Handbook of Materials Failure Analysis

With Case Studies from the Aerospace and Automotive Industries

Edited by
Abdel Salam Hamdy Makhlouf
Mahmood Aliofkhazraei

Handbook of Materials Failure Analysis With Case Studies from the Aerospace and Automotive Industries

Handbook of Materials Failure Analysis With Case Studies from the Aerospace and Automotive Industries

Edited by

Abdel Salam Hamdy Makhlouf

Mahmood Aliofkhazraei

AMSTERDAM • BOSTON • HEIDELBERG • LONDON
NEW YORK • OXFORD • PARIS • SAN DIEGO
SAN FRANCISCO • SINGAPORE • SYDNEY • TOKYO

ELSEVIER

Butterworth-Heinemann is an imprint of Elsevier

Butterworth Heinemann is an imprint of Elsevier
The Boulevard, Langford Lane, Kidlington, Oxford OX5 1GB, UK
225 Wyman Street, Waltham, MA 02451, USA

Notices

Knowledge and best practice in this field are constantly changing. As new research and experience broaden our understanding, changes in research methods, professional practices, or medical treatment may become necessary.

Practitioners and researchers must always rely on their own experience and knowledge in evaluating and using any information, methods, compounds, or experiments described herein. In using such information or methods they should be mindful of their own safety and the safety of others, including parties for whom they have a professional responsibility.

To the fullest extent of the law, neither the Publisher nor the authors, contributors, or editors, assume any liability for any injury and/or damage to persons or property as a matter of products liability, negligence or otherwise, or from any use or operation of any methods, products, instructions, or ideas contained in the material herein.

British Library Cataloguing in Publication Data
A catalogue record for this book is available from the British Library

Library of Congress Cataloging-in-Publication Data
A catalog record for this book is available from the Library of Congress

ISBN: 978-0-12-800950-5

Contributors

Laura Allegrucci
Chemistry Department, Italian Air Force—Flight Test Centre, Pratica di Mare AFB, Pomezia, Rome, Italy

Mikael Amura
Chemistry Department, Italian Air Force—Flight Test Centre, Pratica di Mare AFB, Pomezia, Rome, Italy

Iñaki Armendáriz
Materials and Structures Department, Instituto Nacional de Técnica Aeroespacial (INTA), Torrejón de Ardoz, Madrid Spain

Mohammad Azadi
Fatigue and Wear in Materials (FWM) Workgroup, Irankhodro Powertrain Company (IPCO), Tehran, Iran

Fiona Belben
AWL Materials Technology Laboratory, AgustaWestland Ltd., Yeovil, Somerset, United Kingdom

Manuele Bernabei
Chemistry Department, Italian Air Force—Flight Test Centre, Pratica di Mare AFB, Pomezia, Rome, Italy

Swati Biswas
Gas Turbine Research Establishment, Bengaluru, India

Victor K. Champagne
US Army Research Laboratory, Aberdeen Proving Ground, Adelphi, Maryland, USA

Seyid F. Diltemiz
Turkish Air Force, 1st Air Supply and Maintenance Center Command, Eskişehir, Turkey

Mirko Dinulovic
University of Belgrade, Faculty of Mechanical Engineering, Kraljice Marije 16, Belgrade, Serbia

Kay Ellinghaus
Tenneco GmbH, Edenkoben, Germany

José M. Encinas
Materials and Structures Department, National Institute of Aerospace Techniques (INTA), Torrejón de Ardoz, Madrid, Spain

Ahmed Z. Farahat
Central Metallurgical Research and Development Institute, CMRDI, Helwan, Cairo, Egypt

Mudigere D. Ganeshachar
Gas Turbine Research Establishment, Bengaluru, India

Juan García-Martínez
Materials and Structures Department, Instituto Nacional de Técnica Aeroespacial (INTA), Torrejón de Ardoz, Madrid Spain

Thomas Goehring
Tenneco Inc., Grass Lake, Jackson, Michigan, USA

Roberto González
Materials and Structures Department, Instituto Nacional de Técnica Aeroespacial (INTA), Torrejón de Ardoz, Madrid Spain

Selim Gürgen
Department of Mechanical Engineering, Eskişehir Osmangazi University, Eskişehir, Turkey

Víctor H. Jacobo
Department of Materials Science and Manufacturing, DIMEI Universidad Nacional Autónoma de México Avenida Universidad, Coyoacán, México D.F. Mexico

Adam Kotrba
Tenneco Inc., Grass Lake, Jackson, Michigan, USA

Branimir Krstic
University of Defence in Belgrade, Military Academy, Generala Pavla Jurisica Sturma 33, Belgrade, Serbia

Melih C. Kuşhan
Department of Mechanical Engineering, Eskişehir Osmangazi University, Eskişehir, Turkey

Jivan Kumar
Gas Turbine Research Establishment, Bengaluru, India

Victoria L. Long
National Aeronautics and Space Administration (NASA), Kennedy Space Center, Florida, USA

Limin Luo
Tenneco Inc., Grass Lake, Jackson, Michigan, USA

Abdel S.H. Makhlouf
Manufacturing and Industrial Engineering Department, College of Engineering and Computer Science, University of Texas Rio Grande Valley

Steven J. McDanels
National Aeronautics and Space Administration (NASA), Kennedy Space Center, Florida, USA

Javier S. Millán
Materials and Structures Department, Instituto Nacional de Técnica Aeroespacial (INTA), Torrejón de Ardoz, Madrid Spain

Melany Mioduszewski
Tenneco Inc., Grass Lake, Jackson, Michigan, USA

Teresa L.M. Morgado
Engineering Departmental Unit of Tomar Polytechnic Institute, Escola Superior de Tecnologia de Abrantes do Instituto Politécnico de Tomar, Abrantes, Portugal, and ICEMS-IST-UL—Institute of Materials and Surfaces Science and Engineering, Lisbon University, Lisboa, Portugal

Sangli N. Narendra Babu
Gas Turbine Research Establishment, Bengaluru, India

José Olarrea
E.T.S.I. Aeronáuticos, Universidad Politécnica de Madrid (UPM), Madrid, Spain

Armando Ortiz
Department of Materials Science and Manufacturing, DIMEI Universidad Nacional Autónoma de México Avenida Universidad, Coyoacán, México D.F. Mexico

Edgar A. Ossa
Material Engineering Research Group, School of Engineering, Universidad Eafit, Medellín, Colombia

Marco Paniagua
Material Engineering Research Group, School of Engineering, Universidad Eafit, Medellín, Colombia

Marc S. Pepi
US Army Research Laboratory, Aberdeen Proving Ground, Adelphi, Maryland, USA

Markus Pieszkalla
Tenneco GmbH, Edenkoben, Germany

Igor Radisavljevic
Military Technical Institute, Ratka Resanovica 1, Belgrade, Serbia

Zoran Rajic
Military Technical Institute, Ratka Resanovica 1, Belgrade, Serbia

Edgar I. Ramírez
Department of Materials Science and Manufacturing, DIMEI Universidad Nacional Autónoma de México Avenida Universidad, Coyoacán, México D.F. Mexico

Bosko Rasuo
University of Belgrade, Faculty of Mechanical Engineering, Kraljice Marije 16, Belgrade, Serbia

Marek Rybarz
Tenneco Automotive Polska sp. z o.o. Rybnik, Poland

Varada N. Satish Kumar
Gas Turbine Research Establishment, Bengaluru, India

Rafael Schouwenaars
Department of Materials Science and Manufacturing, DIMEI Universidad Nacional Autónoma de México Avenida Universidad, Coyoacán, México D.F. Mexico

Daniel J. Thomas
College of Engineering, Swansea University, Swansea, UK

Dragan Trifkovic
University of Defence in Belgrade, Military Academy, Generala Pavla Jurisica Sturma 33, Belgrade, Serbia

Zhigang Wei
Tenneco Inc., Grass Lake, Jackson, Michigan, USA

William J. Wolfgong
Raytheon Space and Airborne Systems, Component Engineering Department, McKinney, Texas

Maria C. Wright
National Aeronautics and Space Administration (NASA), Kennedy Space Center, Florida, USA

Xiaolei Xu
Key Laboratory of Ship-Machinery Maintenance & Manufacture Ministry of Communication, PRC, and Department of Materials Science, Engineering Dalian Maritime University, Dalian, PR China

Shang-Kuo Yang
Department of Mechanical Engineering, National Chin Yi University of Technology, Taichung, Taiwan

Zhiwei Yu
Key Laboratory of Ship-Machinery Maintenance & Manufacture Ministry of Communication, PRC, and Department of Materials Science, Engineering Dalian Maritime University, Dalian, PR China

Preface

One of the most common applications of failure analysis is in the Aerospace industry. Planes crashes are memorable to the public, due to the resulting loss of lives of many people and the spiritual injuries suffered by survivors. In 2005, a hydroplane exploded during takeoff from Miami Beach, Florida. The plane was carrying fifteen passengers. During this tragedy, due to an explosion, the plane was engulfed in flame and the right wing was damaged prior to collision with the surface of the water. Experiments on the wreck of the plane indicated that the cracks resulting from fatigue in the right wing of the plane were the cause of the accident. Another example was an incident in Railway Transport in 1998. An express train in Germany went off the rails. The train was travelling on the railway between Munich and Hamburg. At 11 AM, around Eschede (situated 35 miles to the north of Hanover), the train went off the rails. According to reports, some of the passengers had heard a knocking sound. Investigations clarified that the knocking sound was created due to the fracture of one of the wheels, prior to the reversal of the train. Failure analysis is not limited to plane crashes and trains reversals. Failure analysis is the key to failure prevention. Material engineers play the most important role in the investigation of failure analysis and methods of prevention. Therefore, studying materials science and engineering is the door to effective failure analysis and materials protection.

This handbook provides a thorough understanding of the reasons materials fail in certain situations, covering important scenarios, including material defects, mechanical failure as a result of improper design, corrosion, surface fracture, and other environmental causes. The handbook begins with a general overview of materials failure analysis and its importance, and then logically proceeds from a discussion of the failure analysis process, types of failure analysis, and specific tools and techniques, to chapters on analysis of materials failure from various causes.

This handbook contains many real-world failure cases and case studies covering a wide spectrum of materials failure in NASA, aerospace, army, marine, and automotive applications. The editors thank all the contributors for their excellent chapter contributions to this handbook, and for their hard work and patience during the preparation and production of the book. We sincerely hope that the publication of this handbook will help people from Industry and Academia to get the maximum benefits from the experience contained in the published chapters.

Summer 2015
Abdel Salam Hamdy Makhlouf
Mahmood Aliofkhazraei

CHAPTER

1 Strategies for static failure analysis on aerospace structures

Javier S. Millán, Iñaki Armendáriz, Juan García-Martínez, Roberto González
Materials and Structures Department, Instituto Nacional de Técnica Aeroespacial (INTA), Torrejón de Ardoz, Madrid Spain

CHAPTER OUTLINE

Handbook of Materials Failure Analysis With Case Studies from the Aerospace and Automotive Industries.
http://dx.doi.org/10.1016/B978-0-12-800950-5.00001-6

1 INTRODUCTION

Failure analysis comprises the prediction of damage onset on a structure when subjected to loads and environmental conditions. Damages may consist in permanent structural deformations (plastic strains for instance); local damages as cracks for instance, or in general any deterioration of the structure, or lack of functionality. It should be noted that damage onset does not mean the final or catastrophic failure of the structure. Failure analysis also comprises the subsequent progressive failure analysis (PFA) that occurs when the structure is loaded in static or fatigue environments.

In PFA, two features are commonly studied. The first is damage progression before it may reach a critical size producing the final failure. The second is the so-called residual strength, the remaining capability of the damaged structure to withstand loads. In the aircraft sector, it is common to refer the concept of damage tolerance, which means that a structure in presence of undetected damages, either produced by manufacturing defects, fatigue, ambient conditions, or accidental, is still able to withstand the loads produced during its service life. The fail-safe concept is employed and is defined as damage that must not lead to failure before it is detectable by means of inspections. Properly understanding of failure causes and PFA, allows the engineer improving and optimizing the structural design, additionally improving structural reliability.

Instituto Nacional de Técnica Aeroespacial (INTA) is currently involved in developing reliable simulation techniques for damaged structures including PFA. The methodologies are based in the finite element model (FEM) technique and have been applied to typical aerospace structures made in metallic or composite materials, monolithic or sandwich, etc. Some examples are shown below:

- Composite structures with interlaminar delaminations: prediction of delamination growth under static loads.
- Debonding analysis: prediction of debonding onset and growth under static loads.
- Crack growth in thin metallic structures (structures with high plasticity).

Besides accuracy, INTA focuses on developing efficient techniques from a computational point of view (reasonable computation and postprocessing time) as well as understanding and correcting the mesh size effects (FE results dependency on mesh size).

2 DELAMINATION GROWTH IN COMPOSITES

The general trend in modern aircraft structures is the progressive replacement of metallic materials with composites. Composites exhibit superior structural properties such as higher stress allowable, better behavior in fatigue and damage tolerance, less sensitivity to corrosion phenomena, etc. Both the new Airbus A350 and Boeing B787 each with over 50% of their structure made up of composites are illustrations of this tendency. The fuel consumption of these aircrafts is reduced around 20%.

One of the typical failure modes of composite materials are interlaminar delaminations, which means a lack of cohesion between adjacent plies in the laminate. Delaminations can be originated by design features prone to develop interlaminar stresses (curved sections, drop-offs, free edges, etc.), manufacturing defects (shrinkage of the matrix during curing, formation of resin-rich areas, etc.), or accidental causes such as tool impacts. Fatigue loading may create fiber-matrix debonding within the material (interfacial failure) or microscale matrix damage, which eventually leads to interlaminar delaminations.

Delaminations degrade material structural properties and reduce its structural load capacity. Moreover, they are prone to grow when compression and/or out of plane loads (static or fatigue) are applied to the structure. An additional inconvenience of internal damages of this type is that they require complicated and expensive inspections in order to be detected.

The lack of knowledge of the composites damage mechanics regarding delamination for instance, joined with the high dependency of analysis results from material parameters difficult to characterize experimentally, which has traditionally led to rather conservative designs. Moreover, Airworthiness certification requirements are generally more restrictive for composites than for metallic materials. Therefore, when developing a new aircraft model, a more extensive test campaign is often required. Currently, aircraft developers use a strain design approach for composites in order to cover impact damage and to avoid delamination growth. For monolithic laminates, this limit is typically 3500-4000 με, while for other applications, such as honeycomb panels, lower limits are quoted.

Substantial research has been carried out recently to find accurate and reliable simulation methodologies for damaged composite structures, in either static or fatigue load environments. Many authors have characterized delamination growth in composites and one of the tools used is the virtual crack closure technique (VCCT) [1] that requires the calculation of the strain energy release rates (SERR) according to the pure modes of fracture. VCCT requires a predamaged structure, and it is able to predict delamination (or debonding) growth.

In the following sections, a methodology developed at INTA based in VCCT theory, with the ability to predict delamination growth under static loads in composite structures is explained in detail. Included are the tools developed for VCCT application, the benchmark used, the correlation between simulation and tests results, as well as research on FEM mesh size effects.

2.1 VCCT FUNDAMENTALS

VCCT was originally published in 1977 [2], belongs to linear elastic fracture mechanics (LEFM), and, as above explained, it is based on the calculation of SERR, where the strain releases is due to the progress of damage in the structure [1,3–10]. In recent years, several articles have been published assessing the implementation of this technique on FEM commercial software [11,12].

The total SERR requires three components to be calculated: mode I (G_{I}) due to interlaminar tension (opening mode), mode II (G_{II}) due to interlaminar sliding shear (in-plane shear), and mode III (G_{III}) due to interlaminar scissoring shear (out of plane shear). In Figure 1.1, a scheme of the required crack tip forces and displacements near crack tip in a 2D FEM is shown. Based on those forces and displacements, SERR components in modes I and II can be calculated, see Equations (1.1)–(1.3):

$$G_{\mathrm{I}} = \frac{\Delta U_{\mathrm{I}}}{\Delta A} = \frac{\left(\frac{1}{2} F'_{Y} \Delta v'\right)}{\Delta A} = \frac{1}{2} \frac{F_{Y'}\left(v'_{\mathrm{upper}} - v'_{\mathrm{lower}}\right)}{\Delta A} \tag{1.1}$$

$$G_{\mathrm{II}} = \frac{\Delta U_{\mathrm{II}}}{\Delta A} = \frac{\left(\frac{1}{2} F'_{X} \Delta u'\right)}{\Delta A} \frac{1}{2} \frac{F_{X'}\left(u'_{\mathrm{upper}} - u'_{\mathrm{lower}}\right)}{\Delta A} \tag{1.2}$$

$$\Delta A = \Delta a \times t \tag{1.3}$$

In Equations (1.1) and (1.2), ΔU_i are the strain energy increments released in mode i (I in Equation 1.1 and II in Equation 1.2) due to the progress of the delamination area in ΔA (1.3), Δa is the mesh size (see Figure 1.1), t the thickness, F_i the forces (along i direction) in the delamination front previous to the delamination growth, and u_i are

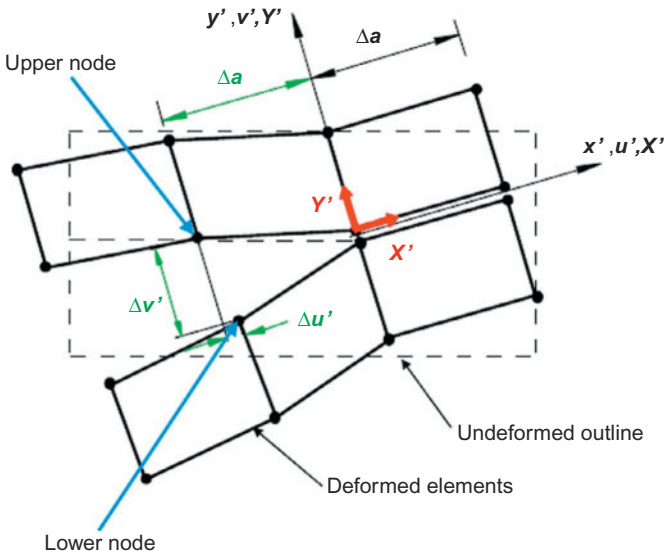

FIGURE 1.1

FEM scheme for VCCT calculations.

the displacements of the delamination front along i direction once the delamination has grown (upper or lower part of the delamination).

When the structural problem shows relevant SERR contributions of the different modes, a mixed-mode failure criterion is required. Usually, the G_{III} contribution to the failure is much lower than the contribution from modes I and II, so a hypothesis can be made in general to eliminate its contribution. One of simplest mixed-mode failure criterion is the linear combination:

$$F = \frac{G_I}{G_{I_C}} + \frac{G_{II}}{G_{II_C}} + \frac{G_{III}}{G_{III_C}} \cong \frac{G_I}{G_{I_C}} + \frac{G_{II}}{G_{II_C}} \quad \text{linear criterion} \tag{1.4}$$

Failure (delamination growth) happens for an applied load such the failure index F equals to 1. G_{I_C} and G_{II_C} are the material interlaminar fracture toughness at modes I and II, respectively. Test methods to derive these critical or allowable values are:

- Mode I: double cantilever beam (DCB) [13].
- Mode II: end notched flexure (ENF), for which a standardized test method is not available yet.
- Mixed mode I and II: mixed-mode bending (MMB) [14].

Besides linear criterion, other mixed-mode delamination growth criteria typically used for composites are shown in Equations (1.5)–(1.7):

$$F = \frac{G_I + G_{II}}{(G_{I_C} - G_{II_C})\mathrm{e}^{\gamma\left(1-\sqrt{1+\frac{G_{II}}{G_I}\sqrt{\frac{E_{11}}{E_{22}}}}\right)} + G_{II_C}} \quad \begin{array}{l}\text{exponential hackle criterion}\\ (\gamma \text{ is a material parameter,}\\ \text{usually between0 and 1)}\end{array} \tag{1.5}$$

$$F = \frac{G_I + G_{II}}{G_{II_C} - (G_{II_C} - G_{I_C})\sqrt{\frac{G_I}{G_{I_C}}}} \quad K \text{ criterion} \tag{1.6}$$

$$F = \sqrt{\left(\frac{G_I}{G_{I_C}}\right)^2 + \left(\frac{G_{II}}{G_{II_C}}\right)^2} \quad \text{quadratic criterion} \tag{1.7}$$

2.2 EXPERIMENTAL BENCHMARK AND FEM SIMULATION

The selected benchmark is a three bonded stringers panel manufactured from Fibredux HTA/6376C, with a single embedded delamination (circular shape, $\Phi = 40$ mm) in one of the bays between fourth and fifth plies. The stiffeners are I shaped, and the panel was tested at QinetiQ at compression static load until final failure [15].

The FEM is prepared using MSC. Nastran, the standard solver in aeronautic industry [16,17]. Composite plate elements (QUAD4) are used for skin and

stiffeners, rigid elements (multipoint constraints or MPC) for the adhesive, and contact elements (GAP) inside the delaminated part. The following FEM boundary conditions reproduce test conditions: clamping at two edges.

A part of the panel FEM is predefined for possible delamination growth. In this section, the skin is divided into two sublaminates: upper and lower, the nodes are linked by MPCs and contact elements. All these FEM features are shown in Figure 1.2. It is assumed that the delamination growth keeps within the initial plane. Additional details of the FE modeling can be found in Refs. [4,7].

To verify the mesh size effect, a typical inconvenience of VCCT simulations, three different FEMs were prepared using different mesh sizes at the delamination area. In Figure 1.3, one of the used FEMs, the FEM 3 with a mesh size of 2.5 mm at the delamination area, is shown.

2.3 FEMs COMPARISON

To check that the three FEMs have similar global behavior, buckling analyses (linear and nonlinear) were made for all them. The FEM buckling loads are also compared with the experimental data available: the delamination buckling load (first buckling

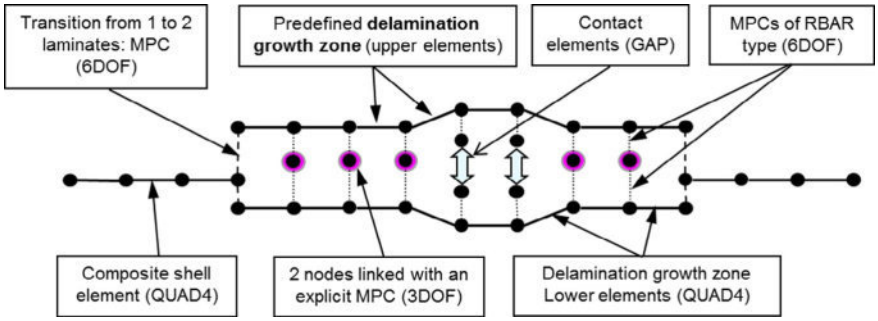

FIGURE 1.2

FEM scheme of delamination growth area.

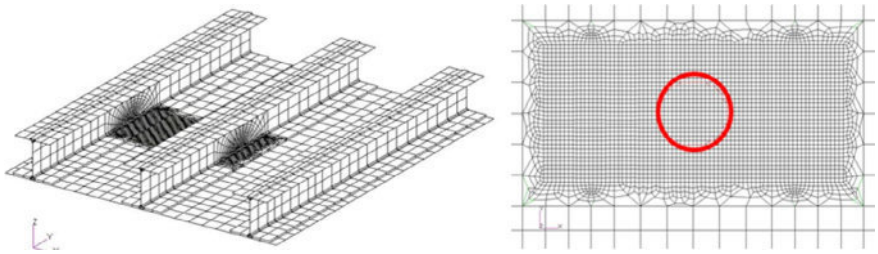

FIGURE 1.3

FEM 3 showing details of the predefined delamination growth zone.

mode) and the skin buckling load (fourth buckling mode). This last buckling mode is local, where the stringers are still able to carry the load, and just the skin in the bay between the stringers is buckled. Details of this comparison can be found in [4,7]. Buckling loads are quite similar among the three FEMs, also correlating well with tests buckling loads.

2.4 DELAMINATION GROWTH TOOL

An in-house delamination growth tool (original code in C++ language) was programmed that uses as inputs the Nastran input file (*.bdf file) and the Nastran results file (*.f06 file, in text format). This tool postprocesses the displacements and force results, calculates SERR components based in VCCT, and it is able to simulate progressive delamination growth. The tool provides different options for delamination growth criteria: linear, power law, K criterion, and hackle exponential, and it is completely automated; once initial FEM is prepared no user intervention is required.

The basis of the tool is the nodal release technique, where the growth of the delamination at a given position is simulated, and the MPC (see Figure 1.2) connecting the two nodes at that position (upper and lower sublaminates) is eliminated. The overall scheme of the tool is carefully explained in [4,7]. Other inputs required by the tool are the G_{I_C} and G_{II_C} values of the composite material.

When the delamination growth tool has finished the calculations, it generates two results files:

- An amplified Nastran results file (*.f06): it collects the FEM results of all load steps (load percentages). Each load step corresponds to a different FEM, because the delamination (shape, size) evolves across the progressive loading.
- A file with the information of "delaminated area versus applied load." This is the main result of the tool that can be used to correlate simulation and test results.

2.5 CORRELATION BETWEEN FEM SIMULATIONS AND TESTS

Figure 1.4 shows the curve "delaminated area (mm^2) versus applied load ($\mu\varepsilon$)" obtained with the delamination growth tool using the most detailed panel FEM (FEM 3) along with the linear failure criterion. Four different load steps (enforced displacement increments) were used for the FEM simulations: 0.1, 0.125, 0.15, and 0.2 mm. Also the experimental curve (green color) is shown for comparison.

The tests performed by QinetiQ were static in compression, until final failure. The damage evolution was monitored during the tests by means of ultrasonic nondestructive inspections (NDI). More information about the performed tests can be found in Ref. [15].

As expected, the increase of the delamination area starts when the panel buckles. The growth velocity (the slope in the figures) is adequate and similar to the experimental curve, although slightly dependent of the load step used. However, the

simulation can be considered a good approach to the tests results. The load-step dependency is studied in next section.

Also a comparison of the delamination shape across the loading process is performed. In Figure 1.5, photos of the delaminated area found by QinetiQ (NDI) are shown. The photos were taken without removing the panel from the test frame [15] and correspond to applied compression loads of 3692 με (Test 1), 4379 με (Test 2), 4862 με (Test 3), and 5255 με (Test 4). In the same figure, the delamination shapes found by the delamination growth tool, using 0.125 mm as load step, and at the same load values, are shown as well.

As it can be seen both experimental and simulation shapes are coherent, and the slight asymmetry of the delamination (see pictures after tests 3 and 4) is captured well in the simulations.

2.6 MESH SIZE EFFECTS

Delamination growth analysis was performed with the three panel FEMs, considering the linear failure criterion, and using different load steps for the Nastran runs. An almost linear dependency was found between the FEM mesh size at the delamination growth area and the optimum load step (the load step that makes simulation results the closest to test results). In Refs. [4,7], additional details of this research are provided. The results of the three optimized FEMs (each one using its optimum load step) agreed very well with the experimental data, as shown in Figure 1.6.

2.7 COMPARISON OF MIXED-MODE FAILURE CRITERIA

A comparison was performed on the different failure criteria implemented in the delamination growth tool: the linear criterion (2), exponential hackle (3), *K* criterion (4), and quadratic criterion (5). It was shown [4,7] that the solution given by the linear and exponential hackle failure criteria were almost identical (that was predictable since both criteria are similar), and provided the best fit with experimental data. The worst solution was given by the quadratic failure criterion.

All criteria predicted quite similar values for the growth initiation load (load at which delamination starts to grows) and for the initial slope of the curve "delamination area versus applied load."

2.8 CONCLUSION AND FURTHER WORK IN DELAMINATION GROWTH ANALYSIS

INTA has researched in the development of FEM simulation methodologies for progressive delamination growth in composites when subjected to static loads. INTA has prepared a tool that uses as inputs the Nastran input (*.bdf) and results (*.f06)

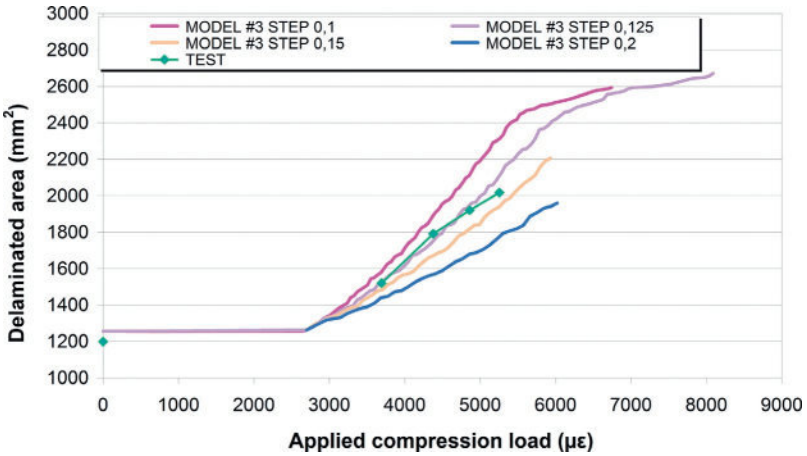

FIGURE 1.4

Comparison between test results and FEM simulation (linear criterion) considering four different load steps.

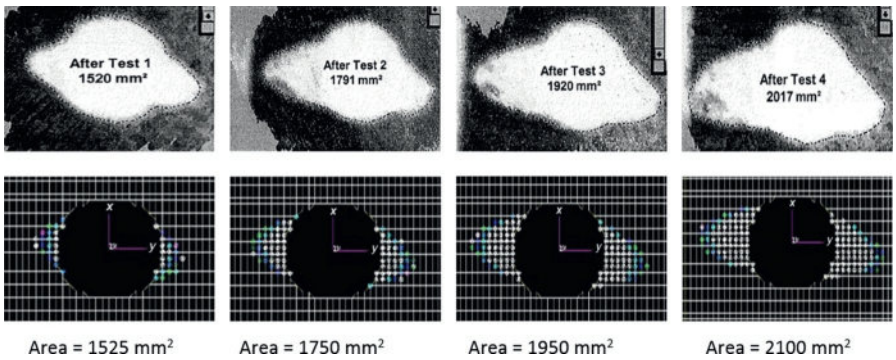

FIGURE 1.5

Delamination evolution found by NDI (above, © QinetiQ Ltd.) and by INTA delamination growth tool (below).

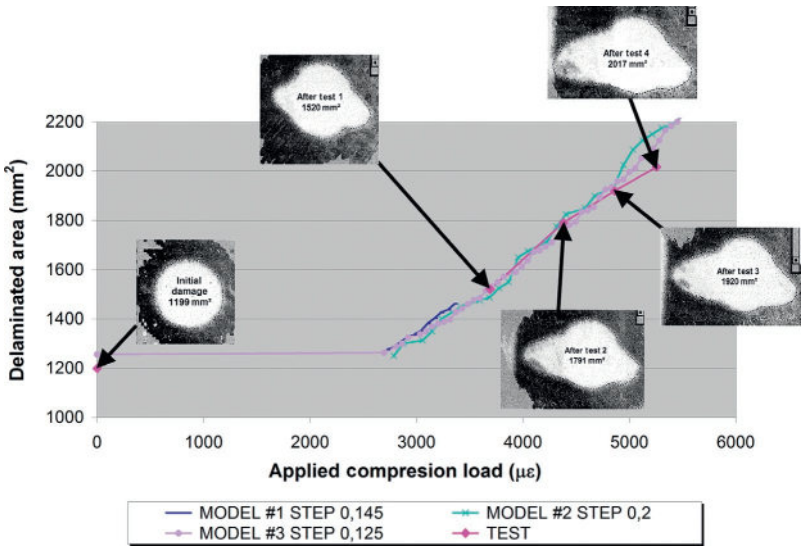

FIGURE 1.6

Comparison of optimized FEMs and experimental curves (delamination photos © QinetiQ Ltd.).

files. The tool is based in VCCT, is automatic, and provides different options for delamination growth criteria.

For validation of the methodology and the tool, the benchmark used is a composite stiffened panel with an initial delamination at one of the bays. A correlation of the evolution of the delamination area with the applied load (between tests and simulations) has been made. Simulation results showed to be consistent with tests, providing an adequate capture of the load that initiates delamination growth, and a similar shape of the delamination across the loading process.

Some studies have been made about mesh size effects, and a dependency almost linear between the FEM mesh size and the optimum load step to be used in the analysis has been found. Different failure criteria have been used for delamination growth, being the best solution given by the linear and exponential hackle failure criteria.

In the future, other experimental benchmarks will need to be evaluated to further validate the methodology shown in this study. Furthermore, other topics will be investigated and taken into account in the simulation including but not limited to: allowing delamination migration, accounting for other types of failure in the composite material (intralaminar cracks for instance), and adaptation of the methodology to impact damage problems.

3 DEBONDING ONSET AND GROWTH

Bonded joints are often used in aircraft structures, particularly in composites. Examples are stiffened panels (joint skin-stiffener), or joints such as skin-ribs, and skin-spar. Bonded joints are quite complicated to analyze even for a simple strength prediction, because the stress distribution at the joints is rather complex and shows high stress concentrations at its ends. PFA in bonded joints is particularly complex to simulate by FEM.

INTA is currently involved in finding robust and reliable FEM simulation methodologies for bonded structures. Up to now, the work done is for DCB coupons (mode I). Two types of adhesives (adhesive film and paste) have been selected for this study, both widely used in aircraft designs and repairs.

INTA has performed detailed FEM simulations of DCB coupons based in cohesive zone (CZ) methodology, a damage mechanics theory accounting for irreversible damage at interfaces, which is well suited to model PFA of delaminations and bonded joints [18–24].

In order to validate CZ FEM results, DCB tests have been carried out at INTA. A detailed correlation simulations—tests is shown in the next sections. The results seem very promising and the correlation achieved is quite accurate. Our next goal is to further develop the methodology for analyzing more complicated structures, and also dealing with mixed-mode problems, for which no established methodology is available.

3.1 DCB COUPON: MODE I INTERLAMINAR FRACTURE TOUGHNESS TEST

DCB coupons are one of the most used experimental tests to characterize fracture toughness of composites or adhesives in mode I (tension mode): G_{I_C}. In Figure 1.7, a scheme of a typical DCB test coupon is shown. It is composed of two identical sublaminates, with an initial debond of length a_0, and subjected to two transverse symmetrical forces F.

The standard employed for the tests is generally ASTM 5528 [13], which was written originally to characterize fracture toughness of resins for composite laminates, and can be used to characterize adhesive fracture toughness G_{I_C}.

Progressive debonding growth takes place in the coupon mid-plane, and during tests the curve "applied force F-opening displacement δ" is recorded. Sometimes, the physical crack length a is also monitored by optical methods. In [13], several data reduction methods approaches are recommended for calculating G_{I_C}: the modified beam theory (MBT), the compliance calibration method (CC), and the modified compliance calibration (MCC) method.

3.2 FE MODELING

The DCB coupons tested at INTA are manufactured with AS fiber and 8552 epoxy resin (pre-preg method), where the initial debond a_0 is 51 mm, and the adhesive is paste Epibond 1590 typically used in repairs. The average adhesive thickness is 0.2 mm. Additional details about dimensions, materials, manufacturing, and laminates lay-ups can be found in [24].

Coupon FEM is prepared by using classical software tools in the aeronautic industry such as Patran [25] for FEM generation and postprocessing, Mentat to model adhesive CZ elements, and finally Marc [26,27] as the FE solver.

In Figure 1.8, the general views of the FEMs can be seen. Unidirectional and fabric plies are modeled by means of solid elements. Adhesive (green color in Figure 1.8) is represented by CZ elements (type 188 in Marc) working in mode I or tension mode. Loads are applied by using MPCs at the left edge of the FEM, as shown in Figure 1.8.

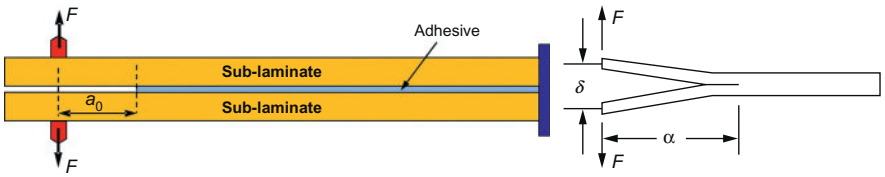

FIGURE 1.7

Scheme of a DCB test.

3.3 CZ FUNDAMENTALS

The basic idea of CZ dates from early 1960s [28], when Dugdale and others introduced models avoiding the unrealistic infinite stresses at crack tip characteristic of the Stress Intensity Factors (SIF) approach.

In FEMs, CZ elements can be considered as interface elements, the traction vector t includes one normal component in tension (mode I), and two tangential (modes II and III), and its mechanical behavior follows a phenomenological separation law of $t = f(\nu)$, ν being he vector of nodal separations (three components as the traction vector) in the CZ element. The typical separation laws are bilinear (used for fragile materials), exponential, and combined linear-exponential (see Figure 1.9), with most of these approaches available in FEM solvers (i.e., Marc, ANSYS, ABAQUS, etc.). The area enveloped by the curve corresponds to the material fracture toughness G_C.

The cohesive law considers a high nonlinear behavior; the first part is linear and reversible, but when separation in the element ν exceeds the critical value ν_c (maximum separation within the elastic regime) the element becomes partially damaged and the behavior is irreversible. If the deformation in the element is high enough ($\nu = \nu_m$) the FEM solver deactivates the element, eliminating its contribution to transmit forces (its stresses are null). By doing so, the debonding onset and the progressive debonding growth are simulated.

The three approaches shown above were tested with the solver Marc, and the exponential approach was finally selected because while it is more adequate to model ductile materials (as it is case of resins or adhesives), the FEM convergence is better.

A typical inconvenience of CZ FEMs is accounting for mixed-mode analysis [29–31], problems for which the CZ element support simultaneously forces and separations in modes I, II, and III. This is not our case; adhesive in a DCB coupon works only in mode I: t is the transverse force (peeling) transmitted by the element, ν the relative transversal separation of CZ element, and G_C value is G_{I_c}.

3.4 MESH DEPENDENCY

It is known that CZ FEMs are mesh dependent, or in other words, CZ FEM results depend on the mesh size (size of the elements in the relevant direction that represent the adhesive in the FEM).

Several researchers have worked in the issue [23,24]. One approach is to adapt adhesive allowables (in this case, the maximum peeling stress) function of the mesh size. The theory is based on Dugdale model for stress state around a crack tip in an elastic-plastic material [28], calculating l_{CZ} the cohesive zone length, where the adhesive length irreversibly damaged when debonding growth is about to start. The issue is that l_{CZ} is rather a small distance, so if the CZ FEM intends to be accurate, its mesh size should be much lower than l_{CZ}. In such a case, the peeling stress distribution and the l_{CZ} itself can be correctly predicted by the FEM.

In our case, a detailed DCB FEM was produced using a mesh size of only 62.5 μm (see Figure 1.10). As it can be seen in the Figure 1.10 the cohesive zone length l_{CZ} is

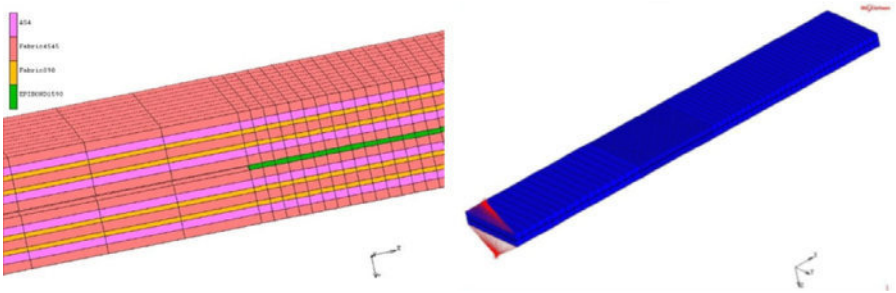

FIGURE 1.8

General view of DCB FEM (Marc).

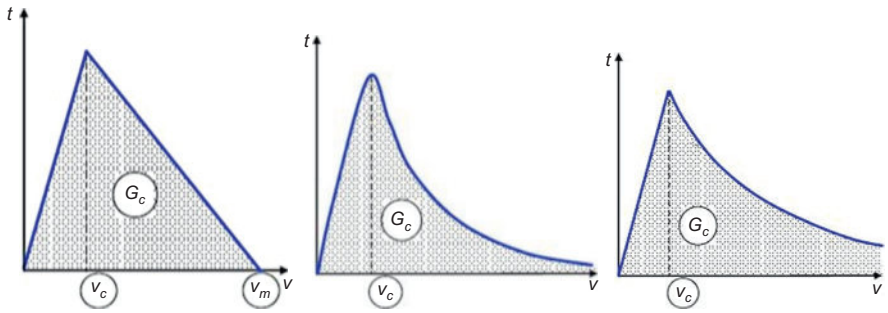

FIGURE 1.9

Options to represent CZ elements mechanical behavior.

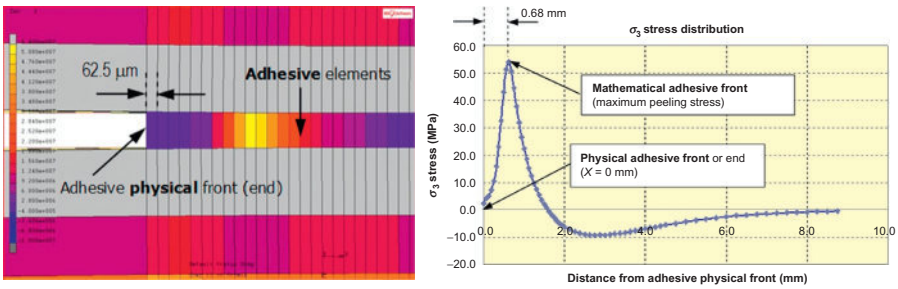

FIGURE 1.10

σ_3 stress (peeling) plot in the adhesive (detailed DCB FEM).

approximately 0.68 mm. The analysis (nonlinear) has been made applying a load to barely reach the first CZ adhesive element showing the maximum deformation capability ν_m, so the element transmits almost no stress; even the element has not been deactivated yet. This is the debonding onset.

This type of detailed FEMs is not practical for progressive debonding simulation of complex structures because of its large size and the difficulties of convergence.

When using a FEM with coarser mesh, l_{CZ} is not accurately predicted by the FEM, nor is, the peeling stress distribution. However, it can be demonstrated that if the allowable peeling stress of the CZ elements σ_0 is adapted function of the mesh size l_e (in this case, the element length along X axis) and N_e the number of adhesive elements in l_{CZ} (general recommendation is $3 < N_e < 5$), the FEM will give accurate results. In (1.8), the equation for the adapted allowable peeling stress of CZ elements is shown, mode details can be found in Ref. [24].

$$\sigma_0^* = \sqrt{\frac{ME_{33}G_{I_C}}{N_e l_e}} \tag{1.8}$$

3.5 EXPERIMENTAL RESULTS

In Figure 1.11, pictures of the mode I DCB tests carried out at INTA are shown. As there is no resultant force in the coupon, there is no need to clamp it at the opposite side of the load application end.

In Figure 1.12, the experimental curves load applied $F(N)$ versus opening displacement δ (mm), are given for the five coupons tested, P1 to P5. As it can be seen, except the coupon P2 that behaves relatively different, there are very slight differences and the mechanical behavior is relatively repeatable for the most important curve characteristics: initial slope, maximum load, and negative curve slope beyond

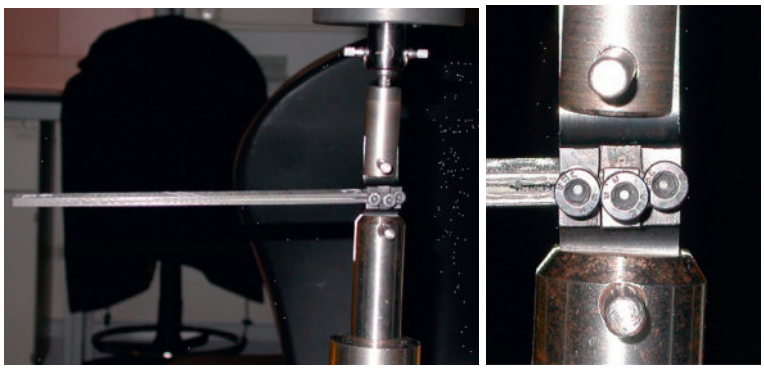

FIGURE 1.11

Experimental tests on DCB coupons.

maximum load. The P2's different behavior is attributed to an inadequate quality control of bonding process.

From these curves, by using MBT and CC methods [13], the adhesive mode I interlaminar fracture toughness G_{I_C} was obtained: 211.7 J/m^2.

3.6 CORRELATION FEM SIMULATION—TESTS

As mentioned above the detailed FEM (mesh size 62.5 μm) was produced only for calibration purposes but not for analysis of the DCB coupon progressive debonding. For this latter purpose, four different FEMs with coarse meshes were prepared. The chosen mesh sizes or element length l_e along X axis (longitudinal coupon axis) in the debonding growth zone are l_e equal to 2, 1, 0.5, and 0.25 mm. Complete details about the four DCB coupon FEMs can be found in Ref. [24]. In Figures 1.13 and 1.14, the FEMs of mesh sizes 2 and 0.25 mm are shown.

As mentioned above, the solver used is Marc, the analyses are of static nonlinear type, and the results requested are stresses in the adhesive elements and node displacements. The value for the adhesive fracture toughness in mode I is $G_{I_C} = 211.7$ J/m^2 as explained above, and the maximum transverse peeling stress σ_0 considered for the analysis is 54 MPa (value derived from manufacturer test data).

In Figure 1.15, the three curves "applied force versus opening displacement" predicted with the DCB FEMs (mesh sizes l_e equal to 0.25, 0.5, and 1 mm) are presented. As shown, the predicted maximum value of the applied force increases with mesh size. This behavior has been reported by other authors and was expected.

Therefore, another set of analyses was carried out adapting the allowable peeling stress of the adhesive CZ elements function of the mesh size l_e and the number of CZ elements in the cohesive zone length N_e, as indicated in Equation (1.8). In Figure 1.16, this adapted peeling stress σ_0^* is shown function of l_e, for two N_e values: 3 and 5. In Figure 1.17, a comparison between the experimental and CZ FEM simulation "load applied versus opening displacement" curves is given. The FEM curves are obtained with the four different FEMs above explained and $N_e = 5$.

All experimental and test curves are quite similar and the correlation is accurate in terms of initial slope of the curve, maximum load, and negative slope of the curve beyond maximum load. It can be concluded that the CZ FEM methodology used is adequate, and that relatively coarse FEMs (for instance, the one with mesh size of 2 mm) can be used to model progressive coupon debonding with high accuracy. Besides accuracy, the proposed CZ methodology overcomes the problem of mesh size dependence.

Other results, not directly comparable with experiments, have been derived from CZ FEMs to verify its robust and coherent behavior such as peeling stress σ_3 distribution in the adhesive and crack length a [24]. Peeling stresses are different for each FEM as expected, but consistent with the adapted allowable value σ_0^* defined at each FEM function of mesh size l_e. On the other hand, the four FEMs predict the same curve "crack length (a) versus applied force," so again mesh size effects are confirmed to be correctly handled and compensated.

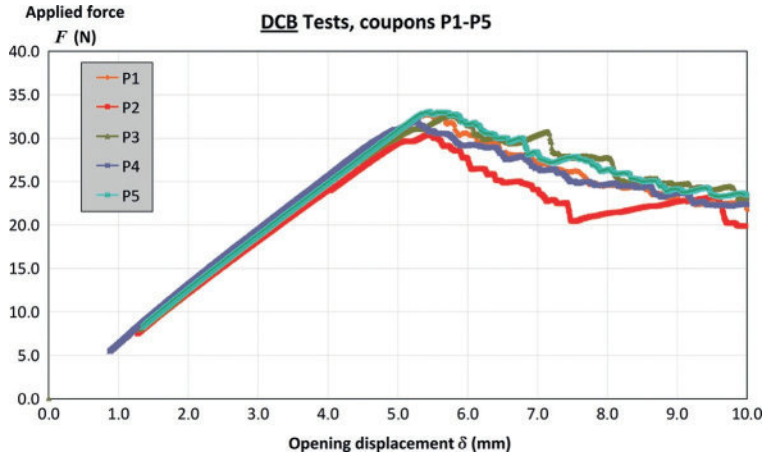

FIGURE 1.12

Experimental DCB curves: applied force F versus opening displacement δ.

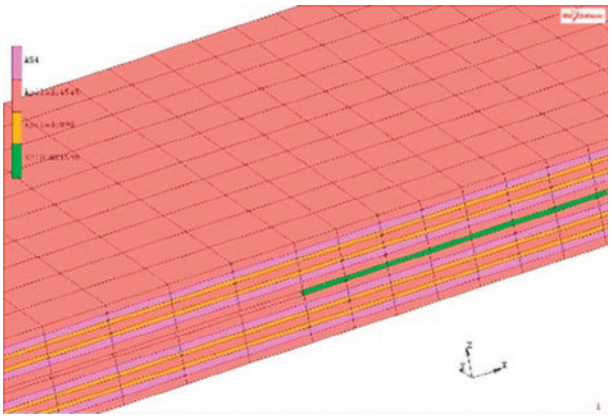

FIGURE 1.13

FEM of mesh size $l_e = 2$ mm (7480 elements).

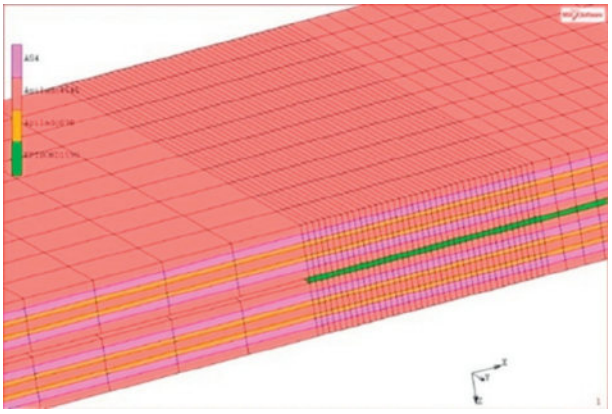

FIGURE 1.14

FEM of mesh size $l_e = 0.25$ mm (12880 elements).

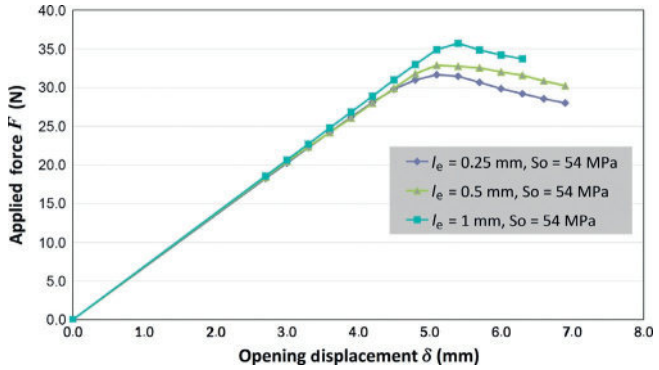

FIGURE 1.15

Curves applied force versus opening displacement found by the nonadapted FEM.

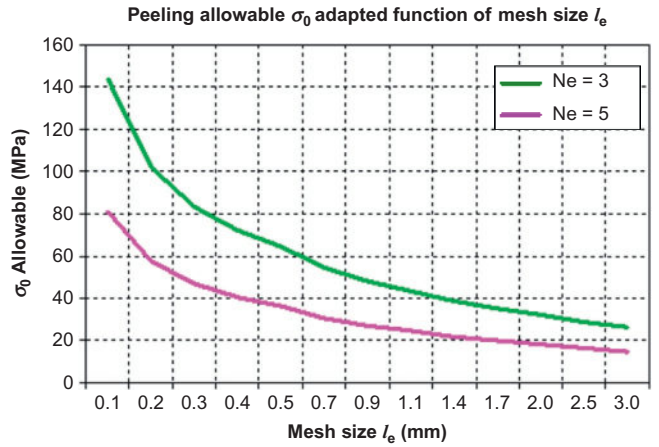

FIGURE 1.16

σ_0 adaptation function of FEM mesh size.

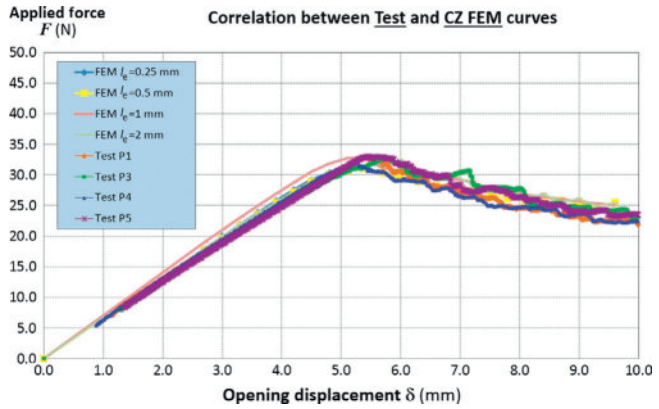

FIGURE 1.17

Correlation between FEM and test "applied force δ opening displacement" curves.

3.7 CONCLUSION AND FUTURE WORK IN DEBONDING ANALYSIS

INTA has researched the development of simulation methodologies for progressive debonding by means of CZ FEMs. The methodology is able to analyze bonded structures working in mode I (tension mode), and has been applied to DCB coupons that have been manufactured and tested at INTA.

A set of FEMs, each using a different mesh size, were prepared with Patran and Mentat (to model adhesive CZ elements). In each FEM, the adhesive allowable peeling stress was modified or adapted as function of its mesh size. Marc was used as FEM solver.

It was found that all FEMs yielded the same results, showing that mesh size dependency, a typical inconvenience of CZ FEMs can be solved. The correlation between FE simulation and test results was found to be accurate. All the relevant parameters of "applied load-opening displacement" curves (initial curve slope, maximum load, and negative curve slope beyond maximum load) were found to be very similar in CZ FEM simulations compared to the experimental values.

In the future, INTA plans to extend the methodology to analyze problems in mode II (ENF coupons for instance) and mixed-mode problems, for which there is currently no established methodology. Moreover, in the future the methodology will be applied to analyze the progressive failure of complicated bonded structures than simple coupons.

4 CRACK GROWTH IN METALLIC STRUCTURES

LEFM methods have been used for calculating the residual strength of cracked metallic aircraft structures, such as the classical SIF approach. Strictly speaking, LEFM is valid for materials failing in a brittle manner [32] or at least for structures that when failing are still mostly in the elastic regime of the material. Most of the metallic alloys used in aircraft structures have considerable ductility, and as the progressive optimization of the structures makes them become increasingly lighter, the stress state in the structure is increasingly within plasticity regime.

Therefore, LEFM was corrected with plasticity factors that still gave valid results while the plasticity in the structure was relatively reduced. Nowadays, typical structures such as stiffened panels in wings or fuselages are very thin, and therefore LEFM gives poor results, sometimes conservative but others, not. To solve this, some elastic-plastic fracture criteria have been developed: J integral, CTOD, CTOA, etc. The criterion known as CTOA (crack tip opening angle) has been used among others by NASA, Boeing, and Lockheed Martin [4,33–39].

In the accompanying sections, the following information will be discussed; a methodology developed at INTA based in CTOA theory, where the ability to simulate progressive crack growth in metallic structures subjected to static loads is explained in detail (crack onset cannot be simulated with this theory), a tool developed for CTOA application, the benchmarks used for validation, and a correlation between simulation and test results. The research is carried out not only for developing a simulation methodology, but also for improving crack growth test methods based in CTOA criterion, which is still an issue under research [40,41].

4.1 CTOA CRITERION—EXPERIMENTAL OBTAINING OF $CTOA_C$

CTOA criterion is based on the hypothesis that for a cracked metallic structure subjected to static loads, stable crack growth occurs at a constant CTOA. That value, known as the critical $CTOA_C$, can be determined by optical microscopy or digital image correlation. Tests performed with different metallic alloys demonstrated that $CTOA_C$ is constant, being a function only of the material (including its thermal condition) and the thickness [33]. This being the main advantage of the criterion, $CTOA_C$ is not dependent on the geometry of the structure analyzed.

In Figure 1.18 it is shown the scheme of a Compact Tension (CT) specimen with an initial crack induced by fatigue. In Figure 1.19 and Figure 1.20, CTOA Tests performed at INTA (Aluminum 2024-T3 CT samples) are shown. A high resolution optical camera was used for $CTOA_C$ determination. (Figures 1.20–1.23).

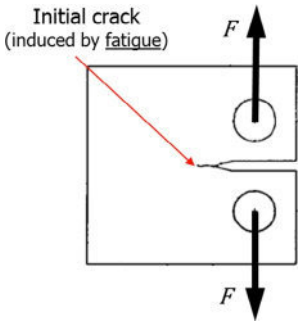

FIGURE 1.18

CT specimen.

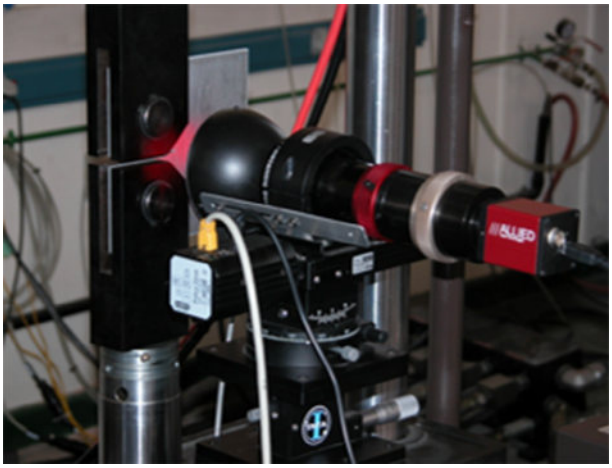

FIGURE 1.19

INTA set-up for CTOA crack growth tests.

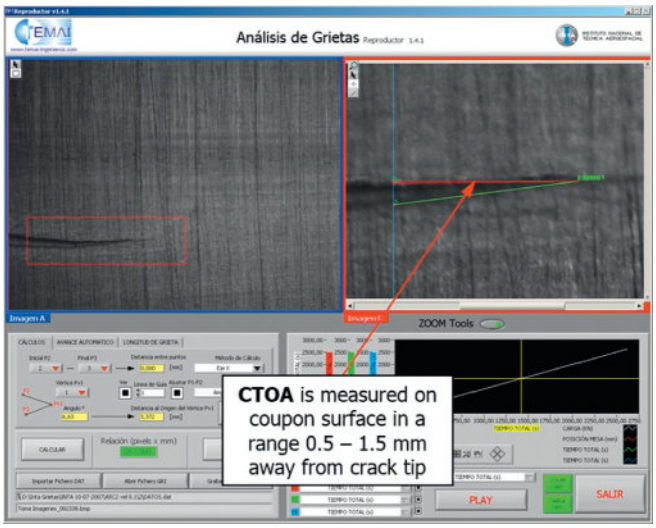

FIGURE 1.20

CTOA identification during tests performed at INTA.

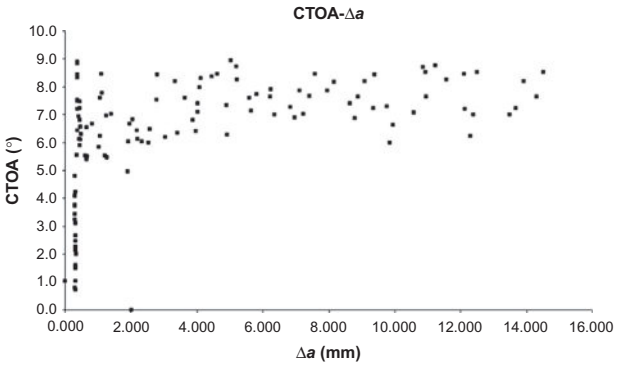

FIGURE 1.21

$CTOA_C$ curve (INTA CT coupon).

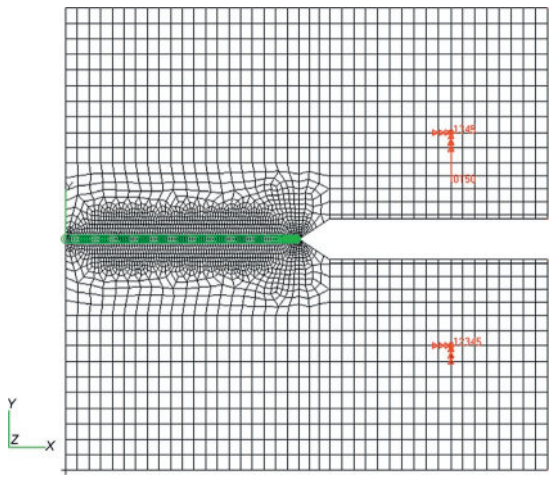

FIGURE 1.22

CT coupon FEM.

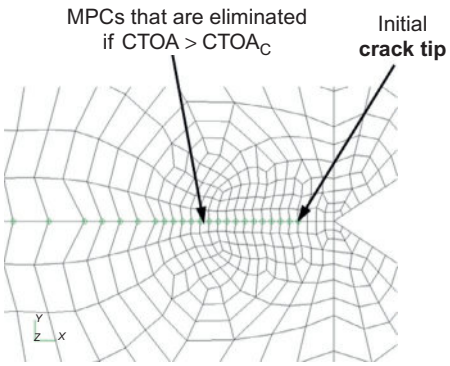

FIGURE 1.23

CT coupon—FEM scheme near crack tip.

4.2 CRACK GROWTH TOOL

The simulation tool developed by INTA has been coded in C++ language and interacts with MSC. Nastran [16,17], the widely used FEM solver in aeronautic industry. To implement CTOA criterion, a predefined crack growth path has to be defined in the FEM in which duplicated nodes (belonging to upper and lower parts of the structure) are joined by MPCs (see Figures 1.22 and 1.23).

The basis of the tool is the nodal release technique. The Nastran run is nonlinear, defining several load steps (percentages of the total applied load). The tool calculates CTOA at the crack tips for each load step. When $CTOA_C$ is reached in the crack tip, the tool modifies the input Nastran file deleting the MPC at the crack tip (simulating this way the crack growth). Then, the tool RESTARTs the Nastran run from that load value. This process is repeated until the crack crosses completely the structure or until maximum load is reached. Therefore, the residual strength curve of the structure analyzed is generated. Additional details are given in Refs. [4,39].

4.3 BENCHMARKS DESCRIPTION

Several benchmarks have been used:

- Coupon level: mode I coupons in aluminum alloy 2024-T3: CT and middle crack tension (M-T). The experimental results have been found from literature [42] and from tests performed at INTA.
- Stiffened panels with different crack configurations and stiffeners shape with experimental results from literature [36]. In the next sections, crack growth simulation results are shown for an integral panel 1 m × 1.9 m, with five Z stiffeners, material aluminum 7475-T7351, and with an initial crack of 150 mm at one of the bays. Details about panel geometry can be found in [36]. The panel has been manufactured and tested by NASA.

4.4 FEM MODELING

Several authors have performed simulations based in CTOA criterion using different structural FEM codes. When using plate elements, some authors define in their FEMs a region around the crack tip in which the plate elements are of plane-strain type [33–36], this is usually called the plain-strain core, while for the rest of the FEM the typical plane-stress elements are used.

The reason for this FEM technique is the triaxial stress state near crack tip induced in a cracked structure subjected to in-plane loads. It is known that in-plane stresses generate not only in-plane deformations, but also transverse deformation according to the material Poisson ratio. The deformation compatibility between the part away from the crack (transmitting in-plane stresses and therefore suffering transverse deformations) and the zone around the crack tip that does not transmit in-plane stresses causes the appearance of transversal stress. The triaxial stress state develops when the structure is thick enough. A criterion widely accepted to estimate the minimum thickness that develops relevant triaxial stress state is given in Refs. [32,43]:

$$t_{min} > 2.5\left(\frac{K_{I_c}}{\sigma_{TY}}\right)^2 \tag{1.9}$$

For aluminum alloys, K_{IC} is about 800 MPa $\sqrt{mm}$ and yield strength σ_{TY} is about 300 MPa [44], which according to the equation above yields $t_{\min} = 18$ mm. This value is much higher than the thicknesses used in the benchmarks analyzed by INTA, so in our studies only plate FEMs of plane-stress type were used.

This assumption was later confirmed experimentally at the coupon tests performed at INTA [39], as the fracture surface failed with a 45° shear lip, and there was considerable yielding prior to fracture, both of which are clear indications of ductile fracture. In opposition, a specimen failing in-plane strain mode, has a flat fracture surface and the plastic zone around crack tip is small (brittle fracture).

The FEMs used are plate elements (QUAD4 mainly) defining a detailed mesh along crack-propagation path. To take into account the plasticity near crack tip, material models used are elastic-plastic according to the Ramberg-Osgood curves [45], and the analyses carried out were nonlinear.

The panel tested at NASA had an initial crack (not centered), therefore FEM models half of the panel (see Figure 1.24) and symmetry conditions are applied only in the *XZ* plane. Additionally, the panels considered a possible crack-propagation bifurcation along two different paths when the crack (initially in the bay) reaches the stiffener, the first crack growth path along the skin and a second one along stiffener web (Figures 1.25 and 1.26).

4.5 CORRELATION SIMULATIONS—TESTS

The simulations were carried out with Nastran (nonlinear analysis) and the above explained in-house crack growth tool. It was found that the results depend slightly on the load applied at each subcase. In general, for higher applied load in each load

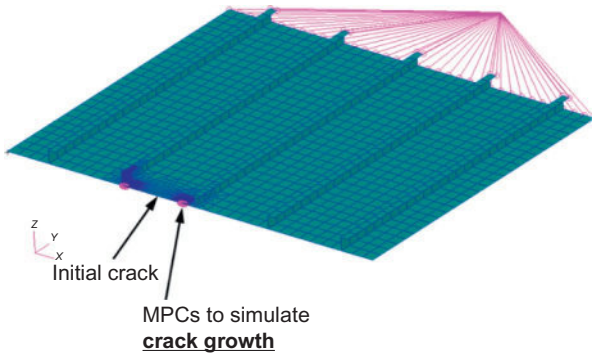

FIGURE 1.24

Stiffened panel FEM.

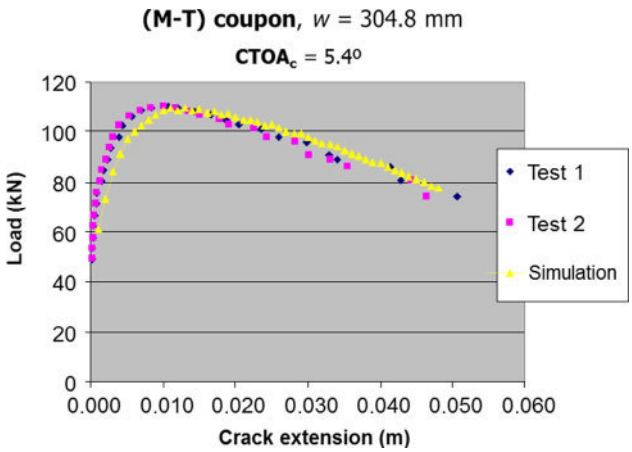

FIGURE 1.25

M-T coupon: comparison of residual strength curves.

step, higher residual strength curves are found. Additionally, it was found, that mesh size slightly influences the FEM results, where the general trend is that when using bigger (coarser) mesh size, the residual strength curve found is higher.

In the figures below, the residual strength curves (load applied versus crack length) found with the crack growth tool are compared with the test curves. The benchmarks that have been selected are M-T coupon in Al 2024-T3, and the NASA panel with five *Z* stiffeners in Al 7475-T351.

As it can be seen, the residual strength curves found by simulation are very similar to the experimental curves, in terms of both the load value that initiates crack growth, and crack growth slope. For the rest of the benchmarks analyzed, the comparison yielded similar results, and therefore it can be concluded that the simulation and tests results are highly correlated.

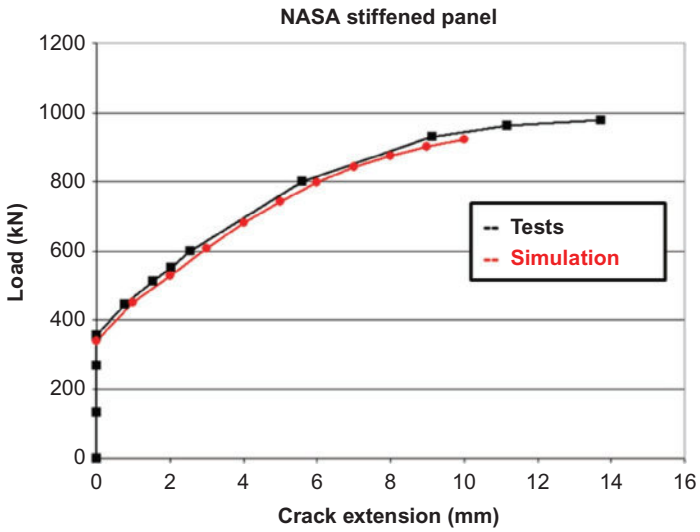

FIGURE 1.26

Stiffened panel: Comparison of residual strength curves.

4.6 CRACK GROWTH IN METALLIC STRUCTURES—CONCLUSION AND FUTURE WORK

INTA has developed a simulation methodology for progressive crack growth in thin metallic structures in which plasticity effects are relevant. In this field, the classical LEFM theories give poor results. A FEM methodology has been developed in which a Nastran FEM interacts with in-house crack growth tool based in CTOA criterion.

Residual strength curves of different coupons and stiffened panels were obtained from the simulations and showed to be consistent with test results.

In the future, INTA plans to verify the methodology in more complex structures, such as aircrafts subcomponents and multiple site damage (MSD) problems, in which various cracks exist and may interact and coalesce.

REFERENCES

[1] Krueger R. Virtual crack closure technique: history, approach, and applications. Appl Mech Rev 2004;57(2):109–43.

[2] Rybicki EF, Kanniken MF. A finite element calculation of stress intensity factors by a modified crack closure integral. Eng Fract Mech 1977;9(4):931–8.

[3] Nilsson KF, Asp LE, Alpman JE, Nystedt L. Delamination buckling and growth for delaminations at different depths in a slender composite panel. Int J Solids Struct 2001;38:3039–71.

[4] San Millán J, Castañón M, Armendáriz I, Gonzalez R, García-Martínez J. Simulation tools for progressive damage, In: NAFEMS World congress, Crete; 2009.

[5] Krueger R, Minguet PJ, O'Brien TK. Implementation of interlaminar fracture mechanics in design: an overview, In: 14th international conference on composite materials (ICCM-14), San Diego; 2003.
[6] Ullah H, Harland AR, Lucas T, Price D, Silberschmidt VV. Finite-element modelling of bending of CFRP laminates: multiple delaminations. Comput Mater Sci 2012;52:147–56.
[7] Armendáriz R González, San Millán J, García-Martínez J. Delamination growth in damage tolerance composite structures. In: 9th international conference on composite science and technology, Sorrento; 2013.
[8] Shokrieh MM, Rajabpour-Shirazi H, Heidari-Rarani M, Haghpanahi M. Simulation of mode I delamination propagation in multidirectional composites with R-curve effects using VCCT method. Comput Mater Sci 2012;65:66–73.
[9] Liu PF, Hou SJ, Chu JK, Hub XY, Zhou CL, Liu YL, et al. Finite element analysis of postbuckling and delamination of composite laminates using virtual crack closure technique. Compos Struct 2011;93:1549–60.
[10] Xie D, Biggers Jr. SB. Progressive crack growth analysis using interface element based on the virtual crack closure technique. Finite Elem Anal Des 2006;42:977–84.
[11] Orifici AC, Krueger R. Benchmark assessment of automated delamination propagation capabilities in finite element codes for static loading. Finite Elem Anal Des 2012;54:28–36.
[12] Leski A. Implementation of the virtual crack closure technique in engineering FE calculations. Finite Elem Anal Des 2007;43:261–8.
[13] ASTM D5528-13, Standard Test Method for Mode I Interlaminar Fracture Toughness of Unidirectional Fiber-Reinforced Polymer Matrix Composites, ASTM International, West Conshohocken, PA, 2013.
[14] ASTM D6671 / D6671M-13, Standard Test Method for Mixed Mode I-Mode II Interlaminar Fracture Toughness of Unidirectional Fiber Reinforced Polymer Matrix Composites, ASTM International, West Conshohocken, PA, 2013.
[15] Greenhalgh E, Meeks C, Clarke A, Thatcher J. The performance of post-buckled CFRP stringer-stiffened panels containing defects and damage. In: 44th AIAA structures, structural dynamics and materials conference, Norfolk; 2003.
[16] MSC Software Corporation. MSC Nastran 2012 Linear Static Analysis—User's Guide; 2012.
[17] MSC Software Corporation. MSC Nastran 2012 quick reference guide; 2012.
[18] Davies GAO, Hitchings D, Ankersen J. Predicting delamination and debonding in modern aerospace composite structures. Compos Sci Technol 2006;66:846–54.
[19] Orifici AC, Herszberg I, Thomson RS. Review of methodologies for composite material modelling incorporating failure. Compos Struct 2008;86:194–210.
[20] Chen J, Crisfield M, Kinloch A, Busso E, Mathews F, Qiu Y. Predicting progressive delamination of composite material specimens via interface elements. Mech Compos Mater Struct 1999;6:301–17.
[21] Segurado J, Llorca J. A new three-dimensional interface finite element to simulate fracture in composites. Int J Solids Struct 2004.
[22] Elices M, Guinea GV, Gómez J, Planas J. The cohesive zone model: advantages, limitations and challenges. Eng Fract Mech 2002;69(2):137–63.
[23] Turon A, Davila CG, Camanho PP, Costa J. An engineering solution for mesh size effects in the simulation of delamination with cohesive zone models. Eng Fract Mech 2007;74:1665–82.
[24] San Millán J, Vázquez L, González R, Matías D, Vergniory U. Progressive failure of composite bonded joints, In: 3rd European conference for aerospace sciences EUCASS; 2009.

[25] MSC Software Corporation. Patran 2012 reference manual—part 3: finite element modelling; 2012.
[26] MSC Software Corporation. Marc 2012 user's guide; 2012.
[27] MSC Software Corporation. Marc 2012 Volume A: theory and user information; 2012.
[28] Dugdale DS. Yielding of steel sheets containing slits. J Mech Phys Solids 1960;8 (2):100–4.
[29] Jansson NE, Larsson R. A damage model for simulation of mixed-mode delamination growth. Compos Struct 2001;53:409–17.
[30] Ruiz G, Pandolfi A, Ortiz M. Three dimensional cohesive modelling of dynamic mixed-mode facture. Int J Numer Methods Eng 2001;52:97–120.
[31] Xie De, Waas Anthony M. Discrete cohesive zone model for mixed-mode fracture using finite element analysis. Eng Fract Mech 2006;73(13):1783–96.
[32] Anderson TL. Fracture mechanics: fundamentals and applications. 3rd ed. Boca Raton, Florida (USA): CRC Press; 2005.
[33] Newman Jr JC, James MA, Zerbst U. A review of the CTOA/CTOD fracture criterion. Eng Fract Mech 2003;70(3–4):371–85.
[34] Seshadri BR, James MA, Johnston Jr WM, Young RD, Newman Jr JC. Recent developments in the analysis of monolithic structures at NASA Langley. In: 6th joint FAA/DoD/NASA conference on aging aircraft, San Francisco; 2002.
[35] Newman Jr JC, Dawicke DS, Seshadri BR. Residual strength analyses of stiffened and un-stiffened panels—part I: laboratory specimens. Eng Fract Mech 2003;70(3–4): 493–507.
[36] Newman Jr JC, Dawicke DS, Seshadri BR. Residual strength analyses of stiffened and unstiffened panels—part II: wide panels. Eng Fract Mech 2003;70(3–4):509–24.
[37] James MA, Newman Jr JC. Three-dimensional analyses of crack-tip-opening angles and d5-resistance curves for 2024-T351 aluminium alloy. ASTM Spl Technical Publ 2002;1406:279–97.
[38] Johnston WM, James MA. A relationship between constraint and the critical crack tip opening angle, NASA Report NASA/CR–2009-215930; 2009.
[39] San Millán J, Valle M, Vázquez Arribas L, González R, García-Martínez J, Salamanca A, et al. Elastic–plastic fracture mechanics in aeronautic metallic structures, In: TCN-CAE-international conference on simulation based engineering and sciences, Venice; 2008.
[40] Sakhalkar A, Frink E, Mahmoud S, Lease K. Crack tip opening angle measurement methods and crack tunnelling in 2024-T351 aluminium alloy. Strain Int J Exp Mech 2011;47(Supplement s1):130–41.
[41] Hashemi SH, Gay R, Howard IC, Andrews RM, Yates JR. Development of a laboratory test technique for direct estimation of crack tip opening angle. In: 15th European conference on fracture; 2004.
[42] Johnston WM. Fracture tests on thin sheet 2024-T3 aluminum alloy for specimens with and without anti-buckling guides, NASA Report NASA/CR-2001-210832; 2001.
[43] ASTM E399-12e3, Standard Test Method for Linear-Elastic Plane-Strain Fracture Toughness KIc of Metallic Materials, ASTM International, West Conshohocken, PA, 2012.
[44] Batelle Memorial Institute. MMPDS-09, Metallic Materials Properties Development and Standardization (MMPDS); 2014.
[45] Ramberg W, Osgood WR. Description of stress–strain curves by three parameters, Technical Note No. 902, National Advisory Committee for Aeronautics; 1943.

CHAPTER

Strategies for dynamic failure analysis on aerospace structures

2

Iñaki Armendáriz*, Javier S. Millán*, José M. Encinas*, José Olarrea†
*Materials and Structures Department, Instituto Nacional de Técnica Aeroespacial (INTA), Torrejón de Ardoz, Madrid, Spain**
E.T.S.I. Aeronáuticos, Universidad Politécnica de Madrid (UPM), Madrid, Spain†

CHAPTER OUTLINE

1 INTRODUCTION

Engineering failure analysis consists of either determining the cause of failure in order to increase reliability or improving and optimizing the performance and design of a given structure. In a dynamic analysis, new parameters are incorporated, mainly

Handbook of Materials Failure Analysis With Case Studies from the Aerospace and Automotive Industries.
http://dx.doi.org/10.1016/B978-0-12-800950-5.00002-8

the inertia forces. If a load is applied sufficiently slowly, the inertia forces can be ignored and the analysis can be simplified as a static one. Any structure can be subjected to dynamic loading; it only needs a load that changes with time quickly in comparison to the structure's natural frequency. Therefore, a dynamic failure analysis consists of determining the cause of a failure when subjected to dynamic loading.

Dynamic loads may involve considerations such as impact, thrust, momentum, vibration, slosh dynamics of fluids, etc. For aircrafts, loading is normally dynamic and is divided into two major categories: limit loads and ultimate loads. Limit loads are often just flight loads of the common flight envelope (maneuvering and gust loads). Ultimate loads are loads that the structure has to withstand a short period of time, for example, crash loads, and certain damages are allowed on the structure. Therefore, maneuvering loads are determined based on the performance limits of the aircraft, and gust loads are determined statistically and they are taken from guidelines or requirements given by the certification authorities. On the contrary, crash loads are bounded by the design objectives; if the structure is not unmanned, it is bounded by the human ability to resist certain level of accelerations. In the case of a turboprop aircraft, a blade loss cannot result in a fatal accident and the airplane must be capable of successfully completing the flight. Other loads that have to be taken into consideration are ground loads. They can come from very different sources, from adverse braking or maneuvering during taxi to impacts with frangible structures or debris.

These last sorts of events are directly connected with the damage tolerance concept. Damage tolerance is a property of a structure related to its ability to sustain defects safely until repair can be accomplished. There are *a priori* harmless load cases that can cause damage; therefore, it is necessary to ensure the continued safe operation of the structure. Damage may result even from low-velocity impact such as tool drops when maintenance is being taken place in the aerospace structure.

On the other hand, there is the frangibility concept where the structure should be damaged and easily broken. In an airport, the structures close to the runway must be frangible such as airport beacons or markers. Particularly, a frangible structure should break, distort, or yield when subjected to sudden collision forces of determined conditions.

This chapter discusses the failure analysis of dissimilar and representative case studies:

- A low-velocity impact in a laminate structure that can be caused by tool drop or impact debris.
- An airport impact with a frangible structure due to a land incident.
- A blade-loss event of a turboprop aircraft due to a crack in the propeller hub.

Each case of study uses a different strategy to analyze the failure due to the distinct natures of the events. However, all of them include a highly dynamic failure simulation, which can involve also prediction of failure sequence.

2 LAND INCIDENTS; LOW-VELOCITY IMPACTS

Composite aircraft structures have become increasingly widespread on civil and military aircraft, and recently on the current drones, unmanned air vehicles or remotely piloted aircrafts. However, these structures are sensitive to low-velocity impact, which may create multiple delaminations through the thickness, as well as matrix cracking, fiber breakage, translaminar delamination, or other damage types [1]. There is no mature methodology that is reliable and fully validated to predict damage initiation and propagation; however, there are many reported efforts [2] and the review [3]. In many cases, damage growth is too rapid, not predictable, and a "no-growth" concept is used in the certification process. Due to this fact, testing is still very expensive and time consuming.

Moreover, impact damage is very complex and the consequences are irregular and variable: multiple delaminations, matrix cracks, etc. [4,5], and imperfections such as dents and other shaped distortions. Furthermore, the damage type depends on several parameters such as lay-up, material, or impact conditions. Due to the complexity of damage, simplifications are necessary to focus just on the most important features.

The primary aim is to develop and verify comprehensive methods for assessing the impact damage and predict the residual strength. In this study case, an example with close interaction between modeling and experimental work is shown. A simulation methodology, finite element model (FEM) technique, is able to accurately predict and characterize the damage produced to composite panels by low/medium velocity impacts. The work is focused in barely visible impact damage panels.

2.1 FEM MODELING AND ANALYSIS

The panels are of two materials, carbon-epoxy laminates IM7/977-2 and IM7/8552. Two configurations are taken into account, each of them showing different size and impact energy (11 and 20 J). The panel thickness is 3 mm and the panel stacking sequence $[(-45, +45, 90, 0)_3]_s$. The benchmark was already explained in detail elsewhere [6].

Panel FEMs were modeled by using Pre/Post MSC.Patran, and the implicit solver MSC.Marc carried out the analysis [7]. The FEM analysis characteristics are nonlinear transient, using a progressive damage model based on stress-based criteria. The criteria take into account the next failure modes: fiber fracture, fiber-microbuckling, matrix failure (tension, compression, and in-plane shear), failure by peeling stress, and failure by interlaminar shear stresses. For all these modes, the criterion used is maximum stress.

The FEMs characteristics are solid elements for the panel. The impactor is modeled as a rigid spherical element. The panel is clamped (*UX*, *UY*, and *UZ*) at panel nodes placed at the clamping ring border ($\phi = 140$ and 220 mm). A picture of the FEMs used in the analysis is shown in Figure 2.1.

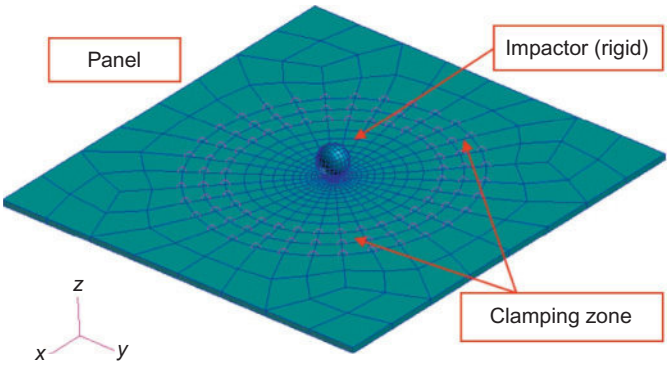

FIGURE 2.1

FEM model.

The FEM results have been studied for each failure index of each failure mode and for each ply. Since the experimental damaged area scans do not indicate the distinct types of failure (delaminations, matrix cracks, fiber fracture) present at the different plies, the correlation tests-FEM analysis is made comparing the damaged area as a whole. In Figure 2.2, the damaged area is compared. In all cases, FEM images, which have been scaled to allow visual comparison, match exactly with test coupon pictures. The white color at FEM images means that failure has occurred in at least

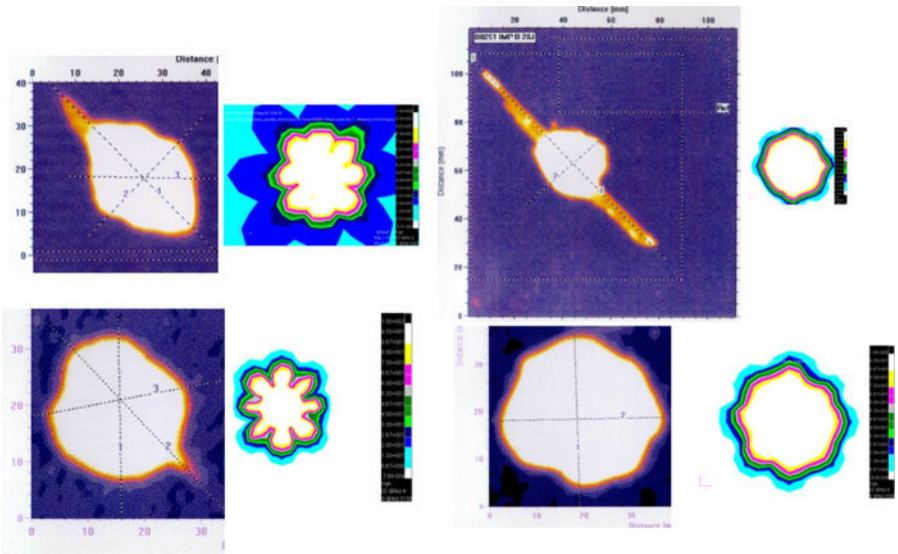

FIGURE 2.2

Comparison between test and FEM results.

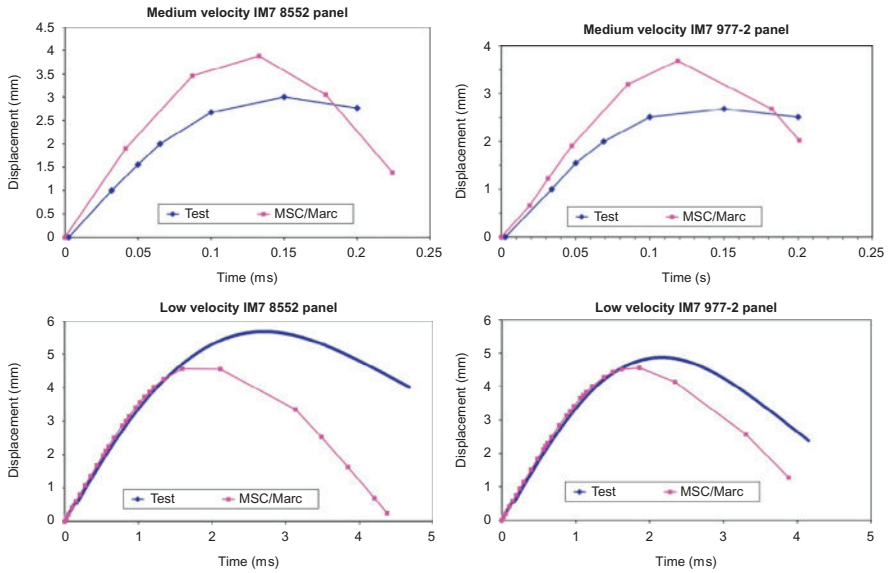

FIGURE 2.3

Deflection versus time plots for the different panels and load cases.

one of the failure modes considered, and it happens in at least one of the plies. Additionally, deflections against time plots of the impactor are correlated between FEM analysis and tests. In Figure 2.3, the deflection against time plots of the impactor is shown for the different panels.

The following conclusions can be extracted from the above FEM-test correlation. The prediction of the damaged area is quite satisfactory for material IM7 8552, while it is only acceptable for IM7 977-2. It seems that the allowable σ_{zz} seems too high and needs to be confirmed with more reliable sources. If allowable σ_{zz} is decreased, damaged area grows and correlates better with test results. The deflection-time plots show very good correlation in low-velocity IM7 977-2 coupons, and only acceptable in the others.

The general conclusion is that the FEM analysis methodology used seems adequate, the correlation between tests and FEM output is at least acceptable, and it is quite satisfactory in some of the panels.

2.2 CONCLUSION AND RECOMMENDATIONS

Prediction of impact response and damage in plain laminates was performed using a closed form quasi-static model and FE models. The closed form model predicted delamination growth using a fracture mechanics criterion (maximum strain). The FEMs were intended as fast design tools and, therefore, used fairly coarse meshes and stress-based failure criteria.

Prior to penetration/rupture, the closed form model was able to predict the response and extent of the delamination zone in drop-weight impacts with reasonable accuracy. The main limitation is the inability to predict the shape of individual delaminations and the extent of other damage types. Additional limitations are the uncertainty in material data.

For future work, it is recommended to either use predictive models for delamination growth based on fracture mechanics criteria, or use other approaches which incorporate the energy absorption during delamination growth.

3 LAND INCIDENTS; FRANGIBILITY OF AIRPORT STRUCTURES

Another application, in which a dynamic failure is present, is a frangibility study of an airport aid structure. There are not many approaches to this field due to the complexity of the simulation [8,9]. Frangibility is defined as the property which allows an object to break, distort, or yield at a certain impact load while absorbing minimal energy, so as to present minimum hazard to aircraft. Most of the suppliers tend to test the impact in order to accomplish the requirements. ICAO "Aerodrome Design Manual" part VI about frangibility [10] describes the minimum requirements to consider a structure as frangible.

- Near the airport runway areas, obstacles must be frangible. They have to withstand static or operational wind loads or jet blast with an appropriate safety factor, but should break, deform, or yield easily when subjected to sudden collision forces of a 3000-kg aircraft in the air and flying at 140 km/h or moving on land at 50 km/h. Therefore, full-scale testing or aircraft impact simulations are performed on these frangible barriers to determine their behavior.
- The frangibility is achieved by means of use of light materials or introducing separation mechanisms that allow the object to break, to deform, or to yield under impact.
- For light masts, a structure can be considered frangible when the impact energy is limited to 55 kJ and the peak force does not exceed 45 kN.

3.1 DESIGN TO BE ANALYZED

The pole under consideration is a tubular mast of 12 m length that fits in a conical and hollow ground support. This mast is used as a light support post in a runway airport area. It consists of a structure composed of unidirectional glass fiber and polyester resin matrix material. In the bottom of the tube are six layers of 1.6 mm, which are gradually disappearing to remain only three in the upper part.

The base is a fabric fiberglass (0°/90°) and a short-fiber mat with polyester resin matrix. In the tapered region of the base are 9 layers and 18 on the collar and on the flat portion thereof.

For the studied mast, the analysis consists of two simulations of impact at 50 km/h (ground plane) and 140 km/h (plane on flight). In these simulations, the plane is modeled as a rigid cylindrical body of 3000 kg.

3.2 NUMERICAL ANALYSIS TOOL USED IN IMPACT PROBLEMS

To perform these impact simulations, MSC.Dytran explicit finite element code is used [7]. MSC.Dytran is a program based on explicit calculation to simulate the dynamic response of systems consisting of solids, structures, and/or fluids. It combines technology of solid and fluid mechanics to facilitate modeling, using an explicit method for the integration of the equations. Also includes a variety of material's types and geometric nonlinearity. The presolver used to build up the element structure is MSC.Patran, which is compatible with this explicit solver. Explicit solvers are used to simulate short-time duration phenomena, such as impacts or crash simulations when the stress wave propagation and the dynamic component are important. The common challenge of these solvers is the large number of time steps needed due to their small size and therefore the CPU time consumed to run the case.

The model consists of 2395 2D plate elements:

- Column: It is a hollow beam with tapered section modeled by 2D elements of composite unidirectional fiberglass and polyester resin. The lower wiring door, which would make the column fragile, is not modeled. Therefore, it is a more conservative case. Each 1.6-mm layer of the laminate is modeled as 2D orthotropic material. From these material properties, different stacks for each section of the column are constructed. The properties are shown in Table 2.1.

Table 2.1 Properties of Composite Material of Each Column and Base Layers

	MAST	BASE
Property	**Value (Units I.S.)**	**Value (Units I.S.)**
Density	1600	1261
Young modulus E11	1.7E+10	1.1E+10
Young modulus E22	6E+9	1.1E+10
Poisson coefficient 12	0.3	0.198
Shear modulus G12	6.5E+9	4.59E+9
Shear modulus G1z	6.5E+9	4.59E+9
Shear modulus G2z	6.5E+9	4.59E+9
Failure stress	6E+7	
Longitudinal tensile failure load	2E+8	2.14E+8
Longitudinal compressive failure load	1.8E+8	
Lateral load tensile failure	1.04E+8	2.14E+8
Lateral load compressive failure	1.4E+8	

- *Impactor*: It is a rigid cylinder of 0.4 m diameter. Its center is located 3 m above the base of the column, and it is made of rigid material with a total mass of 3000 kg.
- *Base*: Mesh of 2D plate elements, with two distinct areas. The tapered region in contact with the column is having 9 layers of composite material, and the neck and the square base 18 composite layers. A fabric (0/90) glass fiber and short-fiber mat with a polyester resin matrix forms each layer. It is modeled from the results obtained in the tests of samples of this material.
- *Ground*: In addition to the mentioned elements, a base is placed at the level where the ground would be found. The ground is modeled because when the column gets out of the conical base during impact cannot go inside it and penetrate the floor. It consists of a rigid mesh of 2D elements with all its nodes simply supported.

The boundary conditions are four points of the square part of the base clamped. Initial speed conditions of 50 and 140 km/h are applied to the impactor. Finally, the following contact conditions are taken into consideration in the problem (Figure 2.4):

- Impactor-column.
- Column-base. In this case, it is considered friction between them, defined by static friction coefficient of 0.6 and dynamic of 0.3.
- Column itself. When bending the column by the shock and collapse, the elements that make up the spine cannot cross one another.
- Column-ground. When the column after the impact is going off the conical base, it cannot go across the floor.

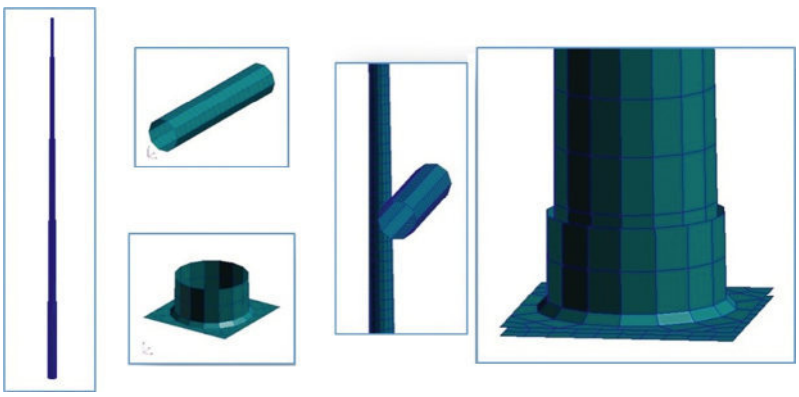

FIGURE 2.4

Column, impactor, and base. Impactor-column and column-base contacts.

3.3 MODEL CORRELATION WITH LATERAL LOADING TEST

A lateral tip load test is performed and the results are:

- Nominal load: 870 N with a deflection of 1225 mm.
- Ultimate tensile 2580 N.

A series of quasi-static simulations of the column subjected to a lateral load (applied in the tip) are conducted increasing from 0 to 2500 N. This is used to validate the properties of the material, the coefficient of friction between the base and the column, and the failure criterion considered.

Analyses were performed with MSC.Dytran. Due to the fact that it is an explicit solver, inertia forces always influence the result of the calculation. Damping is introduced into the system to reduce the effect of inertial forces, minimize computation time, and achieve more reliable results. Two kinds of correlations were performed:

- Validation of material properties.
- Validation of the friction coefficient and failure criteria.

3.4 MECHANICAL PROPERTIES AND FAILURE CRITERION VALIDATION

A set of constant lateral load analyses are performed applying load. This load is low enough not to introduce failure in the material. This deflection is assessed and compared against the one obtained for the rated load (in which the column remained without failure). From these analyses, the damping applied to the rest of the validation process is obtained.

Some of the analyses carried out are:

- Simulating 1 s with increasing load up to 100 N at 0.5 s and constant during the rest of the test. A displacement in the tip between 0.125 and 0.175 m is obtained.
- Simulation of 0.5 s with a constant load of 100 N and damping coefficient of 0.00002. A displacement of 0.125 m is obtained.

The value of the tip deflection during test for the nominal load of 870 N (1.225 m) is extrapolated supposing linear response, obtaining a tip deflection of 0.140 m for 100 N loads. This value is comparable to that obtained in the simulations; therefore, the input values of elastic modulus of the column material are considered valid. In addition, damping values close to 0.00002 are used in the rest of the simulations to reduce computation time.

Analyses with different loads (constant or ramp) are carried out up to 2500 N (Table 2.2). Deflection at nominal load of 870 N is evaluated and compared with test data. Moreover, values of the ultimate load of the column or column-base separation are obtained.

Load is applied gradually (ramp) and damping is introduced to minimize the influence of inertial forces.

Table 2.2 Most Relevant Simulation Results

t [s]	Load (t) [N]	Damping	Max. Deflection. [m]		
			100 N	870 N	2500 N
2	0 (0 s)/2500 (2 s)	0.00002		0.91	7
2	0 (0 s)/2500 (2 s)	0.00001		1.06	9
2	0 (0 s)/2500 (2 s)	0.000005		1.11	9
10	0 (0 s)/2500 (10s)	0.00002		1.08	7.5

The simulations behave linearly at nominal load (870 N). In the test, a deflection at 870 N (1.225 m) was compared with 0.91, 1.06, 1.11, 1.08 m obtained in the simulations (from 10% to 35% less than the nominal value). Therefore, from the frangibility perspective the performance of the simulated column is conservative.

In the case of analysis of 2 s, and damping coefficient of 0.00001, the progress of the fracture was observed at 2500 N. At the upper part of the column, elements begin to break and layers start to separate. It starts a slippage column-base although it did not reach the complete collapse.

Therefore, the simulated column results are conservative from frangibility perspective, since column does not break or exit the base entirely at the value of ultimate load test, as it happens on the test.

3.5 FRANGIBILITY SIMULATION RESULTS

The standard requires two kinds of analyses for frangibility. A case for plane rolling on ground with 50 km/h impact velocity (Figure 2.5) and one airborne with 140 km/h (Figure 2.6) impact speed. The 50 km/h results match the expected behavior in which the column bends and exits the base. The failure mode is separation of components. The 140 km/h results match the expected behavior where the impactor severs the column. The failure mode is brittle.

The energy lost by the impactor, which is absorbed by the column, is 20.6 kJ (50 km/h) and 20.3 kJ (140 km/h). The energy levels are much lower than the allowed value (55 kJ) (Figure 2.7). This is caused by the low module of elasticity of the glass fiber material resulting in brittle material behavior. Moreover, hourglass energy is less than 10% of the overall. Therefore, the results from an explicit analysis point of view are taken as valid.

The maximum impact force for 50 km/h case is 27 kN and the column will be completely separated from the base in 133 ms (Figure 2.8). In the 140 km/h case, it can be observed that the column breaks before 30 ms and the maximum peak force is ~50 kN being conservative. The predicted peak force occurring during the impact event is similar to the specified maximum force of 45 kN. Therefore, it can be potentially concluded that the mast could be considered frangible.

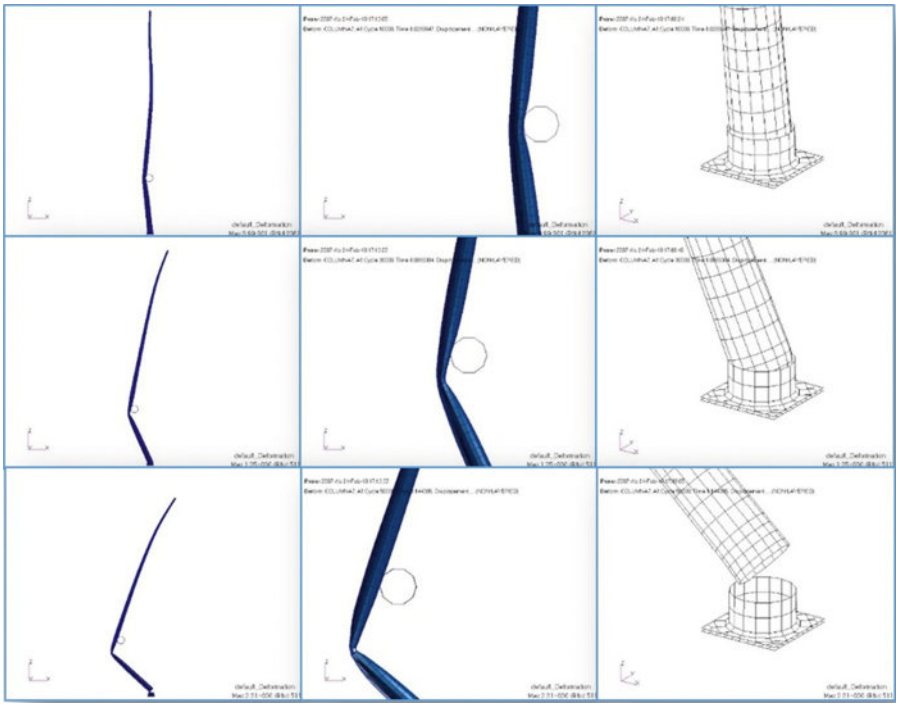

FIGURE 2.5

50 km/h impact. Details around impact area and base.

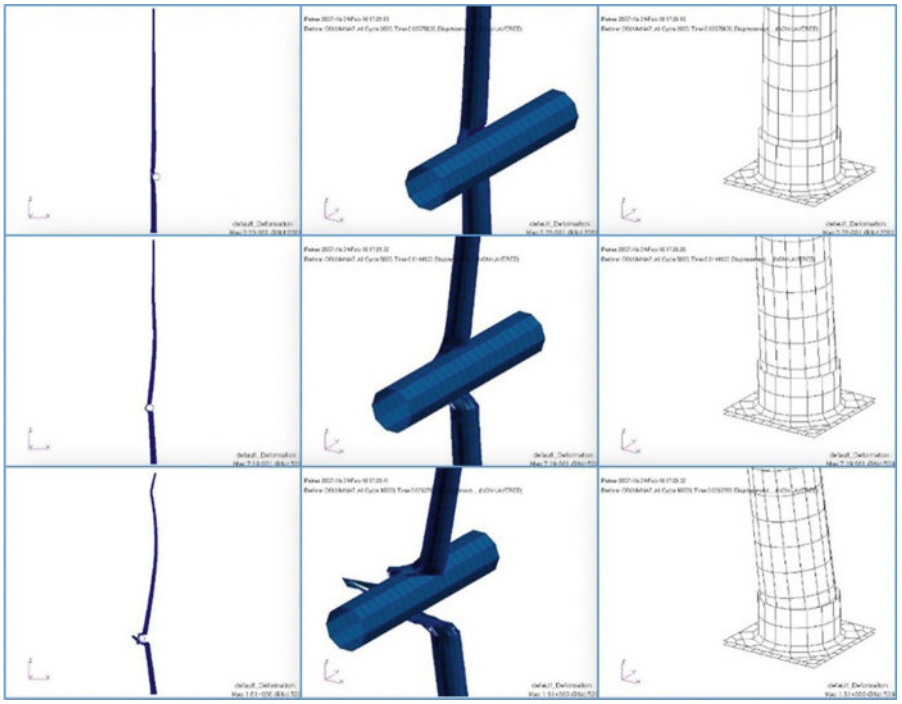

FIGURE 2.6

140 km/h impact. Details of collision area and base.

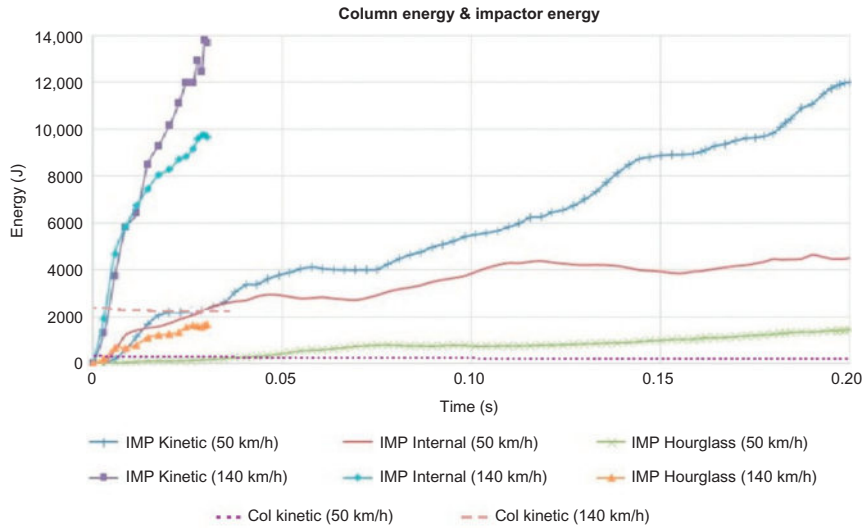

FIGURE 2.7

Impactor energy and column energy.

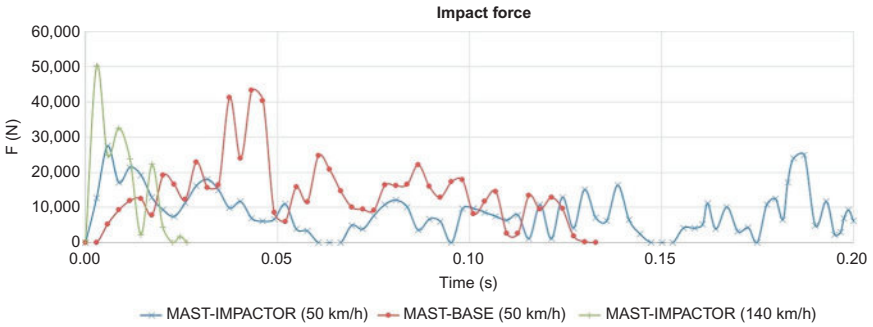

FIGURE 2.8

Impact force.

4 FLIGHT INCIDENTS; BLADE LOSS OF A TRANSPORT AIRCRAFT

Reliability is one of the main concerns in aircraft design and operation. Due to the continuous improvement in this subject, the number of extreme failure events has decreased, although aero engines are operated 1000 h before they are removed from service for scheduled inspection. Even in the unusual occasions of engine

malfunctions, the powerplant installation design makes that no single failure or malfunction will jeopardize the safe operation of the airplane. Each powerplant is isolated from the others and configured in order to stop the rotation of any engine individually if necessary. An inoperative engine does not constitute a safety issue since airplanes are designed to fly under such circumstance.

Several episodes can be the cause of engine malfunction, typically bird strike, hail or ice strike, debris impact, ice formation on the propeller blade, axis, or hub. The most severe failures occur when it is impossible to prevent severe vibration transmission to the structure of the airplane, particularly in the case of a crack in the propeller hub that can possibly result in propeller blade loss. The engine mounting system (EMS) must be designed to absorb these vibrations and, if necessary, detach the engine from the structure before fatal structural damages may occur.

A proper analysis of these failures will improve future designs but is not an easy task due to the nonlinear nature of their dynamics. A reported study [11] explains how to deal with nonlinear topics in structural dynamics. Meanwhile, certification authorities take all of these events into account through modifications of the design loads or by minimizing the hazard to the structure. In this regard, the contribution of design to accidents [12], the key points of aero engine containment requirements in FAR Part 33 [13], the bird strike and icing analysis from a certification point of view [14,15], have all been reported. There are incidents that imply direct consequences to the aircraft structure such as uncontained engine failure, uncontained fan blade impact, and uncontained high-energy rotating machinery failure. These were studied and reported from a certification point of view [16,17]. The analysis of the probability and/or risk of these incidents were also reported [18]. According to the regulation authorities, the airplane must be capable of successfully completing the flight, thus the aero engine has to withstand such a failure without leading to a major hazard to the aircraft. For new propeller developments projects, a full engine test campaign is typically requested by the authorities for certification. Only in case of minor changes from a previous engine design, certification has been allowed without new testing using technical analysis methods. However, as researches keep improving and simulations tools are becoming more reliable, a cost and time saving might be possible in a near future.

Recently, an analytical method for predicting the transient nonlinear response of a complete aircraft engine system due to the loss of a fan blade has been developed by means of a FEM [19]. The response of the structure after a propeller blade loss depends radically on the flight condition, propeller frequency, blade-loss size, angular position where the blade is lost and how it is lost. Furthermore, the flexibility of the wing, the stiffness of this fitting, and the structural damping are also determining factors behind the phenomenon.

Nevertheless, the assumption of deterministic values for certain parameters is difficult to maintain. Some parts of the EMS break (specially the elastomeric devices) during blade loss, and the breaking points or values at which they occur are subject to nondeterministic fluctuations. It is of interest to carry over the analysis to a more

realistic stochastic situation. However, the huge number of relevant variables makes it nearly impossible to do a detailed study of the complete system.

In order to reduce the number of variables in this case study, a more simplified model that keeps the qualitative global behavior of the system is introduced, as obtained and reported in literature [19]. A series of Monte Carlo simulations to deeply analyze the elastomeric collapse sequence is also performed.

4.1 BLADE-LOSS PHENOMENON

A propeller blade progresses through the air along an approximate helical path as a result of its forward and rotational velocity components. To rotate the propeller blade, the engine exerts torque. This momentum is reacted by the blade sections in the opposite direction in terms of lift and drag force components as shown in Figure 2.9. Due to the rotational forces reacting on the air, a rotational velocity remains in the propeller wake with the same rotational direction as the propeller. This rotational velocity times the mass of the air is proportional to the power input. The sum of all the lift and drag components of the blade sections in the direction of flight are equal to the thrust produced. A propeller blade must be designed to withstand very high centrifugal forces. The blade must also withstand the thrust force produced plus any vibratory forces generated, such as those caused by uneven flow fields.

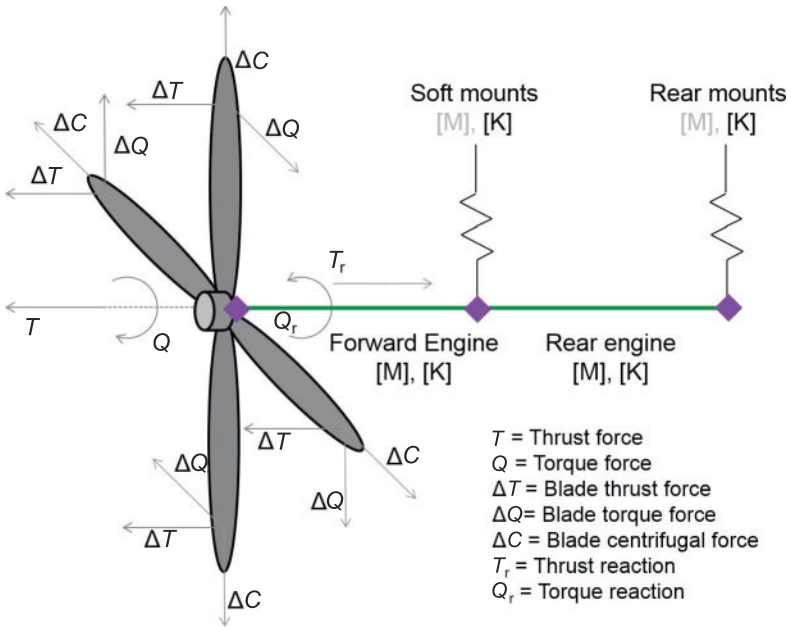

FIGURE 2.9

Aerodynamic forces over the blades and engine and mounts simplified model.

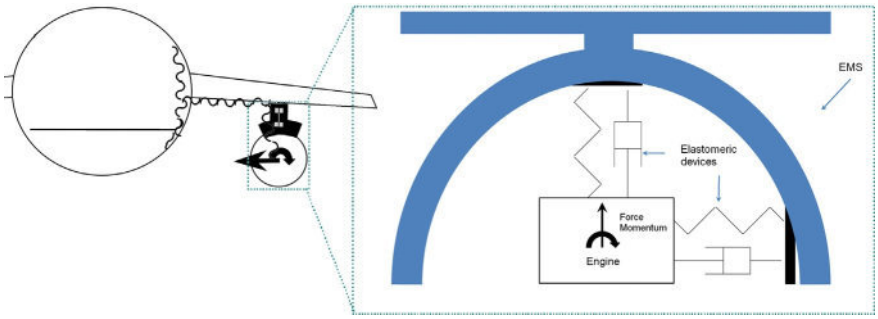

FIGURE 2.10

Vibrations on the aircraft (left) and engine mounting system detail (right).

When a propeller blade is detached, many forces at the broken blade are no longer supported (lift of the blade, drag of the blade, etc.) and there are forces that are no longer compensated, such as the centrifugal force of the blade. These forces for the case of a blade-loss event in a turbofan rotor have been evaluated and reported [20]. These dynamic effects may cause highly dynamic load levels of stress on the engine, EMS, wing, and the rest of the aircraft as shown in Figure 2.10.

In this event, the damage assessment cannot discriminate which damage was due primarily to transients and which was caused by steady-state operation after the blade loss. Even in instrumented tests, it is difficult to ascertain the worst damage due to transients because their duration is very short. It is obvious that damage is inflicted to the engine and its components in various modes. Turboprop engines that lose a propeller blade swiftly start to vibrate powerfully with considerable consequences; material, structural failures, and other damages [21]. Normally, it only causes critical damages at the engine and its support system. The reason why usually the rest of the aircraft does not malfunction is because the engine joining structure absorbs the dynamic loads. If the EMS (typically elastomeric devices) fails, the load path to the wing is interrupted. The devices actually are designed with this purpose: to act as a fuse in order to reduce the risks of critical failure to the rest of the structure.

4.2 DESCRIPTION OF THE MODELS

To analyze and simulate the blade-loss phenomena, a typical turboprop of heavy military transport was chosen. The main aspect of the models includes the dynamic behavior of the engine, particularly its mass and inertia. Moreover, the normal modes of the model must be identical to those of the real structure.

Apart from the main engine model, many of the research efforts are focused on the study of the mounting system stiffness properties. Figure 2.11 shows the type of stiffness. A design optimization of elastomeric material is essential [19]. This

nonlinear problem should consider the elastomeric devices break characteristics in addition to its nonlinear stiffness behavior. Furthermore, the failure criteria for these parts of the structure determine the behavior of the system. Variations in the mounting system due to a failure modify the dynamics of the system and, as a consequence, the failure sequence of the elastomeric devices.

4.3 FEM MODEL AND SIMPLIFIED MODEL

The EMS and the engine are simulated through a FEM code, known as MSC.Dytran [7]. The presolver used to build up the element structure is MSC.Patran. Concerning the engine, the most important aspect to take into consideration is its mass. For this reason, it has been modeled using beam (BAR2) and mass (POINT1) elements, which provide the model the adequate dynamic behavior. The EMS model consists of shell (TRIA3 and CQUAD4) and beam elements that are able to reproduce precisely its structural behavior (Figure 2.12).

In the FEM model, it is necessary to provide nonlinear behavior for the finite elements. Due to the level of stress expected on different parts of the structure, linear material properties are used for the engine and both linear and nonlinear for the EMS. Some of the energy absorbed by the model would be spent on plasticizing the material of the EMS. The nonlinearity has been included through a perfectly plastic criterion in the material for the corresponding 1D and 2D elements of the EMS model. The EMS-wing fitting has been reproduced through elements and its stiffness is changeable. Finally, the wing is replaced nominally by a clamped constraint, since the main interest is determining the forces transmitted to the wing because of blade loss.

In the case of the simplified model, the whole engine has been modeled though limited mass matrixes and stiffness matrixes. However, the structural behavior of the engine close to the forward mount and the rear mounts is ensured. In order to be more accurate, the degrees of freedom of the applied load point have been included (Figure 2.9).

Moreover, some checks between models have been carried out (mass, inertias, normal modes, …). The first modes of the FEM engine and the simplified model are very similar (Table 2.3). The nonlinear behavior of the elastomeric devices has been reproduced exactly. Therefore, the engine plus mounts is correctly reproduced.

4.4 ANALYSIS CONSIDERATIONS, IMPLICIT AND EXPLICIT METHOD, TIME STEP

The critical time-step limit for multidegree of freedom systems is dictated by the highest mode, and consequently, a very small time-step size must be used in order to obtain a stable solution. As previously mentioned, if most of the interesting part of the solution is contained within a few of the lowest modes, it is possible to use a

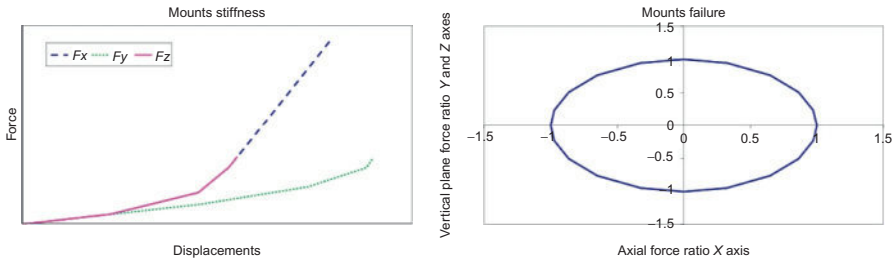

FIGURE 2.11

Mounts stiffness and failure.

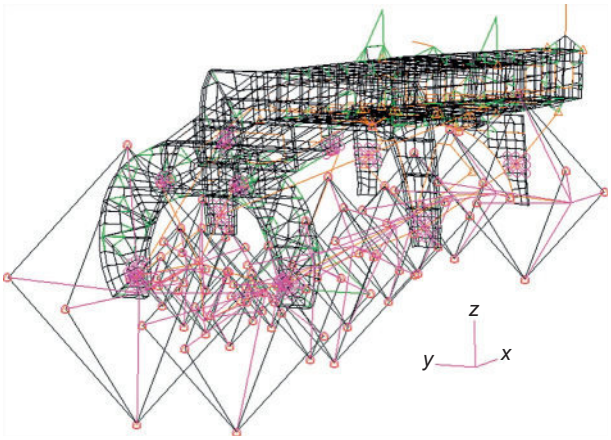

FIGURE 2.12

FEM model.

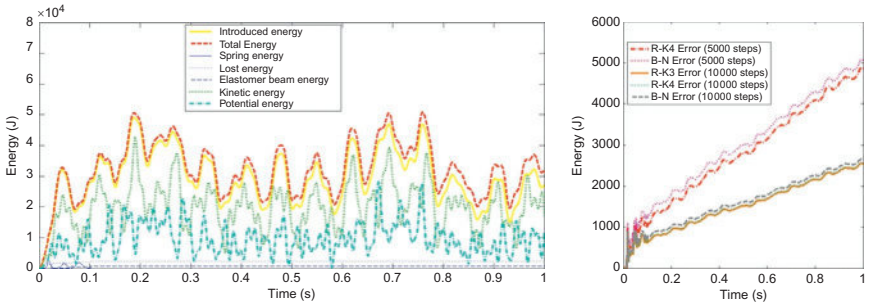

FIGURE 2.13

Energy levels in the nominal simulation (left) and energy errors between schemes (right), both in the simplified model.

Table 2.3 Flexible Modes Error Between Models

Flexible Modes	1st	2nd	3rd	4th
Frequency error (%)	5.05	7.50	8.27	9.99

time-step size considerably larger than the critical limit. The simplified model reduces the modes to take into account and therefore increases the time step. The typical conditional stability equation is:

$$\Delta t \leq \frac{l_c}{c} = \frac{2}{\omega_{\max}} \text{ and } \omega_{\max} \rightarrow \omega_0 = \sqrt{\frac{k}{m}} \tag{2.1}$$

Implicit and unconditionally stable (for linear problems) schemes like the β-Newmark method with $\alpha = 0.5$ and $\beta = 0.25$ are generally preferred to solve this sort of problems. However, implicit method that is unconditionally stable for linear problems may begin to show instability when used for nonlinear problems, especially for long-time simulations. The use of large time steps does not allow accurate resolution of the highest modes. These modes, even though not containing the interesting part of the solution, may still contribute to cumulative errors over long times, and ultimately affect the stability of the solution. This is a reason to analyze the problem through an explicit FEM, which resolves the highest modes contained; however, it requires a large number of time steps (with a relatively low computational cost).

The FEM model uses MSC.Dytran explicit solution technique. It is a transient dynamic code using a central difference scheme to advance in times the velocities and positions of the grid points. In the scheme, it needs to be calculated only once for each time step.

$$v_{n+1/2} = v_{n-1/2} + a_n \frac{\Delta t_{n+1/2} + \Delta t_{n-1/2}}{2} \tag{2.2}$$

$$x_{n+1} = x_n + v_{n+1/2} \Delta t_{n+1/2} \tag{2.3}$$

Use of implicit methods requires solving the system matrix. This factorization of system matrix may be performed once if the system is linear; however, in the nonlinear cases the factorization has to be carried out many times. If the time-step size required is very small, the whole procedure becomes unreachable and time consuming. This is a reason to analyze the problem through a simplified model. For the Runge-Kutta method, the calculation of a vector of internal forces needs to be performed four times. Therefore, it is less expensive than the solution of the system matrix. However, it is the most numerically expensive step in explicit methods, and may be considerable if the calculation of the vector of internal forces involves nonlinear functions.

The elastomeric devices between the engine and the mounting system are nonlinear, it is necessary to include nonlinear stiffness behavior in each axis. Moreover, in the soft mounts, there are different failure criteria depending on the axis. The aim is to obtain ellipsoidal failure criteria curves (abscissa X axis and ordinate YZ plane) where the failure criteria for X and YZ are different (Figure 2.11).

Due to the reasons explained above, the simplified model has been analyzed through different schemes: β-Newmark ($\alpha = 0.5$ and $\beta = 0.25$), third-order Runge-Kutta, and fourth-order Runge-Kutta. It has been checked that they show the same results for the control load case. The energy level achieved during the blade loss, and therefore during the simulation, is an excellent indicator of the appropriate phenomenal development. Figure 2.13 shows the energy levels in the simplified model for the nominal load case simulated through Runge-Kutta and β-Newmark schemes. All of them show the same energy levels (except Runge-Kutta with 5000 steps, which does not converge). The energy error is almost insignificant in all cases; however, it is different between schemes and the time step used. Moreover, it always increases with the number of time steps.

In both models, the forces applied due to the blade loss are converted to energy through the model displacement. Most of the energy is transformed into kinetic energy in the engine. Some of the kinetic energy, determined by the elastomeric properties, reaches the EMS. Additionally, some energy becomes internal energy and more precisely elastic energy. The element deformation absorbs a reversible elastic energy while they are in the linear regime. When the element reaches a plastic level of stress (only possible in the FEM model), this exchangeable energy becomes irreversible. This is also the case for an element failure that can happen in both models. If this occurs, this energy path is no longer possible. These events make each load case different and the simulation progresses and separates each one from the other.

4.5 LOADS AND BOUNDARY CONDITIONS

The loss of a blade introduces a rotary force and a momentum at the hub of the propeller due to the imbalance. The forces depend mainly on the centripetal force caused by the blade lost, whereas the momenta are principally caused by the momentum arm of the lift force that is no longer compensated. Therefore, the loads considered follow the following equations:

$$\begin{aligned} F_y &= -F_c\cos(\omega t), \quad M_y = M_{oop}\sin(\omega t) \\ F_z &= -F_c\sin(\omega t), \quad M_z = -M_{oop}\cos(\omega t) \end{aligned} \tag{2.4}$$

In case of the FEM, the boundary condition is clamped through four nodes (two at the upper middle part in XZ axes, other at the rear part in Z axis, and another between them in Y axis). In case of the simplified model, the boundary condition is camped in two nodes (at the middle part and rear part, both in XYZ axes).

4.6 LOAD CASES ANALYZED

The safety of the aircraft would depend on the selection of the design loads and requirements, which define the structural stiffness, mass, and inertia properties. Several load cases were analyzed during this research; some of them were the initial conditions for blade-loss phenomena and others were different variations of parameters of the blade-loss phenomena itself. Some of the parameters analyzed in the FEM model are:

- *Blade-loss angular position*: The position where and when the propeller is detached may influence the event.
- *Different 1 g initial cases*: Blade loss is mainly studied as an isolated phenomenon; however, since it occurs under a certain flight condition, its influence must be studied.
- *Sensitivity to rpm*: The propeller rotational speed changes with the flight conditions and the effect of this variation in the structure must be analyzed.
- *Sensitivity to EMS-wing fitting stiffness*: As mentioned in previous sections, the EMS stiffness must be studied in depth.
- *Time and shape of the imbalance force*: The load usually is applied instantaneously; however, this entry can be smoother.
- *Blade-loss size*: The blade can come off completely or just partially.
- *Wing flexibility*: The objective is to analyze the influence of a flexible wing (first mode) in the simulation introducing the equivalent stiffness, mass of the wing, and studying the interaction at the first wing-bending frequency.
- *Structural damping*: It influences the response of the structure during the phenomena.

For the simplified model, the following parameters were studied: blade-loss angular position, sensitivity to rpm, blade-loss size, the elastomeric stiffness where the soft and rear mounts stiffness are varied through a parameter (varies the slope of the curves on Figure 2.11 left), and the elastomeric strength where the ellipsoidal failure criteria are expanded or decreased in all mounts through another parameter (larger/smaller ellipses on Figure 2.11 right).

The problem is analyzed in the context of Monte Carlo simulations. The model parameters can be seen in Table 2.4.

The Monte Carlo simulation technique has wide applicability and the accuracy of the solution obtained increases as the number of samples becomes large. As a large number of sample problems need to be solved in order to achieve the required degree of accuracy in the calculation of the statistics of the response, the CPU time consumed is quite significant. However, the model has been simplified and each simulation has a manageable CPU time. The number of each load case set of simulations was between 1000 and 10,000.

The simulations were performed in order to analyze the influence of some parameters, and several results were obtained as spring forces (force against time and fail), elastomeric failure sequence, boundary conditions forces, and model energies. The models and load cases showed different conclusions.

Table 2.4 Variable Modeling

Variable	Variation Type	Interval	Nominal Value
Blade-loss angular position	Uniform	(0°,360°)	0°
Sensitivity to rpm	Uniform	Two typical flight condition with max and min blade frequency	$\omega_{nominal}$
Blade-loss size	Uniform	(0,1)	1
Elastomeric stiffness	Normal	N(1,0.1)	1
Elastomeric strength	Normal	N(1,0.1)	1

4.7 RESULTS

The FEM results showed that the model was suitable to simulate blade-loss collapse sequence. It was also able to run without instabilities until the end of the phenomenon for most of the parametric cases.

- *Blade-loss angular position* (θ): They showed that the physical time needed to detach the engine from the aircraft was higher when the θ values were between 225° and 45° and the number of plasticized elements was higher in the same θ interval.
- *Different 1 g initial cases*: The physical time needed to detach the engine from the aircraft for the sea level at V_b case was much lower than the gravity load case.
- *Sensitivity to rpm*: The results seemed to be dependent on the normal mode frequency that can be excited by the propeller frequency.
- *Sensitivity to EMS-wing fitting stiffness*: The EMS-wing fitting stiffness variation changes the normal modes of the entire system. There were stiffness ratios where the model was less perturbable to the loads applied and it took more time to reach enough energy to detach the engine.
- *Time and shape of the imbalance force*: The variation of the initial load modifies the results; a smoother entry of the load implies higher time required to detach the engine from the wing.
- *Blade-loss size*: The time needed to detach the engine from the aircraft was higher when the detached blade was smaller. The number of plasticized elements was lower when the detached blade was smaller. The velocity of energy absorption was lower when the detached blade was smaller, and hence perturbation reaching the wing was also smaller.
- *Wing flexibility*: A variation in the wing flexibility changes the normal modes of the entire model. Therefore, there are wing flexibilities that make the model less perturbable to the loads applied, and it takes more time to reach a high level of energy.

- *Structural damping*: It influences the response of the structure during the phenomena. The results are not as *a priori* expected, at least for the values studied (typical values of metallic and close to composite materials with high structural damping). The number of plasticized elements was lower when the structural damping was lower. The time needed to detach the engine from the aircraft increased as the structural damping decreased.

The FEM model was simulated using existing explicit finite element method techniques. Using an explicit code was adequate for analyzing the sequence of blade loss and the dynamic phenomena directly related to the loss separation. On the other hand, additional results of large duration, such as those due to the imbalances, could be studied with an implicit code. The simplified model shows additional results, able to combine one, two, or even the five parameters mentioned above (Figure 2.14). The results are:

- *Blade-loss angular position*: The results did not show high dependence in this parameter. The first elastomer break occurred at $t = 0.018$ s (mean) and mainly between $\theta = 170°$ and 200°, and the last was distributed all along θ range. The failure order changed with the parameter variation.
- *Sensitivity to rpm*: The results did not show high dependence in this parameter. The first elastomer break occurred at $t = 0.024$ s (mean) and mainly between $\theta = 260°$ and 350°, and the last was distributed all along θ range.
- *Blade-loss size*: The time needed to detach the engine from the aircraft was higher when the detached blade was smaller. Moreover, the level of energy of the model when the first elastomer breaks followed different and clear patterns. The first break occurred at $t = 0.046$ s (mean) and mainly between $\theta = 0°$ and 50°, the last normally happened between $\theta = 350°$ and 10°. In this parameter, there are very dissimilar evolutions of the simulation, the ratio ranges between different behaviors were 0-0.66, 0.66-0.76, 0.76-0.83, 0.83-0.9, … (Figure 2.15).
- *Elastomeric stiffness*: The results did not show high dependence in this parameter. The first elastomer break mainly occurred at $t = 0.023$ s (mean) and between $\theta = 0°$ and 10°, the last normally happened between $\theta = 350°$ and 0°.
- *Elastomeric strength*: The results showed two dissimilar behaviors with distinct failure order and different energy levels. The first elastomer break occurred at $t = 0.022$ s (mean) and mainly between $\theta = 10°$ and 30° or $\theta = 150°$ and 200°, the last normally happened between $\theta = 350°$ and 10° or $\theta = 50°$ and 90°, respectively.

Monte Carlo technique allows studying the problem with different parameters interactions. Therefore, the variations of each parameter could be classified concerning the variability that produced in the results (Figure 2.16).

The analysis showed that the impact over the results of a variation of the parameters in the study range was different. The evolution of the analysis of changing the blade-loss size can be much different than when changing the elastomer

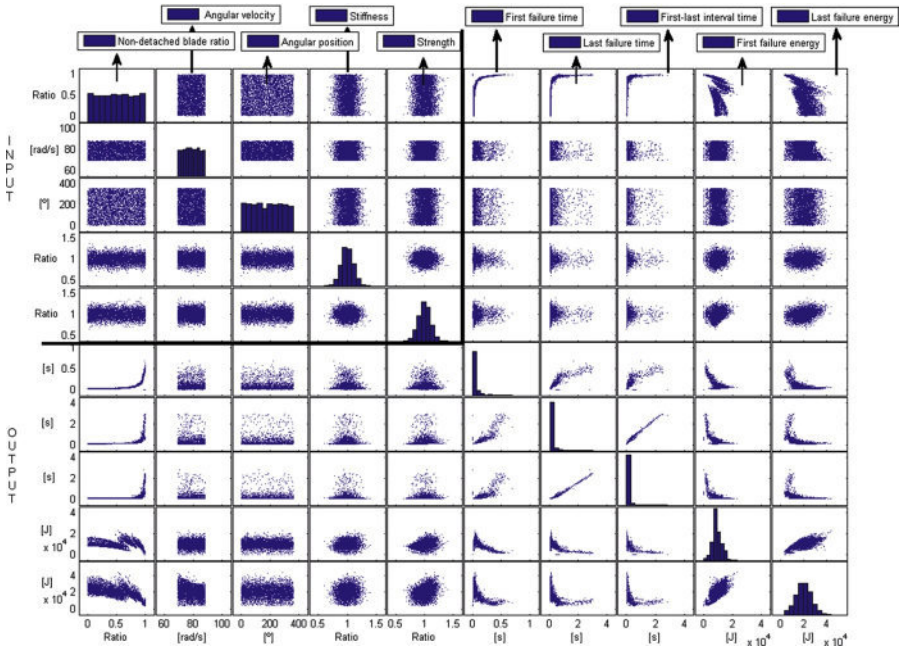

FIGURE 2.14

Matrix correlation for the inputs and some outputs.

stiffness or the engine frequency. In a medium range of variability, there are the elastomeric strength and the angular position of the blade when the blade is detached.

Relevant conclusions can be inferred from the results obtained in this study. The time between the first mount failure and the last mount failure is almost fixed when the blade-loss size varies; it is ∼0.078 s when the nondetached blade size ratio is between 0-0.65 and ∼0.066 s when the nondetached blade size ratio is between 0.65 and 0.75. In the case that the other parameters influence the simulation, the time between the first mount failure and the last mount failure is in more than 80% of the cases between 0.055 and 0.085 s. This can be seen in Figure 2.17.

Finally, an interaction between all the parameters was done and the correlation matrix can be seen in Figure 2.14. The results showed clear and specific patterns between some variables, nondetached blade and all the others, the elastomer strength and all the others, and between the output variables. As an example, the last elastomer failure time and the first-last failure interval time were highly correlated.

4.8 CONCLUSION

Concerning the validity of the research, both models are suitable to simulate blade-loss collapse sequence and are able to run without instabilities until the end of the phenomenon for most of the parametric cases. The model behaves efficiently and

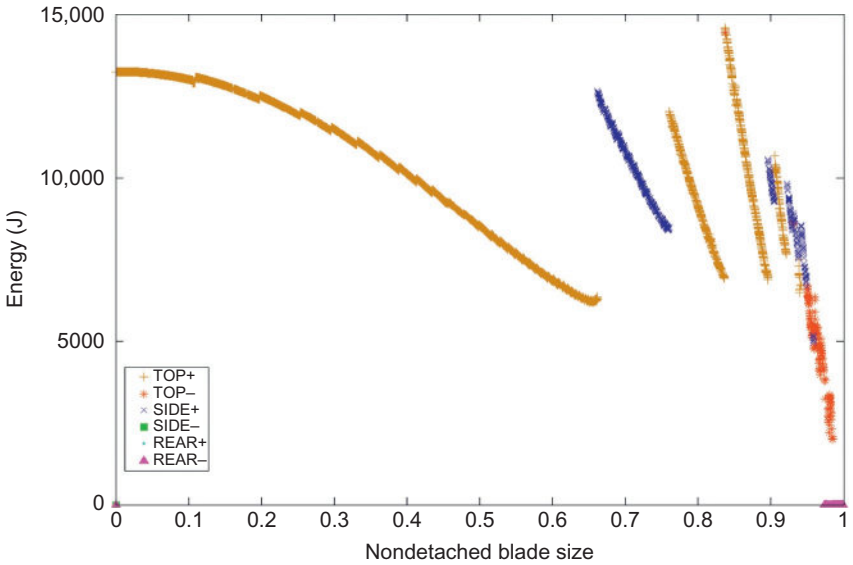

FIGURE 2.15

First failure energy versus nondetached blade ratio.

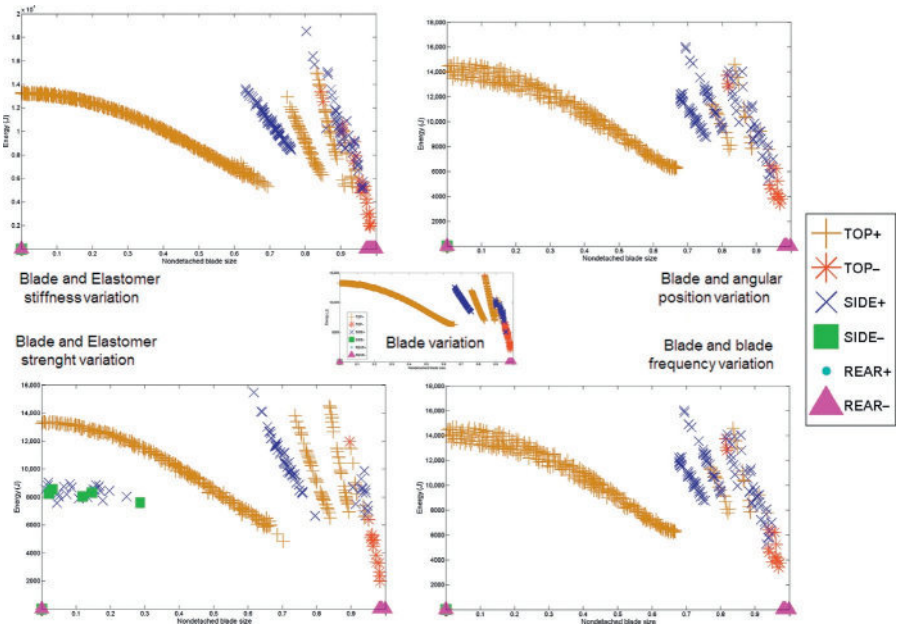

FIGURE 2.16

More parameters variations on first failure energy versus nondetached blade.

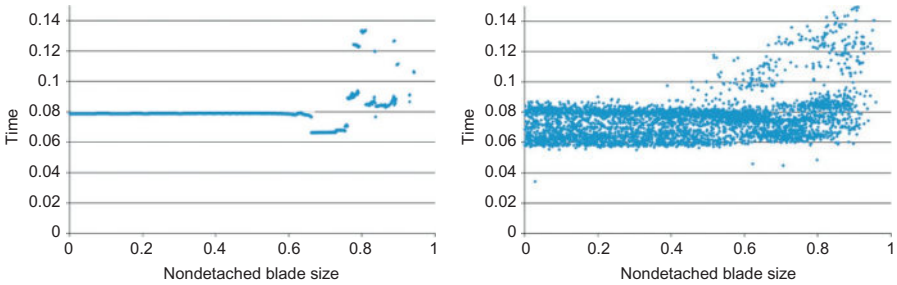

FIGURE 2.17

First-last mount failure time versus nondetached blade with no more variations (left) and all the variations (right).

the energy was checked. The optimization of time step in the FEM model and the simplifications performed in the simplified model were crucial in order to obtain the most adequate solution with the available computational resources.

The models include nonlinear behavior as well as failure criteria. The elastomeric model was able to reproduce the sequence of collapsing. When a soft mount fails, the normal modes of the structure change and so does the dynamic behavior of the system. The simplified model was able to study the range of each parameter where the simulation progressed with the same behavior. Therefore, the model analyses identified why and which parameters were responsible for significant differences in the development of the simulation when there were only small changes in the initial variables.

5 CONCLUSION

This chapter has shown different strategies to study the dynamic failure analysis of several case studies. The investigation examples cover a wide area of the dynamic phenomena. All of the study cases are highly dynamic events, which also involves nonlinear behaviors, damages, and failures.

A low-velocity impact, which can be produced in many situations such as a tool drop, runway hail, and ice pellets, was analyzed. These events open to question the residual strength of the structure and, therefore, its damage tolerance. The case study helped in the knowledge of the impacts themselves and it was able to predict the response and extent of the delamination zone in drop-weight impacts.

In addition, a frangibility study has been presented where the structure has to be broken easily in certain conditions; however, it has to withstand other loads without any damage. This is a concept which engineers are not very familiar with. The case study simulates the event precisely and valuable conclusions were remarked from the different load cases.

Finally, the last case of study shows a simulation of a possible flight incident, the blade loss of a turboprop aircraft. Different models were carried out due to the

complexity of the phenomenon. Moreover, the analyses were performed using distinct strategies, deterministic and statistical methodologies (Monte Carlo technique). Each strategy is able to achieve useful and complementary results. The failure analyses obtain the failure sequence depending on the initial parameters and other useful results.

ACKNOWLEDGMENTS

The chapter was completed; thanks to the inestimable help of the Structure and Mechanism Area team in the National Institute of Aerospace Techniques (INTA). Moreover, it is important to underline also the collaboration relations with Airbus Military and the Universidad Politécnica de Madrid (UPM).

REFERENCES

[1] Richardson MOW, Wisheart MJ. Review of low-velocity impact properties of composite materials. Compos A: Appl Sci Manuf 1996;27(12):1123–31.
[2] Kärger L, Baaran J, Gunnion A, Thomson R. Evaluation of impact assessment methodologies. Part I: applied methods and Part II: experimental validation. Compos A: Appl Sci Manuf 2009;40(1):71–6.
[3] Elder DJ, Thomson RS, Nguyena MQ, Scott ML. Review of delamination predictive methods for low speed impact of composite laminates. Compos Struct 2004;66(1–4):677–83.
[4] Xu S, Chen PH. Prediction of low velocity impact damage in carbon/epoxy laminates. Procedia Eng 2013;67:489–96.
[5] Shi Y, Swait T, Soutis C. Modelling damage evolution in composite laminates subjected to low velocity impact. Compos Struct 2012;94:2902–13.
[6] Lord S. GARTEUR AG28 Impact damage and repair of composite structures, Work element 1:Benchmark test data. QinetiQ/FST/WP041078/A. QinetiQ; 2004.
[7] Corporation MSC.MSC.Marc 2005.MSC.Dytran 2005 and 2008. MSC.Patran 2005 and 2008.
[8] Wiggenraad JFM, de Boer A, Frijns RHWM. Impact simulation of a frangible approach light structure by an aircraft wing section. National Aerospace Laboratory 2000; NLR-TP-2000-618.
[9] Wiggenraad JFM, Zimcik DG. Frangibility of approach lighting structures at airports. National Aerospace Laboratory 2001; NLR-TP-2001-064.
[10] Aerodrome Design Manual. Part 6: Frangibility. ICAO Doc 9157-AN/901 P6; First edition 2006.
[11] Pérez JL, Benítez LH, Oliver M, Climent H. Survey of aircraft structural dynamics nonlinear problems and some recent solutions. Aeronaut J 2011;115(1173):653–668.
[12] Kinnersley S, Roelen A. The contribution of design to accidents. Safety Sci 2007;45(1–2):31–60.
[13] Bin Y. Blade containment evaluation of civil aircraft engines. Chin J Aeronaut 2012;26:9–16.
[14] Guida M, Marulo F, Meo M, Russo S. Certification by birdstrike analysis on C27J full-scale ribless composite leading edge. Int J Impact Eng 2013;54:105–13.

[15] Bin Y, Zhou Y. Icing certification of civil aircraft engines. Procedia Eng 2011;17:603–15.
[16] Zhang H, Li X. Certification considerations for minimizing hazards caused by uncontained turbine engine and auxiliary power unit rotor failure. Procedia Eng 2011;17:521–8.
[17] Wang F, Sun Y, Zeng H. Study of uncontained turbine engine rotor failure airworthiness compliance verification method. Procedia Eng 2011;17:531–41.
[18] Huyse L, Enright MP. Efficient statistical analysis of failure risk in engine rotor disks using importance sampling techniques. 44th American Institute of Aeronautics and Astronautics; 2003–1838.
[19] Armendáriz I, López J, Olarrea J, Oliver M, Climent H. Case study: analysis of the response of an aircraft structure caused by a propeller blade loss. Eng Fail Anal 2014;37:12–28.
[20] Sinha S. Rotordynamic analysis of asymmetric turbofan rotor due to fan blade-loss event with contact-impact rub loads. J Sound Vib 2013;332:2253–83.
[21] Kushan MC, Diltemiz SF, Sackesen I. Failure analysis of an aircraft propeller. Eng Fail Anal 2007;14:1693–700.

CHAPTER

3 The evolution of failure analysis at NASA's Kennedy Space Center and lessons learned

Maria C. Wright, Victoria L. Long, Steven J. McDanels
National Aeronautics and Space Administration (NASA), Kennedy Space Center, Florida, USA

CHAPTER OUTLINE

1 INTRODUCTION

The United States has had four manned launch programs and three station programs since the era of human space flight began in 1961. The launch programs, Mercury, Gemini, Apollo, and Shuttle, and the station programs, Skylab, Shuttle-Mir, and the International Space Station (ISS), have all been enormously successful, not only in advancing the exploration of space, but also in advancing related technologies. As each subsequent program built upon the successes of previous programs, they

Handbook of Materials Failure Analysis With Case Studies from the Aerospace and Automotive Industries.
http://dx.doi.org/10.1016/B978-0-12-800950-5.00003-X

similarly learned from their predecessors' failures. While some failures were spectacular and captivated the attention of the world, most only held the attention of the dedicated men and women working to make the missions succeed.

2 LONG-DURATION SPACE OPERATIONS

2.1 SKYLAB

The first US-made orbiting space station was Skylab. Made from Apollo-era hardware, the experimental space station would serve as a location for science experiments, solar and Earth observations, and evaluation of the response of the human body to a microgravity environment. Three missions to Skylab resulted in over 300 science experiments on solar astronomy, Earth observations, human response to the space environment, and materials science. NASA's Kennedy Space Center was tasked with launching the hardware and the crew using legacy facilities from the Apollo program.

The two primary goals of the Skylab program were to prove that humans could live in space for extended periods of time and to expand our knowledge of solar astronomy using a space-based telescope. Each of the three crews that partook in the Skylab program were trained to use the astronomical telescope, photograph the Earth at selected wavelengths, perform experiments of material behavior in microgravity, and study their own response to space environment through a myriad of medical experiments. Experiments were completed over a period of 171 days and 13 h, including over 200,000 frames returned to Earth from solar astronomy and Earth observations.

Successes from the Skylab program could have been overshadowed by accidental early deployment of a meteor shield during launch which was then torn off by atmospheric drag, causing problems maintaining a constant internal module temperature. A parasol-like shield was designed, then launched, and deployed by the first Skylab crew thus fixing the problem (Figure 3.1). Skylab maintained its near-circular orbit at an altitude of 435 km (270 mile) throughout the life of the program, and remained on orbit for another 5 and 1/2 years until it re-entered Earth's atmosphere and disintegrated over the Indian Ocean and Western Australia in 1979.

2.2 INTERNATIONAL SPACE STATION

Following the successes of the Skylab program, there was great interest within the scientific community to construct another orbiting station for conducting further research that could only be performed in microgravity or low-Earth orbit (LEO). Skylab was not designed to be permanently occupied. In 1984, NASA was given an initiative to design another space station. It was proposed that the new space station would be an international collaboration including Canada, Japan, and the partners of the European Space Agency (ESA) (i.e., Belgium, Denmark, France, Germany, Italy, the Netherlands, Norway, Spain, Sweden, Switzerland, and the

FIGURE 3.1

Skylab orbiting the Earth, as seen by a departing crew capsule after one of the long-duration missions. The parasol-like repair shield is seen at the bottom of the image, a fix that enabled mission and program success.

United Kingdom), with the intention that it be used for space experiments, satellite repairs, and as an intermediate base for space exploration. The concept of space station Freedom arose from these requirements [1]. In the 1990s, the design was streamlined and the international collaboration extended to include Russia, thus the start of the ISS. Five space agencies were an integral part of the construction: NASA, the Russian Space Agency Roscosmos, the Canadian Space Agency, the ESA), and the Japan Aerospace Exploration Agency (JAXA). The first NASA node, Unity, was launched in Space Shuttle Endeavour from the Kennedy Space Center during Space Transportation System (STS) mission 88 in December of 1998. Construction of the ISS was carried out over 14 years with over 115 space flights on five different launch vehicles with coordination of all the international partners and included ESA's Columbus module and JAXA's Kibo module. Figure 3.2 shows the relative length of the "backbone" of the ISS, with a truss length of 357.5 feet, solar array length of 239.4 ft, mass of 924,739 lbs. and habitable volume of 13,696 ft^3 [2].

NASA KSC was responsible for launching 28 major components during station assembly. As various pieces of hardware, including pressurized compartments and structural trusses, were processed at KSC, troubleshooting problems on the ground was of the utmost importance in ensuring successful integration in space. The team knew that there was only one chance to get everything right. However, as meticulous as the NASA and contractor team was from design to launch of hardware, there were unforeseen problems that arose after construction. One such problem necessitated the

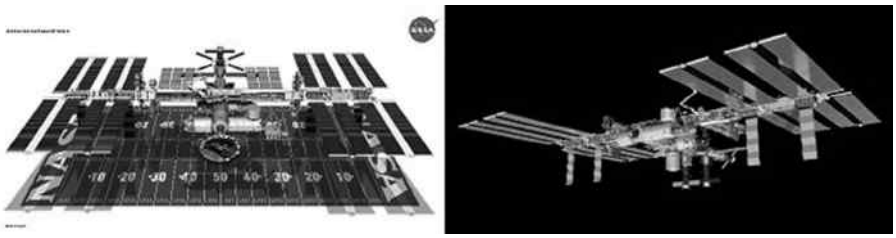

FIGURE 3.2

Relative size of the completed ISS in relation to the U.S. football field (left) and final configuration of the ISS after completion of construction (right).

assistance of engineers across the United States to perform failure analysis on hardware that was already in LEO.

3 FAILURE IN LEO: THE SOLAR ALPHA ROTARY JOINT

3.1 STS-117 MISSION OVERVIEW

On 8 June 2007, the Space Shuttle Atlantis lifted off from Launch Complex 39A at the Kennedy Space Center to deliver the S3/S4 truss segment to the ISS as part of ISS assembly flight 13A. The STS-117 mission was the fifth Space Shuttle launch after the Space Shuttle Columbia disaster and the third ISS assembly mission after the Return to Flight. The hardware delivered during the STS-117 mission was to be located on the starboard side of the ISS and was designated as the S3/S4 truss segments, which was the 8th of 11 total segments that would go on to form the Integrated Truss Structure. The trusses form the 357-ft-long backbone of the ISS and are attached to the pressurized modules that are the living, storage, service, and laboratory space for the ISS crew [3].

The Solar Array Wings are also attached to the Integrated Truss Structure and provide the power to the ISS. The S3/S4 truss segment provided the attach-point for the first set of starboard-side Solar Array Wings and also contained the starboard Solar Alpha Rotary Joint (SARJ), which is the mechanism for rotating the solar arrays for alignment with the sun [3]. The portside SARJ had been installed during the STS-115 mission in late 2006 as part of the mirror-image P3/P4 truss segment and had been in operation since that time [4].

3.2 SARJ HARDWARE OVERVIEW

The SARJ is 10.5 ft in diameter, weighs over 2500 pounds, and is used to position the solar arrays to track the sun during orbit as shown in Figure 3.3. The SARJ is capable of power and data transfer across the rotating joint interface, thereby allowing for a full 360° rotation approximately once every 90 min in sync with the orbit of the ISS [3].

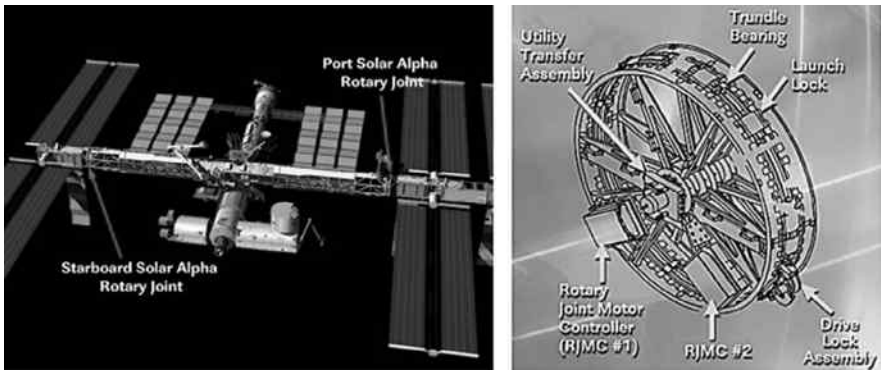

FIGURE 3.3

Location of port and starboard SARJ on the truss of the ISS (left) and details of the SARJ mechanism (right).

The SARJ consists of 2 race rings, 12 independent Trundle Bearing Assemblies (TBAs), 2 Drive Lock Assemblies, and 2 Rotary Joint Motor Controllers. The race rings have a triangular cross-section and are composed of nitrided 15-5 precipitation hardened (PH) stainless steel forgings. The inboard race ring is stationary and the TBAs are fixed to this race ring. The outboard race ring rotates using the Drive Lock Assemblies, which are controlled by the Rotary Joint Motor Controllers. TBA rollers, which are oriented in a triangle that correlates with the race ring cross-section, ride on the outboard race ring and provide a mechanical connection between the two race rings. The rollers are composed of 440C stainless steel and are gold-plated to provide lubrication between the roller surface and the race ring [5].

3.3 STS-117 MISSION DETAILS

After an overnight stay in the Quest airlock in order to remove nitrogen from their bloodstreams, astronauts Danny Olivas and Jim Reilly performed the first extravehicular activity (EVA) for the mission to install the mechanical and electrical connections for the S3/S4 truss segment using the Canadarm 2 with the help of their fellow STS-117 crew [6]. During the second and fourth EVAs, astronauts Patrick Forrester and Steven Swanson removed the launch locks and restraints so that the SARJ would be free to rotate when activated [7]. ISS flight controllers at the Johnson Space Center tested and activated the SARJ, resulting in four fully operational solar arrays powering the ISS by the end of the STS-117 mission. The crew was cleared for landing, returning Astronaut Suni Williams home from a record-breaking 189-day stay aboard the ISS [8].

4 THE PROBLEM

Approximately, 3 months after the installation of the starboard SARJ, the health and status data for the joint revealed a potential issue with the mechanism. The first anomalous sign of a problem was an increasing difference between the velocity that was commanded and the actual velocity of the joint, as seen at Mission Control in the Johnson Space Center. An extensive ground investigation was initiated to find the cause, resulting in the software and controller being cleared, thereby indicating a mechanical problem with the starboard SARJ. Additional signs of an issue were becoming evident and the primary focus was now on the increased current that was necessary to drive the Rotary Joint Motor Controllers, which directly correlated to the SARJ torque. Over a period of 2 months, the necessary current to drive the joint had first doubled and then quadrupled over nominal, indicating that the torque was dangerously close to margin and could possibly lead to an unrecoverable situation [5].

4.1 TROUBLESHOOTING DURING THE STS-120 MISSION

The next planned mission to ISS was STS-120 on Space Shuttle Discovery. STS 120 launched on October 23, 2007 primarily to deliver the Harmony module to the ISS, a water, air, and power hub that would redirect resources to a number of laboratory modules set to launch in 2008. The crew also had a busy EVA schedule involving the relocation of a portside truss segment so that power could be provided from an additional Solar Array Wing [9].

During the second EVA, a task was added to the planned activities for astronaut Dan Tani: to inspect the Multi-Layer Insulation covers on the starboard SARJ for evidence of the cause of the anomalous data, such as a micrometeoroid impact or an interference problem. Upon finding no external cause of the problem, Tani removed the insulation cover and observed apparent metallic debris gathered on the magnetic TBA and a mottled appearance of the race ring surface. Tani gathered fragments using polyimide tape so that the pieces could be returned for analysis by engineers on the ground [10].

Concerns over the damage observed during the inspection resulted in a decision by mission managers to limit the starboard SARJ operation, to inspect the portside SARJ during the third EVA, and to devote the fourth EVA to an in-depth inspection of the starboard SARJ. Astronaut Scott Parazynski reported that the portside race ring had no observable damage, thereby allowing continued operation of the port SARJ [11].

The priority for the fourth EVA abruptly changed when a tear occurred in a blanket during the deployment of a portside solar array, which was one of the Discovery crew's primary mission objectives. With the available time for the STS-120 mission quickly dwindling, the fourth EVA was dedicated to fixing the solar array issue; further inspection of the starboard SARJ was postponed to a later mission [12]. The initial root cause investigation for the SARJ anomaly would be solely dependent on the three pieces of polyimide tape with debris collected during Tani's EVA as shown in Figure 3.4.

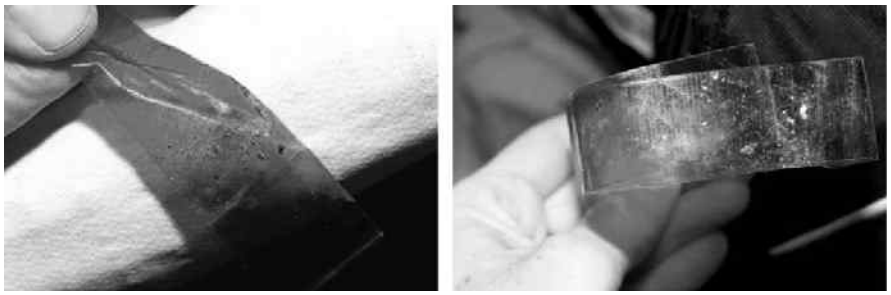

FIGURE 3.4

On-orbit images of debris samples on polyimide tape that needed to be returned to Earth for failure analysis.

Credit: NASA.

4.2 INITIAL KSC SARJ INVESTIGATION

In early November of 2007, materials engineers from across several NASA centers and contractor organizations were in discussions about the potential root cause of the debris generation and developed a test plan to analyze the returning debris. The initial analysis of the debris would determine the failure mechanism based on surface morphology and determine the source of the debris through elemental analysis. The Failure Analysis Laboratory at the Kennedy Space Center was ready to implement that plan when space shuttle Discovery landed in Florida on November 2007 at 1:01 PM. The test plan included photodocumentation, stereomicroscopy, scanning electron microscopy with both secondary and backscattered electron detection, and energy dispersive spectroscopy. Once the initial analysis was completed, further work would be performed to characterize the debris using laser confocal microscopy and metallography. The team initiated the failure analysis as soon as the samples were destowed and delievered to the laboratory, at approximately 4:30 PM, and concluded their initial analysis in less than 10 h. Because of the unique nature of the samples, work had to be expedited yet proper handling and documentation was of the utmost importance. Figure 3.5 shows the team during the removal of the samples in preparation for detailed photodocumentation.

The three pieces of polyimide tape collected by astronaut Tani and returned to Earth were photodocumented and initially observed in a stereomicroscope. The particles sizes for the debris ranged from very fine particulate less than 100 μm up to approximately 1 mm. The first significant observation was apparent machine markings still present on the surface of some of the larger fragments and fracture features visible on other fragments (Figure 3.6). Additionally, the debris was classified as fine particulates, flattened agglomerations, and large chips. The debris had a slight magnetic response [13].

Energy dispersive X-ray spectroscopy (EDS) via a scanning electron microscope (SEM) used in variable pressure low vacuum mode gave the first definitive answer about where the debris originated. The ISS SARJ system engineers had determined that the four most probable sources of the debris were the nitrided 15-5 PH stainless

FIGURE 3.5

Meticulous handling of the starboard SARJ samples was carried out by the team during the investigation.

Credit: P. Marciniak/NASA KSC.

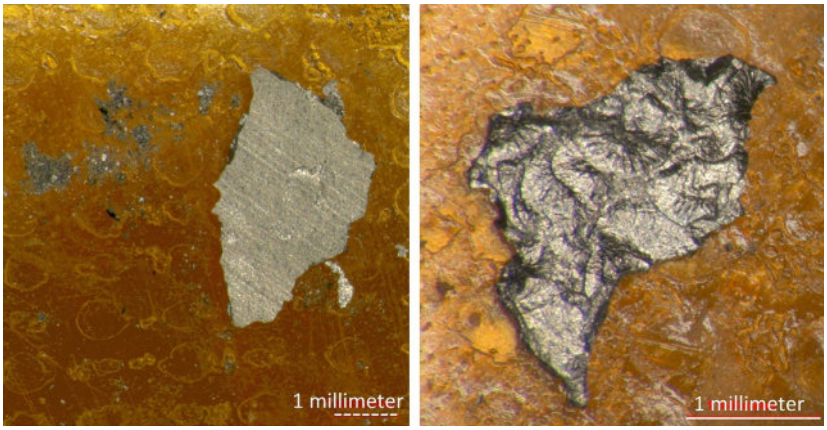

FIGURE 3.6

Stereomicroscopic inspection revealed that the shards included both original surface finish (left) and fracture features (right).

Credit: T. Long & C. Wright/NASA KSC.

steel race ring, the gold-plated 440C stainless steel rollers from the TBA, the gold-plated 13-8 Mo stainless steel pinions, and the nickel-phosphorous plated 17-7PH stainless steel centering springs. Since the EDS analysis clearly showed that the debris shards were composed of 15-5PH stainless steel with nitrogen present throughout the samples, the source of the debris was determined to be the nitrided

case of one of the starboard SARJ race ring surfaces. The only other metal fragments present on the tape were a small number of isolated gold pieces, which originated from the gold-plated 440C rollers.

SEM observation of the debris revealed the clues that started to tell the story about what had happened to the SARJ race ring. The machine markings on some of the larger fragments were again confirmed via the SEM and when one of these fragments was flipped over, fracture features were revealed. The debris shards displayed classic evidence of Hertzian contact stress failure, with fracture paths parallel to the outer surface [14]. These fracture features were relatively brittle in nature, resembling a progressive failure with crack arrest marks clearly evident (Figure 3.7). Niobium-rich precipitates, verified via EDS and typical for this alloy, appeared at the subsurface initiation sites of the fractures.

Laser confocal microscopy (Figure 3.8) and metallography were both used to characterize the thickness of the debris, which indicated that the debris generation was limited to the nitride case. However, M&P engineering was concerned by the observation of extrusion-like damage and agglomerated fine particulate, which indicated that further damage was occurring and failure of the race ring could be exacerbated by the presence of this debris.

4.3 NASA SARJ INVESTIGATION

Further investigation and sampling was necessary to determine why the race ring was failing and what could be done to preserve the operation of the solar arrays. In order for NASA to meet international partner commitments, this investigation had to

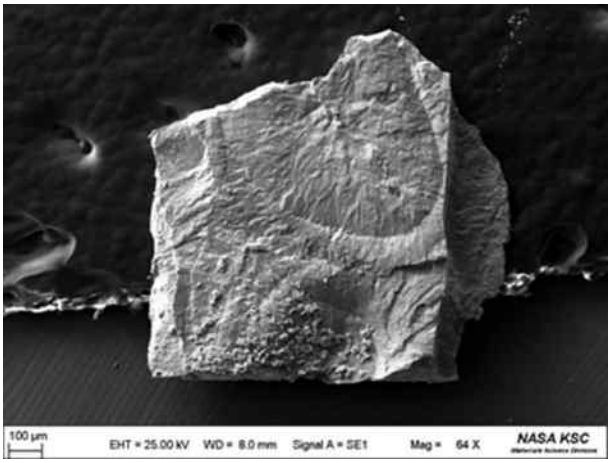

FIGURE 3.7

SEM micrograph of a larger starboard SARJ chip showing subsurface crack initiation at Nb-rich precipitates and crack arrest marks.

Credit: T. Long & C. Wright/NASA KSC.

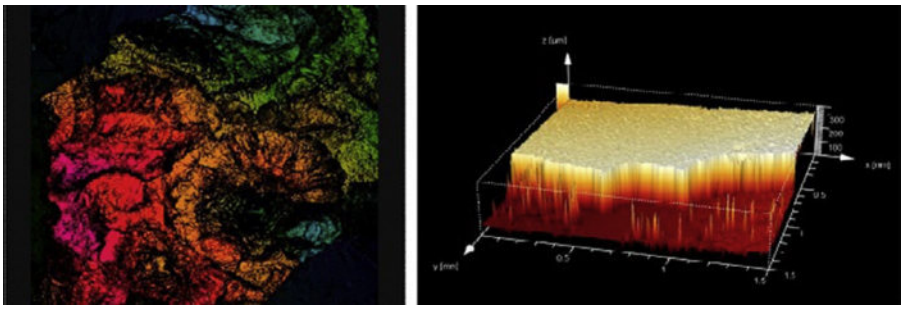

FIGURE 3.8

Laser confocal microscopy was utilized to nondestructively measure the thickness of the starboard SARJ debris.

Credit: C. Wright/NASA KSC.

progress quickly. The addition of the ESA Columbus module and the Kibo Japanese Experiment Module was going to require the power production capability of both the portside and starboard solar arrays [15].

A team comprises civil servant and contractor engineers, scientists, and technicians across six NASA centers and private companies spread throughout the United States spent the next 2 years on the analysis and repair of the starboard SARJ race surface failure [16].

4.4 EXPEDITION 16 SAMPLE ANALYSIS

In December of 2007, approximately a month after the original failure analysis at the KSC laboratory, Expedition 16 astronauts Dan Tani and Peggy Whitson performed a nearly 7-h EVA which focused on inspecting the starboard SARJ race rings and bearings beneath 16 of the 22 drive lock assembly covers. Various amounts of the similar types of debris were observed, while one of the TBAs was removed for evaluation back on Earth. During EVAs 13 and 14, 29 tape samples, containing hundreds of fragments of debris, were collected. High-resolution photographs of the raceway surfaces revealed surface degradation with debris adhering to the TBAs (Figure 3.9).

The 29 tape samples and TBA removed during Expedition 16 could not be returned to Earth until the return of the next Shuttle mission, STS 122, due to space limitations. The samples were finally delivered to the NASA Failure Analysis Laboratory at the Kennedy Space Center in February of 2008 for analysis. Analysis determined that the chips collected during the Expedition 16 EVAs 13 and 14, as well as those harvested from the removed TBA, were similar in appearance, composition, and failure mode to those analyzed from the first SARJ debris samples returned on STS-120. Predominantly, nitrided 15-5PH chips were present as both fine debris and fractured fragments. The fine debris was observed in three forms: as individual particles, as particles agglomerated but with little mechanical adhesion, and as agglomerates that appeared rolled and exhibiting an extruded appearance. It was determined that the majority of the debris was less than 50 μm in diameter and

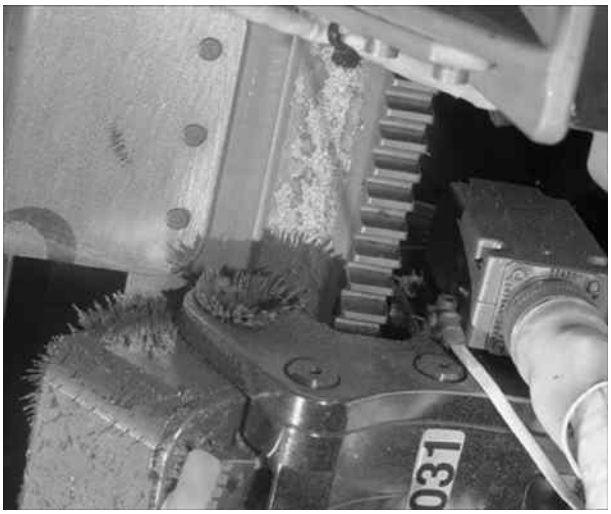

FIGURE 3.9

On-orbit photograph of one of three raceway surfaces of the starboard SARJ during Expedition 16 EVA showing damage to the race and magnetized debris on the TBA.

Credit: NASA.

covered a significant amount of the tapes' surface areas. Based on thickness, composition, and microstructure, fracture was limited to the nitrided case of the primary race ring. Fragment thicknesses were comparable to those from the previous analysis and within the range of the hardened nitrided case specifications, which was required to be less than 170 μm. EDS verified the presence of nitrogen throughout the fragments. Etching of cross-sectional samples revealed the nitrided case layer microstructure and transgranular secondary microcracking. The SARJ fragments did not display a martensitic core microstructure or case-core interface, indicating that the spalling was limited to the nitrided case. Figures 3.10–3.13 show representative samples from the investigation [17,18].

Of particular interest to the Agency-wide investigation team was the presence of gold plating that was the intended lubricant for the contact surface between the 15-5PH race ring and the 440C TBA rollers [19]. The gold plating should have been metallurgically bonded to the substrate, but Figure 3.14 shows that microscopy tape could easily detach the plating in ribbons. Additional investigation by the engineering team revealed that the loss of gold plating was occurring on flight spares, and that artificially aged samples from new gold-plated rollers were experiencing a loss of adhesion due to corrosion at the interface between the plating and substrate. The resulting inadequate lubrication led to high levels of friction and contact between the race ring and the rollers. As subsurface loads transitioned to the case/core interface of the nitride race ring, spalling initiated at subsurface discontinuities, specifically niobium-rich precipitates which acted as stress concentrators. It was theorized that weak magnetic forces in the microgravity environment caused the debris

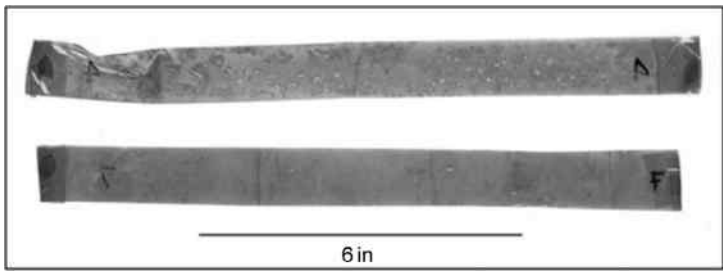

FIGURE 3.10

Photograph of two representative SARJ sample tapes from the Expedition 16 spacewalks showing dust-like fine debris covering the majority of the adhesive tape surface as well as some larger fragments that were evident when visually inspected.

Credit: P. Marciniak/NASA KSC.

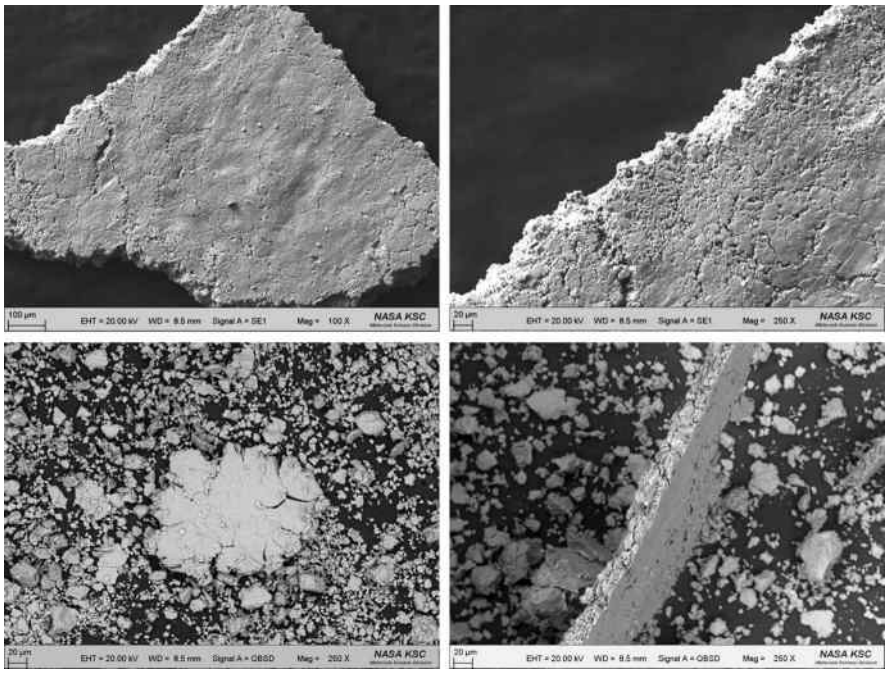

FIGURE 3.11

Representative SEM micrographs of agglomerated (top) and extruded (bottom) SARJ particles from Expedition 16 EVA.

Credit: C. Wright/NASA KSC.

to stay within the SARJ, causing the larger chips to be pulverized and then agglomerate. An additional conclusion by the investigation team was that the SARJ design had a kinematic susceptibility to tip due to roller mistracking, which, combined with the high frictional forces, led to high roller-edge stresses and resulted in the 15-5PH race surface spalling at the nitride case [20].

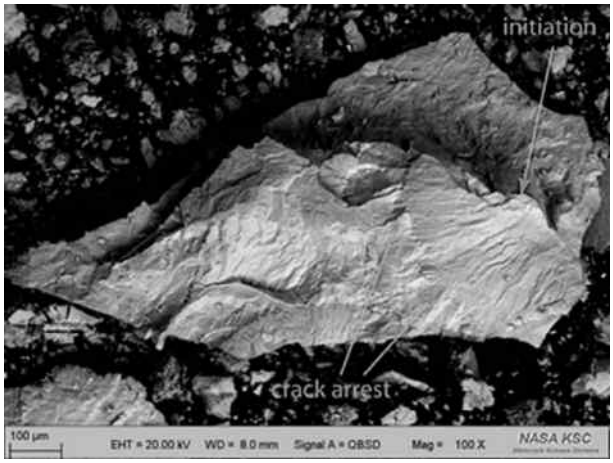

FIGURE 3.12

Fracture features of the Expedition 16 EVA samples were similar to those from the original STS 120 samples, with subsurface crack initiation and crack arrest marks.

Credit: C. Wright/NASA KSC.

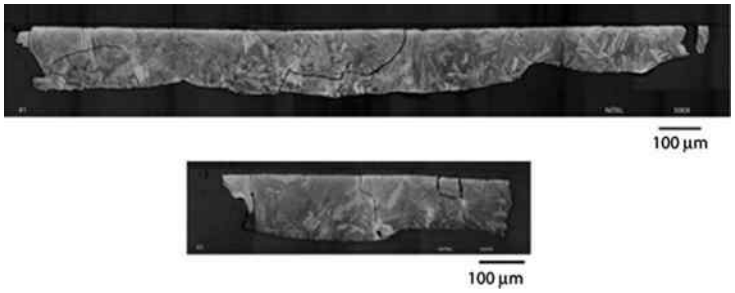

FIGURE 3.13

Etched starboard SARJ fragment showing transgranular crack propagation and fracture within the nitride case of the 15-5 PH race surface.

Etchant: Diluted Nital. Credit: P. Marciniak & B. Tucker/NASA KSC.

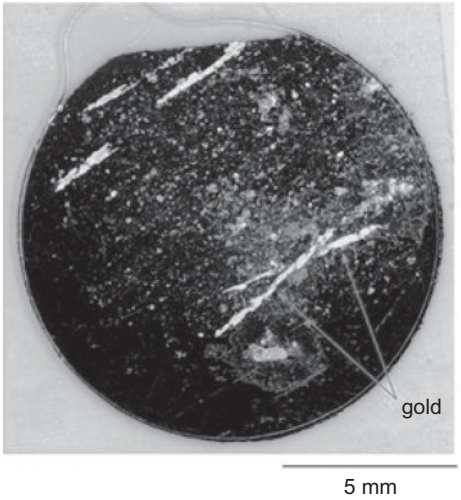

FIGURE 3.14

Stereomicroscope image of TBA sample, taken from an inner 45 roller surface. Gold plating was observed flaking off of the roller sides as samples were prepared.

Credit: C. Wright/NASA KSC.

4.5 POSTANALYSIS ON-ORBIT INSPECTION

The starboard SARJ was not allowed to function in normal mode until the debris was cleaned and the race surface was again considered to be fully functional. During STS-124 in June of 2008, spacewalkers Mike Fossum and Ron Garan demonstrated techniques to clean the debris, including using a specially designed grease gun to lubricate the outer race ring (Figure 3.15), and replaced one of the TBAs [21]. The port SARJ, which was functioning nominally, was inspected. Small amounts of debris were collected and returned to Earth for analysis.

4.6 THE REPAIR ON STS-126, NOVEMBER 2008

After the investigation team concluded that high frictional forces due to a lack of lubrication were causing the spalling, NASA decided to use Braycote grease during the STS-126 mission (Figure 3.16) in November of 2008 to provide a lower coefficient of friction. Braycote grease is vacuum-stable grease that was designed for the extreme environment of space. On the starboard SARJ, the debris was cleaned using terry cloth EVA wipes and a scraper tool for the flattened pieces, followed by a greased wipe on all surfaces. The grease gun that was tested during STS-124 was used to apply the Braycote to both the starboard and the port SARJ race ring surfaces. The SARJs were then rotated to allow the rollers in the TBAs to spread the lubricant. The TBAs on the starboard SARJ that had suspect gold plating and were covered with debris were replaced during an EVA in the course of STS-126 [22]. Although the starboard SARJ has a redundant inboard race ring, it was decided at the time not to use the redundancy so as to maintain an available back-up. At the time it was expected that a long-term fix, including a race re-design, was going to be required.

FIGURE 3.15

Astronauts Mike Fossum and Ron Garan testing a grease gun specifically designed to aid in cleaning of the starboard SARJ race ring debris.

Credit: NASA.

FIGURE 3.16

Astronaut Shane Kimbrough removing debris and applying lubrication around the starboard SARJ during the STS-126 mission's second spacewalk.

Credit: NASA.

However, the cleaning and lubricating procedures' efficacy resulted in reverting to continuous autotrack operations for the starboard SARJ in 2010 [23,24]. Had the permanent repair been necessary, it would have taken 10 spacewalks for installation of a new race ring assembly.

4.7 WHAT ABOUT THE PORT-SARJ?

The port SARJ was inspected during various spacewalks as the starboard SARJ investigation was underway. The port SARJ had been installed and activated during STS-115 in September of 2006 and had been operating nominally. As a preventative measure, the port SARJ was lubricated during STS-126 in November of 2008 and relubricated after 3 years of greased operation in May of 2011 during STS 134 [24]. Analysis of debris sampled during the relubrication operation in 2011 revealed very small amounts of wear debris from the port race ring-nitrided case. It was decided that monitoring of the mechanism would be carried out using telemetry data of the SARJ current loads.

5 CONCLUSION

By its very nature, the exploration of space is wrought with difficulty. Failure is an ever-present possibility. One can either ignore the failure and its cause and press on, or learn from that failure. Failure analysis at the Kennedy Space Center has evolved

from the early space programs to today. Advances in equipment have made the field more portable, usually taking materials engineers and failure analysts to the launch pads, vehicles, and associated facilities to perform *in situ* failure analysis. As NASA continues to extend long-duration missions on the ISS and explore deep space, remote failure analysis is a necessity. Cross-country and international teams comprise experts from government, industry, and academia, working in concert with deployed astronaut crews, must overcome many barriers to communicate the technical facts, while working toward the same goal: the safest possible exploration beyond Earth.

REFERENCES

[1] NASA's Space Station Program: Evolution and Current Status, Testimony before the House Science Committee; April 4, 2001.
[2] International Space Station Facts and Figures, http://www.nasa.gov/mission_pages/station/main/onthestation/facts_and_figures.html; February 6, 2014.
[3] STS-117 Press kit. June 2007, www.nasa.gov.
[4] STS-115 Press kit. August 2006, www.nasa.gov.
[5] The International Space Station Solar Alpha Rotary Joint Anomaly Investigation, NASA; 2009.
[6] STS-117 Status report # 14. June 2007, www.nasa.gov.
[7] STS-117 Status report #20. June 2007, www.nasa.gov.
[8] STS-117 Status report #21. June 2007, www.nasa.gov.
[9] STS-120 Press kit. October 2007, www.nasa.gov.
[10] STS 120 Status report #12. October 2007, www.nasa.gov.
[11] STS-120 Status report #16. October 2007, www.nasa.gov.
[12] STS-120 Status report #18. October 2007, www.nasa.gov.
[13] STS-120 International Space Station (ISS) Starboard Solar Alpha Rotary Joint (SARJ) Debris Analysis, Internal report KSC-MSL-2007–0499.
[14] Wulpi, DJ, Understanding How Components Fail. ASM International, p. 199; 1985.
[15] http://www.thespacereview.com/article/1136/1; May 16, 2014.
[16] Golden J, Martinez J. Examination of Surface Residuals Obtained during Re-Lubrication of the International Space Station (ISS) Solar Alpha Rotary Joint (SARJ). Microscopy and Microanalysis (M&M); 2012.
[17] Wright MC. International Space Station (ISS) Expedition 16 Starboard Solar Alpha Rotary Joint (s-SARJ) Debris Analysis. Internal report KSC-MSL-2008–0099; 2008.
[18] McDanels S, Wright MC, Salazar V, Lubas D, Tucker B. Logistical and analytical approach to a failure aboard the international space station. Society for the Advancement of Material and Process Engineering (SAMPE), Japan International SAMPE Symposium & Exhibition, Tokyo, Japan, 2009.
[19] Basta E, Dagupta R, Figert J, Jerman G, Wright C, Petrakis D. Solar alpha rotary joint anomaly: the materials & processes perspective. In: J. Golden. Aging Aircraft 2009 Conference; 2009.
[20] NASA Engineering Safety Center (NESC) support to the ISS SARJ Investigation, http://www.nasa.gov/offices/nesc/home/Feature_SARJ_051809.html; October 7, 2014.

[21] STS124 (June 2008) Mission Status Updates (http://www.nasa.gov/rss/nasa-pao-rss.xml); June 23, 2014.
[22] STS126 Press kit. November 2008, www.nasa.gov.
[23] Station boss happy with SARJ and water recycler repairs; November 25, 2008, http://www.spaceflightnow.com/shuttle/sts126/081125fd12/index2.html; August 24, 2014.
[24] Golden J, Martinez J. Examination of Surface Residuals Obtained during Re-Lubrication of the International Space Station (ISS) Solar Alpha Rotary Joint (SARJ). Paper presented at Microscopy Microanalysis, Phoenix, AZ, 2012.

CHAPTER

4 Fleet impact resulting from a space shuttle Columbia main engine controller wire failure during Mission STS-93

Steven J. McDanels

National Aeronautics and Space Administration (NASA), Kennedy Space Center, Florida, USA

CHAPTER OUTLINE

Space Shuttle mission STS-93 is notable for being the first NASA mission with a female commander, Eileen Collins, and for launching the Chandra X-ray Observatory, the most advanced X-ray observatory in existence at the time of its launch. It is also notable for bringing to light a concern over the condition of electrical wiring used throughout the orbiter fleet. The Space Shuttle Columbia lifted off from NASA Kennedy Space Center Launch Complex 39B on July 23, 1999 (Figure 4.1). Approximately 5 s after lift-off, NASA flight controllers observed a drop in voltage in one of Columbia's electrical buses [1]. The voltage drop caused a disabling of the primary digital control unit (DCU-A) for the center engine and the backup digital control unit (DCU-B) for the right engine. However, with built-in primary/backup redundancy for each engine, the ascent was able to proceed and a contingency abort was averted despite the loss of redundancy. Once orbit had been achieved, NASA flight controllers requested that the crew verify that the circuit breaker for the suspect main engine controller had indeed opened; the astronauts verified that the breaker had opened, indicating that the issue was local and not wider ranging [1].

Following a successful mission, the Columbia returned to Earth on July 28, 1999; post-flight inspection revealed that a main engine controller wire had arced against the head of an adjacent screw (Figure 4.2). Likewise, a second area of exposed conductor was observed on the same wire approximately 2 in. away from the arced region. The second area of damage was also located above a nearby screw.

Handbook of Materials Failure Analysis With Case Studies from the Aerospace and Automotive Industries.
http://dx.doi.org/10.1016/B978-0-12-800950-5.00004-1

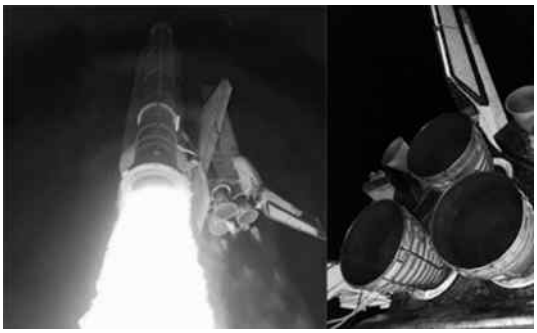

FIGURE 4.1

Launch of STS-93. The Columbia's three main engines functioned nominally despite the loss of redundancy of the primary digital control unit (DCU-A) for the center engine and the backup digital control unit (DCU-B) for the right engine (SSMEs during lift-off, left; SSMEs after touch-down, right).

Credit: NASA.

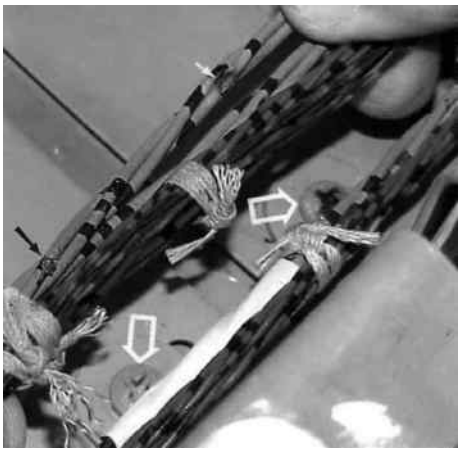

FIGURE 4.2

Arced wire (solid white arrow) and nearby damaged area (solid black arrow) with associated screws (open white arrows) in the midbody aft port-side lower wire tray 11/12 frame.

1 SPACE SHUTTLE COLUMBIA WIRING HARDWARE OVERVIEW

The space shuttles each had over 200 mile of wiring, weighing over two-and-a-half tons, in addition to associated cables, conduits, and trays as well as hardware to house, route, and contain all of the materials. Although the initial investigation focused on only several inches of the wiring, the ramifications extended to all 200-plus miles of wiring aboard the Columbia, and impacted the entire Shuttle fleet [2].

The subject wire provided power to the digital control units and was a 14 American wire gauge (AWG) polyimide-insulated twisted three-wire conductor, with Kapton® polyimide insulation surrounding the nickel-plated copper conductor. The insulation was topcoated with an aromatic polyimide resin color coded to indicate AWG size, with green corresponding to 14 AWG and red to 20 AWG. Although the proximate cause of the loss of signal redundancy was found in the form of a short circuit caused by the wire arcing to an adjacent screw, the root cause of the arcing event had to be ascertained.

2 INVESTIGATION

A failure analysis was initiated to determine the cause of the main engine controller's short circuit. The shorted main engine controller wire and nearby damaged wire were located in the midbody aft port-side lower wire tray 11/12 frame (Figure 4.3). Both the arced screw and the screw beneath the second damaged area had exposed base metal where the screw head slots had been deformed. It should be noted that the wires 180° from the damaged areas appeared undamaged.

The shorted and nearby damaged wires were harvested along with their corresponding screws. Further inspection revealed that an additional seven other wires in the bundle also displayed varying degrees of damage; these wires were likewise removed from service for analysis.

Several intact wires were also removed for laboratory testing in order to simulate various forms of mechanical damage and generate exemplars. This testing consisted of the following methods: a step test, where a person literally stepped on a wire bundle that rested upon a screw head; a shear test that forced a screw head and a torque tip against a wire in an attempt to damage the insulation and conductor; a vibration test to determine if a wire bundle would abrade when vibrated against a screw head; an abrasion test to determine if the polyimide insulation would become damaged by

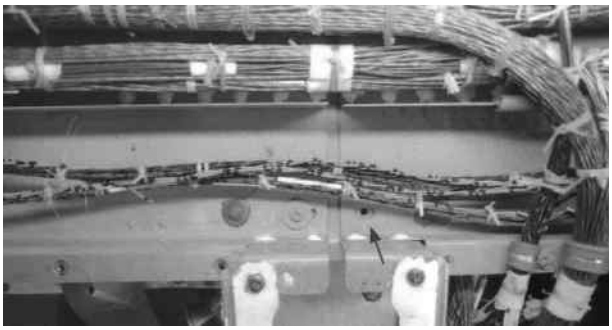

FIGURE 4.3

Shorted wire bundle with arced screw removed (arrow) in the midbody aft port-side lower wire tray 11/12 frame.

rubbing against helical convolex convoluted tubing; and an impact test to determine if convoluted tubing would protect a wire bundle from a foreign object strike, such as by a torque tip or screwdriver bit.

Visual and low-magnification examinations of the various wires were performed. The arced conductor wire (Figure 4.4) displayed several areas of mechanical damage adjacent to areas that appeared melted, corresponding to the region of arc tracking. Dark deposits of apparently burned material were evident over much of the exposed areas. Deposits were also evident covering some of the nearby mechanically damaged area. The topcoat adjacent to the shorted area appeared deformed. Similar examination of the screw head that the wire arced against revealed a definite region of arc-tracking damage (Figure 4.5). Raised areas of bare base metal were also evident on the sides of the slots in the screw head; these raised areas were devoid of paint.

Macroscopic examination of the second damaged area revealed that the insulation had been pushed up (Figure 4.6). Mechanical gouges on the conductors were observed. The directionality of the mechanical damage in this area corresponded well to that of the mechanical damage in the arced region.

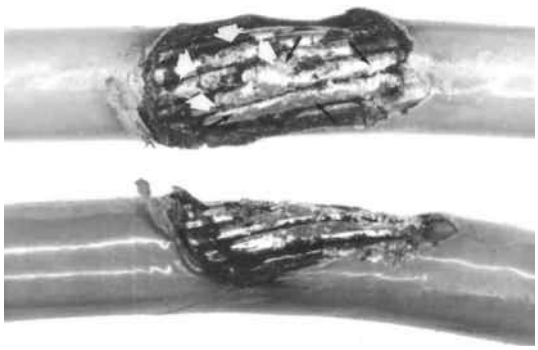

FIGURE 4.4

Rotational view of shorted wire displaying arced region (white arrows) and mechanically deformed region (black arrows).

FIGURE 4.5

Screw head displaying arc tracking and raised areas.

FIGURE 4.6

Mechanically damaged area approximately 2 in. from the shorted section of the main engine controller wire displaying deformation of the conductors and topcoat.

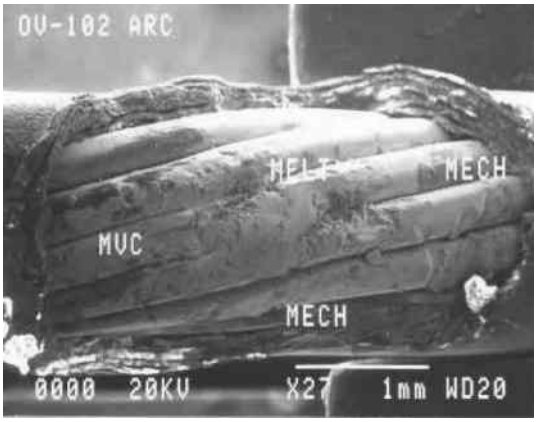

FIGURE 4.7

SEM micrograph of the damaged region of the shorted wire. Mechanical damage is evident on the conductors (denoted "MECH"). The melted region is between the "MELT" and "MVC" zones. Magnification: 27×.

Next, the wires were analyzed via scanning electron microscope (SEM), energy-dispersive X-ray spectroscopy (EDS), and electron spectroscopy for chemical analysis (ESCA). SEM analysis of the shorted wire verified that the polyimide insulation was missing in the arced area, with the wire's conductors clearly evident (Figure 4.7). It should be noted that the damaged insulation was even and smooth, as opposed to serrated. Three distinct topographical features were evident on the shorted wire: a mechanically damaged zone, a melted zone, and a zone displaying microvoid coalescence (MVC). The mechanically damaged zone appeared gouged (Figure 4.8). The damage was directional, roughly tangential to the length of the wire. The central portion of the exposed area contained a mixture of mechanical damage and melted metal (Figure 4.9). The melting was confined to the outer layer of wire strands and did not appear to penetrate to the inner strands. The final region of the exposed area displayed MVC (Figure 4.10), typical of ductile overload. The overload area corresponds to the region where the wire actually melted and fused with the screw head

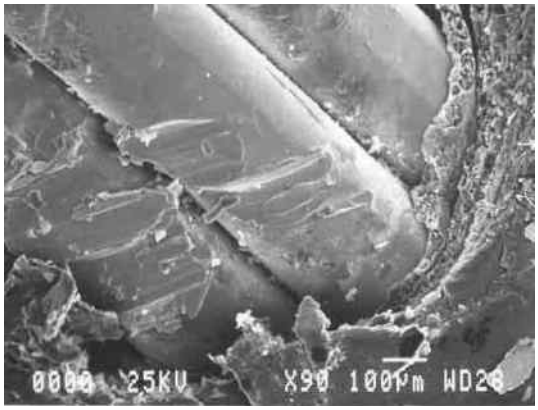

FIGURE 4.8

SEM micrograph of shorted wire displaying mechanical damage to the conductors. Magnification: 90×.

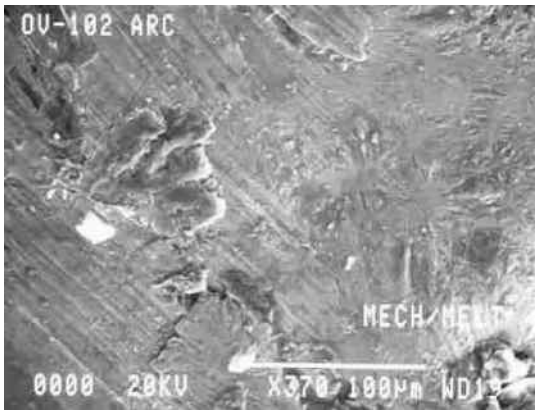

FIGURE 4.9

SEM micrograph of shorted wire illustrating mechanical damage and thermal damage. Magnification: 370×.

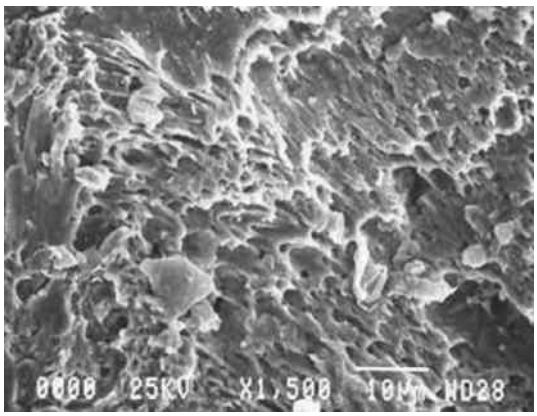

FIGURE 4.10

SEM micrograph of shorted wire displaying MVC, typical of ductile overload. Magnification: 1500×.

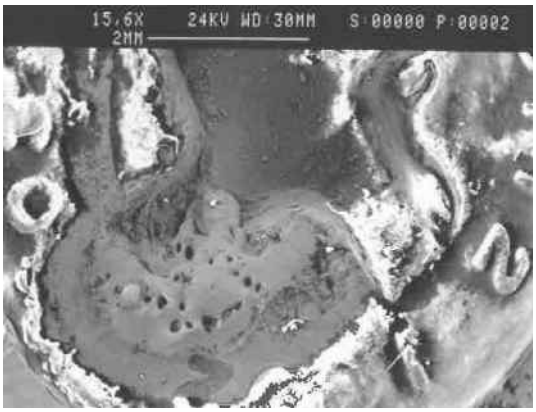

FIGURE 4.11

SEM micrograph of shorted screw head displaying area of resolidified metal and MVC. Magnification: 15.6×.

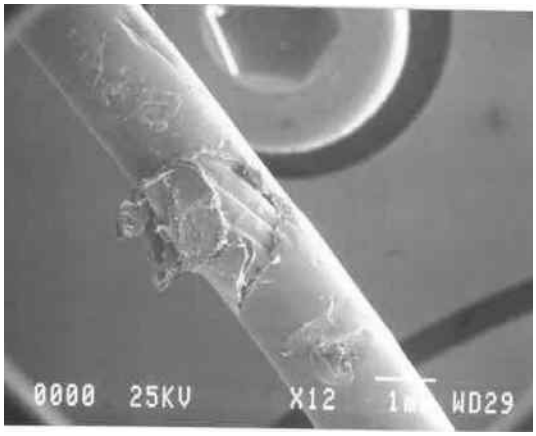

FIGURE 4.12

SEM micrograph of a second damaged area from the shorted wire. The conductors appeared mechanically damaged, with the topcoat pushed back. Magnification: 12×.

(Figure 4.11). SEM examination of the damage 2 in. from the shorted region of the controller wire showed evidence of mechanical damage but no arcing (Figure 4.12).

EDS and ESCA revealed the presence of nickel and copper on the arced screw head in the region of resolidified metal. ESCA, which typically has a surface sensitivity of approximately 10 nm, revealed the presence of an oxide layer on the shorted wire. The depth of this layer was compared to that of three laboratory exemplars: a freshly nicked portion of copper wire, a 2-week-old exposed piece of copper, and a sample that had been exposed a year previously during another investigation.

The depth of the oxide layer on the shorted wire was substantially thicker than that of either freshly exposed exemplar and was approximately four times thicker than the year-old samples. ESCA was then performed on an area of damage near the shorted section of wire that also had damaged conductors. A precise timeframe for when the damage to this region occurred could not be established with certainty, but based upon the topography, directionality, and extent of damage, it likely occurred concurrently to the mechanical damage found in the arced region. ESCA of this additional damage disclosed a substantially thicker oxide layer than that of the fresh exemplars and similar to that of the arced region. The thickness of the oxide layer indicated an approximate exposure time of 4-5 years [3,4].

Of the seven additional wires removed for analysis, neither damage to the conductor nor serration of the insulation was noted (Figures 4.13 and 4.14).

Mechanical tests were performed to duplicate the launch environment and damage characteristics of the service failure. Step tests, even under increasing effort and force, did not damage the conductor when forced against a smooth screw head. SEM examination of the step-test specimens showed only topcoat/insulator damage. No

FIGURE 4.13

Macrograph of typical damage observed on additional wires.

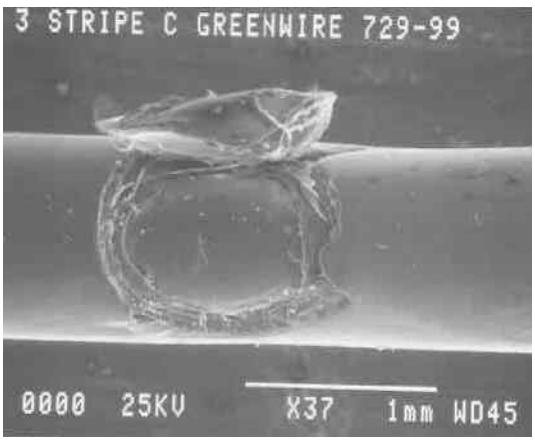

FIGURE 4.14

SEM micrograph of additional wire typifying topcoat and insulation damage. Magnification 37×.

conductor damage was observed (Figures 4.15 and 4.16). However, subsequent step testing performed after the primary investigation was concluded did cause damage to the conductor. Vibrational testing at frequencies ranging from 20 to 2000 Hz and loads varying from 600 to 2100 g damaged the conductor in the 2100 g range. Single event drop testing meant to simulate a sharp object impacting the bundle carried out with drop heights of 1-3 ft and loads of 900-20,000 g did not damage the conductor until 19,050 g were added to the impacting tool. Additional vibrational abrasion and drop testing verified that the convoluted tubing would be damaged before any damage to the conductor would occur.

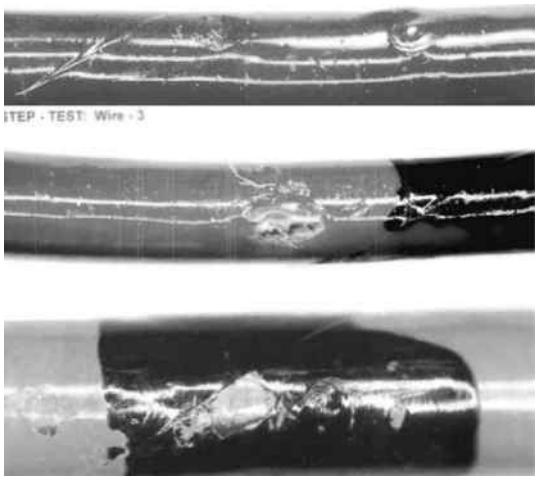

FIGURE 4.15

Typical step-test damage.

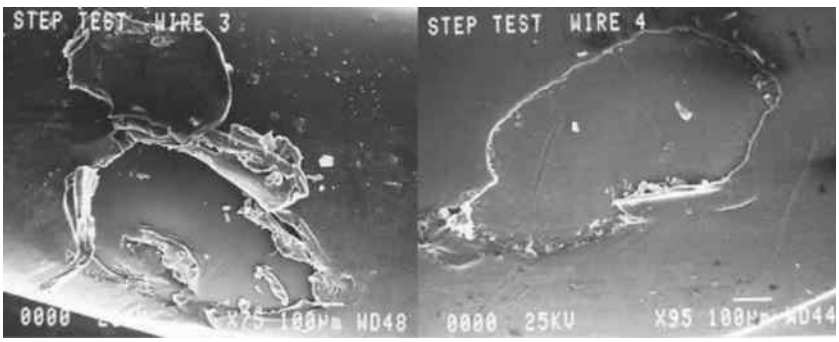

FIGURE 4.16

SEM micrograph of step-test exemplars. Mechanical deformation of insulation is evident with no damage to conductor. Magnification: 75×, 95×.

3 CONCLUSION

The subject main engine controller wire displayed evidence of mechanical damage, both in the arced region as well as the damaged area 2 in. away. ESCA results showed that the oxide layers in these regions were substantially thicker than the oxide layers of recently exposed pieces of conductor. The depths of the oxide layers, along with the fact that the oxide layer was deposited above the mechanical damage, indicated that the arced wire's deformation was present prior to the short. Although oxide would have been deposited during the arcing event, the fact an area which displayed similar mechanical damage to the arced section yet was 2 in. away from the arced region also contained an oxide layer implied that the damage likely occurred at approximately the same time. Maintenance records indicated that the last time these wiring trays were exposed was 4 years prior, which corresponds well to the estimate of the age of the oxide accumulation [4].

It is likely that the exposed base metal of the screw resulted from deformation of the screw head during insertion or removal of the fastener during its service life, possibly during maintenance 4 years earlier. Contact between the exposed conductor and the base metal of the screw head likely resulted due to launch-induced vibration. Once the circuit was energized, a short developed. Chemical testing verified the presence of copper and nickel in the melt zone on the iron-based screw head, indicating that the wire and screw did make contact at some point. The wire fused with the screw until a subsequent applied mechanical force separated them. The MVC on the fused area indicates that the force was a single event, as no evidence of a progressive separation was observed.

Additionally, the fact that the subject wire was damaged in two places, each above screw heads with raised, bare base metal, indicated that similar events may have caused damage to both areas. The mechanical simulation tests showed that vibration and physically stepping on the components when pressed against smooth screw heads would likely have not caused the damage. Although the step tests performed during the investigation did not damage the conductor, even against burred screw heads, subsequent testing was able to damage the conductor by stepping on a simulated bundle using additional orientations of the hardware. If something had been dropped on the wire bundle, the adjacent wires immediately surrounding, as well as those 180° from, the damaged areas might not have been damaged because the bundle could absorb the shock due to its compressibility, however the bundle as a whole would still be forced onto the screw heads, causing localized damage. The two most probable scenarios for the damage occurrence are either a strike with a tool, such as with a torque tip or pliers, or something being dropped or placed on the wire bundle, causing the bundle to be forced against adjacent burred screw heads with raised, bare metal, and damaging the conductors; stepping on the bundle and pressing it against a burred screw head would fall into the latter category.

Three previous occurrences of wires shorting had been reported during the shuttle program to that point. Due to the incidence of arc tracking on STS-93, an

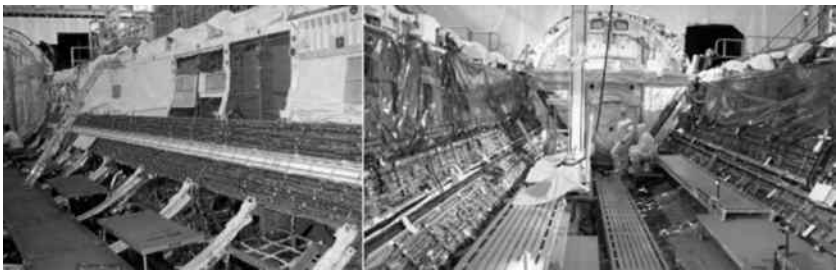

FIGURE 4.17

Orbiter midbody before inspection and during wiring inspection. Tags indicate areas of potential damage to the wiring.

unprecedented inspection of wiring throughout the orbiter fleet was undertaken. Accessible areas as well as critical hard-to-access locations were examined using inspection mirrors, flashlights, and 10× magnification. Manipulation of the wiring was kept to a minimum to lessen the likelihood of introducing any further damage. Between the four orbiters, the Atlantis, the Columbia, the Discovery, and the Endeavour, approximately 3000 suspect indications were identified (Figure 4.17) [5]. Of the 3000 discrepancies, nearly 500 involved exposed conductor. Of the exposed conductors, approximately 150 had mechanical damage, although no additional instances of arc tracking were reported.

Following the inspection of the orbiter fleet's wiring, several lessons were learned. It was recommended that similar screws adjacent to wire bundles be examined to make sure no metal was raised on the screw heads, and also that no screws have bare metal exposed. If any were found, the screws were to be replaced or the raised areas smoothed and the screws repainted. The use of convoluted tubing was recommended as beneficial, both as a physical protection for the bundles, as well as an insulator for any conductors which might become exposed.

Strict adherence to procedures and processes to minimize potential damage during installation and maintenance of wiring and surrounding hardware is imperative. Ongoing training was initiated to ensure that proper precautions were taken when working in or around wiring. Handling and access was also addressed, with the use of temporary workstands and covers to protect vulnerable components being emphasized. Also, the use of convolex convoluted tubing was recommended in high-traffic and critical areas to minimize the likelihood of damage, whether through vibration or impact, as well as to provide protection against similar short circuits.

The lessons learned, both through the failure analysis of the STS-93 main engine controller wire, as well as the fleet-wide inspection which followed, will be incorporated into all subsequent programs. Whether returning to the Moon, landing humans on Mars, or visiting other extra-terrestrial bodies, electrical wiring is a critical component of any spacecraft; ensuring the integrity of such vital hardware is of paramount importance.

ACKNOWLEDGMENTS

The author would like to acknowledge the talents and contributions of:

Peter Marciniak, NASA, Kennedy Space Center
Kirk Scammon, University of Central Florida/Advanced Materials Processing and Analysis Center (AMPAC)

REFERENCES

[1] STS-93 Mission Control Center Status Report # 1. http://www.nasa.gov/centers/johnson/news/shuttle/sts-93/STS-93-01.html.
[2] Managing Electrical Connection Systems and Wire Integrity on Legacy Aerospace Vehicles. S. Sullivan, Kennedy Space Center, National Aeronautics and Space Administration, Kennedy Space Center; George A. Slenski, Materials Directorate, Air Force Research Laboratory Research Laboratory, AFRL/MLSA, Wright-Patterson AFB. Federal Aviation Authority Principal Inspectors and Engineers Aging Aircraft Workshop, Seattle, WA; 2001.
[3] Failure Analysis of a 115 VAC 400 Hz Main Engine Controller Wire From the Midbody Port Side Lower Wire Tray 11/12 Frame From OV-102 That Shorted During the Launch of STS-93, KSC-MSL-0729–1999, S. McDanels, National Aeronautics and Space Administration, Kennedy Space Center; 1999.
[4] ESCA Analysis of Shuttle Columbia Wiring final report. K. Scammon, University of Central Florida/Advanced Materials Processing and Analysis Center (AMPAC); 1999.
[5] Fleet Wire Inspection & Repair Summary. D. White, United Space Alliance Final Report; October 1999.

CHAPTER

5

Fatigue failures of aeronautical items: Trainer aircraft canopy lever reverse, rescue helicopter main rotor blade and fighter-bomber aircraft ground-attack main wheel

Manuele Bernabei, Laura Allegrucci, Mikael Amura

Chemistry Department, Italian Air Force—Flight Test Centre, Pratica di Mare AFB, Pomezia, Rome, Italy

CHAPTER OUTLINE

Handbook of Materials Failure Analysis With Case Studies from the Aerospace and Automotive Industries.
http://dx.doi.org/10.1016/B978-0-12-800950-5.00005-3

1 INTRODUCTION

The evolution of scientific thought has proceeded from lessons learned through trial and error: a "think positive approach" to failures, where accidents and mishaps may become a driving force for enhancing aircraft structures and improving flight safety.

Therefore, the case studies described in this chapter underline the link between causes of failures and activities involving production processes, maintenance, and flight operations.

CASE

Fatigue fracture of an aircraft canopy lever reverse 1

1 INTRODUCTION

During a pre-flight inspection, the canopy of a military trainer aircraft was found to be blocked after reaching approximately 20 cm of its total hinged opening. The aircraft was moved to the hangar and a subsequent inspection revealed that the lever reverse of the canopy had failed in two sections. The lever reverse (evidenced in Figure 5.1), consists of a 7075-T6 aluminum alloy forging, and is the link between the actuator, the torsion bar and the spring of the canopy balancing system, which

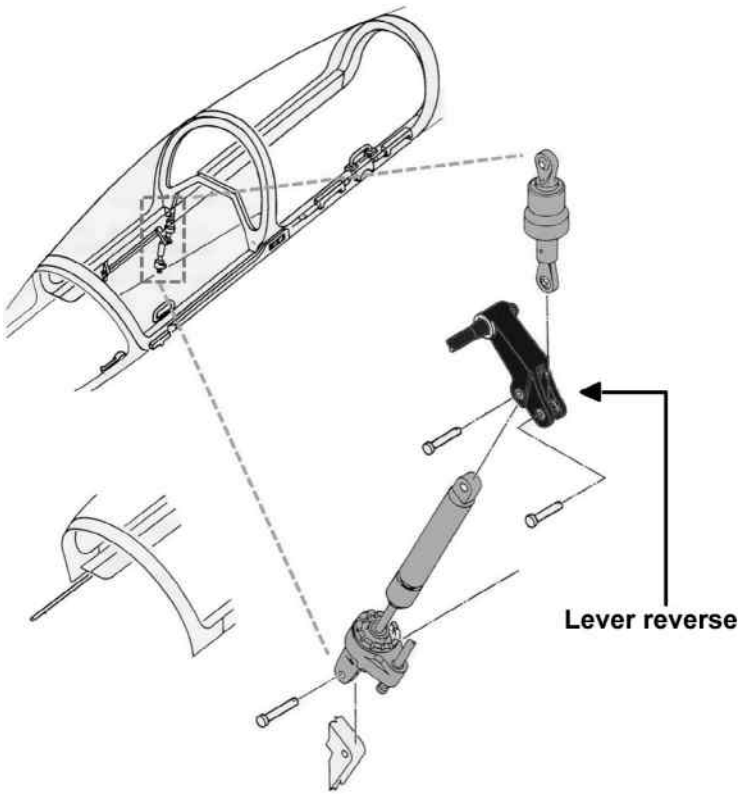

FIGURE 5.1

Schematic view of the canopy balancing system.

enables the opening mechanism. The lever reverse log-report recorded a total life of 300 flight hours since the installation of the canopy, and "on condition" maintenance without nondestructive inspections. In addition, that component is the only one which is known to have suffered failure.

The logbook of the canopy lever reverse revealed that it was recently modified to improve cockpit access during maintenance operations. When it was installed for the first time, the actuator lug featured a two-step elongation process, while on the second release the elongation was a one-step procedure. The second release produced the failure described above and the maximum length of the elongation lug was 1 cm longer than the previously issued part.

Sections containing fracture surfaces of both parts were used for failure analysis, which included visual examination (eye and optical microscopy), material identification (chemical analysis, hardness testing, and metallography), and analysis of fracture surfaces by means of field emission scanning electron microscope (FESEM) and X-ray energy dispersive spectroscopy. In addition, finite element analysis (FEA) and fatigue life assessment were performed to confirm the origin of fracture and to

estimate the number of cycles to failure as well as the stress acting at the time of fracture. The morphological observation of the surfaces revealed that the failure occurred close to the fixing hole of the torsion bar by the propagation of two cracks due to fatigue at the internal edges, thus representing the most stressed areas. In particular, the largest one grew approximately 1.54 cm long and 0.35 deep and was facilitated by pitting, which acted as a stress concentration raiser. Striation counting and calculations showed a relatively high-cycle fatigue and that 81 MPa was a realistic stress magnitude for the lever reverse. No evidence of material deficiencies, fabrication, or maintenance defects was found. Instead, the overlength of the actuator lugs compared with the ones traditionally used was the cause of failure.

Indeed, a mark on the piston due to the action of the cylinder flange was to be found very close to the bottom travel, thus the action of a strong force, estimated at approximately 2760 N. As a consequence of these results, it was recommended that all lever reverses and lugs be inspected immediately and in the event, the actuators removed from service [1].

2 RESULTS

2.1 MACROFRACTOGRAPHY

Figure 5.2 shows the broken component in the as-received condition. The failure occurred close to the fixing hole with the torsion bar. In particular, there is evidence of deep plastic deformations caused either by wear or impact along all the edges of the fixing hole of the torsion bar (see detail of the part A in Figure 5.3) and due to crushing at the lateral surface one (see detail of the part B in Figure 5.3). The crush is located approximately 1 cm far from the fracture surface. The morphology of the fracture surfaces of parts A and B featured three distinct zones. Two of these zones are flat, smooth, and bright surfaces containing beach marks (see zones C and D in Figure 5.4), thus indicating a fatigue crack growth; the third one is rough, dull with coarse grains oriented at about 45° one (see zone E in Figure 5.4), that is the region of the final, unstable fracture. In Figure 5.5, a comparison between the actuator installed on that balancing system and the one traditionally used can be observed. In particular, the lugs of the actuator examined are approximately 1 cm longer (see detail in Figure 5.5).

2.2 MICROFRACTOGRAPHY

Inspection of zones C, D, and E with FESEM was performed on sectioned A and B parts to confirm the fatigue failure and to identify the crack origin sites. In particular, the zone C, representing approximately 19% of the total fracture surface, showed two different morphologies due to stable and unstable fatigue crack propagation, with fatigue striations in the stable one and beach marks alternated to dimples in the other one, respectively (see Figures 5.6–5.8). The striations are also uniformly spaced throughout the fracture surface with a limited amount of associated plastic

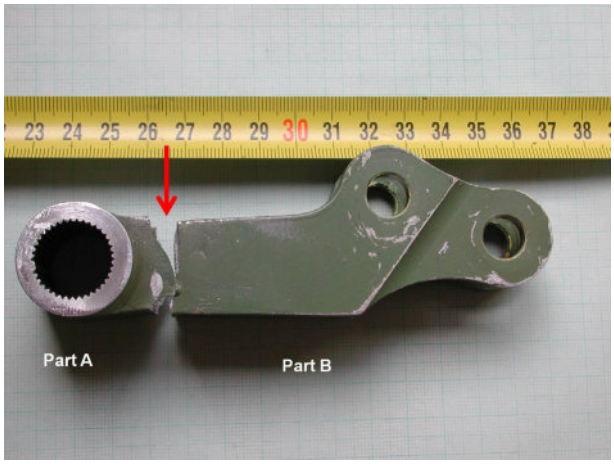

FIGURE 5.2

Macrograph of the two broken pieces of the lever reverse. Zone of failure is denoted by arrow.

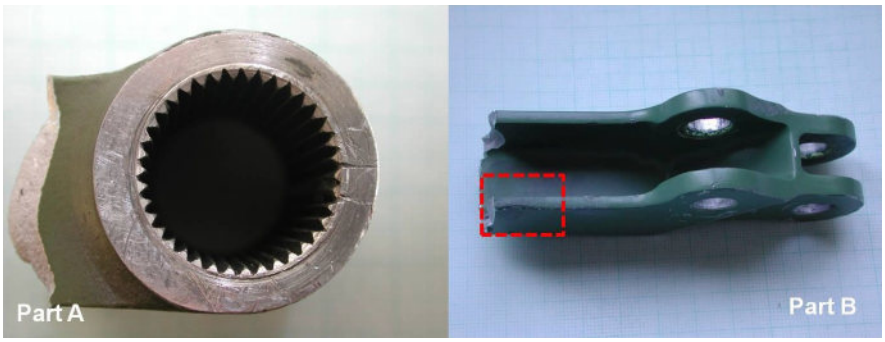

FIGURE 5.3

Macrograph showing plastic deformations of the part A and part B.

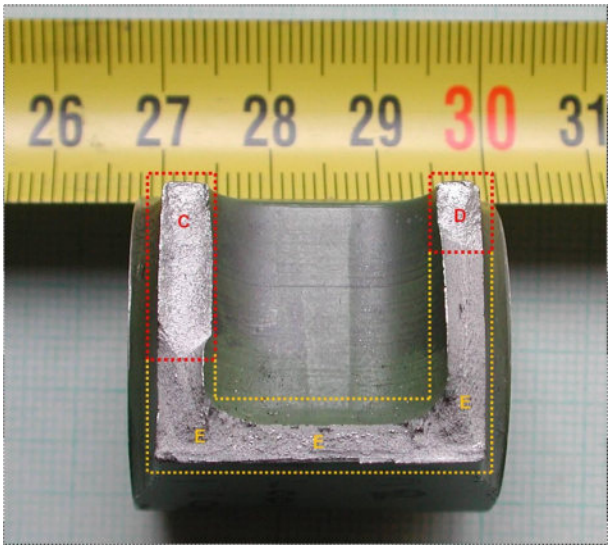

FIGURE 5.4

Macrograph showing zones C, D, and E on fracture surface. Part A.

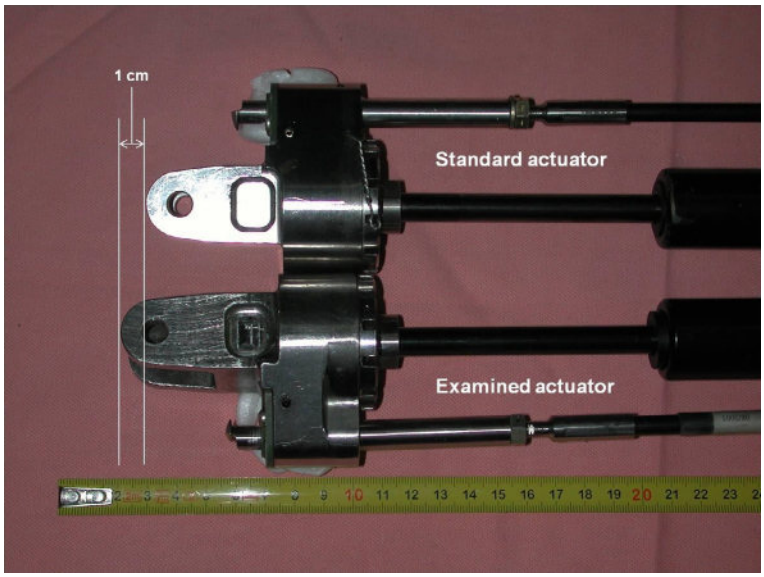

FIGURE 5.5

View of the actuators.

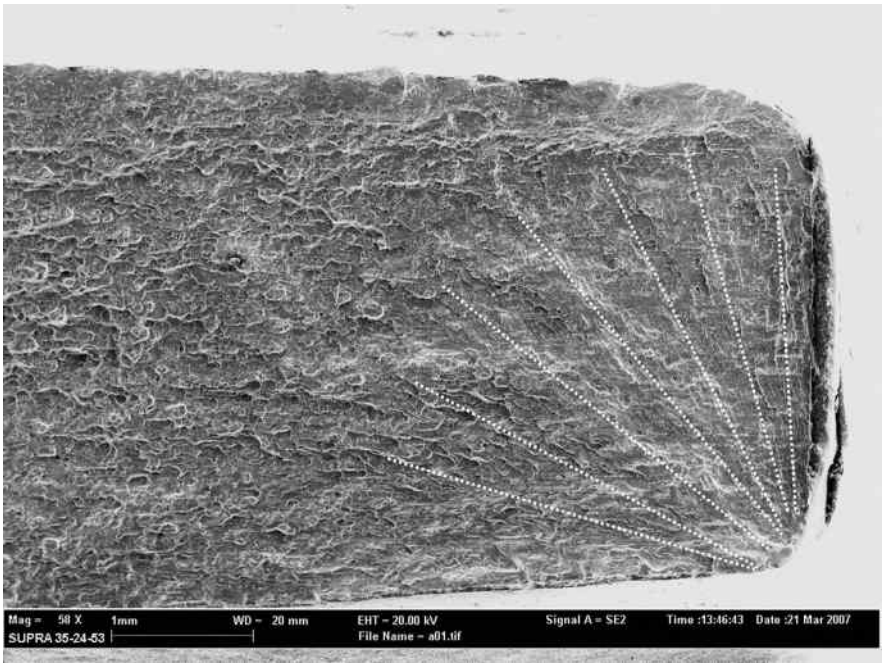

FIGURE 5.6

SEM micrograph of C zone at a location close to the initiation point.

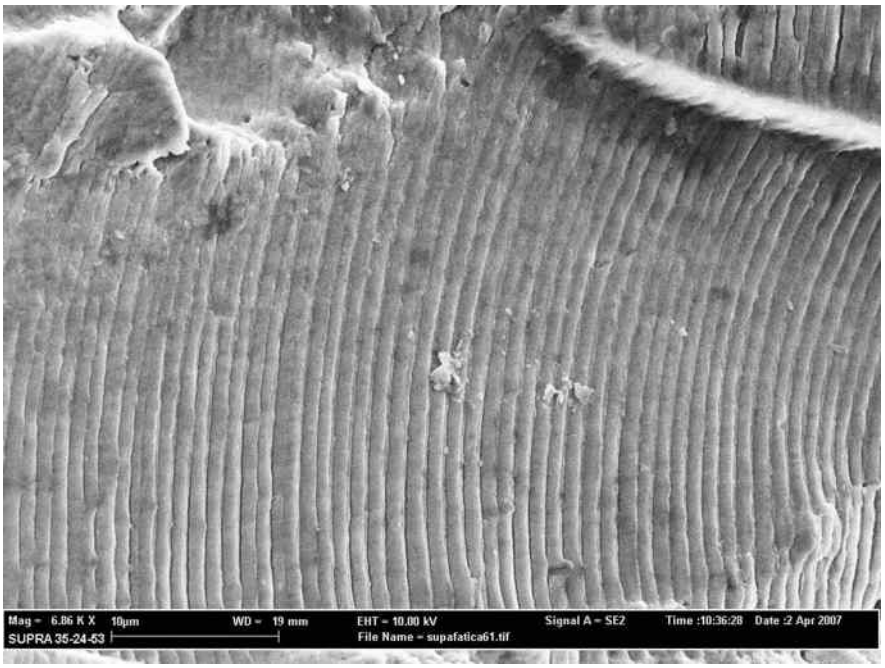

FIGURE 5.7

SEM micrograph of the fracture surface of the crack in the stable propagation. Zone C.

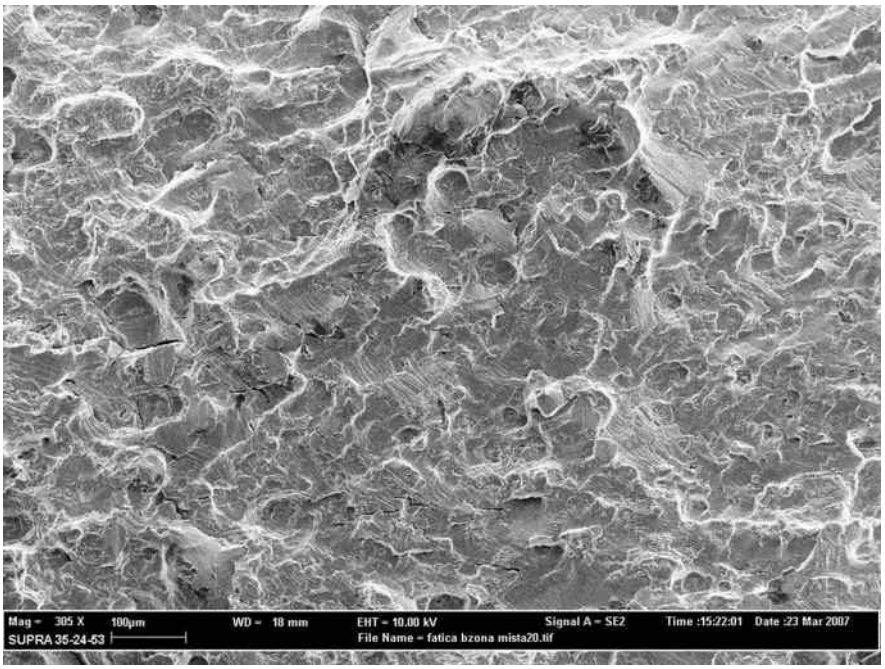

FIGURE 5.8

SEM micrograph of the fracture surface of the crack in the unstable propagation. Zone C.

FIGURE 5.9

SEM micrograph at the crack origin site. Cracking initiated at a pit indicated by arrow. Zone C.

deformation. The striations spacing as well as deformation gradually increased further from the suspected origin site. Tracing back the fatigue evidences, it was identified to be at the internal edge. Detailed microscopy of the site showed presence of a corrosion pit approximately 100 µm deep (see Figure 5.9). A very similar pattern as observed above was found in zone D, representing approximately 8% of the total fracture surface. Conversely, microscopic examination of the initiation site located at the internal edge did not uncover corrosion pits or other anomalous initiating sources. Finally, in zone E, covering approximately 73% of the fracture surface, the predominant pattern was quasi-brittle cleavage rupture, thus representing the final fracture by overload of the lever reverse.

2.3 CHEMICAL ANALYSIS

Chemical analysis results of a lever reverse sample are in accordance with the specification for a 7075 aluminum alloy.

2.4 HARDNESS MEASUREMENTS

Hardness measurements were carried out on the external surface of B part in accordance with the Rockwell standard method and yielded an average value of 80 ± 1 HRB, indicating a T6 tempered condition and a deduced UTS of approximately 500 MPa.

2.5 MICROSTRUCTURAL ANALYSIS

Microstructural examination of the lever reverse was performed on two longitudinal sections of part B in orthogonal direction to the fracture surface. The microstructure revealed features typical of a forging fold with elongated grains and intermetallic phase's precipitates located at grain boundaries (see Figure 5.10). In addition, at the internal edge of the zone C a corrosion pit approximately 100 μm deep was found. No discrepancies were found at the internal edge of zone D.

2.6 MICROANALYSIS

Several areas of the parts were analyzed using an EDX microprobe attached to the FESEM. No other unusual features able to act as initiation sites were found excepting the pit.

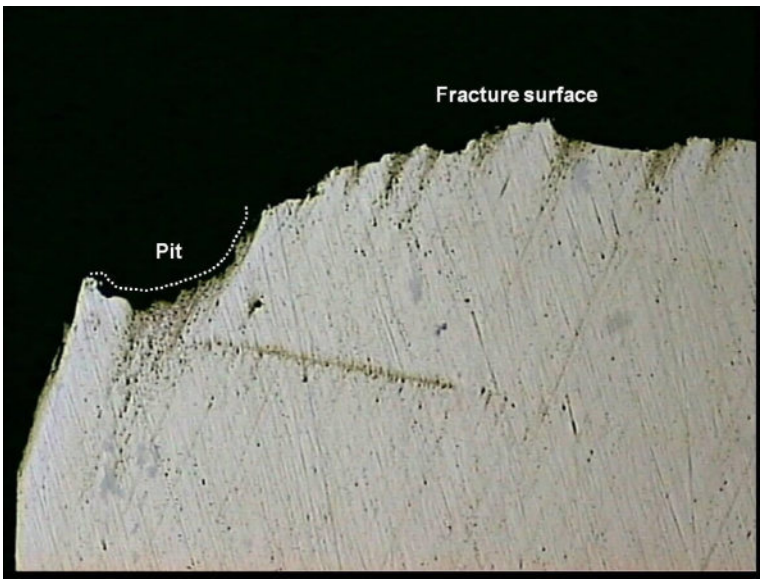

FIGURE 5.10

Optical micrograph showing corrosion pit at a location close to the internal edge. Zone C. 200×.

2.7 FEA

To estimate the force acting in static conditions as well as to identify the stress distribution on the lever reverse a FEA was carried out. Using principles of fracture mechanics, the critical crack size measured on the lever reverse for the deepest one and published fracture toughness data for 7075-T6, resulted in a maximum stress of 81 MPa per fracture, corresponding to 2760 N as the acting force. This is consistent with that found by introducing defects in the lever reverse model deduced from fractographic evidence and repeatedly applying an external load to reach the UTS at the crack tip. In addition, applying the same force to the model in normal conditions, i.e., without consideration of defects, resulted in a stress value of approximately 151 MPa at the internal edges, thus representing the most stressed areas (see Figure 5.11). This stress approaches the fatigue endurance limit of the material under consideration (160 MPa). Furthermore, the results obtained were also used to estimate the total cycles to failure by using Neuber's equation and was equal to approximately 5500 cycles.

2.8 FATIGUE LIFE ASSESSMENT

Average striation spacing was used to provide an estimate of the lever reverse for the number of cycles to failure. The calculation was made considering the fatigue evidences of the C zone fracture surface, which contained the pit corrosion,

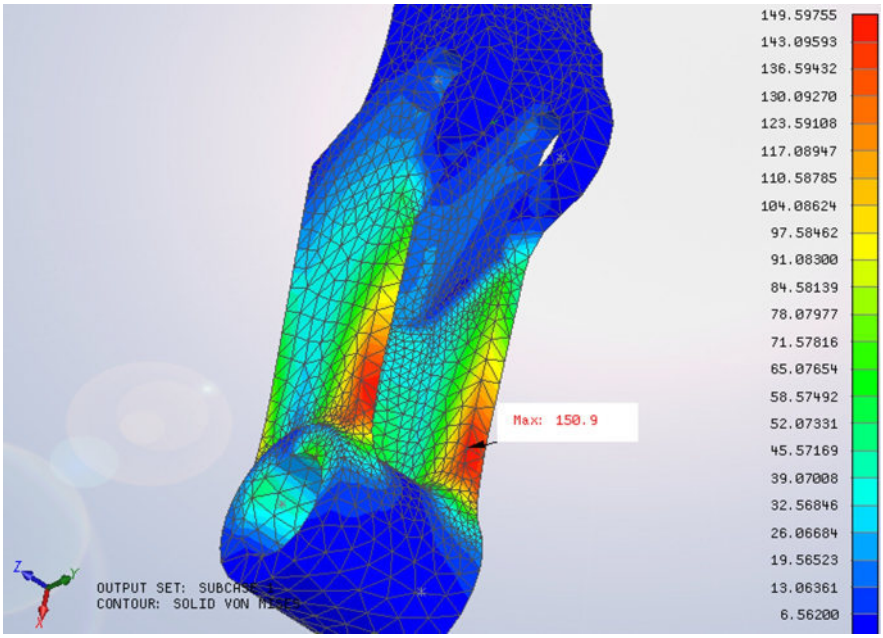

FIGURE 5.11

FEA model showing the most stressed areas of the lever reverse.

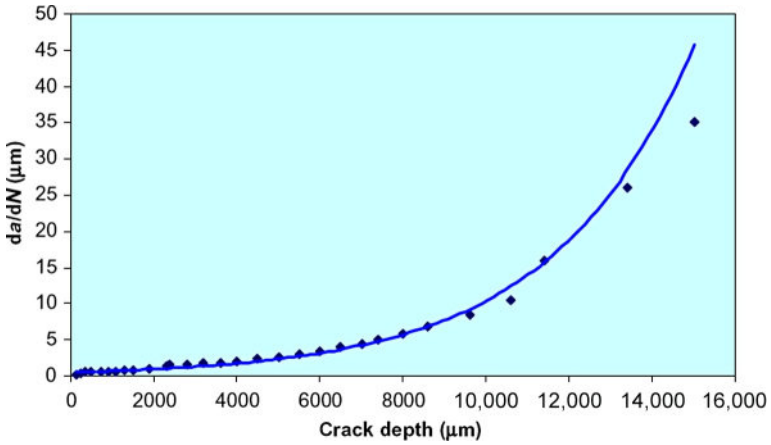

FIGURE 5.12

The general trend.

between 150 µm from the internal edge to approximately 1.5 cm, corresponding to the final overload failure. The general trend is shown in Figure 5.12 and the number of cycles obtained by integrating the exponential curve is of approximately 5900 cycles.

3 ANALYSIS OF THE RESULTS

Fractography established the cracks propagated at the internal edges of the lever reverse at a location close to the torsion bar due to fatigue. In particular, the deepest one grew to approximately 1.54 cm in length before the final rupture and was intensified by pit corrosion about 100 µm deep. The other one grew to approximately 0.6 cm in length and was not associated with any observed defects. FEA also showed how such edges are the most stressed areas of the lever due to their geometrical characteristics. In addition, the striation's structure and spacing were found to be increasingly regular as the cracks grew. In particular, the striations spacing between the point close to the corrosion pit up until transition to the final overload failure was very uniform, with a limited amount of associated plastic deformation. This suggests that only one magnitude of stress was causing the crack growth and that the crack growth mechanism is high-cycle fatigue. Calculations from the number of canopy opening/closing during pre/post-flight operations, both maintenance and inspections and due to the pilot shows, indicated that the canopy would undergo approximately 5400 cycles from its last installation. Although there is some discrepancy between the calculations done and the morphological evidences, the number calculated is consistent with that found by measuring average striations spacing and solving Neuber's equation.

In addition, fractography established that the cracks covered only 27% of the total fracture surface, indicating their propagation did not contribute to the overall fracture process. It is more likely that an anomalous high load event, caused by some incident such as a crash during maintenance operations or service as well as due to design, produced the failure. The effective crack size was sufficiently large to attain K_{IC} value, producing force acting on the component of 2760 N. This is a realistic magnitude value when compared with that obtained by FEA. Because the deep plastic deformation found on the component due to crushing is located on the opposite wall of the edge that originated the deepest crack at a location quite far from the fracture surface, it can reasonably be assumed that the different geometry of the actuator lugs was the proximate cause of failure. Indeed, longer lugs proportionally vary the acting force on the lever, as confirmed by the mark on the piston closer to the flange bottom travel. Although no other failure of this kind had been experienced, there might have been other actuators with analogous geometrical defects. Each of them were immediately inspected for similar defects and, in such cases, removed from service.

4 CONCLUSION

The failure of the lever reverse resulted from high-cycle fatigue caused by the application of an abnormal force due to the overlength of the actuator lugs. The fatigue was also compounded by corrosion pit.

In this case, the modification of the actuator lugs, consisting of a single step of elongation process, and a maximum elongation which was 1 cm longer with respect to the old version, can be considered the main driving force of the failure. In consideration of this fact, the modification on the canopy lever reverse should be completed without failure if a correct FEA evaluation is to be carried out prior to predict the fatigue behavior of the modified component.

CASE 2

Failure of a helicopter main rotor blade

1 INTRODUCTION

A search and rescue military helicopter crashed during a ferry flight to an airport where an exercise was scheduled. All crewmembers suffered fatal injuries. The helicopter veered out of control following the in-flight detachment of one of the five main rotor blades.

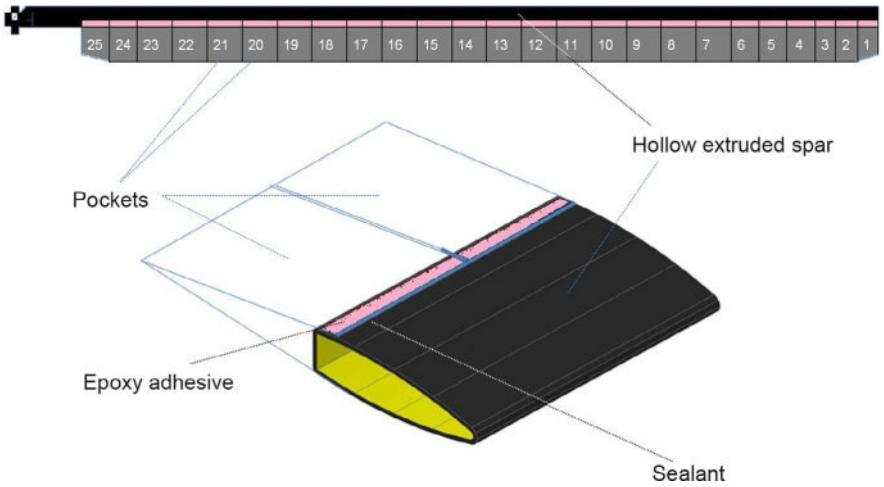

FIGURE 5.13

Helicopter main rotor blade structure.

The Safety Investigation Board found that the largest part of the failed blade detached about 900 m before the wreck, considering the direction of the flight. The failure analysis of the part was conducted in the immediate aftermath: it was immediately apparent that part of the blade had detached first and this caused the helicopter to become uncontrollable. The main rotor blade is about 9 m long. The structural part is a hollow extruded spar made of 6061-T6 aluminum alloy (Figure 5.13, section view), 4.5 mm thick on average. The airfoil geometry is completed by 25 aerodynamic ends named pockets, made of 0.25 mm thick aluminum alloy foils. Each pocket is glued and sealed on the spar (Figure 5.13). Furthermore, the blade is equipped with an *In-flight Blade Inspection System* (IBIS) and the internal part of the hollow spar is filled with nitrogen. If the gas pressure decreases, a warning "blade press" light illuminating in the pilot control panel means that there is the possibility of a blade failure. At the time of the mishap and from the moment the alert signal began, the maximum flight time of the helicopter was 6 h at decreased max speed. It is uncertain whether the blade warning light was alight when the blade detached.

However, it is known that the warning was alight during the second last flight and that the crew was able to reset the IBIS in accordance with the prescribed procedures.

Following, the failure analysis on the aforementioned blade will be illustrated. Fatigue failure initiated at the outer spar surface and propagated along the spar thickness. The observations showed multiple initiation points along an incision on the outer surface. Evidence of the presence of abnormal material was found in the incision: traces of iron. The damage acted as a stress concentration raiser for the normal operative loads.

In addition, fatigue life assessment was carried out to quantify the number of cycles to failure. This was analyzed to introduce NDT inspections along with IBIS and to achieve higher safety standards [2].

2 RESULTS

2.1 FRACTOGRAPHY

The blade fracture occurred between pockets 16 and 17 at the lower corner of the spar section (Figure 5.14, section view, green area). Fractography conducted by means of optical and electronic microscopes showed a progressive fatigue phenomenon.

The fracture started from the outer surface and it spread to the internal surface of the spar. Once the "through-the-thickness" condition was achieved, it continued along the resistant section until the final overload. The fracture surface was divided in two zones named A and B.

Zone A was characterized by an incision located on the outer surface and perpendicular to the blade's longitudinal axis (Figure 5.14, top left, detail of spar section view). The incision was v-shaped (Figure 5.14, 3D reconstruction); it was 2.3 cm in length and 190 μm in depth. Multiple initiation points were found at the incision vertex. From these, beach marks typical of fatigue crack growth departed creating a semi-elliptical front (dashed line in Figure 5.14). The grain morphology was smooth, fine, and bright. After the fatigue achieved the "through-the-thickness" condition, it propagated toward the leading edge and along the backwall (Figure 5.15, top right, detail of spar section view) with flat, coarse grains and beach marks (Figure 5.15).

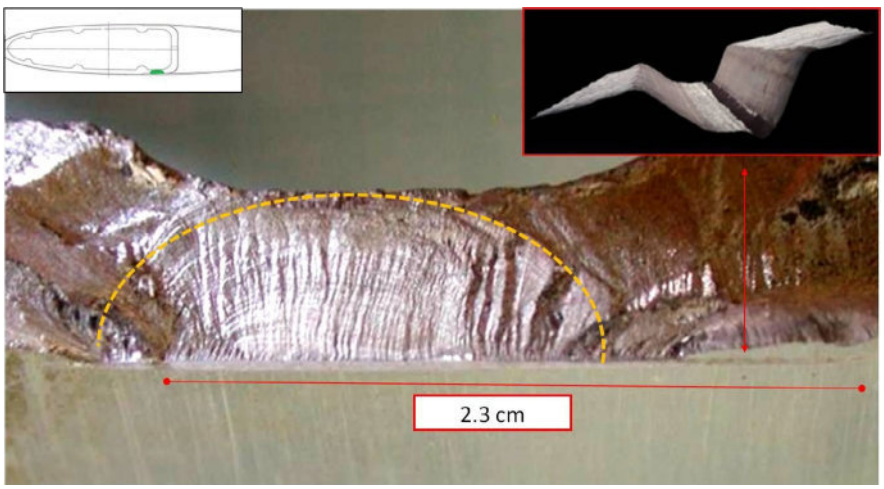

FIGURE 5.14

Blade fracture surface.

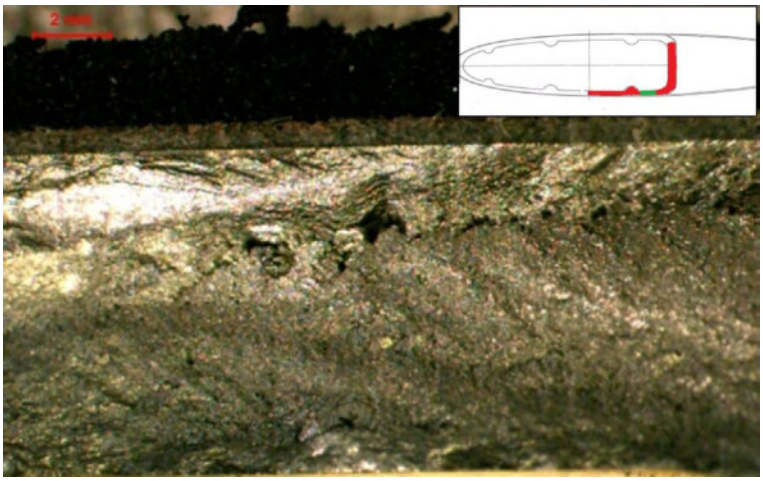

FIGURE 5.15

Fatigue propagation toward the leading edge and along the backwall blade.

This fracture surface part was named Zone B. The remaining part of the fracture surface was rough, dull, characterized by coarse grains, and it was oriented at about 45° to the transversal section. Lastly, evidence of dimpled rupture was found. This resulted from microvoid coalescence denoting final fracture by overload.

2.2 CHEMICAL ANALYSIS

Chemical analysis showed that the spar's alloy was in accordance with the specification for a 6061 aluminum alloy.

The composition homogeneity was verified at the initiation area by an X-EDS microprobe attached to the FESEM. An abnormal presence of iron was found in the incision (Figure 5.16).

2.3 HARDNESS MEASUREMENTS

Hardness measurements were carried out over the external surface of the spar in accordance with the Rockwell T30 standard method and yielded an average value of 48. This is equivalent to 81 Brinell hardness points and compatible with AA6061 T6 tempered condition.

2.4 MICROSTRUCTURAL ANALYSIS

Microstuctural examination, performed on two longitudinal sections made orthogonally to the fracture surface, revealed features typical of a 6061T6 structure.

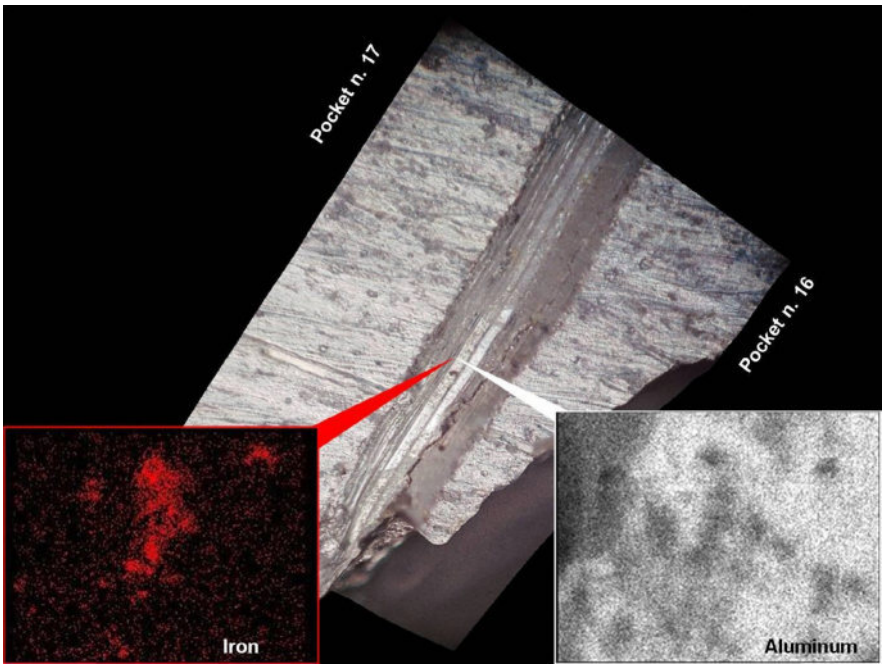

FIGURE 5.16

Abnormal presence of iron found inside the incision.

2.5 FATIGUE LIFE ESTIMATION

Striation spacing was analyzed in order to evaluate fatigue life.

As "a" the variable representing the crack length and "N" the number of load cycles, dA/dn is the crack growth per cycle of stress. Measurements were carried out with sampling techniques by two different investigator teams on the same fracture surface.

Samples were collected every 1000 μm at different magnification, varying from 1000 × to 160,000 ×. Careful examination of the fatigue crack surface showed that striation spacing was found to vary as the crack grew. The striation spacing near the starting point (crack length less than 12 mm) was consistently uniform (Figure 5.17), indicating that only one magnitude of stress was causing crack growth. However, it was not possible to collect any data due to the high magnification required at initial stage area (crack length lesser than 4 mm): 160,000 × was not enough to adequately resolve the image. The striation spacing near the overload was very different and the striations were grouped. In particular, one large striation followed by smaller ones (Figure 5.18), indicates that several stress cycles of different magnitudes were causing crack growth. In such instances, only the larger striations were taken into account.

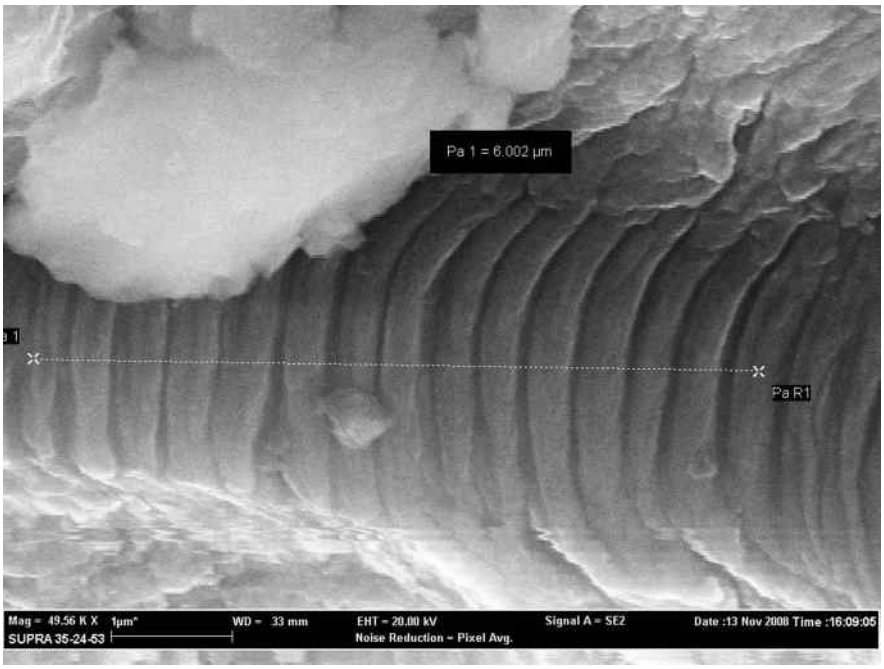

FIGURE 5.17

Striation spacing near the starting point at crack length less than 12 mm.

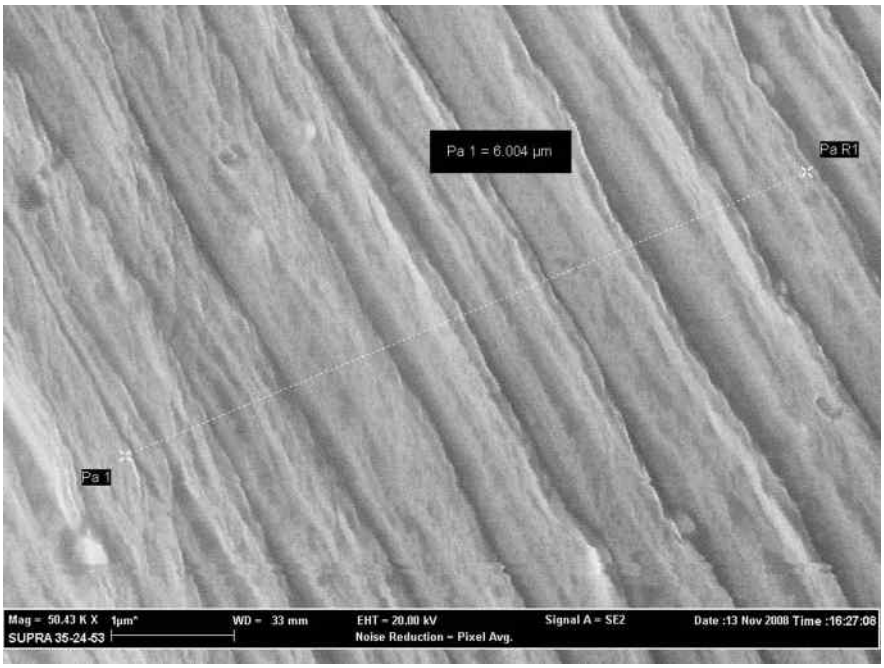

FIGURE 5.18

Striation groups.

In fact, experimental results from a similar blade in operation indicate that there is more than one cycle per revolution. However, they vary greatly in magnitude and some of these stress cycles could be sufficiently small that they may not cause fatigue crack growth in the initial stages of the crack growth.

In order to estimate the fatigue life, the crack growth curve was built by experimental data interpolation from striations counting in Zone B (from the through-the-thickness condition to the final overload) where striation spacing was measurable. Therefore, two experimental fatigue growth curves were obtained by point's interpolation, based on the measurements taken by two different teams.

Thus, the number of load cycles may be estimated as,

$$N = \int_{a_i}^{a_f} f(a)\mathrm{d}a$$

"a_i" was along the beach mark relevant to the condition "through-the-thickness" in direction of the overload and "a_f" was where the overload took place. Finally, "$f(a)$" is the experimental curve obtained by striation counting, $\mathrm{d}N/\mathrm{d}a$.

The flight time needed for the crack to cover the Zone B (from "through-the-thickness" condition to the overload failure) can be estimated taking into account the rotational speed of the main rotor.

The values obtained were 6 h 40 min and 9 h 20 min, consistent with the safety limit imposed by the manufacturer in case of "blade press" warning light: this was a maximum 6 flight hours. However, as it is not clear whether the warning light was on at the time of the accident, the Air Force required an estimation of the total fatigue life in order to implement NDTs in addition to the IBIS system. The method used above could not be adopted due to the impossibility to achieve an accurate striation counting in zone A (before the through-the-thickness stage) that comprised the slow initiation fatigue phase; therefore, the procedure described here was followed.

In general, fatigue phenomena in the stable propagation phase can be analytically described by means of Paris' law:

$$\frac{\mathrm{d}a}{\mathrm{d}N} = C\left[(\sigma_{\max} - \sigma_{\min})F\sqrt{\pi a}\right]^n$$

"$\sigma_{\max}-\sigma_{\min}$" is the difference between maximum and minimum tensile load. This value varies along the spar and in each part of the airfoil section. Unfortunately, the load spectrum was not available, therefore, it was assumed to be constant. This hypothesis is satisfactory because the blade is actually twisted in order to make the load as constant as possible. Based on this assumption, "$\sigma_{\max}-\sigma_{\min}$" could be evaluated from the experimental crack growth curves obtained by striation spacing. In fact, the load on the part of the blade where the crack grew is approximately constant, although the crack velocity changes greatly from the initiation to the stable propagation and to the unstable propagation. "C" and "n" are constants which are relevant for the fatigue properties of the specific material. "F" is the dimensionless geometric factor. Considering the hollow spar similar to a hollow cylinder, "F" is comprised between 0.86 and 1.2 depending on the geometrical parameters (crack length, thickness, and cylinder radius) in the case of a part through crack.

The fatigue curve at the initiation phase is nonlinear. In order to establish NDTs, a simplifying hypothesis was followed to produce a faster fatigue growth, a shorter inspection interval and a higher safety standard. The line tangent to the initial part of the fatigue curve obtained by experimental observation was established in order to approximate the initiation phase. Consequently, it was possible to calculate the fatigue life by integrating the obtained Paris curve with the following expression:

$$dN = \frac{a^{-n/2}\,da}{C[(\sigma_{max} - \sigma_{min})F\sqrt{\pi}]^n} \Rightarrow N = \frac{1}{C[(\sigma_{max} - \sigma_{min})F\sqrt{\pi}]^n} \cdot \int_{a_0}^{a_1} a^{-n/2}\,da$$

In the above equation, a_0 was assumed to be equal to the minimum damage detectable by NDTs, 0-5 mm. a_1 was set as equal to the spar thickness. Taking into account the main rotor angular speed, the number of cycles needed for the crack to grow from 0.5 to 4.5 mm could be correlated to the number of flight hours. The result was a flying time estimation of 200 h.

2.6 NONDESTRUCTIVE TESTING

X-ray nondestructive testings (NDTs) were studied and adopted. A safety factor of 3 would have been feasible to provide an adequate probability of detection and to take into account statistical deviations—the approximations and limitations granted in the fatigue life estimation. However, a unitary safety factor was adopted considering that the overall integrity of the blade was also monitored by the IBIS system, along with X-rays. On the basis of this, the inspection frequency was set to 200 flight hours. This choice allowed the maintenance depot to apply NDTs in the framework of an intermediate inspection, so the time needed to inspect the blades was less detrimental for the operations.

3 BLADE MAINTENANCE

Failure analysis demonstrated that the damage on the external surface of the spar was caused during maintenance activities, therefore these were further investigated.

The maintenance policy adopted for this component was “safe-life” for a prescribed total life of 8000 flight hours. The failed blade log-card recorded 4220 flight hours. In the event of “blade press” warning signal, the blade would undergo static pressure proof testing at the Wing maintenance department in order to find leakage. If leakage was found, then the blade would be returned to the manufacturer for repair. The manufacturer likewise repaired damages to the paint or to the pockets structure. Specifically, pockets must be removed by softening the glue and without using metallic tools.

The iron found in the incision on the spar of the accident was presumably the result of a pocket removal action, produced by a sharp iron-based tool. Considering the blade of the accident and where the crack was found, the 16th pocket was never

changed while pocket 17 was substituted in 1998 at 2724, 25 flight hours. It must be underlined, however, that the mandatory procedures clearly forbid the production of any damage/incision on the spar structure and no iron tools are included in the applicable tools list.

4 CONCLUSION

This study ascertained that the blade failed due to a fatigue mechanism initiated by an incision made on the spar by an iron tool during maintenance activities.

The fatigue life estimation from the "through-the-thickness" state to the final overload was in compliance with the maximum time of flight warranted at the time of the accident, but there was definitely a delay in the activation of the IBIS due to the tightness of the fatigue crack and to the presence of glue required to secure the position of the pockets. Fatigue life prior to the "through-the-thickness" condition was estimated in order to increase the safety of flight and the result was used to establish NDTs every 200 flight hours. Following this study, several other incisions on rotor blades were found.

CASE

Fatigue fracture of a ground-attack aircraft main wheel 3

1 INTRODUCTION

The incident aircraft is a single-engine, fighter bomber, and reconnaissance airplane. In particular, its landing gear has two main wheels and one nose wheel. During a pre-flight taxiing, one of the main wheels of landing gear failed. Following inspections revealed a crack located at the hub housing of the main wheel (Figure 5.19). The wheel is made of 2014-T6 aluminum alloy forging containing a cold-mounted bearing. A nut fitted at the prescribed torque value tightens the wheel assembly. The log-card of the assembly recorded a total life of 299 landings. It also reported that the last eddy current inspection had been conducted at 241 landings. Evidence was collected by visual examination (eye and optical microscopy), materials identification (chemical analysis, hardness testing, and metallography), and fracture surfaces microanalysis based on field emission scanning electron microscope (FESEM) equipped with an X-ray energy dispersive spectroscopy (EDS). Furthermore, finite element analysis (FEA) and fatigue life assessment was carried out to confirm the origin of fracture and to quantify the number of cycles to failure as well as the stress acting at the time of fracture. Finally, all

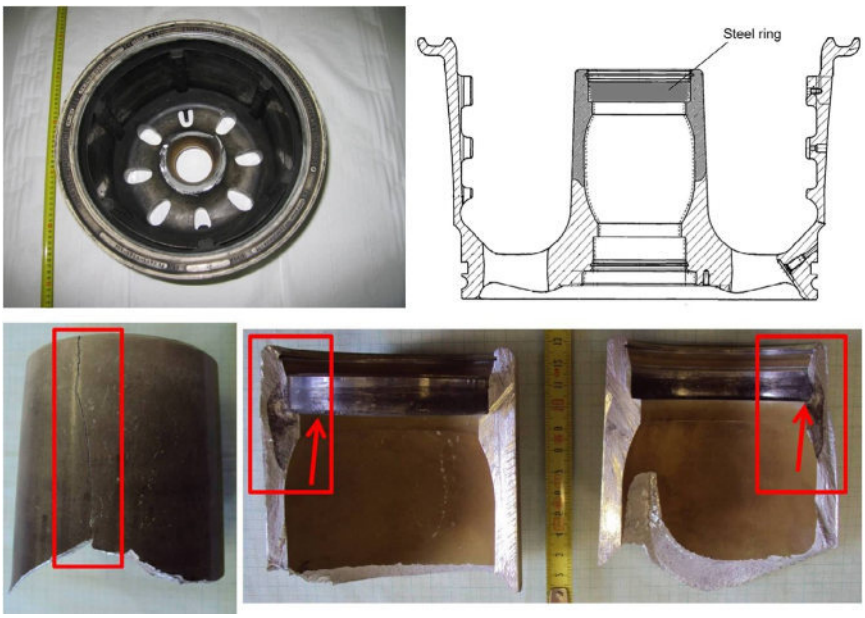

FIGURE 5.19

Fatigue crack in the AA2014 T6 AMX main wheel.

the recorded data were analyzed to improve nondestructive technique (NDT) inspections by using ultrasounds instead of eddy currents. Failure initiated at the bearing cup housing edge and propagated along the hub housing. The crack grew to 30 mm in length and 10 mm in depth. No evidence of material abnormal properties or maintenance defects was found. However, flaws in the installation procedure were detected, as plastic deformations in the initiation area showed. This acted as a stress concentration raiser when routine operative loads were performed. Main wheel maintenance was based on eddy currents inspections which were carried out at every third tyre replacement to minimize the risk of failure. Nevertheless, the failure described here revealed that the NDTs were not reliable [3].

2 RESULTS

2.1 CHEMICAL ANALYSIS

Chemical analysis showed that the main wheel sample was in accordance with the production specification of 2014 aluminum alloy. The composition homogeneity was also verified at the initiation area using an EDX microprobe attached to the FESEM. No unusual features were found.

2.2 MICROSTRUCTURAL ANALYSIS

Microstructural examination, performed on two longitudinal sections made orthogonally to the fracture surface, revealed features typical of a 2014-T6 forging, 5-7 μm grains and irregularly-shaped structure.

2.3 FOURIER TRANSFORM INFRARED SPECTROSCOPY

Fourier transform infrared spectroscopy analysis of black organic material sample found on the fracture surface was consistent with EPDM (ethylene propylene diene material): this consists of rubber commonly used in braking systems. It was extensively scattered also on other wheels that had not suffered any failure, signifying it provided no contribution to the initiation and progression of the rupture mechanism.

2.4 HARDNESS MEASUREMENTS

Hardness measurements were carried out on the external surface of the housing hub in accordance with the Rockwell T30 standard method and yielded an average value of 71. This is equivalent to 153 Brinell hardness points and yields deduced UTS of approximately 520 MPa compatible with AA2014-T6 tempered condition.

2.5 METROLOGIC MEASUREMENTS

The part of the bearing cup that is in contact with the hub housing is a cold installed steel ring (Figure 5.19). Metrological tests ascertained that the diameter was on average 5 μm larger than the design drawing value.

2.6 VISUAL OBSERVATIONS AND MACROFRACTOGRAPHY

The failure of the main wheel occurred at the hub housing which is approximately cylindrical in shape. The fracture started from the lateral surface arriving to the root, where the hub housing is joined to the main wheel body. Thus, the fracture surface was divided in two zones, named A and B. Zone A was at the hub housing root. It was rough, dull, characterized by coarse grains, and it was oriented at about 45° to the transversal section. Moreover, a plastic deformation, associated to the final phase of wheel failure, was observed. Therefore, Zone A was the region of the final, unstable fracture. Zone B was characterized by a crack located along the hub housing lateral surface. In this area, three zones with different morphological features, described in Figure 5.20, characterized the fracture surface.

Area 1: Flat, smooth, and bright with beach marks typical of fatigue crack growth (Figure 5.21). These beach marks were concentric to the initiation point and located on the inner corner of the bearing cup housing. This area was roughly circular with 6.5 mm radius. Beach mark spacing was almost constant, about 40 μm.

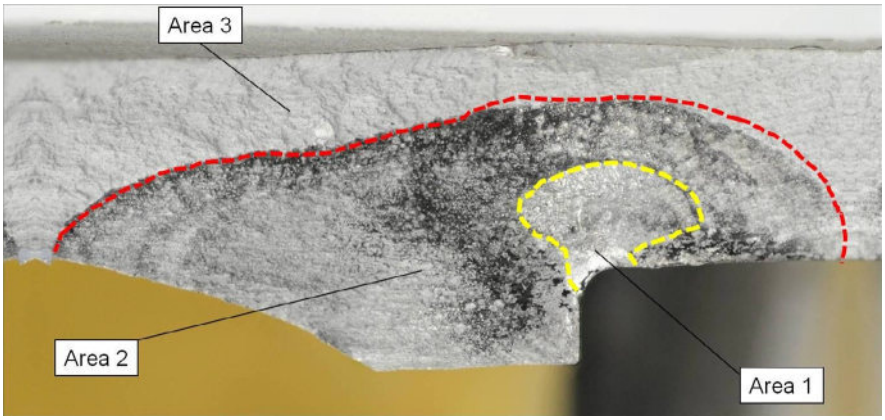

FIGURE 5.20

Fracture surface, area numbering.

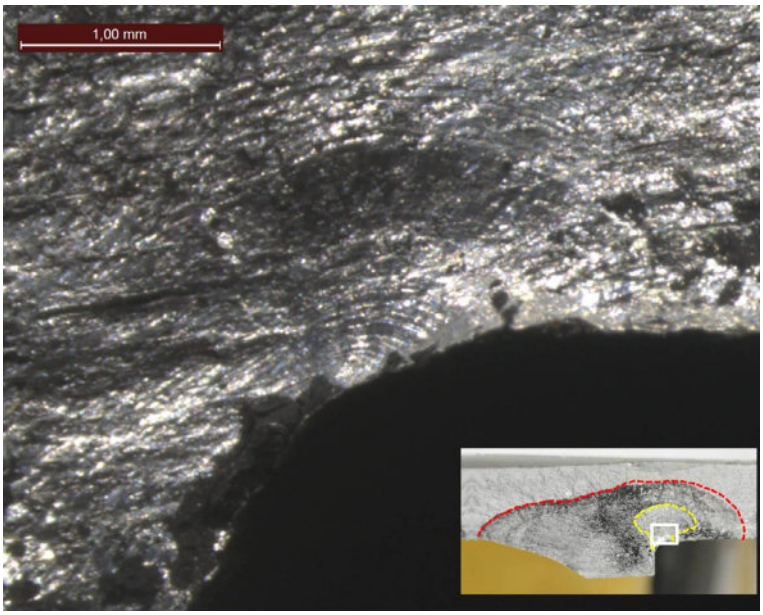

FIGURE 5.21

Area 1.

Area 2: Flat, coarse grains, containing beach marks (Figure 5.22). Fatigue propagated in this area approximately 10 mm toward the bearing cup and approximately 25 mm in the opposite direction.

Area 3: Rough, dull with coarse grains without beach marks and without black residue. These features are consistent with zone 3 being the area in which the final

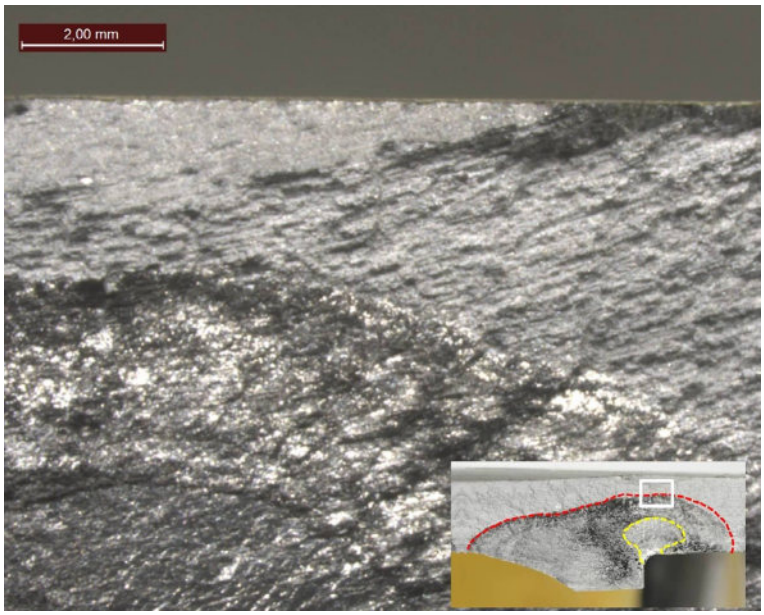

FIGURE 5.22

Areas 2 and 3. Boundary line in red.

phase of the failure occurred. The morphology of the bearing cup housing inner corner was compared with a reference part without defects to gather evidence of the cause of fatigue crack initiation. The comparative observation indicated that the initiation point presented deformations (see sharp transition in Figure 5.23, top). As those defects seemed to indicate faulty installation of the bearing cup, further analyses proceeded to ascertain whether similar features could be found on the diametrically opposed section. Deformations were present and the corner angle was greater than 90° (Figure 5.23, bottom).

2.7 MICROFRACTOGRAPHY

FESEM observations on the fracture surface confirmed the presence of the fatigue crack mechanism. Area 1 showed the morphology of stable fatigue crack propagation with striations concentric to the initiation point. Area 2 showed in turn striations and beach marks, although in this case such features were alternated to dimples, providing evidences of unstable fatigue crack propagation. Lastly, evidence of dimpled rupture was found in Area 3. This resulted from microvoid coalescence indicating final fracture by overload. In general, numerous different striations in terms of spacing and depth were observed. Analysis in a relatively small area displayed regular spacing (Figure 5.24). The lowest value observed was 0.05 μm close to the fatigue initiation point, while the highest was 0.20 μm. The observations conducted in Area

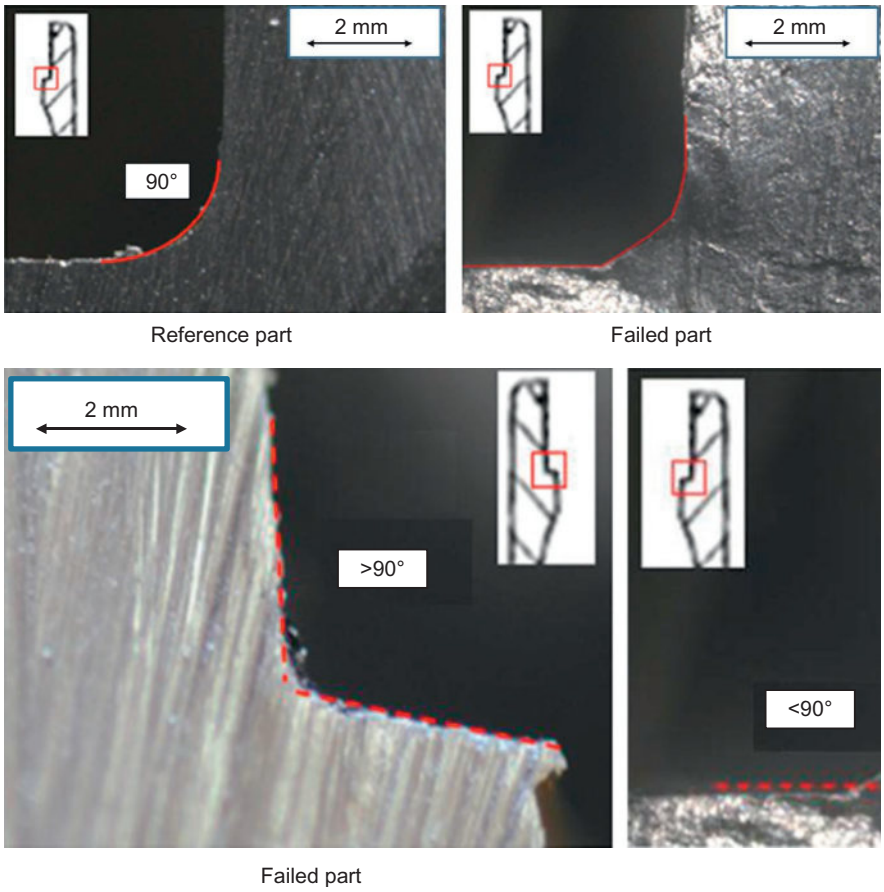

FIGURE 5.23

Curvature comparison. Top figures: fatigue initiation point comparison: failed wheel (right) and reference wheel (left).Bottom figures: featuring of failed wheel in two diametrically opposite points.

1 and Area 2 quantified the magnitude order of the fatigue striations number at 10^5 which is consistent with a high-cycle fatigue mechanism.

2.8 FINITE ELEMENT ANALYSIS

Macrofractography observations suggested the main cause for the fatigue failure was a misalignment between the bearing cup and the housing on the main wheel. FEA was used to evaluate the effect of this misalignment. A 3D model of the wheel was reproduced by the design drawings. 12,599 tetrahedron elements were applied to provide the mesh for the mathematical model. The wheel was supposed to be fixed

FIGURE 5.24

Fatigue striations in Area 1.

at the hub housing root, where the assembly is more rigid in actual fact. FEA included different simulation steps, applied in the following order:

(1) The misalignment of the bearing cup of 0.2°;
(2) The effect of thermal load on the wheel due to cold installation of the bearing cup, −18 °C;
(3) Correct repositioning of the bearing cup resulting from the mounting torque at the nut;
(4) The aircraft weight on the wheel during in-service operations (landings, turns, bumps, and rotations).

Material, contact, and large displacement nonlinearities were taken into account. All loads were applied statically, although in reality, step (4) loads are dynamic. This led to estimate values of stresses that were lower than in actual fact. This hypothesis was considered to be conservative and therefore appropriate for the aims of the simulation. The load sequence (1-4) with average mass configuration 10,000 kg would have produced high residual tensile stresses of about 220 MPa located on the inner corner of the bearing cup housing. Although the values were relatively high, they would have not been able to initiate fatigue because of their static nature: fatigue requires alternate loads to start and then increase. The subsequent periodic application of the

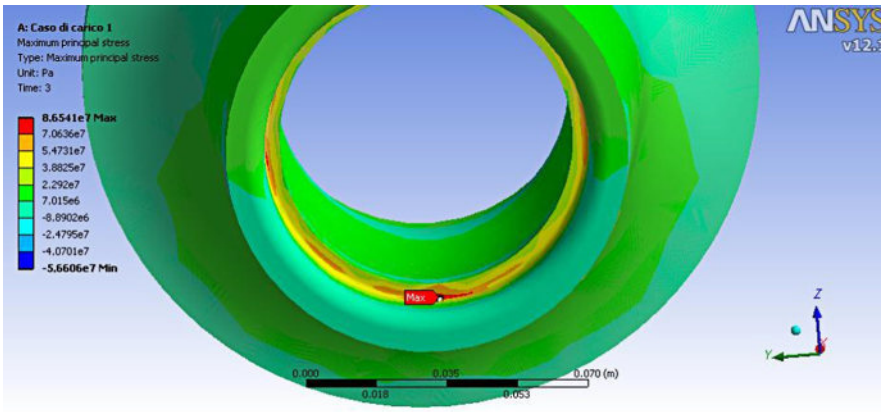

FIGURE 5.25

Stress at the fatigue initiation point.

airplane weight on the wheels due to the in-service operations would have led to about 300 MPa at the initiation site (Figure 5.25). This stress level would be higher than the AA2014-T6 fatigue limit, 125 MPa. Therefore, FEA demonstrated how the misalignment of the bearing cup led to the fatigue initiation.

2.9 MAINTENANCE HISTORY AND NDT EFFICIENCY ASSESSMENT

The main wheels are monitored for structural integrity by eddy current inspections performed only on the external surface (dashed line in Figure 5.26) but they cannot be performed under the bearing zone (line in Figure 5.26). However, no fault was

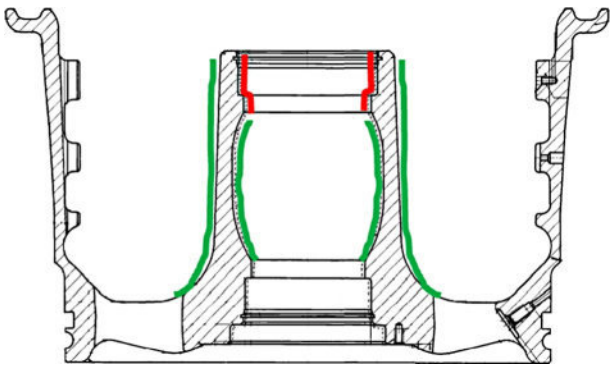

FIGURE 5.26

Eddy currents inspections: accessible area (dashed green line) and not accessible area (dashed red line).

found at the time of the last inspection before failure. Presumably the crack was not large enough to be detected by eddy currents at that time (241 landings, 58 landings before the inconvenience, total life 299 landings). Experimental evaluations were therefore carried out to prepare an alternative and more efficient NDT procedure. Ultrasounds showed higher sensibility due to the wave properties: they propagate through all the thickness. Considering the hub housing thickness at the fatigue initiation point, 10 mm, a lower detection limit of 1 mm was conservatively assumed. In order to estimate the greater reliability of the ultrasounds, fatigue life had to be correlated to the number of landings. These were associated to the beach marks observed during macrofractographic analysis. An approximate fatigue life curve was drawn based on the following maintenance data:

(1) 0 landings, no crack;
(2) 241 landings, no crack detected by eddy currents NDT. The maximum depth of the eddy current test was 0.15 mm from the surface where the probe was positioned; implying that at that time the crack was not subsuperficial. In Area 1, the average beach mark spacing is 40 μm and the estimated radius of Area 1 is about 6.5 mm. The approximate number of landings may be posited as 162. Moreover, Area 1 is where nucleation occurred: during this phase, microcracks expand taking approximately the first 20-40% of total fatigue life (60-120 landings). Area 1 (6.5 mm of propagation) is compatible with 241 landings. This is consistent with no fault being found at the time of the last inspection;
(3) 299 landings, failure of the wheel (crack longer than 25 mm);
(4) The chart in Figure 5.27 was drawn by a linear interpolation of these points (0-241 and 241-299 landings). The linear assumption is realistic in Area 1 of the fracture surface where experimental observation confirmed almost constant average beach mark spacing. Therefore, the cumulative number of landings in the area is approximately a linear function.

Thus, due to the lower detection limit of a 1 mm crack, it is presumable that ultrasounds would allow early detection of a fatigue crack beginning on the inner corner of the housing hub after about 30 landings (arrow in Figure 5.27).

3 DISCUSSION

Chemical analysis and hardness measurements indicated that no unusual features were found in the material. Macrofractography revealed deformations on the inner corner of the bearing cup housing, the initiation point of the rupture mechanism. Microfractography confirmed the nature of the progressive phenomenon: fatigue. The evaluation of the number of fatigue cycles was about 10^5, featuring high-cycle fatigue failure, while the fatigue initiation phase was dominated by heavy load low-cycle phenomena related to the landings. An attempt was made to associate the fractography findings to the in-service loads. Landings were associated to beach marks

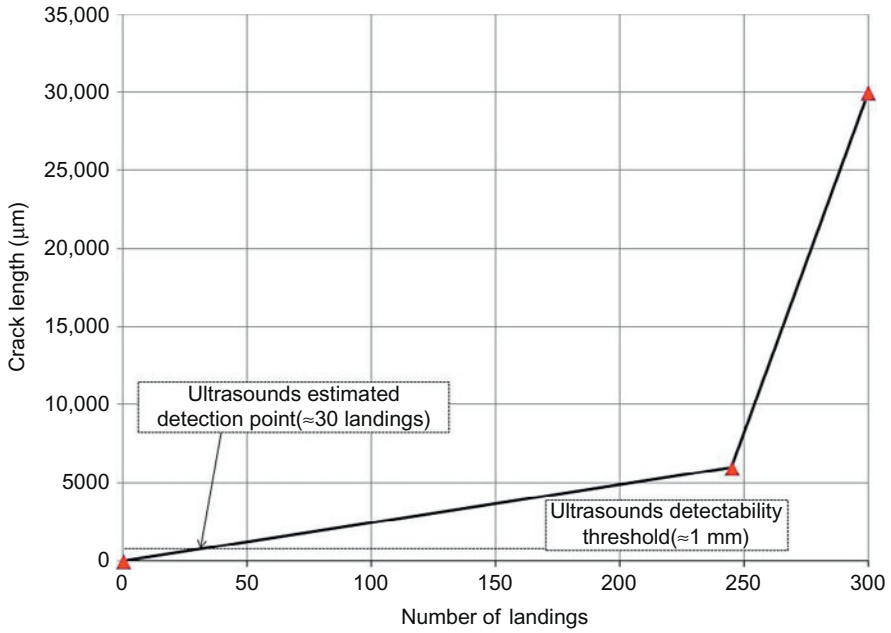

FIGURE 5.27

Fatigue history chart: crack length versus number of landings.

observed by macrofractography: they certainly exerted the greatest solicitation and affected the initiation phase of the progressive mechanism. However, given the estimated order of the magnitude of the striation number (10^5), and considering the inferior total number of landings—299—on the onset of crack growth, other loads such as turns, bumps, and rotations contributed to the fatigue phenomenon. Compatibly with the estimated number of striations, wheel rotations produced the smaller load associated to the fatigue cycles. Vibrations were also taken into account, but they were not considered to provide a significant contribution. In fact, resonance phenomena with rotational components would have led to a higher striation number, around 10^7.

The large number of load cycles was compatible with in-service loads, in particular wheel rotations. These are usually the driving force for such phenomena when associated with this type of component. Moreover, FEA proved that even a slight misalignment of the bearing cup would produce high residual stresses precisely on the inner corner of the bearing cup housing. These would be sufficient to initiate fatigue when the wheel is subject to in-service loads. Metrological measurements highlighted how the diameter of the steel ring installed on the failed wheel was 5 μm larger than the one assumed for reference. This discrepancy certainly increased the stress level. However, this could not be the main cause of the rupture mechanism because it would have resulted in multiple initiation site fatigue. Instead, a single

initiation point was observed. AMX main wheels are monitored for their structural integrity by eddy current NDT every three tyre changes. Such an inspection method is merely superficial and cannot contend with a fatigue mechanism that starts in an area which cannot be directly probed. Furthermore, the eddy current scheduling relies considerably more on tyre consumption rather than on the defect to detect. The limitations which emerged in the case outlined in this chapter and described above showed the hazards of eddy currents failing to detect fatigue cracks. Thus, ultrasounds tests were conducted to find a more effective inspection method. Results highlighted the greater efficiency of ultrasounds compared with eddy currents, thus allowing to earlier detect this type of defect (approximately 30 landings after the initiation of the fatigue crack).

4 CONCLUSION

The ground-attack aircraft main wheel failed because of a high-cycle fatigue mechanism. This was due to plastic deformations induced during the bearing cup installation procedure. In the specific case, a faulty installation procedure was identified as the cause of the wheel failure. In light of this, recommendations were issued in order to improve the procedures and to adopt appropriate NDT techniques to monitor the structural integrity of the wheel.

REFERENCES

[1] Allegrucci L, Amura M, Bagnoli F, Bernabei M. Fatigue fracture of a aircraft canopy lever reverse. Eng Fail Anal 2009;16:391–401.
[2] Amura M, Aiello L, Colavita M, De Paolis F, Bernabei M. Failure of a helicopter main rotor blade. Proc Mater Sci 2014;3:726–31.
[3] Amura M, Allegrucci L, De Paolis F, Bernabei M. Fatigue fracture of an AMX aircraft main wheel. Eng Fail Anal 2013;27:194–202.

CHAPTER

6 Failure investigations of helicopter tail rotor gearbox casings at Agustawestland Limited

Fiona Belben

AWL Materials Technology Laboratory, AgustaWestland Ltd., Yeovil, Somerset, United Kingdom

CHAPTER OUTLINE

Handbook of Materials Failure Analysis With Case Studies from the Aerospace and Automotive Industries.
http://dx.doi.org/10.1016/B978-0-12-800950-5.00006-5

1 INTRODUCTION

Weight saving is a prime consideration in the design and manufacture of helicopters and other aircraft. Reductions in the weight of the aircraft allow for increased payload capabilities or increased flight range due to improved fuel efficiency. For this reason, the low densities of magnesium alloys is very attractive to aircraft designers and for many years magnesium casting alloys have been used successfully for the manufacture of gearbox housings. In addition to their lightness, magnesium alloys also exhibit a good damping capacity, elastically absorbing vibrational energy so that it is not transmitted through the walls of gearbox casings, therefore reducing gearbox noise and vibration [1]. This is a significant benefit to helicopter design where noise and vibration can be a problem and AgustaWestland (and previously Westland Helicopters) has utilized a number of different magnesium casting alloys for the manufacture of gearbox housings.

Despite these advantages, the generally poor corrosion resistance of most magnesium alloys has meant that repair and overhaul costs have generally been high. This is due to a combination of high scrap rates when corrosion damage is severe, or high repair costs when a casing is considered salvageable, the latter being due to the need to dress out any corrosion and re-apply what are in many cases complex surface-protective treatments.

Recent studies at AgustaWestland [2], which compared the corrosion damage on the main, intermediate, and tail gearboxes, have shown that the numbers of cases of unrepairable corrosion are least for the main rotor gearbox and most for the tail rotor gearbox (TRGB). The reason for this variation in corrosion susceptibility is not known, but it is thought that it is possibly related to the downwash from the main rotors directing any rain or sea spray toward the tail of the aircraft.

Fatigue strength is another major consideration when selecting materials for use on helicopters. Fatigue in fixed wing aircraft tends to be primarily low cycle due to take-off and landing loads, whereas fatigue in helicopters is also subject to high-cycle fatigue, due to the cyclic loading introduced by either the main or the tail rotor blades [3].

2 BACKGROUND TO THE PROBLEM

The housing that is the subject of this chapter is shown in Figure 6.1. This is the TRGB center housing from one of our medium-lift helicopters and is a sand casting manufactured from ZE41A-T5 (nominal composition 3.5-5.0% zinc, 0.75-1.75% rare earths (RE), 0.4-1.0% zirconium, remainder—magnesium) to the specification BS L128 which is similar to AMS4439.

FIGURE 6.1

Image showing the port and forward faces of a TRGB center housing.

This alloy generally exhibits minimal microporosity, freedom from microshrinkage, and also exhibits reasonably good room-temperature tensile and fatigue properties [4]. In addition, this alloy is widely used for relatively high-temperature applications (<250 °C) due to its resistance to creep [5]. However, the corrosion resistance of this alloy is generally poor, and during repair and overhaul, corrosion damage at the attachment points of the center housing is frequently encountered due to the surface-protective treatments becoming chipped and scratched.

During routine maintenance of one of these TRGB's, a crack was discovered on one of the webs of the center housing between the gearbox attachment bolt holes. The failure examination of this housing [6] suggested that this crack was due to fatigue and that it had originated at an oxide inclusion.

Failure analysis of magnesium alloy castings can be very difficult due to their rapid oxidation, which can lead to even very recent cracks being heavily corroded. In addition, the absence of clear fracture features [7], such as fatigue striations, and the typical brittle fracture mode can make the analysis of failures by fatigue particularly problematic. The analysis of these failures therefore often relies on the shape of the crack, particularly with respect to any defects or geometrical stress raisers, and the history of the part. This means that detailed information, such as the number of cycles to failure, can rarely be determined in these materials.

Failure investigation records for this aircraft type were reviewed and it appeared that there had only been two previous cases of TRGB housing cracks [8,9], both of which were identified as fatigue cracks and had been attributed to the stress concentration due to an undersize fillet radius adjacent to one of the rear attachment holes on the housing base. The discovery of a crack that was unrelated to the fillet radius and

appeared to be due to a casting defect raised concerns about the casting quality and whether the necessary radiographic inspections had been undertaken. A review of the manufacturing records for this housing was therefore carried out and this revealed that the correct inspections had been undertaken; hence, the size and form of the defect meant that it had not been detected.

To check if other housings containing defects had entered service, an eddy current NDT (nondestructive testing) examination of these center housings, particularly around the webs and base was introduced on new castings, some new built assemblies and others when TRGB's were returned for repair and overhaul. It was hoped that this would provide an understanding of the extent of the problem.

Seventeen housings gave eddy current "indications" and these were subject to very brief failure investigations [10,11]. Some of the indications were found to be due to cracks, but others were found to be due to oxide inclusions which did not appear to have yet initiated fatigue cracks.

Low-magnification microscopic examinations of the cracked housings were undertaken and it was concluded from the "thumbnail" shapes of the cracks that all had been due to fatigue. The cracks in the webs had initiated from trapped oxides and those in the lugs had initiated from an undersize fillet radius. The only apparent exception to this was a casing where web cracks had initiated from a poor surface finish resulting from a fettling operation. In addition to the housings exhibiting indications, approximately 50 housings were found to be fully acceptable with no detectable defects.

As a result of these findings, a decision was made to undertake a number of design modifications to the center housing, including increasing the thickness of the webs, increasing any fillet radii, and also introducing a relatively new casting alloy, WE43A-T6 (nominal composition 3.7-4.3% yttrium, 2.4-4.4% rare earths (RE), 0.4-1.0% zirconium, remainder—magnesium) manufactured to an in-house specification similar to AMS4427. This alloy was under evaluation by our laboratory and was exhibiting comparable fatigue properties and significantly improved corrosion properties in comparison with ZE41A. However, the WE43A was only introduced for use on new gearboxes and ZE41A housings continued to be used on gearboxes already in service.

Experience showed that the ZE41A housings could continue to be used, albeit with the implementation of increased frequency eddy current inspections because, despite the number of these housings in service and the number of cracks discovered, no web cracks had ever propagated into the main body of the housings.

At this time, we received information that a "short-life" ZE41A center housing crack had been discovered. However, this housing had undergone NDT eddy current examination after manufacture and had shown no indications. An investigation, referred to here as "Failure Investigation 1" was therefore undertaken on this part.

3 CASE 1: FAILURE INVESTIGATION 1 (F1)

The cracked TRGB center housing was supplied for investigation together with the information that the crack indication had been discovered during a routine eddy current inspection after 200 h of operation. A review of all the previous TRGB fault investigations was also undertaken.

3.1 PROCEDURE

The housing was examined visually and any identification markings were noted. This allowed the specific casting release documents to be located and checked for compliance. The visual examination of the housing also looked for damage that could have contributed to the initiation of the crack and identified its position.

A section containing the crack was cut from the housing and the crack was broken open to allow the fracture surfaces to be examined, initially using a WILD MAKROSKOP M420 binocular microscope and subsequently using a LEO 1455VP scanning electron microscope (SEM). During the SEM examination, compositional information was recorded using the attached Princeton Gamma Tech IMIX energy dispersive X-ray (EDX) analysis system.

3.2 RESULTS

The certificate of conformity for the casting showed the material properties to be fully acceptable. Further tensile testing was not considered necessary, due to the close relationship between separately cast test bars and the actual casting typically shown by the alloy ZE41A [1].

The crack was located on the port face of the center housing on the central web between the gearbox base and the attachment flange for the output housing. Examination of the fracture surfaces revealed river markings emanating from a small surface breaking casting flaw on the "nose" of the web, beach markings were also visible, see Figure 6.2. It was evident from these features that the crack was due to fatigue and that the crack had initiated at the casting flaw. It had then propagated through the web intersecting a number of other casting flaws. In particular, one very large flaw measuring ≈ 2 mm in diameter was only a few millimeters away.

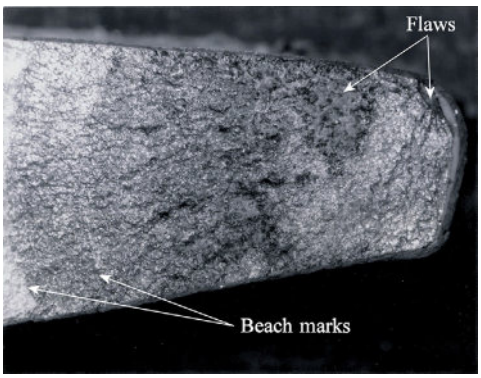

FIGURE 6.2

Image showing one of the fracture surfaces of the fatigue crack in the Port Central Web of the ZE41A housing in Failure Investigation 1.

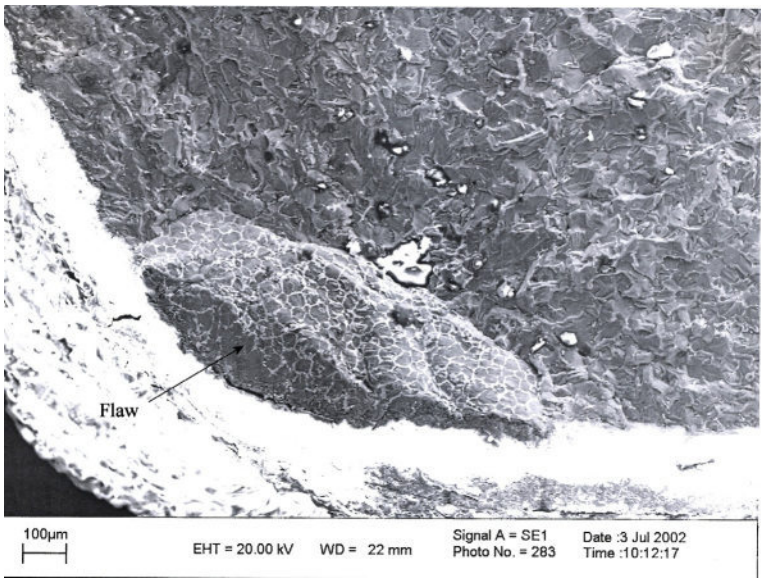

FIGURE 6.3

SEM image showing the casting defect in the origin region of the ZE41A housing web fatigue crack evident during Failure Investigation 1.

The fatigue crack was measured to be 11 mm long and it encompassed the full thickness of the web. The flaw at the origin was approximately 0.9 mm long and 0.3 mm deep.

SEM examination of the fracture surface revealed that the crack origin region exhibited a relatively smooth "as cast" surface with a visible grain structure; see Figure 6.3. This was interpreted as a very small cold shut at the casting surface, possibly resulting from the presence of an entrapped oxide film. Other flaws evident on the fracture surface were also examined and were found to be of a similar appearance to that at the origin.

It was noted that the fracture surface was relatively undamaged. This indicated that the fatigue loading on the web had been wholly tensile.

An EDX spectrum was obtained from a clean area of the fracture surface and the composition was found to be consistent with the alloy ZE41A. An EDX spectrum was also obtained from one of the "film-like" casting defects and it was clear from this spectrum, the reduced count rate and the general appearance of the flaws, that they were thin oxide films.

3.3 DISCUSSION

Similar to the findings of the previously reported failure investigations on TRGB center housings from this aircraft type [6,10,11], a fatigue crack appeared to have initiated from a casting defect in one of the webs and this had propagated into the

web. The defect was identified as a thin oxide film; these are commonly found in magnesium casting alloys [12] when turbulent flow occurs during pouring.

The housing of the current investigation was found to have been subject to a full post manufacture NDT examination and had shown no eddy current indications. However, it is evident that the type of casting flaw present at the origin of this crack would have been difficult to detect by NDT given its small size, orientation, and tightly closed nature. A review of the previous failure investigations [13] revealed that all "used" housings inspected using an eddy current method during repair and overhaul exhibited indications, whereas only one "unused" housing gave an eddy current indication. This suggests that initially the flaws were either tightly closed or "masked" by a layer of metal at the surface (possibly smeared metal from the fettling operation), but when the housing is loaded in service, these flaws open and can then initiate fatigue cracks.

A summary of the findings from the previous failure investigations on these center housings is given in Table 6.1.

This showed that, with the exception of one housing, cracking always involved either the port webs (forward or center) or the starboard rear webs or attachment lug. The formation of cracks at opposite "corners" of the housing base is indicative of vibratory torque loading, with particularly high tensile loads being experienced in the port forward and the starboard rear quadrants. During the early failure investigations, the high stress was noted, but much of the emphasis was placed on the presence of casting defects and dimensional errors. However, the discovery that the cracks affected diametrically opposite corners of the housing indicated that although these features would have been detrimental to fatigue properties, they were not the primary cause of the cracks, but merely examples of the features which high fatigue loads will seek out to act as crack initiation sites. This was corroborated by the fact that one of the foot cracks did not appear to be related to any defects.

It was also noted when compiling the data from previous center housing failure investigations that some of the references to web or feet positions supplied by field service engineers appeared to be incorrect and the port and starboard sides of the gearbox had in a few cases been misidentified. This illustrates the importance of photographic evidence when collecting data.

Although undesirable, casting flaws, particularly in the form of oxides are a common feature of magnesium alloy sand castings. This is because magnesium exhibits a low free energy of formation for its oxide and hence complete prevention of oxide inclusions is virtually impossible [12]. There was no reason to suppose that there had been a significant deterioration in the general casting quality, as these castings had been produced by the same foundry, to the same radiographic standard, throughout the period in question.

It was however considered probable that the fatigue loads acting on the TRGB housing on this aircraft had changed over time. The evolution of an aircraft which has been in service for many years can include significant changes, such as different rotors, different engines, and the incorporation of different mission equipment, all of which can significantly change the weight and dynamics of an aircraft. Furthermore,

Table 6.1 Summary of the Early TRGB Center Housing Failure Investigations Undertaken at AgustaWestland Limited

Casing Modification Standard	Positions of Web Crack Indications	Positions of Base Crack Indications	Defect Identified
A		Starboard, rear	Undersize fillet radius
B		Starboard, rear	Undersize fillet radius
B	Port, forward and port, center		Surface finish
Identification Marks illegible		Starboard, rear	Undersize fillet radius
D	Port, forward	Starboard, rear	Entrapped oxide
B	Port, rear		Entrapped oxide
C	Port, forward		Entrapped oxide
C	Port, forward		Entrapped oxide
C	Port, forward		Entrapped oxide/ surface finish
D	Port, center		Entrapped oxide
D	Port, forward		Entrapped oxide
C	Port, forward and center		Entrapped oxide
D	Port, forward	Starboard, rear	Entrapped oxide in web No obvious defect in foot
D	Port, forward and starboard, rear		Entrapped oxide
D	Starboard, rear		Entrapped oxide
D	Starboard, rear		Entrapped oxide
D	Starboard, rear		Entrapped oxide
D	Starboard, rear		Entrapped oxide
D	Port, forward		Entrapped oxide
D	Starboard, rear		Entrapped oxide
D[a]	Port, center		Entrapped oxide
D	Port, forward and starboard, rear	Starboard, rear	Entrapped oxide

[a]*This housing was investigated in Failure Investigation 1.*

the aircraft on which these particular gearboxes were fitted had seen a weight increase of approximately 30% over its lifetime, which would have put increased stresses on the whole aircraft.

It was considered possible that certain variants of this aircraft may be more susceptible to cracking than others. However, a review of the previous failures [13] revealed that the occurrences of gearbox cracks were not limited to any particular aircraft variant or aircraft operator.

The cause of the apparently increased torsional loading on the TRGB center housing was therefore not specifically determined. However, it was believed that the

introduction of the new stronger and more corrosion-resistant WE43A material, together with increased fillet and corner radii and an increased web thickness would provide a solution.

3.4 CONCLUSION

(i) A through-thickness fatigue crack was discovered in the port center web of this housing.
(ii) There was little damage to the fracture surfaces indicating that the loads on this web had remained tensile.
(iii) The crack had initiated from a small casting flaw, identified as an oxide, at one corner of the web.
(iv) Several other thin oxide inclusions were present on the fracture surface.
(v) This casting had previously been subject to an eddy current examination and no defects had been discovered.
(vi) It is considered that the oxide at the origin was not found by eddy current because of its size, orientation, and geometric characteristics.
(vii) A review of previous failure investigations on these housings has indicated that the incidence of cracking is more likely to be related to the in-service stresses experienced by the housing than to the casting quality.
(viii) A material and geometry change has been implemented on these housings which is hoped to offer a solution to the problem of cracking.

4 CASE 2: FAILURE INVESTIGATION 2 (F2)

Two years after "Failure Investigation 1," reports were received that another cracked TRGB center housing had been discovered during a routine inspection. However, this was of the new design with increased web thicknesses and increased fillet radii. It was also manufactured from the new alloy WE43A.This center housing had reportedly completed less than 70 flying hours.

4.1 PROCEDURE

An investigative procedure similar to that undertaken in Failure Investigation 1 was employed.

4.2 RESULTS

Visual examination revealed a crack in the port forward web. The section of material incorporating the crack was cut from the housing and the crack was broken open to reveal the fracture surfaces. The initial examination, undertaken using a WILD MAKROSKOP M420 binocular microscope, revealed a dull, dark-colored flaw at the nose of the web (see Figure 6.4) with the rest of the fracture surface exhibiting a reflective crystalline appearance.

FIGURE 6.4

Image showing one of the fracture surfaces of the crack in the port forward web of the WE43A housing examined in Failure Investigation 2.

The crack had propagated 13 mm from the nose of the web and there was evidence of a curved crack front at a couple of locations, suggesting that the crack was due to fatigue.

Examination of the fracture surfaces using a LEO 1455VP SEM revealed that the fracture was of a facetted appearance with different fracture planes being evident in adjacent grains (or groups of grains). Although the fracture surfaces did not display fatigue striations or the flat transgranular failure mode typical of other light alloy castings, the fracture features present were similar to those previously seen in fatigue cracks in magnesium alloy castings. An example of a typical transgranular fatigue failure in an aluminum alloy casting has been included for comparison purposes as Figure 6.5.

The defect at the nose of the web measured $\approx$3 mm in width and extended $\approx$1 mm below the surface (see Figure 6.6). Imaging utilizing the back-scattered electron (BSE) imaging mode to provide contrast based on atomic weight, revealed the defect to have a relatively smooth surface in relation to the rest of the fracture. It was also evident on both halves of the fracture. This imaging technique also indicated that the defect was rich in higher atomic number elements. This was confirmed using the attached Princeton Gamma Tech IMIX EDX analysis system which revealed the significant presence of yttrium and neodymium and the minor presence of magnesium.

During the visual examination, a feature was noticed on an adjacent area of the casting. This region was subject to an eddy current inspection which detected a second flaw. The section of material containing this was also removed from the housing and the flaw was sectioned, mounted, and polished prior to SEM examination.

BSE imaging revealed that this feature was a "linear defect" measuring at least 1.5 mm in length and that the two surfaces of this had the appearance of a "skin" that was rich in higher atomic number elements; see Figure 6.7. EDX analysis revealed it to be rich in yttrium and neodymium, similar to the flaw at the crack origin. Figure 6.8 shows a region of this flaw where the "folds" in the yttrium-rich "skin" are clearly visible.

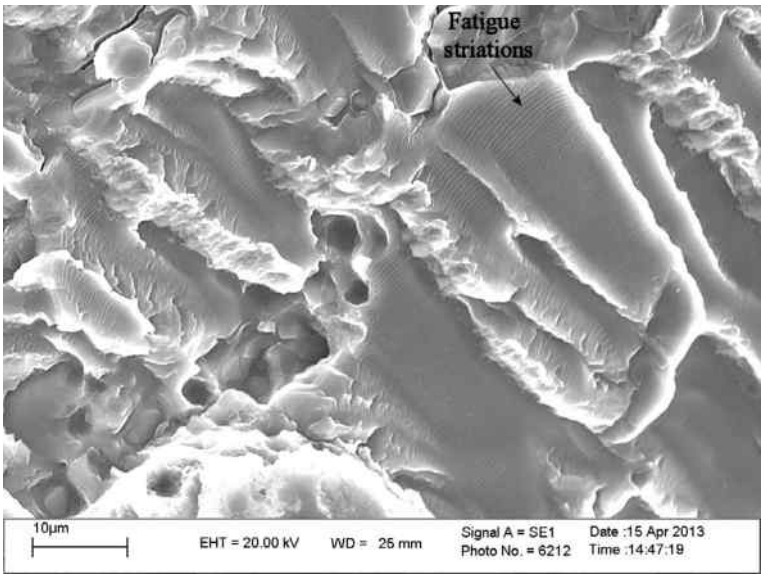

FIGURE 6.5

SEM image showing an example of fatigue striations on the fracture surface of an A357 cast aluminum alloy fatigue fracture.

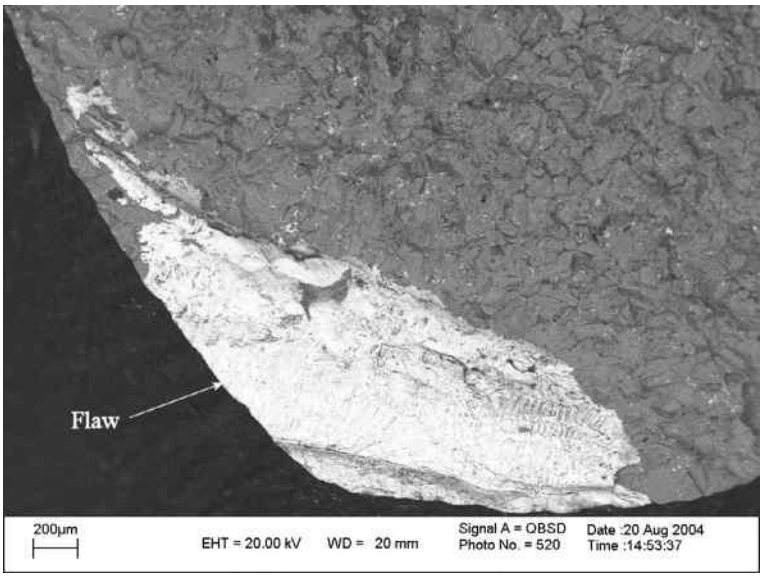

FIGURE 6.6

SEM BSE image showing the casting defect at the origin of the web fatigue crack on the WE43A housing examined in Failure Investigation 2.

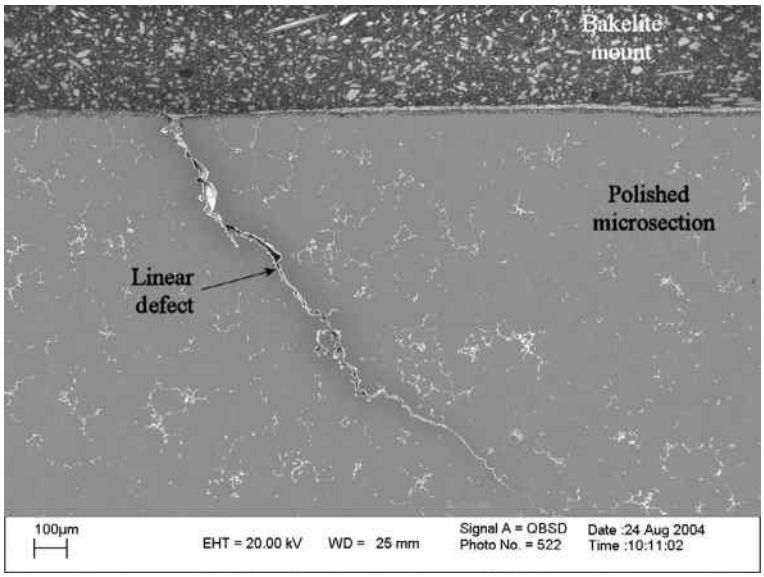

FIGURE 6.7

SEM BSE image showing the linear casting defect in the region adjacent to the cracked web on the WE43A housing examined in Failure Investigation 2.

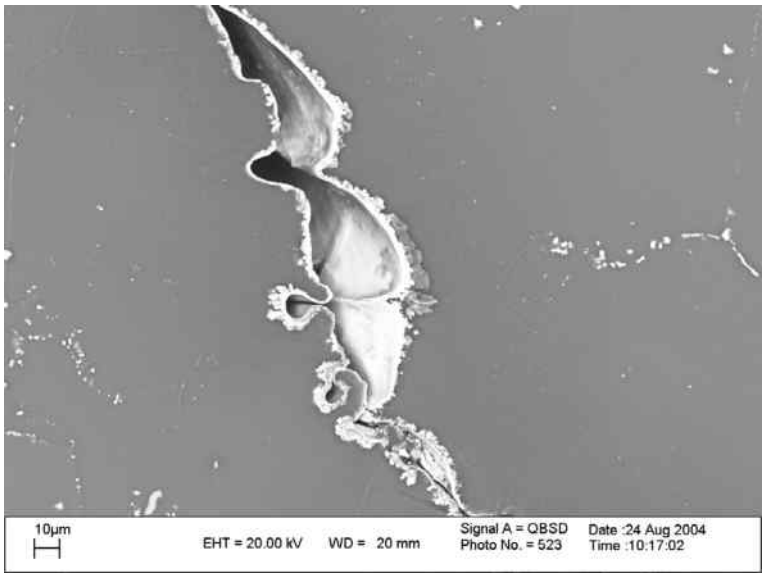

FIGURE 6.8

SEM BSE image showing a fold in the skin-like linear casting defect in the WE43A housing examined in Failure Investigation 2.

4.3 DISCUSSION

The failure of this web was consistent with previous occurrences of cracking in this part.

It appeared that although this housing was manufactured from the new material to the modified design, the large size of the flaw found in the web had negated any benefits of these design changes.

The flaw at the fatigue origin was found on both halves of the fracture surface and the surface of the flaw did not show any fracture features. This indicated that the two halves of the flaw had probably not been in contact over much of the affected area; it was therefore evident that this was similar to the second flaw which had been revealed by microsection. This type of flaw, consisting of a folded oxide film or "skin," occurs as a result of turbulent flow or "waterfalling" (where molten metal falls to a lower level in the mold during casting) and its geometry is particularly damaging to fatigue properties [14]. As WE43A has seen increased use in the manufacture of complex castings, its tendency to form these tenacious oxide films has become more widely reported [15]. It has been found that their presence can be minimized by changes in foundry practice and greater attention to detail in the design of molds, routing of the molten material through the mold and during pouring. However, this can have an impact on component cost [16].

It was considered significant that there were several flaws with high yttrium (and neodymium) levels within the relatively small paint-stripped area on this housing. This suggested that either this region was more susceptible to the formation of defects or that there were similar numbers of defects throughout the housing, but the high stresses in the webs were causing the "skins" here to initiate cracks.

4.4 CONCLUSION

(i) A fatigue crack was present in the port forward web.
(ii) This crack appeared to have initiated from a linear defect that was identified as an yttrium-rich oxide skin.
(iii) A flaw of a similar size and composition was found in the region of the housing adjacent to the cracked web.
(iv) It was not known whether the web region of the housing was more susceptible to the entrapment of oxide skins or whether similar defects were present throughout this housing.

5 CASE 3: FAILURE INVESTIGATION 3 (F3)

Soon after "Failure Investigation 2," reports were received that there had been a second occurrence of cracking of a modified WE43A center housing. It was reported that this housing had completed less than 200 flying hours when the crack was discovered during a routine inspection. This housing was also supplied for investigation.

5.1 PROCEDURE

A similar procedure to that employed within Failure Investigations 1 and 2 was used.

5.2 RESULTS

Visual examination revealed a crack in the starboard rear attachment foot. This crack was broken open and low-magnification microscopy using a WILD MAKROSKOP M420 binocular microscope revealed that despite being close to one of the gearbox attachment holes fitted with a cadmium-plated steel bush, the crack had not broken through to the hole or the lower surface of the housing.

The fracture surface was predominantly of a dull granular appearance but with a more reflective crystalline appearance near the upper and rear surfaces of the foot and near the curved crack front.

It appeared that the crack had initiated at the upper surface of the foot and the fracture pattern indicated that there was probably more than one origin. The first origin appeared to be at or near the corner between the side and top of the base section and there appeared to be a second origin in line with the outer edge of the top hat bush. Examination of the bush and the casting surface in this region did not show any evidence of fretting or wear which might have initiated the crack.

Examination of the fracture surfaces using a LEO 1455VP SEM revealed that the failure was relatively brittle with distinct fracture planes evident. The position of the crack origins was not easily determined as there were no obvious features that would have acted as crack initiators. However, the origins did appear to be in the areas identified with the binocular microscope.

5.3 DISCUSSION

This second occurrence of cracking in a WE43A center housing was particularly significant. The first occurrence (Failure Investigation 2) had been attributed to the presence of a large casting defect in the port forward web. However, the crack within this WE43A housing was in the starboard rear foot and did not appear to relate to any oxides, other casting defects, or significant geometrical stress raisers. In addition, there was some evidence that this crack was multi-origin. This suggested that either this housing was subject to particularly high stresses or that the fatigue strength of this (and possibly other) WE43A housings was lower than anticipated.

5.4 CONCLUSION

(i) A fatigue crack was present in the starboard rear foot of this housing.
(ii) The fatigue crack appeared to have more than one origin on the upper surface of the housing.
(iii) There was no evidence of casting defects or other detrimental features that could have contributed to the initiation of this crack.

6 REVIEW OF MECHANICAL PROPERTIES

Following the discovery of the crack in a WE43A housing that was related to a large inclusion (F2) and, more importantly, the crack in a second WE43A housing (F3), that appeared to be unrelated to any detrimental defects, a decision was made to carry out an evaluation of the static and fatigue strength of the WE43A material. The housing from F3 was utilized in this evaluation and the results were compared with the original WE43A qualification data [17], which had been obtained on a different type of housing.

6.1 PROCEDURE

The housing from F3 was sectioned to produce tensile and coupon fatigue specimens and these were manufactured and tested in accordance with ASTM E8M and E466, respectively.

A sample of material from this casting was also supplied to an outside company for determination of the chemical composition.

Tensile testing was undertaken using a Zwick 1498 500kN tensile testing machine and axial fatigue testing was carried out on a 150kN Amsler Vibrophore. On completion of the fatigue testing, the fracture surfaces were examined using a WILD MAKROSKOP M420 binocular microscope and a LEO 1455VP SEM.

6.2 RESULTS

The chemical analysis revealed that the casting composition fully complied with the in-house material specification, as shown in Table 6.2.

Table 6.3 shows the tensile results obtained from this housing (F3), the mean tensile results from the WE43A qualification castings and the WE43A in-house material specification values.

The tensile properties obtained from this housing fully satisfied the requirements and also exhibited a higher mean 0.2% proof stress and ultimate tensile strength than the qualification castings.

The fatigue results obtained have been plotted in Figure 6.9 together with the qualification fatigue data. It was evident that this housing showed improved fatigue strength, but the standard deviation was nearly twice that of the qualification data. A statistical mean difference test was also undertaken using an internal analytical procedure based on a "student's t" distribution [18] and this revealed that the difference in the datasets was statistically significant.

Examination of the fatigue specimen fracture surfaces was initially undertaken using the binocular microscope. However, the brittle failure mode of the WE43A meant that in some cases it was not obvious where the cracks had initiated and in most cases, the size of the fatigue crack was not clear. Hence, despite the increased time taken to undertake SEM examinations, it was decided that every specimen should be viewed in the SEM.

Table 6.2 Results of the Chemical Analysis Undertaken on the Casting from Failure Investigation 3 and the Compositional Requirements of the WE43A In-House specification

Element	Weight % of Element Measured in the Housing from F3	Compositional Limits of WE43A In-House Specification
Yttrium	3.85%	3.7-4.3%
Neodymium	2.00%	2.0-2.5%
Rare Earths (RE)	2.66% (2.00%Nd+0.06%Yb +0.11%Er+0.28%Dy+0.21%Gd)	2.4-4.4%
Zirconium	0.45%	0.40-1.0 %
Zinc	0.17%	0.2% maximum
Lithium	0.12%	0.2% maximum
Manganese	0.02%	0.15% maximum
Copper	<0.01%	0.03% maximum
Iron	<0.01%	0.01% maximum
Silicon	<0.01%	0.01% maximum
Nickel	<0.005%	0.005% maximum
Magnesium	Remainder	Remainder

Table 6.3 Tensile Results from the Casting from Failure Investigation 3 and the WE43A Qualification Castings Compared with the In-House Material Specification Requirements

Specimen Identity	0.2% Proof Stress (MPa)	UTS (MPa)	% Elongation
T1 (from F3 casting)	189	267	6.0
T2 (from F3 casting)	188	255	4.0
T3 (from F3 casting)	186	266	6.0
T4 (from F3 casting)	189	254	4.0
F3 casting mean properties	188	261	5.0
Mean properties of qualification casting	181	246	5.1
In-house WE43A material specification requirements	≥155	≥225	≥2.0

During the previous gearbox failure investigations, BSE imaging had proved useful because the difference in atomic number between magnesium and yttrium (and the rare earths) is large enough to produce large differences in image contrast. This allowed the higher atomic number yttrium-rich skins to be located easily as they appeared white or off-white. Whereas other oxides, dross, or corrosion would typically be evident as darker regions due to their lower density resulting from the

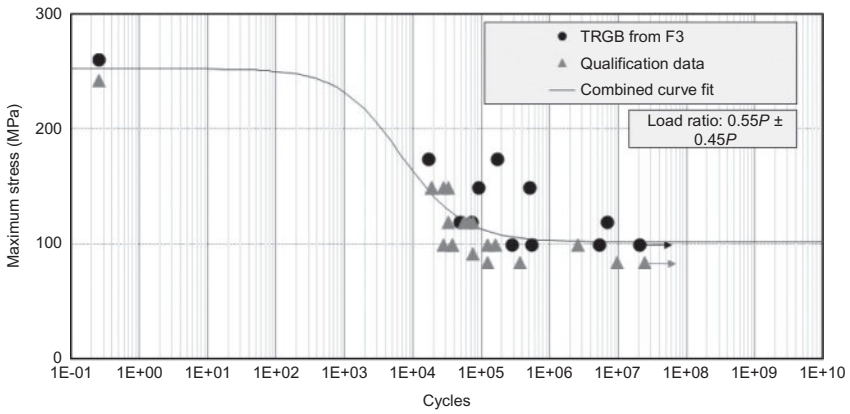

FIGURE 6.9

Fatigue results from the housing examined during Failure Investigation 3 and the WE43A qualification fatigue data.

presence of low atomic number elements, i.e., oxygen, carbon, and silicon. The fatigue specimens were therefore viewed using BSE imaging and during this stage of the examination it was noticed that the BSE imaging mode was also revealing regions of fatigue more clearly than was the case with the SE (secondary electron) imaging mode.

Examples of an SE image and a BSE image of the same area of a WE43A fatigue specimen fracture surface have been included to show these differences (compare Figures 6.10 and 6.11). The fatigue failure shown had initiated from two pores (one only partially shown) and the extent of the fatigue cracks is more easily seen in the BSE image. Another example, from the F3 housing is shown in Figure 6.12 and again this shows the distinction between the fatigue and overload regions quite clearly.

In an attempt at determining how "damaging" yttrium-rich oxide skins are to the fatigue strength of WE43A, the fatigue results were analyzed with respect to the features (if any) at the crack origins. This revealed that porosity was not as damaging to the fatigue properties as linear oxide films and the other slag/drossy inclusions [19]. Unfortunately, the qualification fatigue specimens were no longer available so the relationship between the types of defects and fatigue properties on these specimens could not be determined. However, it was reported that of the 24 fatigue specimens tested, 12 exhibited "oxides" on their fracture surfaces.

6.3 DISCUSSION

The housing examined in F3 had exhibited a fatigue crack, but there were no obvious defects at the origin. This raised the concern that the fatigue strength of the WE43A material may not be representative of the original qualification material. However,

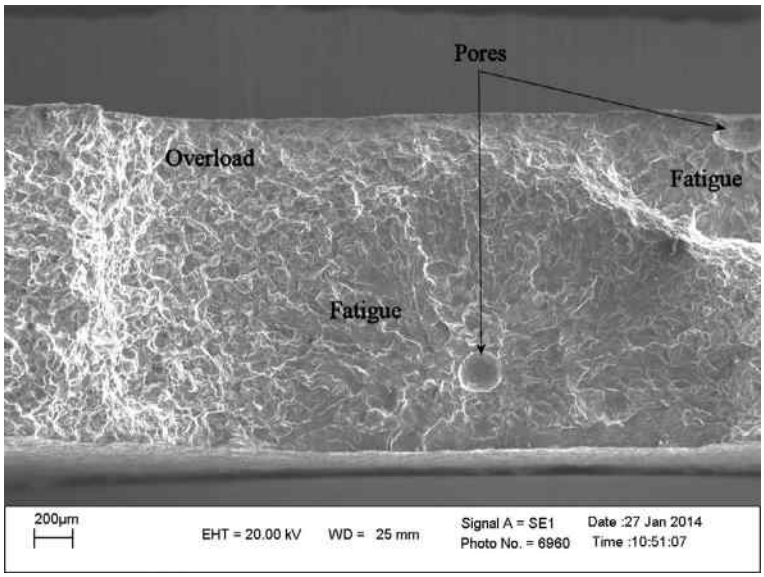

FIGURE 6.10

SEM image showing an example of fatigue cracking from a pore on a WE43A fatigue specimen imaged in the SE mode.

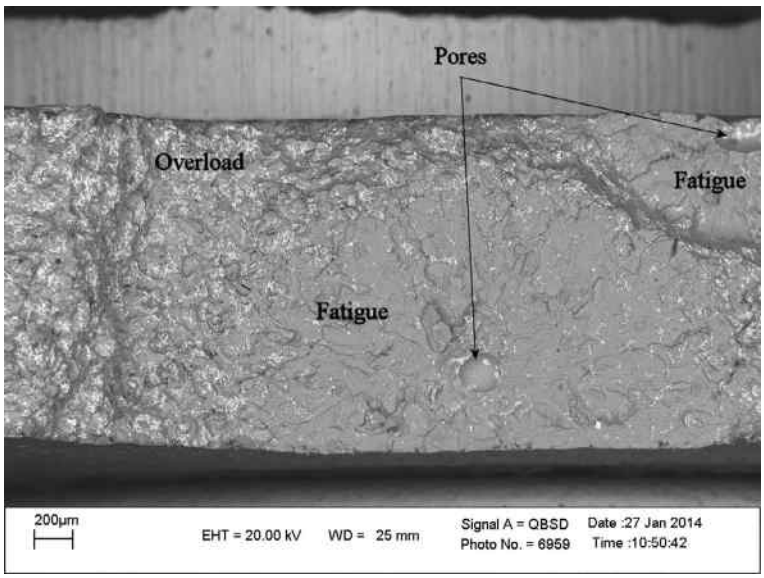

FIGURE 6.11

SEM image showing the same example of fatigue cracking from a pore on a WE43A fatigue specimen as that in Figure 6.10, imaged in the BSE mode.

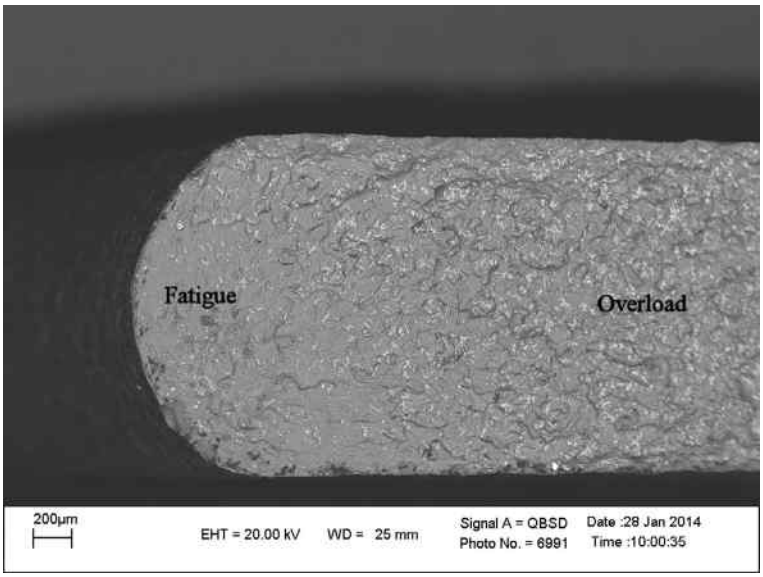

FIGURE 6.12

SEM BSE image of a fatigue specimen from the WE43A housing examined during Failure Investigation 3.

mechanical testing revealed that the tensile and fatigue properties of the F3 housing were better than the qualification castings but the spread of fatigue results was greater. This was attributed to the qualification casting being of a less complex geometry.

Examination of the coupon fatigue specimen fracture surfaces revealed yttrium-rich oxide skins and other detrimental features at the crack origins. The analysis of the fatigue data, with respect to these defects, indicated that the yttrium-rich skins (and other types of oxide films) were more detrimental to the fatigue strength than features such as porosity or shrinkage cavities. This was probably a result of the former's "notch-like" geometry and the latter's small size due to these being "Class A" castings. Yttrium-rich oxide skins have been estimated to reduce the fatigue endurance limit by approximately 13% [20].

During this investigation it was noticed that the BSE imaging mode on the SEM was revealing regions of fatigue more clearly than the standard SE imaging mode. The explanation for this is that in magnesium alloys overload failures are typically intergranular and the grain boundary precipitates in the WE43A alloy are rich in high atomic number elements. Hence, regions of static overload failure in this alloy appear predominantly light in color when imaged using BSE's. In contrast, fatigue failures in magnesium alloys are typically transgranular, and the grain interior of WE43A is richer in magnesium which has a low atomic number. Hence, regions of fatigue are characterized by planar, dark-colored grain interiors, outlined by the lighter grain boundaries when imaged using BSE's.

Consideration has been given to the possibility that the fatigue properties of cast magnesium alloy components may be lower than those of coupon specimens. This is due to the probable presence of surface breaking flaws (oxide skins) in complex regions of a casting. To test this possibility, the webs from this housing were removed, sectioned, and polished and one showed a large (2-mm long) yttrium-rich oxide skin.

6.4 CONCLUSION

(i) Comparison of the coupon fatigue results from the WE43A housing examined during Failure Investigation 3 with those obtained from the WE43A qualification castings demonstrated that the fatigue strength had improved, but that the results exhibited a greater scatter.

(ii) The tensile results obtained exceeded those previously obtained on the qualification castings and satisfied the requirements of the in-house specification.

(iii) Yttrium-rich oxide skins appeared to be present both at the surface and subsurface. These features were found to be more detrimental to fatigue than porosity or shrinkage cavities in these Class A castings.

(iv) The BSE imaging mode on the SEM proved particularly useful in determining the extent of fatigue cracking when analyzing the fracture surfaces of fatigue specimens.

7 OTHER TRGB FATIGUE INVESTIGATIONS

Following these investigations, other small programs of work were initiated. These included comparisons of the effectiveness of different mold-purging techniques on microstructure and fatigue [21]; an evaluation of the benefits of glass bead peening on fatigue [22] and the evaluation of a casting manufactured using a modified feed through the mold [23].

None of the castings produced during these investigations provided significant improvements in the cleanliness of the material or the fatigue properties.

Having amassed a large amount of fatigue data from the WE43A TRGB center housings, it was considered pertinent to undertake some limited coupon fatigue testing on a ZE41A TRGB center housing for comparison.

All these fatigue results have been plotted in Figure 6.13, and it was apparent that the only clear differences between the two materials were that the static strength of ZE41A was lower than that of WE43A and ZE41A did not exhibit any fatigue failures at stresses lower than 120 MPa. However, it is believed that the latter would not be the case if further ZE41A fatigue testing was undertaken, as there had been a relatively short-life failure of one ZE41A specimen tested at 120 MPa. In addition, a previous fatigue evaluation of these two alloys had shown lower fatigue results and wider scatter in ZE41A castings in comparison with the same part cast in WE43A [24].

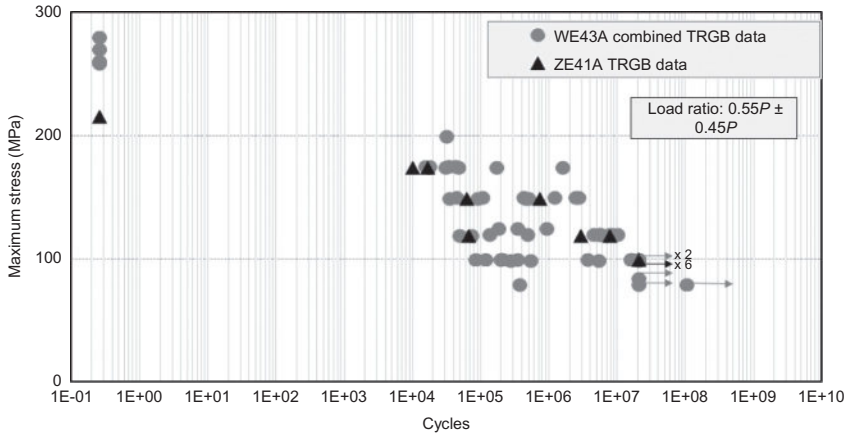

FIGURE 6.13

Comparison between the fatigue results obtained from a ZE41A center housing and those from all the WE43A center housings tested to date.

Examination of the ZE41A fatigue fracture surfaces again showed the benefits of utilizing the BSE imaging mode, as the distinction between regions of static overload and fatigue was even more evident in this alloy. This was due to the numerous zinc-rich particles and precipitates decorating the grain boundaries; see Figure 6.14.

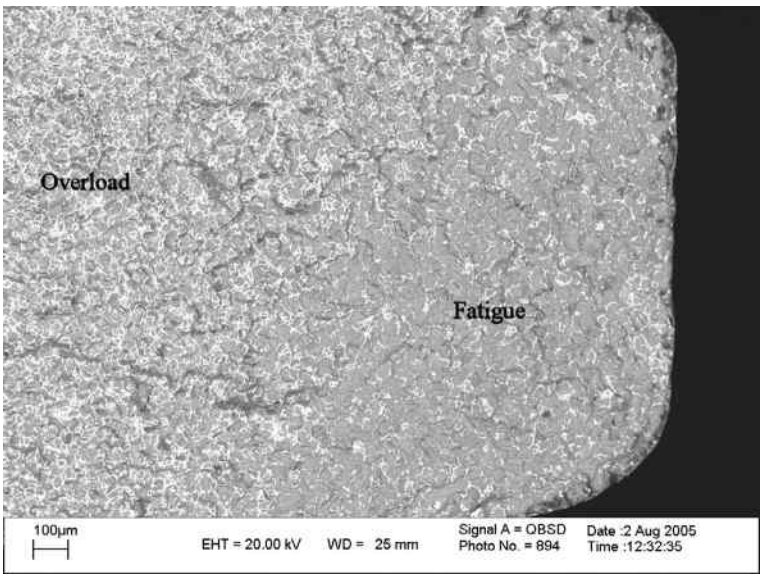

FIGURE 6.14

SEM BSE image of the fracture surface of a fatigue specimen from the ZE41A center housing fatigue tests.

During the fracture surface examinations, it was noted that there were fewer "large" casting defects at the crack origins, when compared with the WE43A fatigue specimens. This confirmed that the latter alloy was more susceptible to the formation and entrapment of oxides, as indicated in the literature [15,16].

8 OTHER FATIGUE FAILURE INVESTIGATIONS

The discovery that BSE imaging in the SEM can quickly, easily, and accurately be used to determine the location and extent of fatigue cracks in some alloys has been beneficial in the analysis of a number of other magnesium alloy casting failures. In addition, this method has also found some use in the investigation of fatigue failures in 7000 series wrought aluminum alloys which also show large numbers of grain boundary precipitates rich in elements denser than the aluminum matrix.

9 HOUSING DESIGN-GOING FORWARD

9.1 CURRENT CENTER HOUSING

The analysis of the fatigue cracks described within this chapter was particularly difficult. The introduction of a new material at the same time as design modifications to the housing in question has meant that the determination of the root cause of cracking has been inconclusive. It appeared from the investigations that the cracks were most likely due to a combination of factors. First, failures in the absence of visible defects confirm that this housing is operating very close to its fatigue limit. Second, the large size (and notch-like geometry) of some of the defects present indicate that the cleanliness of this material was generally unsatisfactory.

Although over recent years fewer occurrences of cracking after short periods in service have occurred, probably as a result of the improvements in casting practice introduced following the early WE43A failures, occasional cracks have still been found during the regular in-service eddy current inspections. The decision was therefore made that the higher costs associated with the use of WE43A and the potentially greater cost required to produce castings of the necessary quality were preclusive to the continued use of this alloy in this application. This housing therefore reverted to being made from the more easily cast (and cheaper) ZE41A material, but with the retention of the improvements in casting process and housing design introduced with the WE43A material. In addition, a more thorough inspection of raw castings and housings in service has been implemented.

Ways of reducing the fatigue loads acting on these housings have also been investigated, but the constraints of adjoining structure means that major design changes are not possible. Hence, material quality improvements and the limitation of any build stresses introduced when mounting the housing onto the gearbox platform are likely to provide the most benefit to the fatigue performance of these gearboxes.

Although this chapter has reviewed a number of gearbox fault investigations concerning cracking, it should be emphasized that by far the biggest cause of scrapped magnesium alloy gearbox housings is galvanic corrosion attack in the vicinity of fasteners.

9.2 GEARBOX HOUSINGS ON NEW AIRCRAFT

The lessons learned from these failure investigations have been taken into account when designing new TRGB's. In particular, the shapes of castings have, where possible, been simplified to ensure better material flow during casting. In addition, as a result of the high scrap rates resulting from corrosion, new designs ensure that there are fewer moisture traps and also benefit from enhanced protective treatments.

In some cases, aluminum alloy investment castings have been used as they can more closely follow a finite element model, therefore reducing the weight of a casting. However, the cost benefits and damping characteristics of magnesium alloys mean that these alloys are still used extensively and as new magnesium alloys are developed, they are also being evaluated.

ACKNOWLEDGMENTS

I would like to thank Dr David Davies for his help and advice in the production of this chapter, Mr Stephen Jenkins and Mr Andy Belben for their editing skills, and AgustaWestland Limited for allowing me to publish this work.

REFERENCES

[1] ASM. Properties and selection: nonferrous alloys and special-purpose materials. 10th ed. ASM handbook formerly metals handbook, vol. 2. Metals Park, Ohio: ASM International; 1995, p. 457–462.
[2] Davies DP, AgustaWestland Internal Report, Reference LR07,131; 06/05/2008.
[3] Aircraft Structural Integrity Course (course notes), DSGT, RAF College Cranwell, UK (ASIC No. 14). Helicopter Structural Integrity Present and Future, P 8-5.
[4] ASM. Properties and selection: nonferrous alloys and pure metals. 9th ed. Metals handbook, vol. 2. Metals Park, Ohio: ASM; 1979, p. 526.
[5] Polmear IJ. Light alloys. 2nd ed. London, England: Edward Arnold; 1989, p. 191.
[6] Coates GF, AgustaWestland Internal Report Reference LR97,143; 30/05/1997.
[7] Fellows John A, editor. Fractography and atlas of fractographs. 8th ed. Metals handbook, vol. 9. Metals Park, Ohio: ASM; 1974. p. 48.
[8] Berners MR, AgustaWestland Internal Report, Reference LR88,158; 13/06/1988.
[9] Berners MR, AgustaWestland Internal Report, Reference LR89,038; 10/03/1989.
[10] Coates GF, AgustaWestland Internal Report, Reference LR98,004; 27/01/1998.
[11] Coates GF, AgustaWestland Internal Report, Reference LR98,242; 16/07/1998.
[12] ASM. Casting. 9th ed. ASM handbook formerly metals handbook, vol. 15. Metals Park, Ohio: ASM International; 2006, p. 96.

[13] Belben FR, AgustaWestland Internal Report, Reference LR02,112; 09/07/2002.
[14] ASM. Failure analysis and prevention. ASM handbook, vol. 11. Metals Park, Ohio: ASM International; 2007, pp. 117–118.
[15] Lyon P. Elektron WE43—foundry processing update. In: Elektron group meetings 27 October-5 November; 2003.
[16] Lyon P. New magnesium alloy for aerospace and speciality applications. In: TMS annual meeting and exhibition, March, Charlottesville, USA; 2004.
[17] Geary B, AgustaWestland Internal Report, Reference LR93,286; 10/08/1993.
[18] IHS Metallic Materials Data Handbook, ESDU00932, Volume 1, Section 1, Issue 9, January 2000, P17, 39.
[19] Belben FR, AgustaWestland Internal Report, Reference LR05,102; 19/04/2005.
[20] Davies DP, Jenkins SL, Belben FR. Survey of fatigue failures in helicopter components and some lessons learnt. Eng Fail Anal 2013;32:134–51.
[21] Belben FR, AgustaWestland Internal Report, Reference LR05,124; 31/05/2005.
[22] Belben FR, AgustaWestland Internal Report, Reference LR06,176; 23/08/2006.
[23] Belben FR, AgustaWestland Internal Report, Reference LR06,147; 27/06/2006.
[24] Geary B. Advances in the application of magnesium in helicopter gearcases. In: Lorimer GW, editor. Proceedings of the third international magnesium conference 10-12 April, Manchester, UK. The Institute of Materials; 1996. p. 565–74.

CHAPTER

Failures of Rotorcraft and Fixed-Wing Aircraft Aerospace Components

7

Victor K. Champagne, Marc S. Pepi
US Army Research Laboratory, Aberdeen Proving Ground, Adelphi, Maryland, USA

CHAPTER OUTLINE

1 INTRODUCTION

All too often, the failure analyst can become preoccupied with trying to pinpoint the cause of a failure to some aspect of the service conditions, without thoroughly understanding how the part was fabricated. It is essential to take a holistic approach and fully understand the exact sequence of manufacturing operations that were performed to make the finished part and that includes knowing the details associated with the raw materials. Attention must be paid to determine if any changes in manufacturing and/or manufacturers had occurred from when the parts were initially made and

Handbook of Materials Failure Analysis With Case Studies from the Aerospace and Automotive Industries.
http://dx.doi.org/10.1016/B978-0-12-800950-5.00007-7

introduced into service to the time of the failure. Such changes include all aspects of the manufacturing process; from raw material suppliers to the paint shop and everything in between. The root cause of a failure is quite often not related to service but a deficiency that was allowed to take place before the part was shipped from the manufacturing plant. Notch-sensitive materials, such as titanium [1], can have a low tolerance for tool marks and other surface flaws, which can lead to premature cracking under the right conditions and ultimately failure. In this chapter, the focus is on the failure of aerospace components due to manufacturing defects. A product is considered defective in manufacture if it "deviates in some material way from its intended design or performance standards based on a manufacturing error" [2]. It is important to know the precise cause of failure because expensive aircraft are at risk and more critical is the fact that human lives are at stake. The primary author has had the benefit of performing failure investigations for over 30 years for the Department of Defense and have worked with the Department of Justice on high-profile lawsuits involving large defense contractors [3,4]. The authors have testified as a technical expert at the US Army Court of Appeals, and in doing so have determined the cause of many failures to be associated with deficiencies from the manufacturing operations. Therefore, the objective in this chapter is to contrast those failures associated with manufacturing to those that are service related. Because of the nature of the case studies presented, it was deemed necessary not to always disclose the manufacturer nor the exact part nomenclature and the associated military aircraft from which it failed.

2 SYNOPSIS OF A UTILITY HELICOPTER FORWARD LONGERON FAILURE

While a mechanic at Fort Rucker was securing the lower left-hand AFT engine cowling fastener to the forward left-hand upper tail boom of a utility helicopter, he discovered that the forward tail boom's bulkhead contained a 5-in. crack at the upper left-hand corner. Closer inspection revealed that the forward upper left-hand longeron had 2 in. broken off. It was determined that the bulkhead was cracked as a result of the longeron failure. It was estimated that the part accumulated 11,476 flight hours, while the actual aircraft had a total of 16,720 flight hours. Figure 7.1 shows the two broken pieces of the longeron, in the as-received condition. The part is fabricated from a 2014 aluminum alloy extrusion. For identification purposes throughout the context of this case study, the fracture half which became detached from the remaining assembly will be referred to as fracture half "A," while the other fracture half will be identified as fracture half "B." It is important to note that the same features and analytical results were obtained for both fracture halves but most of the results presented will be that of fracture half A. Figure 7.2 is a low-magnification fractograph of fracture half A, which clearly revealed evidence of fatigue beachmarks emanating from one end of the "U"-shaped part, as identified by the arrow. The beachmarks, which are fractographic features left behind as a result of an advancing crack front subjected to cyclic loading conditions [5], occurred

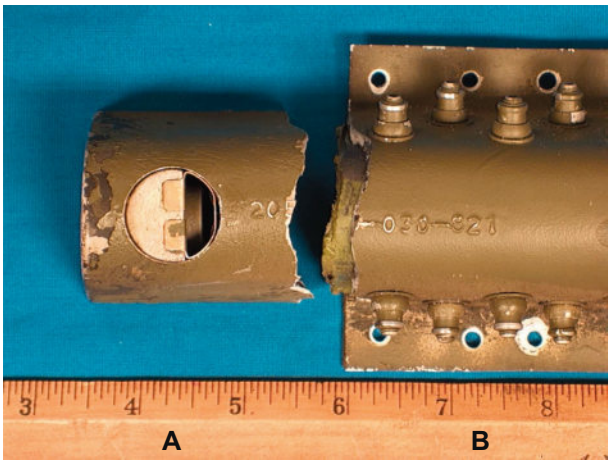

FIGURE 7.1

The two broken pieces of the longeron, in the as-received condition.

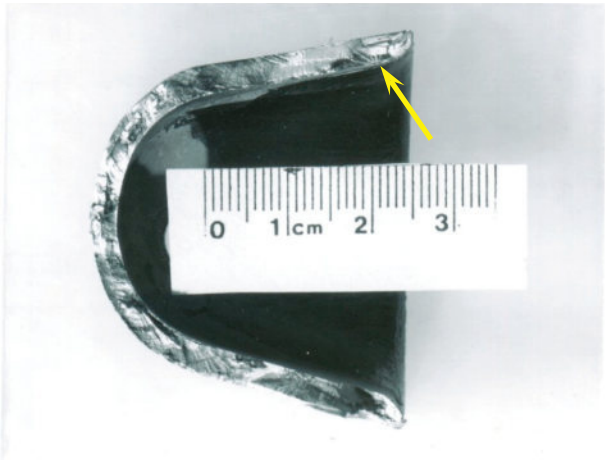

FIGURE 7.2

Low-magnification fractograph of fracture half A. Arrow denotes crack origin and beachmarks formed over approximately 80% of the entire fracture surface.

over approximately 80% of the entire fracture surface. The fracture surface itself contained dark deposits and contaminates at various locations. These regions usually suggest an older region of fracture, when compared to other areas which exhibit a more lustrous appearance; however, such was not the case for this fracture, since the origin was relatively clean. Figure 7.3 is an enlargement of the crack origin of

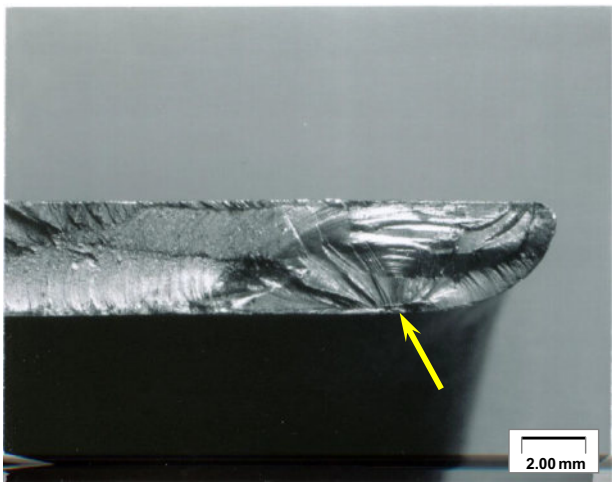

FIGURE 7.3

Enlargement of fracture origin of section A. Note the radial lines converging to a single area identifying the crack initiation site and the many finely spaced beach marks propagating outward from the fracture origin (arrow).

fracture half A. Note the radial lines converging to a single area identifying the crack initiation site and the many finely spaced beach marks propagating outward from the fracture origin. Closer examination of the crack initiation site revealed an anomaly that did not contain any discernible crack arrest markings or other features normally associated with a fracture surface. This area is shown in Figure 7.4 which represents fracture half A and that of fracture half B is depicted in Figure 7.5. In conjunction with this finding, several other surface anomalies were found below the crack origin, running parallel to the fracture (Figure 7.6). These defects were found to be cracks and still contained paint over and within them, substantiating the fact that they were the result of manufacturing (Figure 7.7). The hardness of the component was measured using the Rockwell B Scale (HRB). The part was sectioned such that the hardness could be measured along perpendicular planes (transverse and longitudinal to the extrusion direction). Specification SAE-AMS-QQ-A-367 [6] listed a minimum hardness requirement of 125 Brinell, which correlates to a minimum of 78 HRB using standard conversion charts. There was no significant variation between the 10 readings measured in both directions, and each set of readings conformed to the minimum hardness requirement. The average hardness value obtained in the transverse direction was 80.6 HRB, while that in the longitudinal direction was 80.0 HRB. The electrical conductivity of this component was measured using a DETEK analyzer. Because the process is sensitive to changes in composition and thermal condition [7], electrical conductivity can be used as a qualitative method for determining whether the prior tempering operation was performed adequately for aluminum alloys. The conductivity requirement is 35.0-41.5% International

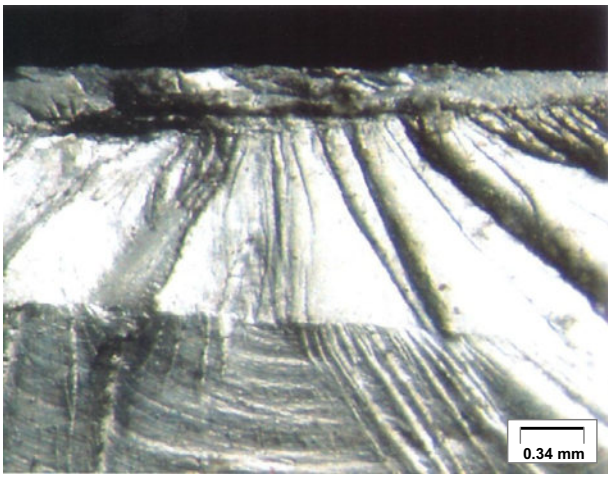

FIGURE 7.4

Closer examination of the crack initiation site of fracture half A revealed an anomaly that did not contain any discernable crack arrest markings or other features normally associated with a fracture surface.

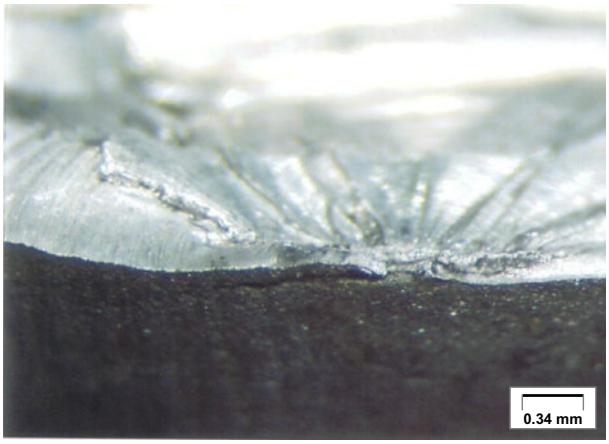

FIGURE 7.5

Closer examination of the crack initiation site of fracture half B revealed an anomaly that did not contain any discernable crack arrest markings or other features normally associated with a fracture surface.

Annealed Copper Standard (%IACS) for 2014 aluminum in the T6 condition [8]. The conductivity compared favorably with the required conductivity for this alloy in the T6 condition. The average conductivity value in the transverse direction was 39.57% IACS and 39.84%IACS in the longitudinal direction. A section of the component was analyzed for chemical composition. The method used for detection was DC

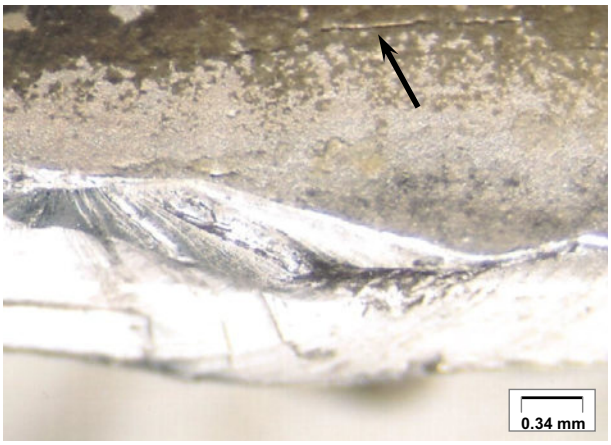

FIGURE 7.6

Surface anomalies found below the crack origin, running parallel to the fracture.

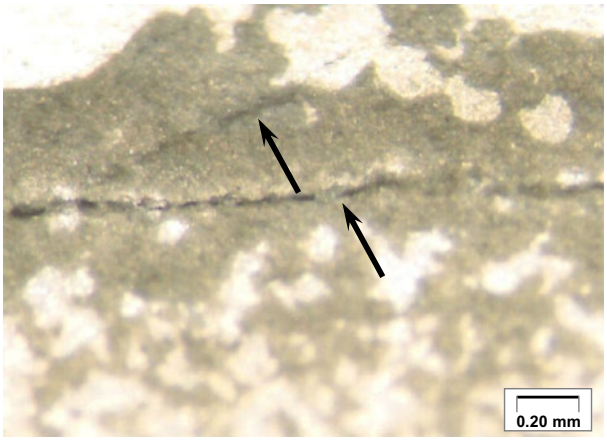

FIGURE 7.7

The defects (arrows) noted in Figure 7.6 extended into the surface of the material and contained paint in some areas, substantiating they were the result of manufacturing.

plasma emission with Beckman SSVI equipment. Specification ASTM E 1097 [9] was used for reference. The chemical composition of this alloy compared favorably with the SAE-AMS-QQ-A-367 requirement. The microstructural and fractographic features of the material were examined by light optical and electron microscopy. The component was sectioned through the fracture surface at the origin and at the center of the "U." Specimens were sectioned on a high-speed diamond wheel cut-off machine, and mounted in a mechanical mount without the use of Bakelite or other

mounting media in order to preserve the fracture surfaces. Rough polishing was accomplished using wet silicon carbide paper, ranging in grit size from 180 to 1200, while final polishing was conducted using silica. Fracture half B was sectioned through the origin, in order to examine the anomaly observed during visual examination using light optical microscopy. Care was taken to section slightly adjacent to the surface anomaly, such that subsequent polishing would result in optimal characterization of the area in question. The anomaly was examined in the as-polished condition, at low and high magnifications. Figure 7.8 shows a cross-section taken through the crack origin in the as-polished condition. Note the recessed area identified by the arrow, which is the surface anomaly observed previously in Figure 7.5. The width of the defect was approximately 0.004 in. Keller's reagent was utilized to reveal the microstructural features of the material as shown in Figure 7.9, which represents the cross-section through the center of the "U." The material was typical of a T6 temper and did not contain any other inherent material defects. Scanning electron microscopy was performed on both fracture halves in order to characterize the surface morphology and to examine the crack origin. Figure 7.10 represents fracture half A. The radial lines converge to a small area on the edge of the concave side of the part. Beachmarks emanate from this region outward toward the opposite side and to the left of the fractograph continuing across approximately 80% of the entire fracture surface. Figure 7.11 shows the fatigue striations predominate over most of the fracture surface, confirming that crack propagation was the result of cyclic loading. The striation spacing varied as did the morphology within the fatigue region. Figure 7.12 illustrates this point. Note the variation in surface topography at low magnification. There were distinct regions of transgranular fracture as Figure 7.13 depicts, while

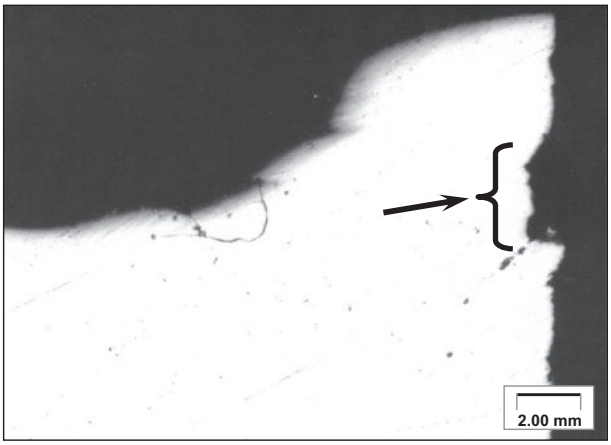

FIGURE 7.8

A cross-section taken through the crack origin in the as-polished condition. Note the recessed area identified by the arrow, which is the anamoly observed previously in Figure 7.5. The width of the defect was approximately 0.004 in.

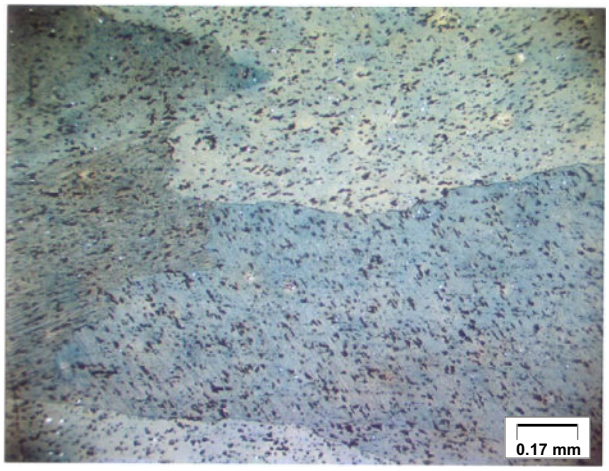

FIGURE 7.9

A cross-section through the center of the "U" was etched with Keller's reagent to reveal the microstructural features of the material. The material was typical of a T6 temper and did not contain any other inherent material defects. Magnification: 60×.

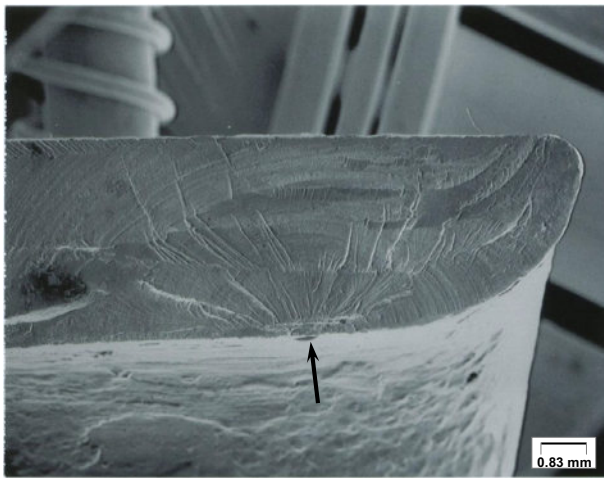

FIGURE 7.10

SEM fractograph of fracture half A. Note that the radial lines converge to a small area on the lower edge of the fracture surface as oriented in the fractograph (arrow). This area was located on the concave (inside) surface of the longeron. Beachmarks emanate from this region outward toward the opposite side and to the left of the fractograph continuing across approximately 80% of the entire fracture surface. The fracture morphology was irreconcilable at the point of crack initiation and what appeared to be an oxide was present.

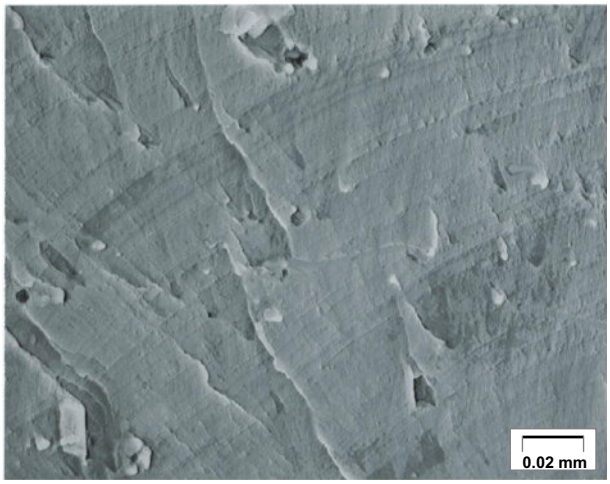

FIGURE 7.11

SEM fractograph of fracture half A showing that the fatigue striations predominate over most of the fracture surface confirming that crack propagation was the result of cyclic loading. The striation spacing varied as did the morphology within the fatigue region.

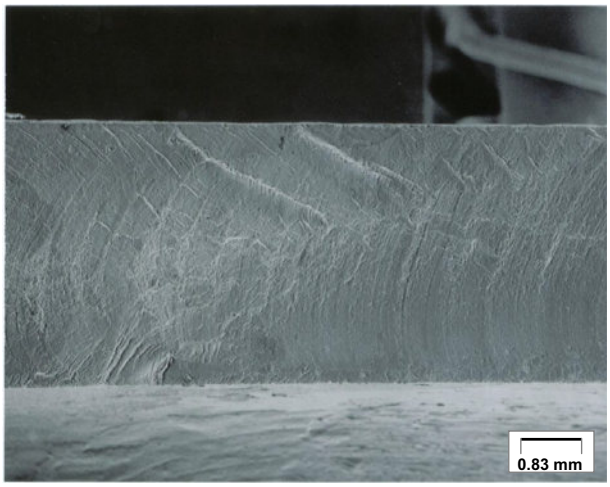

FIGURE 7.12

Note the variation in surface topography at low magnification.

adjacent areas toward the outer edges of the advancing crack front, often consisted of a dimpled morphology (Figure 7.14). The final fracture region at the opposite end of the "U"-shaped part also contained a predominately dimpled morphology, indicative of overload conditions (Figure 7.14). The dimpled structure within the fatigue region most likely occurred as a result of the strength variation of the forging. The outer edges being more compressed would be stronger than the less deformed regions

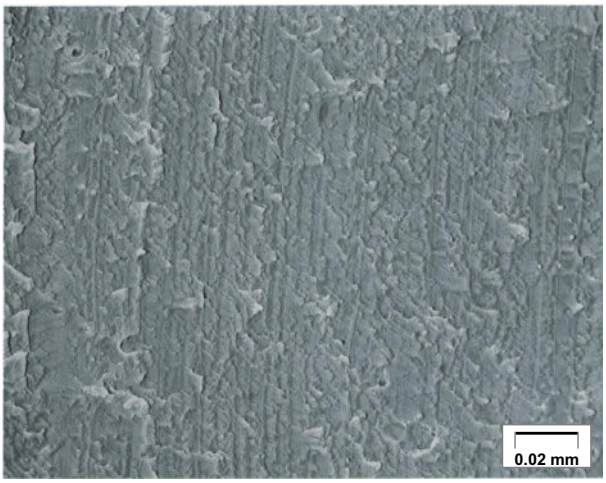

FIGURE 7.13

SEM fractograph of fracture half A showing distinct regions of transgranular fracture.

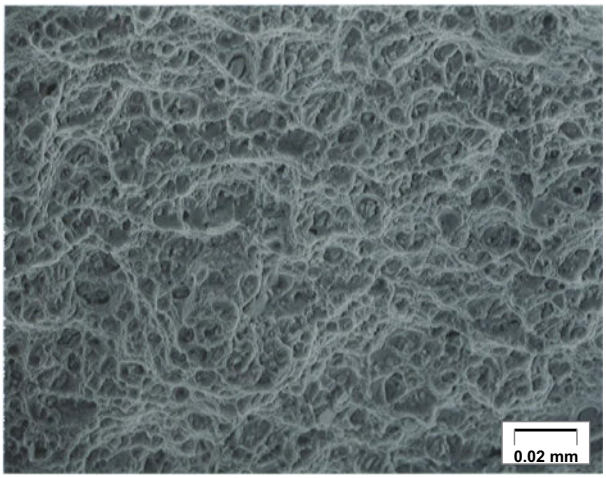

FIGURE 7.14

SEM fractograph of fracture half A showing areas adjacent to those shown in Figure 7.13, toward the outer edges of the advancing crack front, that often consisted of a dimpled morphology. The final fracture region at the opposite end of the "U" shaped part also contained a predominately dimpled morphology, indicative of overload conditions.

in the center. Figure 7.15 is an enlargement of a cross-section taken through the crack origin of fracture half B, which was not mounted in epoxy resin. The fracture morphology was irreconcilable at the point of crack initiation and what appeared to be an oxide was present, as distinguished by the featureless amorphous structure. Figure 7.16 represents the same area at higher magnification. Energy dispersive

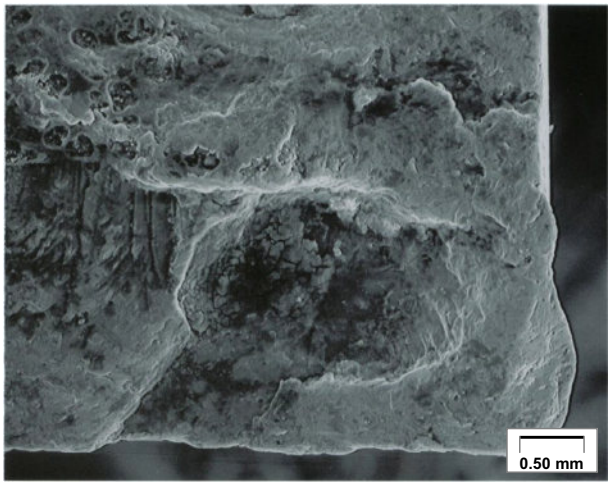

FIGURE 7.15

An enlargement of an unmounted cross-section taken through the crack origin of fracture half B. The fracture morphology was irreconcilable at the point of crack initiation and what appeared to be an oxide was present.

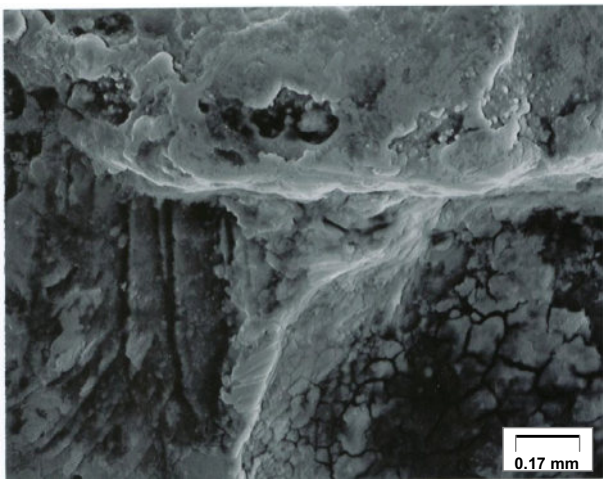

FIGURE 7.16

Photograph of the same area shown in Figure 7.15 at higher magnification. Energy dispersive spectroscopy (EDS) was performed to compare the chemical composition of the alleged oxide product with that of the polished cut surface and also with other areas of the fracture away from the origin.

spectroscopy (EDS) was performed to compare the chemical composition of the alleged oxide product with that of the polished cut surface and also with other areas of the fracture away from the origin. The results support the presence of an oxide as evidenced by high oxygen peaks associated with the oxide, as compared to that of the other areas of the fracture surface and the polished section, which contained little or no oxygen.

2.1 DISCUSSION OF A UTILITY HELICOPTER FORWARD LONGERON FAILURE

The crack initiation site contained an irreconcilable fracture morphology that was covered with what appeared to be a discontinuous heavy oxide layer. EDS analysis revealed the presence of a large oxygen concentration as compared to the remaining fracture surface. The chemical composition of a polished section of the material was also used for comparative purposes and contained a very small oxygen peak. Therefore, it was reasonable to deduce that the layer in question was rich in oxygen. In addition, the thickness of the oxide layer, as well as the physical shape of the area encompassed by it, suggested that it formed by an alternative means other than atmospheric corrosion or fretting. The remaining fracture surface contained the effects of atmospheric corrosion in the form of dark oxide product which was clearly distinguishable from the oxide contained at the crack origin. Fretting would have produced minute, dark oxide particles, and which would have been caused by some type of mechanical action, but this was not observed. The alleged oxide layer and its morphology were consistent with that of a forming defect, such as a lap. Further evidence substantiating this claim was the other laps found on the concave surface of the part during stereoscopic examination (Figures 7.6 and 7.7). A series of these cracks were located adjacent to the crack origin and extended parallel to the fracture. Such a defect would have provided a suitable site for fatigue crack initiation and propagation.

2.2 LESSONS LEARNED FROM A UTILITY HELICOPTER FORWARD LONGERON FAILURE

The component failed as a result of high-cycle fatigue, which originated from an extrusion crack. Approximately 80% of the entire fracture surface contained beachmarks and striations, which indicated an appreciable amount of time before the onset of final fast fracture. This was supported by the 11,476 flight hours accumulated on the part. This information was useful in determining an appropriate inspection interval. If aluminum is forced through an extrusion die with excessive stress or at too high a temperature, cracks can form at the ends or can extend lengthwise. The extrusion cracks on this part extended lengthwise in the extrusion direction and could be prevented by extruding at lower speeds and/or temperatures.

3 SYNOPSIS OF CH-47 CHINOOK SPIRAL BEVEL GEAR FAILURE

A metallurgical investigation of a CH-47D Chinook spiral bevel gear that had catastrophically failed leading to a controlled crash of the aircraft at Ft. Meade, MD was performed after the part was recovered from the crash site (Figure 7.17). The component was fabricated from VASCO X2M carburized steel and it failed due to a fatigue crack, which originated from grinding cracks. The failed component was double carburized. The grinding cracks formed from a microstructure that contained excessive carbides and was the result of an unauthorized grinding operation of the chamfer adjacent to the damping ring groove [10]. This grinding operation was performed in order to meet dimensional requirements and was the final step of the manufacturing process. This sequence was outside the approved specification because a subsequent nital etch inspection was required after any grinding operation to detect thermal damage. In addition, the part would also be required to be stress relieved and subsequently shot peened. The excessive carbides were formed during the carburization heat treatment and were the result of too high a carbon potential. Optical and electron microscopy of the case and core microstructures were performed and the grinding burns were characterized. Figure 7.18 shows an example of the carbide distribution as a result of a low-carbon potential treatment, associated with a certain gear manufacturer, while Figure 7.19 shows that of a high-carbon potential treatment associated with defective gears. Note the difference in carbide distribution between the two. Figure 7.20 shows the ground surface of a defective gear. There is evidence of a rehardening burn (lightly etched surface layer) as well as retempering burn (darker etching layer below the rehardening zone). This region is shown at higher magnification in Figure 7.21. Metallographic examination, combined with microhardness testing, revealed a deeper than acceptable case in the

FIGURE 7.17

Catastrophic failure of the CH-47 spiral bevel gear.

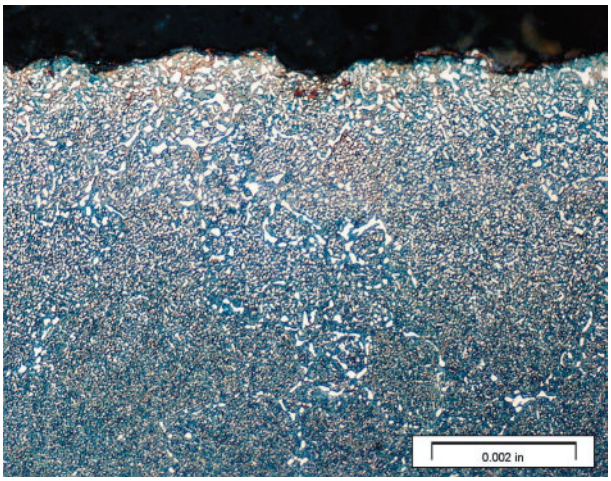

FIGURE 7.18

Typical carbide distribution within the case of a gear heat treated with a high-carbon potential (1.2%). Magnification: 500×.

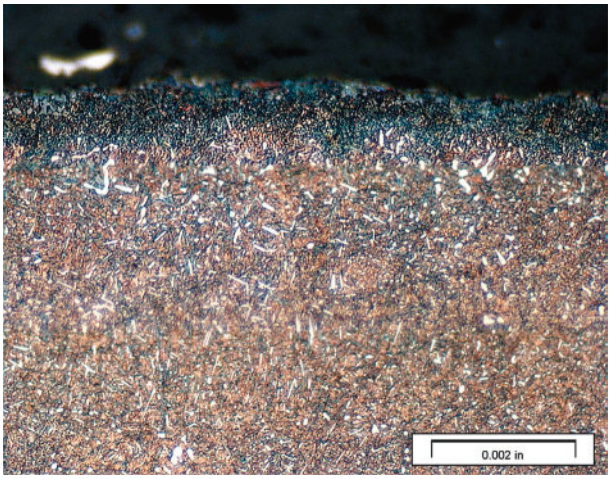

FIGURE 7.19

Typical carbide distribution within the case of a gear heat treated with a low-carbon potential (0.9%). Magnification 500×.

damping ring groove region (origin location). It was later learned that this region was mistakenly subject to a double carburization during processing. A grinding crack was also examined as shown in Figure 7.22. The shape of the crack suggests separation of the case and core. The core structure (Figure 7.23) consisted of a duplex structure of free ferrite and tempered martensite.

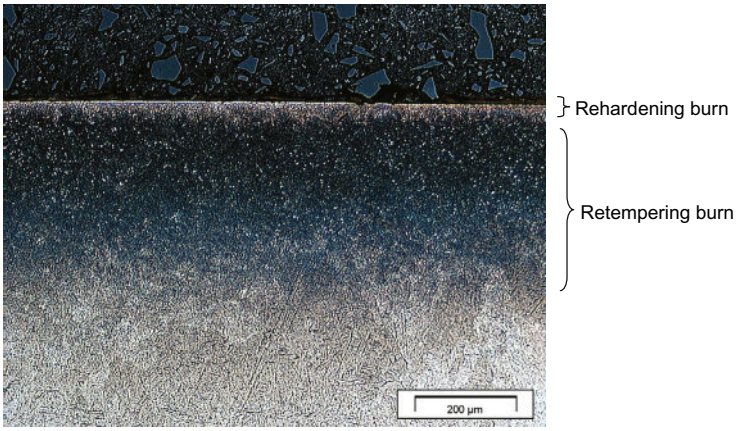

FIGURE 7.20

Rehardening and retempering grinding burns. Magnification 200×.

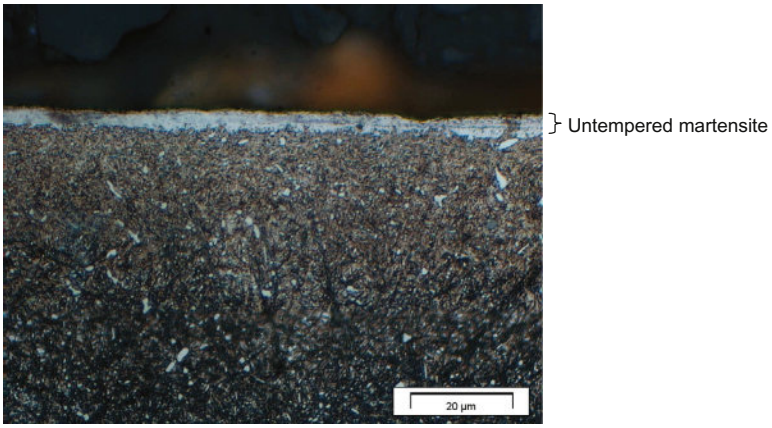

FIGURE 7.21

The rehardening burn shown in Figure 7.12 at higher magnification Note the layer of untempered martensite at the surface. Magnification 1000×.

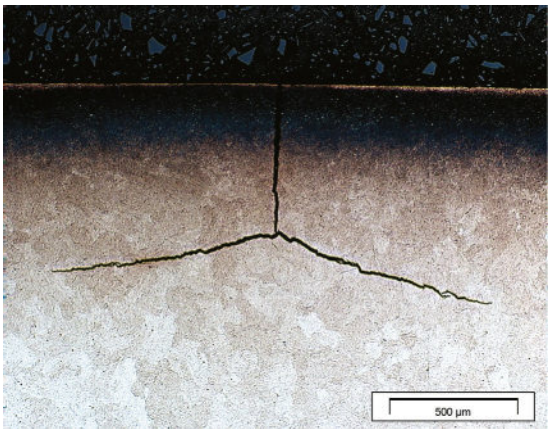

FIGURE 7.22

A grinding crack indicative of defective gears. Crack branching appears to suggest case/core separation. Magnification 50×.

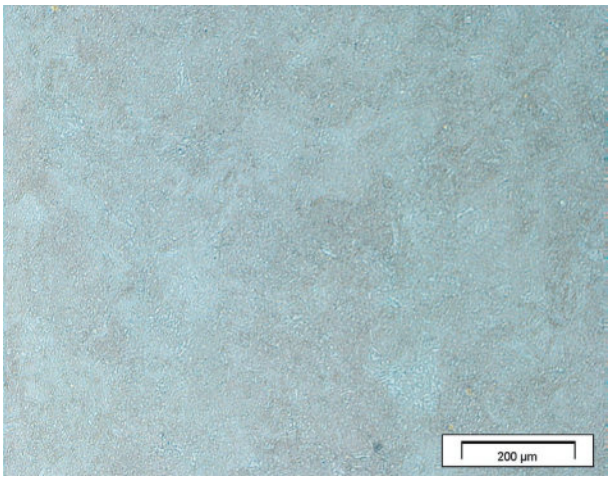

FIGURE 7.23

Typical core microstructure of the carburized gears. Magnification 100×.

3.1 DISCUSSION OF CH-47 CHINOOK SPIRAL BEVEL GEAR FAILURE

Vasco X2M was developed by Teledyne-Vasco of Latrobe, Pennsylvania, as a carburizing grade steel with good, hot hardness for gear and shaft applications [11]. It has essentially the same chemical composition as H-12 hot work die steel, with the exception of lower carbon content.

The X2M variation has further reduced carbon content than the X-2 predecessor. This alloy provides an excellent combination of strength, toughness, and fatigue strength. Very little information exists in open literature with respect to the effects of carbide networks on X2M material properties. With respect to general comments about this structure, *ASM's Handbook on Failure Analysis* states, "Fatigue resistance of a component may be increased by case carburizing, provided the treatment is carried out properly so as to avoid gross structural discontinuities, such as carbide networks" [12]. In addition, Parrish states that "under bending fatigue conditions continuous networks appear to reduce the fatigue limit" and adds that, "when failure eventually occurs, it does so down the carbide network" [13]. Summarizing, Parrish notes that "carburized cases containing free carbides are relatively weak in response to static bending and impact bending." [13]. Statements such as these and those previously referenced are assumed to pertain to all carburizing grade steels. The pre-existing crack was oriented perpendicular to the direction of grinding, indicating the possibility of a grinding crack. Grinding is required to be performed on these gears before subsequent stress relieving and shot peening. However, it was revealed during the investigation that unauthorized rework was performed on the failed gear, whereby grinding was performed after the stress relief and shot peening, for burr removal. Grinding problems can occur if excess heat is

generated at the part surface. Many factors contribute to grinding problems including worn grinding wheels, improper wheels, or removal of too much stock. Any of these scenarios can produce a tempering of the martensitic surface (dark layer), resulting in a reduced surface hardness, as well as a rehardening burn which produces a thin, hard layer of martensite (white layer) at the surface. These two anomalies were noted at the origin of this failure. The presence of continuous carbide networks (CCNs) within the case that contained the grinding burn aggravated the situation. Parrish states that "carbide networks can render a surface sensitive to grinding, the cracks tending to follow the path of the network." [13]. The grinding crack at the origin of the failure being investigated followed the path of the network as evidenced by the intergranular morphology along the 30° taper. Although much is documented concerning the negative aspects of CCNs, their detrimental effects can be minimized by ensuring that no surface defects (such as grinding cracks/burns) exist on the surface of the component. Therefore, it is essential that nondestructive techniques used during the manufacturing sequence (i.e., magnetic particle inspection (MPI), 10× visual inspection, and nital etch inspection) are sensitive enough to reveal grinding cracks and burns.

3.2 LESSONS LEARNED FROM THE CH-47 CHINOOK SPIRAL BEVEL GEAR FAILURE

It was concluded that the failed gear was the result of a crack that had formed during the grinding process and had propagated by a fatigue mechanism, along the carbide network until final fast fracture. Contributory to crack propagation was the presence of carbide networks within the carburized case. Two extraordinary events occurred leading to the demise of the gear: (1) the part was unmasked in the damping ring groove and subjected to a double carburization and (2) grinding was performed as the final step, to provide dimensional tolerance. These events acted to produce excessive carbide formation in the damping ring groove region, as well as undetected grinding burns and cracks within the same area. This deleterious combination coexisted in service until a grinding crack propagated in fatigue to final fast fracture.

4 SYNOPSIS OF THE MS3314 GENERAL-PURPOSE BOMB 1000-POUND SUSPENSION LUG FAILURES

As an F-18 Fighter was landing on an aircraft carrier, a 1000 pound general-purpose (GP) bomb became detached and hit the deck before bouncing off into the ocean, without exploding. Fortunately, these bombs are both mechanically and electronically armed prior to detonation. The mishap was caused by the failure of the suspension lugs used to secure the bomb onto the aircraft. Two suspension lugs are threaded into each general-purpose bomb and used to attach it onto the underside

FIGURE 7.24

Suspension lugs (within highlighted red oval) attached to GP bombs (http://warthognews.blogspot.com/2013_02_01_archive.html).

of Navy aircraft (Figure 7.24). This mishap prompted the Navy to perform a random test sampling of lugs from inventory. Prior to this sampling, each suspension lug was required to be 100% inspected by MPI to detect surface discontinuities. A total of three suspension lugs failed during proof load testing of a small sample size. The proof load testing required the part to sustain a tensile load of 35,000 pounds for 1 min at a 6° angle, as well as 24,000 pounds at a 35° angle for 1 min. These three lugs failed to achieve the 1-min duration before failure occurred. Two of the three failed lugs were sent from the Naval Air Warfare Center (NAWC) for failure analysis. The failure investigation included visual examination, chemical analysis, metallography, hardness testing, scanning electron microscopy, and EDS. Visual examination revealed a blackened region at the crack origin of each failure. In addition, a forging lap was found on the external bail surface of one of the failed lugs. Material sectioned from the failed lugs and subjected to chemical analysis confirmed that the AISI 4340 steel met the required composition and hardness. The microstructure was indicative of quenched and tempered AISI 4340 steel. Metallographic examination adjacent to the blackened regions at the crack initiation sites showed slight carburization upon etching. This indicated that the regions were exposed to high temperatures, such as those performed during heat treatment. A representative forging lap is shown in Figure 7.25. Electron microscopy of the blackened surface revealed a featureless amorphous morphology, which is associated with oxide formation (Figure 7.26). EDS of the blackened regions revealed evidence of a corrosion product or heat treat scale. It was concluded that such a feature could be formed as the result of the forging operation and subsequent heat treatment of the part. Proof testing of hundreds of lugs in inventory revealed that almost 20% contained forging laps and had to be removed.

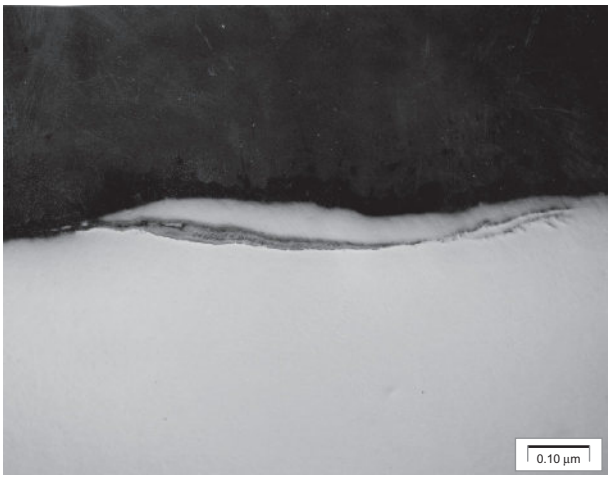

FIGURE 7.25

SEM of dark oxide at crack origin 1000×.

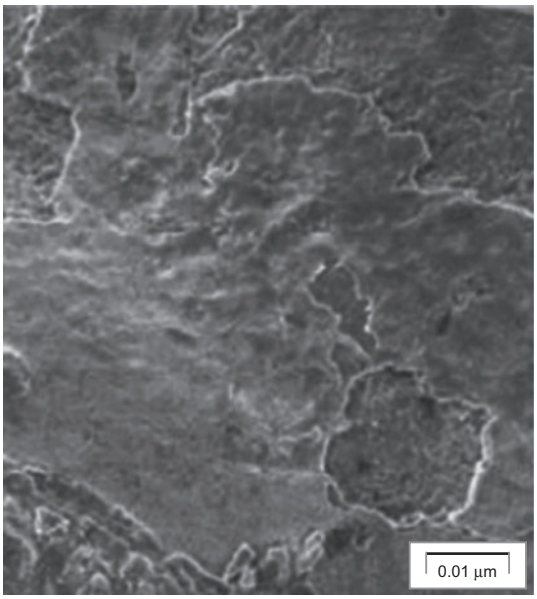

FIGURE 7.26

SEM of dark oxide at crack origin 1000×.

4.1 DISCUSSION OF THE MS3314 GP BOMB 1000-POUND SUSPENSION LUG FAILURES

A lap is caused by the folding over of metal into the surface of the part during forming [14], while a seam is a discontinuity in a part caused by an incomplete joining of material during forming [15]. Proof testing on lugs in inventory was performed in order to determine the extent of the manufacturing defects. When many components failed the proof testing, it necessitated an MPI screening of all parts in inventory, which totaled in the hundreds of thousands. Figure 7.27 is a blacklight photomacrograph showing an example of a forging seam contained within the bail of a lug subjected to this screening. Concurrently, ARL and NAWC representatives visited the manufacturing facility in order to determine how the defective parts had made their way into inventory. It was determined that the contractor was not using an authorized written procedure for MPI. In addition, the contractor was using an MPI procedure that was not capable of detecting defects in certain orientations. This allowed defective components to leave the facility undetected. As for the forging, the manufacturer took steps to minimize the amount of defects, by

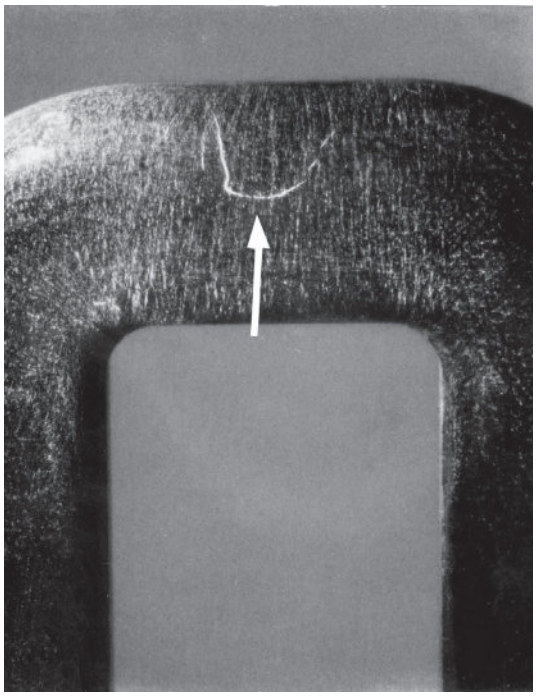

FIGURE 7.27

Black light photo of a forging seam located on the bail section of a lug.

incorporating the use of a forging lubricant while decreasing the impact energy. Proof testing revealed that the lugs were very sensitive to these surface anomalies. It was concluded that the lugs failed due to overload conditions, as determined by the predominantly ductile dimpled fracture surface but was initiated as a result of forging laps.

4.2 LESSONS LEARNED FROM THE MS3314 GP BOMB 1000-POUND SUSPENSION LUG FAILURES

Inadequate process control was found to be the root cause of the suspension lug failures. There were two distinct deficiencies uncovered that involved inadequate controls of certain aspects of the manufacturing process. The first was related to the forging operation and the other to the MPI. Forging laps were eliminated by incorporating a forging lubricant while decreasing the impact energy. The MPI inspection was required on 100% of the parts yet 20% of them contained forging laps that were cause for rejection. An extensive inventory screening process was necessary to prevent any more defective lugs from being used in service, whereby the parts that were supposedly previously magnetic particle inspected were subjected to an additional 100% inspection, consisting of a central conductor shot, as well as a head shot (Figures 7.28 and 7.29). The head shot was added to the MPI procedure. Thousands of lugs were scrapped as a result of this re-inspection, and the warranty clause was invoked by the NAWC.

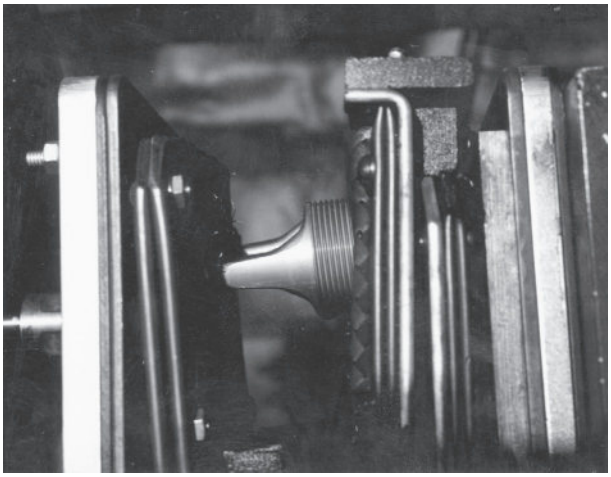

FIGURE 7.28

Magnetic particle inspection procedure incorporating a head shot.

FIGURE 7.29

Magnetic particle inspection procedure incorporating a central conductor shot.

5 SYNOPSIS OF THE AM355 MAIN ROTOR PART FAILURE FROM AN ARMY ATTACK HELICOPTER

A critical flight-safety component fabricated from AM355, a semi-austenitic precipitation hardenable stainless steel, used in an Army attack helicopter failed catastrophically in service causing the aircraft to crash and the loss of all crew members. An in-depth metallurgical analysis of the flight-safety critical component revealed that the premature failure was attributable to fatigue, which was not an anticipated failure mode. Further analysis of material taken from various stages of the processing steps revealed an intergranular surface attack that was later found to be caused by acid pickling, performed during processing of the sheet material at the steel mill. Thick sheets of AM355 stainless steel were rolled into thinner sheets and between each rolling step the material had to be annealed because of excessive work hardening. After the annealing heat treatment, the material formed an oxide layer that was removed by acid pickling. However, if the material remained in the pickling bath too long then the surface would be attacked. It was hypothesized that the surface intergranular attack led to premature crack initiation due to the breakdown of the protective passive layer and/or the stress concentration effect of the attack. A study was conducted to quantify the effects of varying degrees of surface intergranular attack on the fatigue properties of the material. Fatigue specimens were machined from actual components taken from inventory and from fielded components and were subsequently categorized into four groups which described the degree or severity of attack based on appearance and depth

measurement: none, light, moderate, and heavy. Fatigue test data showed a direct relationship between the number of cycles to failure and the severity of surface intergranular attack. It was recommended to eliminate the surface intergranular attack at the steel mill or to remove it altogether with a light sanding operation.

5.1 DISCUSSION OF THE AM355 MAIN ROTOR PART FAILURE

Optical and electron microscopy results revealed that the surface intergranular condition had an effect on the initiation and progression of a fatigue crack front. The intergranular network of attack on the surface of the material had been measured to be approximately 2.5-6.4 μm deep, varying upon the location measured and the coil of material from which the specimens were acquired. The intergranular attack was present on both sides of the material and constituted approximately 2.5% of the total cross-sectional area (using 4.5 μm as the average depth of the intergranular surface attack and the fact that the material was only approximately 0.356 mm thick). The significance of 2.5% of the cross-sectional area being attacked was clearly observed in the SEM analysis and fatigue test data. The intergranular attack lowered the fatigue life of the material simply because the fatigue crack front easily followed the intergranular network of attack near the surface and less energy was required to propagate the crack. The crack progressed along the intergranular network near the surface edges of the specimens that exhibited surface intergranular attack. This mode was not evident on the specimens that did not contain significant surface intergranular attack. It would be expected that having an intergranular network on the surface of the laminates would lower the fatigue life of the material. This was demonstrated in the graphical presentation of the fatigue data. It was clearly observed in all three fits of the data that the specimens with significant surface intergranular attack had lower overall and projected fatigue lives. The tensile data all fell within the normal values for the material. It appeared that the surface intergranular condition did not have a significant effect on the tensile properties of the material. Figure 7.30 shows a secondary crack propagating through the thickness of the strap pack laminate. Also evident on the photo are beach marks from the fatigue crack progression.

5.2 LESSONS LEARNED FROM THE AM355 MAIN ROTOR PART FAILURE

This case study pointed out the fact that attention must be paid to the initial stages of raw material processing at the steel mill and controls be established for detecting surface intergranular attack of AM355 stainless steel as a result of acid pickling between annealing and rolling operations. It was determined that severe intergranular attack of the surface of the part could initiate fatigue cracks and lead to catastrophic failure.

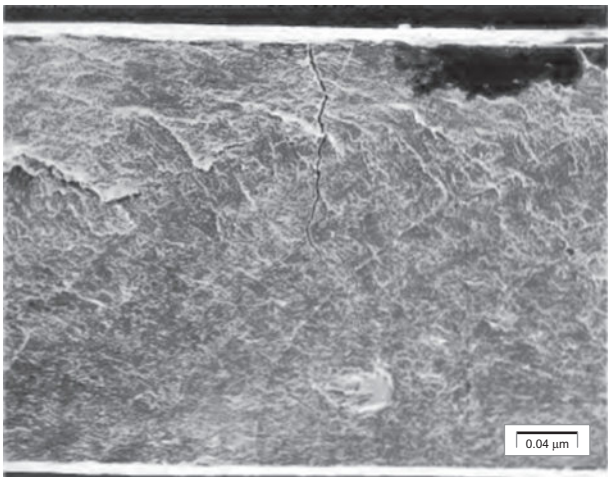

FIGURE 7.30

Secondary cracking noted on a strap pack laminate.

6 CONCLUSION

Process defects that escape a manufacturer's quality control program may lead to subsequent component failure, which could result in a catastrophic accident and potential loss of life. The cost of manufacturing defects to both the Government and the manufacturers is unknown, but is surmised to be in the billions of dollars each year. This chapter has discussed the results of four failure investigations where each failure was shown to have a root cause associated with manufacturing defects from a variety of sources and aerospace materials including (1) extrusion of 2014 aluminum, (2) improper carburizing and grinding of X2M gear steel, (3) forging laps and seams in AISI 4340 steel, and finally (4) aggressive acid pickling of AM355 stainless steel at the rolling mill. It is important to note that a failure investigation must not only include knowledge of the service conditions and environment the part was subjected to, but just as importantly, a full understanding of the primary and secondary manufacturing process steps, to be all inclusive.

REFERENCES

[1] Khataee A, Flower HM, West DRF. New titanium-aluminum-X alloys for aerospace applications. J Mater Eng 1988;10(1):37–44.

[2] 232 F. 3d 754 - Patricia Wheeler v. Ho Sports Inc, 232 F.3d 754 (10th Cir. 2000), Patricia Wheeler, Plaintiff - Appellant, v. Ho Sports Inc.; Premier Ski Boat Corporation, doing business as Waterski America, Defendants – Appellees, No. 99–6039, United States Court of Appeals Tenth Circuit; November 6, 2000.

[3] http://www.bafirm.com/articles/gen/defense_contractor_fraud.html, accessed December 15, 2014.
[4] http://www.justice.gov/opa/pr/2000/August/450civ.htm; accessed December 15, 2014.
[5] Boyer Howard E, Gall Timothy L, editors. Metals handbook—desk edition. Materials Park, OH: ASM; 1985, p. 32–16.
[6] Specification SAE-AMS-QQ-A-367, 22 Feb 2001 Aluminum Alloy Forgings.
[7] Van Horn KR, editor. Aluminum properties, physical metallurgy and phase diagrams—volume I. Materials Park, OH: ASM; 1967, p. 174.
[8] Specification MIL-H-6088, 26 Sep 1997 Heat Treatment of Aluminum Alloys, Table IX, p. 56.
[9] Specification ASTM E1097, 2012, ASTM, WEST CONSHOHOCKEN, PA, Standard Guide for Determination of Various Elements by Direct Current Plasma Atomic Emission Spectrometry.
[10] Pepi M. Metallurgical Examination of Failed Spiral Bevel Gear PI96, Part No. 145D6302, ARL-TR-1432; August 1997.
[11] Fopiano P, Oliver S, Kula E. The effect of heat treatment on the structure and properties of standard and modified Vasco X-2M Steel, AMMRC TR 77–8; March 1977.
[12] American Society for Metals (ASM, Materials Park, OH) Handbook, Volume 11, Failure Analysis and Prevention, Fatigue Failures; 1985.
[13] Parrish G. The influence of microstructure on the properties of case-carburized components; 1990.
[14] ASM Materials Engineering Dictionary, Edited by JR Davis & Associates, ASM International, 1992, p. 246.
[15] Davis JR, editor. ASM materials engineering dictionary. Materials Park, OH: ASM International; 1992, p. 398.

CHAPTER

Suspension and landing gear failures

8

Edgar A. Ossa, Marco Paniagua

Material Engineering Research Group, School of Engineering, Universidad Eafit, Medellín, Colombia

CHAPTER OUTLINE

Handbook of Materials Failure Analysis With Case Studies from the Aerospace and Automotive Industries.
http://dx.doi.org/10.1016/B978-0-12-800950-5.00008-9

1 INTRODUCTION

Landing gears in aircrafts and suspension systems in vehicles play an important role in both kinds of transportation vehicles. Landing gears are designed to support the aircraft while grounded and to withstand high loads during landing without any damage to its structure while providing comfort to the passengers. Despite the rigorous maintenance and part replacements imposed by the different Aviation Administrations, failures in aircraft systems are common. According to Wang and Long [1], who studied causes of failures on Boeing 737-300 aircrafts, failures of landing gear systems account for approximately 9% of the failures suffered on this kind of aircraft (see Figure 8.1). Considering the importance of this system during landing of aircrafts, it is necessary to understand the main causes of failures of these systems in order to avoid any catastrophic incidents involving injures to passengers, or in the worst scenario, loss of lives.

On the other hand, the automotive industry suffers even more failures than the aviation industry, in part because a maintenance program is not usually followed as well as the aviation industry. It is even common that if a vehicle part fails, it is just replaced and the root cause of failure is not investigated in order to prevent future failures. According to Heyes [2], who studied causes of failures of 70 vehicle components, failures of suspension systems account for approximately 13% of the failures of the automotive industry (see Figure 8.2).

Failures of suspension systems are very sensitive as they can cause the loss of control of the vehicle, which can lead to serious accidents and loss of lives. This chapter will be concentrated with a brief description of common reported cases of failures of landing gears and suspension systems in order to provide ideas for the improvement of maintenance procedures and production standards for these components looking onward toward a reduction on recurrence of failures.

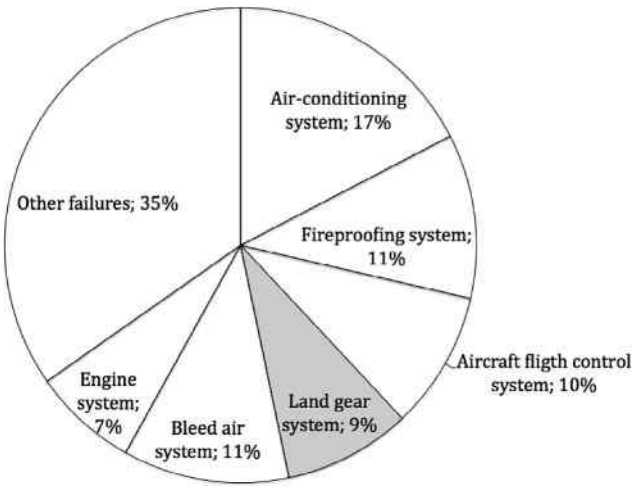

FIGURE 8.1

Main causes of failure of Boeing 737-300 aircraft [1].

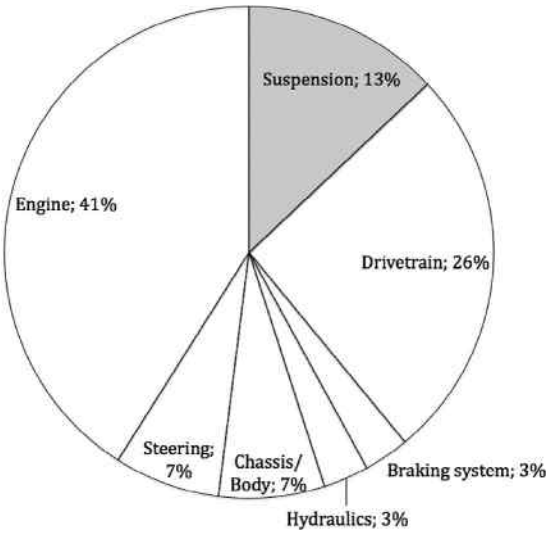

FIGURE 8.2

Main causes of failure of automotives [2].

2 CAUSES OF SUSPENSION SYSTEMS FAILURES

The main causes of failure of the suspension system parts can be divided into metallurgical, design, and processing failures.

2.1 METALLURGICAL FAILURES

Nadot and Denier [3] studied the fatigue failure of suspension arms manufactured by nodular cast iron under low- and high-cycle fatigue conditions finding that casting defects govern the failure initiation of these parts. The low-cycle fatigue was governed by multiple cracks initiated independently from casting defects, while high-cycle fatigue was mainly controlled by surface defects like dross and oxides. They even proposed a tool for fatigue design of components made out of iron castings depending on the expected defect size. This tool can be used to reduce the appearance of these defects and avoid failures.

Prawoto et al. [4] analyzed the main causes of failure of suspension springs, finding that one of the main causes of failure of these components is the amount of inclusions found. They also discussed that as the weight reduction in automotives is becoming more important, the stress levels of suspension springs have been increased dramatically, leading to small window for defects.

Banuta et al. [5] studied the failure of a suspension system ball joint, finding that the presence of inclusions after a welding process caused the reduction of load bearing of the component, leading to failure.

2.2 DESIGN FAILURES

Eryürek et al. [6] studied the causes of failure of suspension springs, finding that the presence of inclusions on the structure and design errors reduced the fracture toughness and safety factors of the components, leading to premature failure of the part. Triantafyllidis et al. [7] studied the cause of failure of a steering knuckle, finding that the design choice of material for the component was incorrect. The part was manufactured using ductile cast iron, which is not the best choice of material for a component subjected to cyclic loads, leading to fatigue failures initiated by surface or metallurgical defects. Ossa et al. [8] studied the failure of a MacPherson suspension ball joint finding that the root cause was high-contact stresses on the element due to improper design. Even after many years of use and design of suspension systems on vehicles, it is common to find a simple design error which can be easily avoided by learning from previously reported incidents and their solutions.

2.3 PROCESSING FAILURES

Das et al. [9] studied the failure of a suspension coil spring after a short period of operation finding that the main cause of premature fatigue failure was improper shot penning of the spring surface, leading to fast crack initiation. Banuta et al. [5] found that an improper welding of a ball joint caused aligned inclusions leading to fatigue failure of the element. Zhao et al. [10] studied the failure mode of torsion beam bars under service conditions finding that the welding was the weakest part in the elements and is prone to failure if care is not taking during the manufacturing process. It is well known that "heat and beat" manufacturing processes are the root cause of many defects, so excessive care must be taken in order to void the generation of defects that can generally cause fatigue cracks in suspension systems subjected to high cyclic loads.

3 CAUSES OF LANDING GEAR SYSTEMS FAILURES

According to reported cases of failure of landing gear system parts, they can be divided into metallurgical, environmental, design, processing, and overload failures.

3.1 METALLURGICAL FAILURES

Azevedo and Hippert [11] and Azevedo et al. [12] studied the failure of a landing gear during a landing operation, finding material recrystallization led to grain boundary precipitation which caused anisotropy of the microstructure, reducing the fracture toughness on the main loading direction, thus initiating the fracture of the element. Recrystallization and grain boundary precipitation is common on alloyed aluminums and in order to avoid a reduction on toughness of the material, it is recommended to evaluate the appearance of this condition on overhauls.

3.2 PROCESSING FAILURES

Niansheng et al [13] studied a leakage failure of a brake nave on a landing gear, finding that rough machining marks and incomplete protective coatings initiated a crack, which further propagated by transgranular stress corrosion. Eliaz et al. [14] investigated the cracking of the main landing gear of a cargo aircraft, finding it to be caused by abusive grinding during an overhaul. The grinding caused localized overheating, which altered the martensitic structure of the material, leading to thermally induced cracks. Bagnoli et al. [15] studied the fatigue failure of a landing gear swinging lever, which turned out to be caused by abnormal silicon concentration of the material due to the manufacturing process of the part during the forging stage. Barter [16] studied the failure of the wing landing gear trunnion fork assemblies of a Boeing 747-300 aircraft. Analysis of the failure showed that deep machining grooves were present as a consequence of poor shot peening, this along with a chemical surface process during manufacture resulted on intergranular attack at the bottom of the grooves, causing cracking and failure of the part.

3.3 ENVIRONMENTAL FAILURES

Azevedo et al. [12] studied the failure of a landing gear during landing, finding material recrystallization leading to grain boundary precipitation, inducing pit cavities associated with intergranular corrosion. This intergranular corrosion reduced the load-bearing capacity of the landing gear, provoking its failure. Lee et al. [17] analyzed the failure of the nose-landing gear hydraulic actuator cylinder of an F-4 aircraft, finding that corrosion pits at the interior of the cylinder initiated fatigue crack growing. This corrosion was attributed to improper maintenance and surface processing of the element. Franco et al. [18] analyzed the failure of a nose-landing gear also finding corrosion pits causing fatigue crack growth of the element. Bagnoli and Bernabei[19]) studied the failure of the main landing gear right wheel of a Piaggio Avant P180 aircraft, also finding fatigue crack growth from corrosion pits promoted by fretting. Fretting in this case removed the protective coating of the element. On landing gears, the environmental effects causing corrosion are important due to the sudden changes of temperature and environments, so the protective coatings of the exposed elements must be checked carefully during overhauls.

3.4 DESIGN FAILURES

The UK Air Accidents Investigation Branch (2010) reported on the crash landing of a Boeing 777 at London's Heathrow airport in 2008 [20]. In this incident, the aircraft crash-landed on soft grass. The landing gear under the nose collapsed, as it should, but the main landing gears beneath the wings did not, finally causing damage to the fuel tank and fuselage. Here, the cause of concern was the "nonfailure" as intended of the landing gear and changes on the designs were proposed in order to ensure failure of the landing gear even on a soft landing. Erasmus et al. [21] studied the failure of a

landing gear strut on a homebuilt motor glider finding that the root cause of failure was deficient design due to use of inappropriate material and design parameters as reduced cross-sections and bend radius in the struts.

3.5 OVERLOAD FAILURES

Ossa [22] studied the cause of failure of the landing gear of a Cessna 402B aircraft, finding that overloading caused the failure, even when optical fractographic evidence showed it to apparently be a fatigue failure. Tao et al. [23] studied the effect of overloading sequences on landing gear fatigue damage finding that the overload effect is stress-state dependent and dominated by local residual and mean stresses. They suggested that the load sequence effect should be considered in fatigue analysis if local yielding exists before or after overloading. Asi and Yesil [24] investigated the failure of a nose-landing gear piston rod end, finding that the piston failed by fatigue with cracks initiated at the surface close to a mechanically damaged region, which caused stress concentration leading to fracture of the element.

4 CASES OF SUSPENSION AND LANDING GEAR SYSTEMS FAILURES

The following sections will explore different failure cases of suspension and landing gear systems in order to explain the main steps followed on the analysis and determination of the causes of their appearances.

4.1 PROCESSING AND DESIGN FAILURE OF A CAR SUSPENSION SYSTEM BALL JOINT

This case describes the analysis and investigation of the causes of the sudden failure of a MacPherson strut suspension system ball joint. The axis of the ball joint element showed a complete fracture, which occurred midway between the top and bottom section changes of the element, as shown in Figure 8.3.

A fractographic inspection of the fractured surface of the element was initially performed using optical microscopy. After this inspection, samples were extracted to analyze the material microstructure and some of the fractographic features by means of scanning electron microscopy (SEM). The microstructural analysis was performed in order to obtain information about previous thermo-mechanical treatments to the element. Optical emission spectroscopy (OES) was used to identify the chemical composition of the failed element. Vickers hardness was also measured on the failed element. It is worth noting that before any measurement was performed, any traces of grease and debris were removed from the element.

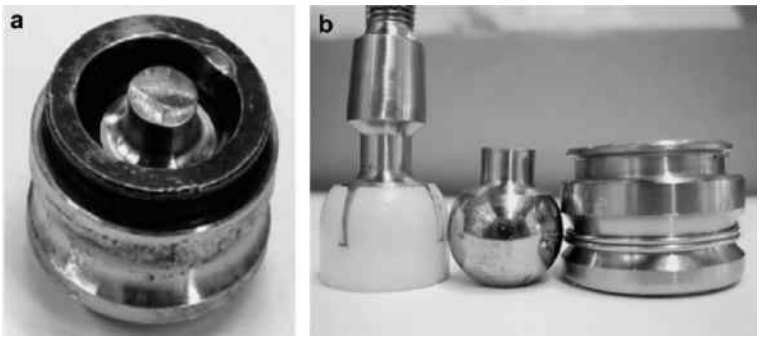

FIGURE 8.3

Ball joint element. (a) Failed ball joint in the cage. (b) Failed and new ball joints out of the cage [8].

4.1.1 Fractographic Study

Figure 8.4 shows a macroscopic image of the fractured surface of the ball joint obtained by optical microscopy. Three different characteristic zones of the fracture are identified in the figure as Zones A through C. Zones A and B indicate opposed zones where the crack growth started. These zones showed a smooth and curved appearance or beach marks. These zones are a clear indication of fatigue failure of the material. Furthermore, in Zones A and B can be appreciated fracture features pointing toward the center of the fracture. These ratchet marks are typical of fracture on elements subjected to high-stress concentrations. Zone C on the other hand shows a rough surface, indicating the final fracture zone of the element; this zone occupying approximately one quarter of the cross-section of the element.

Figure 8.5 shows the fracture zones of the element, where the smooth surface and the beach marks characteristics of fatigue crack propagation can be appreciated, corresponding to Zone A (Figure 8.5a). On the other hand, Figure 8.5b shows Zone C, where the micro-voids characteristic of final ductile fracture of the element can be appreciated.

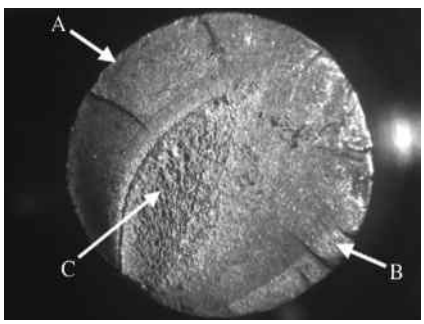

FIGURE 8.4

Fracture surface of the failed ball joint [8].

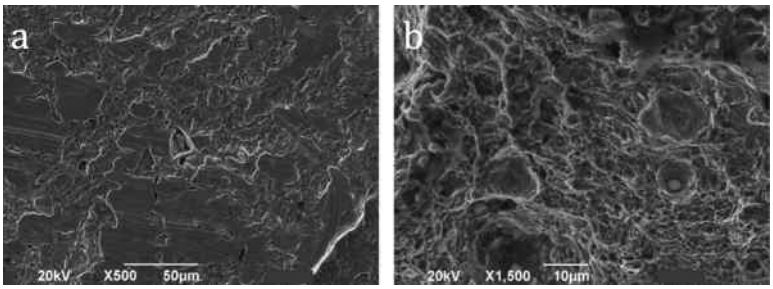

FIGURE 8.5

SEM micrographs of fracture surface. (a) Zone A and (b) Zone C. [8].

4.1.2 *Metallographic Analysis*

According to chemical composition analysis by OES, the ball joint was manufactured using AISI-SAE 5140 steel. Figure 8.6 shows the microstructure of the ball joint element. This micrograph shows a microstructure formed mainly by tempered martensite with acicular grains of ferrite on the grain boundaries (white grains indicated by arrows).

The presence of tempered martensite indicates that the material suffered a heat treatment of quenching and tempering. Despite of the beneficial effect of increasing material toughness of ferrite in low-carbon steels [25–27], it has been found that acicular ferrite can decrease the fracture toughness and mechanical strength of heat treated steels when it appears on tempered martensite grain boundaries [28,29], as in the present case. The presence of acicular ferrite on grain boundaries can also induce a

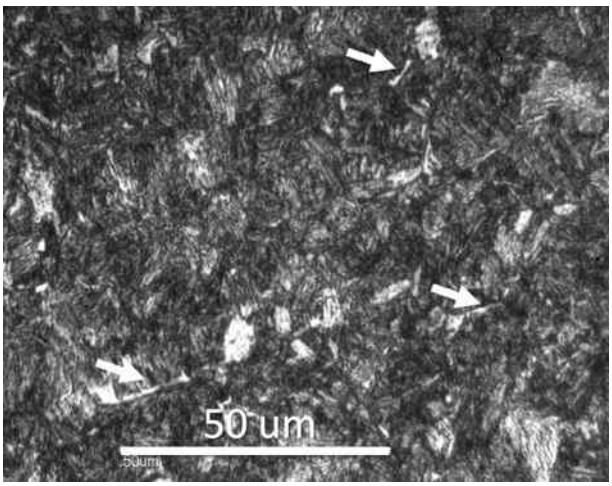

FIGURE 8.6

Microstructure of the material. Etched with Nital 2% [8].

localized reduction on the hardness of the material, reducing the fatigue endurance limit, which along with the reduction on toughness can drastically reduce the life of the component. According to Murakami [30], the uniaxial fatigue strength σ_f can be related with the Vickers hardness HV as:

$$\sigma_f = 1.6\text{HV} \pm 0.1\text{HV} \tag{8.1}$$

The measured bulk Vickers hardness of the failed element was of 353HV. Therefore, using Equation (8.1), the uniaxial fatigue strength of the material can be estimated as 565 ± 35.3 MPa. Alsaran et al. [31] and Bayrak et al. [32] studied experimentally the effect of heat treatment on the properties of AISI-SAE 5140 steel used in the manufacture of suspension system ball joints, finding a fatigue endurance limit of 416 MPa. As Alsaran's endurance limit is lower than the value found using Equation (8.1), and was found experimentally, this value is then used as the bulk fatigue endurance limit of the failed ball joint element studied. Furthermore, Alsaran's value is more conservative.

The Vickers microhardness of the acicular ferrite on the tempered martensite grain boundaries was also measured, finding a mean value of 204HV. Using Murakami's Equation (8.1), the endurance limit for the acicular ferrite approximates to 326 ± 20.4 MPa. Despite the differences found on the endurance limit of the material by using Murakami's or Alsaran's approaches, it is evident that acicular ferrite reduces the endurance limit of the material in approximately 40%. This reduction on endurance limit is considered to be the cause of the fatigue crack initiation on the element, which was further enhanced by the contact stresses highlighted by the ratchet marks present on the fracture surface.

4.1.3 Finite Elements Analysis

Using finite elements analysis (FEA), it is possible to find the locations of high stresses suffered by the analyzed element and their values. In this way, it is feasible to draw specific conclusions on the causes and possible solutions to avoid the recurrence of these kinds of failures. In this analysis, the ball joint was geometrically modeled. The loading, boundary, and contact conditions of the model were given as:

1. A fixed contact in the zone corresponding to the ball.
2. A lateral load assumed constant in this analysis to simplify the modeling, with a value of 500 N and applied at the end of the element. This load value was used according to the experimental study of Ryu et al. [33], who found a value of lateral load of approximately 500 N for a suspension system similar to the one studied here, so it is considered that this load value represents a realistic estimate of the load applied to the element.
3. A lateral contact support patch, corresponding to the support of the axis of the ball joint element with its cage. This contact patch support was applied between the ball and the end of the element where the failure occurred (Figure 8.3) with a rectangular shape as the real shape of contact of the ball joint element against its cage. The rectangle on the contact region had 1 mm thick by 3 mm long around the perimeter of the ball joint element.

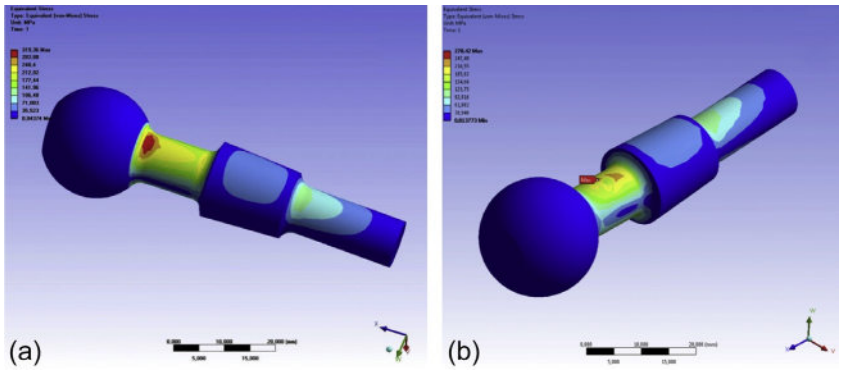

FIGURE 8.7

Equivalent Von Mises stress distribution of the ball joint. (a) Without contact support and (b) with contact support [8].

The analysis and calculations of maximum stresses were performed both with and without the contact support patch, in order to highlight the places of higher stresses in the element. The contact support between the axis of the element and its cage was modeled as frictionless because the failed element surfaces did not show any indications of fretting or wear suggesting friction between them. Figure 8.7a shows the stress distribution on the ball joint element without the contact support patch in place. In this case, the maximum stress was found on the section change between the ball and the axis. This stress reached a maximum value of 319 MPa approximately. On the other hand, Figure 8.7b shows the stress distribution on the element including the contact support patch. In this case, the maximum stress was found on the contact region between the axis of the element and its cage. This stress reached a maximum value of 278 MPa approximately, which is lower than the bulk fatigue endurance limit of this steel under normalized conditions, which reaches to a value of 416 MPa [31]. However, this stress is close to the endurance limit found using Murakami's Equation (8.1) for the acicular ferrite present in the grain boundaries of the material. Also note that the place where this stress is reached corresponds to the place where the fracture occurred in the ball joint element (see Figure 8.3). The smooth beach marks accompanied by ratchet marks and a small final fracture zone (one quarter of the cross-section of the element) confirm that the element suffered high-stress low-cycles fatigue conditions initiated at the acicular ferrite on the grain boundaries, followed by fatigue crack growth.

4.1.4 Conclusion and Recommendations

The analysis showed that the ball joint suffered a fatigue-induced fracture. The fracture initiated at the contact points between the ball joint element and its cage, where a stress concentration was created. Along with this stress concentrator, the presence of acicular ferrite on the tempered martensite grain boundaries reduced the fatigue

endurance limit of the material by almost 40%, initiating cracks that grew with the application of loading cycles until the moment when the sudden failure of the element occurred.

The material used in the manufacture of the ball joint was appropriate for this kind of application. However, defective heat-treating processes reduced the fatigue endurance limit of the material by formation of acicular ferrite on tempered martensite grain boundaries. Further, the reduction of the cross-section on the ball joint element on the region of failure allows the formation of stress concentrators, which further reduce the life of the element. Therefore, the causes of the failure of the ball joint are (i) defective heat-treating process and (ii) defective geometric design of the element cross-section.

In order to reduce the contact stresses on the ball joint element, a change on the geometric design of the element was proposed. It is suggested to modify the geometry of the ball joint to increase the loading section and reduce the contact stresses with the cage. It is also suggested to evaluate the heat-treating processing conditions followed on the manufacture of the element to avoid the formation of acicular ferrite, which further reduces the fatigue endurance limit of the element.

4.2 FAILURE OF A LANDING GEAR DUE TO OVERLOAD

This case describes the analysis and investigation of the causes of the accident of a Cessna 402B civil aircraft with a weight of approximately 28 kN. At the moment of the accident, the aircraft was landing under normal wind and visibility conditions. On landing, one of the main landing gears failed, the failure of the remaining one followed.

Figure 8.8 shows the main landing gear of the Cessna 402B aircraft. Linkage A locks the landing gear at vertical landing position. This linkage is subject to high loads at landing and high shear stresses are applied to the clevis bolts. The failure of the landing gear was initiated on these linkages, and no other failed components were found on the landing gear, consequently the analysis was concentrated on these linkages and their respective bolts.

Figure 8.9 shows the two linkages as received for analysis after the accident. Linkage A1 shows fracture of the bottom clevis, with bolt B1 fractured at one end. Linkage A2 on the other hand, was received with clevis bolt B2 fractured at both ends.

4.2.1 *Fractographic Analysis*

4.2.1.1 Linkage A1

Stereographic examination of the fractured surface of bolt B1 reveals a typical mode II or shear loading fracture, with the arrow indicating the zone where the fracture began (Figure 8.10).

Figure 8.11 shows the fracture surface of the failed clevis of linkage A1. The fracture surface indicates crack-opening mode-I loading failure, initiating the crack at the internal surface of the element as indicated by the arrow.

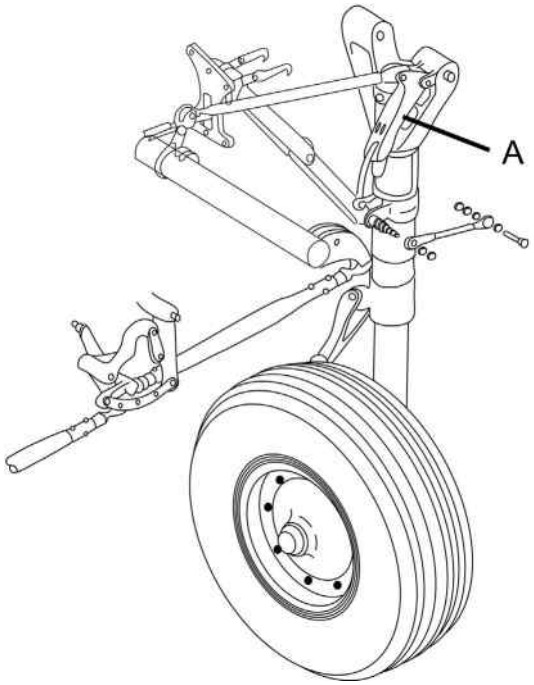

FIGURE 8.8

Schematic showing the Cessna 402 aircraft landing gear. Locking linkage A is shown [22].

FIGURE 8.9

Landing gear left and right locking linkages A1 and A2, respectively. Also shown is the location of the respective failed bolts B1 and B2 [22].

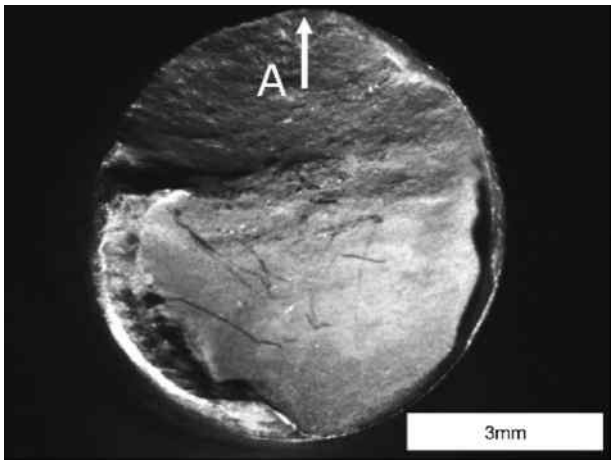

FIGURE 8.10

Stereoscopic micrograph of the fractured surface of bolt B1. The arrow points toward the fracture initiation [22].

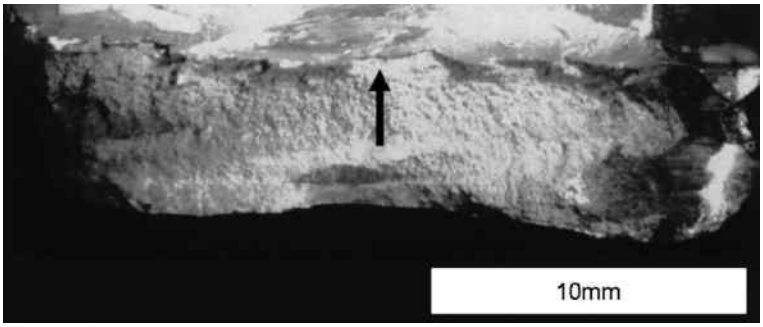

FIGURE 8.11

Stereoscopic micrograph of the fractured surface of the clevis of linkage A1. The arrow points toward the fracture initiation [22].

4.2.1.2 Linkage A2

Figure 8.12a shows the fractured surface of the left-hand side tip of bolt B2. This surface displays similar characteristics to the fracture surface shown in Figure 8.10 for bolt B1, with shear fracture mode prevailing, also accompanied by bending of the left-hand side tip of the bolt. Figure 8.12b, on the other hand shows the fracture surface of the right-hand side of bolt B2. This surface exhibits different characteristics when compared with the respective fractured surfaces of the bolts analyzed previously, with a less rough appearance in Zone A (see Figure 8.12b). This zone also displays what appear to be fatigue beach marks, which along with the straight

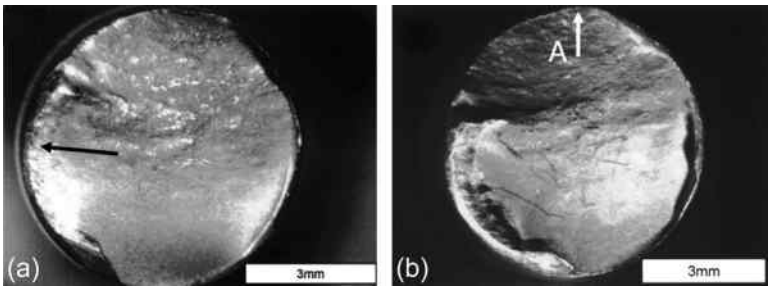

FIGURE 8.12

Fracture surface of bolt B2. (a) Left-hand side and (b) right-hand side [22].

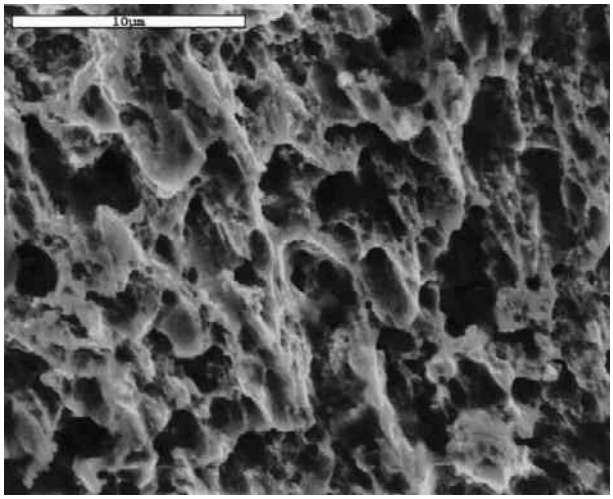

FIGURE 8.13

SEM micrography of Zone A in Figure 8.12, showing ductile shear fracture [22].

right-hand tip fracture could indicate a pre-existent crack in the bolt. However, higher magnification SEM analysis revealed that the failure was indeed caused by shear loading mode as for the other fractured bolt surfaces and no evidence of fatigue was found, as shown in Figure 8.13. These apparent fatigue marks can be misleading and care must be taken in order to asses a realistic failure cause.

4.2.2 *Estimation of Failure Load*

As the landing gear failure was caused by shear loading of clevis bolt B2, the load at landing supported by this bolt can be estimated. The ultimate shear stress of the bolt can be approximated from the empirical expression [34]:

$$\tau_u = \frac{\sigma_{TS}}{1.6} \tag{8.2}$$

where σ_{TS} is the tensile strength of the material. This tensile strength can in turn be estimated using the empirical correlation [34]:

$$\sigma_{TS}(\text{MPa}) = 3.2\,\text{HV} \tag{8.3}$$

where, HV is the Vickers Hardness of the material. The measured Vickers Hardness of clevis bolt B2 was 349 HV, then from Equations (8.2) and (8.3) the ultimate shear stress of the bolt can be estimated as $\sigma_{TS} = 698$ MPa. Finally and considering that bolt B2 failed by double shearing, the ultimate load can be calculated as

$$F_u = 2\tau_u \pi r^2 = 39.5\,\text{kN} \tag{8.4}$$

with $r = 3$ mm.

It is worth noting that the empirical approximations employed (Equations 8.2 and 8.3) were based on quasi-static loading experiments and not on dynamic loading as was the case of the failure being analyzed. It is known however that dynamic shear resistance is higher than static resistance (see, for instance, Ref. [35]). Therefore, the value of F_u must be taken as a lower approximation to the real load supported by the bolt. With this in mind, and recalling that the total weight of the aircraft was 28 kN approximately, the landing to cause shear fracture of bolt B2 had to be abrupt and heavy.

4.3 DISCUSSION

After analyzing the different fracture surfaces of the landing gear, a conclusion of the causes of the accident can be drawn. The failure was initiated by a sudden impact shear load on bolt B2 causing shear fracture leading to lose of all loads bearing capacity of linkage A2 and the corresponding landing gear. As a consequence, the entire landing load was displaced to a lateral loading of the left landing gear causing the shear failure of bolt B1 and subsequent mode-I failure of linkage A1 clevis. In order for the failure to occur in that way, the landing had to be abrupt with the entire load applied to the right landing gear. Therefore, the accident was due to human error and not to material defects.

4.4 FAILURE OF A NOSE-LANDING GEAR AFT LOCK-LINK

This case describes the analysis and investigation of the causes of the failure of the nose-landing gear AFT lock-link of a Boeing 767-200 aircraft. Figure 8.14 shows the nose-landing gear of the aircraft. The AFT lock-link was fractured as shown in Figure 8.15. The element was manufactured using a 7175 Aluminum alloy.

4.4.1 *Fractographic Analysis*

Figure 8.16 shows the fracture surface of the landing gear, appreciated by optical microscopy. This fracture shows two distinctive zones, one clear and semi-circular zone denoted as Zone A, and a darker zone, denoted as Zone B. The fracture began at

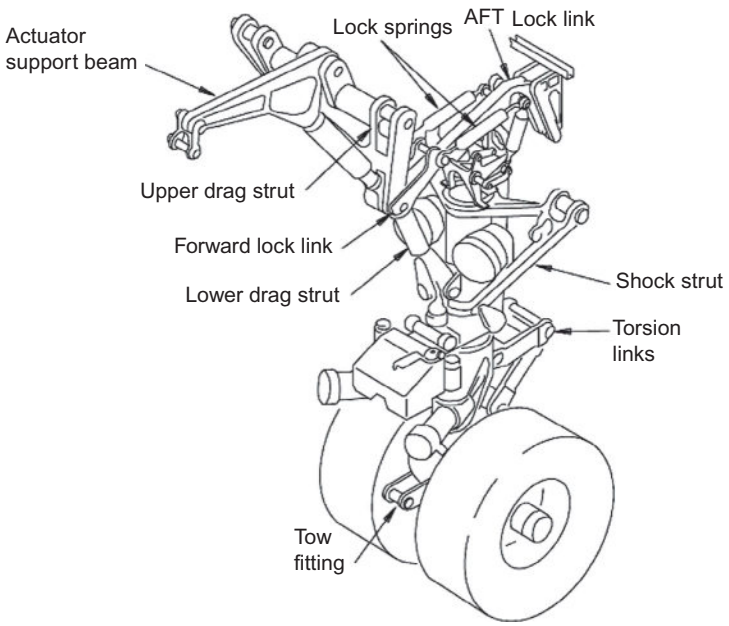

FIGURE 8.14

Schematic showing the nose-landing gear. AFT Lock link is shown.

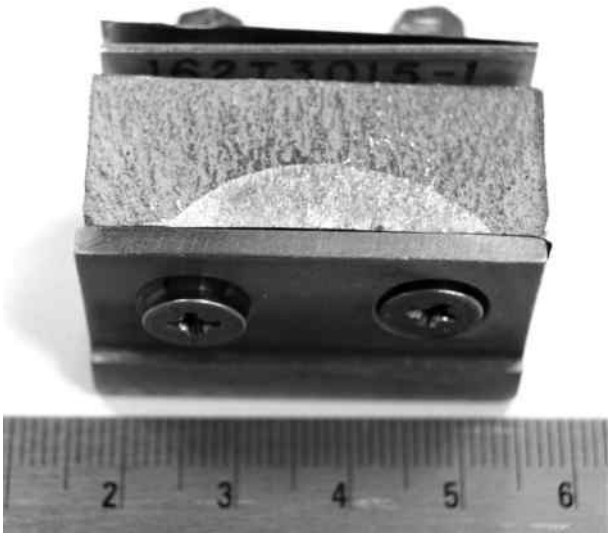

FIGURE 8.15

Failed AFT lock-link with support plate in place.

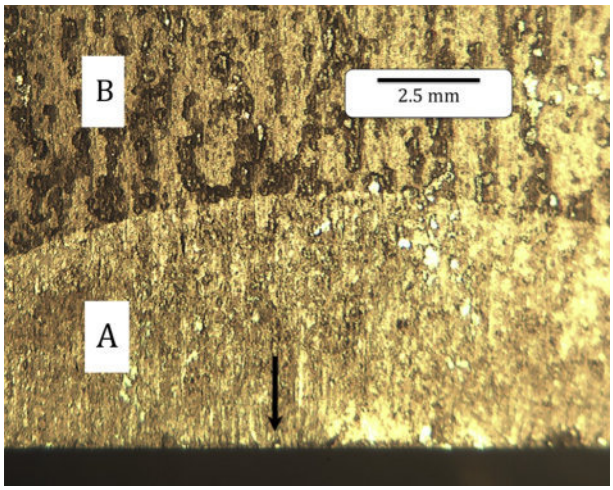

FIGURE 8.16

Fracture surface of the AFT lock-link.

the lower part of Figure 8.16, as indicated by the arrow. This zone coincides with the placement of the support plate of the element.

Figure 8.17 shows Zone A; here the ratched marks can be appreciated, indicating high stresses in the contact area of the support plate.

Figure 8.18 shows a SEM image of Zone A, where the arrow indicates the fatigue crack growing direction. It can also be appreciated that the fatigue crack growing direction runs parallel to a precipitate located at the center of the image.

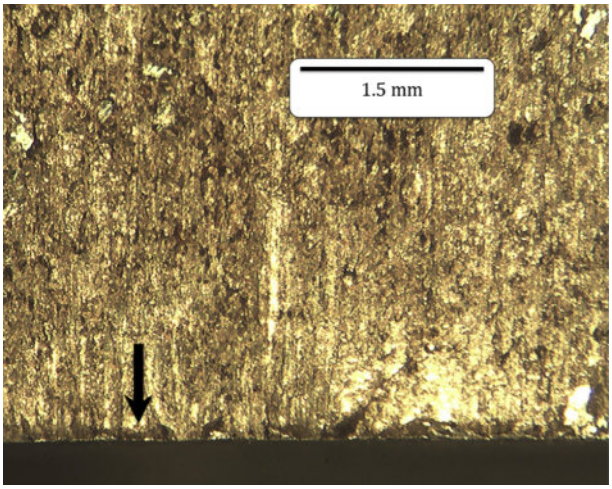

FIGURE 8.17

Fracture surface of the AFT lock-link, Zone A.

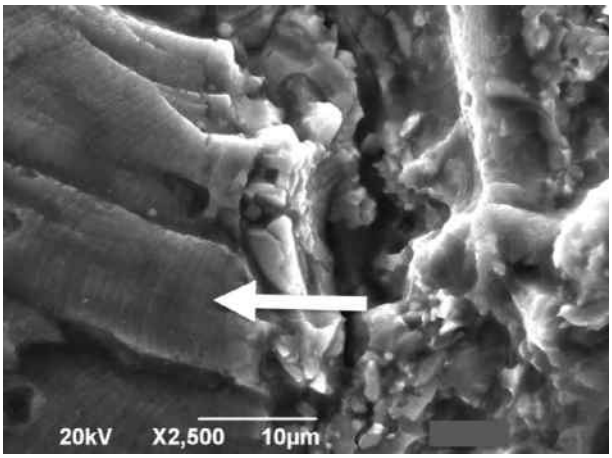

FIGURE 8.18

SEM fracture surface of the AFT lock-link at Zone A. The arrow indicates fatigue-growing marks.

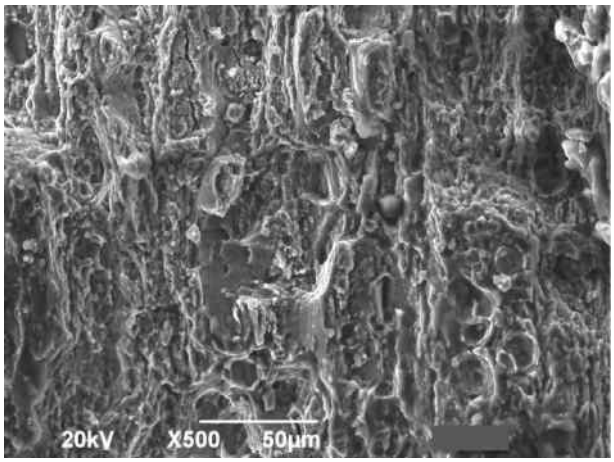

FIGURE 8.19

SEM fracture surface of the AFT lock-link at Zone B.

Figure 8.19 shows the fracture surface of the element on Zone B. Here, the surface is characteristic of ductile fracture with vertically aligned precipitates.

4.4.2 *Metallographic Analysis*

Figure 8.20 shows a metallographic specimen etched with nitric acid (25%) in a zone near to the fracture. Here, the aligned $FeAl_3$ (dark gray) and $MgZn_2$ precipitates (black) inside an aluminum-rich matrix can be seen.

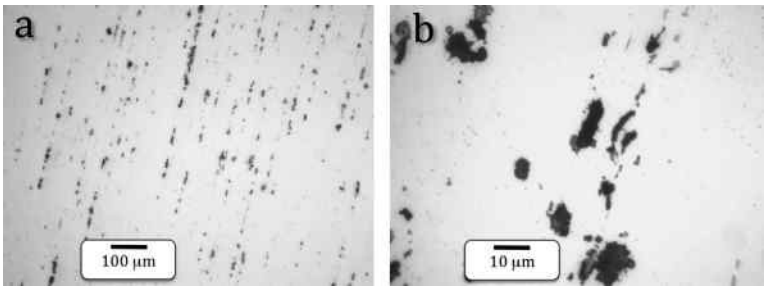

FIGURE 8.20

Microstructure of the AFT lock-link showing aligned precipitation of $MgZn_2$ and $FeAl_3$. (a) low magnification and (b) high magnification.

4.4.3 *Analysis*

The failure of the AFT lock-link was due to the appearance of aligned precipitates and inclusions. These were present in the microstructure of the material in high quantity, which after cyclic loading started fatigue cracks near to the contact region against the steel support plate, leading to the final fracture of the element. In order to reduce or even avoid the appearance of this kind of failures, it is recommended to perform appropriate heat treatments to the material in order to avoid the formation of precipitates, which can cause fatigue crack initiation. It is also important to avoid the presence of contaminant elements like iron on the aluminum alloy. Iron creates $FeAl_3$ precipitates, which reduces considerably the fracture toughness of the material.

4.5 FAILURE OF THE REAR CANTILEVER SPRING LANDING GEAR OF A FUMIGATION AIRCRAFT

A rear cantilever spring landing gear of a fumigation aircraft (Figure 8.21) failed during a landing procedure under normal conditions. The failed cantilever spring was manufactured using an AISI 4340 steel and failed at the same place of support to the aircraft main structure, as shown in Figure 8.22.

Figure 8.23 shows the two fracture surfaces of the cantilever spring. Here, the corroded surface on top of the cantilever with pits near the fracture surface can be appreciated.

Figure 8.24 shows the fracture surface of the spring. Here, the fracture shows two characteristic zones, denoted as A and B. Zone A is where the crack started, and the arrow points toward the point where the crack started to grow, which corresponds to a pit cavity. Zone B, on the other hand is the region of the element, which supported the loads at the final stages of crack growth of the element, as indicated by the river lines.

Figure 8.25 shows a SEM micrograph of the fracture Zone A, close to the starting point of fracture. This fractograph ruled out any possibility of associating this failure

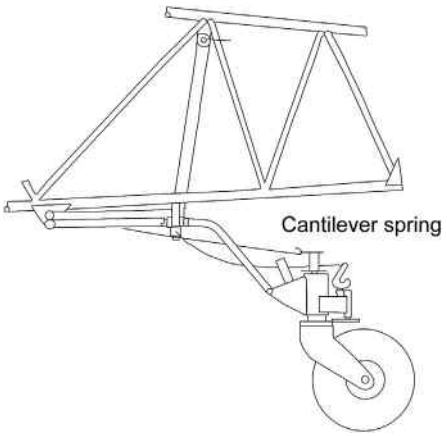

FIGURE 8.21

Schematic of the rear cantilever spring landing gear of a fumigation aircraft.

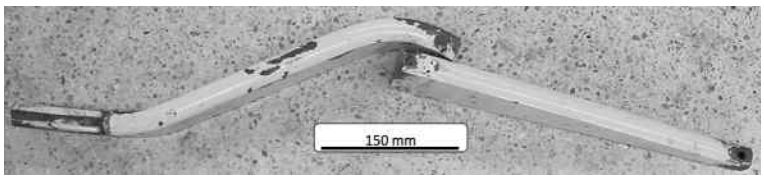

FIGURE 8.22

Failed cantilever spring.

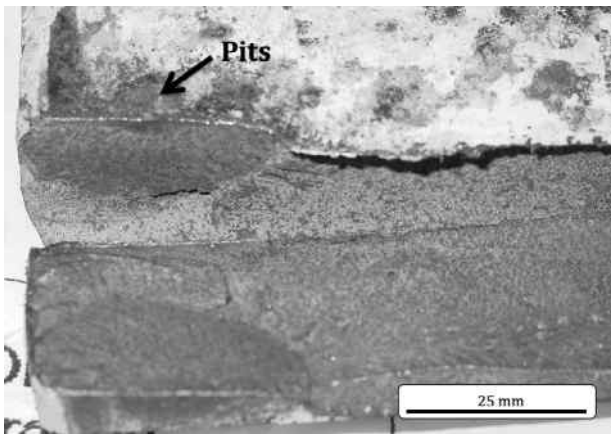

FIGURE 8.23

Top view cantilever spring fracture surfaces.

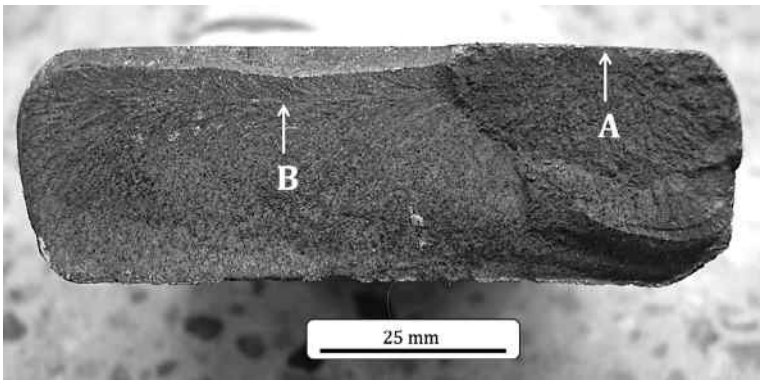

FIGURE 8.24

Fracture surface of the cantilever spring.

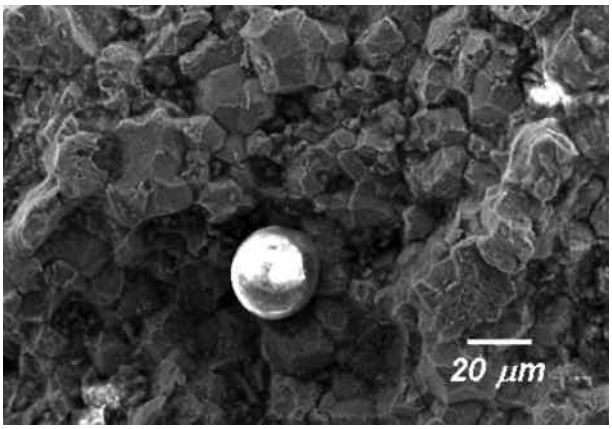

FIGURE 8.25

SEM micrograph of fracture Zone A.

to fatigue. The fracture is completely intergranular, which is an indication of stress corrosion-induced cracking.

Figure 8.26 shows one intergranular corrosion crack growing from a pit on the surface of the cantilever spring. These kinds of cracks were found consistently in different zones near the surface and the fracture zone of the element.

It can be concluded that the failure of the cantilever spring was caused by a defective protective coating in order to prevent surface corrosion. The corrosion pits created intergranular corrosion of the material that further grew cracks due to cyclic loadings during take offs and landings of the aircraft.

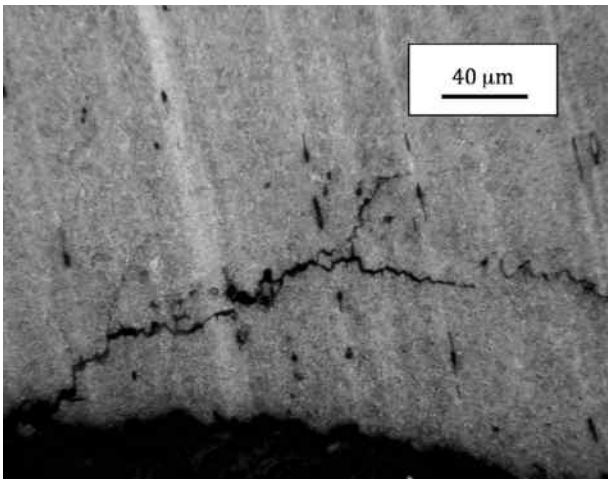

FIGURE 8.26

Intergranular crack growing from the element surface on Zone A.

5 CONCLUSION

Failures of landing gears in aircrafts represent approximately 10% of the total of failures reported for the aerospace industry. These failures are usually associated to metallurgical (e.g., recrystallization and grain boundary precipitation), processing (e.g., machining marks, incomplete protective coatings, and abusive grinding), environmental (e.g., corrosion), design (e.g., improper material selection, reduced cross-sections), and overload causes. These are conditions that can be easily prevented by following good engineering and maintenance practices, which are usually well established in the aerospace industry.

On the other hand, failures of suspension systems in vehicles represent approximately 13% of the total of failures for the automotive industry. These failures are commonly associated to metallurgical (e.g., casting defects, excessive inclusions), processing (e.g., improper shot pinning, welding, machining), and design (e.g., incorrect choices of materials, excessive contact stresses) conditions.

REFERENCES

[1] Wang Y, Long H. Summary and analysis of the aging aircrafts. Fail Procedia Eng 2011;17:303–9.

[2] Heyes AM. Automotive component failures. Eng Fail Anal 1998;4(1):129–41.

[3] Nadot Y, Denier V. Fatigue failure of suspension arm: experimental analysis and multiaxial criterion. Eng Fail Anal 2004;11:485–99.

[4] Prawoto Y, Ikeda M, Manville SK, Nishikawa A. Design and failure modes of automotive suspension springs. Eng Fail Anal 2008;15:1155–74.
[5] Banuta M, Tarquini I, Gauvin B, et al. Failure of a fusion welded ball joint as a result of modification in MnS direction. J Fail Anal Preven 2008;8:426–30.
[6] Eryürek IB, Ereke M, Goksenli A. Failure analysis of the suspension spring of a light duty truck. Eng Fail Anal 2007;14:170–8.
[7] Triantafyllidis GK, Antonopoulos A, Spiliotis A, Fedonos S, Repanis D. Fracture characteristics of fatigue failure of a vehicle's ductile iron steering knuckle. J Fail Anal Preven 2009;9:323–8.
[8] Ossa EA, Palacio CC, Paniagua MA. Failure analysis of a car suspension system ball joint. Eng Fail Anal 2011;18:1388–94.
[9] Das SK, Mukhopadhyay NK, Ravi Kumar B, Bhattacharya DK. Failure analysis of a passenger car coil spring. Eng Fail Anal 2007;14:158–63.
[10] Zhao LH, Zheng SL, Feng JZ. Failure mode analysis of torsion beam rear suspension under service conditions. Eng Fail Anal 2014;36:39–48.
[11] Azevedo CR, Hippert E. Fracture of an aircraft's landing gear. Eng Fail Anal 2002;9:265–75.
[12] Azevedo CR, Hippert E, Spera G, Gerardi P. Aircraft landing gear failure: fracture of the outer cylinder lug. Eng Fail Anal 2002;9:1–15.
[13] Niansheng X, Peidao Z, Chunhu T. Failure analysis and prevention of a brake nave on a landing gear. Eng Fail Anal 1996;3(3):211–8.
[14] Eliaz N, Sheinkopf H, Shemesh G, Artzi H. Cracking in cargo aircraft main landing gear truck beams due to abusive grinding following chromium plating. Eng Fail Anal 2005;12:337–47.
[15] Bagnoli F, Dolce F, Colavita M, Bernabei M. Fatigue fracture of a main landing gear swinging lever in a civil aircraft. Eng Fail Anal 2008;15:755–65.
[16] Barter SA. Investigation of a Boeing 747 wing main landing gear trunnion failure. Eng Fail Anal 2013;35:387–96.
[17] Lee HC, Hwang YH, Kim TG. Failure analysis of nose landing gear assembly. Eng Fail Anal 2003;10:77–84.
[18] Franco L, Lourenco N, Graca M, Silva O, Campos P, von Dollinger C. Fatigue fracture of a nose landing gear in a military transport aircraft. Eng Fail Anal 2006;13:474–9.
[19] Bagnoli F, Bernabei M. Fatigue analysis of a P180 aircraft main landing gear wheel flange. Eng Fail Anal 2008;15:654–65.
[20] UK Air Accidents Investigation Branch. Report on the accident to Boeing 777-236ER, G-YMMM, at London Heathrow Airport on 17 January 2008. Aircraft accident report 1/2010; 2010.
[21] Erasmus DJ, Hattingh DG, Young AB, Els-Botes A, James MN. Design of a motor glider landing gear strut—the role of failure analysis in structural integrity. Eng Fail Anal 2014;41:30–8.
[22] Ossa EA. Failure analysis of a civil aircraft landing gear. Eng Fail Anal 2006;13: 1177–83.
[23] Tao JX, Smith S, Duff A. The effect of overloading sequences on landing gear fatigue damage. Int J Fatigue 2009;31:1837–47.
[24] Asi O, Yesil O. Failure analysis of an aircraft nose landing gear piston rod end. Eng Fail Anal 2013;32:283–91.
[25] Bol'shakov VI, Laukhin DV, Sukhomlin GD, Kuksenko VI. Effect of heat treatment on formation of acicular ferrite and on the properties of low carbon microalloyed steels 10G2FB and 09G2S. Met Sci Heat Treat 2004;46(11–12):545–50.

[26] He K, Edmonds DV. Formation of acicular ferrite and influence of vanadium alloying. Mater Sci Technol 2002;18:289–96.
[27] Mazancova E, Rucka Z, Mazanec K. Comparison of microfractographic behaviour of acicular ferrite and bainite and hydrogen cracking resistance. Arch Mater Sci 2007;28 (1–4):95–9.
[28] Huang Z, Yao M. Effect of arrangement of acicular ferrite in a Widmanstatten microstructure on the fracture of mild steel. Mater Sci Eng A 1989;119:211–7.
[29] Ossa EA, Paniagua M. Failure analysis of a fastener system and its analytical prediction. In: SAMPE conference, Baltimore, MD, USA; 2009.
[30] Murakami Y. Metal fatigue: effects of small defects and non-metallic inclusions. Oxford, UK: Elsevier; 2002.
[31] Alsaran A, Karakan M, Celik A. The investigation of mechanical properties of ion-nitrided AISI 5140 low-alloy steel materials characterization. Mater Charact 2002;48: 323–7.
[32] Bayrak M, Ozturk F, Demirezen M, Evis Z. Analysis of tempering treatment on material properties of DIN 41Cr4 and DIN 42CrMo4 steels. J Mater Eng Perform 2007;16 (5):597–600.
[33] Ryu YI, Kang DO, Heo SJ, Yim HJ, Jeon JI. Development of analytical process to reduce side load in strut-type suspension. J Mech Sci Technol 2010;24:351–6.
[34] Jones DRH. Engineering Materials 3. Oxford: Pergamon Press; 1986.
[35] Zhang H, Zhou M, Hu S. Impact strength measurement of spot welds. Proc Inst Mech Engrs B 2001;215:403–41.

CHAPTER

Fatigue as a cause of failure of aircraft engine cylinder head

9

Branimir Krstic*, Bosko Rasuo†, Dragan Trifkovic*, Igor Radisavljevic‡, Zoran Rajic‡, Mirko Dinulovic†

*University of Defence in Belgrade, Military Academy, Generala Pavla Jurisica Sturma 33, Belgrade, Serbia**

University of Belgrade, Faculty of Mechanical Engineering, Kraljice Marije 16, Belgrade, Serbia†

Military Technical Institute, Ratka Resanovica 1, Belgrade, Serbia‡

CHAPTER OUTLINE

1 INTRODUCTION

The most frequent cause of fatal aircraft accidents, without taking into account pilot errors, is a mechanical failure of different structural elements, propulsion, and other systems of aircraft. In modern aerospace industry, considered today as the technological leader in developing and applying new materials and highly sophisticated technical systems, an increasing level of reliability in service is being requested from these elements. This is in direct contradiction to demands of long endurance while

Handbook of Materials Failure Analysis With Case Studies from the Aerospace and Automotive Industries.
http://dx.doi.org/10.1016/B978-0-12-800950-5.00009-0

under increasingly complex dynamic loads of high intensity as well as a work in severe operating conditions. This antagonism, further pronounced in aviation through the demand for flight safety, directly imposes an imperative that a catastrophic failure must not occur in flight. Because of that, it is necessary to continuously undertake some specific preventive measures during a whole life cycle of aircraft. Unfortunately, despite all this, failures continue to occur, and in a case of vital elements, fracture can lead to fatal consequences to human lives, complete loss or, at very least, cause damage to property. Therefore, today across the world, specific methodologies for failure investigation of responsible structures are being developed and applied extensively. Scientific discipline, known as forensic engineering, widely uses these methodologies, especially in aviation industry in order to help accidents investigation and their future prevention.

The subject of this study includes mechanical failures of aircraft engine CHs that are very demanding in terms of complexity of exact determining of their failure causes. First, fractures often occur due to simultaneous action of several factors. Second, a crack initiates from multiple origins and, finally, mechanism of crack spreading is usually a combination of fatigue and overload. In addition, cracks in cylindrical elements quite often are developed on the inner, difficult to access, surface and are revealed only when they reach the outer surface or when cause final fracture.

Taking into account all stated specificities of aircraft engine CH, a reliable methodology for analysis of failure causes of aircraft engine CHs is developed in this study. This methodology should enable forensic engineers to determine an exact cause(s) of failures and consequently to propose appropriate preventive and corrective measures.

The results of the research are verified through analysis of the two real mechanical failures of aircraft engine CH that have occurred during the flight. The failures were due to cracking the CHs of the piston engine Lycoming IO-360-B1F, built in the training aircraft Utva-75 (Figure 9.1). In addition, these failures have occurred in

FIGURE 9.1

Utva-75 training aircraft.

aviation of some other countries, as evidenced by reports of relevant aviation authorities stated below.

In the Airworthiness Directive [1] AD 2008-19-05, issued by Federal Aviation Administration (FAA) of U.S. Department of Transportation, it was stated that 45 engine failures with the CH separation due to cracks at the CH to the cylinder barrel interface in the cylinder assemblies (CH and cylinder barrel) had been reported until 2008. Since 2000, the National Transportation Safety Board of the United States (NTSB) has examined numerous aircraft piston engine cylinder assemblies (documented in the NTSB case numbers: ENG07WA032, ENG07SA033, and WPR09SA476) that failed due to fatigue cracking that initiated in the root of the CH thread, eventually resulting in loss of compression and/or separation of the CH into two pieces [2]. During the 2009/2010, the Transportation Safety Board of Canada—Operational Services Branch in engineering reports [3,4] presented in detail the results of two investigations of aircraft engine failure involving the CH separation. In both cases, the separation of the CH occurred due to the fatigue cracks that developed at the root of the CH thread. Some other observations have also shown that a CH can fail due to fatigue cracking that initiated away from the root of a CH thread [5,6].

2 DESCRIPTION OF FAILURES

Two piston engines of the training aircraft Utva-75 malfunctioned during the flight mission within the period of 4 months, due to the fatigue cracking of their aluminum cast CHs. In the both cases of failures, the training aircraft Utva-75, with two pilots on board, was on a training flight, when pilots reported an engine problem. Shortly after departure, the pilots heard a very loud "bang" and the engine began to run rough and vibrate. The engine working parameters degraded rapidly and pilots decided to perform a forced landing. In the first case of failure (Failure Case I), the aircraft was in close proximity to a home base, where the crew performed a forced landing. In the second case of failure (Failure Case II), forced landing was performed at the nearest suitable airport equipped with one grass runway, approximately 80 km away from the home base. In both aforementioned force landings, neither the pilots were injured nor the aircraft was damaged. However, the on-the-spot visual inspection of the both engines revealed cracks in the CHs between the fifth and the sixth cooling fins (counting from the barrel). The engines were removed from the aircraft and the damaged cylinder assemblies were sent to the Military Technical Institute (MTI), Structural and Technical Materials Laboratory, to determine the cause(s) of the failures.

The failed CHs presented in this study belong to a four-cylinder, direct drive, horizontally opposed, air-cooled engine of the training aircraft Utva-75 that had an accident. The cylinders assemblies are of conventional air-cooled construction and include two major parts, the CH and the cylinder barrel. The CHs were manufactured from an aluminum-casting alloy 242.0 (according to American National Standard

Institute designation system) with a fully machined combustion chamber. The cylinder barrels are machined from chrome nickel molybdenum steel AISI 4140 (according to American Iron and Steel Institute designation system) forging with deep integral cooling fins and have a smooth bore that houses the piston. The CH and the cylinder barrel are joined by heating the CH to about 350 °C then screwing it onto the cylinder barrel [2]. As the CH cools and shrinks onto the cylinder barrel, an interference fit is produced, locking the parts together at the threads and at an adjacent plain diameter, which is commonly referred to as a shrink band. Shrink bands are features on the cylinder barrel and in the CH marked with red and blue arrowheads in Figure 9.2. The engine specifications [7] are presented in Table 9.1.

In the Failure Case I, the damaged cylinder assembly was installed on the engine in the number one position (Figure 9.3), and at the time of the occurrence flight, the engine had accumulated 1560 flight hours since new and 360 h since overhaul. The last periodic (50 h) compression test was conducted at either 1545 h of total flight time or 15 h before accident. In the Failure Case II, the damaged cylinder assembly was installed on the engine in the number four position (Figure 9.3). The engine had accumulated 1389 h since new and 189 h since overhaul. The last compression test was conducted at 1349 h of the total flight time (40 h before accident).

According to the technical specifications provided by the manufacturer, this engine's time between overhauls (TBO) is 2000 h. For damaged cylinder assemblies, the result of differential pressure test was significantly below the minimum allowable value of 70 psi, required by the manufacturer [8], as shown in Table 9.2.

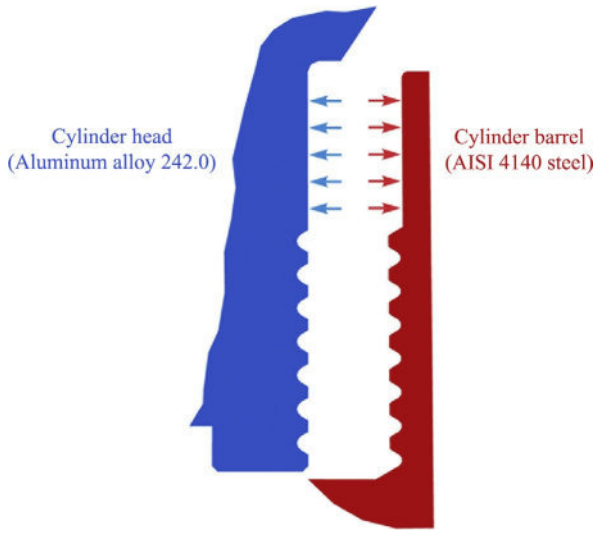

FIGURE 9.2

Longitudinal section view of the cylinder assembly.

Table 9.1 Lycoming IO-360-B1F Engine Specifications

Parameter	Value
FAA-type certificate	1E10
Rated horsepower	180 hp
Rated speed	2700 rpm
Bore	0.130 m
Stroke length	0.111 m
Volumetric displacement	5.893 L
Number of cylinders	4
Compression ratio	8.5:1
Firing order	1-3-2-4
Spark occurs	25° before top dead center
Propeller drive ratio	1:1
Propeller drive rotation (viewed from rear)	Clockwise

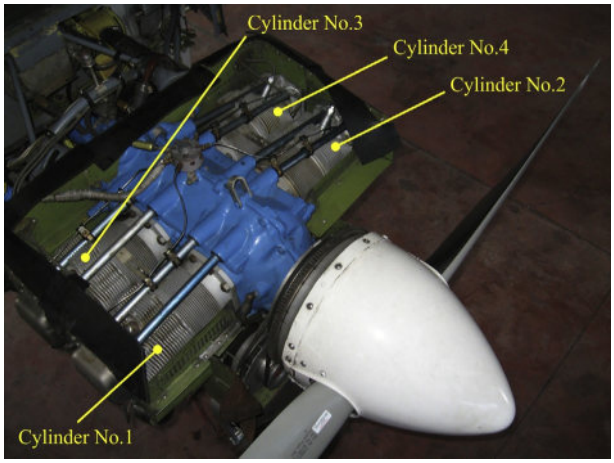

FIGURE 9.3

Lycoming IO-360-B1F engine.

Table 9.2 Compression Test

	Cylinder			
	Cylinder No.1	Cylinder No.2	Cylinder No.3	Cylinder No.4
	Compression reading (psi)			
Failure Case I	64	72	74	72
Failure Case II	70	76	78	64

3 EXPERIMENTAL DETAILS

This section presents a detailed description of the failure analysis procedure employed for determining the root cause(s) of the both mentioned failures.

Immediately, after damaged cylinder assembly was received for examination at the MTI Structural and Technical Materials Laboratory, an external visual inspection by unaided human eye was conducted. The location of the crack in the CH was identified and documented. Since the CH was not completely broken into two pieces, it was then mechanically opened due to the necessity of performing the fractographic analysis of the fracture surface. The first step was visual examination by unaided human eye. The fracture surface, attached to the upper part of CH, was then cut off into ring shape to allow introducing it under stereomicroscope. The macroscopic analysis of the fracture surface was undertaken using Leica M205A stereomicroscope at low magnification ($\leq$50). The obtained ring with fracture surface was ultrasonically cleaned at slightly elevated temperature in a citrus-based liquid degreaser. Then it is cleaned in acetone and ethanol to eliminate residues produced by the combustion. The microfractographic analysis of the most interesting areas of the fracture surfaces was done using JEOL JSM-6610LV scanning electron microscope (SEM). Deposits, clearly visible under SEM, were analyzed by energy dispersive spectroscopy (EDS) in SEM. Specimens for metallography were cut perpendicular to the fracture surface, at the location that approximately corresponds to the main fatigue crack origin. The metallographic preparation included wet mechanical grinding, using silicon carbide papers down to 2500 grit. This was followed by polishing using 7/5, 5/3, and 3/2 μm diamond paste and final polishing with 1 μm diamond paste. The sample was examined in the as-polished condition under LeitzMetalloplan light microscope. The microstructure of metallographic specimens was analyzed and compared to the microstructure of the sample cut away from the fracture surface. The chemical composition of the CH material was determined by X-ray fluorescence spectroscopy (XRF) chemical analysis method. The Brinell hardness test of the material was conducted using a 2.5 mm diameter hardened steel ball with a 612.9 N load applied for a period of 30 s (HBS 2.5/62.5/30″). The hardness measurements were taken from the "ring" plane, opposite to the fracture surface. To identify the stress state of the cylinder assembly related with in-service condition, a structural FE analysis was carried out using CATIA V5R22 Generative Structural Analysis Workbench. For this purpose, 3D solid model of the cylinder assembly, identical to the physical one of the engine, was developed using CATIA V5R22 and applied with a nominal load of the engine.

4 RESULTS

4.1 VISUAL INSPECTION

The damaged cylinder assemblies, photographed in the as-received condition, are shown in Figure 9.4 and 9.5. As seen from the aforementioned figures, both CHs had cracked between the fifth and the sixth cooling fins. The clearly visible crack

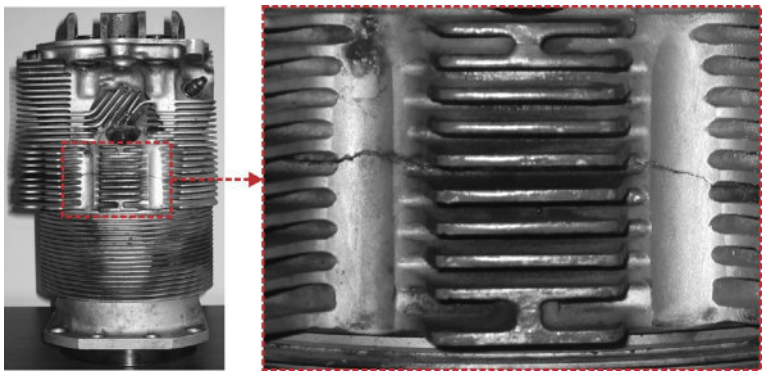

FIGURE 9.4

Cylinder assembly photographed in the as-received condition with close-up view of the crack in the CH I (Failure Case I).

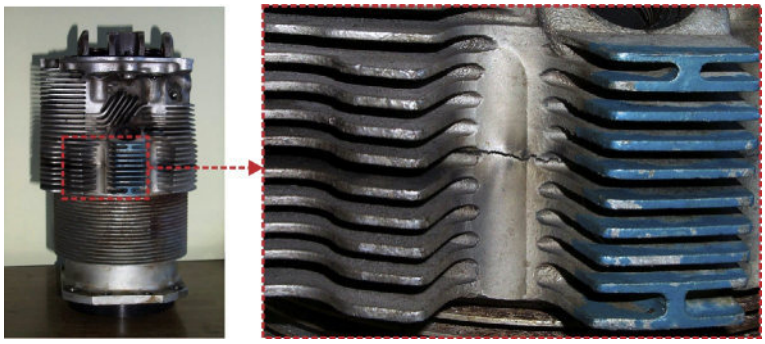

FIGURE 9.5

Cylinder assembly photographed in the as-received condition with close-up view of the crack in the CH II (Failure Case II).

had an approximately 0.5 mm width and extended about 80% of the CH circumference. The crack propagation plane in the failed CHs runs through the position of the top plane of cylinder barrel (Figure 9.6).

4.2 MACROFRACTOGRAPHY

4.2.1 Macrofractography of the CH I (Failure Case I)

The initial visual inspection of the mating fracture surfaces of the CH I (Figure 9.7), using the unaided human eye, indicated the presence of five different morphologies, marked as A, B, C, D, and E in Figure 9.8. The sector A, located on the exhaust side of the CH I, showed a flat and smooth surface. Features characteristic of fatigue fracture can be clearly distinguished. These are ratchet marks, which represent steps between fatigue crack regions propagated from different origins (the larger of them

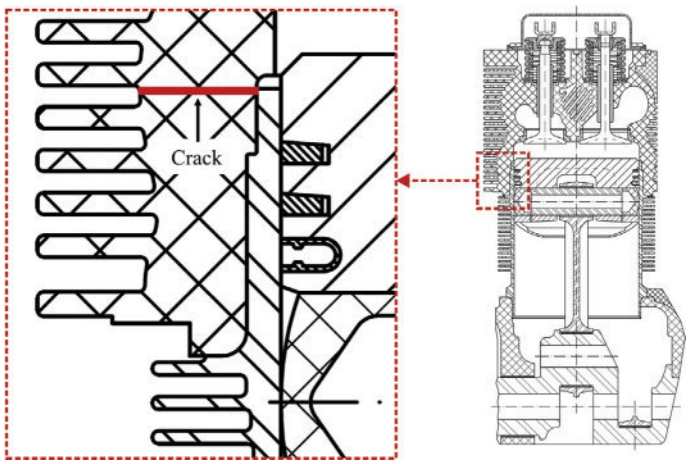

FIGURE 9.6

Schematic drawing of cylinder assembly, piston, and valve components with close-up view of the crack position in the CH.

FIGURE 9.7

Mating fracture surfaces of the CH I obtained after the crack was mechanically opened.

are marked with arrowheads in Figure 9.9a). The additional examination of fracture surface of the sector A under stereomicroscope confirmed that the fatigue crack initiated from different origins located on the inner edge of the CH I (Figure 9.9b). The fatigue crack had propagated slowly over this sector. The sector A has an obvious thumb-nail-shaped boundary with the sector B. The main macroscopic feature of the slant fracture surface of the sector B (Figure 9.10a), approximately 45° to the CH I axis, is a rough and dull texture, which suggests ductile fracture under mostly

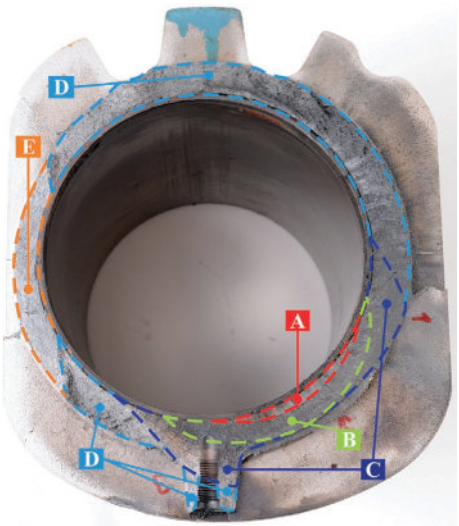

FIGURE 9.8

Macrograph showing characteristic morphologies on the fracture surface of CH I.

tensile loads. Moreover, a narrow rim of overstress fracture extends around almost the entire outer circumference of the slant fracture. However, in this stage of fracture life, the crack depth reached the outside surface of the CH I (arrowhead in Figure 9.10b). The sector C of the fracture surface revealed the presence of macroscopic crack beach marks (arrest lines), which suggest that the crack propagated in a fatigue mode (Figure 9.11). The sector D represents the fracture surface of unstable fracture with a rough, dull, and coarse grainy morphology, where the overload was the main fracture mechanism. This final overstress fracture of the CH I wall occurred when the crack had reached a critical size. The sector E covers about 20% of cross-section of the CH I. Actually, this sector is area of mechanically forced open fracture characterized by the bright appearance resulting from the reflective qualities of cleaved crystals. In addition, the visual inspection disclosed a varying degree of exposure of the fracture surface to the combustion gases. Consequently, almost the entire fracture surface of the CH I, except sector E, was significantly contaminated by these gases. No evidence of macroscopic plastic deformations was found on the fracture surface.

4.2.2 *Macrofractography of the CH II (Failure Case II)*

Three distinct areas of apparent morphologies were noticed on the mating fracture surfaces (Figure 9.12) of the CH II (marked as A, B, and C in Figure 9.13). A rather smooth and flat surface of the sector A, with clearly visible beach and ratchet marks (Figures 9.14 and 9.15), undoubtedly evidenced that the fatigue was involved. This sector extends about a quarter of the CH II circumference and appears to cross the

FIGURE 9.9

(a) View of the sector A of the fracture surface depicting ratchet marks (arrowheads) and (b) stereomacrograph showing the sector A of the fracture surface with multiple ratchet marks along the inner edge of the CH I (arrowheads).

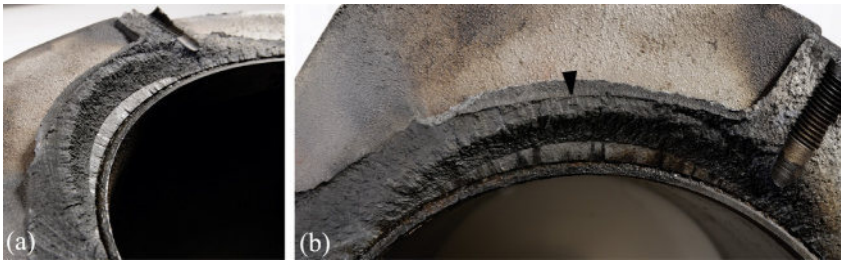

FIGURE 9.10

(a) Macrograph showing the slant fracture surface of the sector B and (b) place where the crack depth reached the outside surface of the CH I (arrowhead).

entire thickness of the CH II wall in the middle. By tracing back the beach marks, the fracture origin area was also found to be at the internal surface of the CH II. The fracture surface of unstable fracture, sector B, exhibited a rough, dull with coarse grainy morphology, which is common for an overstress fracture mode. This final overstress fracture of the CH II wall occurred when the total area of the crack had reached a critical size. The sector C of fracture surface, obtained after the crack was mechanically opened, was characterized by the bright appearance due to reflective qualities of cleaved crystals and represented about 25% of the CH II cross-section. Similar to the Failure Case I, areas of apparent fatigue and overstress fracture (sectors A and B) were also significantly contaminated by combustion gases. No evidence of macroscopic plastic deformations was found.

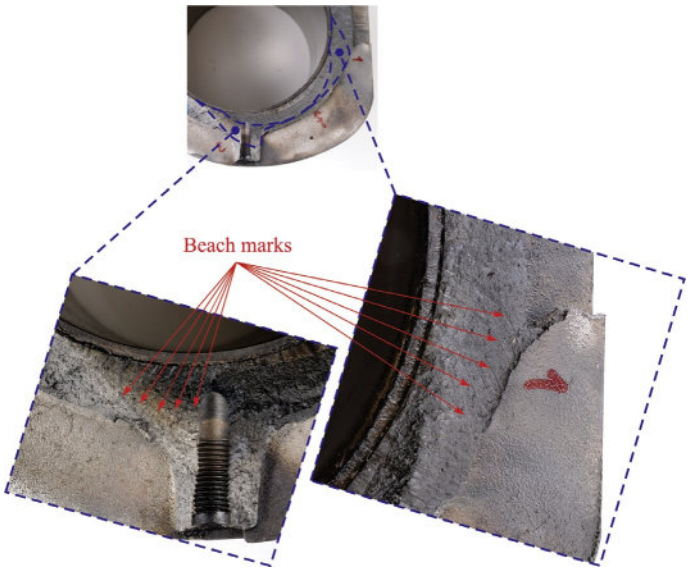

FIGURE 9.11

Macrograph montage of the sector C of the fracture surface showing the fatigue beach marks.

FIGURE 9.12

Mating fracture surfaces of the CH II obtained after the crack was mechanically opened.

4.3 MICROFRACTOGRAPHY

As mentioned in the previous section of the chapter, the mating fracture surfaces of the both CHs, CH I and CH II, were covered by large amounts of deposits (except the areas of mechanically forced opened fractures), which were impossible to remove using nondestructive methods. Therefore, the SEM examination did not provide detailed information about mechanisms leading to failures. Regardless of the presence

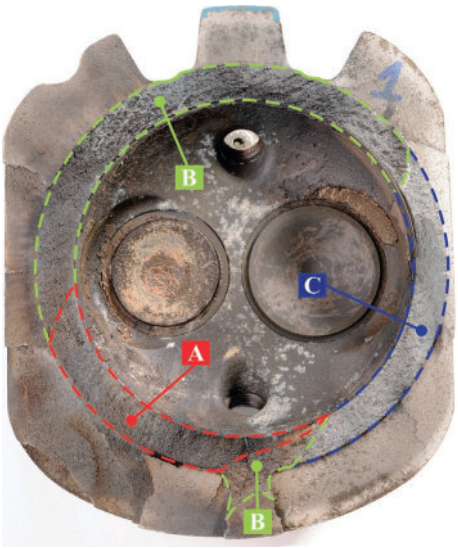

FIGURE 9.13

Macrograph showing characteristic morphologies on the fracture surface of CH II.

of deposits, the SEM examination of the most interesting areas of the fracture surfaces (sector A on fracture surfaces of the CH I and the CH II) revealed the fine ratchet marks along the entire fracture nucleation region on the both CHs inner surfaces (Figure 9.16a). In addition, this confirmed the macroscopic observation about the existence of multiple fatigue fracture origin sites (Figure 9.16b).

EDS analysis indicated that deposits on the fracture surfaces, clearly visible on SEM images (Figures 9.17a and 9.18a), contained high concentrations of lead and bromine (Figures 9.17b and 9.18b), which undoubtedly suggested that they originated from combustion of aviation gasoline. Aviation gasoline normally contains lead, while bromine is an additive, which scavenges lead by forming volatile lead bromine [9].

4.4 METALLOGRAPHY

Metallographic examination of the casts was performed on five longitudinal sections of the CHs (one section of the CH I and four sections of the CH II) in a direction perpendicular to the fracture surface. The samples were prepared at the locations indicated by dotted lines in Figures 9.19a and 9.20. These locations approximately corresponded to the main fatigue crack origins. The sections were examined in the as-polished condition under light microscope. They discovered a presence of casting defects in both CHs materials. A large amount of microporosity, in form of grouped shrinkage pores surrounded by primary dendrites and eutectic phase [10], was found near to the both CHs surfaces (Figures 9.19b and 9.20). Some of these microporosities reached approximately 400 μm in length (Figure 9.19c). Intergranular cracks, formed by linking up of other shrinkage pores in material, were also observed (Figure 9.19d). The

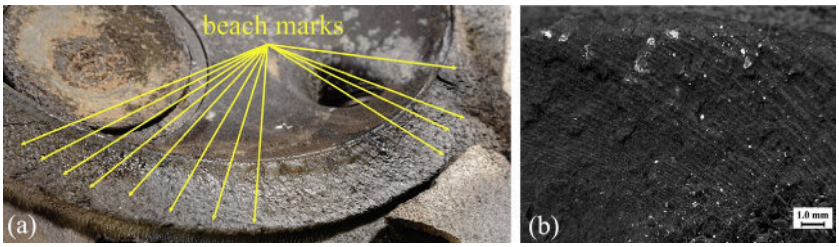

FIGURE 9.14

(a) Macrograph showing beach marks in the sector A of the fracture surface of CH II and (b) stereomacrograph of beach marks in the sector A.

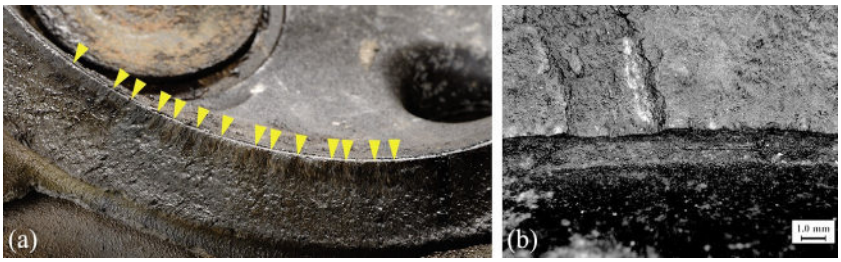

FIGURE 9.15

(a) Macrograph showing ratchet marks in the sector A of the fracture surface of CH II (arrowheads) and (b) stereomacrograph of ratchet marks in the sector A.

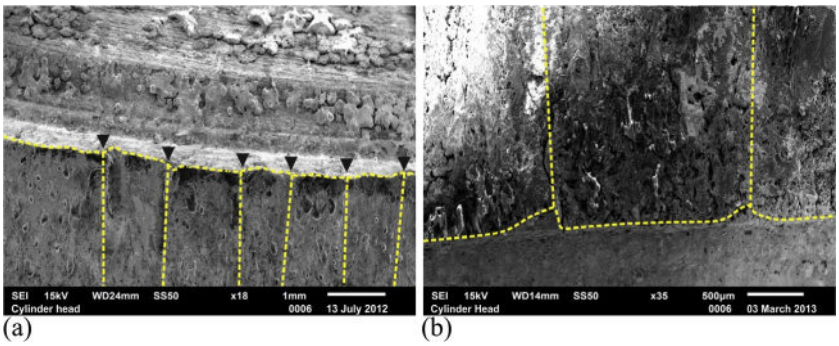

FIGURE 9.16

(a) Fatigue fracture surface of the sector A of CH I shows evidence of fine ratchet marks (arrowheads) and (b) one of the multiple fatigue origin sites on the inner surface of the sector A of CH II.

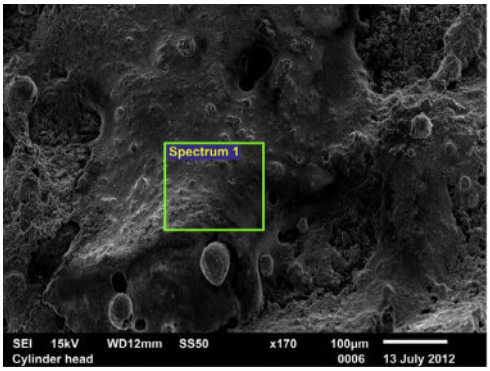

(a)

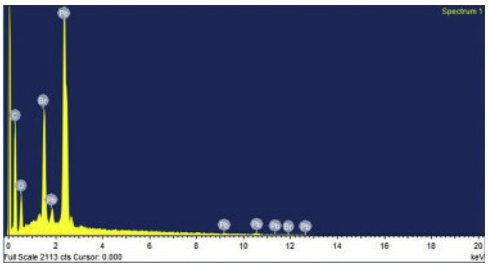

(b)

FIGURE 9.17

(a) Fatigue fracture surface of the sector A of CH I covered by deposits and (b) EDS spectrum from deposit (region marked in (a)).

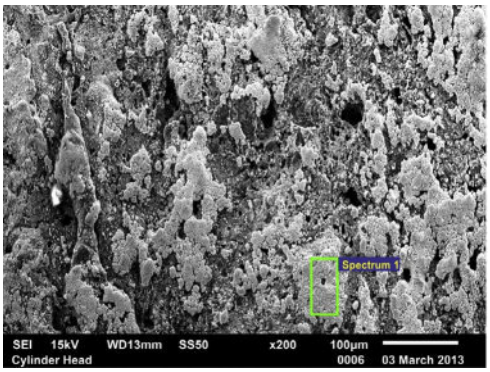

(a)

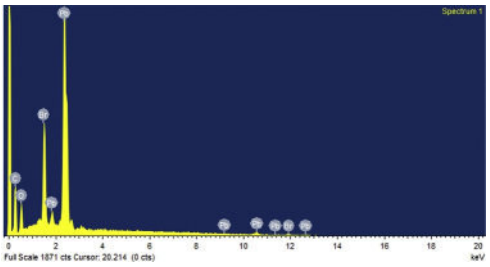

(b)

FIGURE 9.18

(a) Fatigue fracture surface of the sector A of CH II covered by deposits and (b) EDS spectrum from deposit (region marked in (a)).

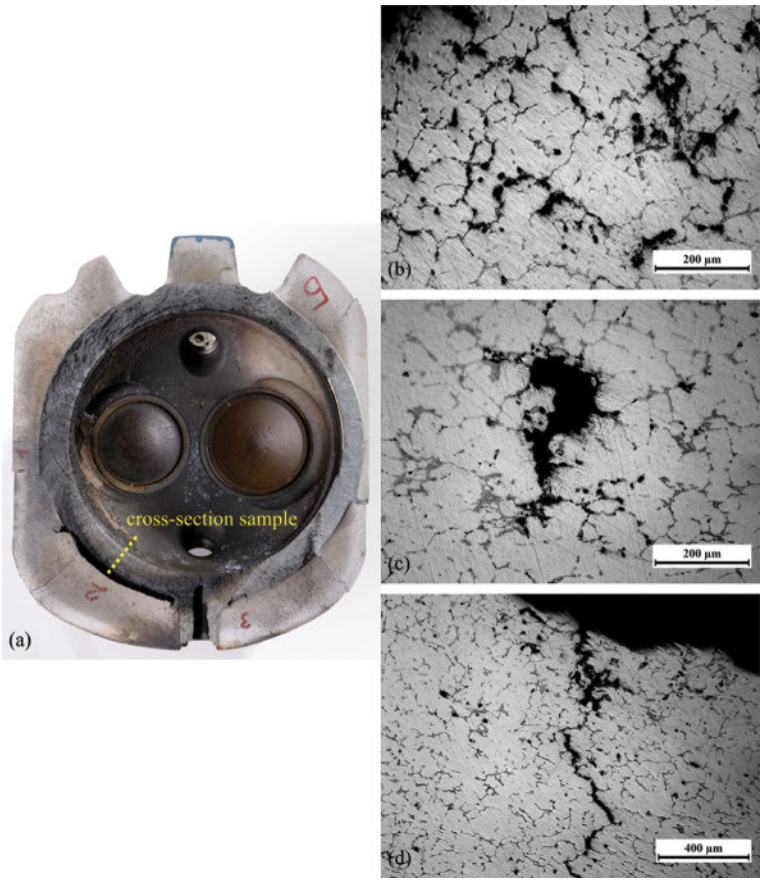

FIGURE 9.19

(a) Macrograph of fracture surface of CH I with location where metallographic sample was taken, (b) grouped shrinkage pores in CH I material, (c) typical shrinkage pore (black) surrounded by primary dendrites (white) and eutectic phase (gray needles in a white matrix), and (d) intergranular crack due to the linking of shrinkage pores.

microstructure revealed the typical structure of an aluminum-copper casting alloy with intermetallic phases precipitates located at the grain boundaries [11] (Figure 9.21).

4.5 CHEMICAL COMPOSITION

Chemical analysis results of the CH I and CH II samples indicated that the casts were actually made of a 242.0 aluminum-casting alloy. Shown in Table 9.3 are the chemical compositions of the both CHs materials, as well as the standard specification for 242.0 aluminum alloy. Due to its excellent high-temperature strength, the mentioned aluminum alloy is the most common alloy used in manufacturing of air-cooled cylinder heads in the aviation industry [12].

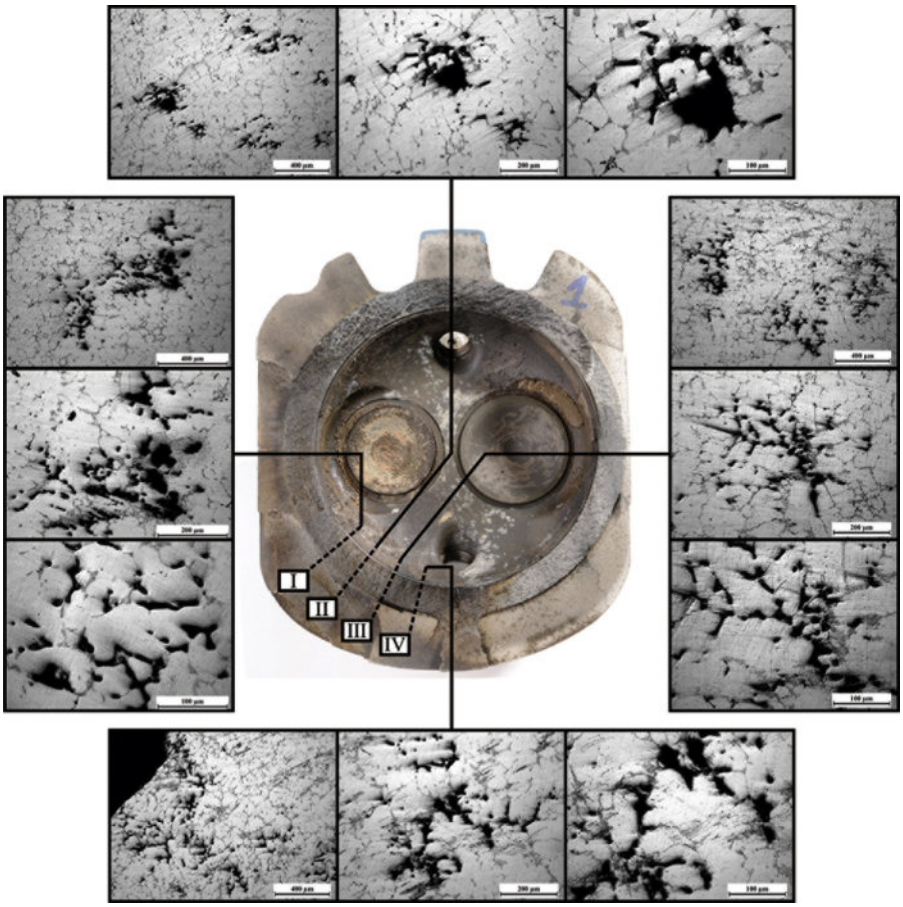

FIGURE 9.20

Macrograph of fracture surface of CH II showing locations where metallographic samples were taken with optical micrographs of samples I-IV.

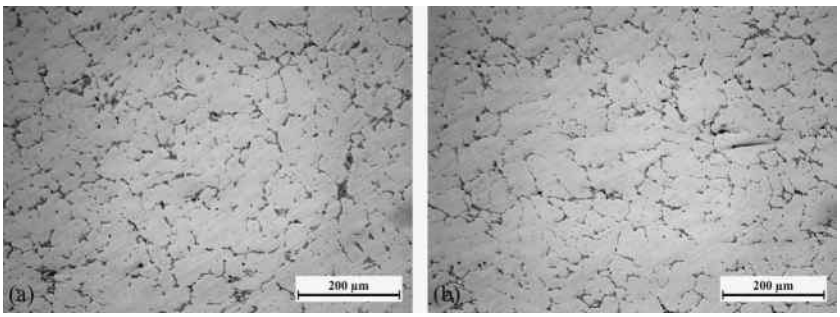

FIGURE 9.21

(a) Optical micrograph of the CH I microstructure and (b) optical micrograph of the CH II microstructure.

Table 9.3 Cylinder Head Chemical Composition (wt.%)

	Element									
Content	**Cu**	**Mg**	**Mn**	**Si**	**Fe**	**Ni**	**Ti**	**Cr**	**Zn**	**Al**
Material of the CH I	4.28	1.65	0.03	0.22	0.24	1.90	0.22	0.20	–	Bal.
Material of the CH II	4.05	1.49	0.03	0.33	0.21	1.89	0.20	0.19	–	Bal.
Standard specification	3.5-4.5	1.2-1.8	≤0.35	≤0.7	≤1.0	1.7-2.3	≤0.25	≤0.25	≤0.35	Bal.

4.6 HARDNESS MEASUREMENTS

For the purpose of comparability of the testing results with the standard specifications [13], the hardness measurements were carried out on a polished cross-section surface of the CH (ring plane opposite to the fracture surface) in accordance with the Brinell standard method [14]. The measurement points were radially distributed at the equal angular spacing of 45° (blue points in Figure 9.22). In the case of the CH I, the obtained hardness value at the measurement point 6 did not match the standard specification and was significantly higher than those recorded in other measurement points were. Bearing in mind that the location of this measurement point corresponded to the central portion of the crack origin zone, additional measurements were performed at points in the immediate vicinity of the measurement point 6 (red points in Figure 9.22). The final hardness data obtained from the testing are given in Table 9.4.

4.7 FINITE ELEMENT ANALYSIS

To identify the stress state of the cylinder assembly related with in-service condition, a structural FE analysis was carried out using CATIA V5R22 Generative Structural Analysis Workbench. For that purpose, the plausible 3D solid model of cylinder

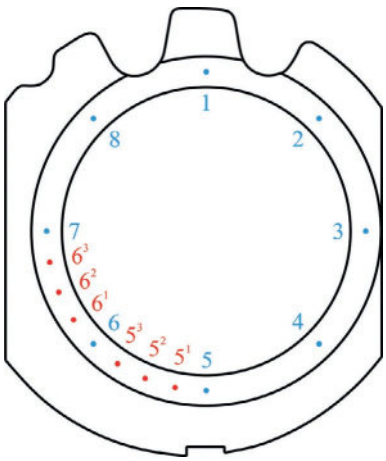

FIGURE 9.22

Distribution of the hardness measurement points around CH wall circumference.

Table 9.4 Hardness measurements

	Measurement point													
	1	2	3	4	5	5^1	5^2	5^3	6	6^1	6^2	6^3	7	8
	Hardness (HB)													
CH I	71	75	76	76	86	93	100	102	111	102	96	92	87	71
CH II	73	74	72	75	79	–	–	–	81	–	–	–	78	76

assembly was developed, as shown in Figure 9.23a. The appropriate materials were applied to the solid models of the members of cylinder assembly, aluminum-casting alloy 242.0 to the CH and AISI 4140 steel to the cylinder barrel. In order to create the FE model, the continuum of cylinder assembly geometry was discretized by 4-nodes tetrahedral solid elements. The selected mesh size for the cylinder barrel and CH was 1.5 and 1.0 mm, respectively. In total, the FE model of the cylinder assembly consisted of 1,378,196 nodes and 5,920,151 elements (Figure 9.23b). Based on the previously mentioned method of mounting the CH on the cylinder barrel, the contact zone between the CH and the cylinder barrel was constructed as a pressure fitting connection with positive overlap parameter [15]. Considering that the hold-down flange of the cylinder barrel is attached to the crankcase by studs and nuts, the nodes of the flange were fixed by restraining all degrees of freedom. The rest of the cylinder assembly remained unrestrained.

The CH is predominantly subjected to surface load, associated with gas pressure. In this study, the mean effective pressure represented the gas pressure. The calculation of this pressure was carried out applying the following equation [16]:

$$\text{mep} = \frac{P n_R \times 10^3}{V_d N} \tag{9.1}$$

where mep is the mean effective pressure (kPa), P is the rated power delivered by the engine (kW), n_R is the number of crank revolutions for each power stroke per cylinder ($n_R = 2$ for four-stroke cycles), V_d is the volumetric displacement (dm^3), and N is the rated rotational speed (rps). Inserting the requested parameters values into the above equation, the mean effective pressure was calculated as follows:

$$\text{mep} = \frac{\frac{180}{1.36} \cdot 2 \cdot 10^3}{5.893 \cdot \frac{2700}{60}} \approx 998\,\text{kPa} \tag{9.2}$$

The obtained value is within the range of typical values of the mean effective pressure for naturally aspirated spark ignition engines [16] (850-1050 kPa). This pressure

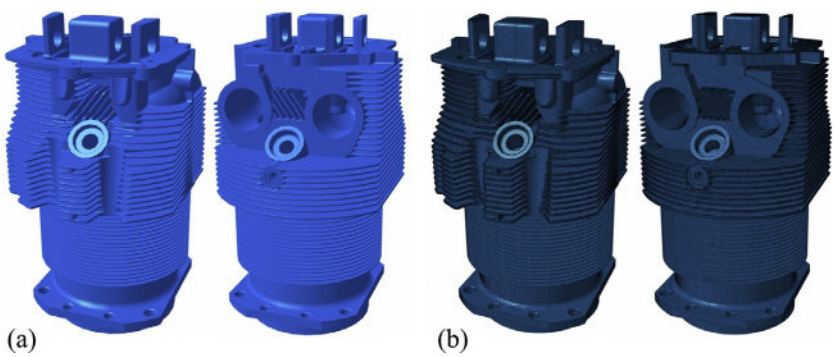

FIGURE 9.23

(a) 3D solid model of the cylinder assembly (view from the front and rear side) and (b) FE model of the cylinder assembly (view from the front and rear side).

was applied to all entities of the inner surfaces of the cylinder assembly geometry that are in contact with combustion gases.

The stress distribution of the cylinder assembly was obtained according to the Von Mises stress criterion. The FE analysis confirmed that the crack origins were located at the most stressed area of the cylinder assembly (i.e., on the inner flange fillet of the exhaust side of the CH). The stress maximum value is 24.8 MPa, which is less than yield strength of 242.0 aluminum-casting alloy. However, this stress in combination with high concentration of shrinkage pores can lead the crack to initiate. The node where stress reaches the maximum value, Figures 9.24 and 9.25, corresponds to the central portion of sector A, Figures 9.8 and 9.13.

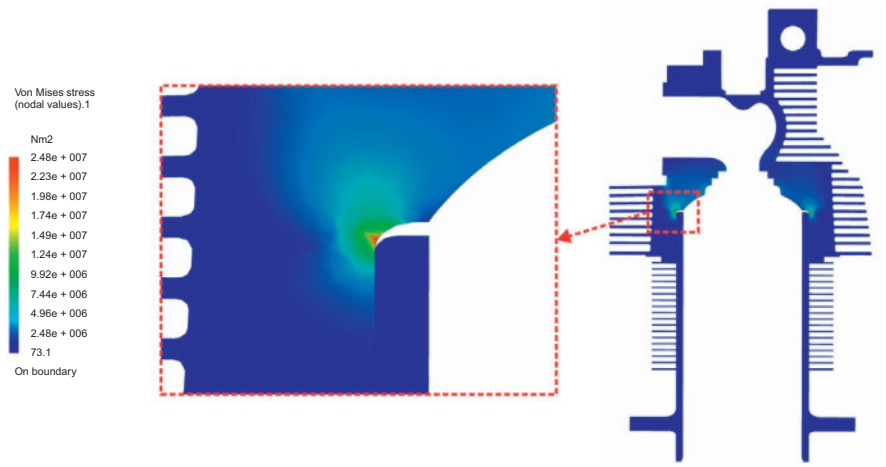

FIGURE 9.24

Stress distribution on the longitudinal section of the FE model through the node with maximum stress value.

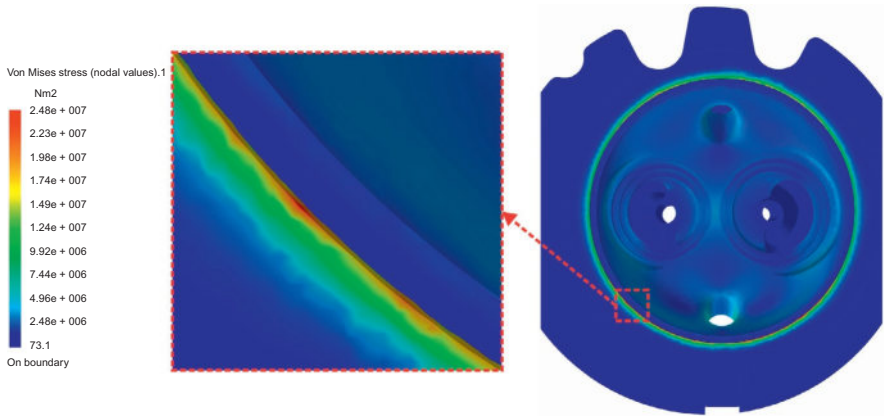

FIGURE 9.25

Stress distribution on the cross-section of the FE model through the node with maximum stress value.

5 DISCUSSION

The next step in this forensic expertise is an analysis of the obtained results in order to find exact answers to crucial questions. First of all what happened, why and how it happened? If these questions are not precisely clarified, inadequate corrective and preventive measures may be proposed.

Fractography features revealed fatigue as the main cause of the failures for CHs. Tracing the fatigue evidences in form of ratchet and beach marks, the crack origin region was determined. The fatigue originated from multiple origins located on the inner flange fillet of the CHs, which suggested that it was not a single particular defect that caused fatigue crack nucleation. Also, the FE analysis confirmed that the fatigue crack origins were in correspondence of the most stressed area of the CH. Merging initially occurred cracks into the single one, the crack front profile grew across the CH wall with semi-elliptical surface shape. In the Failure Case II, the fatigue crack propagated slowly in radial direction all the way through the CH II wall. In the Failure Case I, the fatigue crack propagated slowly in radial direction up to about 30% of the wall thickness of the CH I. Since the fatigue crack covered substantial portion of the local CH I wall thickness, the load capacity of the remaining local cross-section of the CH I wall has been significantly reduced. Further, the reduced load capacity combined with the local material porosity contributed to the crack advance up to the outer surface of the CH I by the overload mechanism. The evidence of abnormal combustion that could boost overload fracture as well was not found. However, when the crack had reached the outer surface of the CH, the gases from the combustion chamber started to leak outside through the crack. Therefore, the pressure loads were reduced and the process of overloaded fracture in the Failure Case I was stopped. It is most likely that both the engines continued work in that state until final fracture. The evidence for this statement is the presence of large amount of combustion residues that had been deposited in the surrounding area of external edge of the crack and on the mating fracture surfaces. While the gas was leaking, it was acted on mating fracture surfaces in both axial directions accelerating subsequent fatigue appearance. Then final overstress crack of the remaining load-bearing cross-section of the CH wall occurred when the total area of two fatigue cracks, on left and right side, reached the critical size. The final overstress crack did not totally separate CH into two parts, due to a sharp decrease of gas pressure caused by huge leaking.

Metallographic examination revealed the presence of casting defects in CHs' materials exactly at the area where cracks initiation began. The observed subsurface shrinkage pores were mostly in the range of 100-300 μm. The largest of these pores had a length of about 400 μm. Intergranular cracks in material in fracture initiation area were formed by linking up of shrinkage pores. The failures of aeronautical and engineering components due to the presence of casting defects are widely studied and reported [17–20]. Such defects, determining the fracture initiation site, compromise the mechanical properties as well as the fatigue of the material [21]. They have a detrimental effect on fatigue life by shortening not only the fatigue crack propagation but also initiation period. The decrease in fatigue life is directly correlated with the increase of defect size [22–24]. Also, the fatigue life of cast aluminum alloys

containing defects can be one or two orders of magnitude lower than indefect-free cast components [25–30]. Further, the complex geometry of the CH body, with distinct change in the section thickness, combined with the casting process parameters (i.e., inadequate pouring temperature, insufficient number of pouring gates, inadequate gate cross-section, excessive pouring temperature, or inadequate feeding) also represent other sources of failure [5,6]. The significant increase of the hardness of the CH material in cracks initiation region is frequently correlated with toughness loosening and therefore may assist the fast crack propagation [31,32]. Chemical composition and microstructure were found in conformity with those expected from the selected aluminum-casting alloy. It is worth mentioning that the other series of such cylinder assemblies also had a history of these two CHs separation due to fatigue cracking and was covered by the manufacturer's bulletin [33] and the Federal Aviation Administration Airworthiness Directive [1]. Early detection of the crack in the CH is crucial in order to prevent the engine power loss and possible engine failure caused by separation of a CH, which can potentially lead to loss of aircraft control. The manufacturer's bulletin [33] precisely defines inspection procedures to determine the existence of crack in the CH. For damaged cylinders (Cylinder No.1 in Failure Case I and Cylinder No.4 in Failure Case II), the results of the last conducted periodic compression test (Table 9.2) were not in agreement with the minimum value, required by the aforementioned bulletin. During compression test, the cylinder pressure gauge readings (64 psi) were below the minimum allowable value of 70 psi [33]. In this case, the soap bubble leak check is a reliable verification method, but there is no evidence that it had been done. It is most likely that the cracks already had reached the thickness of the CHs, at the time when the last periodical inspections were carried out. Since the aircraft returned in service after these inspections, the cracks continued to grow and finally led to a complete failure of cylinder assemblies.

6 CONCLUSION AND RECOMMENDATIONS

Taking into account all findings, it is clear that the main reason for the failure of the two CHs, that belong to two different aircraft engines, was fatigue. This phenomenon was promoted by a pre-existing material defect and identified as a high concentration of shrinkage pores in the most stressed region on the inner flange fillet of the exhaust side of the CH. The defect is probably caused during the manufacturing stage of the casting. These two case studies, as well as others previously reported [1–4], showed the repetitive and therefore systematic problems with the CH of air-cooled, and horizontally opposed, aircraft piston engines.

Based on the obtained results, the following recommendations can be proposed:

- Changes in the CH design should include new geometry without sharp edges in the zone of high-stress concentration;
- Locally increase the wall thickness of the CH in the crack initiation zone;

- Introduce some necessary changes in casting process to avoid forming porosity in material;
- Strictly respect the prescribed maintenance procedures and periodically inspect presence of cracks.

ACKNOWLEDGMENTS

The authors would like to acknowledge Military Technical Institute (Ministry of Defense of the Republic of Serbia) for experimental program. The University of Defence in Belgrade has supported this research within the project No. VA-TT/02/13-15 titled "Contribution to the development of the forensic engineering in the domain of the failure analysis of cylindrical structures." The last but not the least special thanks to the Transportation Safety Board of Canada—Operational Services Branch for providing free access to their engineering reports on similar investigation.

REFERENCES

[1] Airworthiness Directive (AD), Federal Aviation Administration of the USA; 2008-19-05.
[2] Safety Recommendation A-12-7, National Transportation Safety Board of the USA; 2012.
[3] Guertsman V, Dionne S, Crosby T, Engineering report number LP085/2009, Transportation Safety Board of Canada; 2009.
[4] Guertsman V, Dionne S, Crosby T, Engineering report number LP077/2010, Transportation Safety Board of Canada; 2010.
[5] Krstic B, Rasuo B, Trifkovic D, et al. Failure analysis of an aircraft engine cylinder head. Eng Fail Anal 2013;32:1–15.
[6] Krstic B, Rasuo B, Trifkovic D, et al. An investigation of the repetitive failure in an aircraft engine cylinder head. Eng Fail Anal 2013;34:335–49.
[7] Operator's manual- Textron Lycoming O-360, HO-360, IO-360, AIO-360, HIO-360 & TIO-360 series aircraft engines, Part No. 60297–12, Rev. No. 60297-12-6, Textron Lycoming; 2000.
[8] Overhaul manual-Lycoming Direct Drive Aircraft Engines, Part No. 60294–7, Rev. No. 60294-7-10, Textron Lycoming; 2007.
[9] ASTM Standard D910-11, Standard Specification for Aviation Gasolines, ASTM International, West Conshohocken, PA, DOI:10.1520/D910-11, www.astm.org; 2011.
[10] Anson JP, Gruzleski JE. The quantitative discrimination between shrinkage and gas microporosity in cast aluminum alloys using spatial data analysis. Material Characterization 1999;43:319–55.
[11] Zolotorevsky VS, Belov NA, Glazoff MV. Casting aluminum alloys. In: Structure and microstructure of aluminum alloys in ascast state. Oxford: Elsevier; 2007. p. 95–183.
[12] Rasuo B. Aircraft production technology (in Serbian). In: Aluminum and aluminum alloys. Belgrade: University of Belgrade; 1995. p. 1–36.
[13] Kearney AL. Properties of cast aluminum alloys. In: ASM handbook. Properties and selection: nonferrous alloys and special-purpose materials, vol. 02. Material park, OH: ASM International; 1990. p. 152–77.

[14] SRPS EN ISO 6506–1:2011, Metallic materials—Brinell hardness test—part 1: test method (ISO 6506:1:2005), Institute for Standardization of Serbia, www.iss.rs; 2011.
[15] Trifkovic D, et al. Failure analysis of the combat jet aircraft rudder shaft. Eng Fail Anal 2011;18:1998–2007.
[16] Heywood JB. Internal combustion engine fundamentals. In: Engine design and operating parameters. New York: McGraw-Hill; 1988. p. 50–1.
[17] ASM. Handbook of case histories in failure analysis, vol. 1. Materials Park, OH: ASM International; 1994.
[18] ASM. Handbook of case histories in failure analysis, vol. 2. Materials Park, OH: ASM International; 1994.
[19] Bagnoli F, Dolce F, Colavita M, Bernabei M. Fatigue fracture of a main landing gear swinging lever in a civil aircraft. Eng Fail Anal 2008;15:755–65.
[20] Bhaumik SK, Sujata M, Venkataswamy MA. Fatigue failure of aircraft components. Eng Fail Anal 2008;15:675–94.
[21] Bagnoli F, Bernabei M, Ciliberto A. Failure analysis of an aircraft auxiliary power unit air intake door. Eng Fail Anal 2011;18:284–94.
[22] Couper MJ, Nesson AE, Griffiths JR. Casting defects and the fatigue behavior of an aluminium casting alloy. Fatigue Fract Eng Mater Struct 1990;13:213–27.
[23] Grbovic A, Rasuo B, Vidanovic N, Peric M. Simulation of crack propagation in titanium mini dental implants (MDI). FME Trans 2011;39:165–70.
[24] Wang QG, Apelian D, Lados DA. Fatigue behavior of A356-T6 aluminum cast alloys, part I, effect of casting defects. J Light Metals 2001;1:73–84.
[25] Maksimovic S. Fatigue life analysis of aircraft structural components. Sci Tech Rev 2005;1:15–22.
[26] Skallerud B, Iveland T, Harkegard G. Fatigue life assessment of aluminum alloys with casting defects. Eng Fracture Mech 1993;44:857–74.
[27] Kuwazuru O, Murata Y, Hangai Y, et al. X-ray CT inspection for porosities and its effect on fatigue of die cast aluminium alloy. J Solid Mech Mater Eng 2008;2:1220–31.
[28] Gao YX, Yi JZ, Lee PD, Lindley TC. The effect of porosity on fatigue life of cast aluminium-silicon alloys. Fatigue Fract Eng Mater Struct 2004;27:559–70.
[29] Yi JZ, Gao YX, Lee PD, Lindley TC. Microstructure-based fatigue life prediction for cast A356-T6 aluminum-silicon alloys. Metall Mater Trans B 2006;37:301–11.
[30] Yi JZ, Gao YX, Lee PD, Flower HM, Lindley TC. Scatter in fatigue life due to effects of porosity in cast A356-T6 aluminum-silicon alloys. Metall Mater Trans A 2003;33:1879–90.
[31] Mateo A, Heredero F, Fargas G. Failure investigation of a centrifuge duplex stainless steel basket. Eng Fail Anal 2011;18:2165–78.
[32] Boljanovic S. Fatigue strength analysis of a semi-elliptical surface crack. Sci Tech Rev 2012;LXII(1):10–6.
[33] ECi Mandatory Service Bulletin, No.08-1, Rev.3 of 19 August 2008, Engine Components International, San Antonio, TX.

CHAPTER

Analysis of an engine bevel pinion failure

10

Swati Biswas, Mudigere D. Ganeshachar, Varada N. Satish Kumar, Jivan Kumar, Sangli N. Narendra Babu

Gas Turbine Research Establishment, Bengaluru, India

CHAPTER OUTLINE

1 INTRODUCTION

A spiral bevel pinion is used for power transmission in an aircraft engine. Unlike the gears with the plain contour, these spiral pinions (or gears) are used to transmit motion between parallel or crossed shafts or between a shaft and a rack by meshing teeth that lie along a helix at an angle to the axis of the shaft [1]. Because of this angle, mating of the teeth occurs such that two or more teeth of each gear are always in contact. This condition permits smoother action than that of spur gears with straight contours. As the teeth get engaged and dis-engaged continuously with the meshing components during the operations, the pinion and gear teeth undergo wear damage. Because of this reason, the teeth are subjected to case hardening treatment invariably. The process results in very high hardness (excess of 60Rc) at the surface imparting excellent wear resistance in the meshing flanks. The core hardness is maintained low (around 40-45Rc).

Handbook of Materials Failure Analysis With Case Studies from the Aerospace and Automotive Industries.
http://dx.doi.org/10.1016/B978-0-12-800950-5.00010-7

This design of the gears and pinions allows to have the best balance of toughness in the components with wear resistance capabilities at the meshing flanks.

Despite making the best efforts in component design, its assembly and usage, failures of the pinions and gears are encountered in aerospace and automobile industries as well as in machineries used in several other industries. Depending on the service conditions, the gears and pinions experience failures, generally from the teeth locations [2–4] because of the transmitted loads and rotational speed. The common modes of failures include wear [2], scoring [5], spallation [6], surface contact fatigue [7,8], tooth bending fatigue [9–11], etc., and are well reported.

Starzhinskii et al. have classified [2] different types of failure mechanisms of gears in engineering systems. Wear is the mechanism of surface deterioration of the meshing gear teeth. There are two distinct modes of wear—abrasive and adhesive [1]. In case of abrasive wear, the mating surface material gets continuously removed and does not get accumulated on the surface. This type of damage is initiated with light scratches; the intensity gradually increases and finally leads to scoring. Adhesive wear occurs on sliding surfaces when the pressure between the contacting asperities is sufficient to cause local plastic deformation and adhesion [1]. Whenever plastic deformation occurs, the energy expended to produce the deformation is converted to heat. The first indication of trouble is a glazed surface, followed by galling, then by seizure. Spallation is the formation of microscopic craters in the contact regions of the gear teeth [12]. With the increasing amount of spallation, fatigue crack initiates from the craters leading to the fracture of the teeth. This failure mechanism is generally referred to as surface contact fatigue. As the name suggests, the fatigue failure is initiated by material removal process on the contacting surfaces of the gears. This mode of gear and pinion failure is very common in engineering practice [13]. The review article by Fernandes et al. clearly specifies whenever two curved (usually convex) surfaces are in contact under load, the contact occurs along a line or point, or, depending on the elastic constants of the materials concerned, along a very small circular or elliptical area. As a result of such small contact areas, the shear (Hertzian) stresses which develop at and near the surface are consequently very high. The maximum shear stress occurs at some distance below the surface. When the contacting stresses are repetitive, as is the case on the active flanks of gear teeth, the cyclic compressive stresses induced cause differing elastic and plastic behavior in the near-surface material. Depending on the microstructure and grain orientation of the material in this region, internal stress concentrations are formed which can ultimately lead to crack initiation. Damage due to contact fatigue in gear teeth usually occurs in one of three areas, viz along the pitch line, in the addendum (i.e., above the pitch-line), and in the dedendum (i.e., below the pitch line) [1]. Root bending fatigue is another common mode of gear failures where fatigue failure is initiated at the root region of the gear teeth. The maximum tensile stresses occur at the root radius on the meshing (i.e., loaded) flank of the gear tooth, while the maximum compressive stresses occur at the root radius on the passive flank. With the cyclic variation in loads characteristic of gear operation, these regions become preferential sites for fatigue crack initiation [14].

Apart from the above mentioned failure modes, gears and pinions are also reported to malfunction due to the presence of mechanical stress concentration [15,16], unacceptable metallurgical constituents [17,18], and a corrosive environment [19]. Manufacturing and assembly defects [20] also result in premature failure of the gears. Xu et al. [15] reported premature fatigue failure of a diesel engine gear shaft from the grove region. In this case, the small fillet radius of the upper groove provided a stress concentration level in root fillet region and created the conditions responsible for the fracture of the gear shaft. Park et al. described a fatigue failure of a planetary gear carrier from the stress concentration resulted by the presence of a blow hole. Fatigue failure of an elevator drive shaft from a key way with ungenerous radius of curvature [21] has also been reported by Göksenli et al.

In this chapter, the authors describe the analysis of a premature failure of a developmental engine bevel pinion.

2 BACKGROUND INFORMATION ABOUT THE FAILURE

An abrupt failure of an engine bevel pinion was reported during test runs. Prior to the failure, the component completed approximately 1300 h of testing. Strip examination after the event revealed that a portion of the spiral bevel pinion of engine gear box was fractured (Figure 10.1) and ejected out of the test setup. This caused secondary damages to the front cover plate of the test assembly. The balance portion of the bevel pinion remained positioned in the pinion housing (Figure 10.2). However, the rotation of the bevel pinion was arrested. The engine pinion housing was sheared into two halves (Figure 10.3). Top end splines of the vertical quill shaft (mating with engine bevel pinion) were found completely worn out and the bottom splines (mating with engine gear box bevel pinion) were intact (Figure 10.4).

The fractured bevel pinion pieces, broken pieces of pinion housing, and the vertical quill shaft were examined to find out the reason of failure. The bevel pinion and the quill shaft were fabricated from a low-alloy case-carburizing grade steel with a carburized gear teeth, where as the pinion housing was made out of a α-β titanium alloy.

FIGURE 10.1

Fractured spiral bevel pinion piece found outside the test setup after failure.

FIGURE 10.2

Fractured bevel pinion in the housing.

FIGURE 10.3

Photograph of the pinion housing after the failure.

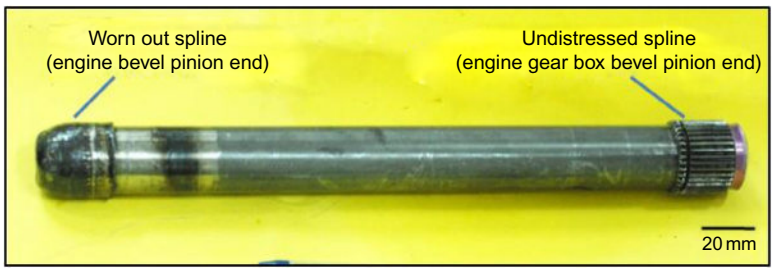

FIGURE 10.4

Photograph of the vertical quill shaft showing worn out splines and bluish tint on the shaft.

3 INVESTIGATIONS

3.1 VISUAL AND STEREO-BINOCULAR

3.1.1 Fractured Piece of the Bevel Pinion

The fractured piece of the bevel pinion was observed visually and under stereo-binocular microscope (Figure 10.5). The fractured surface revealed the presence of "clam shell marks" or "beach marks" indicating that the bevel pinion has failed in a progressive mode (i.e., fatigue). Tracing back the orientation of the beach marks, the crack origin was found to be at the bottom surface of the gear wheel where an extraction hole was present. It may be noted here that one crack front was at the right side of the extraction hole which was found to propagate almost the entire length up

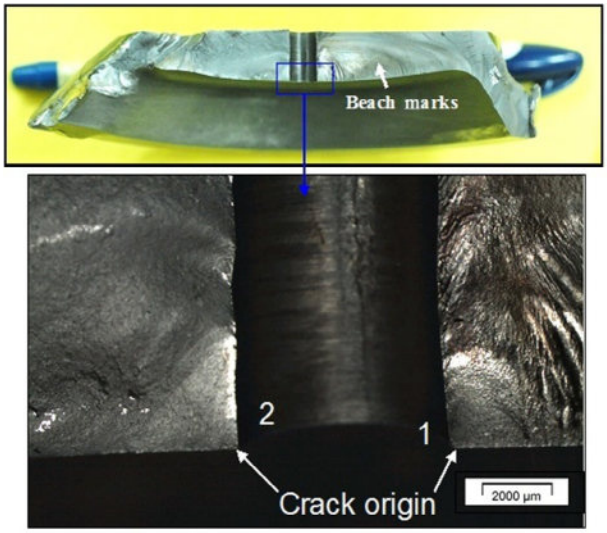

FIGURE 10.5

Fractured surface of the failed bevel pinion showing beach marks and fatigue crack origin.

to the gear teeth (with crack origin at location 1 as shown in Figure 10.5). One more crack front was present at the left side of the extraction hole (crack origin region indicated as 2 in Figure 10.5). In this case, the fatigue crack was found to propagate a short distance (approximately 15-20% of the fractured surface). The remaining area was found to have fractured by overload. A third crack front was identified at the gear teeth region; i.e., at the extreme end of the first crack front (Figure 10.6). The crack propagation area for this crack front was also relatively smaller than the first crack front. Considering the fact that fatigue crack propagation region was higher for the first crack front than the third crack front, it appeared most probable that the crack front "1" had originated first and then propagated. As it reached the gear teeth root region, the high-stress concentration at this region had resulted in the third fatigue crack origin.

The extraction hole was studied further to ascertain if any abnormalities were present which might have caused the fatigue crack initiation. The extraction hole surface at the fatigue crack origin region was free from any distress (Figure10.7).

When the mating surface of the fractured bevel pinion was observed, it was noticed that the extraction hole continued further in length (Figure 10.8). This resulted in an "L"-shaped geometry at the gear shaft-gear wheel junction (Figure 10.9). It must be noted here that the fatigue crack origins at both sides of the extraction hole were located at the corner of this "L" shape. A photograph of the bottom surface of the bevel pinion at the other extraction hole is presented in Figure 10.9. The edges of the holes were found to be very sharp.

The bevel pinion had three extraction holes. Since the fatigue crack origin was found at the edge of one extraction hole, the other two extraction holes were also

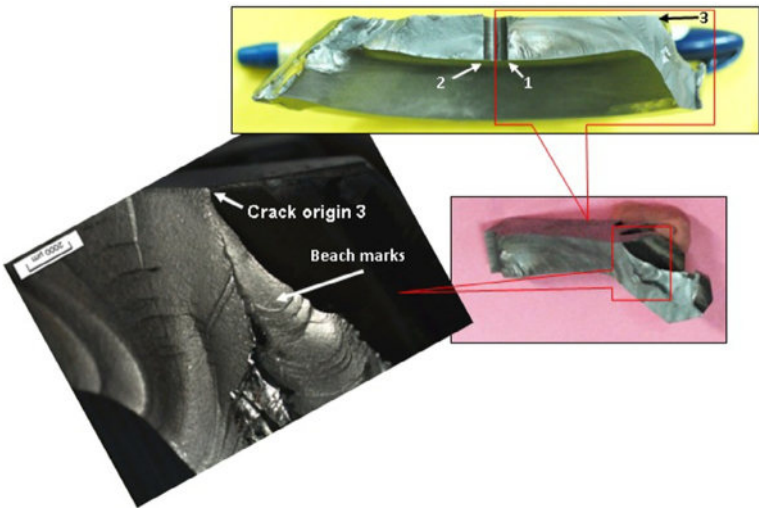

FIGURE 10.6

Fatigue crack at the gear teeth root region.

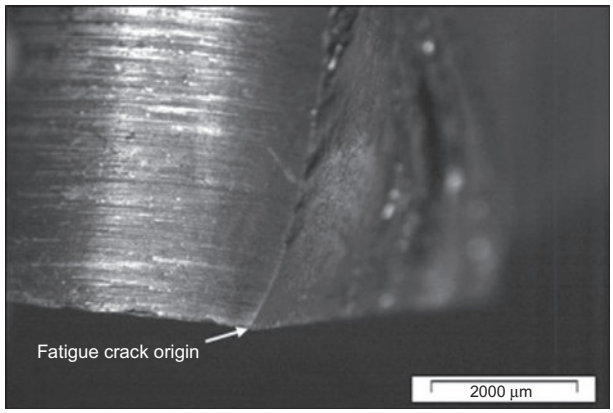

FIGURE 10.7

Condition of the extraction hole at the fatigue crack origin 1.

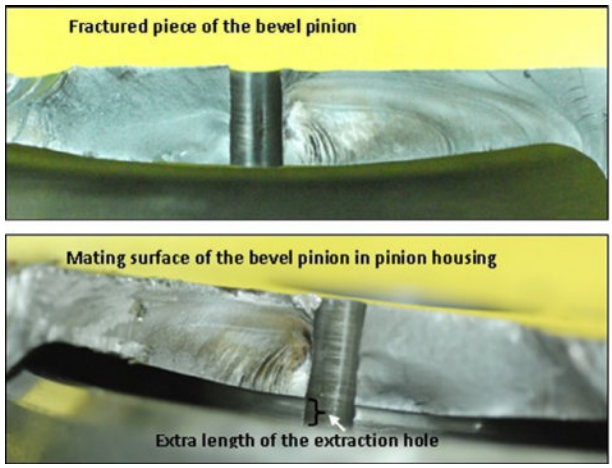

FIGURE 10.8

Mating fractured surfaces of the bevel pinion showing more length at one side of the extraction hole.

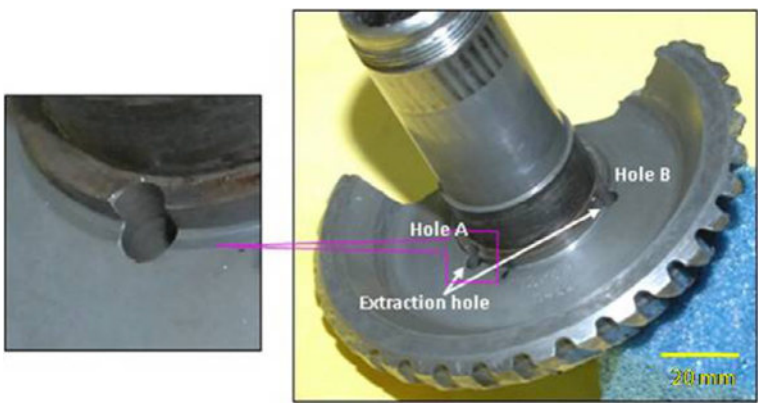

FIGURE 10.9

Extraction hole geometry at the bottom of bevel pinion (gear shaft-gear wheel junction).

checked for presence of any abnormalities under stereo-binocular microscope. Both of them exhibited the presence of cracking around the gear shaft extending from both the corners of the "L"-shaped contour of the hole (Figures 10.9 and 10.10). Hole "A" revealed the existence of multiple cracks from the edge. This observation was later reconfirmed by magnetic particle inspection (MPI). Sharp machining marks were also observed near hole "A."

3.1.2 Pinion Housing

The pinion housing was found to have fractured into two pieces (Figure 10.2). The top portion of the pinion housing was deformed. The edges of the fractured piece revealed evidence of shearing (Figure 10.11) indicating that failure of the pinion was secondary in nature.

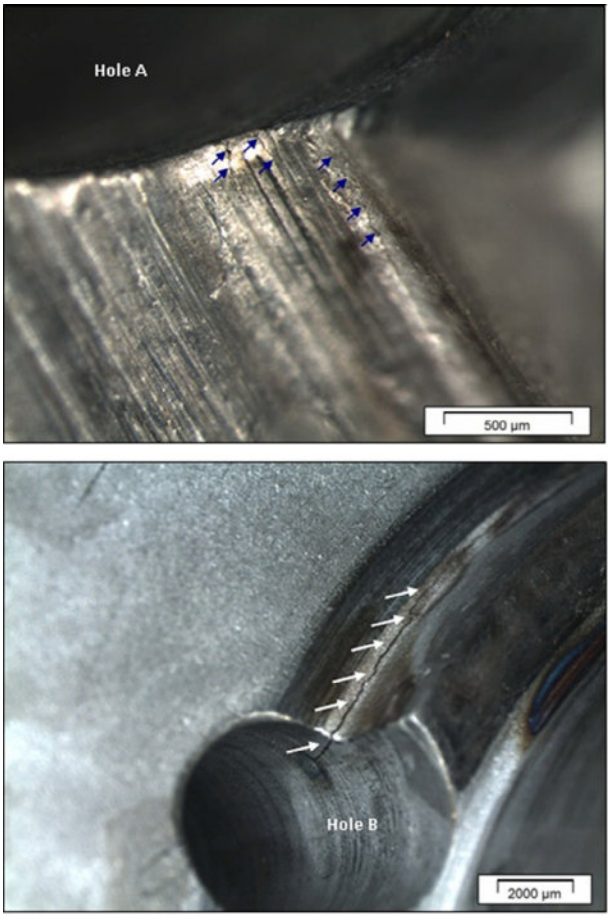

FIGURE 10.10

Crack (indicated by arrows) at edges of the extraction hole of the bevel pinion.

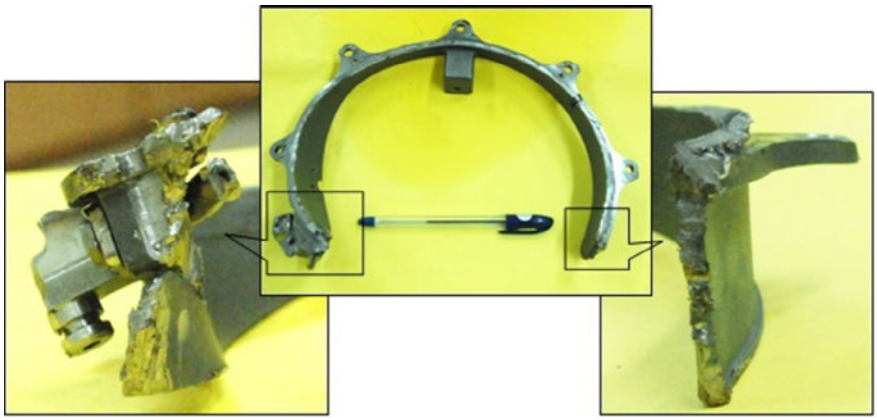

FIGURE 10.11

Top portion of pinion housing after failure.

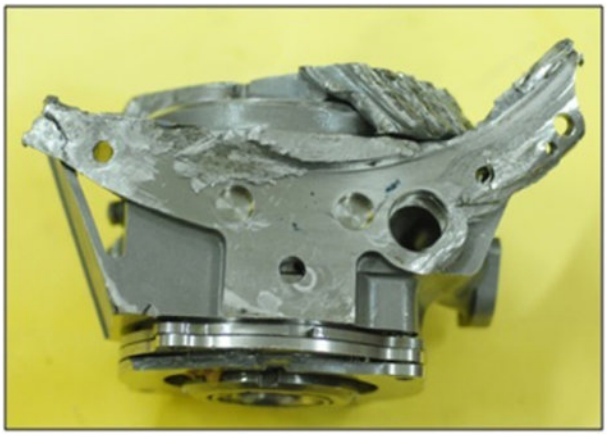

FIGURE 10.12

Secondary damages on the pinion housing.

The bottom portion of the pinion housing was still holding a portion of the bevel pinion after the failure (Figure 10.2). Extensive damages (impact and abrasion marks) were noticed on this part as well (Figure 10.12).

3.1.3 *Vertical Quill Shaft*

The vertical quill shaft also showed extensive damage on the top end (Figure 10.3). The splines at this end were completely worn out. The splines at the bottom end of the shaft were more or less intact. This indicated stoppage of rotation of mating components at the top end of the shaft, while the bottom end was still rotating. It must be

noted here that the top end splines were meshing with the failed bevel pinion shaft. Therefore, it appears most probable that after the dislodgement of the portion of the bevel pinion, the remaining portion of the bevel pinion stopped rotating. As the other end of the shaft was still rotating, the top end splines got worn out during this process. The bluish tint on the shaft also appeared to have resulted from the friction between the shaft and it's mating part. Therefore, it was concluded that the damages on the vertical quill shaft were secondary in nature.

3.2 MICROHARDNESS AND OPTICAL MICROSCOPY

A suitable sample was cut from the gear and prepared metallographically for a microhardness measurement. The case hardness on the flank region of the gear teeth was 62-63Rc, where as core hardness was 42-44Rc. Case depth was found to be around 0.9 mm (Figure 10.13) and meeting the specification requirement. Core hardness indicated that the material was in hardened and tempered condition. Optical microstructure also revealed the presence of a tempered martensitic structure at the core (Figure 10.14).

3.3 SCANNING ELECTRON MICROSCOPY

Since, visual and low-magnification studies revealed features of progressive failure in the case of bevel pinion, only a bevel pinion piece was subjected to further higher magnification electron microscopic studies. Suitable pieces were cut from the fractured piece of the pinion to accommodate into the scanning electron microscope (SEM) chamber. No metallurgical abnormalities such as inclusions or compositional heterogeneity were identified at the crack origins. The crack origin region of the

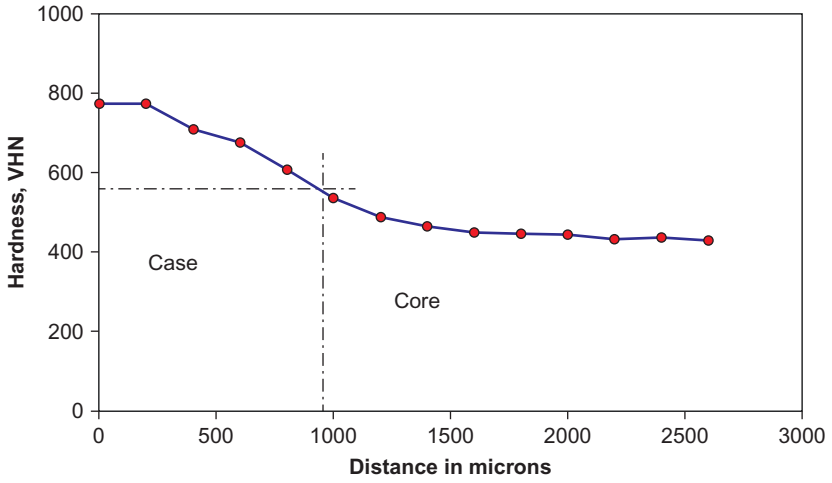

FIGURE 10.13

Microhardness profile at one of the gear teeth flank region.

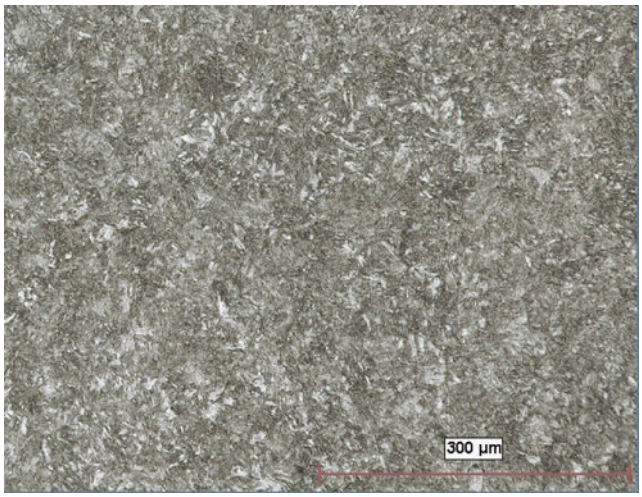

FIGURE 10.14

Microstructure of the gear material at core revealing tempered martensitic structure.

crack front "1" (Figure 10.5) under SEM is presented in Figure 10.15. Semi-quantitative composition analysis using energy-dispersive spectrum (EDS) at the crack origin region also confirmed that the composition was conforming to the low-alloy case-carburizing grade steel (Table 10.1).

4 ANALYSIS OF FAILURE CAUSE

Fractographic features indicated that the bevel pinion failed by a progressive mode (i.e., by fatigue). Three crack fronts were observed. Two of them were found to be initiated from the diagonally opposite corners of the extraction hole. The third fatigue crack origin was located at the root of one of the gear teeth. No metallurgical abnormalities were identified at the fatigue crack origins. However, edges of the extraction holes were very sharp. The radius of curvature of the fillet was found to be 0.23-0.25 mm. The stress concentration factor at the edges of the circular hole was three times the average stress level which was further aggravated by the presence of sharp fillet at the hole edge. This high-stress concentration factor is believed to be the reason for fatigue crack nucleation from the edges of the extraction hole. Premature failure of the components by fatigue initiated at sharp corners are reported in literature [22,23] as well. The existence of cracks was also identified at the other two extraction holes of the bevel pinion. This observation further strengthened the view. As the fatigue crack was found to propagate almost over the entire fractured surface, it is expected that operating loads at the gear wheel failure location was relatively lower. Therefore, the failure involved low stress-high cycle fatigue.

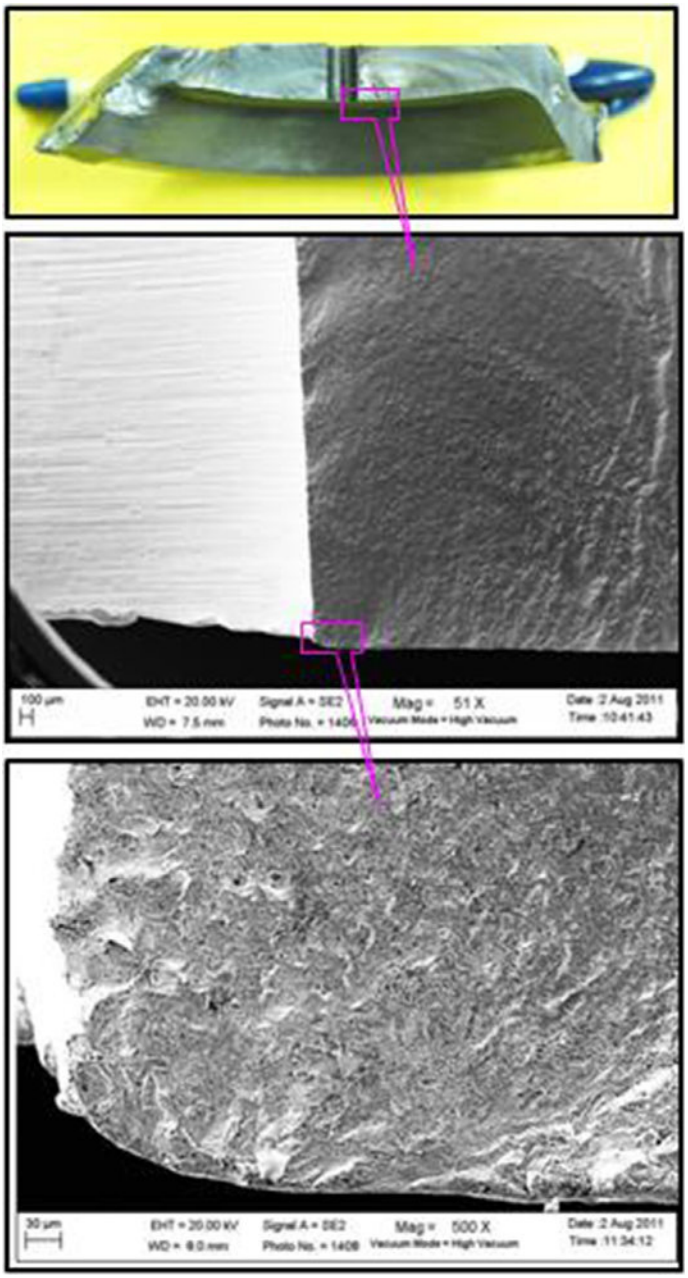

FIGURE 10.15

Crack origin "1" under scanning electron microscope.

Table 10.1 Chemical Composition at the Crack Origin "1"

Elements	Weight %
Si	2.60
Cr	2.20
Fe	Balance
Ni	2.68
Ti	3.77
Al	1.10

Failure of the other components, namely, pinion housing and vertical quill shaft were secondary in nature and occurred subsequent to the dislodgement of the bevel pinion.

5 CONCLUSION

The spiral bevel pinion failure was caused by fatigue crack initiation and propagation from the sharp corner of the extraction hole. As the crack propagated and finally reached an unstable size, a portion of the pinion was dislodged causing secondary damages to the other components in the assembly, namely, the pinion housing and vertical quill shaft.

6 RECOMMENDATION

A more generous radius of curvature at the fillet region was proposed as a preventive measure.

ACKNOWLEDGMENTS

The authors are thankful to Director, GTRE, for permitting to publish these results. The support extended by the members of Gear Box Design Group and Gear Box Testing group by giving the relevant information about the failed parts and NDT-QAG by carrying out magnetic particle inspection in the failed component are gratefully acknowledged. The authors express their gratitude toward Technical Director and Associate Director of Materials Application Group for their continuous support and guidance.

REFERENCES

[1] Alban LE. Failure of gears. ASM handbook. Failure analysis and prevention, vol. 11. Materials Park, OH 44073-0002: ASM International; 2002, pp. 2544–2590.

[2] Starzhinskii VE, Soliterman YL, Goman AM, Osipenko SA. Forms of damage to gear wheels: typology and recommendations on prevention. J Frict Wear 2008;29(5):343–53.

[3] Ozturk H, Yesilyurt I, Sabuncu M. Detection and advancement monitoring of distributed pitting failure in gears. J Nondestruct Eval 2010;29(2):63–73.
[4] Mackaldener M, Olsson M. Tooth interior fatigue fracture—computational and material aspects. Int J Fatigue 2001;23:329–40.
[5] Muhammad W, Ejaz N, Rizvi SA. Failure analysis of high-speed pinion gear shaft. J Fail Anal Prev 2009;9(5):470–8.
[6] Endo H, Randall RB, Gosselin C. Differential diagnosis of spall versus cracks in the gear tooth fillet region. J Fail Anal Prev 2004;4(5):63–71.
[7] Benedetti M, Fontanari V, Ho B. Influence of shot peening on bending tooth fatigue limit of case hardened gears. Int J Fatigue 2002;24:1127–36.
[8] Li S, Kahraman A. A micro-pitting model for spur gear contacts. Int J Fatigue 2014;59:224–33.
[9] Jonck J, Slabbert GA. Analysis of a failed spur gear from a Vibro-Hammer. Eng Fail Anal 2013;34:511–8.
[10] Pandey RK. Failure analysis of coal pulveriser gear box. Eng Fail Anal 2007;14 (4):541–7.
[11] Nejad AR, Gao Z, Moan T. On long-term fatigue damage and reliability analysis of gears under wind loads in offshore wind turbine drivetrains. Int J Fatigue 2014;61:116–28.
[12] Suresh S. Fatigue of materials. 2nd ed. The Edinburgh Building, Cambridge CB2 2RU, UK: Cambridge University Press; 2003, p. 458.
[13] Fernandes PJL, McDuling C. Surface contact fatigue failures in gears. Eng Fail Anal 1997;4(2):99–107.
[14] Fernandes PJL. Tooth bending fatigue failures in gears. Eng Fail Anal 1996;3(3):219–25.
[15] Xu X, Yu Z. Failure investigation of a diesel engine gear-shaft. J Fail Anal Prev 2009;9 (6):572–6.
[16] Park S, Lee J, Moon U, Kim D. Failure analysis of a planetary gear carrier of 1200HP transmission. Eng Fail Anal 2010;17(2):521–9.
[17] Xu X, Yu Z. Failure investigation on the cracked diesel engine ring gears. J Fail Anal Prev 2009;9(4):335–41.
[18] Netpu S, Srichandr P. Failure of a helical gear in a power plant. Eng Fail Anal 2013;32:81–90.
[19] Lee H, Hwang Y, Kim T. Failure analysis of nose landing gear assembly. Eng Fail Anal 2003;10:77–84.
[20] Fakhfakh T, Walha L, Louati J, Haddar M. Effect of manufacturing and assembly defects on two-stage gear system vibration. Int J Adv Manuf Technol 2006;29:1008–18.
[21] Göksenli A, Eryürek IB. Failure analysis of an elevator drive shaft. Eng Fail Anal 2009;16:1011–9.
[22] Bhaumik SK, Rangaraju R, Parameswara MA, Venkataswamy MA, Bhaskaran TA, Krishnan RV. Fatigue failure of a hollow power transmission shaft. Eng Fail Anal 2002;9(4):457–67.
[23] Qylafku G, Azari Z. Application of a new model proposal for fatigue life prediction on notches and key-seats. Int J Fatigue 1999;21:753–60.

CHAPTER

11 Failure due to synergistic fracture and pitting corrosion of ruptured bolts in a LARZAC engine of Alpha Jet

Ahmed Z. Farahat*, Abdel S.H. Makhlouf†
*Central Metallurgical Research and Development Institute, CMRDI, Helwan, Cairo, Egypt**
Manufacturing and Industrial Engineering Department, College of Engineering and Computer Science, University of Texas Rio Grande Valley†

CHAPTER OUTLINE

1 INTRODUCTION

According to the report of Snecma Safran group, France, for the MILITARY AIRCRAFT ENGINES about LARZAC®04 [1], "The Larzac® is a proven, highly reliable jet engine featuring easy maintenance and low cost of ownership. It is mainly designed to power single or twin-engine trainers and light tactical support aircraft". Figure 11.1 shows the different components of the LARZAC engine and the arrows point to the position of the bolts under investigation. Six ruptured bolts samples have been provided for investigation. Figure 11.2 shows the failure zone in one of the bolts.

Handbook of Materials Failure Analysis With Case Studies from the Aerospace and Automotive Industries.
http://dx.doi.org/10.1016/B978-0-12-800950-5.00011-9

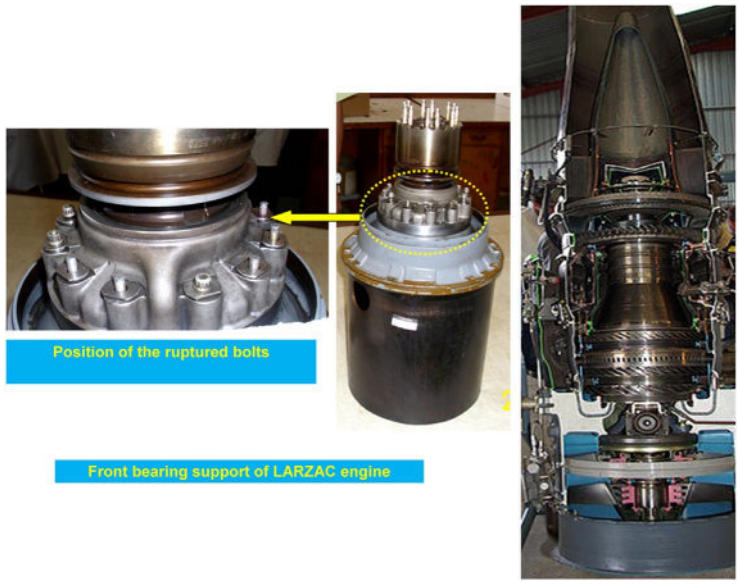

FIGURE 11.1

The LARZAC engine with the position of the ruptured bolts.

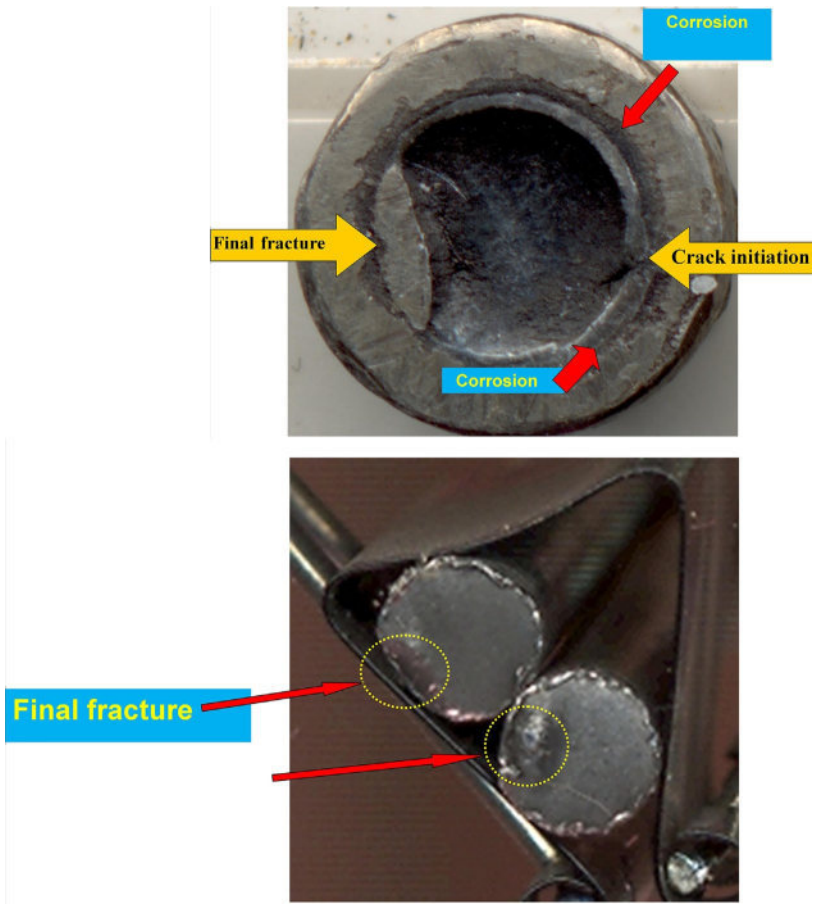

FIGURE 11.2

Macrograph images for the damaged bolts (head (above) and shank (down)).

Table 11.1 The Standard Chemical Analysis of the Bolts

Element	C	Si	Mn	Cr	Ni	Fe
Wt.%	0.32 0.40	0.15 0.35	0.40 0.80	0.30 0.70	1.25 1.75	Base

2 LABORATORY EVALUATION OF THE DAMAGED BOLTS

According to the chemical analysis (Table 11.1), the composition bolts material is confirmed to German standard 36 NiCr6 Din No. 1.5710. The material is heat-treated steel and used in the manufacturing of bolts. The material hardness $HV_{0.1} = 350$-400 Kg/mm^2.

The six bolts samples received for failure analysis are first examined visually with the aid of a low-power stereomicroscope and photographed. In addition, sections from the bolts heads and shanks were examined utilizing a scanning electron microscope equipped with an energy dispersive X-ray analysis system (SEM-EDS). This permits a much more detailed examination of the bolts surface under the deposits together with the identification of elemental species at specific locations within the deposits. This analysis was found very useful to provide additional clues as to the failure mechanism. For example, the finding of sulfur and chloride salts in the deposits provides a clue that media was concentrating to high aggressive solids values in those areas, indicating the potential for pitting corrosion at the surface.

3 FAILURE ANALYSIS SUMMARY

The investigation of the bolts failure followed a series of steps each designed to answer specific questions.

3.1 PHYSICAL AND VISUAL EVALUATION OF THE BOLTS SAMPLES

Physical examination of the bolts specimen showed severe fracture in addition to some dark areas that could be originated as corrosion products (Figure 11.2). The occurrence of fracture has been confirmed in all bolts specimens. In some samples (Figure 11.2), the crack initiation zone has also been identified.

3.2 SURFACE EXAMINATION USING SEM IMAGES

The examination utilizing the SEM provides detailed information on the surface conditions in the area of failure and on the spatial location of components of the

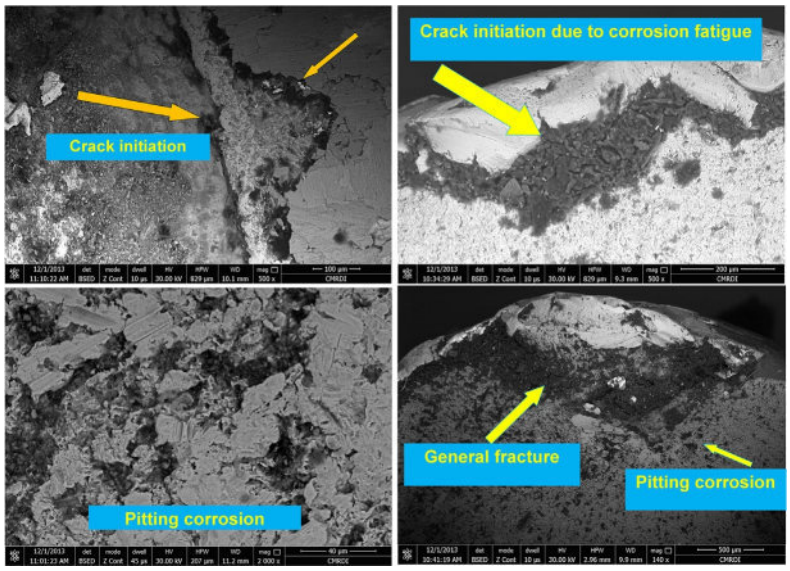

FIGURE 11.3

SEM analysis of the bolts showing well-defined pitting corrosion and fracture.

deposits. SEM analysis of the bolts specimen showed well-defined pitting attack- and transgranular fracture which point to the occurrence of corrosion and severe vibration. The cracks initiation and fracture have also been evidenced (Figure 11.3). SEM-EDS analysis revealed formation of pitting corrosion which can be attributed to the presence of high chloride and sulfur content as explained in Section 3.3.

3.3 CHEMICAL COMPOSITION EXAMINATION

The microprobe analysis of the deposits (dark color) formed at the pitting corrosion areas was performed using EDS. EDS provides specific information on the chemical composition of the deposits, which can be correlated with data on media contamination and the chemical composition of the bolts material. The analysis of deposits formed at the bolts specimen revealed presence of corrosive sodium chloride and sulfur at the pitting zones (Figures 11.4–11.6). Chloride and sulfur are well-known reasons for occurrence of pitting corrosion on steel substrates.

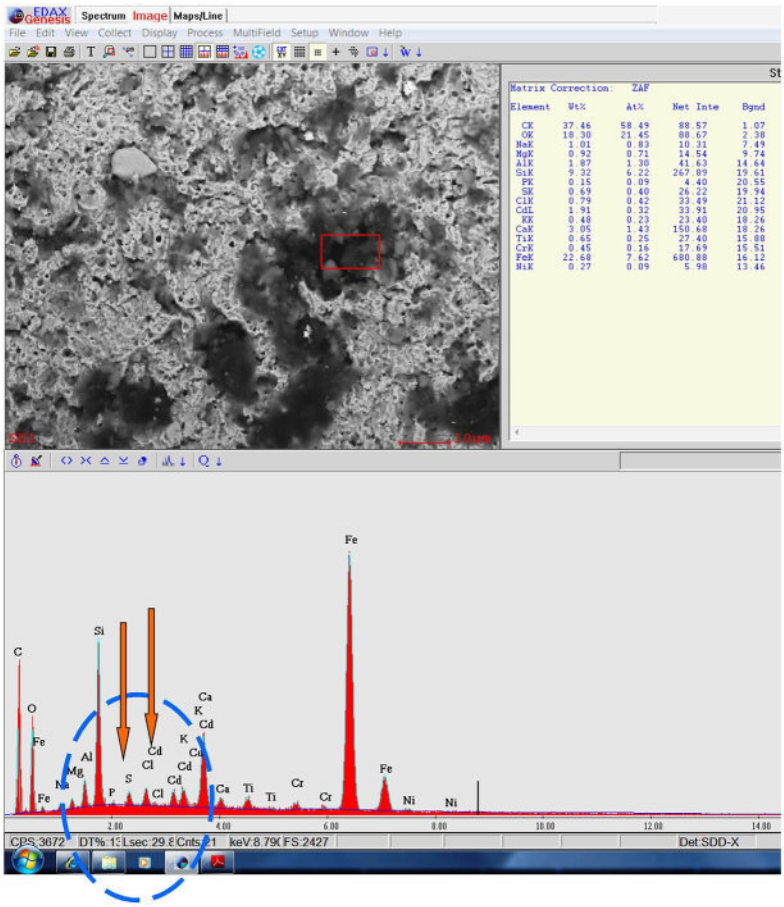

FIGURE 11.4

Surface analysis using EDS of the deposits formed over the pitting zone.

4 CONCLUSION

1. Failure due to fracture and pitting corrosion was observed in six bolts used in the front bearing support of LARZAC engine.
2. The failure occurred due to a synergistic effect between corrosion and vibration.
3. SEM micrographs showed that the main mode of failure was pitting corrosion (by the proven presence of corrosive chloride and sulfur) and fracture (possibly due to a vibration originated from a failure in the rolling bearings) as evidenced by macro- and micrographs examination.

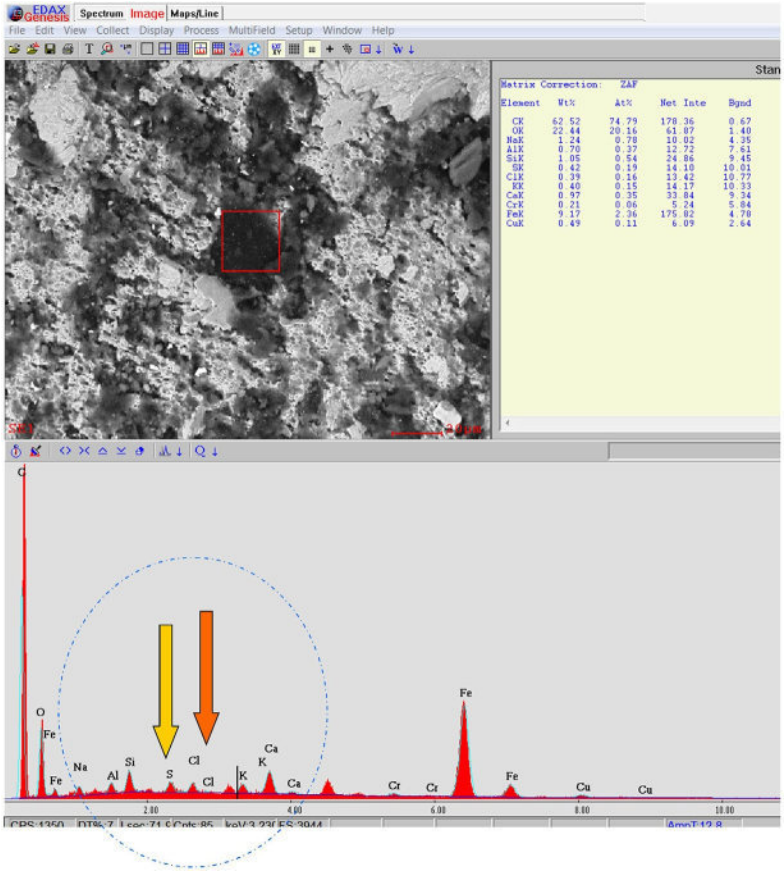

FIGURE 11.5

Surface analysis using EDS of the deposits formed over the pitting zones.

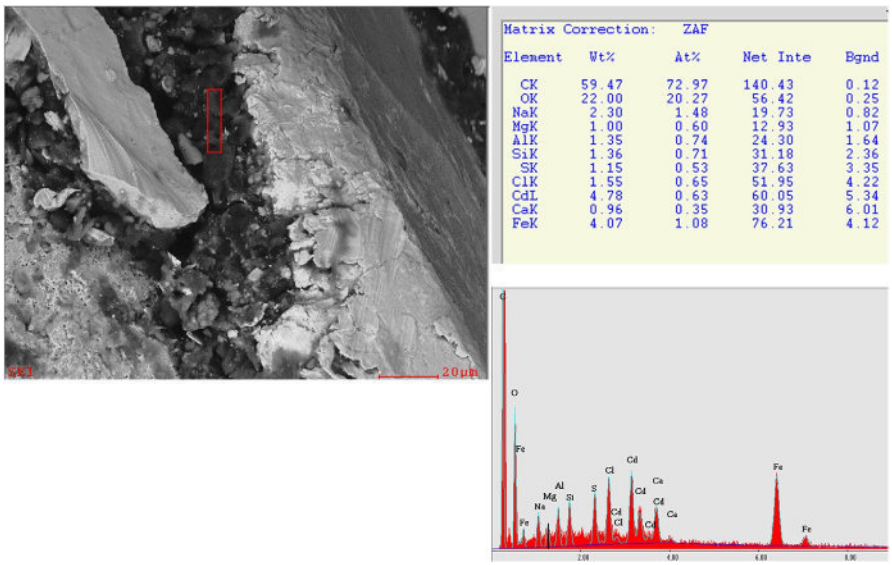

FIGURE 11.6

Surface analysis using EDS of corrosion fatigue crack initiation zones.

5 RECOMMENDATIONS

1. Based on the surface examination and chemical analysis, the reason(s) for the failure in the rolling bearings should be investigated so the vibration originated from them can be avoided and hence, the chance for fracture/corrosion failure under investigation will be minimized.
2. Aggressive chloride and sulfur salts were found to have a catastrophic effect at the materials causing pitting corrosion and initiate cracking. Corrosion of any or all components of bolts or bearing can result from ingress of water, moisture or other liquid, or from deterioration of the lubricant. Accordingly, a scheme to avoid such corrosive salts should be considered.

REFERENCE

[1] http://www.snecma.com/IMG/pdf/LARZAC_Anglais.pdf accessed May 7, 2015.

CHAPTER

12 A failure-processing scheme based on Kalman prediction and the reliability analysis for 25 kVA generators used on IDF

Shang-Kuo Yang
Department of Mechanical Engineering, National Chin Yi University of Technology, Taichung, Taiwan

CHAPTER OUTLINE

1 INTRODUCTION

The power system of an Indigenous Defensive Fighter (IDF) is divided into the left-side system and the right-side system, and the generator of each side supplies power to the corresponding load of the fighter respectively. Because the rated output of each

Handbook of Materials Failure Analysis With Case Studies from the Aerospace and Automotive Industries.
http://dx.doi.org/10.1016/B978-0-12-800950-5.00012-0

generator is 25 kVA, each generator can sufficiently supply the power needed by the whole aircraft. An IDF has a load-switching mechanism that is designed for failures of the generators, i.e., in case any one of the two generators on an IDF fails, the load of the failed generator can be switched to the other one within 50 ms. Accordingly, the two generators can not only supply power to their own load but also can play the role of a backup device to each other. Unfortunately, the availability of these newly developed generators has not been good since they were installed on IDFs. The requirement of high reliability for the generators of a fighter is not satisfied due to the frequent failures.

The frequent failures of the generators result in the following two problems:

(1) An IDF has been equipped with a monitoring system to know if the AC power source has failed or not and then to take corresponding measures. However, from the moment when the system detects the abnormal output of the generator (over (low) voltage, over (low) current, over (low) frequency, etc.), judges the power source failed, and then completes the load switching, the irregular output of the failed generator within this time frame has already harmed many important systems of the aircraft as well as the generator itself.

(2) According to the maintenance record of the 25 kVA generators in the air force of Taiwan, the mean repair time for failed generators is 8 months. The long repair time substantially reduced the recurring use rate of the generators. This situation makes IDFs to be AOGs (aircraft on ground) and immensely degrades the availability of IDFs.

To solve the aforementioned problems, the most effective method is to improve the reliability of the 25 kVA generators so as to reduce the occurrence of failures. Generally, the engineers will execute the failure cause analysis to find the weakest parts and components and then perform engineering improvements on them. By promoting the reliability of components, the goal of upgrading the whole generator system may be achieved. However, the engineering improvement for high failure rate parts and components of the generators has been done continually after they were installed on IDFs and yet the generators still failed frequently. Through a detailed investigation, the engineers reported that the cause of the problem was the structure of the generators. The generators were required to be small and light at the design phase. It was found that the designed structure cannot reliably endure the operating rotational speed of 13,750–25,000 rpm. Consequently, to thoroughly solve the problem, the structure of the generators needs to be redesigned. Due to the expense and the execution schedule, opinions among the user, the aircraft manufacturer, and the generator supplier differed from each other on this issue, thus the structure redesigning has not been accomplished at this time. Accordingly, how to effectively promote the reliability of 25 kVA generators while under restriction so that the structure cannot be modified is the aim of this study.

This study proposes a failure-processing scheme for 25 kVA generators, that is, establishing a state-prediction mechanism based on the state-estimation function of the Kalman filter to predict the occurrence of failures by estimating the future state variables of a 25 kVA generator and cooperating with the functions of load switching

and system reset of IDFs in order to switch the load of the abnormal generator prior to its actual failures. The structure of the state-estimation function of the Kalman filter has been performed on a DC motor [1] to predict the failure-occurrence time by estimating the future state variables. The resultant prediction errors are acceptable. Furthermore, this study analyzes the reliability of 25 kVA generators that are equipped on IDFs under the current mutual backup configuration, and the results are compared with the reliabilities of three other configurations: single generator, active redundancy, and passive redundancy of generators so as to know the effect of redundancy design.

2 25 kVA GENERATOR

A 25 kVA generator, as shown in Figure 12.1, is one of the most important components in the power system of an IDF. The main function of the generator is to convert the power of the Airframe Mounted Accessory Drive Gearbox on an IDF to the 115 V, 400 Hz, 3-phase AC power system. A 25 kVA generator is composed of two subassemblies: (1) generator and magnetics assembly (GMA) and (2) inverter. The GMA generates AC power with frequency range from 1370 to 2500 Hz and then feeds the power to the inverter. The output of the inverter is 270 V DC power that is then converted by the generator control unit (GCU) to a fixed voltage (115 V), fixed frequency (400 Hz), and 3-phase-4-line AC power for the use of the whole aircraft. The main specifications for the generators are listed in Table 12.1 [2].

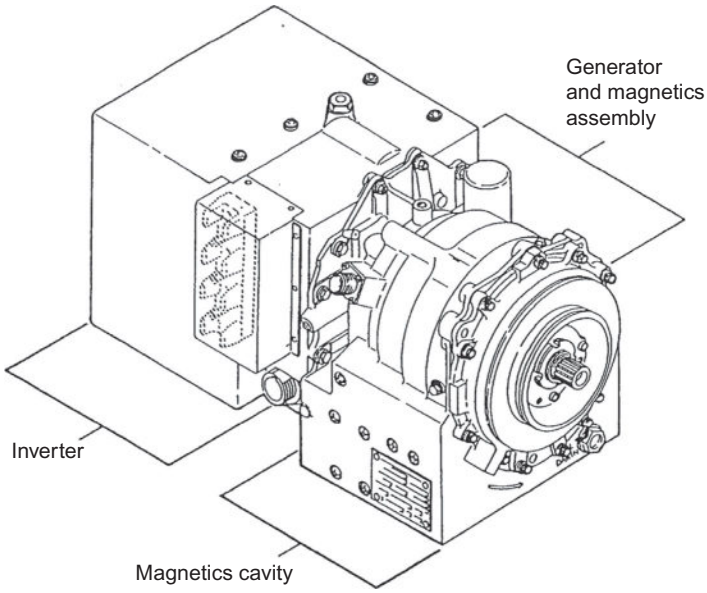

FIGURE 12.1

The assembly of a 25 kVA generator.

Table 12.1 Main Specifications for the 25 kVA Generators

Rating (kVA)	25 (Continuous)
	37.5 (5 s)
Rating (Speed)	13,750–25,000 rpm
Voltage, AC	200 Vrms L-L
Phase	3
Power factor	0.75 lagging to 1.0
Frequency (H)	400 ± 1
Size (in.)	$9.97H \times 8.67W \times 20.7L$
Weight (dry)	57.1 lbs

3 KALMAN FILTER AND THE SIMULATION SYSTEM

3.1 KALMAN FILTER

The block diagram of a discrete system is shown in Figure 12.2. The state equations [3] are

$$X_{k+1} = \Phi_k X_k + B_k U_k + W_k \tag{12.1}$$

$$Y_k = H_k X_k \tag{12.2}$$

$$Z_k = Y_k + V_k \tag{12.3}$$

State estimation aims to guess the value of X_k by using measured data, i.e., $Z_0, Z_1, \ldots, Z_{k-1}$. Let $a \geq b$, define the notation $\hat{(\cdot)}_{a/b}$ as the estimate of (.) at time $a\ T$ based on all known information about the process up to time $b\ T$. Accordingly, $\hat{X}_{k/k-1}$ is called the prior estimate of X, and $\hat{X}_{k/k}$ is called the posterior estimate of X [4].

The Kalman filter is a copy of the original system and is driven by the estimation error and the deterministic input. The block diagram of the filter structure is shown in Figure 12.3. The filter is used to improve the prior estimate to be the posterior estimate by the measurement Z_k. A linear blending of the noisy measurement and the prior estimate is written as given in Ref. [4]

$$\hat{X}_{k/k} = \hat{X}_{k/k-1} + K_k\left(Z_k - H_k \hat{X}_{k/k-1}\right) \tag{12.4}$$

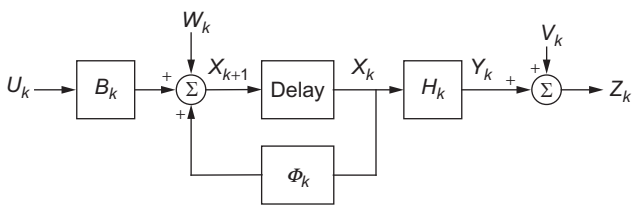

FIGURE 12.2

Block diagram of a discrete system.

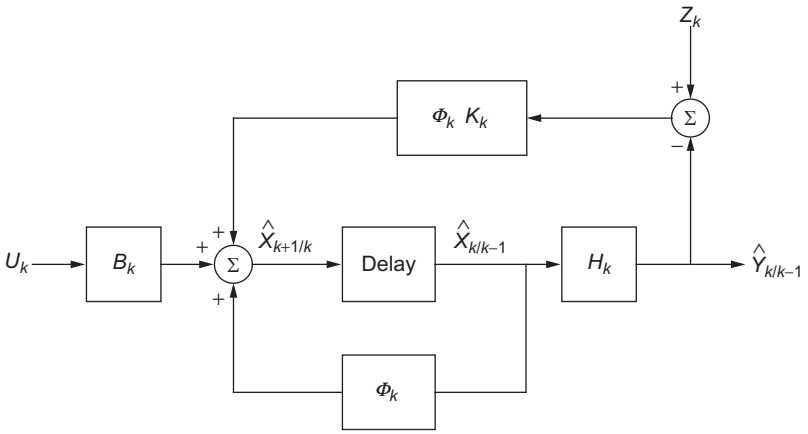

FIGURE 12.3

Block diagram of the Kalman filter.

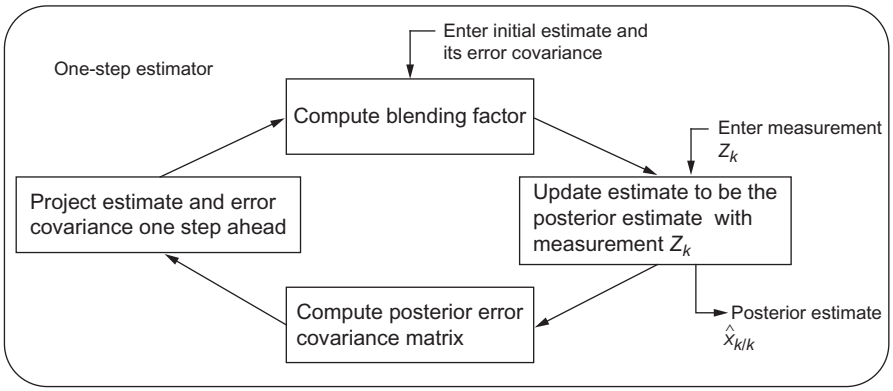

FIGURE 12.4

One-step estimator.

where K_k is a blending factor for this structure. As depicted in Figure 12.3, the one-step-ahead estimate is formulated as:

$$\begin{aligned}\hat{X}_{k+1/k} &= \Phi_k \hat{X}_{k/k-1} + \Phi_k K_k \left(Z_k - H_k \hat{X}_{k/k-1}\right) + B_k U_k \\ &= \Phi_k \left[\hat{X}_{k/k-1} + K_k \left(Z_k - H_k \hat{X}_{k/k-1}\right)\right] + B_k U_k \\ &= \Phi_k \hat{X}_{k/k} + B_k U_k\end{aligned} \tag{12.5}$$

According to the aforementioned statements, recursive steps for constructing a one-step estimator are summarized in Figure 12.4. However, initial conditions, i.e., $\hat{X}_{0/-1}$, $P_{0/-1}$, Φ_0, H_0, Q_0, and R_0 have to be known to start recursive steps.

3.2 STATE-SPACE MODELS OF THE GENERATOR

3.2.1 *Continuous State-Space Model*

The block diagram of a synchronous generator is shown in Figure 12.5 [5]. Choosing the deviation of the rotor speed $\Delta\omega_r$ and the deviation of the rotation angle $\Delta\delta$ as state variables, the state vector of the synchronous generator is represented as $X=[\Delta\omega_r \Delta\delta]^T$. The continuous state equations can be derived from the motion equations of the generator as follows:

$$\frac{d}{dt}\Delta\omega_r = \frac{1}{2H}(T_m - T_e - K_D\Delta\omega_r) \tag{12.6}$$

$$\frac{d}{dt}\delta = \omega_0\Delta\omega_r \tag{12.7}$$

Equation (12.6) can be linearized as:

$$\frac{d}{dt}\Delta\omega_r = \frac{1}{2H}[\Delta T_m - \Delta T_e - K_D\Delta\omega_r] \tag{12.8}$$

Employing $\Delta T_e = K_s\Delta\delta$ leads to:

$$\frac{d}{dt}\Delta\omega_r = \frac{1}{2H}[\Delta T_m - K_s\Delta\delta - K_D\Delta\omega_r] \tag{12.9}$$

Again, (12.7) can be linearized as:

$$\frac{d}{dt}\Delta\delta = \omega_0\Delta\omega_r \tag{12.10}$$

Consequently, according to (12.9) and (12.10), the continuous state equations of the synchronous generator are written as:

$$\frac{d}{dt}\begin{bmatrix}\Delta\omega_r \\ \Delta\delta\end{bmatrix} = \begin{bmatrix}-\frac{K_D}{2H} & -\frac{K_S}{2H} \\ \omega_0 & 0\end{bmatrix}\begin{bmatrix}\Delta\omega_r \\ \Delta\delta\end{bmatrix} + \begin{bmatrix}\frac{1}{2H} \\ 0\end{bmatrix}\Delta T_m \tag{12.11}$$

$$Y = [1 \;\; 0]\begin{bmatrix}\Delta\omega_r \\ \Delta\delta\end{bmatrix} \tag{12.12}$$

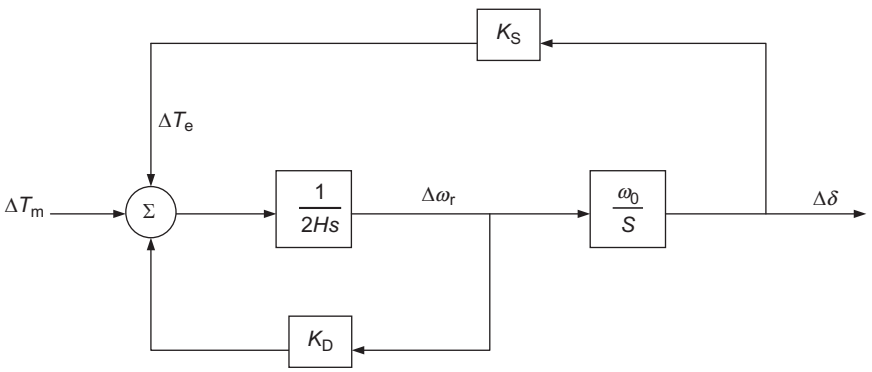

FIGURE 12.5

Block diagram of a synchronous generator.

3.2.2 Discrete State-Space Model

In order to derive the discrete state equations of a system from its continuous state equations, the continuous state equations are formulated as [6]:

$$\dot{V}(t) = A_c V(t) + B_c U(t) \tag{12.13}$$

$$Y(t) = C_c V(t) + D_c U(t) \tag{12.14}$$

Let $\Phi_c(t) = L^{-1}[(sI - Ac)^{-1}]$ be the state transition matrix of Equation (12.13), where L^{-1} denotes the inverse Laplace transform and Equation (12.13) can be rewritten as:

$$\dot{V}(t) = \Phi_c(t - t_0)V(t_0) + \int_{t_0}^{t} \Phi_c(t - \tau)B_c u(\tau)\mathrm{d}\tau \tag{12.15}$$

where t_0 is the initial time, $t = kT$ (T is the time interval for the discrete system). For emphasizing $u(t)$ as the output of a zero-order hold, the representation of $u(t)$ is changed to $m(kT)$, i.e., $u(t) = m(kT)$ when $kT \le t < kT + T$. Substituting $m(kT)$ into Equation (12.15) yields:

$$\dot{V}(kT + T) = \Phi_c(T)V(kT) + m(kT)\int_{T}^{kT+T} \Phi_c(kT + T - \tau)B_c\mathrm{d}\tau \tag{12.16}$$

Comparing (12.16) with (12.17),

$$X(kT + T) = A_d X(kT) + B_d m(kT) \tag{12.17}$$

If $X(kT) = V(kT)$ then the following equations can be derived:

$$A_d = \Phi_c(T) \tag{12.18}$$

$$B_d = \int_{kT}^{kT+T} \Phi_c(kT + T - \tau)B_c\mathrm{d}\tau \tag{12.19}$$

And the output equation (12.14) can be rewritten as:

$$\begin{aligned} Y(kT) &= C_c V(kT) + D_c U(kT) \\ &= C_d X(kT) + D_d m(kT) \end{aligned} \tag{12.20}$$

Moreover, the B_d in (12.19) can be further simplified. Substituting ($kT - \tau = -\sigma$) into (12.19) yields:

$$B_d = \left[\int_0^T \Phi_c(T - \sigma)\mathrm{d}\sigma\right]B_c \tag{12.21}$$

Again, let $\tau = T - \sigma$, Equation (12.21) can be written as:

$$\begin{aligned} B_d &= \left[\int_0^T \Phi_c(T - \sigma)\mathrm{d}\sigma\right]B_c \quad = \left[\int_T^0 \Phi_c(\tau)(-\mathrm{d}\tau)\right]B_c \\ &= \left[\int_0^T \Phi_c(\tau)\mathrm{d}\tau\right]B_c \end{aligned} \tag{12.22}$$

Finally, the discrete state equations are formulated as:

$$X(kT + T) = A_d X(kT) + B_d m(kT) \tag{12.23}$$

$$Y(kT) = C_d X(kT) + D_d m(kT) \tag{12.24}$$

where $A_d = \Phi_c(T)$, $B_d = \left[\int_0^T \Phi_c(\tau)\mathrm{d}\tau\right]B_c$, $C_d = C_c$, $D_d = D_c$.

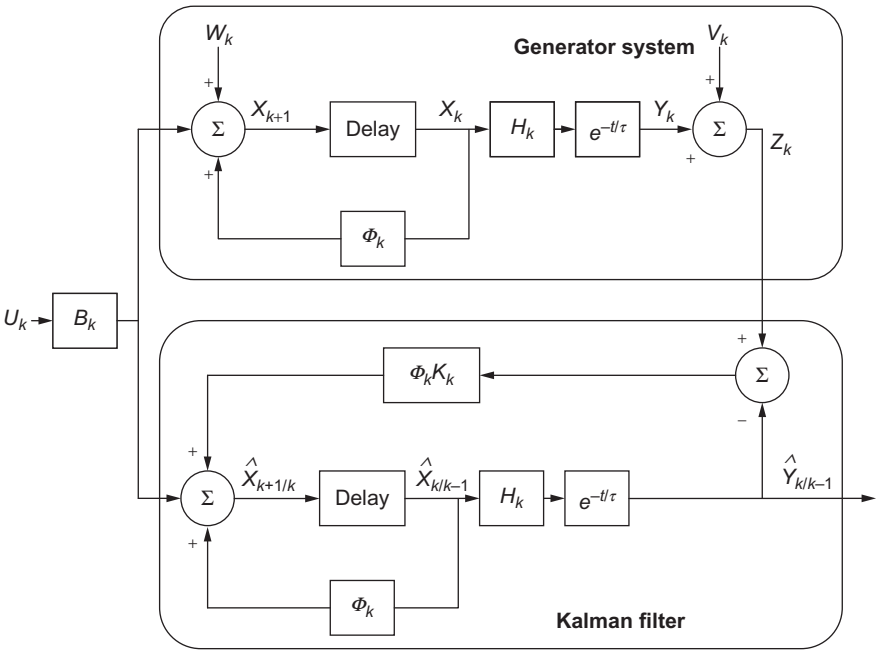

FIGURE 12.6

Block diagram of the simulation system.

3.3 AGING MODEL

To account for the aging failure modes and the exponentially distributed failure times t_i, an exponential attenuator, represented as $e^{-t/\tau}$, is placed at the output end of each motor system as well as the Kalman filter. The block diagram of simulation system is shown in Figure 12.6. The symbol τ of the attenuator in Figure 12.6 denotes the failure time constant of the generator, which varies with failure times that are generated by Monte Carlo simulation (MCS) [7].

4 SIMULATIONS AND RESULTS

4.1 PARAMETERS

The following parameters are used to conduct the failure prediction:

(1) The failure thresholds of the generator are defined as the rotational speed that is $\pm 5\%$ different than the rated value. That is, the generator is judged to fail if the rotational speed drops to 95% (13,063 rpm) of the rated low value (13,750 rpm) or rises to 105% (26,250 rpm) of the rated high value (25,000 rpm).

(2) According to the maintenance documentation [8], the mean time between failures (MTBFs) of the generators is 783.5 h.

(3) Sampling interval T is respectively chosen as 5, 20, and 60 min to be the increment time for every step in Kalman predictions. Due to the 50 ms load switching time on IDFs, T should be longer than 50 ms.
(4) Disturbance W_k has mean 0 and variance 0.01 N m [9].
(5) Measurement error V_k for $\dot{\theta}$ has zero mean and the standard deviation is 1% full-scale accuracy [10] of the measurement.
(6) Other parameter values for 25 kVA generators are listed below [11].
Synchronizing torque coefficient $K_S = 0.755$
Damping torque coefficient $K_D = 9.98$
Inertia constant $H = 19.1$ MW s/MVA

Substituting the parameters K_S, K_D, and H into Equations (12.11) and (12.12), the continuous state-space equations for low and high rated rotational speeds of the generator are written as:

(1) low rated rotational speed:

$$\frac{\mathrm{d}}{\mathrm{d}t}\begin{bmatrix}\Delta\omega_r\\ \Delta\delta\end{bmatrix} = \begin{bmatrix}-0.261176 & -0.019764\\ 8639.37 & 0\end{bmatrix}\begin{bmatrix}\Delta\omega_r\\ \Delta\delta\end{bmatrix} + \begin{bmatrix}0.002618\\ 0\end{bmatrix}\Delta T_\mathrm{m}$$

$$Y = [1 \;\; 0]\begin{bmatrix}\Delta\omega_\mathrm{r}\\ \Delta\delta\end{bmatrix}$$

(2) high rated rotational speed:

$$\frac{\mathrm{d}}{\mathrm{d}t}\begin{bmatrix}\Delta\omega_\mathrm{r}\\ \Delta\delta\end{bmatrix} = \begin{bmatrix}-0.261176 & -0.019758\\ 15{,}707.96 & 0\end{bmatrix}\begin{bmatrix}\Delta\omega_\mathrm{r}\\ \Delta\delta\end{bmatrix} + \begin{bmatrix}0.002618\\ 0\end{bmatrix}\Delta T_\mathrm{m}$$

$$Y = [1 \;\; 0]\begin{bmatrix}\Delta\omega_\mathrm{r}\\ \Delta\delta\end{bmatrix}$$

4.2 NUMBER OF SIMULATION SAMPLES

For the purposes of reducing the prediction error and increasing the accuracy of the simulation results, the number of simulation samples should be determined. According to the central limit theorem [12]:

(1) If the population is normally distributed, the distribution of the sample mean is normal.
(2) If the population is large but not normally distributed, the distribution of sample mean approaches is a normal distribution provided that the sample is large.

Estimators follow the normal distribution if the sample size is sufficiently large. The sample size of 30 is a reasonable number to use [12]. The larger the sample size, the smaller the estimated error becomes, which tends to zero when the sample size approaches infinity. Hence, the number of simulation samples is determined as 100 in this study.

4.3 RESULTS: COMPARISON BETWEEN KALMAN PREDICTION AND MCS

Simulations in this study were performed by using MATALAB.

(1) Failure simulations of the rated low rotational speed

Figure 12.7 shows the results of 100 simulations of failure times generated by MCS and predicted by Kalman filter for $T = 60$ min. The differences between them are shown in Figure 12.8. The mean value (μ) and the standard deviation (σ) of the differences for the 100 simulations are -20.71 and 47.19 min, respectively. The negative sign of the mean value indicates that the failure time predicted by

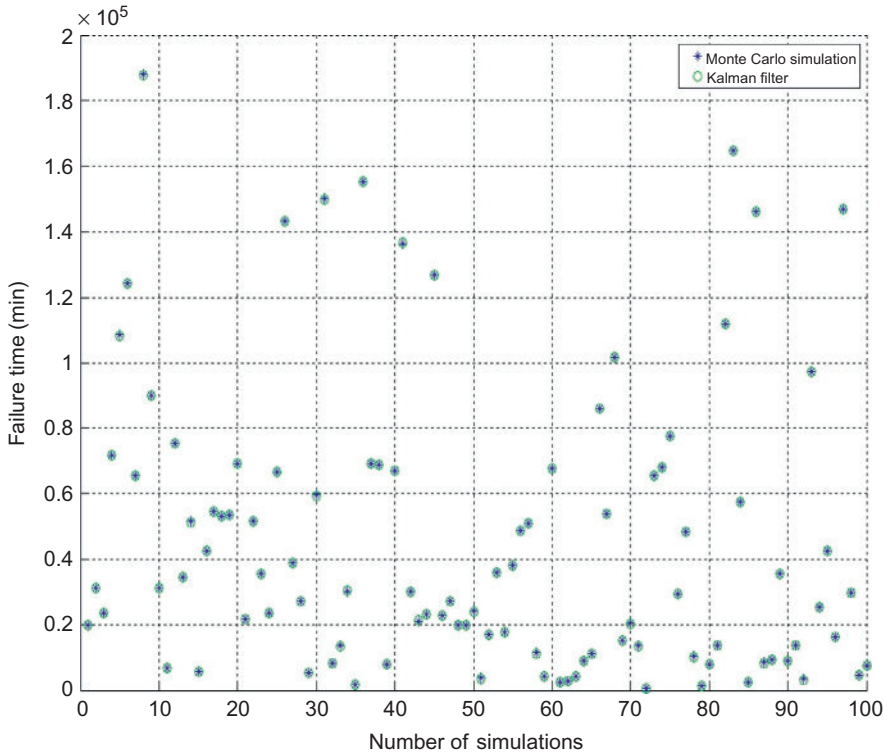

FIGURE 12.7

Failure times generated by Monte Carlo simulation and predicted by Kalman filter when $T = 60$ min (for failure simulations of the rated low rotational speed).

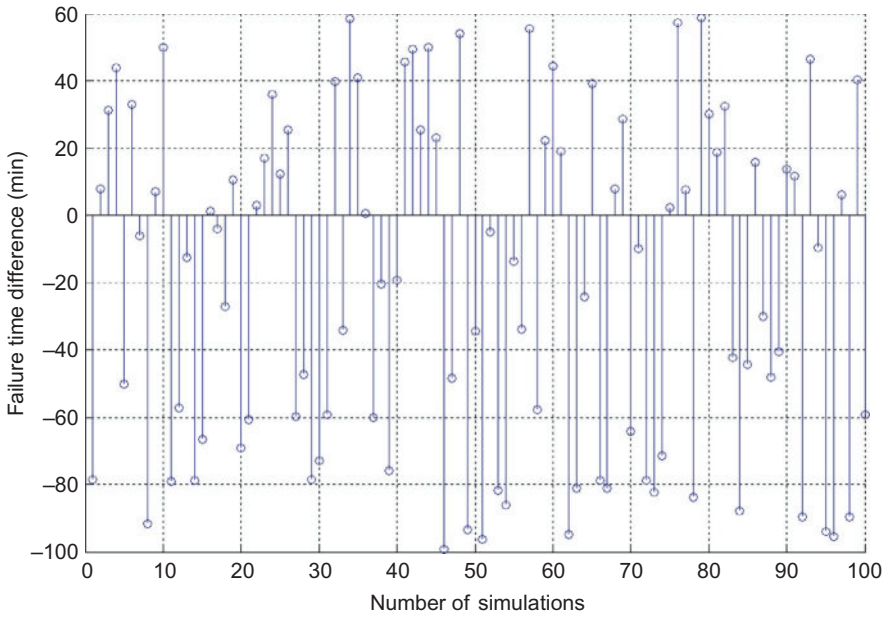

FIGURE 12.8

Differences between failure times calculated by Monte Carlo simulation and Kalman prediction when $T=60$ min (for failure simulations of the rated low rotational speed).

Kalman filter is prior to the time generated by MCS. According to the Z formula [12], the error (E_r) for estimating the mean value of the sample population can be calculated by:

$$E_r^2 = \frac{Z_{\alpha/2}^2 \sigma^2}{n}$$

where n is the number of simulation samples, and α is the significance level. The Z value for a 99% confidence level $(1-\alpha)$ is 2.575 [12]. Solving for E_r gives:

$$E_r = \frac{(2.575)(47.19)}{\sqrt{100}} = 12.15\,(\text{min})$$

According to the above data, there is 99% confidence that the interval for the mean value of the time differences is -20.71 ± 12.15 min, i.e., from -8.56 to -32.86 min.

Results for simulations of $T=20$ min and $T=5$ min are shown in Figures 12.9–12.12. The mean value and the standard deviation of the failure time differences between MCS and Kalman prediction, the E_r value, and the confidence interval with 99% confidence level for the estimations are listed in Table 12.2. Results in Table 12.2 show that the shorter the T is, under the same confidence level, the smaller the mean value (μ) and the narrower the confidence interval becomes.

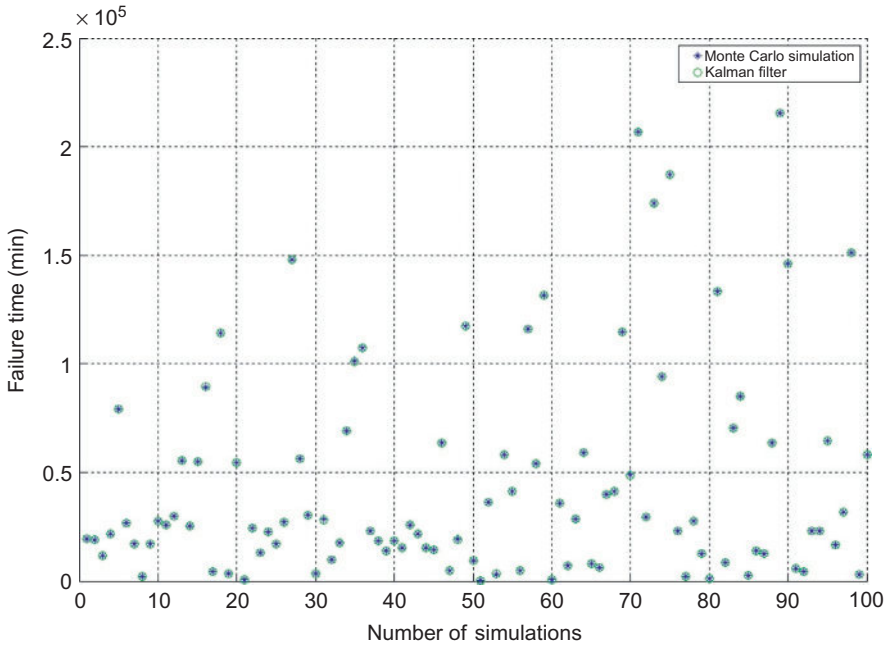

FIGURE 12.9

Failure times generated by Monte Carlo simulation and predicted by Kalman filter when $T = 20$ min (for failure simulations of the rated low rotational speed).

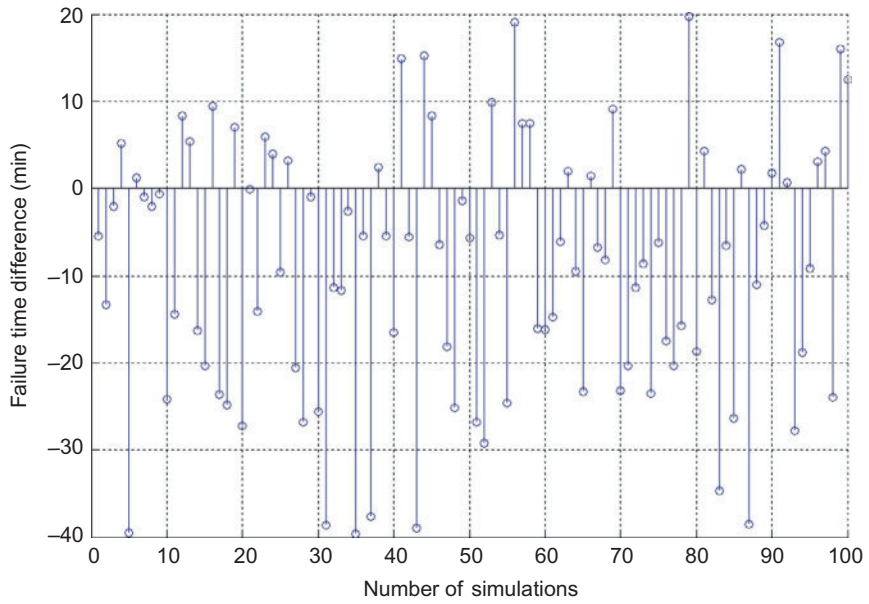

FIGURE 12.10

Differences between failure times calculated by Monte Carlo simulation and Kalman prediction when $T = 20$ min (for failure simulations of the rated low rotational speed).

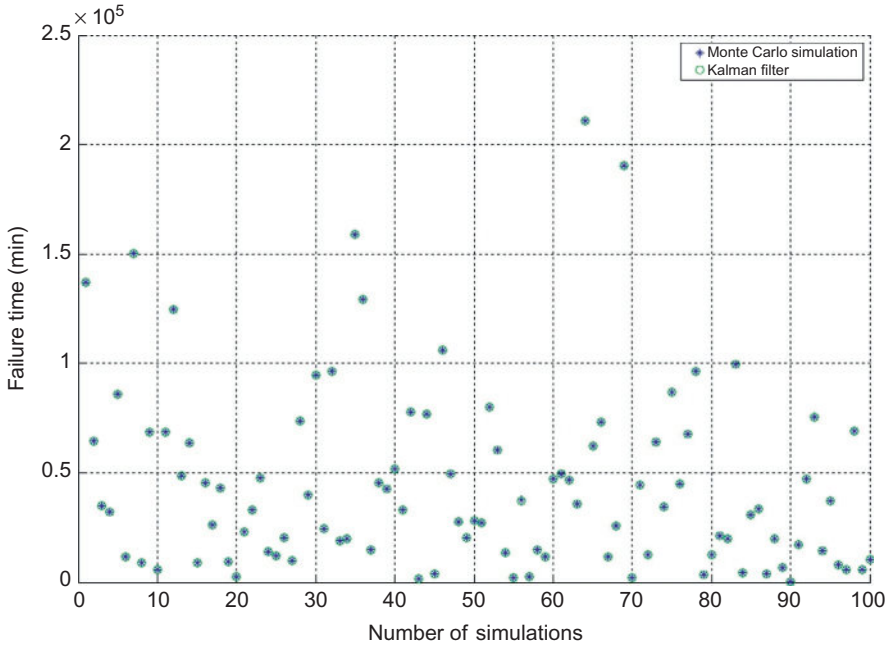

FIGURE 12.11

Failure times generated by Monte Carlo simulation and predicted by Kalman filter when $T=5$ min (for failure simulations of the rated low rotational speed).

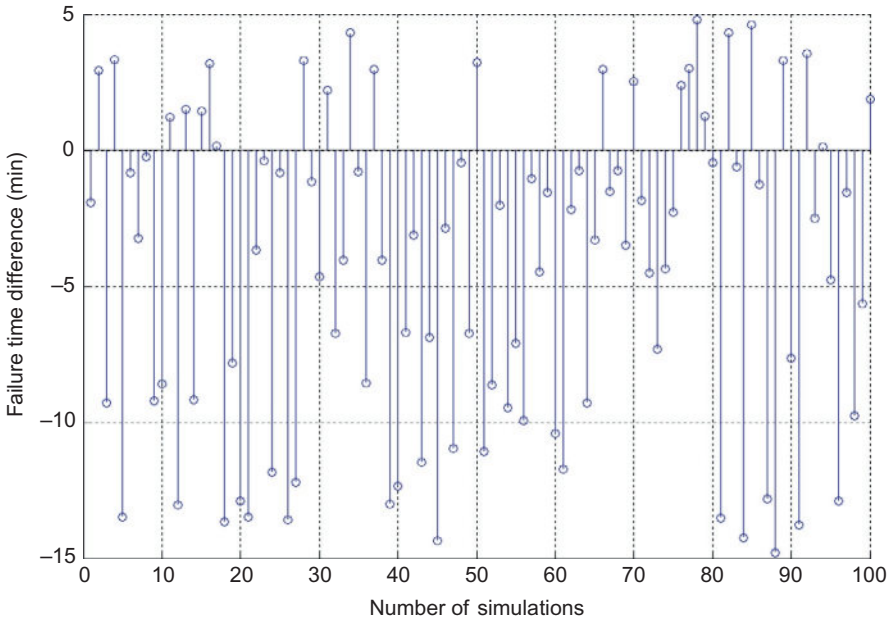

FIGURE 12.12

Differences between failure times calculated by Monte Carlo simulation and Kalman prediction when $T=5$ min (for failure simulations of the rated low rotational speed).

Table 12.2 Estimation Results with 99% Confidence Level for Simulations of the Rated Low Rotational Speed

T (min)	μ	σ	E_r	Confidence Interval
60	−20.71	47.19	12.15	(−8.56, −32)
20	−9.21	14.7	3.79	(−5.42, −13)
5	−4.49	5.83	1.43	(−2.99, −5.99)

(2) Failure simulations of the rated high rotational speed

In a similar manner, failure simulations of the rated high rotational speed are conducted. The results of 100 simulations of failure times generated by MCS and predicted by Kalman filter for $T=60$ min, $T=20$ min, and $T=5$ min are presented in Figures 12.13–12.18, respectively. For these simulations, the mean value (μ) and the standard deviation (σ) of the failure time differences between the results calculated by MCS and Kalman prediction, the E_r value, and the confidence interval with 99% confidence level are listed in Table 12.3. The trend of the results is similar to the trend of the results that are obtained in the rated low rotational speed simulations.

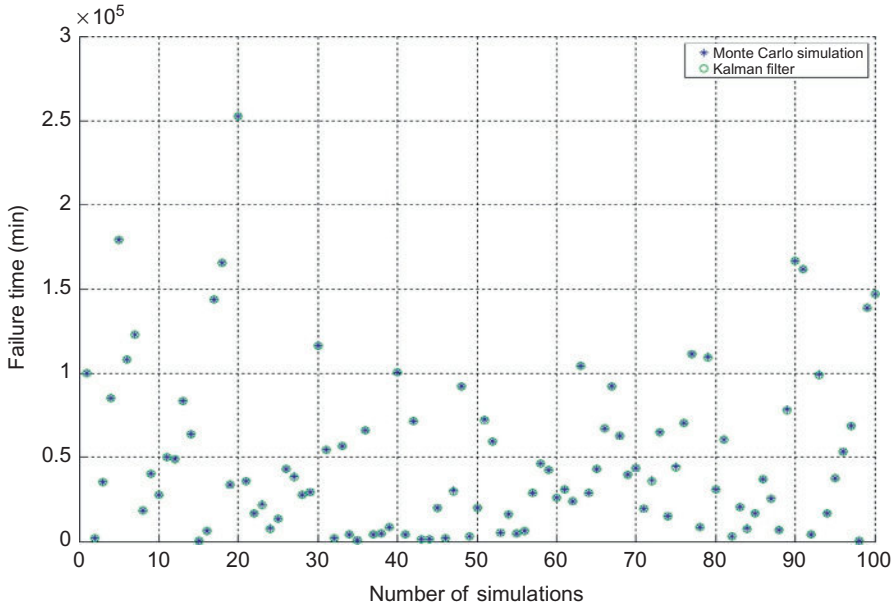

FIGURE 12.13

Failure times generated by Monte Carlo simulation and predicted by Kalman filter when $T=60$ min (for failure simulations of the rated high rotational speed).

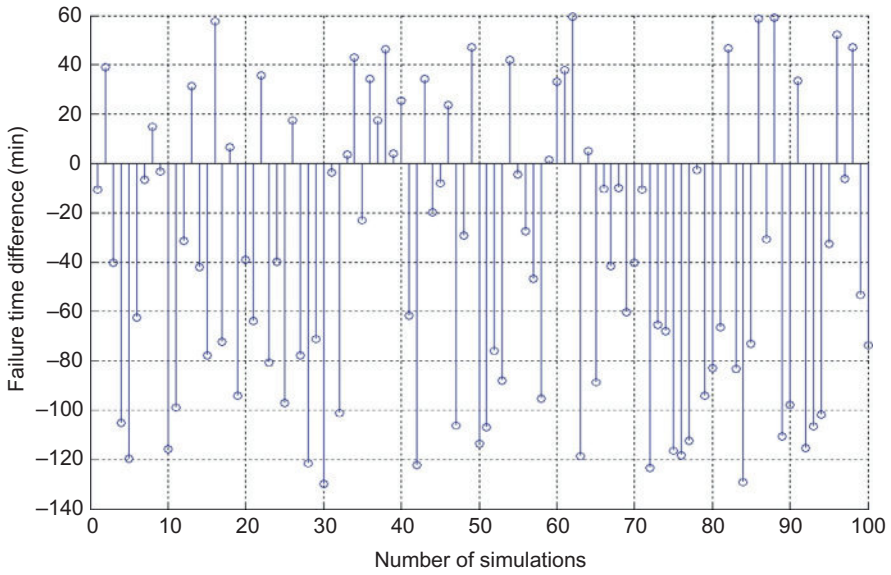

FIGURE 12.14

Differences between failure times calculated by Monte Carlo simulation and Kalman prediction when $T=60$ min (for failure simulations of the rated high rotational speed).

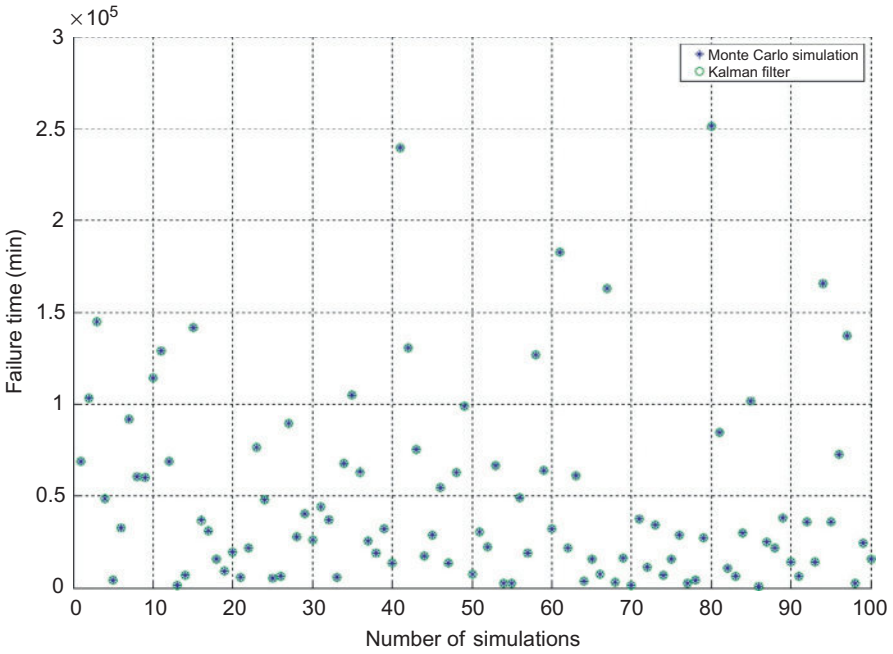

FIGURE 12.15

Failure times generated by Monte Carlo simulation and predicted by Kalman filter when $T=20$ min (for failure simulations of the rated high rotational speed).

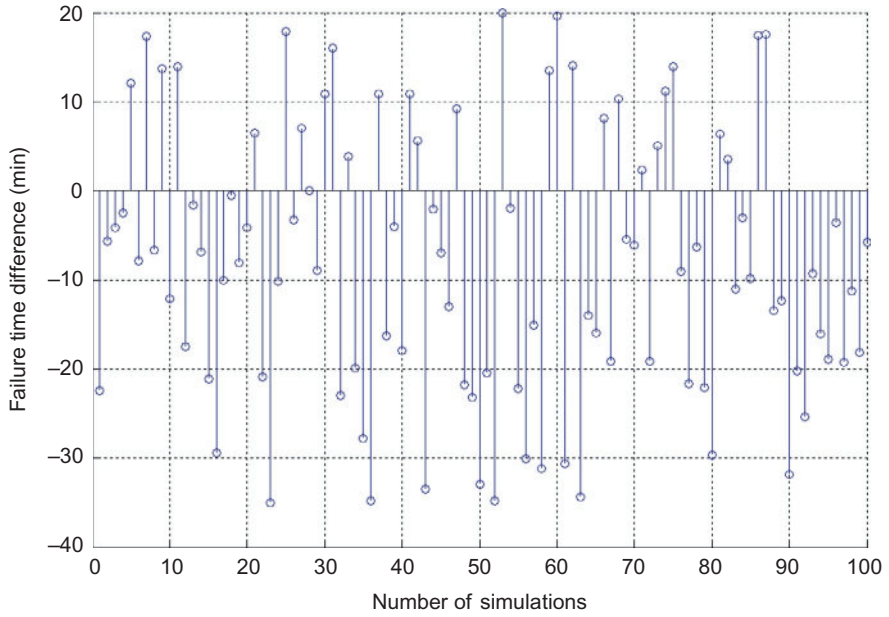

FIGURE 12.16

Differences between failure times calculated by Monte Carlo simulation and Kalman prediction when $T=20$ min (for failure simulations of the rated high rotational speed).

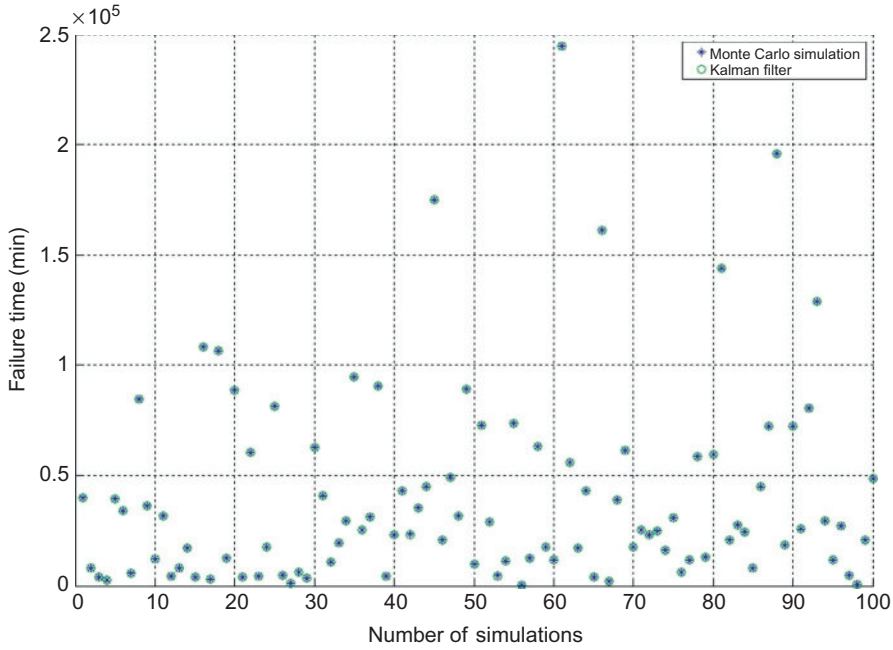

FIGURE 12.17

Failure times generated by Monte Carlo simulation and predicted by Kalman filter when $T=5$ min (for failure simulations of the rated high rotational speed).

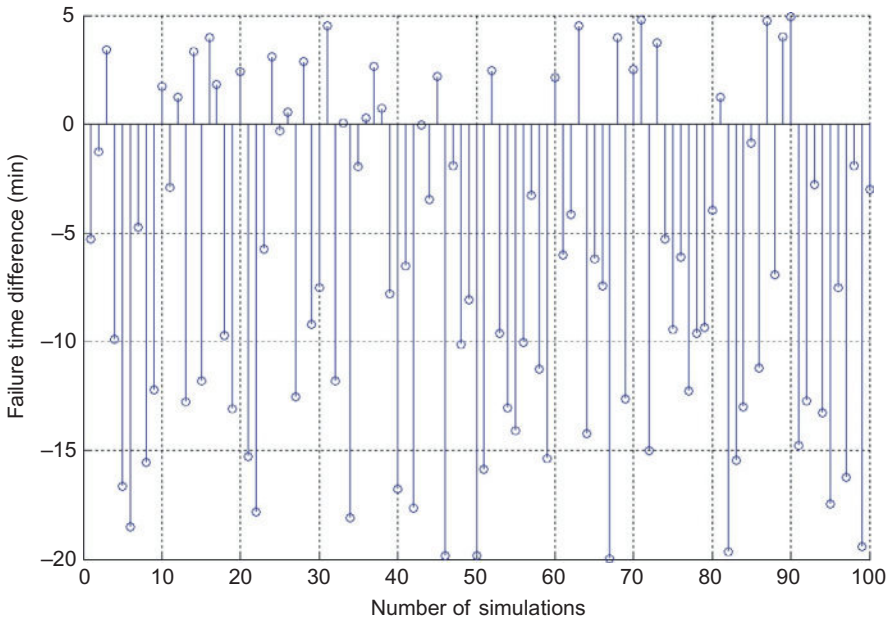

FIGURE 12.18

Differences between failure times calculated by Monte Carlo simulation and Kalman prediction when $T=5$ min (for failure simulations of the rated high rotational speed).

Table 12.3 Estimation results with 99% confidence level for simulations of the rated high rotational speed

T (min)	μ	σ	E_r	Confidence Interval
60	−39.22	57.92	14.91	(−24, −54)
20	−8.17	15.21	3.92	(−4.25, −12)
5	−6.93	7.60	1.96	(−4.87, −8.79)

5 FAILURE PROCESSING SCHEME

Based on the failure prediction function of the Kalman filter, this study proposes the failure-processing scheme for the 25 kVA generators as follows.

(1) Enhancing the equipped failure-processing function of the aircrafts.

Although, an IDF has been equipped with a monitoring system to indicate whether the AC power source has failed or not; however, this system does not take any action to avoid the occurrence of failures. The load switching is done after the occurrence of a failure anyway. The prediction capability of

the Kalman filter can enhance the failure-processing function of the system from mending after failure to preventing beforehand. Whenever the Kalman filter has estimated that one of the two generators is going to fail, a message will be sent to the corresponding GCU to complete the load switching before the failure actually occurs. The switching mechanism for failures of the 25 kVA generators is shown in Figure 12.19.

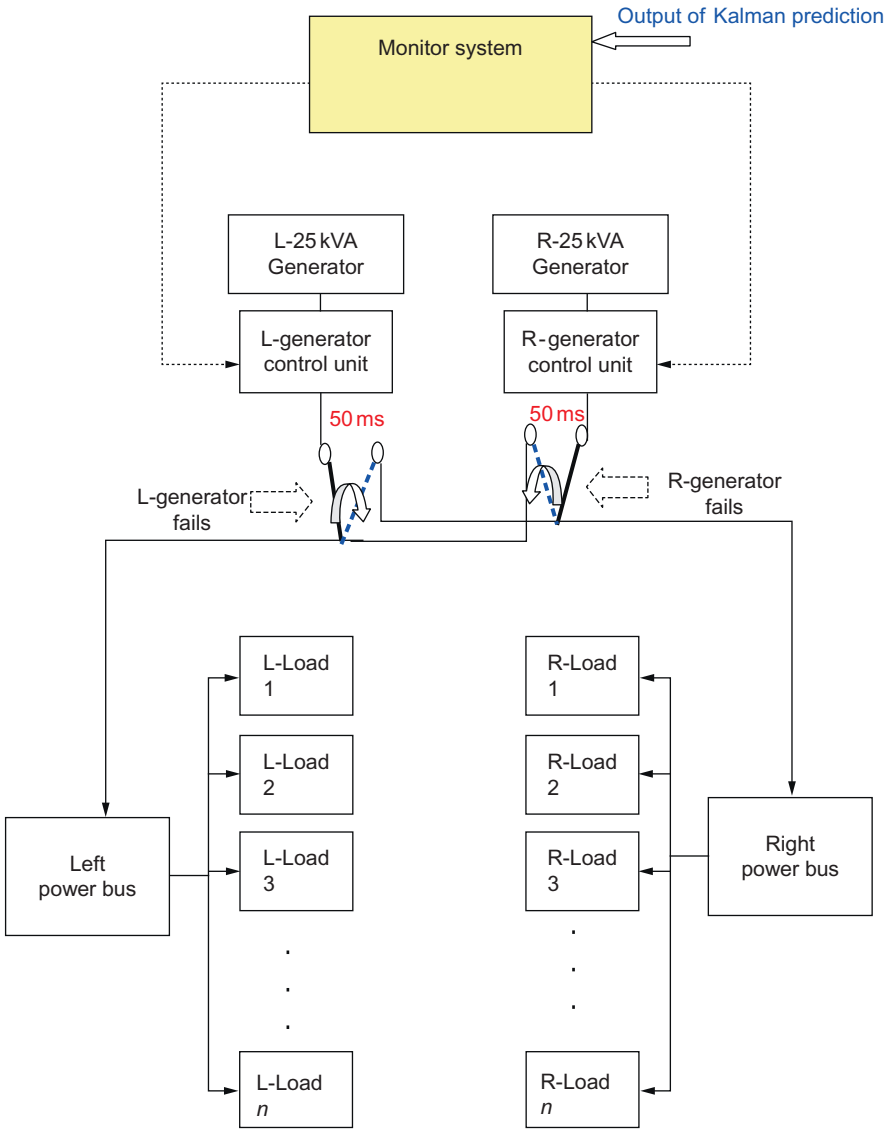

FIGURE 12.19

Switching mechanism for failures of the 25 kVA generators.

(2) Performing the isolated check by resetting the GCU.

According to past experience, sometimes a failure of the generators is temporary. Therefore, the generators are equipped with a reset function that can restart the failed (unloaded) generator and switch the load back to the original generator if the failed one has been restarted successfully. Therefore, the temporary failure can be eliminated. Combining this function with the Kalman prediction, the generator that is predicted to fail can be separately checked by resetting the GCU on the aircraft. On the other hand, if the restart is not successful, preventive maintenance should be done on that generator after the aircraft returns to the base in order to avoid actual failures or further damages. Hence the life of the generator can be extended.

6 DISCUSSIONS

(1) The proposed method in this study is exemplified by a synchronous generator, which is treated as a system. The procedure can be executed on a multicomponent system if state equations for the components can be constructed. Performing the procedure on either the multicomponent system as a whole or each of the components individually is equally feasible. For a complicated or large system, the proposed method can be performed on those elements in minimum cut sets that are constructed by fault tree analysis or the Petri net model for failure [13].

(2) Regarding multiple failure modes, they can be modeled to become modules, such as an attenuator for simulating an aging failure mode for a generator exemplified in this chapter, and placed at the system model output end to extend the proposed method. As depicted previously, the system model may be single component or multicomponent. Whether the failure modules are placed in serial, parallel, or other forms can be determined by system failure analysis [13]. As for a multicomponent system with multiple failure modes, the system can be taken apart, separated into several components, and placed in the related failure module(s) at the output end of each component to perform state estimation by Kalman filter for each.

7 RELIABILITY ANALYSIS

Assuming the failure rate of a random failed 25 kVA generator is λ, the reliability of the single generator is written as:

$$R(t) = e^{-\lambda t} \tag{12.25}$$

A configuration of redundancy is commonly used to promote the reliability of a system. For comparing the effect of redundancy design, reliabilities of three different configurations of redundancy for the two 25 kVA generators on an IDF are calculated.

(1) Active redundancy

The active redundancy is defined as that of two generators supplying power in parallel to the whole aircraft at the same time, and the system fails only if the two generators are failed. The reliability of this configuration (R_A) is formulated as [7]:

$$\begin{aligned} R_A(t) &= R + R - R \times R \\ &= 2e^{-\lambda t} - e^{2\lambda t} \end{aligned} \tag{12.26}$$

(2) Passive redundancy

The passive redundancy is defined as only one generator supplying power to the whole aircraft at a time, and the backup generator taking over if the operating generator fails. Assuming the failure rate of the switching device is p and the backup generator will not fail under the standby state, the Markov states and the state transition diagram of this configuration are described in Figure 12.20. Since state No. 3 will never happen, state transition equations for the other three states are derived as:

$$\frac{\mathrm{d}}{\mathrm{d}t}P_1(t) = -(1-p)\lambda P_1(t) - p\lambda P_1(t) = -\lambda P_1(t)$$

$$\frac{\mathrm{d}}{\mathrm{d}t}P_2(t) = (1-p)\lambda P_1(t) - \lambda P_2(t)$$

$$\frac{\mathrm{d}}{\mathrm{d}t}P_4(t) = \lambda P_2(t) + p\lambda P_1(t)$$

Hence, the reliability of the configuration (R_P) is:

$$R_p(t) = \sum_{i \in o} P_i(t) = [1 + (1-p)\lambda t]e^{-\lambda t} \tag{12.27}$$

Generator	State No.			
	1	2	3	4
Main	O	F	O	F
Backup	O	O	F	F

O : Operational, F : Failed

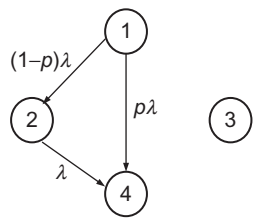

FIGURE 12.20

Markov states and the state transition diagram for the passive redundancy.

Table 12.4 Reliabilities Among Four Configurations for Mission Time from 100 to 800 h

	Reliability (h)							
Configuration	**100**	**200**	**300**	**400**	**500**	**600**	**700**	**800**
Single generator	0.8802	0.7748	0.6819	0.6003	0.5283	0.4651	0.4093	0.3603
Active redundancy	0.9856	0.9493	0.8988	0.8402	0.7775	0.7138	0.6511	0.5908
Passive redundancy	0.9925	0.9725	0.9430	0.9066	0.8654	0.8211	0.7749	0.7281
Present IDF's mutual backup	0.9856	0.9492	0.8988	0.8401	0.7775	0.7138	0.6511	0.5907

(3) Present IDF's mutual backup

The configuration of the present IDF's mutual backup has been described in the introduction section of this study. The function of this configuration is similar to the active redundancy except the switching device that should be included. Accordingly, the reliability of this configuration (R_I) is expressed as:

$$R_I(t) = \left(2e^{-\lambda t} - e^{2\lambda t}\right)(1-p) \tag{12.28}$$

Allowing $\lambda = 0.001276$ and $p = 0.0001$ [8], according to Equations (12.25) through (12.28), the reliabilities of the above four configurations for mission times from 100 to 800 h are calculated every 100 h. The results are shown in Table 12.4. The reliability roll-off trend of each configuration is shown in Figure 12.21. It is seen that the present IDF's configuration has very close results to the results of the active redundancy while the passive redundancy is the best among them.

8 CONCLUSION

The failure-processing scheme for improving the availability of the 25 kVA generators on an IDF has been presented. The scheme uses the state-estimation function of the Kalman filter to predict the occurrence of failures by estimating the future state variables of a 25 kVA generator and cooperating with the functions of load switching and system reset of IDFs in order to switch the load of the abnormal generator prior to its actual failure. This scheme has been verified by computer simulations. Comparing the failure times predicted by the Kalman filter with the results generated by MCS, no matter the low rated rotational speed simulation or the high rated rotational speed simulation, resultant errors are acceptable. The estimated mean value and the confidence interval of the mean of the estimated failure time difference between the

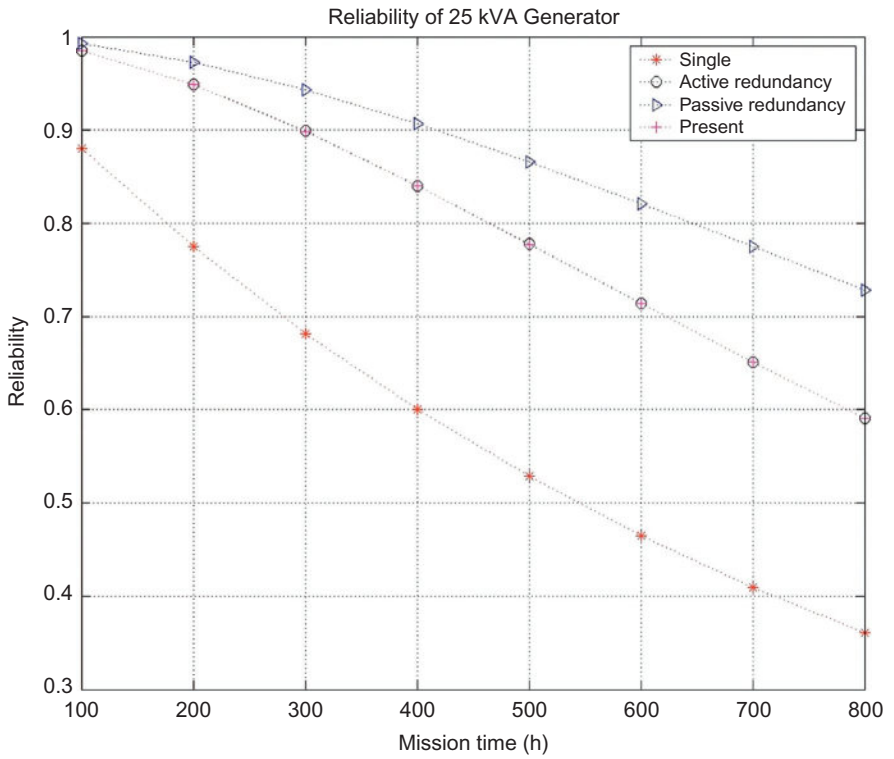

FIGURE 12.21

Reliabilities comparison among the four configurations.

results calculated by Kalman prediction and MCS is smaller if the increment time for every step in Kalman predictions is shorter. That is, the prediction accuracy is higher. Reliabilities of four configurations are compared as well: single generator, active redundancy, passive redundancy, and present IDF's mutual backup. The results show that the single generator has the largest roll-off rate and the passive redundancy has the best effect among the four configurations. The proposed scheme provides adequate time to perform a preventive maintenance on the generators such that not only the impact resulting from the irregular power on systems of the aircraft is mitigated but also it effectively improves the availability of the 25 kVA generators.

NOMENCLATURE

$\boldsymbol{A}_c, \boldsymbol{B}_c, \boldsymbol{C}_c, \boldsymbol{D}_c$	Coefficient matrix of the state equation for a continuous system
$\boldsymbol{A}_d, \boldsymbol{B}_d, \boldsymbol{C}_d, \boldsymbol{D}_d$	Coefficient matrix of the state equation for a discrete system
$\boldsymbol{A}^T$	Transpose matrix of A

A^{-1}	Inverse matrix of A
B	Damping coefficient
B_k	Coefficient matrix for the input term of a discrete state equation
H_k	Measurement sensitivity matrix
K_k	Kalman gain
$P_{k/k-1}$	Estimation error covariance matrix
Q_k	Plant noise covariance matrices
R_k	Measurement noise covariance matrices
U_k	Control input of a discrete state equation at state k
V_k	Noise, measurement error vector
W_k	Disturbance, system stochastic input vector
X_{D0}	Initial states resulting from deterministic input
X_k	System state vector at state k
X_{S0}	Initial states resulting from stochastic input
Y_k	System output vector at state k
Z_k	Output measurement vector
Φ_k	State transition matrix
ω_r	Angular speed of the rotor, electrical rad/s
ω_0	Rated speed of the rotor, electrical rad/s
δ	Rotation angle of the rotor, electrical radians
T_m	Mechanical torque, N m
T_e	Electromagnetic torque, N m
K_S	Synchronizing torque coefficient, pu torque/rad
K_D	Damping torque coefficient, pu torque/pu speed deviation
H	Inertia constant, MW s/MVA

REFERENCES

[1] Yang SK. An experiment of state estimation for predictive maintenance using Kalman filter on a DC motor. Reliab Eng Syst Saf 2002;75(1):103–11.

[2] Sundstrand, Technical Manual USC 8A6-7-201-3, Generator, AC Part No. 950 F220-1; 1996.

[3] Anderson BDO, Moore JB. Optimal filtering. Englewood Cliffs, NJ: Prentice-Hall; 1979.

[4] Brown RG, Hwang PYC. Introduction to random signals and applied Kalman filtering. New York: Wiley; 1997.

[5] Kundur P. Power system stability and control. New York: McGraw-Hill; 1994.

[6] Phillips CL, Nagle HT. Digital control system analysis and design. Englewood Cliffs, NJ: Prentice-Hall; 1990.

[7] Rao SS. Reliability-based design. New York: McGraw-Hill; 1992.

[8] Handbook of Total Logistic Support System, Aerospace Industrial Development Corporation, Taiwan, 2007.

[9] Chiang-Lin CY. Parameter estimation and fault diagnosis on the thermal network by applying the extended Kalman filter and the expert system. [M.S. thesis]. Taiwan, Republic of China: National Chao Tung University; 1991.

[10] Webster JD, Palla's-Areny R. Sensor and signal conditioning. New York: Wiley; 1992.

[11] Prime item product fabrication specification for Indigenous Defensive Fighter: 25kVA Generator System. Specification:AC8-70-002C; Aerospace Industrial Development Corporation, Taiwan, 1992.
[12] Black K. Business statistics, contemporary decision making. Los Angeles: West Publishing; 1997.
[13] Yang SK, Liu TS. Failure analysis for an airbag inflator by Petri nets. Qual Reliab Eng Int 1997;13:139–51.

CHAPTER

Fatigue failure in aircraft structural components

13

Selim Gürgen*, Melih C. Kuşhan*, Seyid F. Diltemiz†
*Department of Mechanical Engineering, Eskişehir Osmangazi University, Eskişehir, Turkey**
Turkish Air Force, 1st Air Supply and Maintenance Center Command, Eskişehir, Turkey†

CHAPTER OUTLINE

1 INTRODUCTION

Fatigue is a failure process developed by the effect of the cyclic loadings. Failure in the material can occur at the stress levels below the monotonic yield strength of the material [1]. Fatigue was first recognized in 1830s. A civil servant named Wilhelm Albert introduced the first metal fatigue test in 1837. The test was performed with actual conveyor chains under real conditions as in the Clausthal mines in Germany [2]. Albert made the test to find the cause of the chain failure in the service and reported that the failure was arising from repetitive loading not overloading [2,3]. This phenomenon was called fatigue and this term was used in print for the first time in 1854 [3].

Fatigue is the most common cause of the failures in metals with an estimation of 90% frequency [4]. The first known fatigue failure was recorded as Versailles railway accident in 1842 [2]. During the journey, one of the axles of the locomotive was broken due to metal fatigue and the carriages passed over the locomotive [2,3]. In aviation industry, Comet airliner crashes are the typical examples of metal fatigue failure. In 1954, Comet air crashes happened within successive 3 months. Injury patterns in both crashes exhibited that the aerial window mounted to the cabin roof by riveting

Handbook of Materials Failure Analysis With Case Studies from the Aerospace and Automotive Industries.
http://dx.doi.org/10.1016/B978-0-12-800950-5.00013-2

produced microcracks around the rivet holes. Repeated pressurization of the aircraft cabin accelerated the crack propagation by the effect of metal fatigue. Then the joining section of the aerial window could not withstand the internal pressure of the aircraft cabin and the fuselage exploded catastrophically in the sky. It was later proven by the conducted investigation tests that up to 70% of the aircraft's ultimate stress accumulated on the corners of the aircraft's windows [5]. Today, aircraft failures due to metal fatigue are at the lowest level with respect to the failures happened before [6].

Fatigue in metallic materials develops under three stages which are crack nucleation, crack propagation, and failure. Crack nucleation is the spark of the fatigue mechanism and can be easily emerged by the effect of environmental influences. For example, some of the manufacturing processes such as machining leave tool traces or scars on the material surfaces and create crack origins. Crack nucleation generally locates at the plastic strain accumulation regions such as sharp notches, nonmetallic inclusions or crack-like defects [1]. In crack propagation stage, material is subjected to interrupted loadings. Failure surface includes striations and each striation displays a time interval which crack propagation happened. Striation width increases with increasing the stress level. Finally, in the failure stage, reduced cross-sectional area of the material cannot bear the acted loads and the material ruptures. Failure surface shows either ductile or brittle fracture characteristics depending on the material. Generally, this stage passes very fast and rupture occurs suddenly. In ductile fracture, plastic deformation takes place and the failure is procrastinated for a while. However, failure is seen without plastic deformation in brittle fracture [4].

Fatigue is very important failure mechanism that has to be taken into consideration under dynamic loadings for the structural integrity. According to Schijve, polished surfaces including about 100-μm length crack can reduce the material's fatigue life of 60% to 80% [6].

In engineering design, fatigue in metallic materials is characterized by determining their endurance limits under repeated loadings. For this purpose, a series of specimens are subjected to specified stress amplitude (S) until failure. Then each number of cycles to failure (N) is plotted as the abscissa with respect to the applied stress as the ordinate. This graph is called *S-N* diagram of the material. Generally, number of the cycles to failure is plotted in logarithmic form since the number of the cycles is quite extensive. *S-N* curves after a certain number of cycles show horizontal trend for most of the materials. This trend indicates a maximum stress level which causes no failure in the material. Therefore, fatigue limits of the materials can be determined from the *S-N* diagrams. However, for some materials such as aluminum, *S-N* curves never become horizontal. For this kind of materials, fatigue limit is defined as the stress at a specified number of cycles (e.g., 5×10^8 for aluminum). Typical values are available in the handbooks of the engineering materials [7]. Figure 13.1 shows *S-N* curves of two different materials. Material-1 exhibits a fatigue limit of S_1 where the stable trend is attained at the number of cycles N_1. Material-2 does not exhibit a fatigue limit. However, S_2 is assumed as fatigue limit which is the stress at the number of cycle N_2 for Material-2.

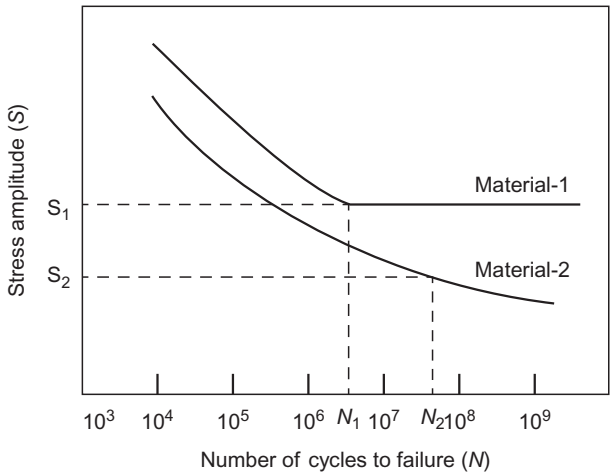

FIGURE 13.1

S-N curves of different materials.

2 FAILURE ANALYSIS OF AN AIRCRAFT PROPELLER

Cessna-185, known as Skywagon, is a single engine aircraft which is updated from model 180. Basically, model 185 has strengthened fuselage and more powerful engine with respect to the model 180. The first flight of the model 185 was performed in 1960. In 1962, military version was introduced. This version was denoted by U-17. Cessna-185 has a piston aircraft engine and crankshaft of the engine is connected to a propeller with two blades [8]. General appearance of a Cessna-185 is shown in Figure 13.2.

FIGURE 13.2

Cessna-185 during takeoff.

The aircraft mentioned in this case study is a U-17B which is a variant of model 185 produced for military purpose. The power unit of the aircraft is a 300 HP (224 kW) Continental IO-520-D piston engine. The failed propeller on the tip of the crankshaft was made of 2024 aluminum alloy. 2000 series high-strength aluminum alloys are widely used in the aerospace industry due to their high resistance to crack growth, good repairability, and high damage-tolerance properties. Moreover, 2000 series are also known as aerospace aluminum alloys and their strengths are comparable to steel [9].

After the investigation of the failed propeller, it was shown that failure of the propeller took place by breaking one of the blades during the flight. The propeller was assembled to the aircraft in 1970 and had 1850 total flight hours. Moreover, the last inspection was performed just 50 flight hours before the accident.

During the service life, all aircraft are inspected by scheduling certain periods. In these inspections, non-destructive testing (NDT) is used to check the components. Among the NDT methods, fluorescent penetrant inspection (FPI) is the most common technique to detect the flaws on the part surfaces. Inspection procedure of the propeller is performed by disassembling the propeller from the engine, removing the surface paint, and applying FPI, respectively. After cleaning the inspection surface, fluorescent penetrant is applied. Low-viscosity penetrants are chosen to easily penetrate into the defects on the surface. Excessive penetrant is removed and then surface stays waited for the penetrant-filled defects. Next, a powder material called developer is applied which absorbs the trapped penetrant from the defects and makes the indication visible. Most of the penetrants are visible under ultraviolet light. Therefore, inspection is performed in dark rooms by using ultraviolet radiation. Besides, visible penetrants under day light are available in the industry. Scratches, dents, and collapses are usual flaws in the inspections because the propellers are open to airborne strikes.

2.1 PROPELLER AFTER FAILURE

The fracture line separated the blade into two pieces. The upper piece was lost during the accident and the lower piece stayed connected to the propeller hub. Fracture was located at one third of the total length from the blade root as seen in Figure 13.3. There were many deformation points on the blade surface as given in Figure 13.4. The deformed areas provided the intense clue that the failure was induced by foreign object damage.

Since 2024 aluminum alloy includes copper, it is susceptible to stress corrosion crack (SCC). SCC is crack propagation by the effect of tensile stress and corrosive environment. Material susceptibility is the complementary parameter in the process. Tensile stress takes part in the process to open cracks on the material surface. SCC formation is seen under sustained loading which is either applied stress or residual stress. Cold forming, welding, machining, and heat treatment are main sources to store the residual stress into materials [10]. SCC initiative environments change according to the materials. For aluminum alloys, chlorides and seawater are effective mediums. In the aircraft components, flight conditions induce underestimated cracks by the effect of fatigue. After condensation of water inside the cracks, SCC is easily

FIGURE 13.3

Broken propeller blade.

FIGURE 13.4

Deformation points on the blade surface.

initialized by the conjoint action of chemical reaction and tensile stress. Deposition of water containing Cl^- ions brings in convenient environment for SCC by considering the extensive usage of aluminum alloys in the aircraft [10,11]. SCC is rare but very dangerous that ends up with catastrophic failures. It is very common to clad the surface of the 2000 series aluminum alloys with high-purity aluminum against the chemical reactions. This process improves the passivation of the surface and protects the material against the aggressive environments [11].

Investigation was focused on the crack surface to search for corrosion in this vicinity. But it was seen that there were no intensive corrosion, oxidation, or deposition of dirt on the crack surface explaining SCC.

2.2 FAILURE MECHANISM OF THE PROPELLER BLADE

Remaining components after an accident have great importance to understand the root cause of the problem. For this reason, the broken blade was investigated profoundly in this accident. Investigation was conducted by evaluating stereo microscope and scanning electron microscope (SEM) images.

Crack surface had two different planes which were tagged by Zone-I and Zone-II as given in Figure 13.5. Zone-I was at the leading edge side and perpendicular to the XZ plane, whereas Zone-II was at the trailing edge side and had about 45° angle to the XZ plane as seen in Figure 13.6. The surface characteristics of these two planes were relatively different. Zone-I had brighter surface due to its smooth surface, whereas Zone-II had dull surface resulting from roughness making the light less reflected.

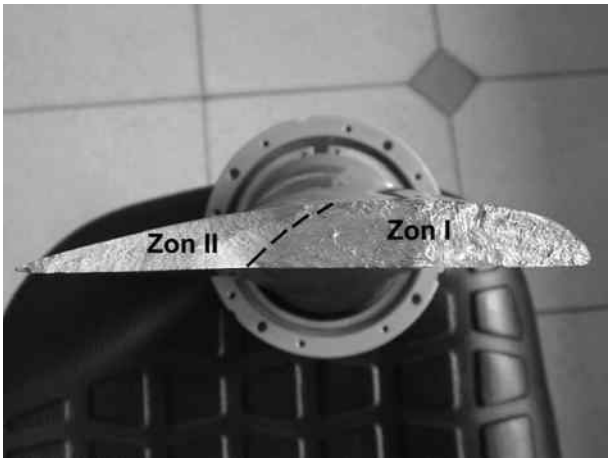

FIGURE 13.5

Zone-I and Zone-II on the crack surface of the propeller blade.

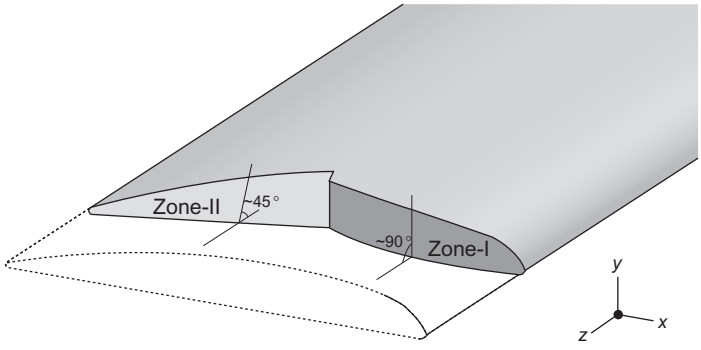

FIGURE 13.6

Characteristics of the crack surface.

FIGURE 13.7

SEM image of the propeller blade Zone-I.

Examination of the Zone-I showed that the fatigue striations were obvious under the microscope as seen in Figure 13.7. These striations were in the semi-elliptical circles form and result of the cyclic loadings. The striation circles overspread from a center point, which was the starting point of crack propagation, located at the lower surface of the blade. Generally, cracks launch from a surface flaw rather than in-body flaws and cyclic loadings accelerate the crack growth process. These flaws can be scratches, notches, burrs, or dents where the local stresses are prone to increase. Geometrically, these kinds of discontinuities cause notch effect by the effect of increased local stresses and facilitate the microcrack formations. Once a crack starts off, it moves on until failure of the structure. In addition to this, since the discontinuities are formed as a result of an impact, strain hardening takes place on the impact areas. Locally strain-hardened areas increase the hardness of the material and initialize brittle crack propagations easily [12].

In the broken propeller blade case, the starting point of the crack was a dent on the lower surface as shown in Figure 13.8. The dent size was explained by a depth of 140 μm and a width of 3060 μm.

After discovering the crack propagation source, investigation was focused on this point to reveal the root cause. The findings were weird that the dent was covered by paint. Figure 13.9 shows the SEM image of the paint layer on the dent area.

Maintenance reports showed that the propeller was inspected 50 flight hours before the accident. In the inspection process, blade paint was removed from the part surface and then inspection was performed against the surface problems. However, there was no defect detection in the maintenance reports. If the dent had been formed before the last inspection, residual paint should have been on the crack surface. Because after the inspection, the blade was painted again therefore, the microcracks on the dent area must have included paint debris. On the contrary, microcracks were such tiny that the paint could not penetrate into despite the capillary effect [13].

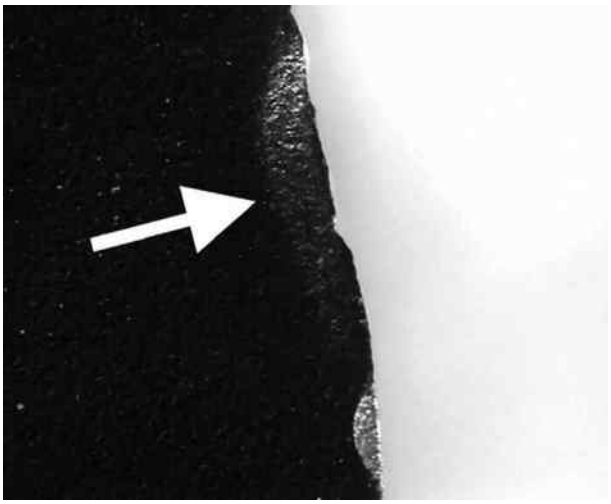

FIGURE 13.8

Crack propagation point.

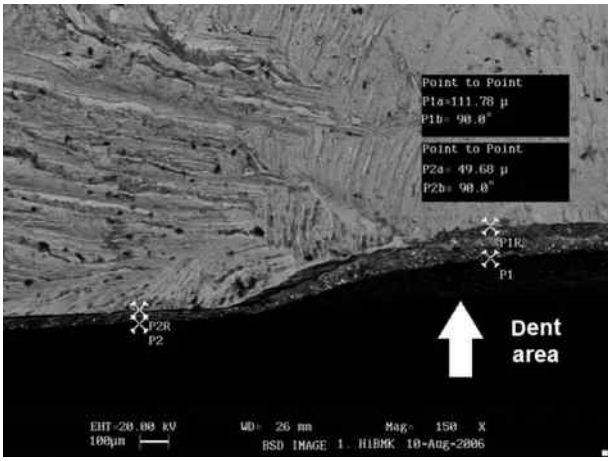

FIGURE 13.9

SEM image of dent area.

Another scenario is that the dent was formed after the last inspection by striking of foreign object without peeling the paint. In the airborne strike, the paint on the blade must have been flexible to be able to stay clean on the surface. To show the possibility of this scenario, paint layer flexibility test was conducted. In the test, a painted surface was deformed by using Brinell hardness indenter (BMS HB-3000B, 1st Air Supply and Maintenance Center Command, Turkey). There was no paint spalling or peeling after the test. It proved the flexibility of the paint layer but never simulated the real impact conditions.

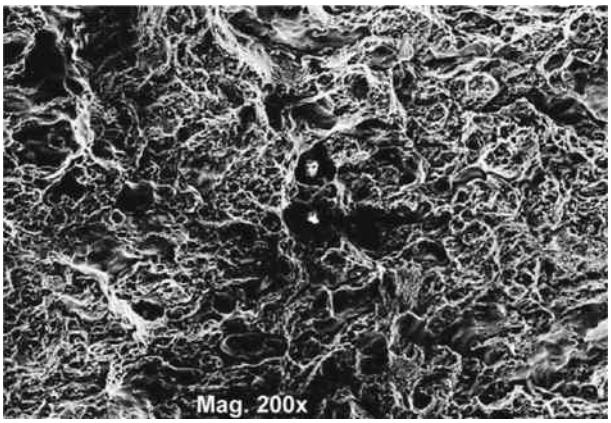

FIGURE 13.10

SEM image of the propeller blade Zone-II.

In the examination of Zone-II, the crack surface had dimpled appearance as seen in Figure 13.10. This kind of crack surface including little holes indicated a ductile-type fracture under monotonic loadings [4].

It was obvious that the dent on the lower surface of the blade was formed by impact of a foreign object. The dent was the key point for the failure mechanism because it brought about the notch effect and initialized microcracks. During the service time, microcracks propagated by the effect of the cyclic loadings. Fatigue striations were the intense proof on the Zone-I. After the fatigue striations reached the end point of the Zone-I, the blade kept a critical cross-sectional area which was not enough to carry the acted loads. Eventually, the critical cross-sectional area was exposed to a ductile-type fracture and Zone-II was formed.

Investigation also revealed the fatigue characteristics by evaluating the fatigue striations on the Zone-I. If the fatigue area increases, the structure is said to be exposed to low-magnitude cyclic loading with high number of cycles which is shortly high-cycle fatigue (HCF). Conversely, if the fatigue area decreases, high-magnitude cyclic loading with low number of cycles, as known as low-cycle fatigue (LCF), is seen on the structure. For Zone-I, the fatigue was in the trans-regime.

In HCF, stress levels on the structure are lower and deformations are elastic. Therefore, large numbers of cycles are required to cause failure. Generally, numbers of cycles greater than 10^4 to 10^5 are seen in HCF. However, stress levels cause plastic deformations and the failure occurs at the low numbers of cycles such as less than 10^4 to 10^5 in LCF [4].

2.3 DISCUSSION ON THE FAILURE OF PROPELLER BLADE

The failure mechanism after the dent formation is given above. As explained, the failure developed as a result of typical fatigue in the ductile material. However, the root cause of the failure was the dent and it was debatable whether

the dent was formed before the last inspection. About this issue, two estimations are given below:

(i) Dent was formed by an airborne strike after the last inspection and the paint was flexible enough to compensate the impact energy. Therefore, the paint remained on the dent surface without any damage (i.e., spalling, peeling).

(ii) Dent was formed by an airborne strike before the last inspection and the inspection could not reveal it. Also, the paint while painting process could not penetrate into the microcracks that the investigation detected no paint debris on the crack surface.

The second estimation is more possible that the measurements of the paint thicknesses introduced realistic clues. According to the measurements, thickness of the paint layer was 50 μm on the correct surface and 112 μm on the dent area. It means that the dent was formed before the last inspection and acted as a pool on the surface during the final painting process. Consequently, the paint deposition was located inside the dent.

3 FAILURE ANALYSIS OF A FLAP ACTUATOR ROD

F-4 Phantom is a supersonic combat aircraft produced for the United States Navy by McDonnell Aircraft (later McDonnell Douglas). The first flight was performed by XF4H-1 prototype in 1958. After proving its power and versatility, F-4 was also spread to the U.S. Marine Corps and the U.S. Air Force. The Great Britain was the first foreign customer for the Phantom. After 1960s, the Phantom was recognized globally and exported to many countries. The main operators are Egypt, Germany, Greece, Iran, Israel, Japan, South Korea, Spain, Turkey, United States, and United Kingdom [14,15].

F-4 was widely used during the Vietnam War, especially for the ground attack and reconnaissance missions. Today, the Phantom is retired by some of the user countries. However, it serves as reconnaissance and interceptor fighter in the F-4 active countries. Figure 13.11 shows an F-4 Phantom fighter during takeoff.

FIGURE 13.11

Phantom during takeoff.

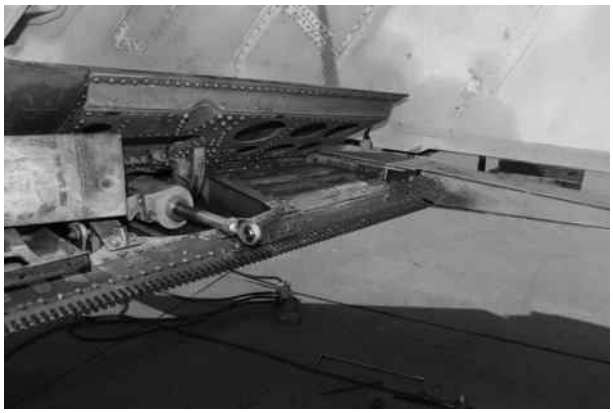

FIGURE 13.12

An actuator located inside the wing.

The case study is about the failure of a Phantom flap actuator rod. Basically, an actuator is a kind of motor that converts energy into mechanical motion. In terms of the energy source, actuators are divided into different groups such as electric, hydraulic, and pneumatic [16]. In the aircraft, main application areas of actuators are landing gears and control surfaces such as rudder, ailerons, elevators, stabilizers, spoilers, and flaps. These structural units lead the air flow by the motion of the actuator mechanisms. Since the actuators are directly related to the aircraft control so the flight safety, they play critical roles during the flights. Figure 13.12 shows an actuator mounted within the interior of a fighter wing responsible for the control surfaces.

In this case study, one of the flaps lost the mobility during the flight. Fortunately, the aircraft could make the landing safely and the investigation procedure was carried out to find the root cause of the problem. First inspection revealed that the cap section of the actuator rod was broken. The rod had a ball bearing inside the hole drilled on the cap section and the failure occurred near along the diameter of the hole. Figure 13.13 shows the failed section of the actuator rod.

3.1 FAILURE MECHANISM OF THE ACTUATOR ROD

Macroscopic examination showed that the cap section of the rod was broken clearly and that there were no evidence of dent, scratch, or deformation neck in the vicinity of the crack. General condition of the rod was good out of the crack zone. There was no evidence of dirt explaining corrosion on the crack surface. Corrosion on the parts can cause fatigue damages particularly in contact surfaces (e.g., surface between hole and ball bearing). Therefore, avoiding of contact fatigue is very important for the structural reliability. Corrosion fatigue is formed by the combined effect of cyclic stress and corrosive environment in the structure. This term should not be confused with stress corrosion crack. In corrosion fatigue, corrosion decreases the strength of the material and

FIGURE 13.13

Failed section of the actuator rod.

the material fails at lower stresses. Dynamic forces act on the aircraft components inevitably and most of the failures are in the category of fatigue fractures [17,18].

At the beginning of the investigation, the crack surface was divided into two regions due to different surface characteristics. The smooth regions with shiny appearance were labeled by Zone-I and the dull regions were labeled by Zone-II as seen in Figure 13.14.

In the microscopic examination, stereo microscope and SEM images were employed. The images were evaluated and for Zone-I, it was stated that there were fine fatigue striations which were stemmed from cyclic loading as seen in Figure 13.15. Propagation points of the striations indicated that V-shaped dents around the hole had started the crack growth (Figure 13.16). The V-shaped dents were formed at the junction of the hole and the ball bearing to fix the bearing secure inside the hole.

In the Zone-II examinations, the failure was explained as a typical ductile fracture. SEM images showed that the Zone-II had rough surfaces including equiaxial dimples as shown in Figure 13.17. These surface characteristics explained that the component was subjected to uniaxial tensile loading rather than shear loading. Because, ductile materials develop microvoids inside the body and since the loading

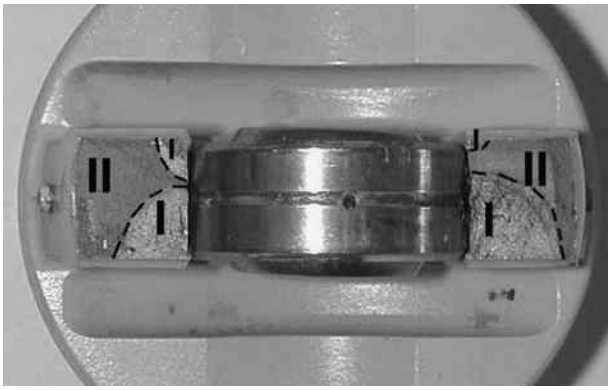

FIGURE 13.14

Zone-I and Zone-II on the crack surface of the actuator rod.

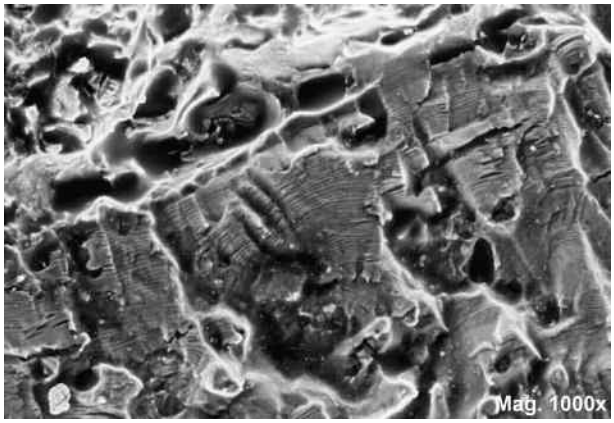

FIGURE 13.15

SEM image of the actuator rod Zone-I.

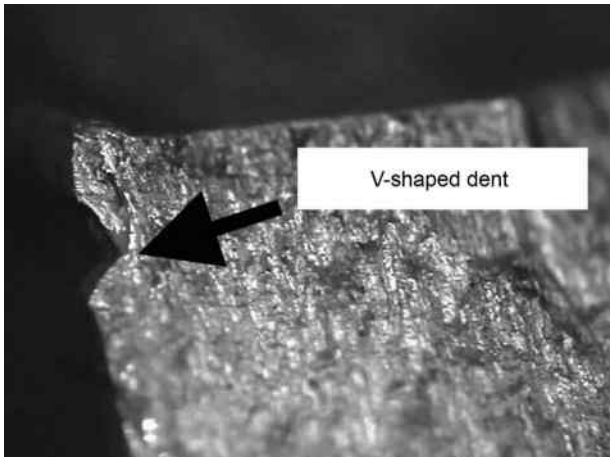

FIGURE 13.16

V-shaped dent as crack propagation point.

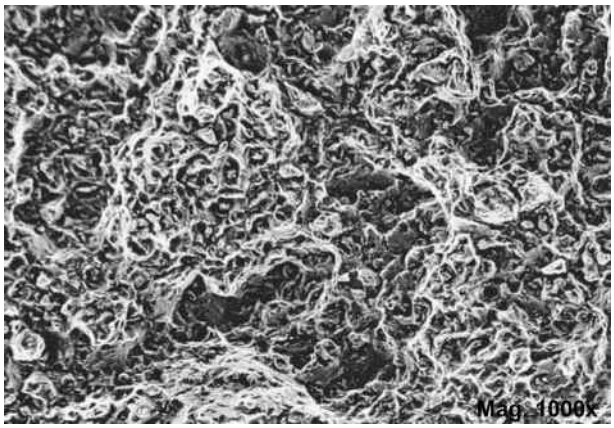

FIGURE 13.17

SEM image of the actuator rod Zone-II.

acts perpendicular to the fracture surface, the microvoids are elongated in the normal direction of the fracture surface. Fracture line intersects the microvoids and they are seen as spherical dimples under the microscope. However, in the shear loadings, dimples are seen in elliptical or C-shaped form because of the horizontal elongation of the microvoids with respect to the fracture surface.

3.2 DISCUSSION ON THE FAILURE OF ACTUATOR ROD

According to the investigation results, fatigue crack initiation was stemmed from the V-shaped dents which were design errors to constraint the ball bearing in the hole. Microcracks nucleated in the sharp root of the dents and propagated by the effect of cyclic loadings in the part. Finally, the cross-sectional area was so reduced that the rod cap ruptured.

Loading characteristic was also understood from the investigation that the cap section of the rod was subjected to double bending in the service. There were four crack initiation sites on the fracture surface. Furthermore, as seen in Figure 13.14, the fatigue areas (Zone-I) were wider at the bottom side than at the upper side of the fracture surface that unsymmetrical bending acted on the component.

The problem source was found as the V-shaped dent which accumulated the stress and expedited the crack growth. The V-shaped dent was a design error, which was performed by squeezing operation in assembly stage, and must have replaced by a safe method. Figure 13.18 shows a recommended forming method with larger root radius to distribute the stress accumulation while constraining the ball bearing inside the hole. Additionally, locations of the squeezing operation were very important in terms of failure since the maximum stresses affect certain sections of the rod cap. Locations of the V-shaped dents are given by circles and the recommended locations where the stresses are less during the service conditions are given by lines in Figure 13.19.

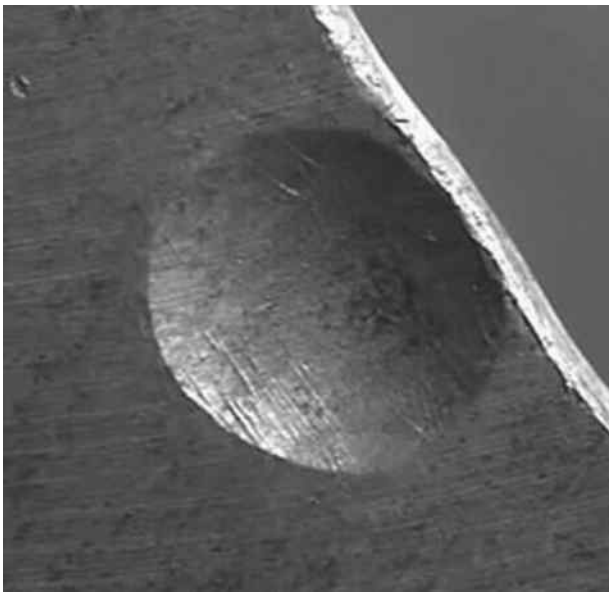

FIGURE 13.18

Recommended squeezing point with larger root radius.

FIGURE 13.19

Actual (circles) and recommended (lines) locations of the squeezing operation.

4 CONCLUSION

Aircraft components are exposed to complicated loadings during the flights. Static loadings act on the components at the steady-state conditions. However, dynamic loadings are more prominent since the conditions are changeable while flying. Each part of the aircraft responds dynamically to the forces acting during the flight phases such as taxi-bump or landing. Moreover, the structure exhibits more intense response in the extreme conditions such as gusts or bird strikes.

Cyclic loading is a kind of dynamic loading that may end up with material fatigue. Fatigue is the most common cause of structural failure in the aircraft. For this reason, service lives of the components are described by flight hours and the components are substituted after certain periods in the aircraft by considering material fatigue limits.

REFERENCES

[1] Schijve J. Fatigue crack closure: observation and technical significance. In: Newman JC, Elber W, editors. Mechanics of fatigue crack closure. Philadelphia: ASTM; 1988. p. 5–34.
[2] Schütz W. A history of fatigue. Eng Fract Mech 1996;54(2):263–300.
[3] Pook LP. Historical background. In: Metal fatigue what it is, why it matters. London: Springer; 2007. p. 7–13.
[4] Callister WD, Rethwisch DG. Failure. In: Materials science and engineering: an introduction. Hoboken, NJ: John Wiley & Sons; 2010. p. 235–80.
[5] 'Metal fatigue' caused Comet crashes. In: BBC On This Day 1950–2005, http://news.bbc.co.uk/onthisday/; 19 October 1954.
[6] Newman JC Jr. Advances in fatigue and fracture mechanics analyses for metallic aircraft structures. NASA Langley Technical Report Server 2000;210084:1–45.
[7] Hibbeler RC. Mechanical properties of materials. In: Mechanics of materials. Upper Saddle River, NJ: Pearson Prentice Hall; 2005. p. 85–113.
[8] Lee HC, Hwang YH, Kim TG. Failure of aircraft propeller assembly. Eng Fail Anal 2004;11:305–12.
[9] Kushan MC, Zafer N. Structural materials of aeroplanes (in Turkish). In: I. Ulusal Metalurji ve Malzeme Günleri. Eskisehir. p. 368; 2004.
[10] Lynch SP. Mechanistic and fractographic aspects of stress-corrosion cracking. In: Raja VS, Shoji T, editors. Stress corrosion cracking theory and practice. Philadelphia: Woodhead; 2011. p. 1–130.
[11] Davis JR. Environmentally assisted cracking. In: Corrosion of aluminum and aluminum alloys. Ohio: ASM International; 1999. p. 99–134.
[12] Kushan MC, Diltemiz SF, Sackesen I. Failure analysis of an aircraft propeller. Eng Fail Anal 2007;14:1693–700.
[13] Kushan MC, Erdem M, Saracyakupoglu T. EB Varestraint test method and an application. In: 23rd International Council of Aeronautical Sciences. Congress, Toronto; 2002. p. 8–13.

[14] Jackson R, editor. McDonnell F-4 Phantom. In: The encyclopedia of aircraft: over 3,000 military and civil aircraft from the Wright flyer to the Stealth bomber. San Diego: Thunder Bay; 2004. p. 336–7.
[15] Kushan MC. F-4 Phantom. In: A'dan Z'ye Dunya Ucakları ve Helikopterleri (in Turkish). Eskisehir: Nisan. p. 63; 2004.
[16] Gomis-Bellmunt O, Campanile LF. Actuator principles and classification. In: Design rules for actuators in active mechanical systems. London: Springer; 2010. p. 3–28.
[17] Kimura Y, Sekizawab M, Nitanai A. Wear and fatigue in rolling contact. Wear 2002;253:9–16.
[18] Bhaumik SK, Sujata M, Venkataswamy MA. Fatigue failure of aircraft components. Eng Fail Anal 2008;15:675–94.

CHAPTER

14 Chemical analysis techniques for failure analysis: Part 1, common instrumental methods

William J. Wolfgong

Raytheon Space and Airborne Systems, Component Engineering Department, McKinney, Texas

CHAPTER OUTLINE

Handbook of Materials Failure Analysis With Case Studies from the Aerospace and Automotive Industries.
http://dx.doi.org/10.1016/B978-0-12-800950-5.00014-4

1 INTRODUCTION

Chemical analysis techniques are often crucial in determining root cause during failure analyses and compliment other methods such as visual examination, microscopy, and physical analyses. These methods are employed to determine the chemical compositions of materials to answer questions such as: was an assembly constructed with the proper materials in the proper ratios; is contamination present which could contribute to failures and if so what is its nature and source; are materials releasing volatile compounds which can contribute to failures; what is the composition of the atmosphere within a specific environment.

In this chapter, the operating principals of many of these techniques are discussed. Examples of how these methods may be applied to failure analyses as well as inherent limitations are also highlighted. In the second part of this work, specific examples (case studies) are given to demonstrate how these methods are applicable to real-world failure analysis challenges.

2 BASIC OPERATING PRINCIPLES, APPLICATIONS, AND LIMITATIONS OF COMMON TECHNIQUES

As is common with most all technical fields, the analytical sciences rely on a variety of techniques which are most commonly referred to using acronyms; these are defined as each technique is introduced and described in this section. Each of these is the subject of books and book series, graduate classes, doctoral dissertations, and advanced research applications. However, only a basic understanding is necessary for most of the general engineering and scientific populations whose job descriptions include failure analysis. This is important as during initial phases of failure analyses, very often, decisions are made concerning analytical method selection for root cause determinations. A good understanding of the various analytical techniques, even for nonexperts in material science, leads to more efficient failure analysis routes hastening time to resolution and cost of root cause determination.

For example, if the goal of an analysis is to simply verify that the proper class of polymer was used in a specific application, a simple infrared spectrum will often provide a very quick and relatively inexpensive answer. On the other hand, if the analyst selects an elemental analysis technique such as energy dispersive spectroscopy (EDS) using a scanning electron microscope (SEM) the analysis is likely to be much more costly and is incapable of supplying the desired information.

In most cases, with regard to the amount of sample available for analysis, the more the better. Also, the ability to analyze samples without regard to maintaining sample integrity, i.e., destructive analysis, is desirable. While ideal, these circumstances are more often the exception and not the rule. With this in mind, a basic understanding of the sample size requirements for the various techniques is useful. Also, what constitutes a destructive analysis is not always as straightforward as it may seem and such knowledge can help guide proper technique selection. Another concern, that quite often is overlooked, is the fact that form of the sample may dictate available methodologies; not all techniques are capable of analyzing liquids or gases or even solids.

No single technique can answer even a fraction of the possible outcomes desired of a total materials analysis; there are no universal methodologies. For example, as is quite often the case, quantitative information is desired. While many techniques provide such information, sensitivities are often orders of magnitude different by comparison. Case in point, elemental analysis using SEM/EDS is very common; however, the detection limits are generally only about 0.2-0.5% per element, are extremely sample dependent, and suffer from the semi-empirical nature of the calibrations (some samples simply cannot be accurately analyzed using this method). On the other hand, atomic emission spectroscopy (AES) is typically sensitive to most elements in the low to subparts per billion range, is destructive, often complicated by matrix concerns, and can involve tedious sample preparation and method development. In some cases, SEM/EDS may offer the more judicious route while in others AES may be more practical.

In the following section, a brief description of the operating principles of common instrumental chemical analysis techniques is discussed. Many times we tend to think of such machines as "black boxes" in which samples are placed and information is generated—that is with little or no knowledge of what is actually going on inside the box. Even a basic understanding of operating principles allows for more judicious choice of which technique/s to be selected for a given failure analysis making for a more efficient analysis plan.

2.1 ELECTRONIC TRANSITIONS: THE UNDERLYING PHYSICAL PHENOMENA RESPONSIBLE FOR MANY OF THE TECHNIQUES

Most elemental detection techniques rely on some phenomena related to electronic transitions—that is, electrons transitioning between orbitals in the atoms of the analytical samples [1,2]. At the atomic scale, energies are quantized (they occur at discreet levels) and do not exist in a continuum of possible energy states such as phenomena described by classical physics. This is fortunate because it allows for unambiguous detection of elemental compositions of materials under investigation. For example, the energy of a specific electron transition of iron will be unique to only iron as would similar transitions for cesium or chromium or the rest of the elements. At times, a particular technique may not have the sensitivity to resolve energetically closely spaced phenomena, hence there is the possibility that an assignment could mislabeled. However, most techniques have straightforward means of resolving such ambiguity.

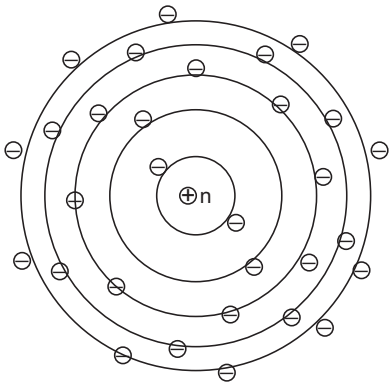

FIGURE 14.1

Electron orbitals around an atom's nucleus.

Figure 14.1 illustrates a simplified representation of an atom; most electrons occupy orbitals with much more complicated shapes than spheres as implied here [3]. This familiar representation has a central circle with the symbol of "+" representing the positively charged nucleus with "n" charges or protons which is an element's atomic number. Note that electron orbitals do not always contain the same number of electrons nor are they at the same distance from the nucleus. The net effect is that the innermost shell, comprises only two electrons, is exposed to the full nuclear charge with no other electrons "shielding" them from this charge. As a result, these electrons are very tightly held and it takes a large amount of energy to remove these from an atom. However, as shown in this figure, the outermost electrons are partially "shielded" from the full force of the nuclear charge by those occupying closer orbits; this diminishes the nuclear charge these electrons are subjected to [4]. Because these electrons are effectively shielded from the full force of the nuclear charge, they are more loosely held and the energy to remove, or excite, these electrons is lower than that of inner shell electrons. As will be shown, these phenomena are the basis of various forms of elemental detection methods.

2.2 ABSORPTION SPECTROSCOPIES

Absorption spectroscopies refer to those that depend on analysis of the radiation absorbed by a sample. Common examples include ultraviolet/visible light absorption (UV/Vis) spectroscopy, atomic absorption (AA) spectroscopy, and Fourier transform infrared (FTIR) spectroscopy.

Figure 14.2 illustrates the principle of AA spectroscopy in which an atom absorbs the light of an incident photon exciting an electron from the ground energy state to a higher energy state. The frequency of the light absorbed is specific to the elements present in the sample and the amount of light absorbed is proportional to concentration which is the basis of quantitative analysis [5].

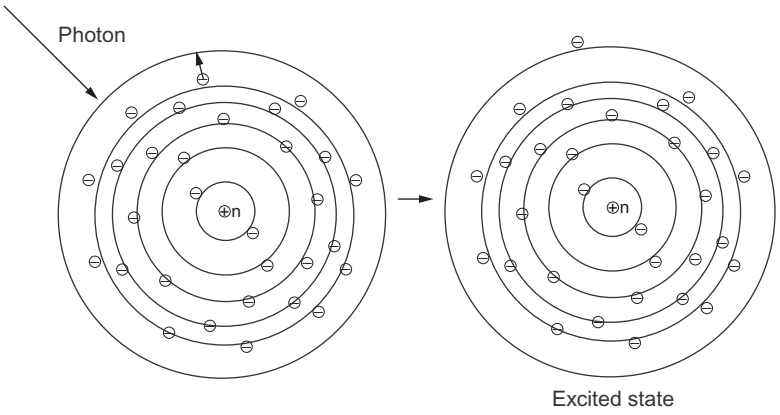

FIGURE 14.2

Atomic absorption, the basis of AA spectroscopy.

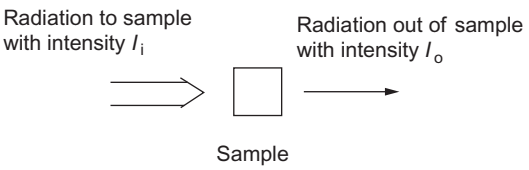

FIGURE 14.3

Absorption spectroscopies rely on recording the amount of incident energy absorbed by the samples of interest.

As opposed to AA, FTIR relies on the absorption of photons in the infrared region raising molecules from a ground vibrational state to an excited vibrational state [6]. While the energy diagrams used to illustrate such phenomena are different than that shown in Figure 14.2, the same principle of absorption of energy leading to a chemically excited state applies. In both, the absorption of energy by the sample is recorded (Figure 14.3).

2.3 EMISSION SPECTROSCOPIES

As opposed to absorption spectroscopies, detection of energy emitted by samples, most commonly photons, is the basis of emission spectroscopic methods. These methods include AES, EDS, wavelength dispersive spectroscopy (WDS), X-ray photoelectron spectroscopy (XPS)—also referred to as electron spectroscopy for chemical analysis (ESCA), Auger electron spectroscopy, and X-ray fluorescence (XRF) spectroscopy.

Figure 14.4 illustrates the basis of AES. Energy is imparted to atoms of samples under investigation via collisions with particles in a plasma causing an outer shell electron to transition to a higher electron shell (the resulting atom is in an excited state). The electron then quickly relaxes back to the ground state emitting a photon

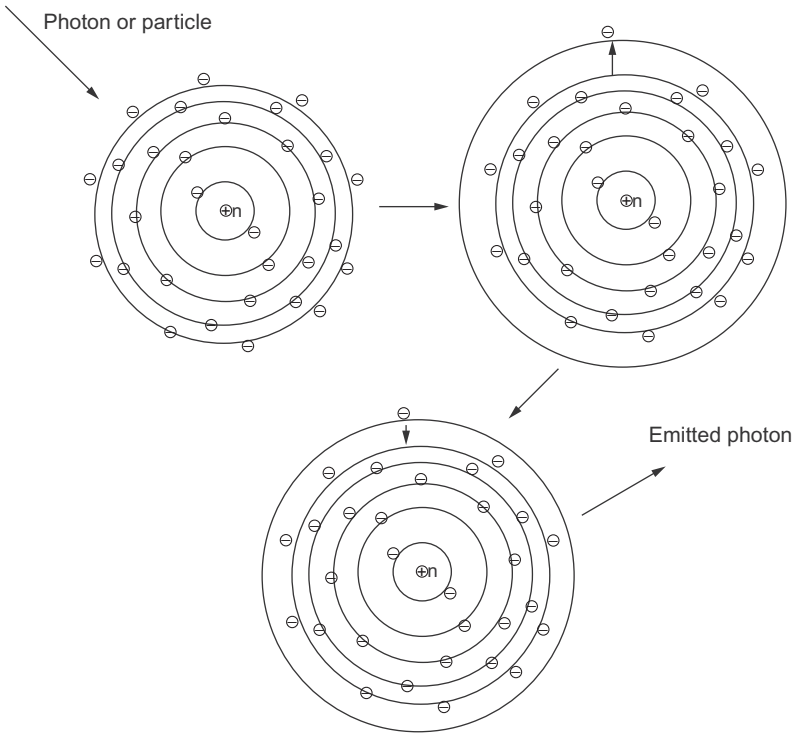

FIGURE 14.4

Mechanism of atomic emission spectroscopy.

that is equal to the energy difference between the two orbitals in which the electron transitioned (being outer shell transitions, these are relatively low-energy photons in the ultraviolet and visible range of the electromagnetic spectrum).

In the cases of EDS, and WDS spectroscopies, high-energy electrons (typically between 5 and 30 kV) impact the atoms of the analytical samples and cause inner shell electrons to be ejected (inner shell electrons are tightly held requiring energetic electrons to dislodge them). Electrons from higher shells then transition down to fill the ejected electron vacancies resulting in emission of X-rays (being inner shell transitions the emitted energy is in the X-ray range of the electromagnetic spectrum) [7]. XRF operates on a very similar principle with exception of the exciting energy being in the form of X-ray photons.

Because an electron beam is necessary for EDS and WDS spectroscopies, these are most commonly coupled to a scanning electron microscope (SEM) and the samples must be analyzed under high-vacuum conditions. On the other hand, as the samples under analysis when using XRF are subjected to an X-ray beam, they may be analyzed under ambient conditions.

The basis of XPS spectroscopy is similar to those just described with the sample being excited by an X-ray beam[8]. A distinct difference, however, is that the energy

of the ejected electrons are what is recorded by the spectrometer. Because the energy of the electron is not just a function of atomic orbital electronic transitions but also molecular orbital transitions, molecular information such as the type of bonding that exists between atoms of molecules can be deduced by analysis of the emission spectra. This technique thusly provides elemental information as well as some molecular bonding information. Auger electron spectroscopy provides similar information as XPS but relies on an electron beam to dislodge electrons for analysis [8].

2.4 GENERIC SPECTROMETER

Most of the techniques discussed herein are some form of spectroscopy. While the specifics of the design and operation of the spectrometers themselves vary considerably depending on technique, they all have several attributes in common [9]. A generic spectrometer is displayed in Figure 14.5.

Figure 14.5 displays a very simple spectrometer design. While these are technique dependent, they all have several features in common:

(1) An excitation source. This source may be a hot filament to provide infrared radiation, a laser to provide a source of photons, or perhaps an X-ray source. Alternately, it may be an electron beam or a plasma torch. Regardless of type, these all provide a source of energy to interact with the analytical samples.

(2) A means to place the sample within the spectrometer. This is not trivial and the peculiarities of each method often require radically different sample presentation methods. For example, many techniques require the sample to be placed within high-vacuum environments with a means of electrically grounding the sample. Others require that the sample be made into a fine atomized vapor mist or be placed at a specific angle with regard to the source and detector.

(3) A means to separate multiple energy signals generated by the spectrometer into discrete signals. One of the first such devices was the prism. As shown in the diagram, and encountered in grade school science classes, this is a device which allows for the separation of light of multiple frequencies; diffraction gratings are more common for such purposes in modern spectrometers. In many

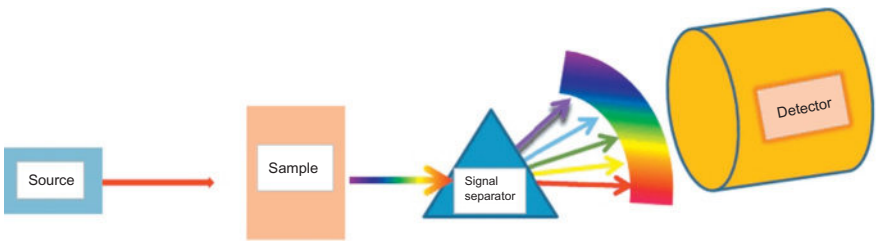

FIGURE 14.5

A generic spectrometer.

cases this stage of the spectrometer is more complicated than prisms or diffraction gratings and employs devices such as interferometers or ion optics as well as others.

(4) A means to detect the differentiated signals generated by the technique. There are a variety of detector designs which range from bolometers, charge-coupled devices (CCDs), photomultiplier tubes, electron multiplier tubes, and many others.

It should be pointed out that some designs allow for steps 3 and 4 of the spectrometer design components to be combined into a single step or device.

2.5 RAMAN SPECTROSCOPY, MASS SPECTROMETRY, AND CHROMATOGRAPHY

The basis of mass spectrometry (MS) and Raman spectroscopy, while unrelated to each other, are distinct from the previous examples and are neither emission nor absorption spectroscopies. Additionally, chromatographic separations are used for materials identifications but are not a spectroscopy at all and rely on mechanisms distinct from all other methods discussed. As a result, the principles of these are presented in this section separately.

2.5.1 *Raman Spectroscopy*

Raman spectroscopy is related to infrared spectroscopy (i.e., FTIR) in that transitions involving molecular vibrations are responsible for the resulting spectra. As a result, interpretation of infrared and Raman spectra is essentially identical [10]. However, the physical phenomena that lead to the recorded spectra are quite different. The exact nature of the Raman effect is beyond the scope of this work; however, the effect itself is rather straight forward [11].

When monochromatic light is incident on a material, the vast majority of the light that is reflected is of the same wavelength as the incident beam (this is termed Rayleigh scattering). This is intuitive and is why, for example, when a green laser hits a material we see the green light of the laser that is reflected from its surface. However, about one in a million or so of the reflected photons are shifted from the wavelength of the incident beam. The energies of these shifted photons result from the same molecular transitions responsible for infrared spectroscopy; hence, the spectra are essentially identical (at least with regard to the wavelengths of the relative Raman shifts which occur in the infrared region). When a material's molecules are in the ground state, the shift in frequency is to longer wavelength hence lower energy photons—these are called Stokes lines as they appear in the Raman spectrum or the effect in general is termed Stokes shift. Alternately, when a material's molecules are in an excited state, for example, as a result of heating, the photon shift is to shorter wavelength hence higher energy photons—these are called anti-Stokes lines as they appear in the Raman spectrum or the effect in general is termed anti-Stokes shift.

The absolute shift resulting from the chemical bonding of molecules, be it Stokes or anti-Stokes, is of the exact absolute amount. Therefore, it is only necessary to plot the shifts of one of these phenomena for chemical interpretation of Raman spectra. As Stokes lines are almost always the more intense of the two, Raman spectra are conventionally plots of only Stokes lines (Figure 14.6).

2.5.2 Mass Spectrometry

MS, also termed mass spectroscopy, is actually not a spectroscopy at all; it does not rely on detection of electromagnetic energy (this is sometimes referred to as mass selective detection). However, as the resulting plots resemble electromagnetic spectra in appearance; this is most commonly referred to as a spectroscopy (Figure 14.7).

There are several variations of MS which differ primarily in how analyte molecules are introduced into the mass spectrometer as well as how they are ionized to allow for mass separation and detection [12]. The focus of this work will be limited to gas chromatography/mass spectrometry (GC/MS).

In the most common applications of MS, the masses of molecules, and the pieces which make them up are detected. In this sense, the spectrum is like a puzzle which can be reconstructed to determine molecular identities.

In Figure 14.8, hypothetical molecule ABC is ionized under high-vacuum conditions to form the positive ions with the mass of the whole molecule ABC and masses of fragments of the parent molecule plotted. Molecules, and their fragments, are ionized such that they can be focused using magnetic and electrical fields allowing for their separation and mass determination. The detected masses are plotted in the manner of the spectrum shown in Figure 14.7, the mass spectrum of *para*-xylene,

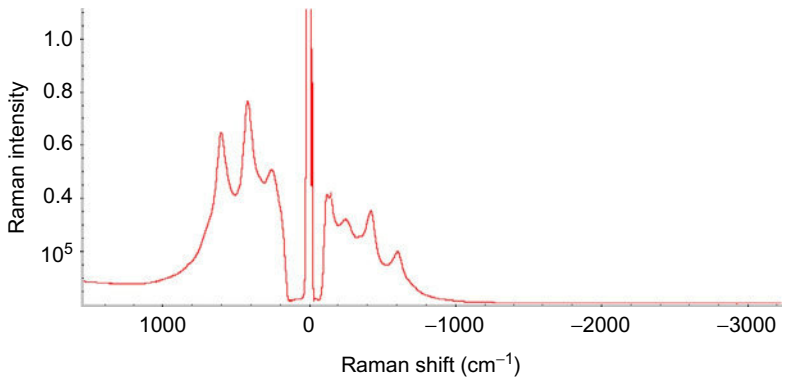

FIGURE 14.6

A Raman spectrum showing both Stokes and anti-Stokes shifts. The central clipped band, 0 cm^{-1}, is from the excitation laser. Stokes bands tend to be more intense and as a result anti-Stokes shifts are generally ignored.

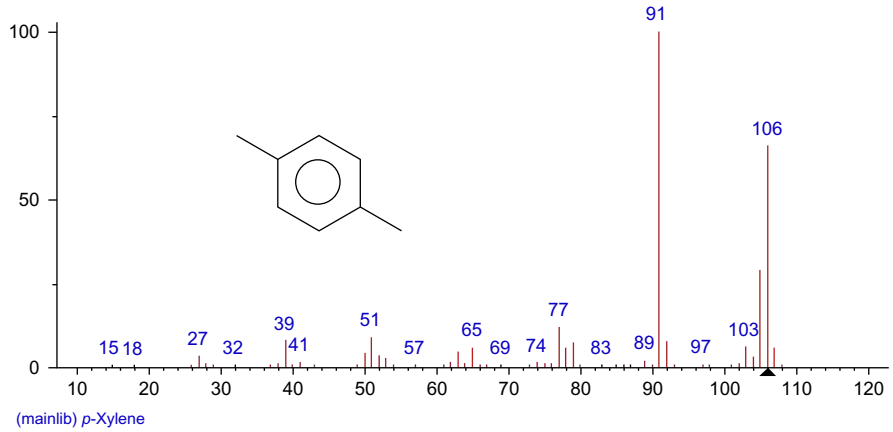

FIGURE 14.7

Typical mass spectrum (*para*-xylene).

$$ABC \Rightarrow ABC^{+} + AB^{+} + BC^{+} + A^{+} + B^{+} + C^{+}$$

FIGURE 14.8

Masses of the ions of hypothetical molecule ABC are detected and recorded.

with the *x*-axis a plot of atomic mass units and the *y*-axis normalized to 100% corresponding to the most intense mass signal. In the spectrum of *para*-xylene, the masses result from the following considerations:

(1) The molecular formula of *para*-xylene is C_8H_{10}.
(2) The exact mass of the most abundant isotope of carbon is 12 amu and the nominal mass of the most abundant isotope of hydrogen is 1 amu.
(3) 10 hydrogen atoms and 8 carbon atoms equal a mass of 106 amu which is a prominent mass of the highest mass cluster.
(4) Carbon also has an isotope of nominal mass 13 amu with a ratio of about 1.1% that of carbon 12. Because *para*-xylene has 8 carbon atoms, there is an 8.8% chance that at least one is a carbon-13 isotope and the mass spectrum of *para*-xylene will have a mass 107 in the spectrum that is 8.8% as intense as the mass at 106 amu.
(5) The remainder of the detected masses are fragments of C_8H_{10} which occur with intensities that make logical chemical sense.
(6) Because masses of fragments of molecules as well as atoms themselves are detected, both molecular and elemental data are directly detected using MS.

2.5.3 Chromatography

The term chromatography implies the study of colors and is a seeming misnomer when considered in terms of how the method is applied in the modern context. However, it was coined by Mikhail Semyonovich Tsvet, who is credited with the invention of chromatographic methods, as he used it to separate plant pigments which were evident as colored bands in the chromatographic column [13]. While there are various chromatographic methods, all are based on the separation of the individual components which make up a mixture. To accomplish this separation, a sample is passed through a column, a hollow tube with specific material, the stationary phase, packed in the center or coated on its inner walls [14]. The sample is carried through/past the stationary phase by a carrier, either a solvent or a gas, known as the mobile phase. The role of the stationary phase is to interact with the individual components of sample mixtures selectively retaining them in the column longer than would be necessary to pass through by the action of mobile phase alone. This is accomplished by judicious selection of a stationary phase with attention being placed on its chemical characteristics. If a component interacts strongly with the stationary phase it is retained longer by the column than components which interact less strongly and hence take longer to pass through the column. The result is a chromatogram as shown in Figure 14.9.

Because the retention times are highly reproducible, typically within 0.01 min, the time it takes for a material to elute from the column can be used for identification. For example, if it is found in an ion chromatography analysis that chloride elutes at 2.22 min (this is found from analyzing a known chloride standard) and an unknown sample produces a peak at 2.23 min, it is assumed that the unknown contains chloride. However, it is possible that differing materials may co-elute and such

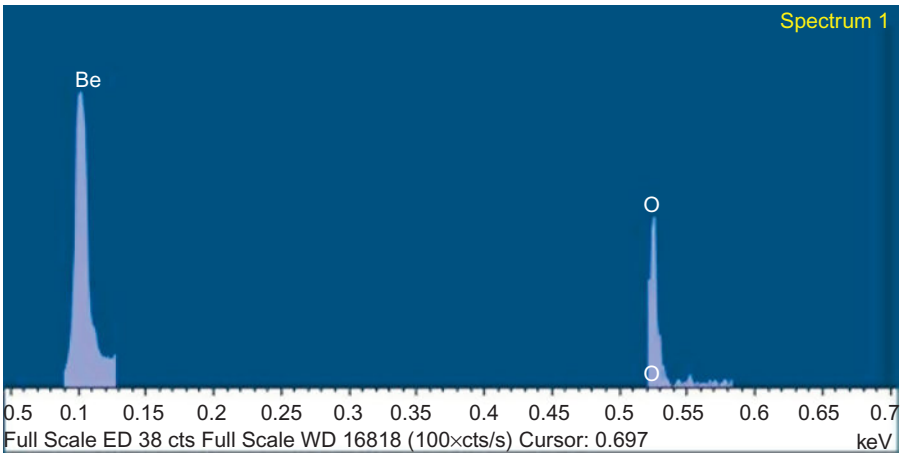

FIGURE 14.9

A typical chromatogram.

assumptions can be incorrect. Use of detectors which provide insight into chemical compositions, such as MS and FTIR, can circumvent this ambiguity.

In Figure 14.9, a comparison of three ion chromatograms, the *x*-axis is time (minutes) and the *y*-axis is conductivity in micro Siemens (an intensity measurement). Each peak represents detection of a unique compound. The purple trace represents a standard containing 2.5 ppm each of fluoride (1.72 min), chloride (2.73 min), nitrate (5.02 min), bromide (5.64 min), sulfate (9.81 min), and phosphate (11.80 min). This was used to establish retention times of the various ions for identification in test samples (a flux and a transducer extract) and the peak intensities are used for quantitative analysis. The flux sample chromatogram is presented as the black trace, and the transducer extract chromatogram is the blue trace. If a peak or peaks observed in either the flux or transducer chromatograms corresponds to those in the standard, it may be assumed that they arise from the same ion of the standard. This illustrates one of the strengths of chromatography: the ability to separate complex mixtures such that the individual components can be characterized individually. This is distinct from most all other analyses techniques which typically detect a weighted average of all compounds present often leading to very complex data.

3 A BRIEF REVIEW OF SPECIFIC TECHNIQUES

In this section, a discussion of the more common chemical analysis techniques used during failure analyses are presented. Included are basic principles (relying heavily in the material presented in the previous sections), strengths, and limitations of each technique, as well as sample considerations inherent to each method.

3.1 ATOMIC EMISSION SPECTROSCOPY

AES sometimes referred to by the acronym OES (optical emission spectroscopy), is an elemental analysis technique with detection limits of subparts per billion for most elements. As the name implies, it relies on the detection of light emitted by atoms, and very simple compounds (oxides, nitrides, etc.), of excited atoms/simple compounds. To excite these species, such that they will emit sufficient light to allow for routine detection, samples are most commonly exposed to plasma. In the case of inductively coupled plasma (ICP) excitation-based AES, liquid samples are atomized into an extremely fine mist and aspirated into a plasma torch. Atoms of the samples emit characteristic light while residing in the torch, which is detected and quantified by the spectrometer. Mostly all materials, if not already liquids, can be converted to liquids by digestion methods (e.g., dissolving in acid) allowing for routine elemental analyses. Additionally, full-scan emission spectra can be obtained from unknown samples to allow for elemental characterization.

Figure 14.10 displays five of the most intense iron emission lines detected during the analysis of an alloy sample. While there are many more detectable lines,

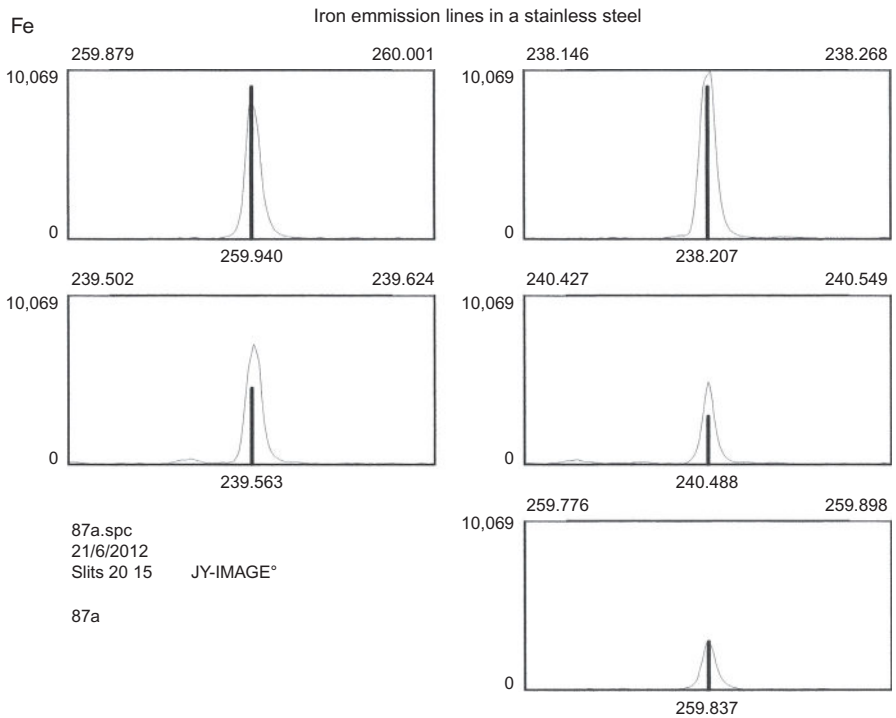

FIGURE 14.10

Five intense emission lines of iron in a stainless steel.

identification of these five is sufficient to qualitatively determine that iron is present in the sample. Quantitative analysis of the sample was performed by comparing the areas under the curves to those of known standards.

Advantages include: extremely high sensitivity; almost full elemental coverage without need for specific excitation sources such as encountered with AA spectroscopy; linear range of several orders of magnitude; very accurate quantification at low concentrations; by using bulk samples a true bulk analysis is obtained (this is often difficult or impossible for many other methods); the ability to analyze most any sample type even with limited availability (most commonly samples are about 0.1-1 g but can be as small as a few milligrams); even gases may be analyzed when introduced into the torch using methods such as gas chromatography (not common but possible).

Disadvantages include: cumbersome sample preparation (an exception being pure liquids such as plant waste water samples); the need to generate calibration curves from samples as similar in all respects as the samples under investigation (so-called matrix matching); initial method development is often time consuming and tedious; in the case of failure analyses method development will often be necessary each time a new sample type is encountered; relatively long analysis times; the method is inherently destructive.

Another way to excite samples into a plasma state is to cause them to spark by application of electrical current. This technique is simply referred to as "spark" and the analysis is often called "spark analysis." This method results in the same types of spectra as that of ICP excitation.

Advantages include: calibration-free quantitative analyses (calibration curves are established at machine set-up only and are checked periodically and easily corrected for drift); the ability to detect nitrogen and carbon in alloys; less matrix matching concerns than ICP; very quick analyses; extremely accurate quantification results; very high sensitivity (not quite as sensitive as ICP but more so than most other elemental analysis techniques); full-scan capabilities allow for unknown materials identification which is often automated requiring little user input.

Disadvantages include: the fact that samples are limited to only those that are conductive (i.e., metals), relatively large sample sizes are required (typically 1×1 in. or more samples are ideal), and the method is inherently destructive.

Another feature of spark analysis, which at times is considered a disadvantage but at other times an advantage, is the fact that only the outermost layer of a sample is characterized. If overall bulk analysis is desired, this can limit the methods applicability. On the other hand, if the goal of the investigation is to only analyze the plating or clad layer, this method is well suited for such purposes.

Failure analysis applications of OES include: alloys verification; process bath (e.g., conversion coating, plating, cleaning, etc.) contamination and composition analysis; high-purity metals, for example, four or five "9s" (99.999% purity) gold, analysis and verification; ceramic and glass composition verification; trace elemental analysis of unknown materials.

3.2 GAS CHROMATOGRAPHY/MASS SPECTROMETRY

3.2.1 *Mass Spectrometry*

As previously mentioned, there are many methods to ionize molecules as well as a multitude of mass detection methods [12]. For the purposes of this work, only electron impact ionization (EI) is mentioned and the nuances of various mass detector designs are not discussed.

During electron impact ionization MS, analyte molecules are bombarded with energetic electrons (70 V by convention). This causes the molecules to lose one of their own electrons becoming ionized with a net positive charge [15]. This process is illustrated in Figure 14.11 for molecular nitrogen.

The MS community, by convention, selected 70 V as the energy of the electron beam that is employed to ionize molecules during standard applications. This was chosen as it only takes electrons of about 3-20 V to ionize molecules in the gas phase and the extra energy imparted to the molecules, using the 70 V source, allows for the fragmentation to aide in molecular identification. Additionally, when 70 V EI ionization is employed, the spectra are extremely reproducible resulting in the creation of mass spectral libraries with hundreds of thousands of entries. These spectra are akin to fingerprints allowing for identification of molecules, in most cases, with a

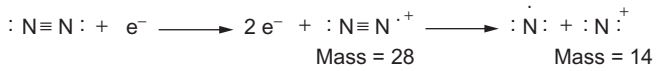

FIGURE 14.11

Molecular nitrogen ionization.

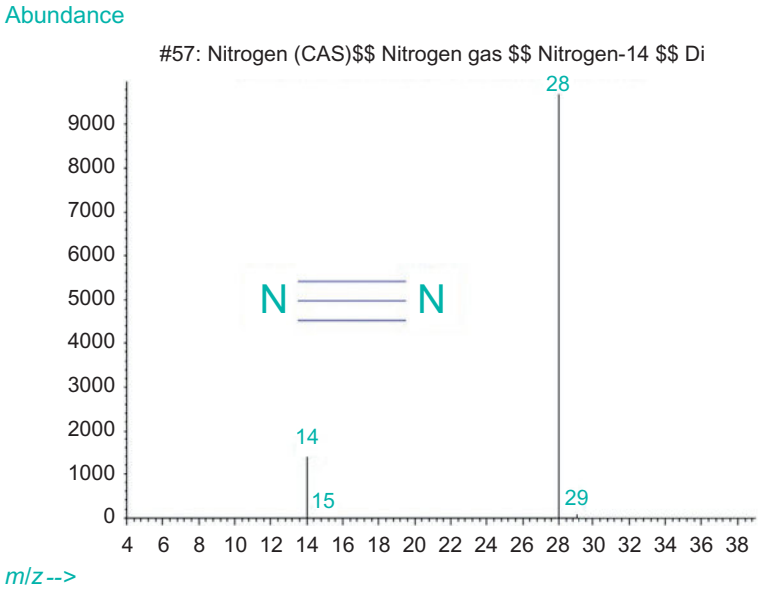

FIGURE 14.12

Mass spectrum of nitrogen.

high degree of confidence (mass spectral database matching is the most reliable of the spectroscopic database matching methods in the author's experience) (Figure 14.12).

3.2.2 *Gas Chromatography*

Gas chromatography can be used only to detect volatile components of a mixture or components which can be made to become volatile as it requires their conversion to the gaseous phase. Many organic compounds, and to a much lesser degree inorganic compounds, can be detected in this fashion. Separation is accomplished both by differences in volatility (the use of column oven programming is employed as a basis of component separation) and by selective interactions with the stationary phase [16].

While the term gas chromatography may imply the ability to only analyze gaseous samples, this is in fact not true. GC/MS allows for characterization of all types of samples and analysis of gaseous samples, particularly with regard to failure analysis, is in fact infrequent when compared to liquids and solids analyses. Liquid

samples are often created by extracting materials of interest; for example, an oily residue on a component or additive in a polymer, with solvent and injecting the resultant solutions into a heated port which converts these to volatile materials. Solids are also very commonly analyzed using thermal stripping methods (heating a sample in the carrier gas to liberate volatile materials) or pyrolysis (thermally fragmenting large non-volatile compounds into smaller volatile fragments).

The chromatogram is generated by measuring the total ion current recorded by the mass spectrometer on the *y*-axis versus time on the *x*-axis (Figure 14.13). Not obvious in the chromatogram shown in Figure 14.13, is that at each point in time there is a corresponding mass spectrum. For example, if the chromatogram was generated by collecting spectra at a rate of 10/s, within a 1-min window 600 spectra would be recorded and available for analysis. Figure 14.14 displays the 574th mass spectrum recorded to create the chromatogram displayed in Figure 14.13.

Advantages include: the "go to" method of gas analysis (most analytical methods cannot analyze gases); the ability to separate components of mixtures allowing for characterization independent of each other; mass spectral database matching provides high-confidence results; the ability to characterize liquids, and solids in addition to gasses; the method can be considered nondestructive in many cases, for example, when analyzing solvent rinses of surfaces; extreme sensitivity (molecules are typically detected at nanogram levels); and the ability to quantify component concentrations over several orders of magnitude with high accuracy.

Disadvantages include: compounds must have some, if limited, volatility when heated to around 300 °C; because of the volatility requirement many compounds and materials are inaccessible; in some cases, the technique is destructive.

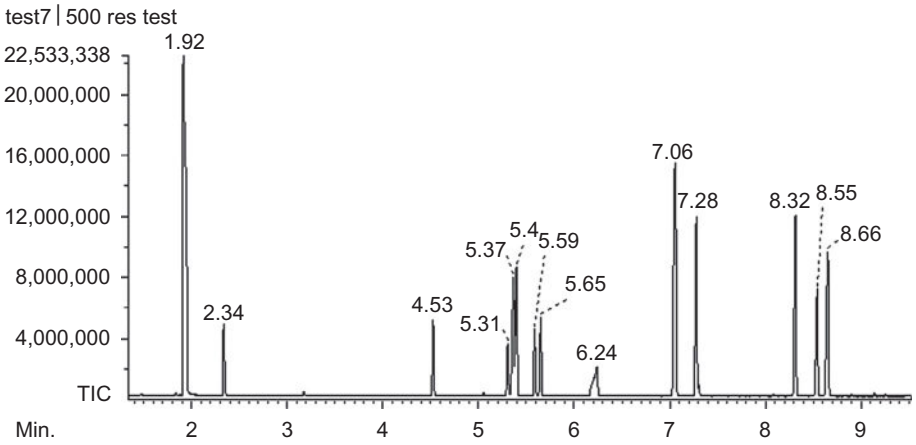

FIGURE 14.13

Example gas chromatogram. Each "peak," labeled by retention times, represents a unique material detected.

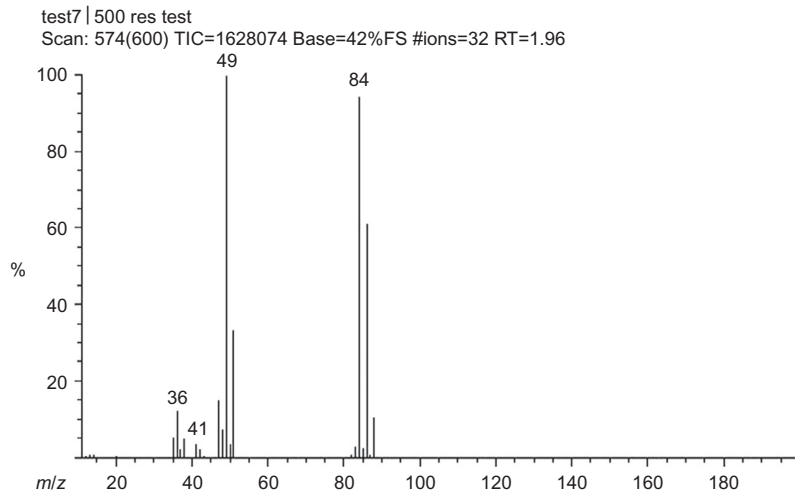

FIGURE 14.14

Mass spectrum collected at 1.96 min (scan 574) from chromatogram displayed in Figure 14.13. This shows that methylene chloride was present in the sample.

Example failure analysis applications include: determination of "outgassing" (gases released by materials typically upon heating) which may redeposit as films, contribute to corrosion, impact electrically sensitive contact surfaces, etc.; product composition comparisons for verification of a contaminant or to determine slight lot variations; product specific compound, "marker compound," identification for contamination source verification; identification of additive and blend variations of closely related polymers (confirming that the correct polymer was utilized); unambiguous lubricant identification when more general methods such as FTIR fail.

3.3 FTIR SPECTROSCOPY

Infrared spectroscopy, applying electromagnetic radiation in the mid-IR region (2500-16,000 nm), is useful for revealing structural information of molecules. As a result, this technique can be used for assignment of exact identity, or failing that the chemical class of the materials under investigation. The technique relies on the fact that compounds absorb infrared radiation in a predictable fashion as a function of the types of chemical bonding present. A plot of the attenuation of the infrared source, via absorption by the sample, as a function of wavelength (by convention absorbance versus wavenumber, reciprocal wavelength in centimeters) results in the infrared spectrum. It has been likened to a fingerprint in that, at least in theory, no two compounds produce identical spectra. As a result, spectra of unknown materials can be searched against spectral databases to aid in their identification.

The FT or Fourier transform of the acronym refers to the collection technique most commonly applied with modern infrared spectrometers, namely, all wavelengths of energy are collected simultaneously using an interferometer based spectrometer. A Fourier transform is necessary to convert the time domain data from the interferometer output to the frequency domain data creating the spectrum.

Four common types of sampling techniques are described in Figures 14.15–14.18: transmission, reflectance, grazing angle reflectance, and attenuated total reflectance (ATR). In transmission spectroscopy, the radiation passes directly through the sample while in reflectance spectroscopy the radiation passes through the sample, is reflected off the surface under the sample, and passes through the sample again. In standard reflectance techniques, the incident beam is nearly perpendicular to the reflective surface and the analyzed "depth" is approximately two times the sample thickness. In grazing angle reflectance, the incident radiation is nearly parallel to the sample and the analyzed depth is many times the sample thickness. When using ATR spectroscopic methods, a sample is simply placed in contact with an ATR crystal. In the schematics of Figures 14.15–14.18, if $I_o < I_i$, radiation was absorbed by the sample. The frequencies of the absorbed radiation are indicative of the types of chemical bonds present in the sample. An example spectrum, of ethanolamine, is displayed in figure 14.19. Figure 14.20 highlights the chemicals bonds which lead to the bands in the spectrum.

Advantages of this method include: the spectra are rich in molecular information which is lacking in most other methods; an almost universal technique with most material types including both organic and inorganic easily characterized; spectra

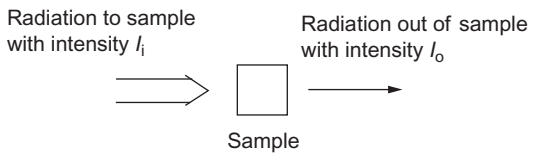

FIGURE 14.15

Transmission spectroscopy.

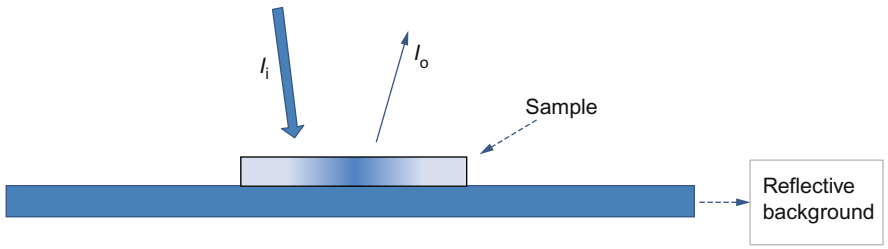

FIGURE 14.16

Standard reflectance spectroscopy.

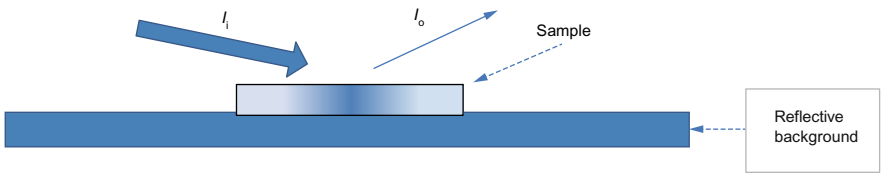

FIGURE 14.17

Grazing angle reflectance spectroscopy.

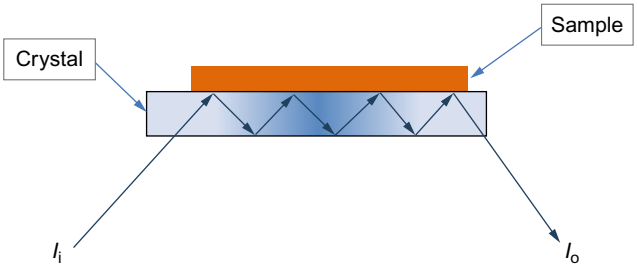

FIGURE 14.18

Attenuated total reflectance (ATR) spectroscopy.

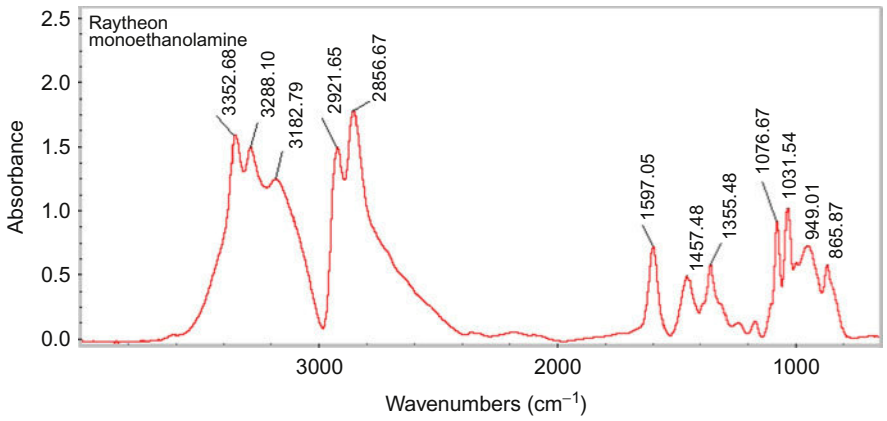

FIGURE 14.19

Spectrum of ethanolamine.

are akin to fingerprints in that database matching can be performed; with FTIR microscopic methods, analysis of small, microscopic samples (fractions of a milligram) is routine, and when performing reflectance methods the spatial resolution is about 10 μm; in most cases, spectral collection is quick; in many cases, the technique is noninvasive, hence, nondestructive.

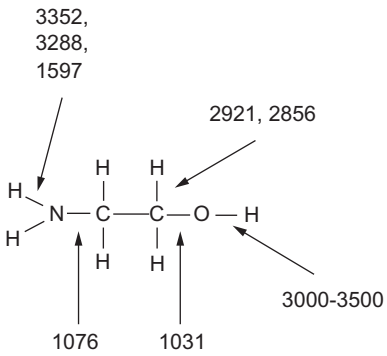

FIGURE 14.20

Bonds responsible for characteristic absorptions of ethanolamine.

Disadvantages include: many times the data is ambiguous and difficult samples require a highly trained operator; difficulty to inability to detect trace contaminants; the lower spatial resolution is about 10 μm (this was also listed as an advantage); while database matching is possible it is far from "foolproof," quantitative analysis is difficult and the sensitivity is low (lower detection limit for individual components of mixtures in most cases is in the percent range); sample preparation can be tedious; in some cases, the method is destructive.

Example failure analysis applications include: materials verification; contamination analysis; microscopic materials and contamination analysis; degree of cure studies of some polymers; oxidative attack of materials analysis; gas analysis when coupled to a thermogravimetric analyzer (TGA) or GC.

3.4 RAMAN SPECTROSCOPY

While the physics of the Raman effect are quite different than that of infrared spectroscopy, the two methods are related with both providing chemical bonding information as they are sensitive to molecular vibrations. It is useful to think of Raman spectroscopy as a related complimentary technique to infrared spectroscopy (FTIR). In fact, the spectral bands which result from the same type of chemical bonding occur at the same relative Raman shift as the frequency of infrared spectra.

Note that the Raman and infrared spectra of cyclohexane, Figure 14.21, have many bands in common. Also note that some bands are more intense, or even missing, when comparing the two spectra. This results from a convenient difference between the methods; the types of bonds that are strong in Raman tend to be weak in the infrared and vice versa, the techniques being complimentary. In fact many materials that are inaccessible by one of these methods may be analyzed using the other. For example, Raman spectroscopy is able to analyze pure materials such as silicon or pure carbon compounds such as nanotubes, graphite, and diamond-like films. These are inaccessible using infrared spectroscopy. While infrared spectroscopy is the more common of

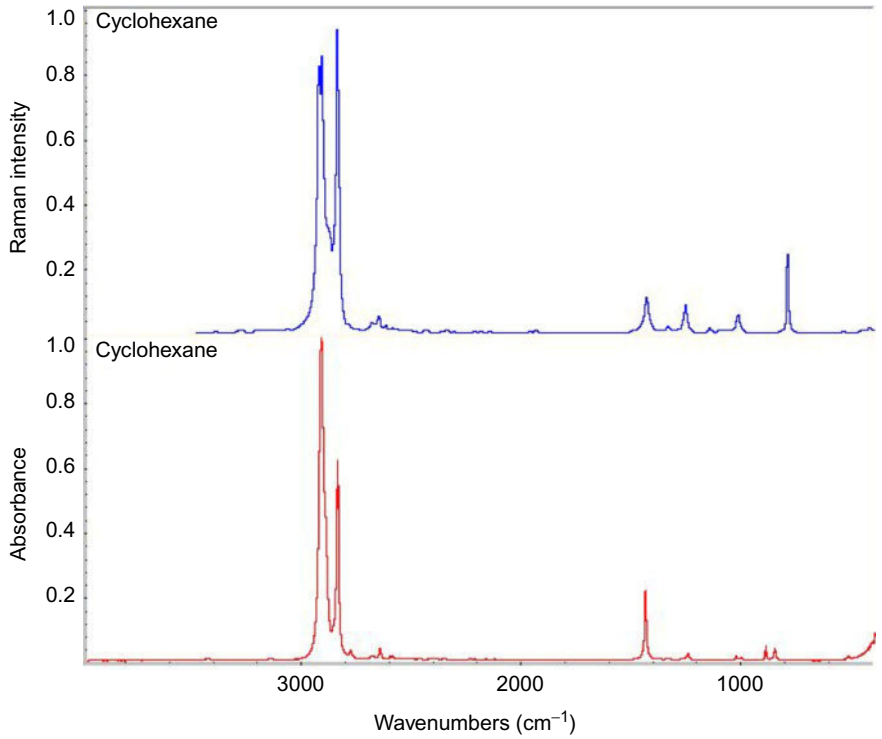

FIGURE 14.21

Comparison of Raman spectrum of cyclohexane (top) to infrared spectrum of cyclohexane.

the two techniques, Raman spectroscopy expands a lab's capabilities to analyze samples beyond the limitations of infrared spectroscopy [17].

Advantages include: smaller area of analysis than with FTIR, sometimes referred to as "spot size," of about 1 μm; the ability to depth profile using confocal microscopy (that is analyzing different layers of materials simply by focusing into them); in most cases, sampling is very simple by just aiming the laser and collecting the spectra (no sample preparation at all); a result of the last advantage is that most times the method is nondestructive; the ability to analyze some materials that simply are not accessible using other methods; the ability to collect stress maps of materials such as silicon wafers; orientation analysis; spectra are like fingerprints that can be compared to databases for materials identification.

Disadvantages include: many times fluorescence overwhelms the Raman effect making spectral collection difficult to impossible; dark samples tend to absorb the Raman shifted light; less universal than FTIR; higher cost of ownership than FTIR; the laser can burn samples; database matching is more quirky than that of FTIR resulting from differential laser response and other features such as spectral alignment and calibration requirements.

Example failure analysis applications include: materials analysis of cross-sections; analysis of materials not accessible to other methods such as FTIR; analysis of materials under glass or the layers of a laminate nondestructively using confocal capabilities; stress analysis of semiconductors; degree of cure analysis of polymers.

3.5 EDS AND WDS

EDS is one of the better known methods applied to failure analysis and is also referred to as energy dispersive X-ray (EDX) spectroscopy and even EDAX which was a pioneering company in the development of the method. WDS is less well known but is a related technique that is typically an addition to an existing EDS system.

An important limitation of both methods is that because samples must be exposed to vacuum conditions, gases cannot be analyzed and liquids are limited to those that have very limited volatility and will not contaminate the system (some labs will not perform any liquids analysis out of contamination concerns).

The X-ray detection methods of EDS versus WDS are fundamentally different; the energy of the X-rays are detected using EDS, while the wavelength of the X-rays are detected using WDS. However, when used in conjunction, they complement each other overcoming limitations inherent in each technique independent of each other. These methods are usually coupled to electron microscopes which provide the electron beam for sample excitation.

It is important to stress that only elemental information is provided and many times false assumptions as to the identity of unknown materials result. For example, it is not uncommon when carbon is detected to assume an organic material is present. From elemental data alone this is a guess, many times a good one, but examples of inorganic carbon are numerous including carbonate corrosion products. Case in point, lead carbonate is often the major contributor of tin/lead solder corrosion. Attributing carbon found on such solder to organic contamination, for example flux residue, in this case would be incorrect. Also, as some elements are not easily detected (nitrogen, boron, and beryllium) and others (hydrogen, helium, and lithium) are not detectable at all leading at times to materials misidentifications. This is pointed out as care should be exercised when assigning absolute materials identification when applying these methods.

As mentioned, both these methods are capable of detecting elements present in samples and additionally can quantify amounts present. EDS is the lower resolution method of the two and peak overlap is a common problem; that is two peaks resulting from two different elements may overlap, obscuring each other and making identification difficult. However, there are methods to overcome this limitation. Despite this fact, at times from EDS spectra alone, unambiguous peak assignment may be impossible. Also an element of interest may be present below the detection limit of EDS (typically about 0.2-0.5%). In these cases, WDS is often applied to overcome these limitations.

Figure 14.22 highlights typical EDS output. In this case, the spectrum suggests a stainless steel. The quantification results indicate that this is likely a 300 series and is a good match to alloy 316.

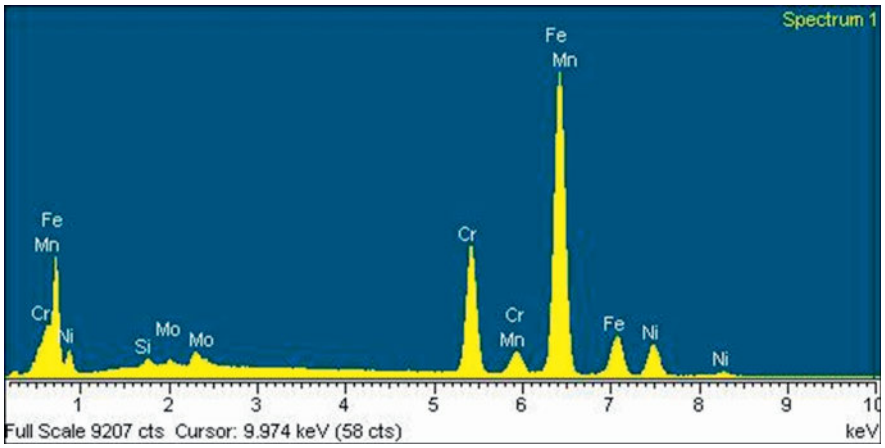

Element	Weight %	Atomic %
Si	0.54	1.08
Cr	17.53	18.80
Mn	1.45	1.47
Fe	66.61	66.50
Ni	11.11	10.55
Mo	2.76	1.60
Totals	100	100

FIGURE 14.22

EDS elemental spectrum and quantification results.

Advantages of EDS include: a relatively quick elemental analysis technique (in most cases); elemental coverage for all but the lightest elements (carbon and above are detectable, boron is problematic); quantitative elemental data; the ability to scan areas (raster scanning) and single spots; a large spatial range from about 1 mm^2 to $submicron^2$; elemental spectra are linked to image data generated by electron microscope; elemental maps, "dot maps," can be generated from the data; depth information is possible using variable excitation voltages and modeling packages such as Monte Carlo simulations; generated data are from only the top couple of microns of the material under investigation (surface sensitive); while many consider this a destructive technique, particularly in the case of electronic components, it is in fact not in many cases (e.g., in most cases electronic components are not damaged by the electron beam).

EDS disadvantages include: because of the most common detector designs, nitrogen produces a very weak response making its detection unreliable for most materials; generated data are from only the top couple of microns of the material under investigation complicating bulk analyses; it is a relatively insensitive method with lower detection limits in the percentage range; only elemental data is generated; quantitative analysis of heterogonous materials often results in inaccurate data;

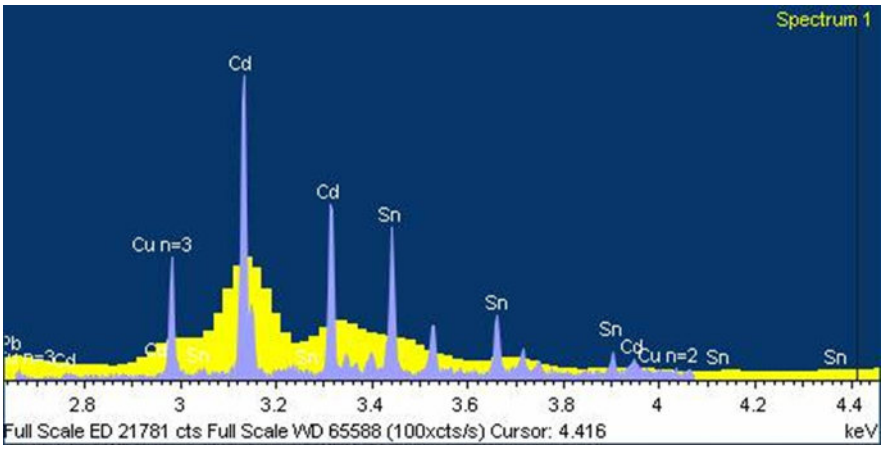

FIGURE 14.23

This example highlights the resolution advantage of WDS compared to EDS. The EDS spectrum is the lighter trace and is composed of about four to five relatively broad peaks. The WDS spectrum is the darker trace composed of about 15 well-defined peaks.

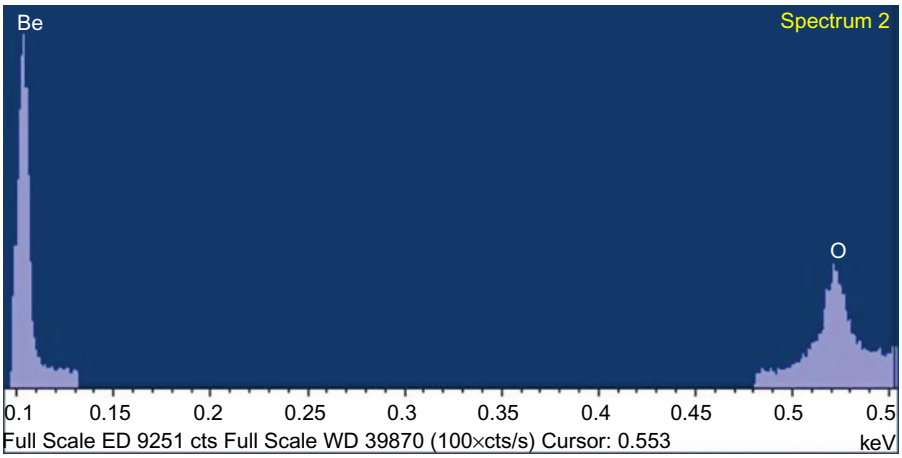

FIGURE 14.24

The extended elemental range of WDS is highlighted (EDS is extremely poor at detecting Be). Suspect beryllium oxide was readily detected.

samples must be submitted to vacuum conditions; chamber dimensions often limit the size of samples which may be analyzed (large chamber systems do get around this limitation but are the exception, not the rule); nonconductive samples may need to be coated with a conductive film usually resulting in the analysis being destructive.

WDS advantages include: better sensitivity than EDS with about 1-3 orders magnitude increase for most elements; extended elemental range down to beryllium; quantitative analysis can be more accurate than EDS (Figures 14.23 and 14.24).

WDS disadvantages include: slow collection times; only spot mode detection is possible (cannot raster large areas); calibrations are more involved than those of EDS; quantitative analysis of heterogonous materials often results in inaccurate data; samples must be submitted to vacuum conditions; chamber dimensions often limit the size of samples which may be analyzed (large chamber systems do get around this limitation but are the exception not the rule); nonconductive samples may need to be coated with a conductive film usually resulting in the analysis being destructive.

Example failure analysis applications include: materials verification based on elemental analysis; nondestructive alloy verifications, small-area elemental analyses such as those revealed by cross-section samples.

3.6 XPS AND AUGER ELECTRON SPECTROSCOPY (AES)

XPS, also referred to as ESCA, and AESusually simply called Auger spectroscopy, are related methods primarily distinguished by how analytical samples are excited [18]. They are emission methods distinct from others discussed thus far. They both offer the advantage of providing elemental as well as molecular bonding information [8]. An example XPS spectrum is displayed in figure 14.25.

An important limitation of both methods is that because samples must be exposed to vacuum conditions gases cannot be analyzed and analysis of liquids is limited to those with minimal volatility (some labs will not perform any liquids analysis out of contamination concerns).

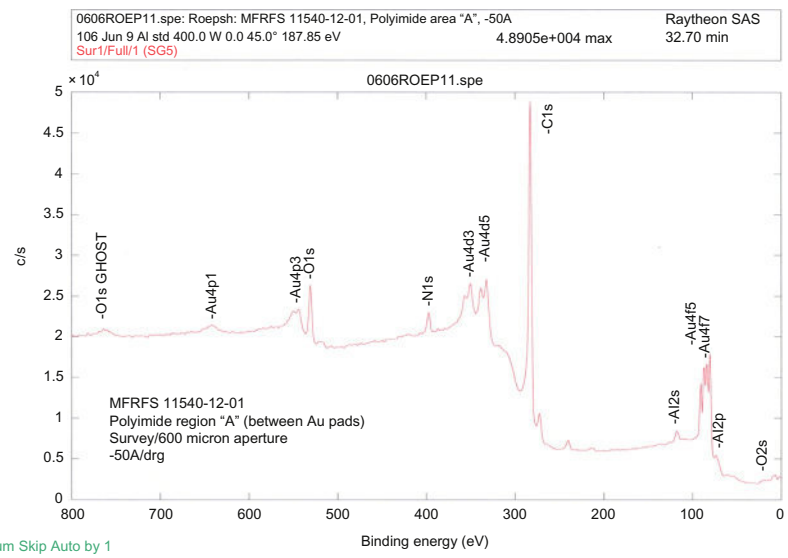

FIGURE 14.25

Typical XPS spectrum. Gold, oxygen, nitrogen, aluminum, and carbon detected. Electron orbital assignments are listed with identified elements.

XPS relies on application of X-rays of a known energy. These collide with electrons in the atoms of the molecules of interest causing some to be ejected from the sample. On the other hand, AES relies on the collision of electrons from an electron beam to dislodge and eject electrons from the sample atoms. The energies of theses ejected electrons are measured and are the basis of the generated elemental and molecular information. Both methods are extremely surface sensitive.

Advantages of these methods include: molecular bonding as well as elemental information is provided; extreme surface sensitivity with the lower limits of depth analyses in the tens of Angstroms (single atom radii range from about 0.5-2 Å hence, 10 Å is only a few atoms thick).

Disadvantages include: these tend to be costly analyses; ultrahigh vacuum conditions are necessary; a result of the vacuum requirement is that sample size is limited; these are most commonly destructive to the samples; samples must be handled with extreme care as even slight handling contamination can complicate analyses; samples require charge grounding and dissipation; sensitivity is low (comparable to that of EDS methods).

Example failure analysis applications include: materials verification based on elemental and molecular information; nondestructive alloy verifications, analysis of extremely thin contamination layers (10s of atoms thick).

4 MISCELLANEOUS TECHNIQUES

The previous discussion covers only techniques which are the most common and are highlighted by examples given in next chapter. While not comprehensive, the following is a list of other techniques which are applied to failure analyses with only a brief description.

4.1 KARL FISHER TITRATION

This is a method of determining the water content of liquids and some solids. This is most commonly carried out using automated systems [19].

4.2 SECONDARY ION MS (SIMS)

This is a type of MS which uses an ion beam to ionize materials for mass spectral detection from sample surfaces. Detection limits are extremely low and the method is extremely surface sensitive. Depth profiling is also commonly carried out [20].

4.3 XRF SPECTROSCOPY

This is an emission spectroscopy used for elemental analyses. It is very commonly used to determine plating thicknesses. Most common designs are insensitive to elements below aluminum on the periodic table [21].

4.4 RESIDUAL GAS ANALYZERS

These are mass spectrometers which can be applied to a number of applications such as real-time monitoring of gas flows. However, within the electronics industry the method is commonly used for analysis of the gases within sealed components [22].

4.5 ULTRA VIOLET/VISIBLE (UV/VIS) SPECTROSCOPY

This is an absorption spectroscopy of light in the UV/Vis region of the electromagnetic spectrum (150-800 nm). It is most commonly used for quantitative analyses of components of liquids. The spectra are not as chemically information rich as vibrational spectroscopies (i.e., FTIR and Raman) [23].

4.6 NEAR INFRARED (NIR) SPECTROSCOPY

An absorption spectroscopy that detects absorption of electromagnetic radiation in the NIR region (800-2500 nm) of the electromagnetic spectrum. It is most commonly used for quantitative analyses of liquids. The spectra are not as chemically information rich as other vibrational spectroscopies (i.e., FTIR and Raman) [24].

4.7 LIQUID CHROMATOGRAPHY/MASS SPECTROMETRY (LC/MS)

Like GC/MS, this method can provide compositional information of mixtures by providing mass spectra of the separated compounds. This method uses a liquid as the mobile phase. Database matching such as that of GC/MS is not possible [25].

4.8 ION CHROMATOGRAPHY (IC)

This is a form of liquid chromatography in which dissolved ions are separated based primarily on interactions with the stationary phase; however, the mobile phase strength is also used to effect separations. In general, the charge to size ratio of the analyte ions is the largest contributor to retention. For example, smaller singly charged ions tend to elute sooner than larger ions and singly charged ions tend to elute sooner than multiply charged ions. This method is commonly used for quality control and monitoring of various processing operations; however, it can be applied to failure analyses [26].

4.9 AA SPECTROSCOPY (AA)

This is an elemental analysis technique similar in many respects to ICP/AES with the exception that it is an absorption spectroscopy and not an emission spectroscopy. The torch is most commonly acetylene/nitrous oxide. A weakness with regard to failure analysis is that specific element lamps must be used and full elemental scans of unknowns are not possible. This is most commonly a quality control technique [27].

REFERENCES

[1] McGregor D, Kull C, Gehlhausen J, Viscomi A, Wu M, Zhang L, et al. Direct determination of nonmetals in solution with atomic spectrometry. Anal Chem 1988;60 (19):1089A–98A.

[2] Olefjord I. Brune D, editor. Surface characterization. Weinheim, Germany: Wiley-VCH Verlag GmbH; 1985. p. 291–319.

[3] Pauling L. The nature of the chemical bond. Application of results obtained from the quantum mechanics and from a theory of paramagnetic susceptibility to the structure of molecules. J Am Chem Soc 1931;53(4):1367–400.

[4] Reed J. The genius of slater's rules. J Chem Educ 1999;76(6):802–4.

[5] This is a good general reference for all types of spectroscopy discussed herein. Parker S (editor) In: McGraw-Hill Encyclopedia of Chemistry. McGraw-Hill; 1982. p. 980–6.

[6] Dows D. On the origin of characteristic group frequencies in infrared spectra. J Chem Educ 1958;35(12):629–33.

[7] Goldstein J, Newbury D, Joy D, Lyman C, Echlin P, Lifshin E, et al. Scanning electron microscopy and X-ray microanalysis. 3rd ed. New York, New York: Springer; 2007, pp. 297-353.

[8] Schreifels J, Turner N. Surface analysis: X-ray photoelectron spectroscopy and Auger electron spectroscopy. Anal Chem 2000;72:99R–110R.

[9] James J. Spectrograph design fundamentals. Cambridge University Press; 2007.

[10] Lin-Vien D, Colthup N, Fateley W, Grasselli J. The handbook of infared and Raman characteristic frequencies of organic molecules. London: Academic Press; 1991.

[11] Gershon S, Dean J. The chemist's ready reference handbook. McGraw-Hill; 1989. pp. 9.1-9.9.

[12] McLafferty F, Turecek F. Interpretation of mass spectra. 4th ed. Sausalito: University Science Books; 1993, pp. 1-17.

[13] Tswett M. Adsorptionanalyse und chromatographische Methode. Anwendung auf die Chemie des Chlorophylls [Adsorption analysis and chromatographic method. Application to the chemistry of chlorophyll]. Ber Dtsch bot ges 1906;24:384–93.

[14] One common exception is the method "Thin Layer Chromatography" (TLC) which relies on a sample moving over a plate coated with stationary phase by capillary action.

[15] Electrons may also be captured by the molecules creating negatively charged ions. These can also be detected by the system when used in negative ion mode. However, this mode has disadvantages compared to cation mode and is used only in special cases.

[16] Rood D. A practical guide to the care, maintenance, and troubleshooting of capillary gas chromatographic systems. 2nd ed. Heidelberg: Huthig GmbH; 1995, pp. 9-16.

[17] Wolfgong W, Colangelo J. Raman spectroscopy as a valuable tool for failure analysis. Spectroscopy 2004;9–14.

[18] AES has also been used to describe Atomic Emission Spectroscopy in this work. As the acronym is applied to both methods, it was decided not to limit its use to one and not the other.

[19] Scholz E. Hydranal—manual Seelze: Sigma-Aldrich Laborchemikalien GmbH; 2012. pp. 1-6, http://creschem.com/sites/default/files/Hydranal_Manual.pdf, last accessed 1/28/2015.

[20] Vickerman J, Briggs D, editors. ToF-SIMS, surface analysis by mass spectrometry. Chichester: IM Publications and Surface Spectra Limited; 2001.

[21] Beckhoff B, Kanngießer B, Langhoff N, Wedell R, Wolff H, editors. Handbook of practical X-ray fluorescence analysis. New York, New York: Springer; 2006.
[22] MIL-STD-883J TM 1080. Test method standard microcircuits.
[23] Perkampus H. UV-Vis spectroscopy and its applications. New York, New York: Springer; 2012.
[24] Siesler H, Ozaki Y, editors. Near-infrared spectroscopy: principles, instruments, applications. Weinheim (Germany): Wiley-VCH; 2002.
[25] McMaster M. LC/MS: a practical users's guide. Hoboken: Wiley; 2005.
[26] Fritz J, Gjerde D. In: Ion chromatography. Weinheim: Wiley-VCH; 2009.
[27] Welz B, Sperling M. Atomic absorption spectrometry. Weinheim: Wiley-VCH; 1999.

CHAPTER

15 Chemical analysis techniques for failure analysis: Part 2, examples from the lab

William J. Wolfgong

Raytheon Space and Airborne Systems, Component Engineering Department, McKinney, Texas

CHAPTER OUTLINE

1 INTRODUCTION

The following examples were chosen to highlight how various chemical analysis techniques aided in failure analyses of a variety of system and device types investigated by the Raytheon failure analysis labs, McKinney, TX. Examples are presented by common failure modes.

Handbook of Materials Failure Analysis With Case Studies from the Aerospace and Automotive Industries.
http://dx.doi.org/10.1016/B978-0-12-800950-5.00015-6

2 OUTGASSING—GASEOUS MATERIALS LEADING TO FAILURES

Outgassing, sometime called off-gassing, is the release of gaseous compounds by materials. This phenomena, quite logically, is typically accelerated by heat. This is of such industrial importance that NASA has compiled a listing of tens of thousands of material's outgassing properties [1].

Gases that are released often are native to the materials in forms such as polymer additives, residual solvents, process chemicals, and others. Alternately, gases may be generated by decomposition of materials which can happen very slowly, failures not obvious for months or years, or very rapidly such as in high-temperature or high-load environments. Failures can occur as a result of outgassing by a number of mechanisms including, corrosion of metals, deposition of films on optics and other sensitive areas, release of explosive and flammable gases, and many others [2,3].

2.1 SULFUR-CONTAINING GASES LEADING TO SILVER CORROSION

It has long been known that certain, not all, sulfur compounds can lead to the oxidation of silver resulting in silver sulfide tarnish [4]. Particularly troublesome are simple gaseous species such as hydrogen sulfide, simple thiols, carbon disulfide, and sulfur oxides [5]. Common sources of such gases are the decomposition of organic materials (swamps and similar environments such as water tanks can present higher than normal levels), engine exhaust, thermal degradation of materials, chemical production environments, and others.

In this example, thin film resistors were reported to be failing for high resistance or electrical open; resistors were electrically measured with a digital multi-meter and were found to be open or exhibiting exceedingly high resistance. Scanning electron microscopy/energy dispersive spectrometry (SEM/EDS) analyses of the resistor showed evidence of a nodule growth at the termination solder metallization/resistive element interface consistent with silver sulfide corrosion (Figure 15.1). Cross-sectional examination confirmed the formation of silver sulfide (corrosion) at this interface which resulted in an open between the solder termination and the resistive element on both ends of the resistor (Figure 15.2).

Two approaches at remediation are common in such cases: seal the components to minimize atmospheric exposure or eliminate the sources of the sulfur-containing gases. In this, and many other examples, it has been found easier to eliminate the sulfur sources than sealing the components. Of course, to achieve such an outcome the sources of sulfurous gases must be identified. Gas chromatography/mass spectrometry (GC/MS) methods are ideal for such purposes, and as a result, a number of likely candidates native to the system including a dampening foam judged to be the most likely source were screened.

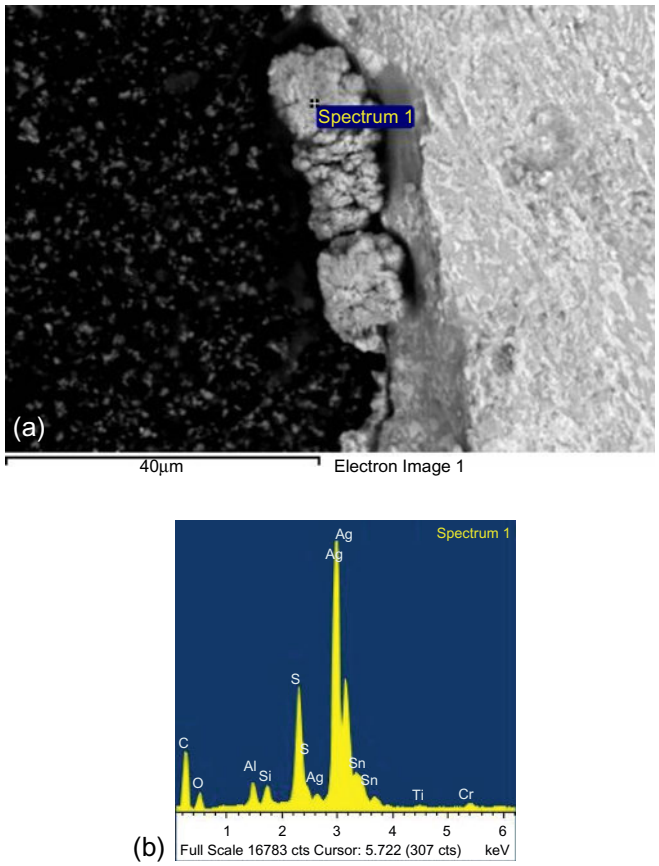

FIGURE 15.1

15.1(a) Silver nodules were analyzed as shown at location of spectrum 1. The spectrum, 15.1(b), indicates that the nodules are silver sulfide as indicated by the high levels of silver (Ag) and sulfur (S) at the resistor termination (other detected elements are consistent with the package construction).

About 50 mg samples of the various system construction materials were placed in quartz sample tubes for thermal striping analysis. These were ballistically heated to 100 or 150 °C for 3 min; these temperatures were chosen to accelerate release of absorbed gaseous compounds while not inducing thermal decomposition of the materials themselves, directly in the carrier gas stream of the GC.[1]

[1]The experimental parameters used for this example were as follows: An Agilent 30-m Gas Pro 0.32-mm (I.D) column was used for the gas separations. The injection was carried out using a split ratio of 7:1. The GC was programmed with an initial setting of −60 °C and held for 3 min. This was then ramped at a rate of 20 °C/min to 0 °C with no hold time followed by an oven ramp at 50 °C/min to 220 °C. This was then maintained for 3 min. The mass spectra were scanned from 10 to 350 amu.

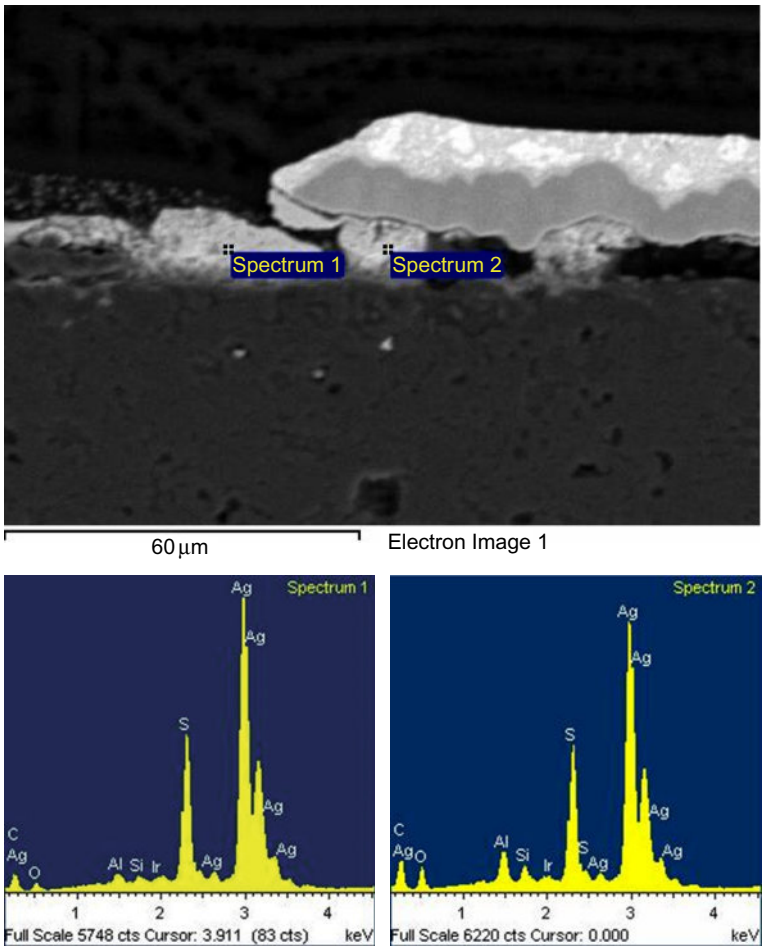

FIGURE 15.2

The elemental spectra, as obtained from areas indicated in the image (spectrum 1 and spectrum 2) of the termination in cross section, show that the electrical contact has been compromised at the termination by formation of silver sulfide (Ag and S in the spectra).

Of the materials tested, the suspected foam was in fact determined to be the source of the sulfurous gases.

In the chromatogram displayed in Figure 15.3, each peak represents a different detected gas. The compounds represented by each peak are identified from the corresponding mass spectra. For example, hydrogen sulfide was identified as shown in the mass spectral database match in Figure 15.4. Other sulfurous gases such as sulfur dioxide, methane thiol, carbonyl sulfide, and carbon disulfide were also identified.

To further characterize the foam, infrared spectroscopy was performed. This was chosen to perhaps yield insights as to why this material is a source of sulfurous gases.

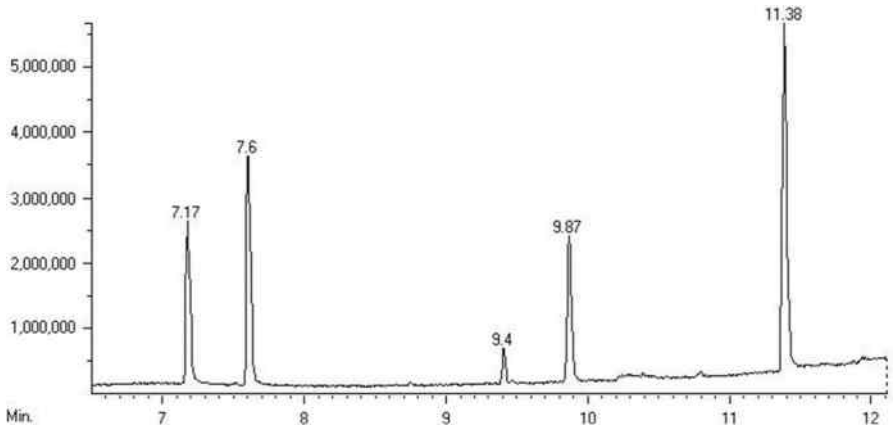

FIGURE 15.3

Chromatogram of evolved gases.

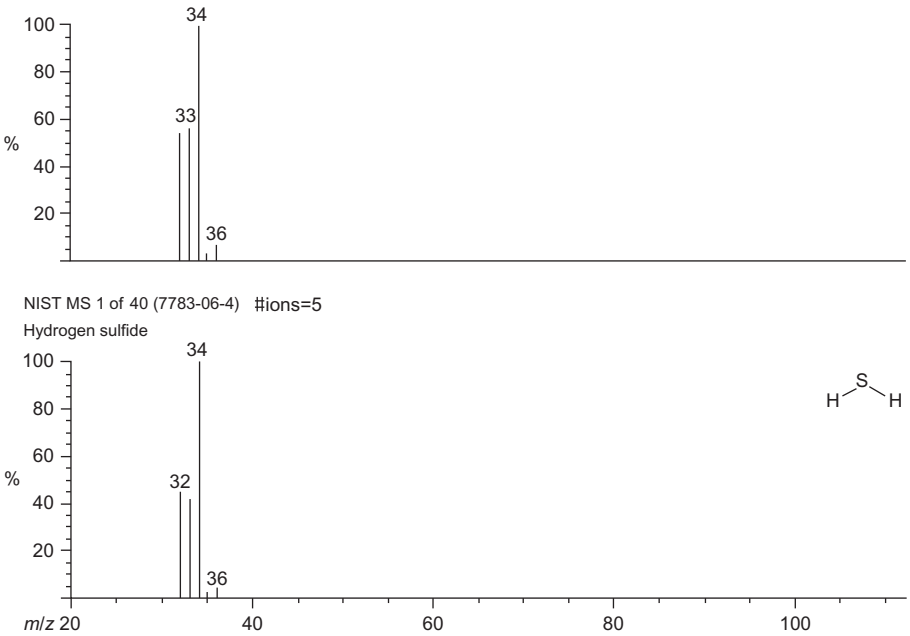

FIGURE 15.4

Database match of mass spectrum recorded from sample (top) to reference spectrum of hydrogen sulfide (bottom).

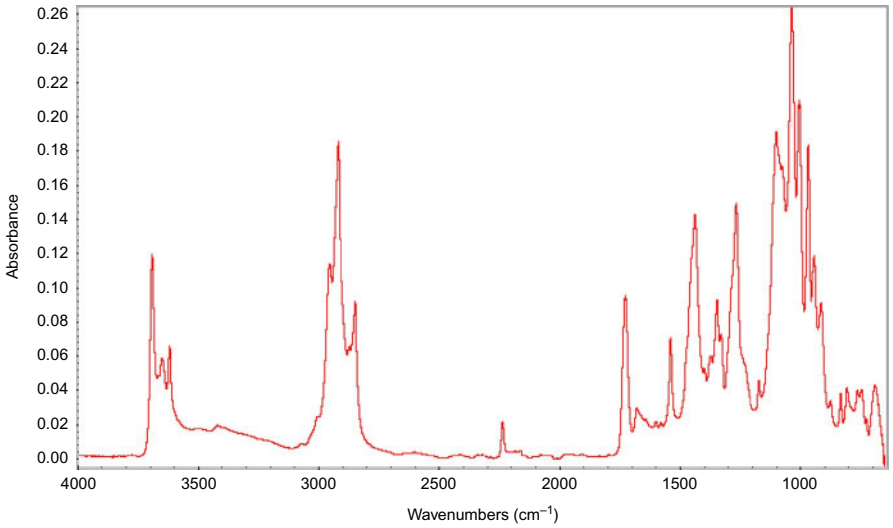

FIGURE 15.5

Infrared spectrum of dampening foam.

In this case, attenuated total reflectance (ATR) sampling methods were employed. Database searching was performed after applying appropriate ATR corrections.[2]

The infrared spectrum displayed in Figure 15.5 of the dampening foam, shown to be the sulfurous gas source, shows that it is silicate mineral filled (large bands centered around 1000 and 3600 cm^{-1} are from the filler). Additionally, the band centered around 2220 cm^{-1} is also very informative showing that this is likely a nitrile rubber blend. Figure 15.6 displays the infrared spectral database matching results of the nonsilicate bands showing that the foam is in fact a rubber blend that contains acrylonitrile as part of the formulation.

The finding that the foam is composed of a butadiene/acrylonitrile blend is significant. This results from the fact that these are polymers formed from monomers of a class of compounds called "olefins." Such monomers contain carbon=carbon double bonds which are commonly "vulcanized" (cross-linked) with elemental sulfur [6].

It should be pointed out that not all olefins are vulcanized using sulfur. However, it has been our experience that batch variation can occur such that when purchasing a blend from a supplier at time *x* it may not be sulfur vulcanized, but at time *y* it may be. Care must be taken to specify sulfur-free polyolefins if sulfur gas generation is deemed problematic.

[2]ATR spectra are not representative of traditional transmission spectra which compromise most commercial libraries. The effects of ATR sampling are typically slight but result in peaks being shifted and at different intensities than those of the database spectra. Mathematical corrections are chosen which take into account ATR parameters allowing for higher quality database matching results.

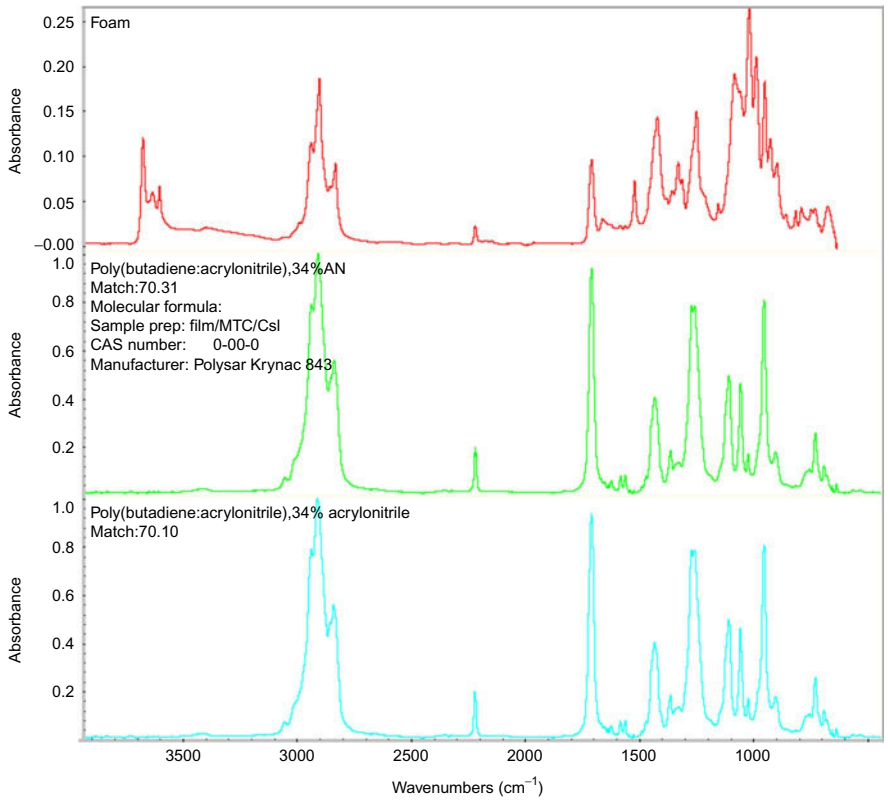

FIGURE 15.6

The foam spectrum matches butadiene acrylonitrile blend reference spectra.

Further testing, as well as applying chemical logic, revealed that polyolefin rubbers in general, and polysulfide rubbers in particular, are high-risk materials with regard to sulfur outgassing, while those that are silicone based or urethane based are low risk. These results were used as guidelines in future foam purchases for sensitive systems. The failures have not been observed with this particular assembly on systems which used these alternate foams.

2.2 CONDENSABLE MATERIALS ANALYSIS

This example is not a failure analysis, *per se*, but rather illustrates the results of material testing during design stages of a system exposed to high-vacuum conditions. The system in question is particularly sensitive to compounds which are released from materials via outgassing that can redeposit at sensitive areas, known as condensable materials. Of the construction materials used, an adhesive was a suspect source of outgassing condensables.

As applied, the adhesive could be expected to be exposed to temperatures ranging from ambient to 250 °C. Additionally, complicating the analyses and the application, the adhesive is exposed to ultra-high-vacuum conditions during use. Initial testing was performed using thermal stripping methods via placing the adhesive directly in the carrier gas stream of the GC and heating for predetermined times at predetermined temperatures (no samples were heated for longer than 2.5 min, 300 °C max. temperature tested). The chromatogram collected when the adhesive was stripped at 150 °C is displayed in Figure 15.7.

Over the course of these analyses, a number of materials were observed with onset temperatures (lowest temperature at which materials start to be detected) and rate laws determined. These were used, in part, to judge which released compounds may be expected to be condensable.

The materials were identified by analysis of the mass spectra. Most of these were discounted as possible condensable compounds as they were volatile solvents such as methanol and methyl ethyl ketone (MEK). However, about 6-10 materials, such as phenol and bisphenol-A, were considered to likely be condensable (Figures 15.8 and 15.9). When the testing progressed to the analysis of actual condensed materials under vacuum conditions, weaknesses in the approach became apparent. Additionally, a fortuitous discovery was made concerning some of the test equipment.

Standard test methods for determining condensable compounds evolved from materials involve heating samples, under vacuum or at ambient depending on the needs, and collecting the liberated materials on cooled surfaces (a kind of purge and trap) [7,8]. These collected materials are then weighed for quantitative analyses. In this example, the condensable materials released by the adhesive under high-vacuum conditions were collected and quantified according to test method ASTM E595.

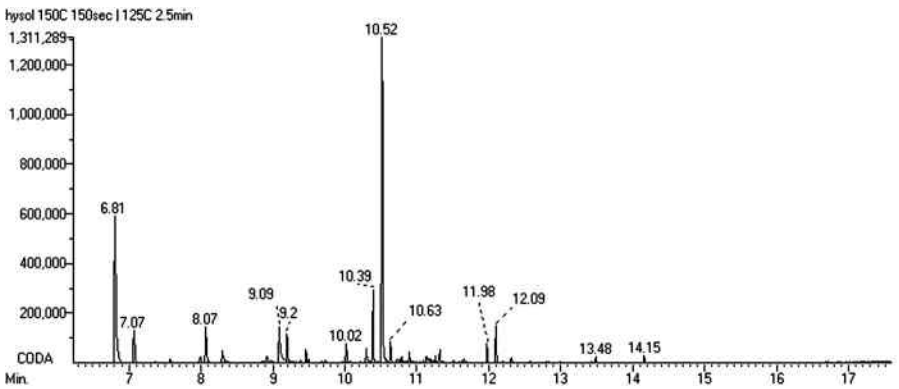

FIGURE 15.7

Typical chromatogram of material released from adhesive when tested using thermal stripping methods.

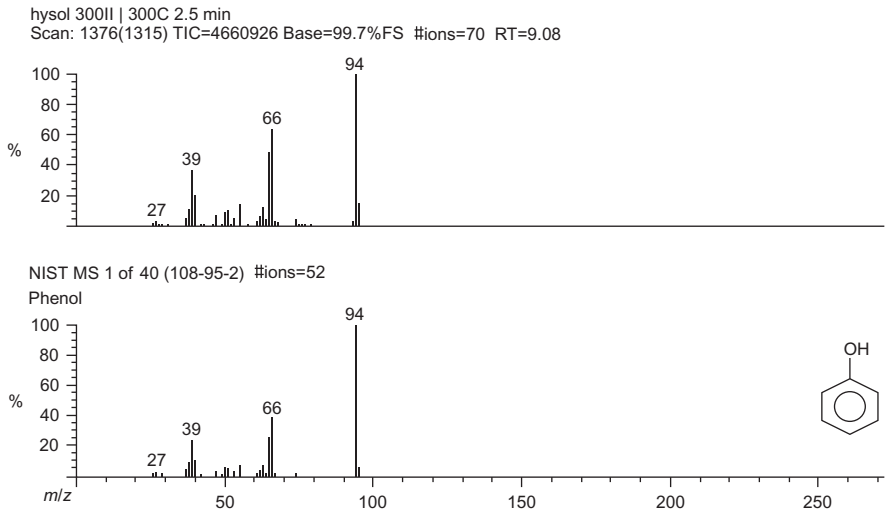

FIGURE 15.8

Phenol identified from mass spectral database matching.

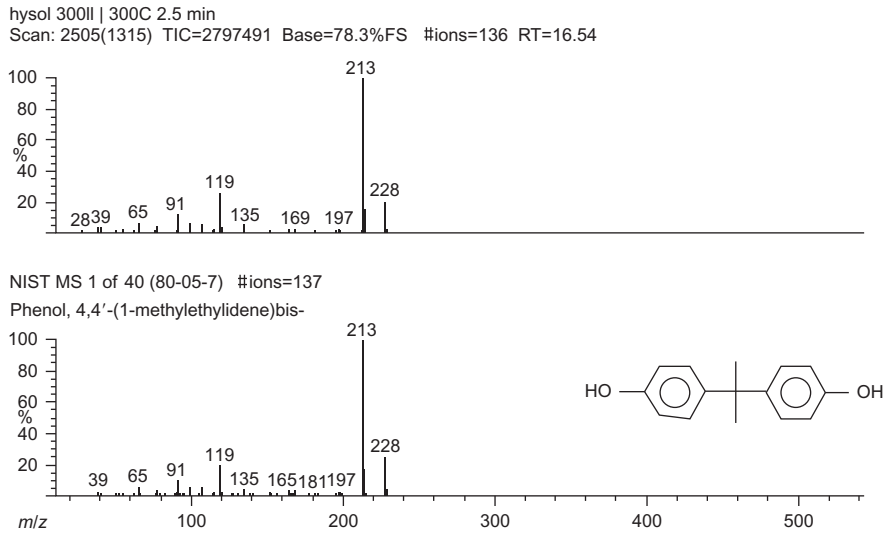

FIGURE 15.9

Bisphenol-A identified from mass spectral database matching.

While such methods are useful for quantitative analysis of condensable materials evolved during testing, they are very poor for all but the most basic materials identification purposes. In these cases, GC/MS as well as Fourier transform infrared (FTIR) analyses of the collected residues are ideal for such purposes and offer advantages to other methods such as the addition of residual gas analyzers (RGAs) to the test equipment. The results were initially more confusing than insightful.

The infrared spectra displayed in Figure 15.10, indicating that the residue was primarily composed of epoxy ethers and some silicones, where initially very hard to explain. This results from the fact that the data collected thus far had not identified any such materials. While the GC/MS data collected from the condensed materials explained the infrared spectra (following discussion), it still could not explain how initial screening missed the detection of these compounds.

Compounds detected in the chromatogram displayed in Figure 15.11 are of those that were condensed on cooled (25 °C) aluminum collectors when the test samples were heated under ultra-high-vacuum conditions (the residues were dissolved in chloroform and injected for analysis). Bisphenol-A, which was expected, was identified; however, the remainder of the materials were reactive epoxies and phenyl/methyl silicones (Figures 15.12 and 15.13).

It was quickly determined that the silicone contribution was from the diffusion pump oils used with the vacuum system of the condensable materials test equipment. Additional analyses, not presented herein, showed that these silicones were fully

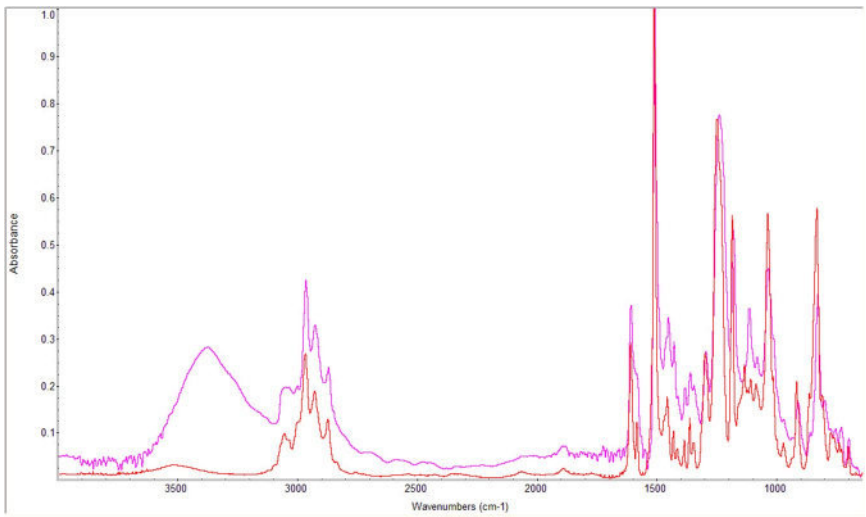

FIGURE 15.10

Comparison of calculated spectrum of an EPON-type epoxy with contributions from a phenyl/methyl silicone (red) to the spectrum of the condensable materials (purple).

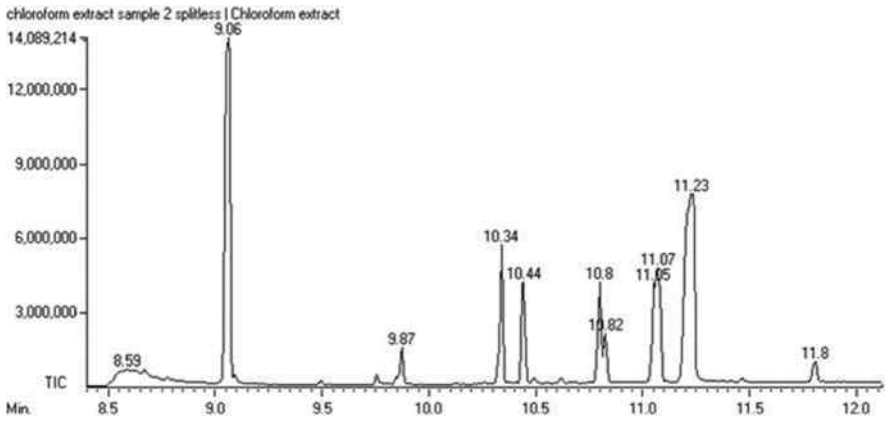

FIGURE 15.11

Condensable materials chromatogram.

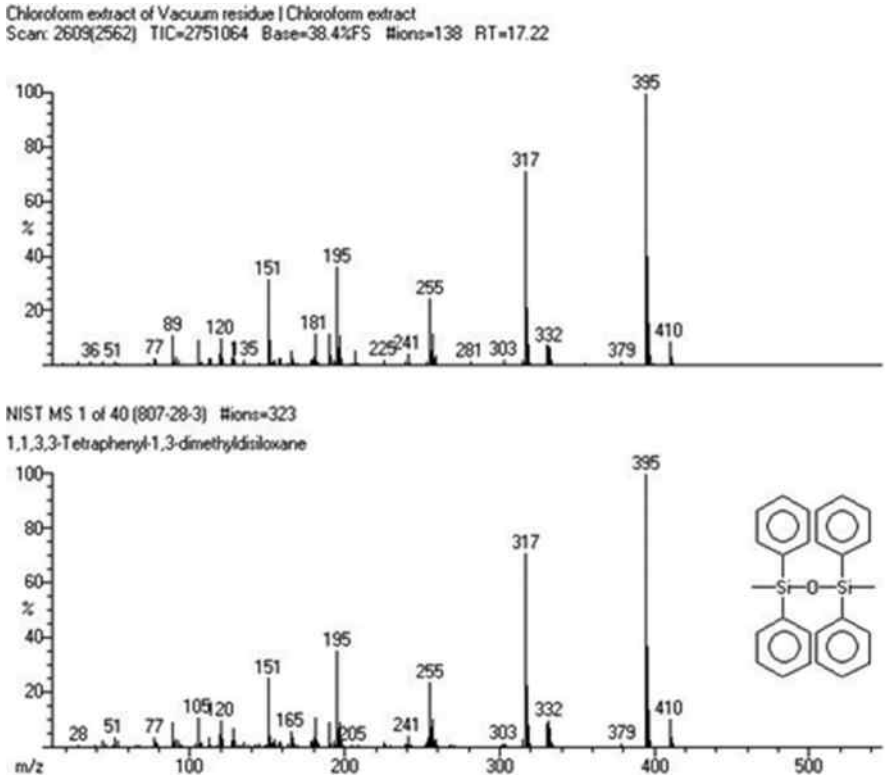

FIGURE 15.12

A phenyl/methyl silicone identified from mass spectral matching.

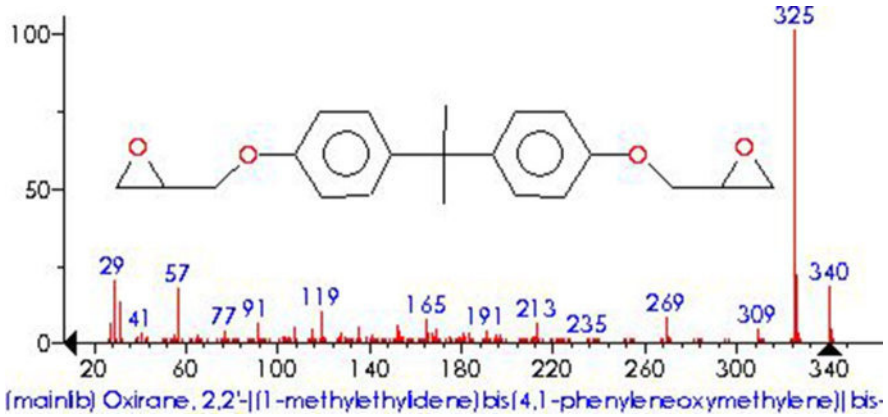

FIGURE 15.13

Diglycidyl ether of Bisphenol-A (an EPON-type epoxy).

consistent with this oil. It was realized that addition of pump oil traps was needed to prevent such contamination and insure that erroneous weights were not determined for the materials assumed to be condensed from the test material alone.

The identification of unreacted epoxy compounds at this stage, and not during the initial testing phase, was found to result from a weakness in the initial testing procedure. That is, while the initial testing method, thermal stripping, was able to detect materials which were released relatively quickly, it was not capable of detecting materials which evolved over relatively slow rates (in this case, the unreacted epoxy compounds). This results from the fact that the initial thermal stripping experiments were carried out over a maximum time period of 2.5 min, while the condensable trapping method was carried out over a period of 24 h. This latter method allowed for collection and concentration of the epoxy compounds which were released at a very slow rate and missed by the initial testing protocol. As such a trapping GC/MS method in which the materials were heated for a few hours rather than less than 3 min would have allowed for their detection if such a method was chosen initially instead of thermal stripping. Fortunately, this was accomplished, however not by design, by analyzing the condensed materials collected from a standard mass analysis technique. Additionally in the process, a flaw in the test equipment was found.

3 CONTAMINATION AT ELECTRICAL CONTACTS

Contamination of electronic components is a very common failure mechanism. The role of the chemical analyst is not to simply identify contaminates but to also assign sources and suggest remediation. In fact, while in many cases chemical identification can be the straight forward, source identification can be much more difficult. Use of product specification datasheets, material safety data sheets (MSDS),

and consultation with manufacturers and suppliers are commonly required for source identification.

Chemical contamination at electrical contacts typically manifests as intermittent contacts, high resistance, or open conditions when the contaminant is an insulator. Cases in which the contamination is an electrolyte (salt containing) or a conductor (i.e., metallic debris), the failures manifest as leakage pathways and shorts.

3.1 AN EXAMPLE OF AN ELECTRICALLY RESISTIVE FAILURE RESULTING FROM CONTAMINATION AT CONTACT SURFACES

The devices in this case are dies from wafers used for higher level component construction. The dies are tested using probes which make contact with the die pad surfaces (Figures 15.14 and 15.15). Test failures reached 100% for some wafers and extensive failure analyses were initiated. SEM/EDS was chosen as the initial investigatory technique. Both the pad surfaces and the test probe tips were thusly characterized (Figure 15.16).

Spectrum 1 displayed in Figure 15.16 is that of a noncontact surface of the die. It is consistent with the expected silicon nitride passivation. Spectrum 4 is of a contact surface. Of particular note is the detection of fluorine which was completely unexpected (C, Al, and Si were easily rationalized, while detection of O was troublesome). When the probe tips were analyzed (not shown), sulfur was detected in addition to fluorine. Neither fluorine nor sulfur was expected. At this stage, it was clear that contamination at electrical contact surfaces was the cause of the test failures.

As the EDS data is elemental in nature and gives no molecular information, only supposition as to the source of the contamination was possible. However, detection of fluorine is somewhat unique, fluorine not being typical of common contaminants,

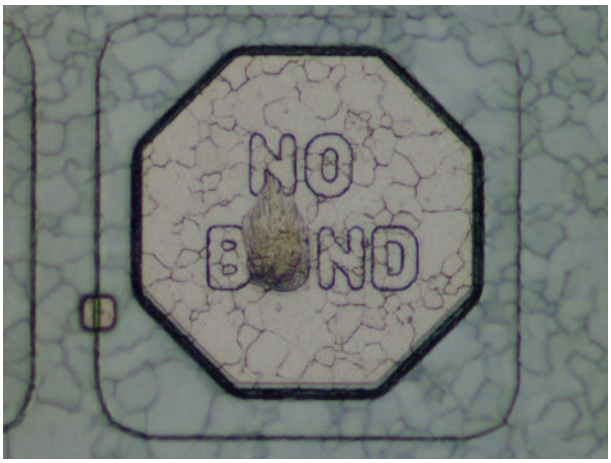

FIGURE 15.14

Probe mark on die after test failure.

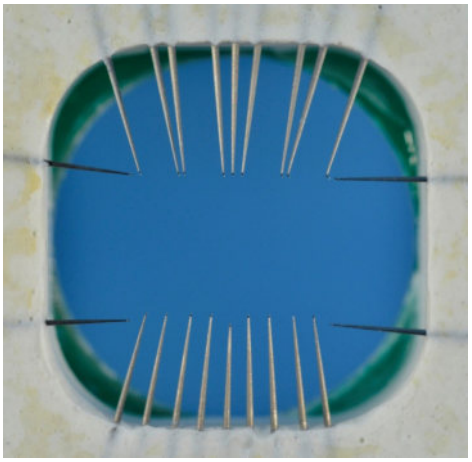

FIGURE 15.15

Probes used to test die.

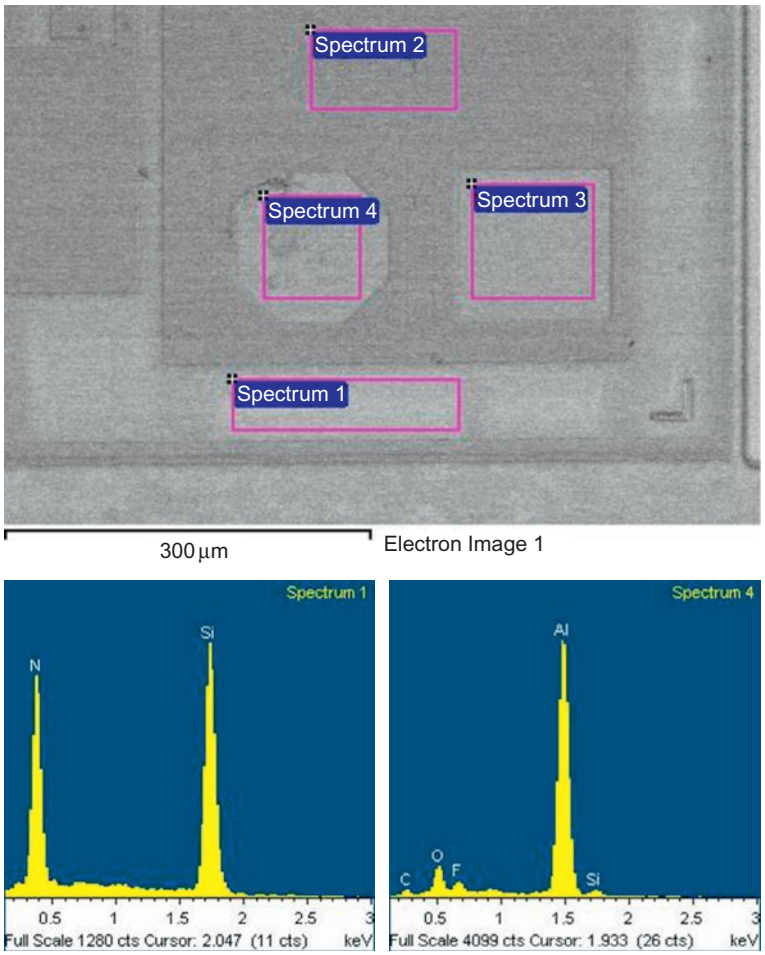

FIGURE 15.16

EDS analyses were obtained by rastering the areas shown for spectra 1 - 4. Spectrum 1 is of a non-contact area and displays the expected elements Si and N of silicon nitride passivation. Spectrum 4 is of a contact area and the detection of carbon (C), oxygen (O), and fluorine (F) in addition to the aluminum metalization are indicative of the presence of contamination.

which allowed for some theorizing as to likely sources. For example, the prevailing initial theory was that fluorocarbon contamination accounted for the failures. It was thought that packaging, both that used for storage and shipping of the wafers and the test probes, could be the source of such a contaminant. Raman and FTIR spectroscopies as well as pyrolysis-GC/MS were chosen to test this theory—all of which are very sensitive for fluorocarbons.

FTIR analyses of the probe and pads surfaces were carried out using both normal angle and grazing angle reflectance microscope FTIR techniques. Collection of Raman spectra were attempted using 532- and 780-nm laser sources. At none of the surfaces analyzed were fluorocarbons, or for that matter organic materials, identified. In fact, the analyses strongly suggested inorganic contamination. Raman and FTIR analyses of packaging materials also did not indicate the presence of fluorocarbons. Finally, pyrolysis-GC/MS analyses all but assured that there were no sources of fluorocarbons in the suspected packaging.

A secondary theory was that the contamination resulted from unintentional implantation during plasma etching of the wafers. Such a mechanism is well known and occurs as a result of the energetic environment of the plasma [9]. Additionally, fluorine implantation could explain the detection of oxygen at the aluminum pad surfaces via fluoride-catalyzed corrosion.

This supposition seemed even more likely upon consultation with the wafer manufacturer who revealed that sulfur hexafluoride was the plasma gas used with these wafers. This mechanism, implantation during sulfur hexafluoride ion etching, would also explain the sulfur that was detected along with fluorine on the probe tip surfaces.

While all the data seemed overwhelming that the contamination occurred during plasma etching, the primary customer still believed that fluorocarbon contamination was the source of the residue. As a result, Auger spectroscopy was chosen as the final arbiter for two primary reasons: it is an extremely surface-sensitive technique which could overcome possible sample thickness limitations of the aforementioned FTIR and Raman methods, and it provides chemical bonding as well as elemental information. Because of the latter consideration, this method could determine if the detected fluorine is bonded to carbon (C-F bonds), as would be expected of fluorocarbon contamination, or is in the form of inorganic fluorine, such as aluminum fluoride, resulting from implantation during plasma etching.

The Auger spectrum displayed in Figure 15.17 is similar to the previously presented EDS spectra in that carbon, oxygen, fluorine, and aluminum are detected (in this case, sulfur is also detected), however, also plotted is the kinetic energy of the ejected Auger electrons. This energy is what yields insight into the chemical bonding, or environment, of these species.

Analysis of the fluorine binding energy yielded the following conclusion: "The data showed that the F 1s peak appears to be at one binding energy (BE), which indicates that the majority of the F atoms are in the same chemical state. The measured BE was ~687.0 eV, which is approximately 1.0 eV higher than the reported standard value for AlF_3 - $3H_2O$. This BE is 2.0 eV less than that for perfluoroalkane materials, indicating that it is not likely to be present as such. There is evidence that some

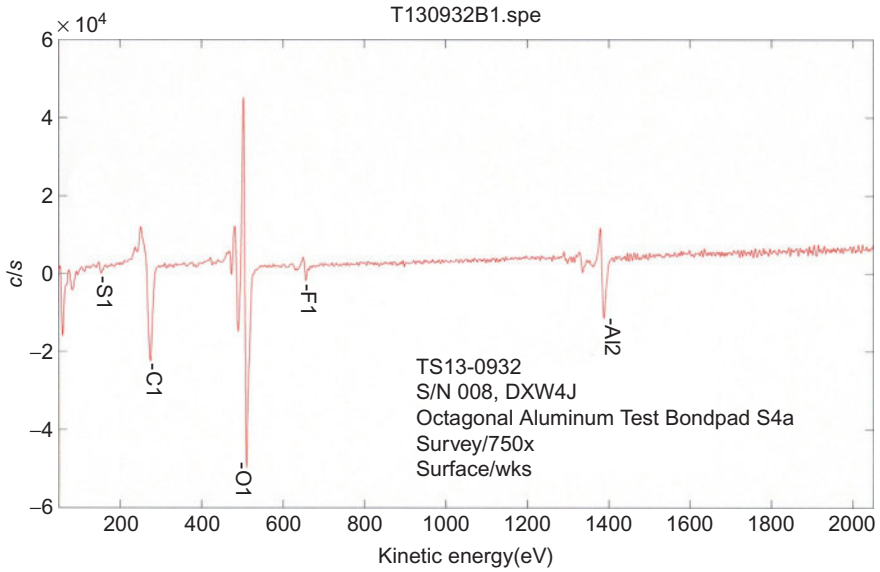

FIGURE 15.17

Auger spectrum from bond pad surface.

charge shifting (an increase of at least 0.5 eV) is occurring near the Al bond pads, which would tend to bring the BE for the F more in line with that for aluminum trifluoride trihydrate. However, based on the stoichiometry of the F to the Al atoms as well as these energy shifts, it is more likely that the F exists as randomly distributed atoms within an aluminum oxide matrix than as the aluminum trifluoride trihydrate." [10] In other words, this analysis proved that the fluorine was deposited via ion etchant gas and was not present as a result of fluorocarbon contamination. The finding of sulfur further supports this conclusion.

The root cause in this case was determined to be implantation of etchant gas atoms into the aluminum pads. Fluorine in particular catalyzed the formation of electrically insulating aluminum corrosion products. These built up over time on the test probe tips leading to the observed failures. The questionable wafers were quarantined and the test probes replaced. These measures proved to mitigate the failures.

3.2 INTERMITTENTS AND OPENS DURING OPERATION OF A SLIP RING

A slip ring is a device which allows for electrical continuity during rotation of contact surfaces. Typically, one of the contact surfaces is fixed while the other exhibits rotary motion. These devices are used on a number of applications including rotating turrets, electric motors, and any type of application in which an electrical contact may be expected to be maintained during rotational motion between contacts. In

the design discussed herein, the contact was made between stationary brushes and rotating "platters" with circular brush tracks.

This particular failure was exhibited in a complex assembly consisting of several layers of platters with dozens of individual brush platter/contact pairs. The failures manifested as intermittent electrical contacts as the slip ring rotated resulting in data corruption. This lead to the essential shut down of an entire program with assembly halted until root cause and mitigation could be resolved. While this analysis involved several layers of investigation and was a considerable undertaking, only some of the select chemical analyses results are discussed herein.

As the failures were intermittent in nature, an obvious contributing factor was the presence of insulative materials at the brush/platter interface. Initial investigations were carried out using SEM/EDS and SEM/wavelength dispersive spectroscopy (WDS) methods.

Displayed in Figure 15.18 is the condition of the brush contact surfaces as revealed by SEM imaging. The lighter colored areas, at the contacts interfaces (contact was made at a region in the middle of image), result from the presence of gold which was transferred from the platter contacts. The darker residues result from the presence of lower atomic weight elements such as silicon, oxygen, and carbon. Figure 15.19 was a typical EDS spectrum recorded from these areas.

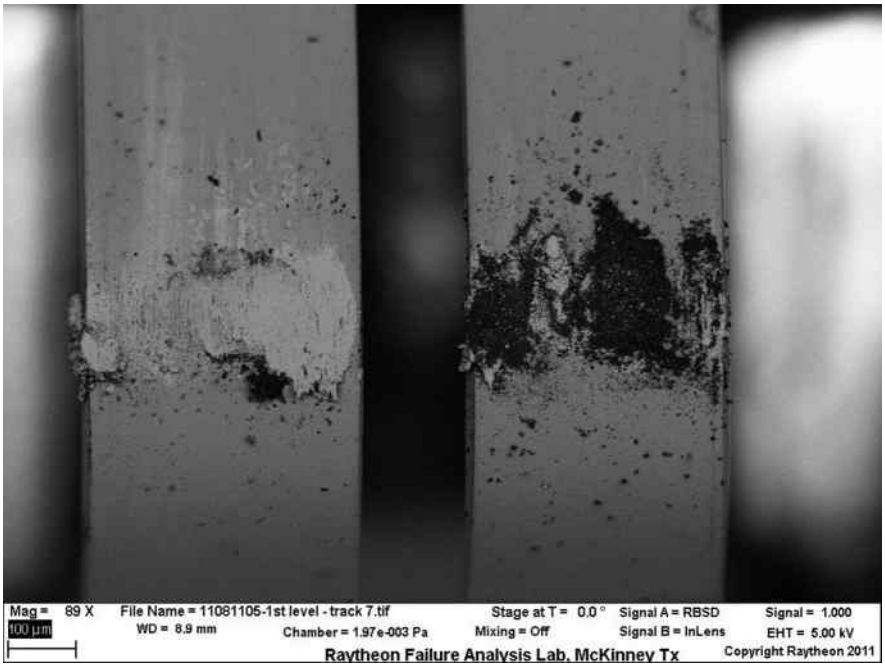

FIGURE 15.18

SEM image of residues on brush surfaces.

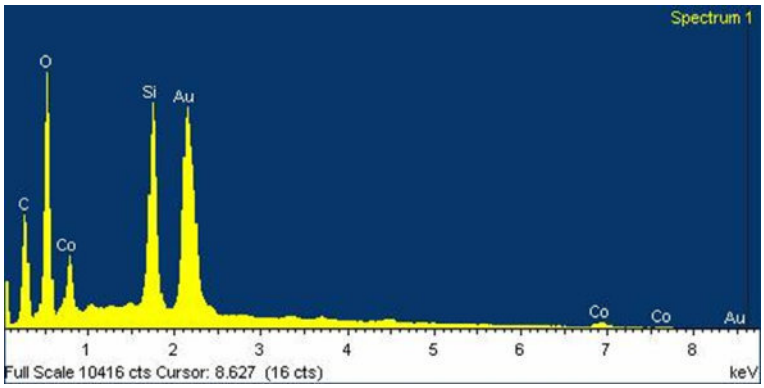

FIGURE 15.19

Typical EDS spectrum of residues on brush contacts.

Identification of silicon, carbon, and oxygen strongly suggested the presence of insulating materials such as silica, silicones, and organic residues. Additionally, it was determined that the oil base of the grease used to lubricate the contacts was not detectable on the platter surfaces (FTIR and GC/MS analyses not reported herein). This lead to an assumption that the oil was not present due to some mechanism such as migration while the grease soap thickeners, which are much less mobile, could still be present at the surfaces conceivably contributing to residue formation. The thickeners of the grease were determined to be soaps of barium and calcium upon consultation with the manufacturer. As these elements were not detected using EDS methods, WDS was pursued to further investigate this supposition. This method was chosen to take advantage of the lower elemental detection limits.

Figure 15.20 shows that barium and calcium were detected in the contact residues. This supported the supposition that grease additives contributed to the residue formation.

As silicones, silica, and organic residue were suspect in the residues, an investigation utilizing FTIR methods was also undertaken. Spectra were recorded using both microscope reflectance and transmission methods.

The spectra displayed in Figure 15.21 are indicative of the presence of both carboxylate salts (bands above 1200 cm^{-1}) and silica and/or silicone materials (bands below 1200 cm^{-1}). The carboxylate salts were rationalized as being present in the form of the aforementioned grease additives. On the other hand, the source of silica/silicones was not immediately clear.

Because silica (silicon dioxide) and silicones have chemical bonds in common, the spectra share overlapping bands. To try and understand if either or both these species were present in the residues, a careful examination of the spectra was undertaken.

Displayed in Figure 15.22 is a comparison of the theoretical band positions resulting from silicones and silica, shown as individual peaks, versus the actual residue

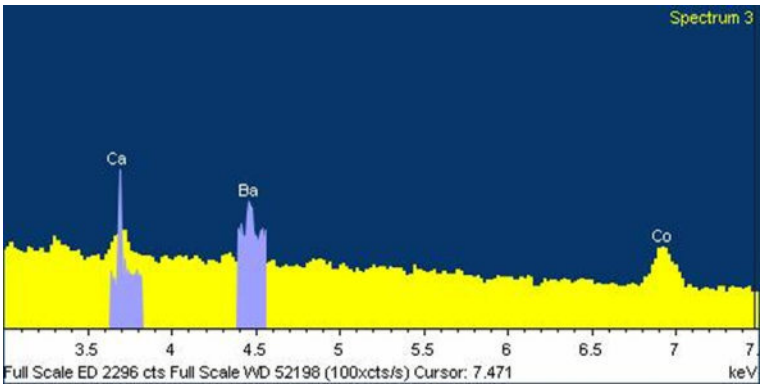

FIGURE 15.20

WDS spectrum showing the presence of calcium (Ca) and Barium (Ba) in the contact surface residues.

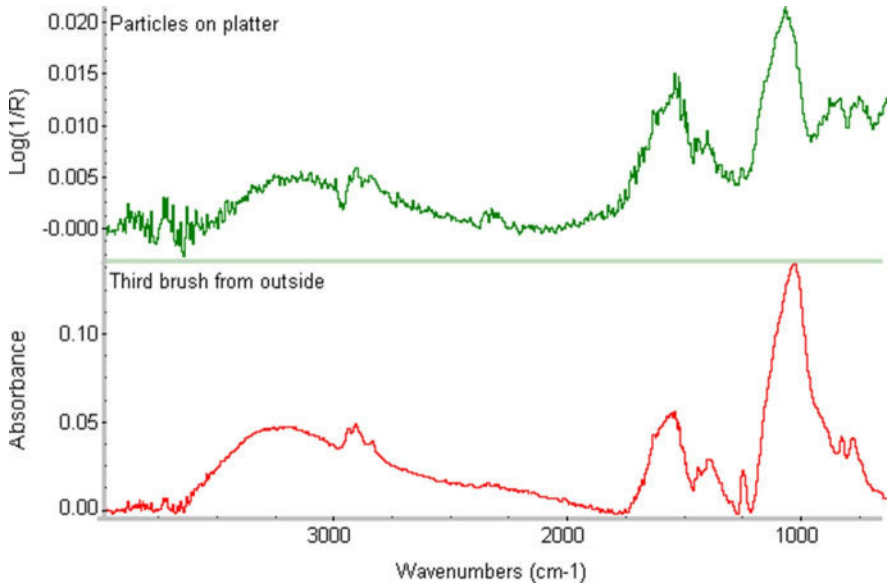

FIGURE 15.21

Typical infrared spectra recorded from residues.

spectrum shown as the continuous line. The following explanations are useful in interpreting the data:

(1) From 1250-1290 cm^{-1} are the C-H deformations of silicones which are inherently strong absorptions.

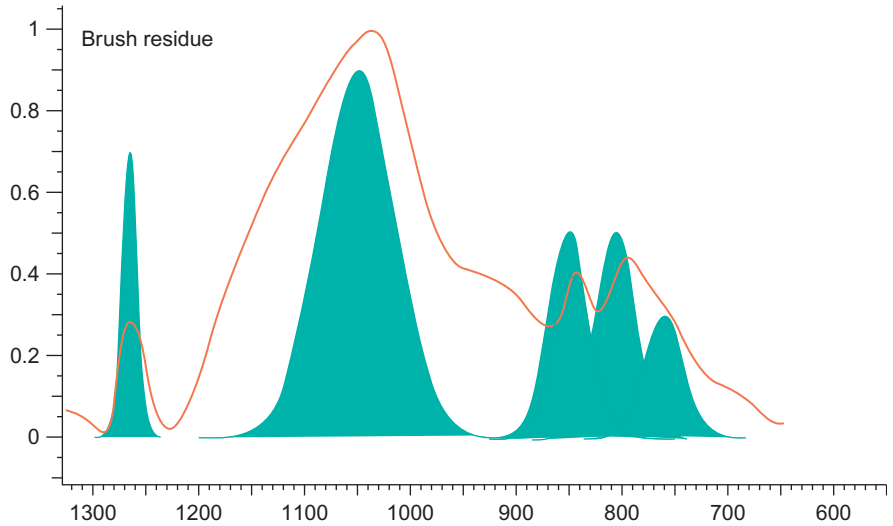

FIGURE 15.22

Analysis of silica/silicone region of FTIR spectrum.

(2) From 960-1150 cm^{-1} is an Si-O-Si stretching band which is an inherently very strong absorption. Note: this bonding is present in both silica and silicones.
(3) From 840-860 cm^{-1} is a Si-C stretch which is an inherently strong absorption. This is common to silicones resulting from an $Si(CH3)_2$ grouping.
(4) From 750-770 cm^{-1} is a Si-C stretch from an $Si(CH3)_3$ grouping which is an inherently strong absorption (also common to silicones).

Careful analysis of the intensity data of the various peaks from the collected spectra, applying mathematical modeling, revealed that both silica and silicones were present at the contact surfaces. As these are both electrically insulative, their presence could help explain the failures. Furthermore, consultation with the manufacturer revealed that the assemblies had several potential sources of silicone contaminants (most being potting compounds).

One of the mechanisms of silicone deposition, leading to the contact surface contamination, was shown to result from the slip rings being submerged in isopropyl alcohol during a processing step; the alcohol was dissolving silicone oils allowing for redeposition. Additionally, the construction material immediately adjacent the contact surfaces of the platters was determined to be composed of a highly silica filled polymer. Sand blasting of this material was shown to lead to silica particles become dislodged with some contributing to the contact surface residues.

Corrective actions included changing of the platter polymer to one that was not silica particle filled, removing silicone potting materials from the construction, and application of a different contact lubricant. These measures, along with others, lead to complete resolution of these failures.

4 A SURFACE APPEARANCE QUESTION

One of the more common questions asked of labs is "Why does my surface look like something is on it; what is it?" For example, this is very commonly encountered with gold-coated electrical bond pads used with electronic devices, particularly those with the presence of microtopography. In these cases, it is most commonly determined that surface topography interacting with light causes the macroappearance, suggesting the presence of a foreign material [11]. However, there are certainly circumstances in which surface appearance anomalies are caused by contamination. When such contamination is relatively plentiful and thick, the analyses are typically straightforward. On the other hand, even extremely thin-surface contamination can cause surface appearance changes, and in these cases, the analyses can be challenging. One such example is highlighted in the following discussion.

4.1 INVESTIGATION OF DISCOLORED WAFERS

The wafers displayed in Figure 15.23 are polyimide coated; the light green wafer represents the appearance prior to a plasma-etching step while the darker green wafer is of the appearance after the etching. Etching was performed to increase adhesion of additional layers of polyimide, which were to be subsequently applied, and to clean the surface. The customer's supposition was that the procedure had created carbon black, via decomposition of the polymer, leading to the darker appearance. There was also concern that any type of contamination would alter the properties of the coatings.

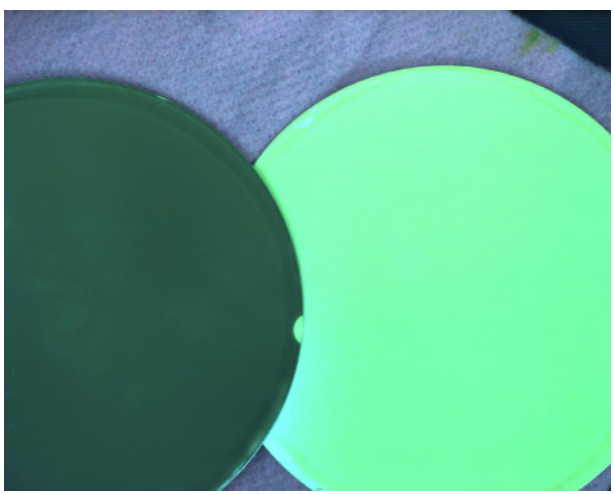

FIGURE 15.23

Polyimide-coated wafers. The darker sample is post-plasma etching.

The initial investigation was carried out using FTIR methods employing a microscope ATR accessory. This was chosen as it is relatively quick and could indicate if a mechanism such as oxidative damage had occurred. However, FTIR spectroscopy is insensitive to carbon black, if it was in fact the culprit. The spectra were indistinguishable between the two samples, and as a result, this approach was deemed insufficient.

Raman confocal microscopy was chosen next as it is very sensitive to the various allotropes of elemental carbon and the confocal capabilities allow for depth profiling. The analysis was performed by defocusing the laser just above the surface of the samples to allow for detection of surface composition followed by collection of spectra upon focusing into the samples.

The top spectrum displayed in Figure 15.24 was collected from the dark sample surface and shows the presence of alumina (the bands above about 3500 cm^{-1} are plasmon bands resulting from exciting alumina with a 532-nm laser). Conspicuous by its absence are any bands associated with elemental carbon—this seemingly discounts the initial hypothesis. On the other hand, when the laser was focused into the sample, bottom spectrum in Figure 15.24, polyimide bands are also observed. This demonstrates that alumina is a surface contaminant residing on the polyimide surface. The sample which was not etched did not have indications of the presence of surface alumina.

While Raman spectroscopy is generally not a "surface-sensitive" technique, the excitation depth is typically around 2 μm, it is very sensitive to certain materials. For example, alumina produces a very intense Raman response when analyzed using a 532-nm laser and miniscule amounts present as extremely thin layers can be detected. However, there was concern that more than just the presence of alumina could account for the darker appearance, post-plasma etch, and it was theorized that other extremely thin-surface contaminants were also present. SEM/EDS/WDS

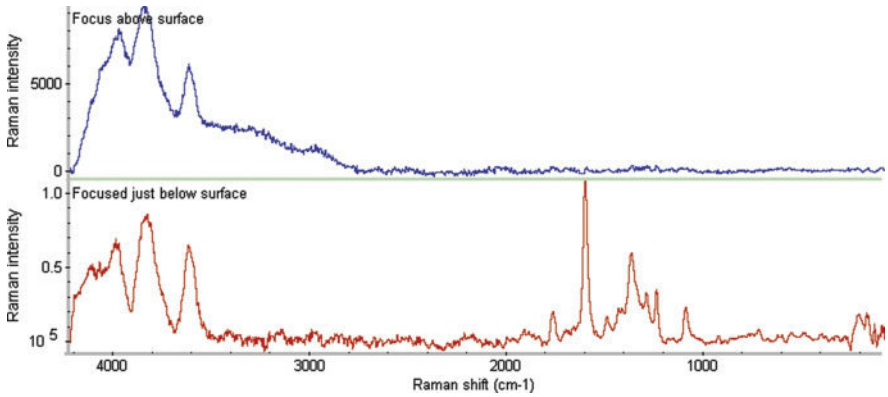

FIGURE 15.24

Top spectrum was collected when defocused above the dark wafer sample. The bottom spectrum was collected when focused into the sample.

Table 15.1 All Elements Are Listed in Atomic Percent

Sample	Carbon (%)	Nitrogen (%)	Oxygen (%)	Aluminum (%)	Titanium (%)	Tungsten (%)
Not plasma etched	89.2	3.25	5.9	0.5	–	–
Plasma etched	57.3	1.68	28.9	5.8	2.51	3.29

Other trace elements make up the remainders.

analyses were carried out but did not detect such materials. As a result, an XPS investigation was chosen to further investigate this possibility.

In this case, only elemental information was collected from just the top 10 Å of the samples. The results, as shown in Table 15.1, were enlightening.

The data presented in Table 15.1 show that the plasma-etched wafer has surface titanium and tungsten contaminants as well as the previously mentioned alumina. The lower detection (% when compared to nonetched sample) of carbon and nitrogen are rationalized as resulting from a lesser surface contribution of the polymer because of the presence of the contaminants. The significant increase in the level of oxygen detected on the plasma-etched sample is consistent with the presence of alumina and suggests the tungsten and titanium species are most likely oxides (waters from hydration may also contribute). The combination of all of these materials at the plasma-etched surface can easily account for the darker appearance. This also confirms that contamination, which could potentially affect device performance, is present.

On-site investigations, as well as discussions with the customer, revealed that the wafers were held in place with devices that were coated with thin layers of titanium and tungsten coated on top of aluminum. The failure mechanism was determined to be deposition of the element oxides as a result of the plasma-etching process. Care to minimize exposure of this material to the plasma environment eliminated the failures.

5 FAILURES AS A RESULT OF CLEANING

At first thought it may seem counterintuitive that the cleaning of components and assemblies would lead to failures. After all, the purpose of cleaning is to remove contamination and ensure more reliable products. The modes of failures that result from cleaning are varied ranging from the presence of residual cleaners at unexpected places leading to shorting, insulative failures, and optics hazing, or due to the presence of contaminates from the use of improper or dirty (i.e., used) cleaners which can lead to similar results.

5.1 SHORTING CONNECTORS

In-line aqueous board cleaners are used to clean a number of assemblies including flex circuits with attached connectors. These cleaners have a few features in common such as the presence of water, the presence of saponifiers which are basic compounds

that help convert insoluble flux acids into water soluble salts, the presence of surfactants which allow for better surface wetting, and the presence of other materials such as organic solvents and protective additives.

A particular consequence of the presence of surfactants in cleaners is that they allow for the entry of chemicals into small crevices and openings. However, because of the high surface tension of deionized (DI) water used to rinse assemblies in the final stage of the overall cleaning process, it is common that the cleaner chemicals are not removed from these areas during rinsing [12]. Such was the case in the following example.

A connector at the end of a flex circuit was brought to the lab which was exhibiting shorting failures between pins and from pins to case. This was occurring relatively quickly during initial testing.

The connector displayed in Figure 15.25 has three distinct cavities internal to the construction. Additionally, a silver metal grounding ring encircles these cavities. Closer inspection revealed extreme corrosion and electromigration between the pins and from some pins to the case (Figures 15.26–15.28).

As shown, Figures 15.25 and 15.26, electromigration of lead from tin/lead solder as well as silver from the grounding frame was noted on the internal cavity surfaces of the connector. For such phenomena to occur, the connector must have had power applied while wet, or at least with significant humidity present [13]. Discussions with the customer revealed that the flex circuits and connectors had passed through an in-line cleaner system. This led to the belief that the ingress of cleaner chemicals, which cannot be washed out by the DI rinse phase, accounted for the failures. The saponifier, in particular, would accelerate these phenomena as it is both corrosive and an electrolyte. Chemical investigations started with the collection of Raman

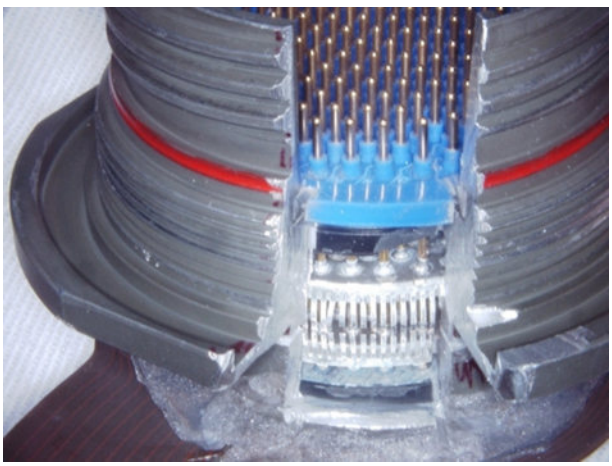

FIGURE 15.25

Overall construction of connector after a section was removed.

FIGURE 15.26

Note white corrosion residues.

spectra for the white residues. This method was chosen as it was fast and the spectra were simple to collect.

The Raman spectral data presented in Figure 15.29 indicate that the residue is largely composed of lead carbonate, an expected corrosion product. However, this does not yield insights into how the electromigration leading to corrosion occurred. To further test the assumption of in-line cleaner ingress, GC/MS methods were chosen.

As cleaning solution ingress into unexpected places is a well-known failure mechanism, the cleaner chemistry had been fully characterized by the time this analysis was undertaken. Of particular note is that the cleaner contains "marker" compounds of limited volatility (they do not evaporate over time), indicating that such ingress has occurred. Of these, a couple of surfactants as well as an alcohol of the cleaner are commonly detectable even after extended periods of time.

To prepare the analysis samples, methanol was gently rinsed over the internal connector surfaces and the resulting solution was allowed to evaporate. The residue thusly formed was reconstituted with about 20 µl of methanol. Of this, 1 µl was injected for analysis. The chromatogram displayed in Figure 15.29 was the result.

The findings of in-line cleaner marker compounds, as revealed by analysis of the relevant mass spectra, verified that ingress into the connectors coupled with applied voltage lead to the reported failures (Figure 15.30). Remediation in this case involved purchasing screw caps from the supplier which were put over the tops of the connectors prior to exposure to in-line cleaning operations thusly eliminating cleaner intrusion.

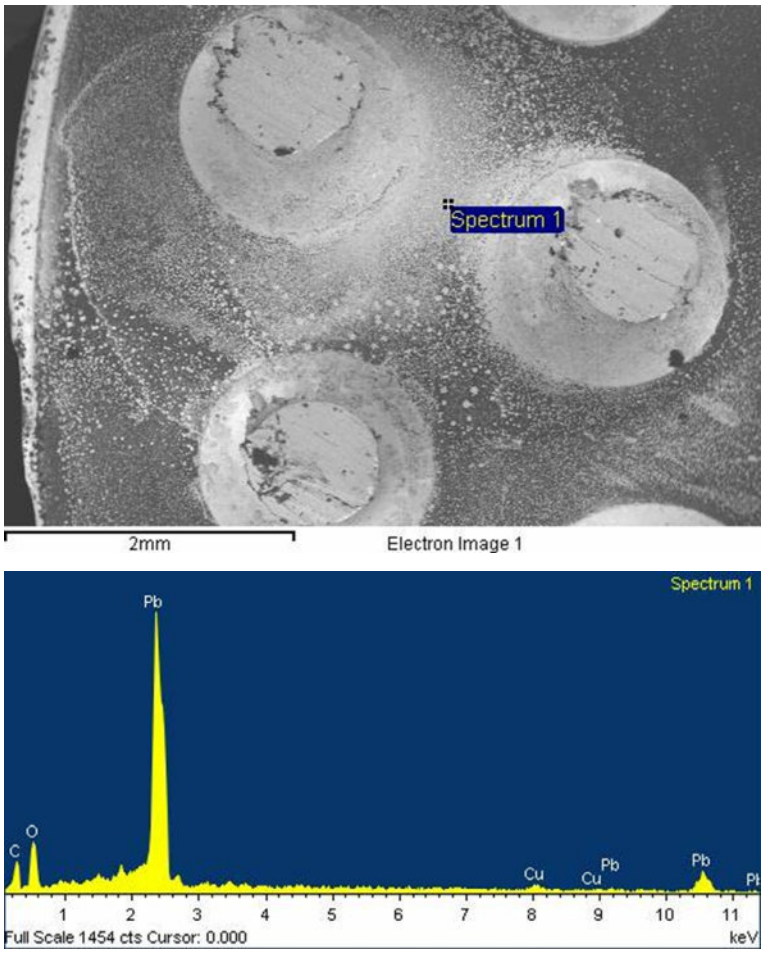

FIGURE 15.27

Spectrum 1, collected from the spot indicated in the image, shows that electromigration of lead occurred between pins.

6 A METALLURGICAL EXAMPLE

Historically, incorrect chemical composition of metals is a very uncommon failure mechanism. More commonly, forging defects such as improper tempering and related concerns are the root cause of failure. However, as the use of improper alloys or compositional deficiencies is very intuitive and also easily analyzed, failure analysis labs are often asked to verify if improper chemical composition of metals contributed to failures. The example chosen here is seemingly straightforward, but as it will be shown, highlights one of the more common chemical analysis technique pitfalls: the inherent limitations of individual methodologies.

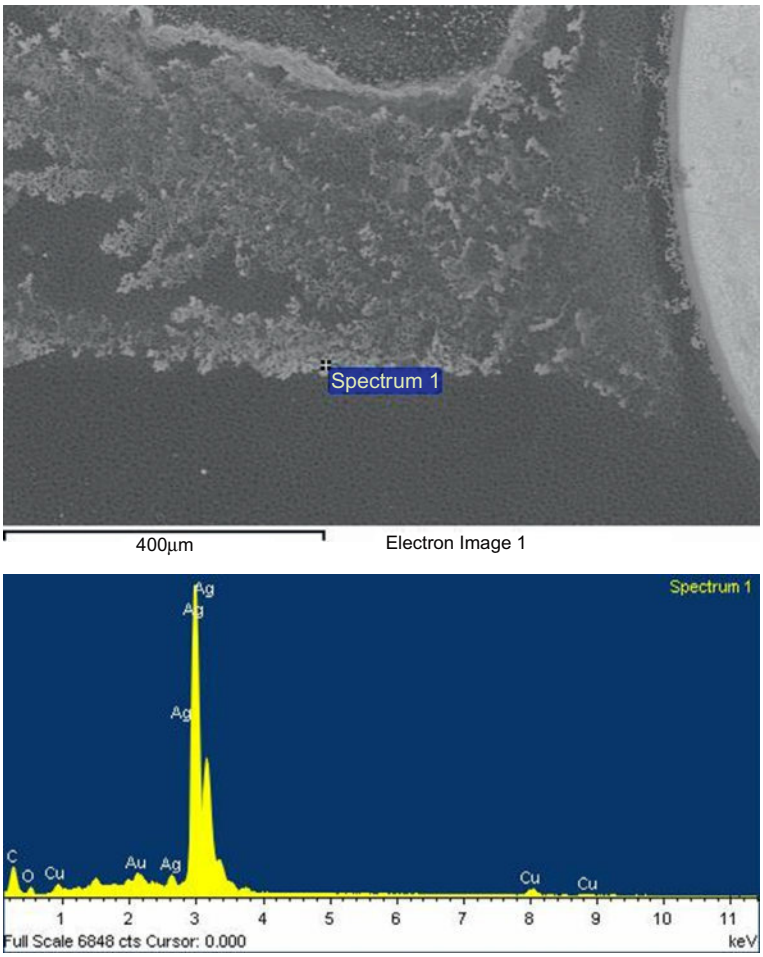

FIGURE 15.28

Spectrum 1, collected from the spot indicated in the image, shows that electromigration of silver occurred between a pin and the case.

In this example, an aluminum housing failed via fracture and was brought to the lab for analysis. The specified alloy was to meet AMS4218 requirements (7.0Si-0.35Mg). Initial investigations were carried out using SEM/EDS methods and the results suggested that the alloy did not meet requirements; the percent weight of silicon was consistently determined to be about 12%, not the nominal value of 7%. This led to the conclusion that an improper alloy had been used. The customer, and initially the lab, thought that the root cause had been determined. However, caution was urged and further analyses were requested, as EDS methods are known, at times, to yield faulty quantification data, particularly when analyzing inhomogeneous

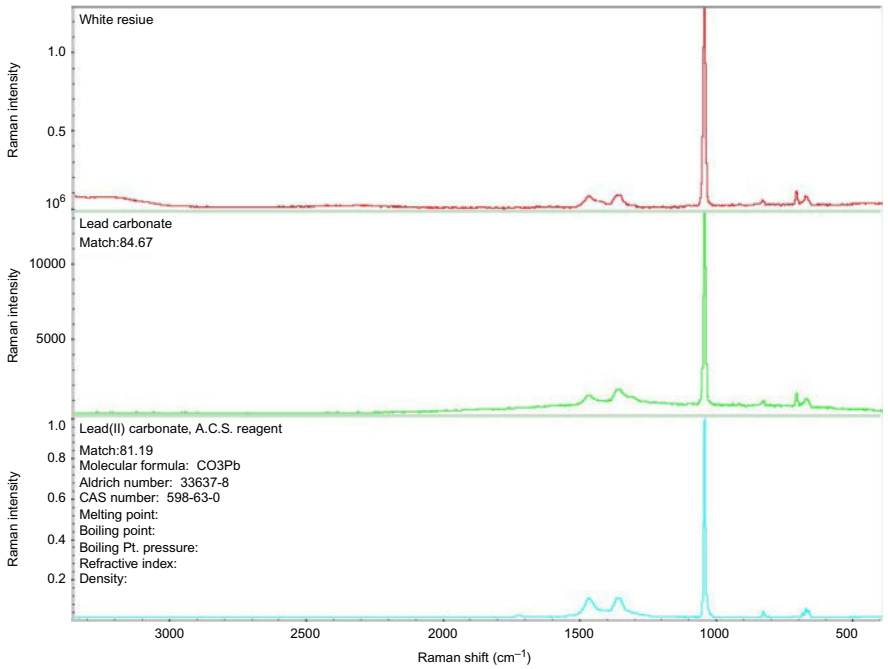

FIGURE 15.29

Raman spectrum of white residue between pins (top) database matches to lead carbonate (bottom two spectra).

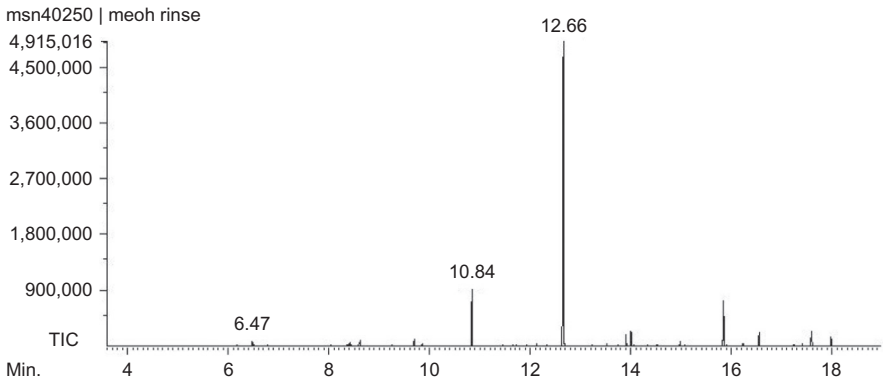

FIGURE 15.30

The labeled peaks were identified from the mass spectra as components of the in-line cleaner.

Table 15.2 ICP/AES Analysis Results Compared to Requirements

Composition Requirements, wt.%			Housing	
Element	**Min**	**Max**	**Element**	**wt%**
Silicon	6.5	7.5	Silicon	6.95
Iron	–	0.20	Iron	0.12
Copper	–	0.20	Copper	0.01
Manganese	–	0.10	Manganese	0.0
Magnesium	0.25	0.45	Magnesium	0.39
Zinc	–	0.10	Zinc	0.0
Aluminum		Remainder	Aluminum	Remainder

materials (high-silicon aluminum alloys are inhomogeneous with the silicon existing primarily as distinct phases). Additionally, EDS methods cannot detect the trace elements required of the specifications. Inductively coupled plasma/atomic emission spectroscopy (ICP/AES) methods were chosen to verify or rule out the assumption that the improper alloy had been used.

The data displayed in Table 15.2 show that the alloy did in fact meet specification and the initial assumption that an improper alloy had been used was based on a commonly encountered problem when relying solely on EDS data: the inability, in some cases, to properly quantify elemental levels of inhomogeneous samples.

When this data was presented to the customer, as well as the SEM operator, there was some resistance. After all, both parties had thought they had found root cause and EDS analyses are fairly accurate in most cases. To put any uncertainty to rest, a third method, spark emission spectroscopy, was employed using a third-party laboratory. The results were essentially identical to the ICP/AES data listed in Table 15.2 and the assumption of improper alloy use was discarded. Further analyses showed that forging defects led to the observed failure. Remediation involved screening for assemblies built from the suspect lot.

7 CONCLUSION

The examples discussed herein were chosen to highlight how chemical analyses techniques may be applied toward failure analyses. The examples cited are certainly not exhaustive and there are a host of other methods available. However, the techniques discussed in this chapter, as well as part one of this book, were chosen as they are the most common of the chemical analyses methods employed during failure analyses. The author's intention was to provide a basic understanding of the principles of operation of these methods and to show how they may be applied to the multitude of chemical analysis challenges presented to the failure analyst.

REFERENCES

[1] The data is available from http://outgassing.nasa.gov/. Last accessed 1/28/2015.
[2] Wolfgong W, Wiggins K. The silicone conundrum. J Fail Anal Preven 2010;10(4):264–9.
[3] Wolfgong W. The Silicone conundrum part II: "Low outgassing" silicones. J Fail Anal Preven 2011;11(3):215–21.
[4] Hillman C, Arnold J, Binfield S, Seppi J. Silver and sulfur: case sudies, physics, and possible solutions. In: SMTA international conference proceedings, October, 11; 2007.
[5] The Journal's EditorialStaff. Silver to black–and back. J Chem Educ 2000;77(3):328A.
[6] Fisher H. Natural and synthetic rubbers. J Chem Educ 1942;19(11):522.
[7] ASTM 1559–09. Standard test method for contamination outgassing characteristics of spacecraft materials.
[8] ASTM E595. Standard test method for total mass loss and collected volatile condensable materials from outgassing in a vacuum environment.
[9] Kurihara K, Egami A, Nakamura M. Structure of surface reaction layer of poly-Si etched by fluorocarbon plasma. J Vac Sci Technol 2006;24(2):286–90.
[10] From correspondence. Carl Townsand. Mechanical Analysis, Materials and Test Equipment Department; Raytheon, El Segundo, California.
[11] Olefjord I. In: Brune D, editor. Surface characterization. Weinheim, Germany: Wiley-VCH Verlag GmbH; 1985. p. 82–3.
[12] Wolfgong W. Cleaning COTs parts in military applications. Circuits Assembly 2006;20(10):18–21.
[13] Krumbein S. Metallic electromigration phenomena. 33rd meeting of the IEEE holm conference on electrical contacts, Chicago, Illinois, September 21-23, 1987. IEEE Trans Comp Hybrids Manuf Technol 2002;11(1):5–15.

CHAPTER

16 Characterization of steel cut-edge properties for improved life predictions for preventing automotive structural failure

Daniel J. Thomas
College of Engineering, Swansea University, Swansea, UK

CHAPTER OUTLINE

1 CUT-EDGE CHARACTERISTICS PROPERTIES

Durability requirements for safety-critical advanced high-strength steel structures used in automotive chassis and suspension applications are significantly influenced by the conditions of the cut-edges produced during component manufacture as shown in Figure 16.1. High-performance AHSS's exhibit an increased sensitivity to fatigue cracks as a consequence of their cut-edge properties. The deployment of AHSS grades is commercially critical to the automotive sector, allowing for increased strength in automotive chassis components along with associated weight savings of up to 30%. However, there is also the increased risk of fracture, which makes cut-edge study an important aspect of durability research.

The issues pertaining to fatigue are the key limiting factor to the wider use of high-performance steels in demanding structural applications. The majority of steel components produced for service as automotive structures are primarily manufactured using the mechanical blanking process. This can produce a rough cut-edge which results in the formation of a fatigue crack initiation as shown in Figure 16.2.

The clearance between the punch and die is the chief factor in determining the formation of surface roughness features, residual stresses, and surface work

Handbook of Materials Failure Analysis With Case Studies from the Aerospace and Automotive Industries.
http://dx.doi.org/10.1016/B978-0-12-800950-5.00016-8

FIGURE 16.1

Automotive press stamping lines, which are used to mechanically blank steel profiles [1].

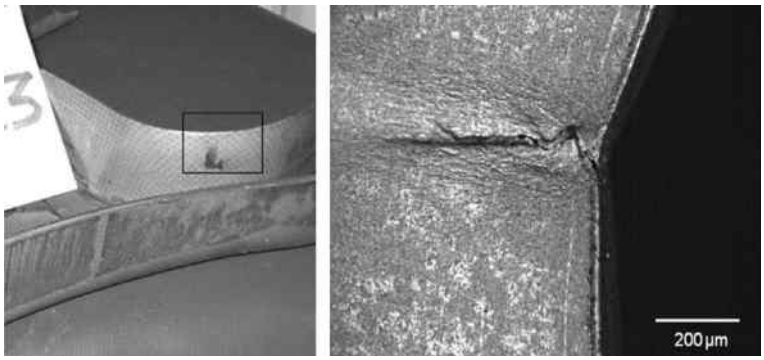

FIGURE 16.2

Suspension arm with a mechanical cut-edge fatigue crack emanating from a point of high stress.

hardening exponents of mechanical cut-edges. Van-Goethem and Ament [2] observed that the formation of the critical burr feature arises mainly at clearances over 20% of the workpiece thickness, and this region can act as an initial point for fatigue cracks to initiate.

The mechanical punch-die clearance used in industry ranges from 5% to 15% of the sheet thickness, with the 5% value corresponding to a clearance applied during the assembly of the punch, and up to 15% as the punch wears down. Between a clearance of 10% and 15% of the sheet thickness, Marronne et al. [3] established that the fatigue strength decreases. As soon as this critical value is exceeded, the effect of cutting becomes increasingly significant with the fatigue strength reduction, which may reach 20% in comparison with polished cut-edge fatigue lives.

Optimizing the clearance between the punch and die as Parsons [4] suggested is the single most important factor toward producing the smoothest mechanical cut-edge. However, clearances outside 10-15% of the sheet thickness can result in the fatigue strength decreasing significantly. This can result in a reduced fatigue resistance because the small defects produced during the cutting process act as stress raisers. If the clearance is correctly chosen, the shearing cracks produced at the respective top and bottom shear edges meet to give an optimum mechanical surface.

Early research by Carlsson et al. [5] has shown that the optimum clearance between punch and die in order to minimize surface roughness is 6-10% of the workpiece thickness. Laser cutting offers a desirable alternative to mechanical blanking, with its high flexibility and its ability to cut sheet components with intricate geometries at high precision. Cut-edge surface alterations formed during CO_2 laser cutting as Meurling et al. [6] observed are a result of material deformations produced by the laser beam during the cutting process. It is these alterations that significantly influence the fatigue properties of components. However, it is also necessary to consider other effects of the process on the material. Interaction of the laser beam with the material will lead to localized heating and cooling and the development of a heat-affected zone (HAZ), the properties of which are influenced by the laser power and traverse cutting speed parameters.

The key types of cut-edges found in automotive components are shown in Figure 16.3. Each edge type has a different characteristic surface and internal microstructural transformation properties. CNC milled edges have the characteristic fine vertical surface striations present with a R_a roughness of 0.2 μm and a slight increase in hardness of $10H_v$ in the cut-edge surface region, due to induced plastic deformation of the subsurface layer microstructure. The microstructural properties of the DP600 fracture zone 60 μm from the cut-edge surface displayed a high degree of grain compression, which influences the hardness properties of the cut-edge. Indeed, the elongations of both the ferrite and martensite grains demonstrate the high level of distortion that the workpiece undergoes during the mechanical cutting process.

Figure 16.4 shows the surface properties of two mechanically blanked automotive AHSS grades. AHSS such as XF350 grade appeared to be sensitive to low clearances ranging between 4.95% and 8.25% resulted in a high proportion of damage to the lower part of the cut-edge, which reduced as the clearance increased. At lower clearances, DP600 steel grade is observed to have smaller smooth zones and the formation of a

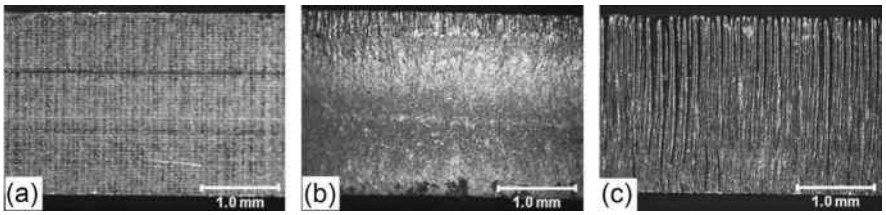

FIGURE 16.3

Surface micrographs of optimum DP600 AHSS automotive cut-edges generated using (a) CNC milling, (b) mechanical blanking, and (c) laser cutting processes.

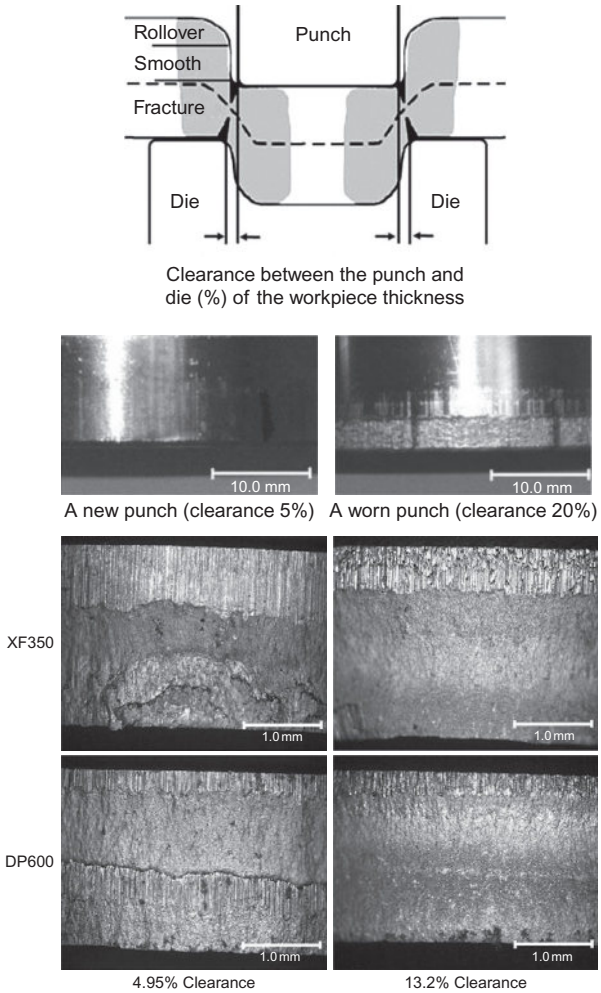

FIGURE 16.4

(a) Definition of mechanical clearance, showing the region of localized plastic deformation and the mechanical cut-edge zones and (b) surface micrographs of mechanical cut-edges generated using low and high clearances.

secondary smooth zone. At higher clearances, the surface profile remained relatively uniform with no further damage observed in both the top and bottom regions.

Mechanical cut-edges display two characteristic surface features, a smooth zone in which the steel workpiece has been sheared between the punch and the die, and is also a region in compression. Following this there is the formation of a fracture zone, in which the steel is torn apart and is a region that is in tension. The mechanical cut-edge surface has a R_a roughness of 3.4 μm and a hardness which is increased by $120H_v$ on average of the parent material. There is also the formation of a burr

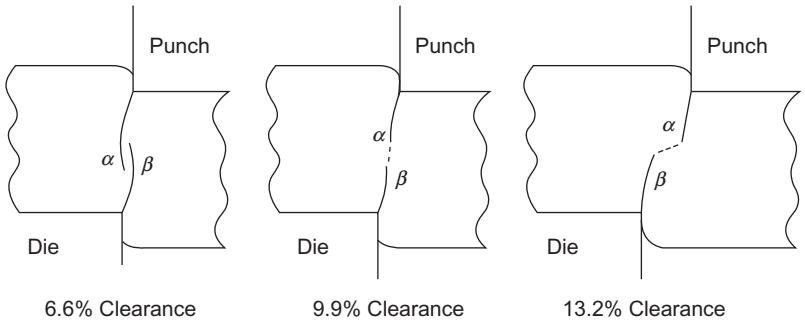

FIGURE 16.5

The formation of mechanical cut-edges at each clearance; α is the crack forming from the top, and β is the crack forming from the bottom.

feature on the underside of the cut-edge, which is formed as the punch exits through the bottom of the workpiece.

The clearance is responsible for the surface cracks formed at the top and bottom of the workpiece, and when they meet, the steel will separate into two pieces. The clearance is the chief component responsible for determining the quality of the cut-edge surface, internal and fatigue performances of mechanical cut-edges. As shown in Figure 16.5, deformation produced during the cutting process is in the form of a highly localized shear. If the clearance is correctly chosen, then the shearing cracks produced at the respective shear edges meet to give the optimal mechanical cut-edges. A clearance which is too low will not only result in overlapping of the top and bottom cracks, resulting in increased damage to the cut-edge surface, but also have the secondary effect of increasing tool wear.

Conversely, a clearance which is too high increases work hardening as the steel is increasingly pulled outward; but this does not necessarily result in a lower quality mechanical cut-edge being produced. The surfaces of laser cut-edges are characterized by the formation of surface striations, which are important toward determining the overall quality of laser cut-edges. The HAZ microstructure is formed with the appearance of a thin layer up to 400 μm thickness which is almost entirely composed of martensite. The cut-edge quality and striation properties of laser cut-edges can vary widely with only slight changes in the cutting process parameters.

Laser cut-edges of steel tend to display improved fatigue strength in comparison with mechanical cut-edges. This was explained by Meurling et al. [7] that there are a larger number of accumulated defects on the surface of the mechanical cut-edge fracture zones in comparison with those of laser cut-edge surfaces. Marronne et al. [3] has shown an increase in the fatigue strength of laser cut-edges in comparison with those that have been punched for a range of steels.

However, slight variations in laser power and cutting speed resulting in nonoptimum process parameters significantly modify the cut-edge properties. The increase in the width of the kerf, which is the slot produced during the laser cutting process further increases the size of striations. Striations are the primary factor determining

laser surface roughness and the formation of these features is the most critical characteristic property formed during the laser cutting process. As it was observed by Yilbas [8], striation properties relate to both the laser cutting process parameters used and the workpiece properties.

The nature of the laser cutting process is how a pattern of striations, which are the overlaps of molten steel, are deposited. An important factor for producing a high-quality laser cut-edge surface is the generation of a periodic pattern of striations. Figure 16.6 shows the roughness data for laser cutting parameters of XF350 and DP600 in which the lowest R_a roughness values were found when using low speed (1500 mm/min) and low power (800 W) set of cutting parameters. This indicates that it is the combined laser power and traverse cutting speed that produces the optimum cut-edge surface. These results suggest that maintaining the correct balance between traverse cutting speed and power are paramount in producing the highest quality laser cuts. However, maintaining the correct balance between power and traverse cutting speed, while using a low shielding gas pressure, resulted in the most uniform surfaces with the absence of laser-induced irregularities. If the speed was increased above a threshold level without altering the power, then the surface roughness features increased dramatically.

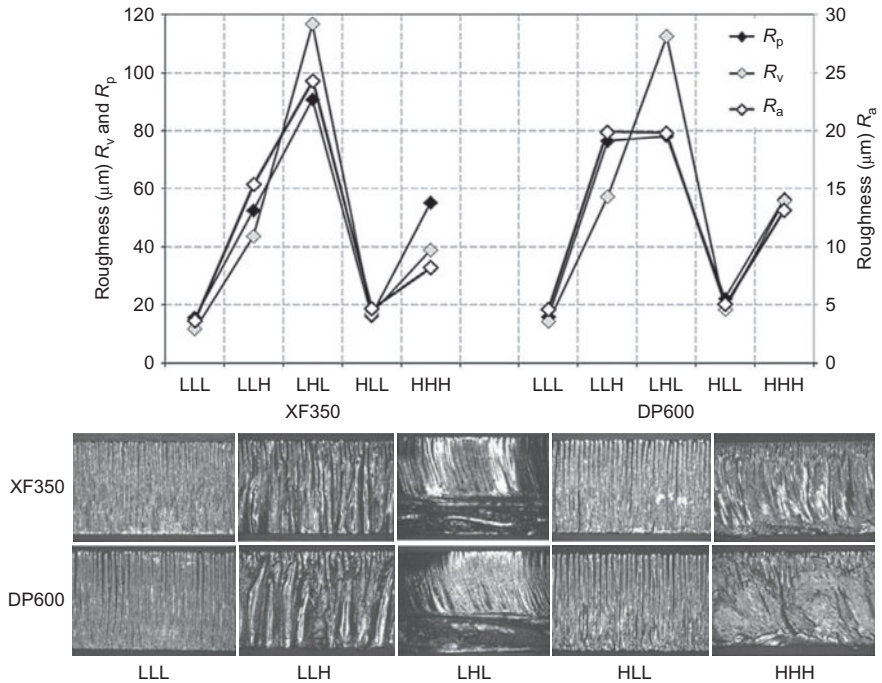

FIGURE 16.6

R_a, R_v, and R_p roughness properties and surface micrographs of different quality laser cut-edges of two AHSS grades, XF350 and DP600.

The microstructural properties of the fracture zone 60 μm from the cut-edge surface have a high degree of grain compression as shown in Figure 16.7a; this influences the hardness properties of the cut-edge and increases the hardness by $100H_v$. The elongation of both the ferrite and the pearlite grains demonstrates the high level of distortion that the workpiece undergoes during the mechanical cutting process.

The surfaces of laser cut-edges are characterized by how the formation of striations, which are the overlaps of molten steel, are deposited as wave features. An important factor for producing a high-quality laser cut-edge surface is the generation of a periodic pattern of striations. Transverse to the cut-edge is a 100 μm in thick martensitic HAZ microstructure as shown in Figure 16.7b. Due to the phase transformation of this material during the laser cutting process, the hardness of this region is increased by $180H_v$.

The fine transition boundary between the heat-affected material and the parent microstructure is shown in Figure 16.8. It is the thickness and properties of this region that allow the effect of the laser parameters on the microstructure to be understood.

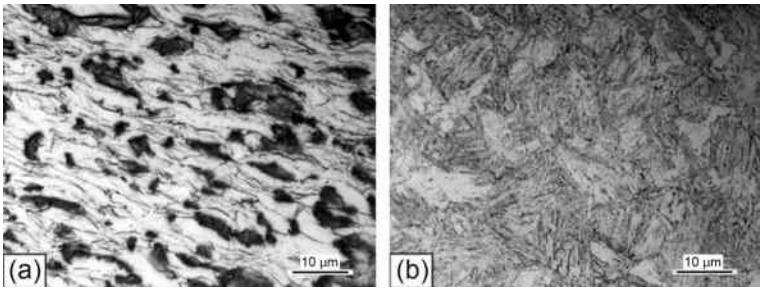

FIGURE 16.7

Near-edge microstructural properties of (a) mechanical and (b) laser cut-edge.

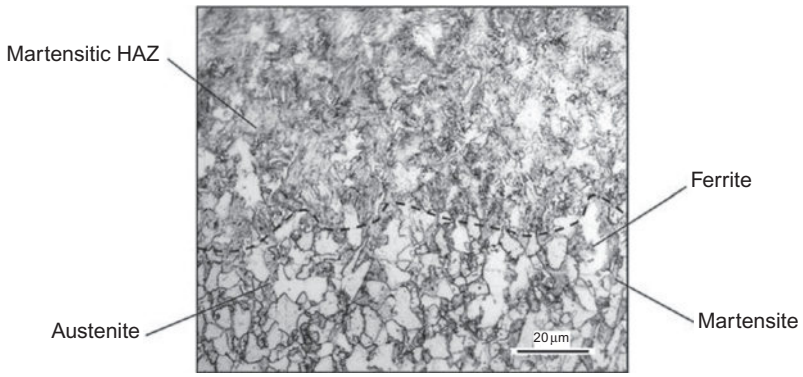

FIGURE 16.8

The fine HAZ transition boundary with the parent material formed using laser cutting.

2 CUT-EDGE FATIGUE CRACK INITIATION AND GROWTH

The mechanical cut-edge S-N fatigue performance of AHSS grade S355MC for a range of mechanical clearances is presented in Figure 16.9a. It was observed that mechanical cut-edges generally gave a reduction in fatigue life and was particularly evident in high-cycle fatigue (HCF) life. The only exception to this was that cut-edges generated using a high clearance displayed an increase in life at higher stresses and this resulted in the fatigue curve crossing over the smooth-edge curve.

The fatigue data shown in Figure 16.9b demonstrates that DP600 exhibited an increased sensitivity to the influence of mechanical cut-edges. Further to this, each mechanical cut-edge clearance displayed a reduced fatigue performance when compared with smooth edges and this effect was more significant at lower stresses.

The defect properties of the cut-edge undergo a process of stress concentration under loading, in which the cut-edge surface characteristics are even more significant. It is the surface properties of mechanical cut-edges that have a critical number of work-hardened surface notches that act to significantly reduce the fatigue life. The stress-life fatigue curves of the different laser cut-edges of S355MC are shown in Figure 16.10a.

It was observed that there is again a cross-over that occurs in the fatigue curves of the cut-edges. In this case, cut-edges generated using low-speed laser parameters showed an increased fatigue life when compared to smooth edges at high stresses and a slight reduction at low stresses. Using medium- or high-speed laser speed process parameters was shown to significantly reduce fatigue performance. In this case, laser cut-edges appeared to have little effect on the fatigue life of DP600, except when high cutting speed process parameters are used as shown in Figure 16.10b in which there is a dramatic decrease in the fatigue life.

Under higher applied loads, crack initiation components fail rapidly, and the condition of the cut-edge is therefore critical toward determining the life of a potential application. The sensitivity of laser edges to fatigue was shown to be limited due to the cut-edge striations. It is this surface characteristic which distributes the stress rather that concentrates it at the trough of a notch as was the case with mechanical cut-edges (Figure 16.11). The fatigue lives of smooth and laser cut-edges in comparison with those that have been generated mechanically were significantly different under both coupon testing and four-point loading as shown in Figure 16.12. These results demonstrate the importance of cut-edges on the resulting fatigue lives of vehicle structures.

Fatigue lives and crack growth curves when comparing the fatigue lives of the TopHat structures with each cut-edge type; it was evident that they have a significant influence on the durability as shown in Figure 16.13. Smooth and laser cut-edges were observed to outperform mechanical cut-edges by a factor of three. This also relates to the fatigue coupon test data in which there was the same degree of difference toward the HCF end of the *S-N* curves.

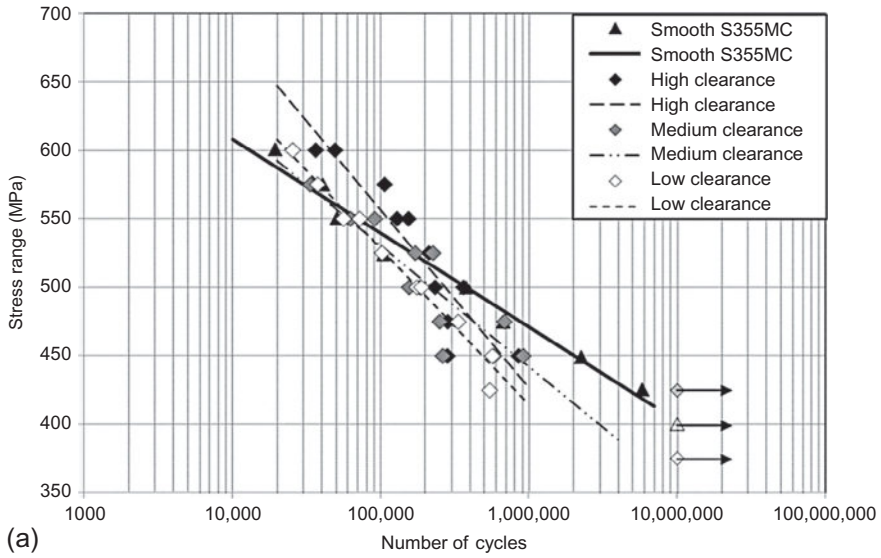

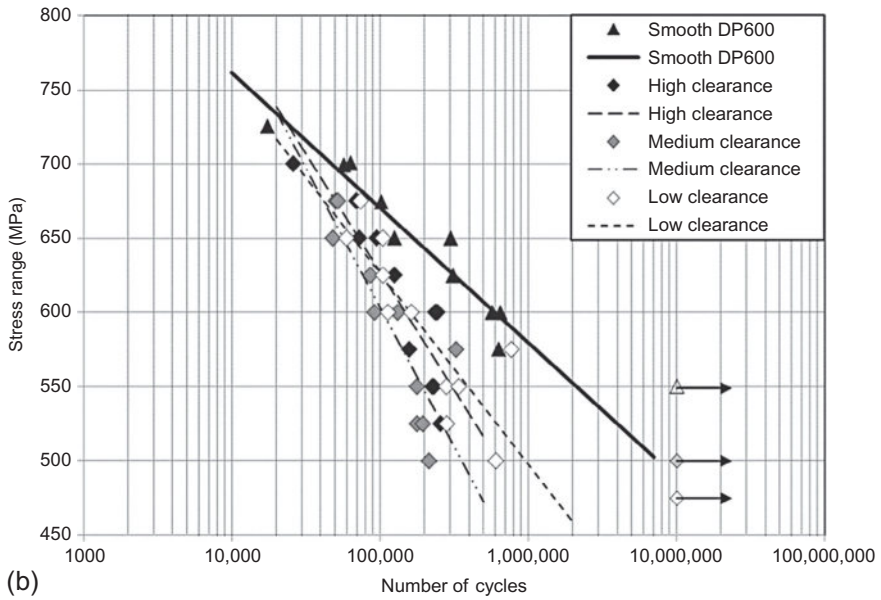

FIGURE 16.9

S-N fatigue curves of (a) S355MC and (b) DP600 mechanical cut-edges with low—6.6%, medium—9.9%, and high—13.2% clearances in comparison with smooth data.

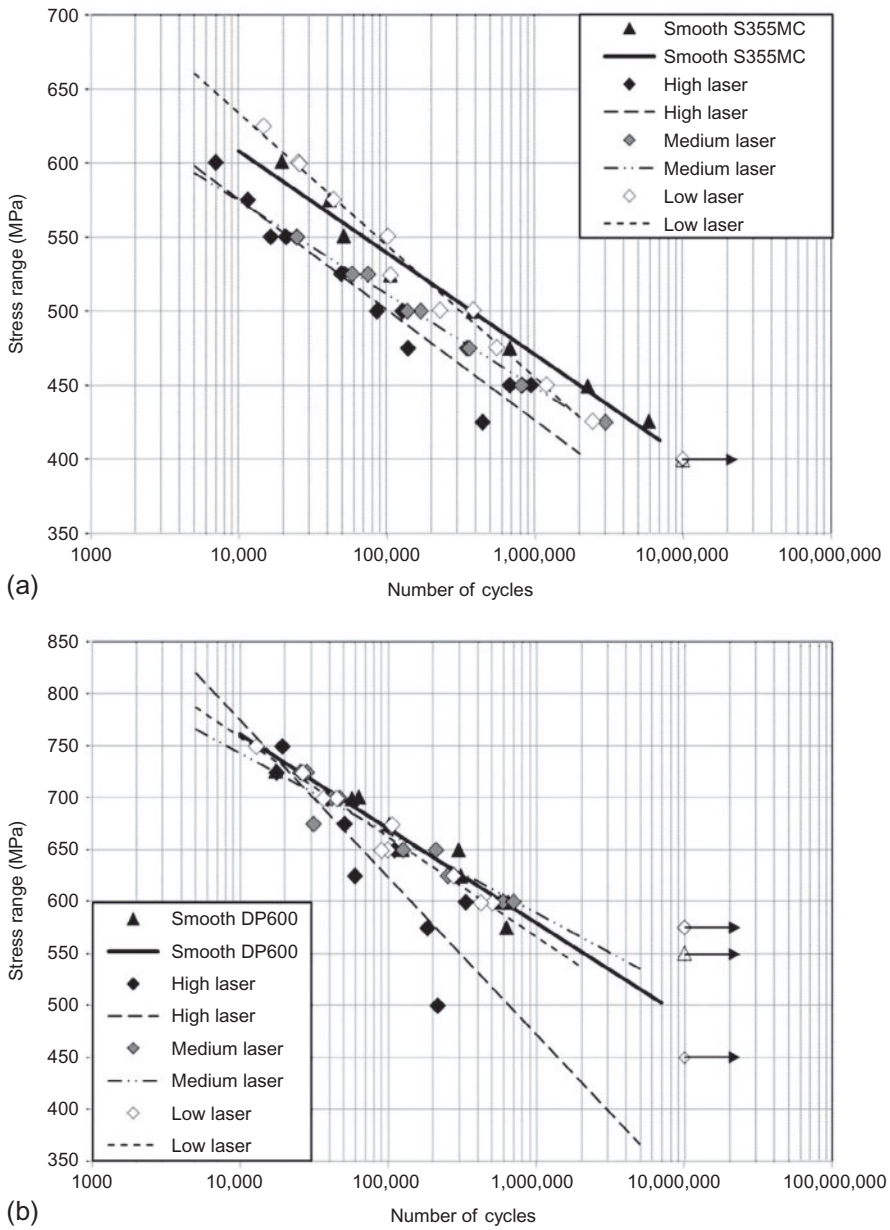

FIGURE 16.10

S-N fatigue curves of (a) S355MC and (b) DP600 laser cut-edges produced using a low cutting speed 1500 mm/min, medium cutting speed 3000 mm/min, and a high cutting speed of 4500 mm/min, clearances in comparison with smooth data.

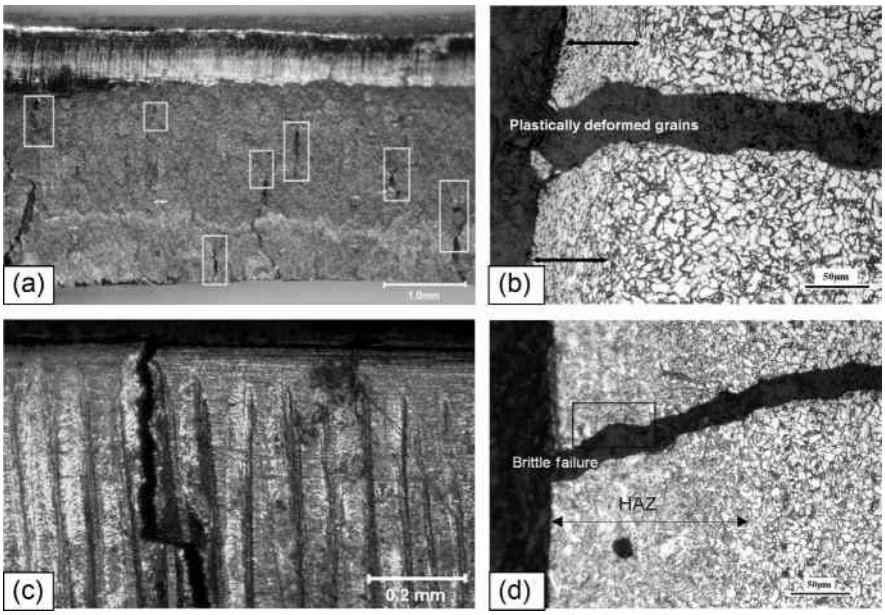

FIGURE 16.11

Micrograph of DP600 cut-edges with (a) the formation of multiple crack initiations from a mechanical cut-edge, (b) micrograph of a mechanical cut-edge fatigue crack initiation, (c) micrograph of the initiation of a laser cut-edge fatigue crack, and (d) micrograph of a fatigue crack initiating from the trough of a cut-edge.

At a load of 20 kN, the improved fatigue performance of laser cut-edges in comparison with smooth was quite evident. When compared with smooth data, these results suggest that in addition to the striations present on laser cut-edge surfaces, the phase-transformed material in the HAZ can also improve the fatigue life. In the case of mechanical and laser cut-edges, there was a significant level of variability in the fatigue data when compared with that of smooth data. This suggests that the surfaces produced by cutting processes can significantly influence the time to crack initiation and is based on the edge inconsistencies produced by the cutting processes.

The measurements of fatigue crack growths as shown in Figure 16.14 provided a basis to understand the propagation life subsequent to crack initiation under the various applied loads. It was measured that applied sinusoidal wave loads of between 20 and 24 kN resulted in gradual crack growth, with further increases in the load leading to rapid failure of the component.

During the process of four-point bend loading, stress was nominally applied equally to each side of the TopHat structure. Because only one side of the structure will fail first, a fatigue crack grows to a significant length from this region while the other side remains unaffected. At a sinusoidal wave peak load of 28 kN, following

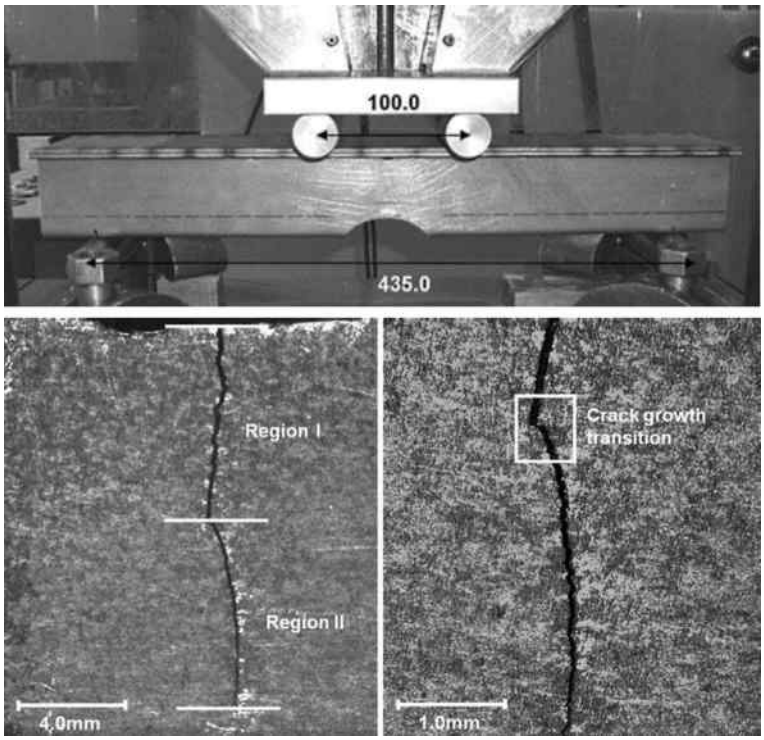

FIGURE 16.12

A TopHat structure under the process of sinusoidal wave four points loading. Under this loading regime, there is a change in crack orientation during its propagation process.

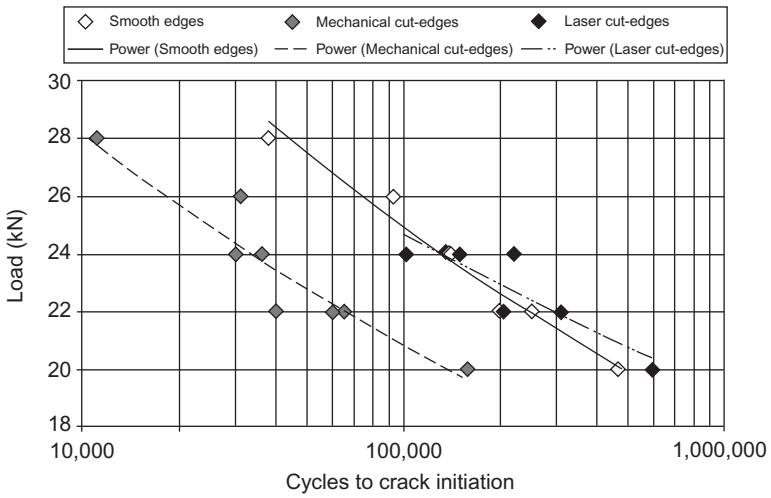

FIGURE 16.13

Comparison of the crack initiation lives of TopHat structures cut-edges.

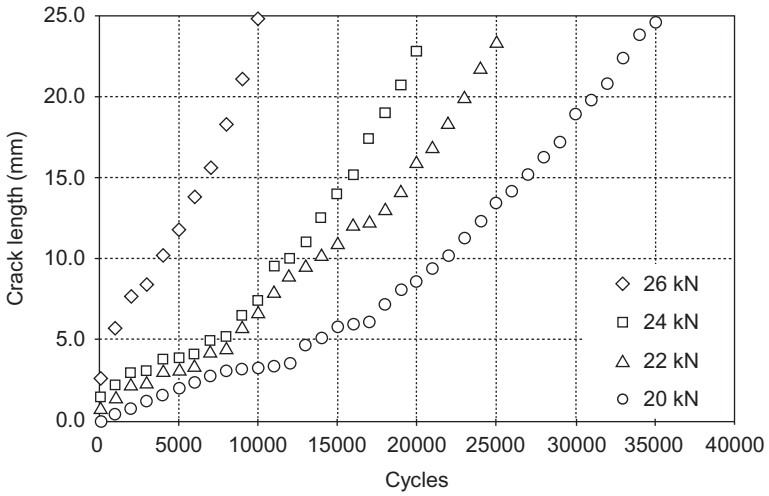

FIGURE 16.14

Fatigue crack growth, measured from TopHat structures under sinusoidal wave loading.

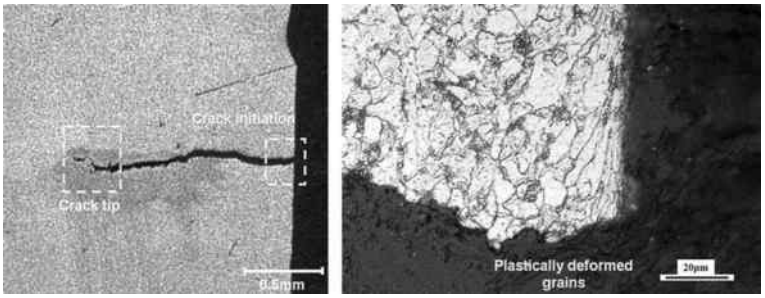

FIGURE 16.15

Smooth-edge region I crack propagation and the microstructure of the region around the crack initiation.

initiation the crack growth was very rapid in which there were lines of plastically deformed grains ahead of the crack growth line and then sudden failure of the component within 1000 cycles of initiation.

Plastically deformed grains in the near-edge region and the notch defects produced during the mechanical cutting process act as stress raisers and the starting point of a crack. Under the process of sinusoidal loading, the orientation properties of the crack were observed to change as shown in Figure 16.15. Over the 25.0-mm length, where the fatigue cracks are grown, it was clear to observe the region I and region II crack growth regimes.

Observations made of the crack growth from the cut-edges of the TopHat structures are revealed to be characteristically straight under region I crack growth.

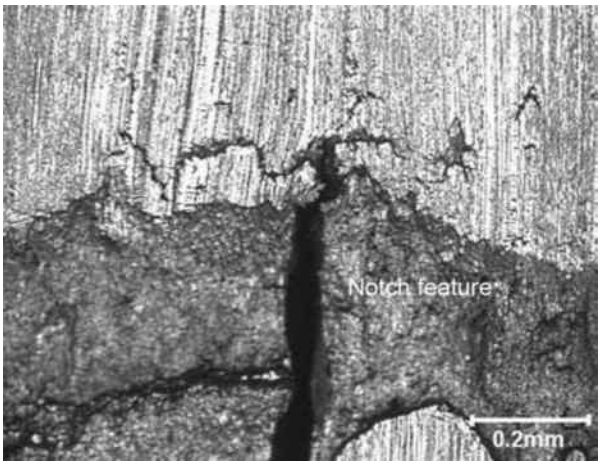

FIGURE 16.16

Surface of the fatigue crack initiation from a mechanical cut-edge notch.

However, the more the crack grew into region II growth, the more the inconsistent it became as shown by observations made of the crack tip behavior. Microstructural examination of the crack growth revealed the elongation of grains at the region where the crack initiated as shown in Figure 16.16. This indicates that under the process of sinusoidal loading there is a localized region of plastically deformed grains, which have been deformed before the formation of the region I crack growth.

At a load of 20 kN, mechanical cut-edge cracks were observed to initiate from notch features. This suggests that it is the cut-edge surface properties that are of critical importance particularly under HCF testing. These observations suggest the reason why mechanical cut-edges displayed a dramatic decrease in fatigue life.

Particularly, under strain control loading, the notches formed on the surface of the mechanical cut-edge specimens act to disperse stress concentrations and the reduction in fatigue life when compared with smooth specimens is not as significant. However, in the process of TopHat loading the properties of the cut-edge are critical at the apex of the hole in which there is a localized region of plastically deformed grains, which form during the first cycle. The notch features on the surface of mechanical cut-edges as a result are influenced negatively by this factor due to stresses being increasingly intensified from this region.

3 PRESTRAIN FATIGUE LIFE PERFORMANCE

The cut-edge condition also has an important influence on the formability capacity of AHSS automotive structures. AHSS also were observed to display a decreased level of formability in the surface regions because mechanical punched edge hole-flanging capacity is dependent on ductility and the surface quality of the cut-edge produced.

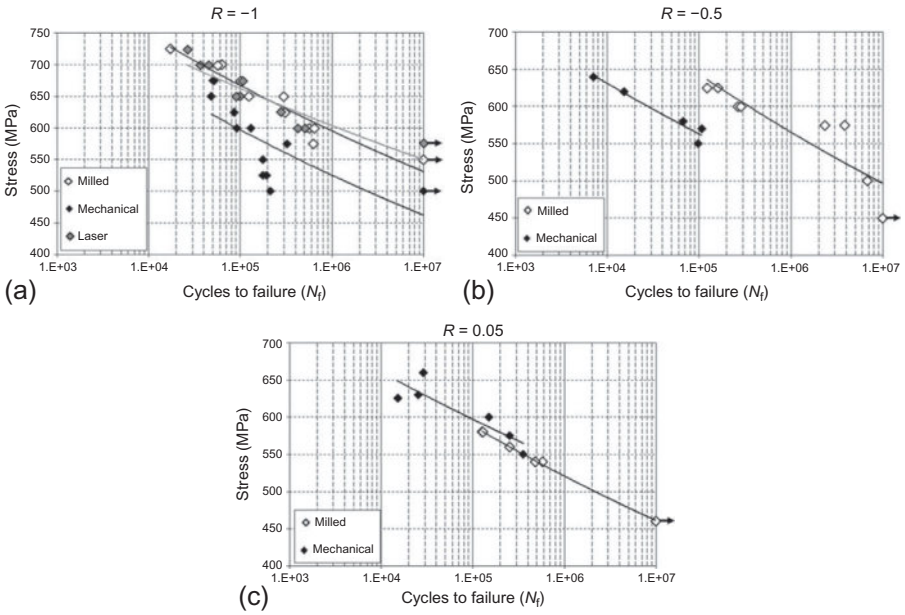

FIGURE 16.17

S-N fatigue curves of cut-edges under stress ratios of (a) $R=-1$, (b) $R=-0.5$, and (c) $R=0.05$.

The fatigue lives shown in Figure 16.17 indicate that DP600 exhibits an increased sensitivity to the influence of mechanical cut-edges at stress ratios of $R=-1$ and $R=-0.5$ in comparison with smooth-edge data. Mechanical cut-edges have increased compressive residual introduced stresses due to increasing deformation of the microstructure. This results in a reduction in fatigue life due to the rougher surface notches formed on the cut-edge surfaces. As a result, mechanical cut-edges appeared to display an increased reduction in fatigue strength under reversed loading.

When using laser process parameters, these displayed fatigue lives equivalent to those of smooth edges now with decreased life. When added to the increased cost of laser cutting, it is clear that operating conditions can be tightly controlled to produce adequate fatigue performance. Under $R=0.05$ loading, there is no component of compressive loading and no difference between the fatigue lives of smooth and mechanical cut-edges. These results suggest that it is the component of compressive stress that has a negative effect on the fatigue life of mechanical cut-edges.

The key to generating optimum fatigue performance of laser cut-edges is the formation of a periodic pattern of striations. The influence of cut-edges on both steel grades is more significant at low stresses and this is due to the fact that HCF properties depend strongly on the cut-edge surface characteristics. At a high number of cycles, any defects formed during the mechanical cutting process act as stress raisers and are a source of localized plasticity and consequently crack initiation.

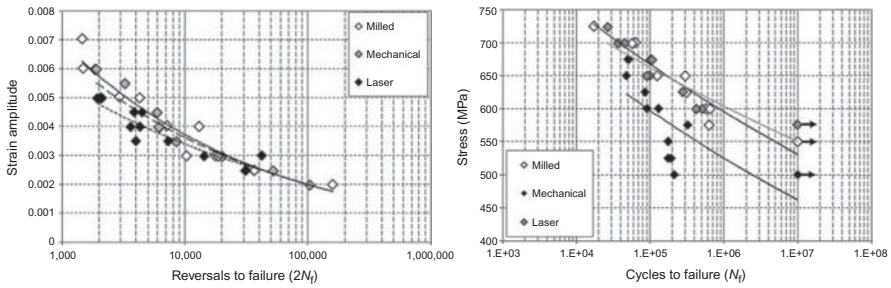

FIGURE 16.18

Total E-N and S-N fatigue data of smooth, mechanical, and laser cut-edges.

Shown in Figure 16.18 are the *E*-N and S-N lives to crack initiation, in which it can be seen that, under higher levels of strain, laser cut-edges display a reduced life relative to that of milled and mechanical cut-edges. Under lower strain levels, the effect of cut-edges is of less significance. A crack propagating through the microstructure of the steel is shown in Figure 16.19 in which the crack grew transgranularly through the microstructure forming daughter cracks running at 90° to the crack growth direction.

The initiation of a fatigue crack from cut-edges is then followed by the crack growth, which was observed to be brittle, and the increased dependence on surface finish is responsible for the tendency on the part of crack lines to fan out under low stresses. As was observed, compressive residual stresses formed due to the martensitic transformation during cyclic loading can act as an extra advantage in AHSS steels helping them to retard the fatigue crack growth.

The fatigue performances of mechanical cut-edges under different levels of prestrain are shown in Figure 16.20. Under LCF loading, the influence of prestrain is more pronounced, and thus it is quite obvious that the 8% prestrain results in a significant reduction in fatigue life. Prestrains of less than 1-5% under higher stress show better fatigue lives than both smooth edges and laser cut-edges toward the higher stress range of the fatigue curves.

Toward the HCF end of the graphs, the effect of prestraining resulted in a gradual reduction in fatigue life over laser and smooth edges. However, up to a prestrain level

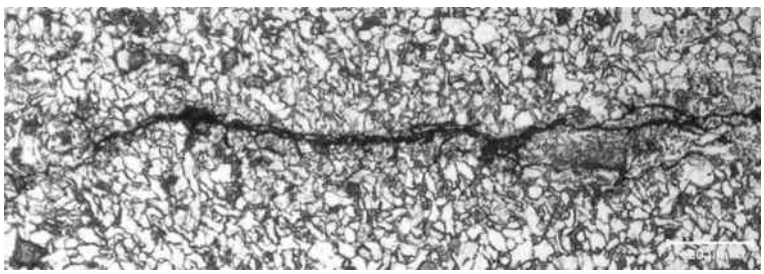

FIGURE 16.19

Fatigue crack propagating through the microstructure of DP600.

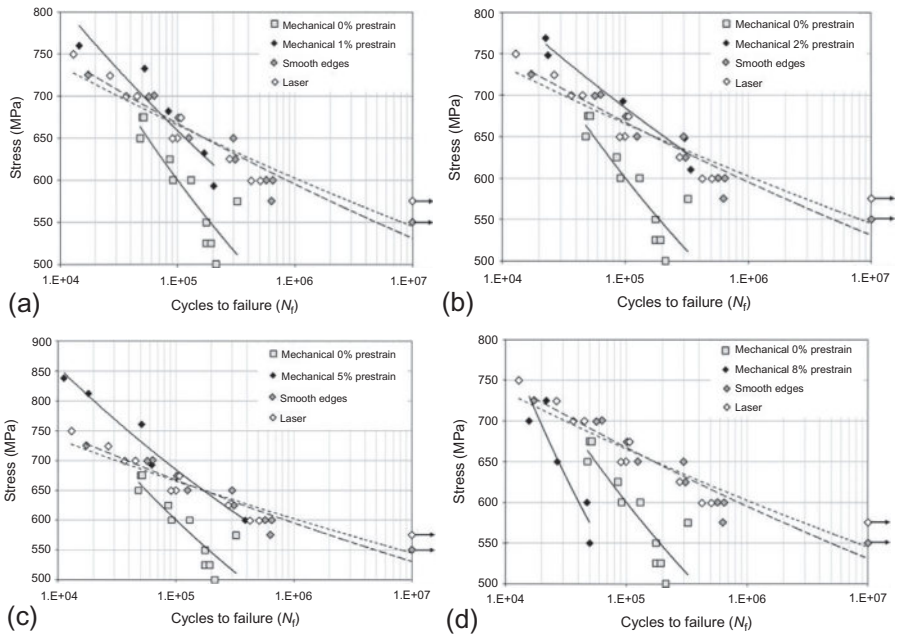

FIGURE 16.20

Comparison of S-N prestrainings of (a) 1%, (b) 2%, (c) 5%, and (d) 8% on the lives of mechanical cut-edges versus 0% prestraining to mechanical cut-edges, smooth edges, and laser cut-edges.

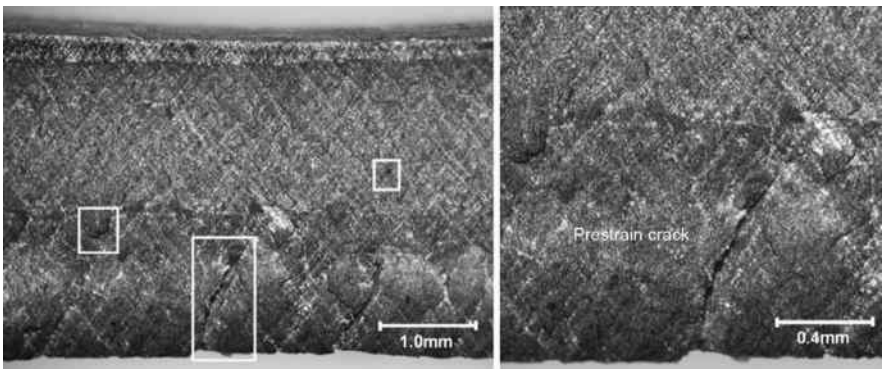

FIGURE 16.21

Micrograph of a mechanical cut-edge surface after an 8% prestrain has been applied.

of 5%, there is a large increase in fatigue life over mechanical cut-edges that have not been prestrained. At a prestrain of 8%, mechanical cut-edges as shown in Figure 16.21 display a number of prestrain-induced cracks at the rougher lower region of the mechanical cut-edge, and these features resulted in a large reduction

in life over all cut-edge types. The influence of prestrain can have characteristically damaging effect on the fracture zone of mechanical cut-edge surfaces. The imperfections in the lower region of the fracture zone are where, under prestraining, cracks can open up into a larger rupture.

At a prestrain of 8%, there are a number of cracks that have formed toward the bottom of mechanical cut-edges and occurred when strain limits of the cut-edge were exceeded. Therefore, the size of the fractured zone is important in terms of understanding the fatigue performance, as it is the roughest region of a mechanical cut-edge and has the presence of tensile residual stresses. Rapid transformation of austenite to martensite at first is due to the nucleation sites introduced by the deformation. However, an excessive strain can retard the transformation, eventually bringing it to a halt as is the case at higher 8% level of strain. This mechanical stabilization process later is a characteristic feature of displacive transformations.

4 FATIGUE LIFE PREDICTION

Current research work outlines the development of an improved finite element (FE)-based life prediction method, based on strain-life fatigue data of S355MC steel cut-edges. The resulting best method of predicting fatigue lives of cut-edges using the Coffin-Manson method has been determined as providing the best means for predicting the durability of high-strength steel components. This process has been validated using a bespoke laboratory test component representative of those in automotive chassis and suspension assemblies. The outcome of this work is that it allows increased reliance on FE life predictions rather than extensive physical laboratory testing.

The fatigue data as shown in Table 16.1 was collected from E-N coupon data using linear regression to determine the fitted or 50% probability of failure curves. This data was inserted into the MSC. Fatigue database that was used to determine FE model predictions of the number of cycles to crack initiation from the TopHat structure under loading. The strain-life method is the most conventional and is based on a zero mean-stress Coffin-Manson relationship, shown in Equation (16.1)

$$\frac{\Delta\varepsilon}{2}=\frac{\sigma'_f}{E}(2N_f)^b+\varepsilon'_f(2N_f)^c \tag{16.1}$$

Table 16.1 Cut-Edge E-N Fatigue and Cyclic Stress-Strain Coefficients Used to Make Fatigue Life Predictions

Cut-Edge Type	E-N Fatigue and Cyclic Stress-Strain Coefficients					
	σ'_f(MPa)	b	ε'_f	c	K'(MPa)	n'
Smooth	1133.34	−0.13156	0.51144	−0.60978	1053.67	0.18415
Mechanical	870.63	−0.09719	0.46243	−0.65107	778.41	0.12604
Laser	893.12	−0.10372	0.12072	−0.47101	1280.87	0.20852

However, fatigue tests of the TopHat component in the current study were conducted at the fatigue stress ratio of $R = 0.1$. Fatigue load cycles that have a positive mean stress are known to cause more fatigue damage than a cycle which has zero or negative compressive mean stress. The Smith-Watson-Topper (SWT) parameter, as shown in Equation (16.2), is one of the methods to account for the effect of mean stresses in the strain-life approach.

$$\frac{\Delta\varepsilon}{2}\sigma_{\max} = \frac{(\sigma'_{\mathrm{f}})^2}{E}(2N_{\mathrm{f}})^{2b} + \sigma'_{\mathrm{f}}\varepsilon'_{\mathrm{f}}(2N_{\mathrm{f}})^{b+c} \tag{16.2}$$

In addition to the SWT method, the Morrow mean-stress correction, as shown in Equation (16.3), has also been used as a third method of fatigue prediction for comparison with test results.

$$\frac{\Delta\varepsilon}{2} = \frac{(\sigma'_{\mathrm{f}} - \sigma_{\mathrm{m}})}{E}(2N_{\mathrm{f}})^{b} + \varepsilon'_{\mathrm{f}}(2N_{\mathrm{f}})^{c} \tag{16.3}$$

When comparing the three life prediction methods above, the method most appropriate for estimating fatigue lives of automotive chassis components with exposed cut-edges can be determined. To achieve this, results from the three different methods of life predictions using MSC.Fatigue are compared with the crack initiation lives from the laboratory tests, in which cracks initiated from the highest stress point at the apex of the cut-edge hole as shown in Figure 16.22.

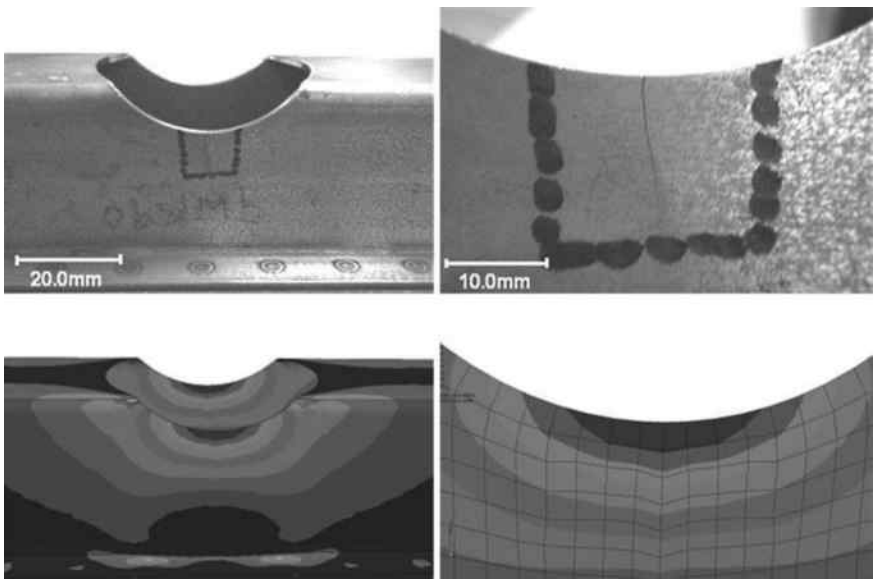

FIGURE 16.22

The critical region on the structure showing the location of maximum stress from where a crack initiates.

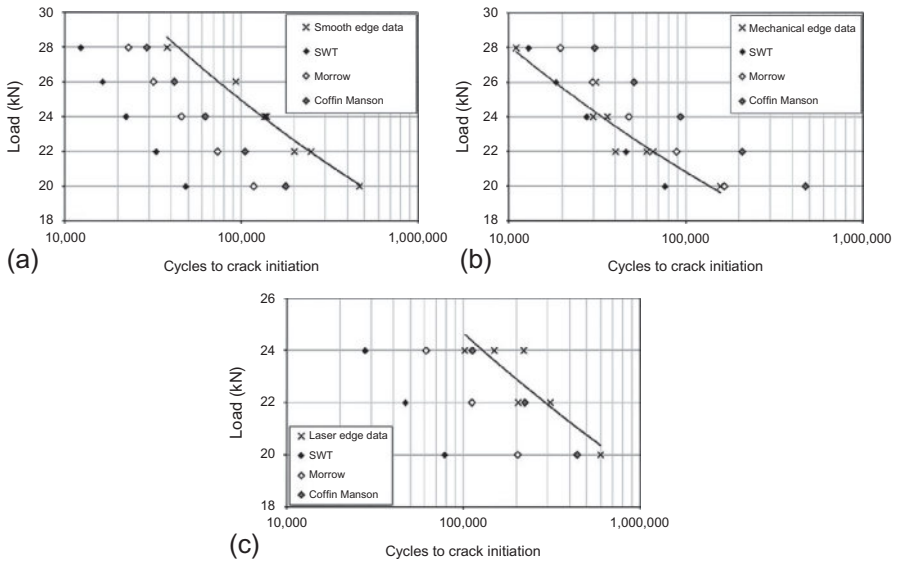

FIGURE 16.23

Fatigue lives to initiation of TopHat structures with (a) smooth, (b) mechanical, and (c) laser cut-edges as compared with FE life predictions.

Comparisons of the FE-based life predictions with those of the physically loaded TopHat components are shown in Figure 16.23. Examining the test-prediction results overall, it appears that both Coffin-Manson and Morrow methods generated acceptable levels of fatigue life predictions, suggesting that as expected it is the fatigue load range that dominates fatigue damage and the effect of mean stress may be secondary. However, if mean-stress effect is indeed taken into account in life assessments, Morrow's correction method provides a more accurate level of life predictions, while the SWT method tends to over-compensate for the mean-stress effect.

The present test-prediction correlation study suggests that the mean-stress effect may be ignored by simply performing fatigue life study based on the Coffin-Manson equation. However, if the mean-stress effect is to be included, the Morrow method produces an overall reasonable level of life estimation. One explanation to support this notion for the suitability of Morrow's method for cut-edge fatigue life predictions may be due to the fact that the mean-stress correction is introduced only to the first elastic strain-life term of the Coffin-Manson equation. The elastic strain versus life term mainly affects fatigue performance in the HCF region. This is consistent with the finding that the difference in fatigue performance between each cut-edge type mainly in the HCF region, as shown in Figure 16.18. The SWT method, on the other hand, corrects the mean-stress effects for both the LCF and the HCF regions, resulting in an overcorrection on the whole as shown in Figure 16.24.

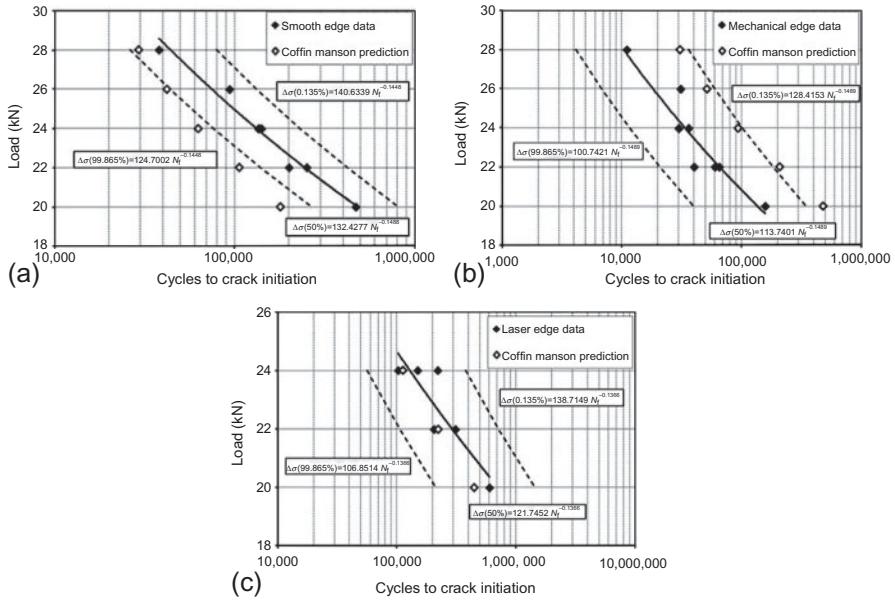

FIGURE 16.24

Comparison of the FE-based (Coffin-Manson) prediction against physical test data for (a) smooth, (b) mechanical, and (c) laser edges with linear regressions.

Increasing the maximum applied load alters the distribution and intensity of stresses, critically at a localized region at the apex of the cut-edge hole. When considering the Morrow method of prediction in comparison with the average fatigue lives of the physically tested structures, the results are quite accurate, particularly under higher applied loads. It is clear that fatigue coupon specimens with mechanical cut-edges tested under S-N loading were also observed to display a significant decrease in fatigue life particularly under HCF loading. For high stresses, the effect is minimized since specimens undergo more plastic deformation and surface features are less critical.

However, the differences at the HCF end of the curve demonstrate the importance of cut-edges on the resulting fatigue lives of structures. Observations made of the crack initiations revealed that the surfaces of mechanical cut-edges showed a high degree of surface damage within the fracture region and this was critical in reducing the fatigue life.

It is due to the increased level of damage induced to mechanical cut-edges that the SWT method may be a more accurate for predicting fatigue life of rough cut-edges. However, the no mean-stress correction method appeared to offer the most accurate prediction for smooth and laser cut-edges. When accounting for the variability of the data in comparison with the Coffin-Manson life prediction compared closely within the 0.135% and 99.865% probability of survival curves for each set of data.

Furthermore, although mechanical and laser cut-edges displayed a wider degree of scatter than smooth cut-edges, the predictions offer on average a uniform correlation.

CAE-based fatigue life estimations of complex components, such as those in automotive chassis and suspension assemblies, can be based on strain-life (*E-N*) approaches derived from the Coffin-Manson relationship. This is based on the fact that the root cause for fatigue crack initiation is localized cyclic plastic strain. However, tensile stress also plays a role and in situations where there exists significant positive mean stress. As a result of this, the SWT and Morrow methods can also be adopted to correct for the mean-stress effects on fatigue life—particularly the case when damaging cut-edge surface features are present.

This current method outlines the development of an improved CAE life prediction method based on strain-life fatigue data of steel cut-edges. This process has been validated using a bespoke laboratory test component representative of those in automotive chassis and suspension assemblies. The resulting best method of predicting fatigue lives of vehicle components can allow automotive designers to increase their reliance on CAE life predictions rather than carrying out extensive physical laboratory tests. This can significantly decrease the time it takes to validate new structures and to facilitate the rapid deployment of new lighter gauge AHSS grades to the automotive vehicle sector.

At a high number of cycles, differences were observed as edge surface characteristics become more critical. It is the conditions at the notch root that increase the sensitivity to surface finish and this factor is important when down gauging future steel grades. This is due to their inherent sensitivity for fatigue cracks initiating from cut-edges. Using the fatigue data generated from specimens with the relevant cut-edges, the present study demonstrated an improved CAE-based approach for predicting the fatigue lives to crack initiation. The strain-life approach based on the Coffin-Manson relationship and Morrow's mean-stress correction method, on balance, offers acceptable fatigue life predictions for smooth, mechanical, and laser cut-edges.

5 CONCLUSION

The fatigue lives of smooth and laser cut-edges in comparison with those that have been generated mechanically were significantly different under both coupon testing and four-point loading. These results demonstrate the importance of cut-edges on the resulting fatigue lives of vehicle structures. Under higher applied loads, following crack initiation the components fail rapidly and the condition of the cut-edge is therefore critical toward determining the life of a potential application. The sensitivity of laser edges to fatigue was shown to be limited. This is due to the cut-edge striations. It is this surface characteristic which distributes the stress rather than concentrating it at the trough of a notch, as was the case with mechanical cut-edges. At a high number of cycles, differences were observed as edge surface characteristics become more critical. It is the conditions at the notch root that increase the sensitivity to surface finish

and this factor is important when down gauging future steel grades due to their inherent sensitivity for fatigue cracks initiating from cut-edges. Using the fatigue data generated from specimens with the relevant cut-edges, the present study demonstrated an improved CAE-based approach for predicting the fatigue lives to crack initiation. The strain-life approach based on the Coffin-Manson relationship and Morrow's mean-stress correction method, on balance, offers acceptable fatigue life predictions for smooth, mechanical, and laser cut-edges.

Research is currently working to develop improved CAE life prediction methods based on strain-life fatigue data to predict cut-edge fatigue performance of complex components. This process has been validated using a bespoke laboratory test component representative of those in automotive chassis and suspension assemblies. The defect properties of the cut-edge undergo a process of stress concentration under loading, in which the cut-edge surface characteristics are even more significant. It is the surface properties of mechanical cut-edges that have a critical number of work-hardened surface notches that act to significantly reduce the fatigue life.

REFERENCES

[1] Thomas DJ, Whittaker MT, Bright GW, Gao Y. The influence of mechanical and CO_2 laser cut-edge characteristics on the fatigue life performance of high strength automotive steels. J Mater Process Technol 2011;211(2):263–74.

[2] Van-Goethem RPM, Ament PCH. Influences of some parameters on the sheet cutting process of cold and hot rolled steel. Corus Technical Report. Reference Source Number 10325; 2000.

[3] Marronne E, Labesse-Jied F, Galtier A, Robert JL. Influence of a cut edge on steel sheets fatigue properties. Fatigue 2003;4:2003.

[4] Parsons AS. The formula for successful punching, http://www.thefabricator.com/Punching/Punching Article.cfm?ID=1415 (last accessed April 4, 2014); 2006.

[5] Carlsson B, Larsson J, Nilsson T. Dual phase steels for auto body design forming and welding aspects. Borlange, Sweden: SSAB Tunnplat AB; 1984, p. 1–14.

[6] Meurling F, Melander A, Linder J, Larsson M, Trogen H. The influence of laser cutting on the fatigue properties of thin sheet steels. Swedish Institute for Metals Research Report IM-3691; 1998.

[7] Meurling F, Melander A, Linder J, Larsson M. The influence of mechanical and laser cutting on the fatigue strengths of carbon and stainless sheet steels. Scand J Metall 2001;30:309–19.

[8] Yilbas BS. The analysis of CO_2 laser cutting. Proc Inst Mech Eng B J Eng Manuf 1997; 211(3):223–32.

CHAPTER

17 Failure analysis cases of components of automotive and locomotive engines

Zhiwei Yu, Xiaolei Xu

Key Laboratory of Ship-Machinery Maintenance & Manufacture Ministry of Communication, PRC
Department of Materials Science, Engineering Dalian Maritime University, Dalian, PR China

CHAPTER OUTLINE

Handbook of Materials Failure Analysis With Case Studies from the Aerospace and Automotive Industries.
http://dx.doi.org/10.1016/B978-0-12-800950-5.00017-X

1 CASE 1: BRITTLE CRACKING OF GEAR-TEETH DUE TO SEGREGATION OF EXCESSIVE INCLUSIONS

1.1 BACKGROUND

Two gears from the same production batch were found to crack after the finishing processes of carburization-quenching and following high-temperature tempering. Therefore, the subsequent heat treating processes (quenching and low-temperature tempering) and machining operations (spraying sand and grinding) could not be conducted. No additional detailed fabrication-related information was provided. The two cracked gears were made of 20CrMnTi steel (C: 0.17-0.23, Si: 0.17-0.37, Mn: 0.80-1.10, $P \leq 0.035$, $S \leq 0.035$, Cr: 1.00-1.30, $Ni \leq 0.30$, $Cu \leq 0.30$, Ti: $0.04 - 0.10$, Fe: balance). According to the heat treating specification, the gears were required to satisfy the following requirements: (a) a carburized case depth greater than 1.6 mm, (b) a case hardness of Rockwell 59-62, (c) a core hardness of Rockwell 36-44.

1.2 OBSERVATION RESULTS

1.2.1 Visual Observations

Two cracked gear-teeth are shown in Figure 17.1 as they were received. Visual inspection revealed that the cracks were situated at the groove root and were along the axial direction. The cracks were found throughout the entirety of the grooves and the axial length was about 146 mm. Fracture surfaces of two cracked teeth prepared by opening cracks showed similar fractographic features, as shown in Figure 17.2. Dark brown fracture surfaces and the presence of oxidation film on the fracture surfaces suggest that the fracture surfaces underwent a process of high-temperature oxidation after the cracking of the gear-teeth. No obvious plastic deformation was observed on the fracture surfaces. The fracture surfaces close to the groove showed opposite chevron crack propagation markings [1,2], as marked by dotted arrows in Figure 17.2. The chevron points toward the origin of the fracture. Hence, it can be determined that the crack origins were about 3.3-3.5 mm from the groove and

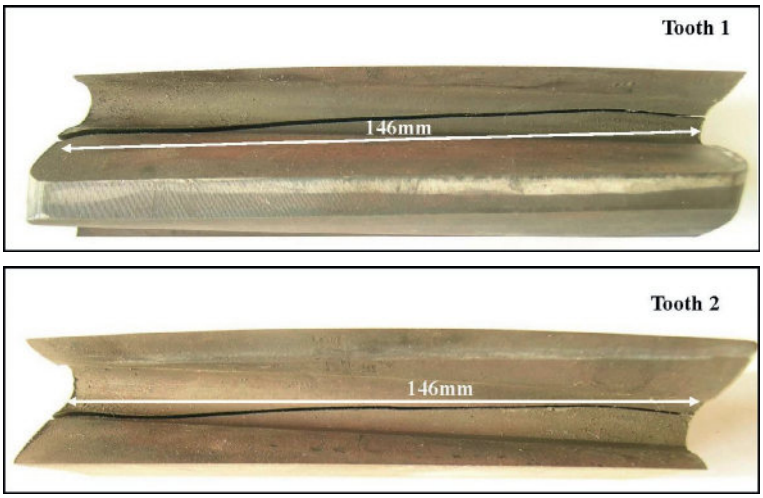

FIGURE 17.1

As-received cracked teeth.

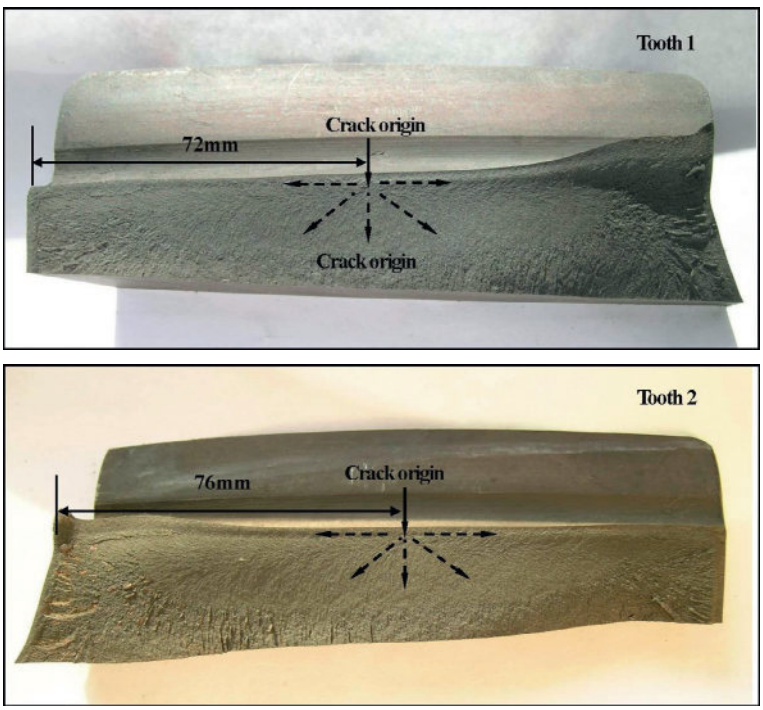

FIGURE 17.2

Macro-fracture surfaces.

situated at the midlength of the tooth. Tracing the crack propagation marks, it can be deduced that the crack propagation rate along the direction parallel to the groove was faster than along the direction vertical to the groove. The failure nature of the two gear-teeth can be attributed to a one-time instantaneous cracking event [2,3].

1.2.2 SEM Observations

A discontinuous oxidation layer was found covering on the fracture surfaces, but the point-like feature in crack origins and radioactive crack propagation marks were clearly revealed by scanning electron microscope (SEM) (Figure 17.3a and c). After the fracture surfaces were cleaned repeatedly by supersonic vibration in acetone solution, large nonmetallic inclusion clusters containing numerous small particles of 5-30 μm in diameter were found in multiple locations of the crack origin regions (Figure 17.3b and d). Based on the morphology and the present position of the particles, it can be deduced that the particles in the crack origins did not originate from the coverings on the fracture surfaces, but were from the raw material. Theses inclusions are of the type generally associated with ingot segregation patterns. Energy dispersive X-ray (EDX) analysis (Figure 17.4) indicated that the particles were mainly Al_2O_3 complex metallurgical inclusions.

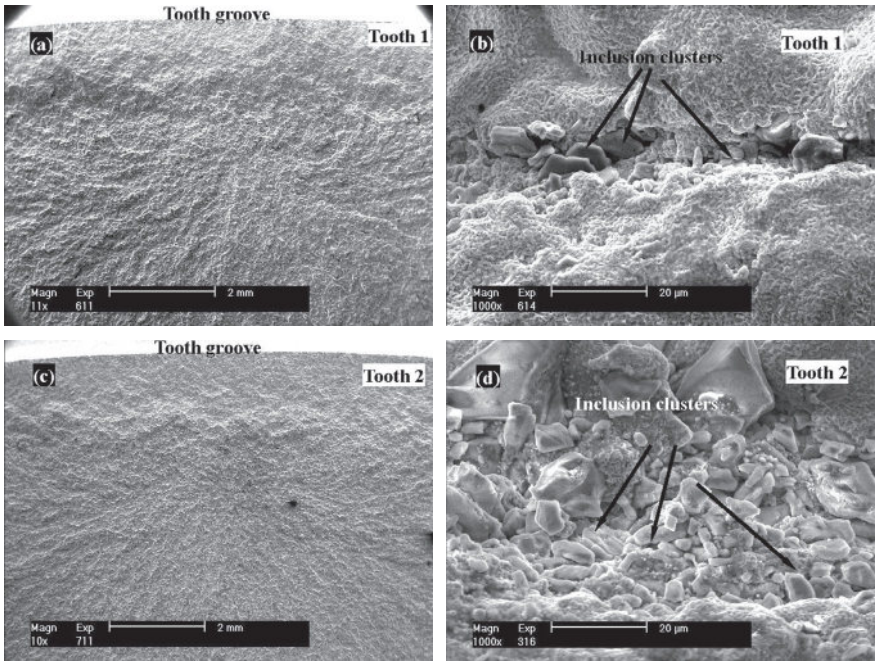

FIGURE 17.3

SEM observation on fracture surfaces: (a,c) general view, (b, d) showing inclusion clusters in crack origins.

1.2.3 Metallurgical Examination

The cross-sections of the cracked teeth close to the crack were prepared for metallurgical examination. The microstructure of the tooth profile region and the core for the two cracked gear-teeth revealed same metallurgical features. The representative photographs showing the carburized layer are shown in Figure 17.5a and b. The

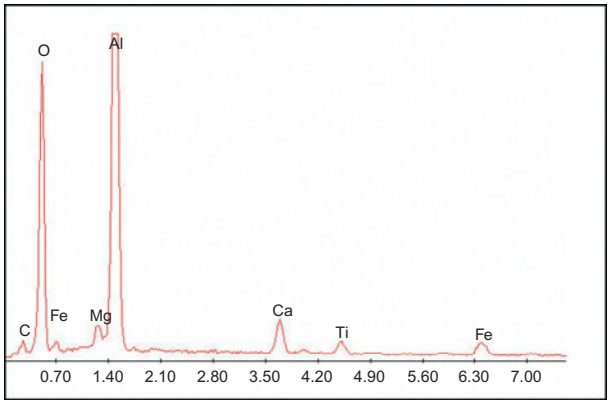

FIGURE 17.4

EDX spectrum taken from the inclusions in the crack origin (tooth 2).

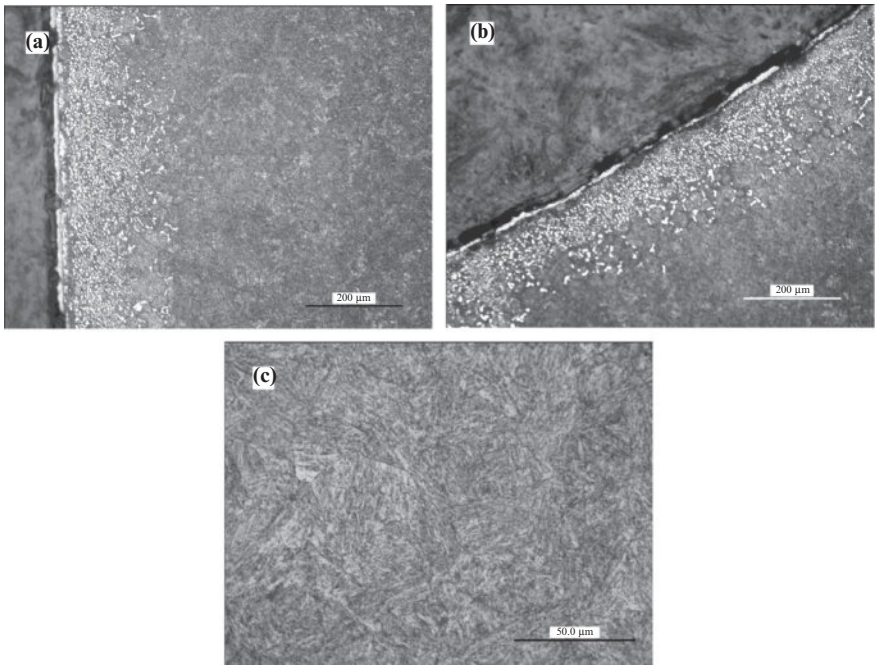

FIGURE 17.5

Microstructure of cracked tooth (tooth 1): (a) carburized layer (pitch region), (b) carburized layer (groove region), and (c) core.

carburized layer was composed of a fine acicular martensite, retained austenite, and both particle-like and discontinuous network-like carbides. The core was composed of low-carbon lath-martensite (Figure 17.5c). It should be mentioned that the presence of excessive carbides, especially network-like carbides in the case layer, may induce the brittle cracking of carburized tooth. However, fractographic investigation indicated that the cracking of teeth in this study was not related to the presence of carbides in the case layer. Additionally, the examination on the chemical composition of the failed gear materials showed that the two failed gears were fabricated from 20CrMnTi steel as specified.

The surface hardness and core hardness of cracked teeth were measured, but the values could not be compared with the specified values because the heat-treatment steps required were partly performed on the failed gears.

1.3 FAILURE CAUSES ANALYSIS

The two cracked teeth within the study had similar metallurgical and fractographic features. The axial cracks appeared on the grooves of the two cracked teeth. The crack initiation was at nonmetallic inclusion clusters at the case/core interface; it did not originate at the surface.

A number of Al_2O_3 complex inclusion clusters were found in the crack origin zones. Here, the difference in expansion coefficients between the inclusion and the matrix is greater as expected. The expansion coefficient of Al_2O_3 is $8 \times 10^{-6}/K°$, but the expansion coefficients of ferrite and martensite are $14.8 \times 10^{-6}/K°$ and $11.5 \times 10^{-6}/K°$, respectively. A greater tensile stress field would be produced in the matrix around the Al_2O_3 inclusions because Al_2O_3 inclusions produce smaller volume contractions during quenching-cooling. Moreover, the compressive stress would be produced on the carburized surface but the tensile stress would be on the subsurface [4]. The crack origins of the teeth were just situated at 3.3-3.5 mm location below the groove (subsurface region), which is the location of the tensile stress region. During carburization-quenching, the tensile stress field in the matrix around inclusions would add with the tensile stress field in the subsurface. The cracks initiated instantaneously and propagated radioactively with inclusion clusters as center. So crack origins of the two gear-teeth were situated at the inclusion clusters region and presented point-like feature. Since the presence of tensile stress in the subsurface region of the carburized component can be attributed to normal phenomenon, it can be concluded that the inclusion clusters were the leading factors of the gear-teeth cracking.

1.4 CONCLUSION

The two cracked gear-teeth revealed the same fractographic characteristics. The axial and throughout cracks appeared at the tooth groove location of the failed gears. Crack initiation was from the nonmetallic inclusion clusters at the case/core interface. Crack origins showed point-like features and the fracture mode of the gears attributed to instantaneous cracking. The cracking of the two gear-teeth was confirmed to have occurred during the carburization-quenching process. The presence

of a number of Al_2O_3 complex inclusion clusters in the crack origin zones was mainly responsible for the cracking of the gear-teeth.

1.5 RECOMMENDATIONS

Improvement of steel purity is suggested to prevent future gear failures. Since metallographic purity testing is always destructive, it is never sufficient for the detection of the largest inclusions, which is seldom event. Casual inspection by nondestructive testing technique is recommended [5].

2 CASE 2: FATIGUE FRACTURE OF FUEL INJECTION PIPE BECAUSE OF SURFACE MACHINING DENT

2.1 BACKGROUND

A high-pressure fuel injection pipe from a truck diesel engine was returned to the manufacturer because the pipe was broken into two sections after about 3650 km of service (see Figure 17.6). The fractured pipe was assembled on the second cylinder of 6-cylinder diesel engine. The pipe is made of No. 20 steel ($C \leq 0.17$, $Si < 0.30$, Mn: 0.40-0.70, $P < 0.025$, $S < 0.025$). The specified mechanical properties were as follows:

Ultimate strength: 340-470 MPa; yield strength: $\geq$235 MPa; elongation: $\geq$30%; core hardness: $\geq$HV 150.

2.2 OBSERVATION RESULTS

From Figure 17.6, it can be seen that the fracture occurred at a bending position. SEM observation of the fracture surface revealed the beach marks (Figure 17.7a) and the fatigue striations (Figure 17.7b) reflective of fatigue crack propagation. From the bowing direction of the beach marks, it can be determined that the fatigue crack

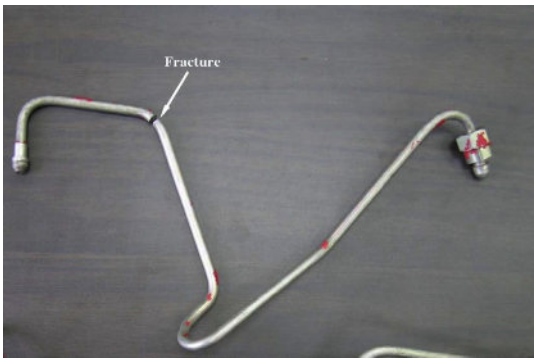

FIGURE 17.6

Cracked fuel injection pipe.

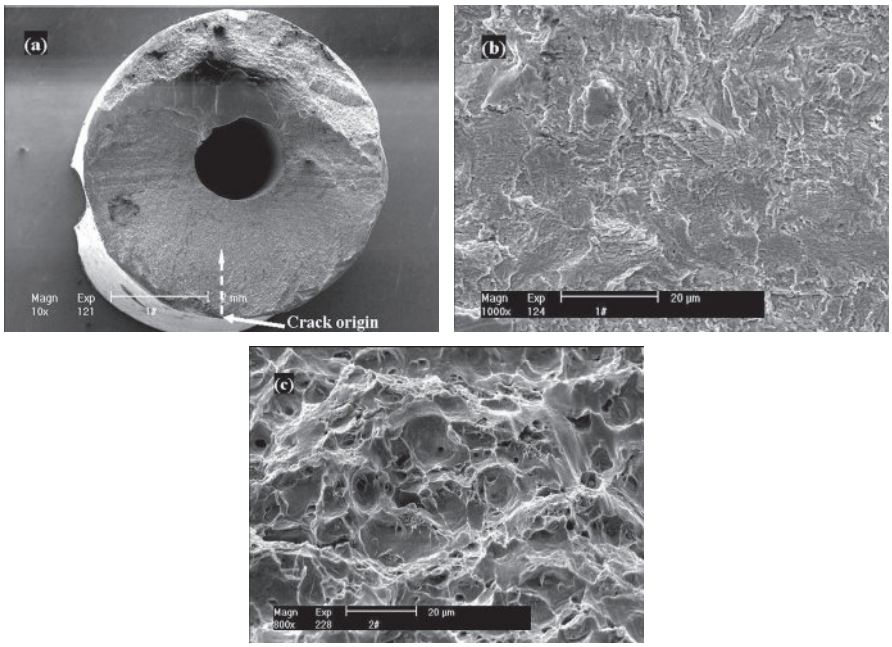

FIGURE 17.7

SEM observation on fracture surface of pipe: (a) general view; (b) crack propagation zone showing fatigue striations, and (c) final fracture zone showing dimples.

origin initiated from the concave side of bending fillet and propagated toward the convex side along the radial direction, as marked by dotted arrows in Figure 17.7a. It is suggested that the unidirectional bending fatigue is the dominant failure mechanism of pipe. The dimples are presented on the instantaneous fracture zone (Figure 17.7c). The final fracture area is about one-third of the whole fracture and the larger final fracture area suggests that the load which pipe bore was greater before fracturing.

It is highlighted that the original machining dent was revealed on the external wall of the pipe in the crack origin region (Figure 17.8) by SEM.

The microstructure of the radial section close to the crack origin was observed by optical microscope (OPM). The microstructure of the pipe was composed of ferrite and a small amount of pearlite (Figure 17.9) without the occurrence of decarburization on the surface of pipe wall, which is the normal microstructure of this grade of steel. Additionally, the chemical composition of pipe material corresponds to the specification.

Two tensile samples extracted from the straight sections of pipe were prepared. The results of tensile properties are shown in Table 17.1, along with the core hardness. It can be seen that the values of mechanical properties are within the range of the specified values.

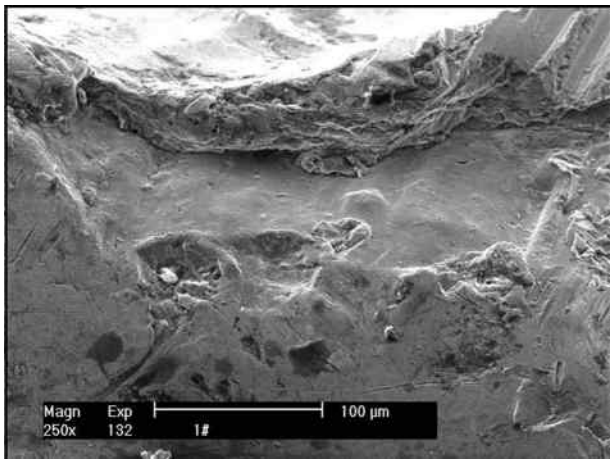

FIGURE 17.8

SEM observation on external wall of pipe in crack origin zone showing machining dent.

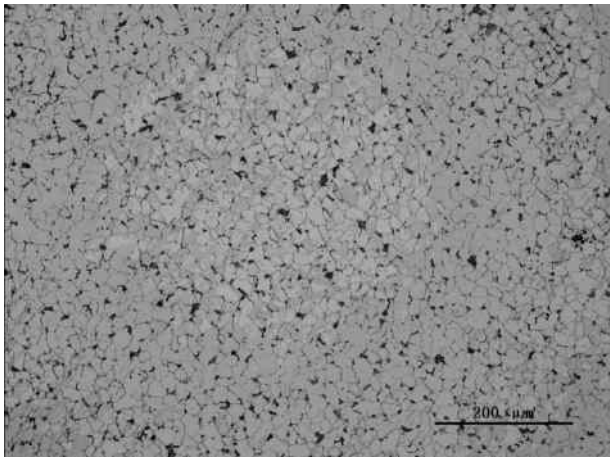

FIGURE 17.9

Microstructure of cracked pipe material.

Table 17.1 Examination Results of Mechanical Properties

	Yield strength, MPa		Ultimate strength, MPa		Elongation, %		Hardness, HV_1	
Obtained	Readings	Average value	Readings	Average value	Readings	Average value	Readings	Average value
	283, 252	267.5	395, 363	379.0	42.4, 41.7	42.1	172, 178, 172, 183	176
Specified	≥235		340-470		≥30		≥150	

2.3 FAILURE CAUSES ANALYSIS

Based on the metallographic examination and the evaluation of mechanical properties, the pipe material corresponds to the technical demand. Therefore, the fracture of the pipe is not associated with the material manufacture and the heat-treatment process.

From fractographic features, it can be concluded that the fatigue fracture was the dominant failure mechanism of the pipe. SEM observation revealed the presence of an original machining dent on the external wall of pipe and the fatigue crack origin of pipe is close to the machining dent. Fatigue failures start at the most vulnerable point in a dynamically stressed area, typically a stress raiser, which may be mechanical, metallurgical, or a combination of two [3]. The initiation of a fatigue crack is very susceptible to surface damage [6] and the machining dent or press pit typical of mechanical stress raiser just supplies the crack initiation site in this case. Additionally, the local concentration of stresses does not reduce the static strength but often leads to failure by fatigue [7]. Specifically, surface machining defects at the tensile stress concentration location may more easily cause crack initiation and propagation during service and lead to premature failure. Unfortunately, the concave side of pipe, the crack initiation site, just bore tensile stress during process of assembling pipe and in service of pipe, which facilitated to initiation and propagation of crack. It can be concluded that due to its presence, the machining dent on the external wall of pipe is the most likely reason for the unidirectional bending fatigue fracture of the pipe.

2.4 CONCLUSION

Unidirectional bending fatigue fracture took place on the pipe. The crack origin initiated from the external wall of the concave side at a bending fillet of pipe, on which the machining dent is presented, and propagated toward the convex side along the radial direction. The machining dent on the external wall of pipe is mainly responsible for the fatigue fracture of pipe. The greater tensile stress acted on the concave side of pipe during assembling pipe and service facilitated initiation and propagation of fatigue crack.

3 CASE 3: FATIGUE CRACKING OF CARBURIZED PLUNGER-SLEEVES DUE TO RAW MATERIAL DEFECT AND IMPROPER HEAT TREATMENT

3.1 BACKGROUND

Two of six plunger-sleeves were found not to supply oil when a truck diesel engine was serviced for about 2 weeks. The plunger-sleeves were disassembled from the engine and were sent to laboratory for examination to determine the cause of failure. The failed plunger-sleeves were made of 20CrMn steel. The surfaces of the internal hole and external circle, except for section A (marked in left illustration of Figure 17.10), are required to be carburized. The surface hardness of the carburized position is specified as HRC 60-64 and the case depth as 0.40-0.70 mm.

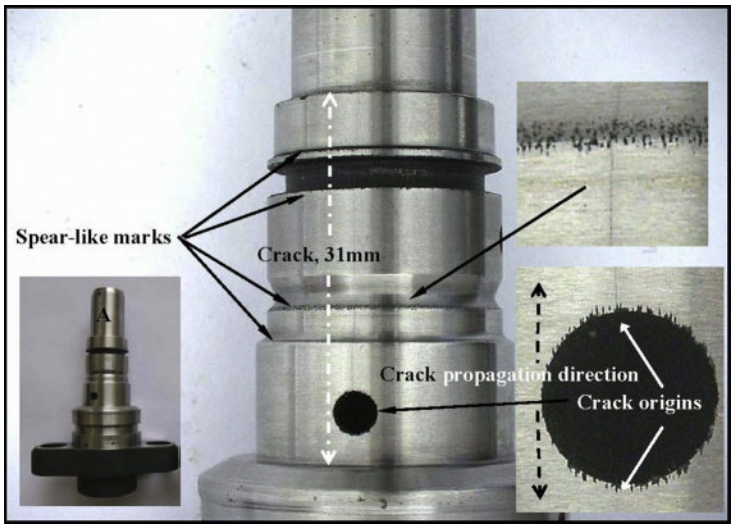

FIGURE 17.10

Cracked plunger-sleeve.

3.2 OBSERVATION RESULTS

3.2.1 Observations on Surface Damage

The plunger-sleeves were examined both visually and with the aid of a stereo-microscope. This examination revealed that all the cracks appearing on the failed plunger-sleeves were along the axial direction of the plunger-sleeve and through the oil-hole. A representative cracked plunger-sleeve is shown in Figure 17.10. The crack at the upper and lower edges of oil-hole was not well aligned and the width of the crack decreased in distance from the oil-hole. It was concluded that the crack originated from the upper and lower edges of oil-hole and propagated oppositely along the axial direction. A lot of black spear-like marks along the axial direction were found at the fringe of oil-hole and the transitional steps of different journals (seen in Figure 17.10).

SEM observations indicated that the black spear-like marks at the fringe of the oil-hole were spear-like blunt openings along the axial direction (Figure 17.11). It was noted that the main cracks at the edges of the oil-hole initiated from the spear-like openings (Figure 17.11b and c). The main crack at both edges of the oil-hole was sharp and the crack presented as tortuous (Figure 17.11d).

3.2.2 Observations on Fracture Surface

The fracture surface was prepared by pulling the crack apart. Intensely concentrated black spear-like marks appeared at the edges of the interface between the radial machining section and fracture, as shown in Figure 17.12.

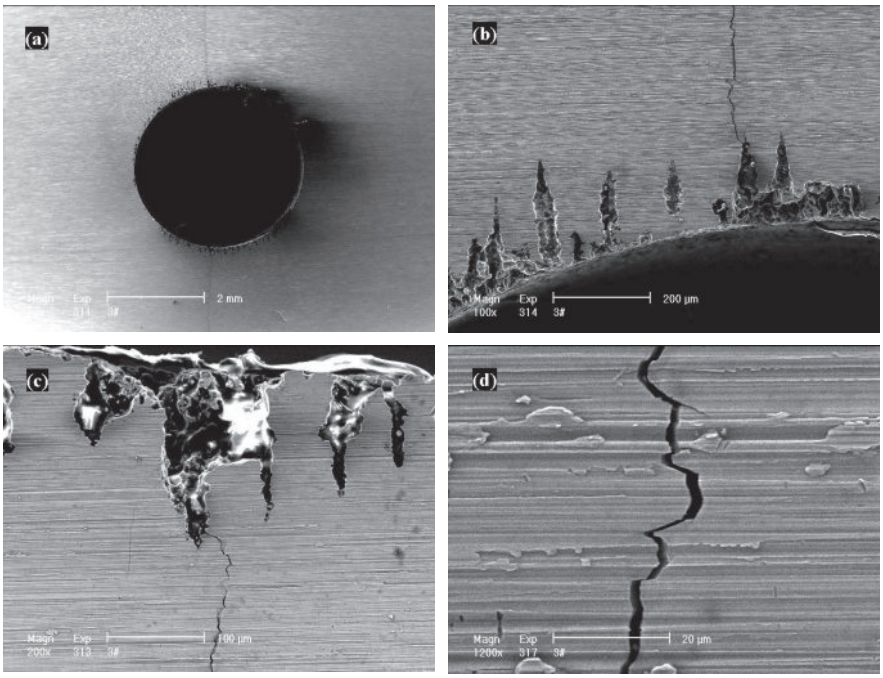

FIGURE 17.11

SEM observation on external surface in oil-hole region showing black spark-like openings and main cracks: (a) general view, (b) at upper edge, (c) at low edge, and (d) tortuous crack morphology.

Beach marks showing fatigue crack propagation [2] were seen in the region close to the oil-hole. From the orientation of beach marks, the crack's origins initiated from the internal wall of the oil-hole edge and propagated toward the external circle (indicated by dotted arrows in Figure 17.12). The axial banded region was exhibited in the middle of the fracture (marked in Figure 17.12). The crystalline fracture morphology can be observed within about 0.5 mm range from the internal hole and the external circle surfaces (marked by double arrows in Figure 17.12).

SEM observation indicated that the fracture surface was smooth and in the crack origins close to internal hole, the crack propagated mainly in the intergranular mode (Figure 17.13b and c). Fatigue striations were observed in the crack propagation region (Figure 17.13d). The axial banded region in the middle of the fracture contained some axial rod-like inclusions (Figure 17.13e). It is concluded that the plunger-sleeve started to crack in the intergranular mode and propagated in fatigue.

The spear-like openings also appeared on the fracture surface connected with the oil-hole (Figure 17.13a–c). There are mostly the elongated inclusions on the extended lines of the spear-like openings (Figure 17.13c). It is suggested that the spear-like openings must be related to the elongated inclusions.

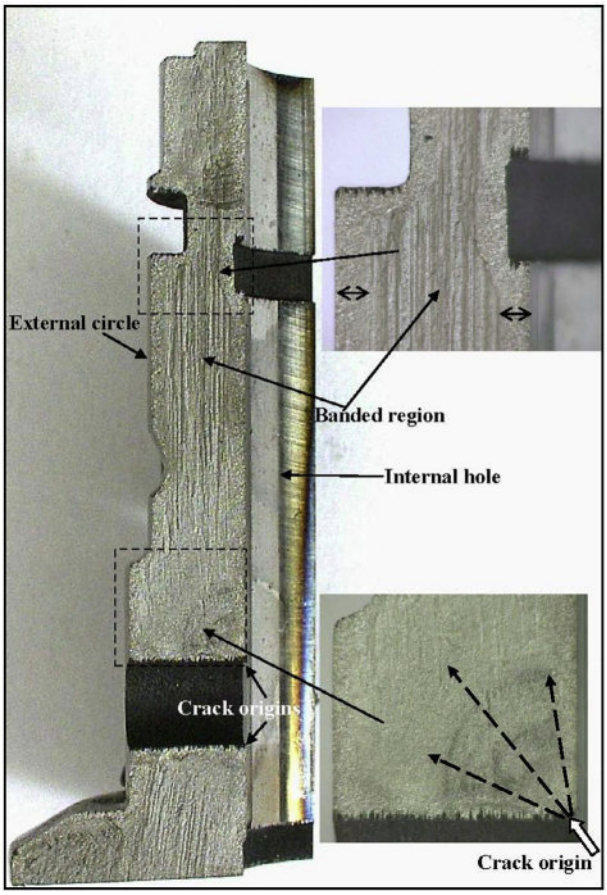

FIGURE 17.12

Macro-fracture surface of cracked plunger-sleeve.

It was noted that a lot of pits along the axial direction are presented on the internal surface of oil-hole (seen in Figure 17.13a).

Intergranular fracture morphology was revealed in 0.4-0.5 mm regions from the surface of the internal cavity and external circle (Figure 17.13f), which is related to the presence of the carburizing layer [8,9].

3.2.3 Microcomposition Analysis on Inclusions on the Fracture Surface

EDX analysis (Figure 17.14) performed on the axial elongated inclusions on the fracture surfaces and in the core material revealed that the elongated ones were sulfide of manganese, MnS.

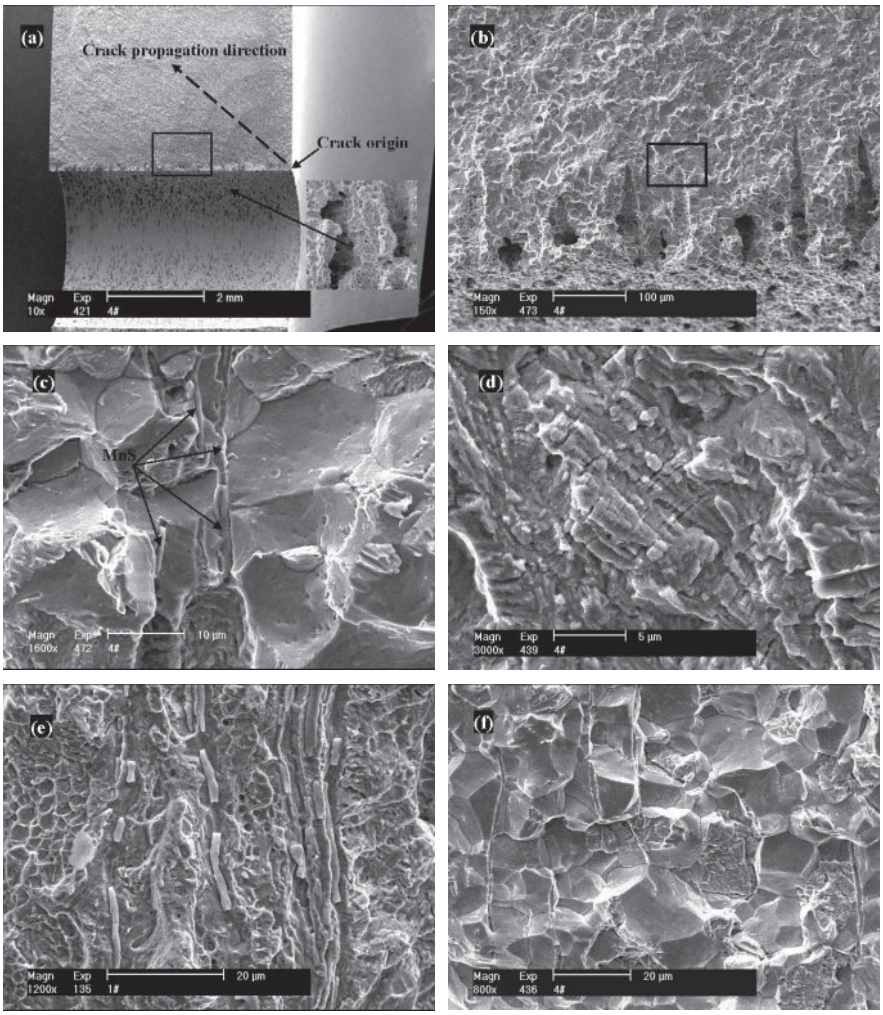

FIGURE 17.13

SEM observation on fracture surface: (a) general view, (b) boxed region in (a) showing intergranular cracking and spear-like pits and openings, (c) boxed region in (b) showing spear-like pits connecting with elongated MnS inclusions, (d) crack propagation region showing fatigue striations, (e) middle region on the fracture surface showing axial banded structure, and (f) intergranular fracture morphology in carburized depth of external circle.

3.2.4 Microstructure Examination

The longitudinal section of the plunger-sleeve was prepared for metallurgical examination. The core microstructure is composed of tempered martensite and fine elongated MnS inclusions were seen along the axial direction of the plunger-sleeve (Figure 17.15a). The carburized layer is composed of martensite and retained

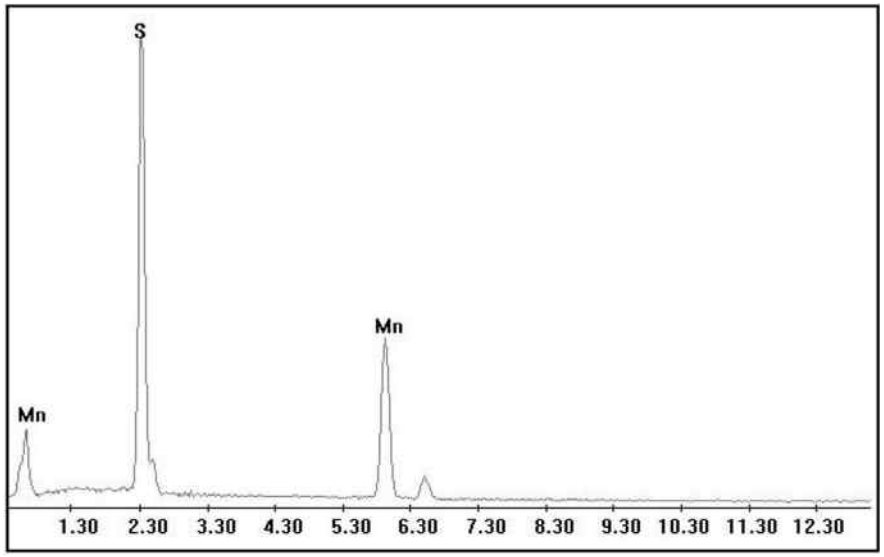

FIGURE 17.14

EDX spectrum taken from the inclusions on the fracture surface (Figure 17.13e).

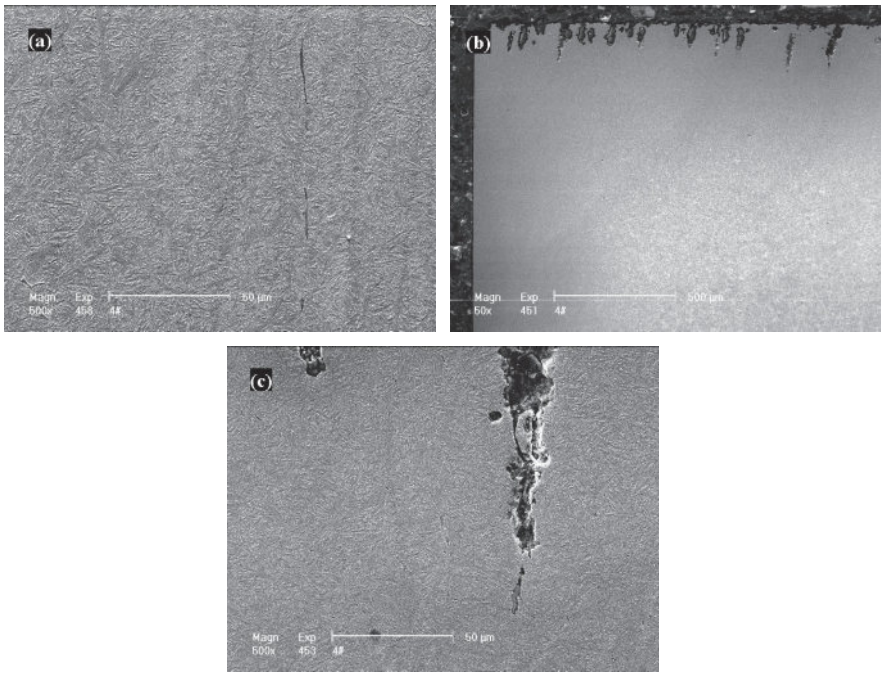

FIGURE 17.15

Microstructure of failed plinger-sleeve: (a) core, (b, c) surface layer region of oil-hole.

austenite (Figure 17.15b and c), which is normal microstructure of the grade of the steel. It was noted that the spear-like openings at the edge of oil-hole were always aligned to MnS stringers (Figure 17.15b and c). In other words, the spear-like openings propagated along MnS-inclusion stringers.

3.3 OXIDATION AND CARBURIZING SIMULATION TESTS IN LABORATORY

Based on the fractographic and metallographic observations, the axial spear-like openings appearing at the edges of oil-hole and the platform always propagated along the axial elongated MnS inclusions, but the spear-like openings were not observed nearby the elongated MnS inclusions in the interior region of the plunger-sleeve. OPM observation on the nonetched specimens exhibited more clearly the morphological difference of MnS in the core and in carburizing layer, as shown in Figure 17.16. It is implied that the appearance of the spear-like openings was not only related to the carburizing temperature but also closely related to the reactions of MnS with carbon or oxygen. In order to determine the formation mechanism of the openings and validate the failure nature of the plunger-sleeve, carburizing and oxidation simulation tests were carried out in the laboratory.

Y40Mn steel (C: 0.37-0.45; Si: 0.15-0.35; Mn: 1.20-1.55; Fe: balance) with greater amount and large MnS stringers (Figure 17.17a) was selected to be carburized and oxidized at different temperatures for various time so as to observe the evolution of the MnS inclusions in both processes. When the specimen was oxidized 5 min at 800 °C, a thin oxidation film peeled from the specimen's surface. SEM observations on the subsurface of the specimen that was oxidized showed that the MnS inclusion had debonded from the matrix and the parts of MnS had fallen off (Figure 17.17b). Some MnS inclusions on the subsurface pulled out from the matrix completely to form pits with rising oxidation temperature and time (Figure 17.17c). However, pulling-out MnS inclusions from the matrix did not occur on the specimens

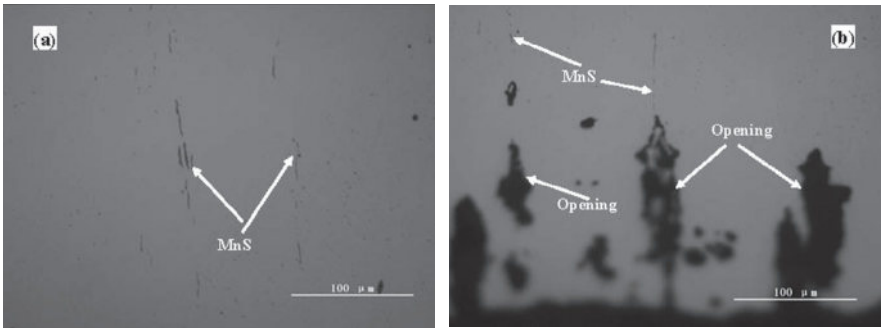

FIGURE 17.16

OPM observation on the nonetched specimens showing MnS morphology in core and in carburizing layer: (a) core and (b) edge at oil-hole.

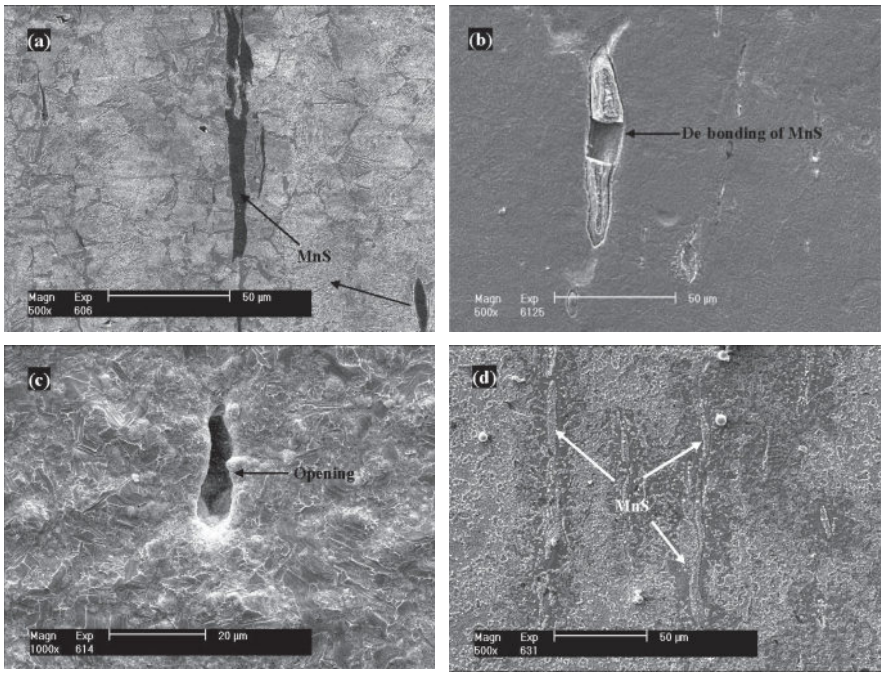

FIGURE 17.17

Evolution of MnS inclusions on subsurface in process of oxidation and solid carburizing tests: (a) showing MnS stringers in original material, (b) showing MnS inclusion debonded and pulled out from matrix after oxidizing at 800 °C for 5 min, (c) showing MnS inclusion pulled out from the matrix completely and forming the opening after oxidizing at 920 °C for 240 min, and (d) showing complete MnS-inclusion morphology after solid carburizing at 920 °C for 240 min.

that were solid-carburized and gas-carburized (Figure 17.17d). It is suggested that the reaction of MnS inclusion with oxygen was mainly responsible for pulling-out MnS inclusions from the matrix and formation of pits.

3.4 FAILURE CAUSES ANALYSIS

The plunger-sleeve material in this case contained numerous axial elongated MnS inclusions. Thermodynamic data showed that alloy elements had different affinities for oxygen [10]. Si, Mn, and Cr should oxidize in gas-carburizing atmosphere, while Fe, Ni, and Mo are not expected to oxidize. Therefore, the elongated MnS inclusions on the surface of the plunger-sleeve would react more preferentially with the oxygen in the carburizing atmosphere of excessive oxygen when an unsuitable gaseous media was operated. The following reaction may occur:

$$MnS + O \rightarrow MnO + S$$

MnS inclusions debonded and pulled out from the matrix to form pits. The pits at the edge of the oil-hole became the spear-like openings. In addition, sulfur (element S) may segregate at the grain boundaries to weaken the grain boundary cohesion, so the intergranular fatigue crack initiation was always observed in the carburized layer of oil-hole. Under the action of the alternative circumferential stress at the oil-hole, the fatigue crack initiated from the end of the spear-like opening at the edge of oil-hole and propagated along the axial direction so that the longitudinal cracking occurred on the plunger-sleeves.

3.5 CONCLUSION

The numerous elongated MnS inclusions along the axial direction of the plunger-sleeve were found in the material. Axial elongated MnS inclusions on the surface of the plunger-sleeve debonded from the matrix and pulled out from the matrix to form the spear-like openings at the edges of the oil-hole in unsuitable gas-carburizing operation due to excessive oxygen content in the carburization atmosphere. Under the action of the alternative circumferential stress at the oil-hole, the fatigue cracks initiated from the end of the spear-like opening at the edges of oil-hole and propagated along the axial direction so that the longitudinal cracking occurred on the plunger-sleeves.

3.6 RECOMMENDATIONS

1. Problems in furnace-atmosphere control during carburizing are relatively common causes of spear-like openings on the plunger-sleeve and steps should be taken to ensure that the furnace is thoroughly purged prior to carburizing and positive atmospheric pressure maintained throughout the carburizing cycle.
2. Steel purity should be improved. High-powered metallographic examination on axial banded inclusions of raw material should be performed. Furthermore, it is recommended that 20CrMn steel be substituted by 20CrMo steel to decrease the presence of the MnS inclusions.

4 CASE 4: INTERGRANULAR FRACTURE OF CARBURIZED SPLINED-SHAFT DUE TO CASE INTERNAL OXIDATION AND DEFECTIVE DESIGN

4.1 BACKGROUND

A truck diesel engine splined-shaft fractured after being in service for 7-8 h. The as-received fractured splined-shaft is shown in Figure 17.18. It can be seen that the transverse fracture occurred at the root fillet between the tooth portion and the cylinder portion and no obvious macro-plastic deformation was observed. The failed splined-shaft was made from 20MnCr5 steel. The external surface of a spline-shaft is required to be carburized. The surface hardness is specified as HV_{10} 675-770 and the depth of carburized layer as 0.30-0.80 mm.

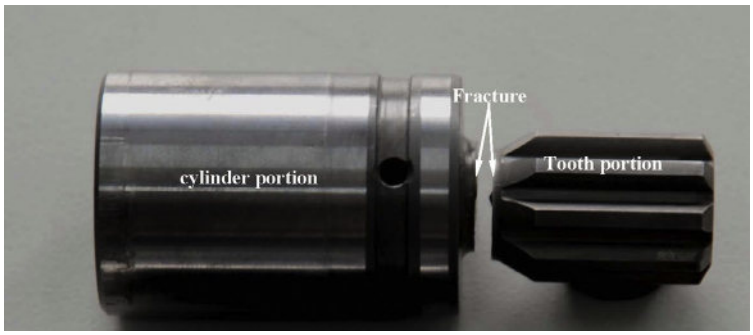

FIGURE 17.18

Fractured splined-shaft.

4.2 OBSERVATION RESULTS

4.2.1 Fractographic Observation

Low-powered SEM observation (Figure 17.19a) indicated that the fracture surface close to the center hole was rough and slightly convex, characterized by a "center of twist" [11] and the circular shear traces surrounding the center of twist were found on the fracture surface. It is concluded that the failure mode of the splined-shaft was torsion fracture and the twist final fracture zone was situated at the fringe of center hole. Unfortunately, due to the mutual rubbing of the matched fracture surfaces, the crack origin and the crack propagation direction could not be distinctly discerned.

High-powered SEM observation indicated that the fracture surface exhibited generally circular parabola shallow dimples (Figure 17.19b) and contact scrape marks along the dragged direction of the parabola dimples appeared in the local regions of fracture (Figure 17.19c). It was noted that within about 20 μm from the internal hole, the fracture morphology was brittle, and in particular, intergranular, as shown in Figure 17.18d and e. The intergranular facets found were associated with dimples or ductile tears [12,13], and some particle-like substances were found on the intergranular facets (marked by arrows in Figure 17.19e). EDX analysis indicated that these particle-like substances were oxide compounds of Cr, Mn, Si (seen illustration in Figure 17.13e). Additionally, in the instantaneous fracture region close to the hole, deeper parabola dimples were observed (Figure 17.19f).

The fracture surface of the failed splined-shaft, especially on the outer periphery, had been worn intensely, so the fractographic features representing a carburized surface were not revealed. However, the presence of the intergranular decohesion features on the fracture surface of internal hole implied some brittle failure mechanism occurred on the splined-shaft and the brittle fracture may relate to the case layer on the splined-shaft. To investigate the relation of intergranular fracture to the case layer, a fracture was manufactured artificially. The semicircle transverse section was removed from the tooth portion and a transverse notch was

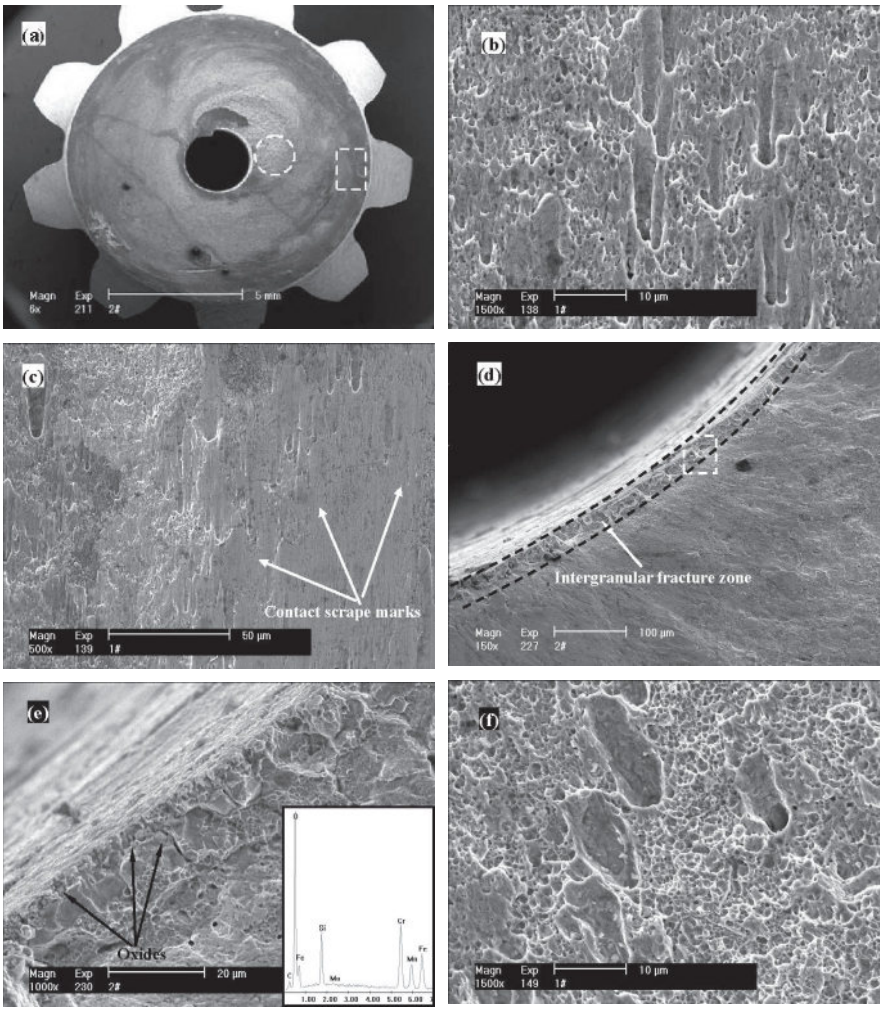

FIGURE 17.19

SEM observation on fracture surface and EDX spectrum of inclusions: (a) general view, (b) boxed zone in (a) showing parabola dimples, (c) showing scrape marks, (d) region close to internal hole, (e) boxed zone in (d) showing intergranular facets associated with dimples and precipitates and EDX spectrum, and (f) circled zone in (a) showing dimple morphology in the instantaneous region.

made in the matrix by spark-cutting, then section from the matrix was broken off toward the tooth portion to obtain identical orientation fracture with the original fracture of the failed splined-shaft. Low-magnified SEM observation indicated that the fracture surface had a different appearance in the outer and inner regions (Figure 17.20a). In the outer region of 0.7-0.8 mm from the surface the fracture

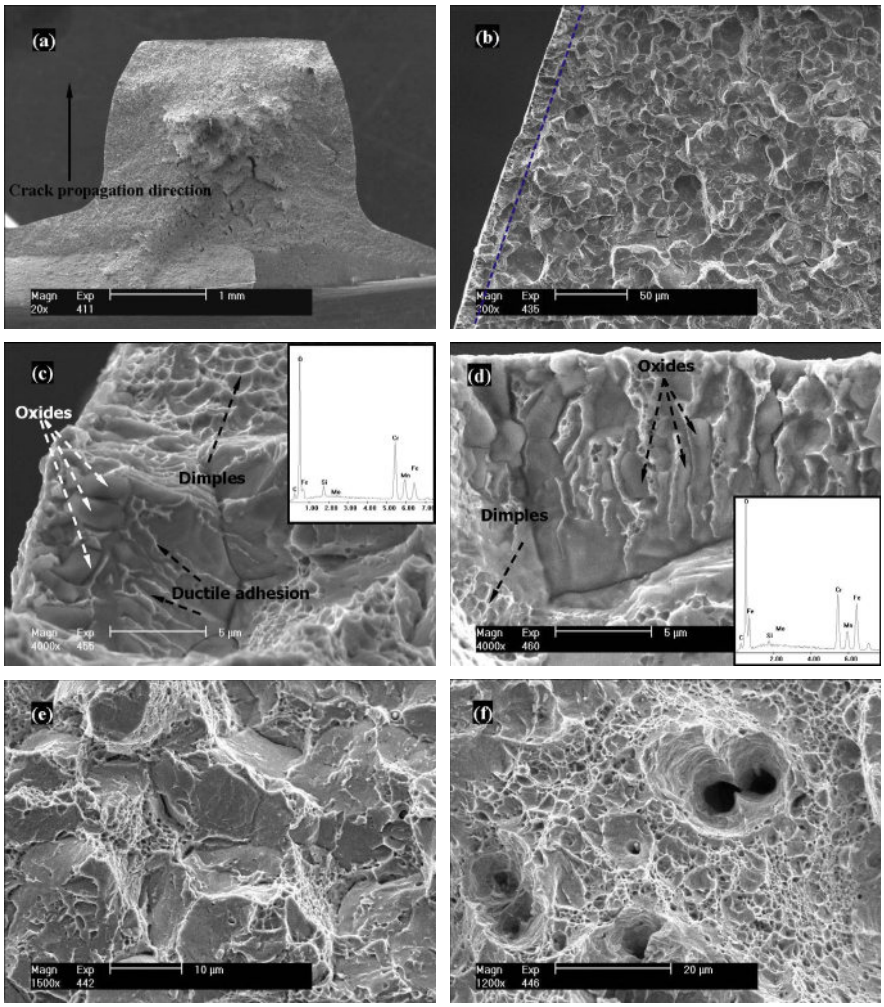

FIGURE 17.20

SEM observation on the fracture surface prepared artificially and EDX spectrum of inclusions: (a) general view, (b) showing the interface corresponding to internal oxidation layer, (c) showing intergranular facets associated with the oxides and dimples (at the flank) and EDX spectrum, (d) showing intergranular facets associated with the oxides and dimples (at tooth groove) and EDX spectrum, (e) showing intergranular fracture in subsurface corresponding to carburized layer, and (f) showing dimple morphology in the middle region.

surface was brittle but ductile in the tooth center. High-magnified SEM observation revealed that in the carburized area of about 0.5 mm from the surface, the fracture mode was predominately intergranular (Figure 17.20b). An obvious interface was revealed at the location of about 20 µm from the surface (marked in Figure 17.20b

by dotted line). However, a close examination of Figure 17.20c and d showed particle-like or rod-like substances at the intergranular facets. As proven by EDX analysis, these substances were also oxide compounds of Cr, Mn, and Si (seen in illustration in Figure 17.20c and d). It is highlighted that the dimples or ductile tears were observed at separated grain facets (Figure 17.20c and d). The fractographic features were similar to those presented in the internal hole region of the serviced fracture of splined-shaft. This indicated that the cracking occurred by microvoid coalescence alongside grain boundaries, typical of a crack propagation by a ductile intergranular mode [12,13]. This behavior is known to result from highly localized plastic deformation within relatively "soft" zones alongside grain boundaries [14], e.g., troosite or pearlite network [14]. It is well known that the occurrence of the internal oxidation on the carburized layer can induce the formation of nonmartensitic structure alongside the grain boundaries, e.g., pearlite, troosite, or bainite [14]. The following microstructure observations will demonstrate the appearance of a thin film of nonmartensite structure on the grain boundary in the case layer. The presence of nonmartensite structure alongside grain boundaries becomes relatively "softer" than the acicular martensite. In summary, the above results indicate that the fracture mechanism was ductile intergranular cracking related to precipitation of intergranular oxides. The oxide particles were not presented on the intergranular facets in subsurface, but dimples were still observed on the individual intergranular facets (Figure 17.20e). The middle region of the tooth was characterized by a dimpled ductile fracture (Figure 17.20f).

4.2.2 Microstructure Examination

The longitudinal (through the fracture surface) and transverse sectional specimens were prepared for metallugical examinations. Visual examination indicated that the carburizing operating was conducted on the external surface of splined-shaft. A relatively thin macro case layer was observed on the internal hole surface, suggesting that operating of preventing penetration was not performed on the internal hole surface.

Longitudinal and transverse sectional microstructures were observed by OPM and SEM. A typical microstructure of the carburized layer in the etched condition is shown in Figure 17.21. As shown, the microstructure of carburized layer mainly consisted of the tempered acicular martensite and the retained austenite without intergranular network-like carbides. It was found that black intergranular network-like structure were presented in the carburized layer of the external surface and the internal hole surface of the splined-shaft (Figure 17.21a). Precipitates were seen along the grain boundaries (Figure 17.21b). As proven by EDX analysis, these precipitates were also oxide compounds of Cr, Mn, and Si (seen in illustration of Figure 17.21b), in accordance with the precipitates on the intergranular facets of the fracture surface. It is suggested that the internal oxidation near the surface occurred, which is a typical phenomenon in gas-carburized steel [14]. The depth of internal oxidation is approximately 20 μm. It is highlighted that the region of

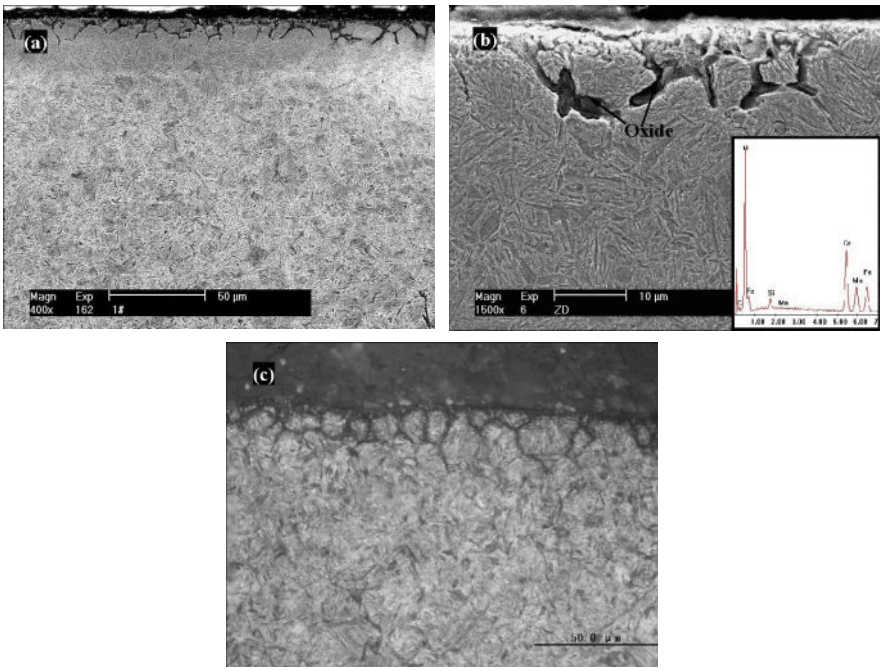

FIGURE 17.21

Microstructure of carburized layer and EDX spectrum of inclusions: (a) SEM observation showing internal oxidation morphology (tip region), (b) showing oxides in the grain boundaries and EDX spectrum, and (c) OPM observation showing nonmartnesite thin film alongside the grain boundaries in the internal oxidation zone.

internal oxidation presents grain boundary "cavities" (Figure 17.21a and b), which is suggested that theses oxidized grain boundaries were favorable sites for crack initiation. Nonmartensite structures were clearly observed in OPM, as shown in Figure 17.21c. From Figure 17.12c, a thin film of "dark phase" [15] of about 1-μm thick alongside grain boundaries was revealed in the internal oxidation layer, whose metallurgraphic features were identical with nonmarteniste as described in the documents [14–17], troosite, or pearlite. The microstructure of core was primarily composed of tempered lath-martensite.

Additionally, the composition examination indicated that the splined-shaft was made from 20MnCr5 steel. The hardness profiles in the tip, pitch line, groove, and internal hole regions from the surface to the interior were measured to evaluate the case depth. The results indicated that the case depth of the tooth portion was generally about 0.55-0.62 mm, which corresponded to the specification (0.30-0.80 mm), and the case depth of internal hole was relatively shallow, about 0.20 mm. The surface hardness is HV_{10} 719 (average value of three readings), which is in accordance with the specification (HV_{10} 675-770).

4.3 FAILURE CAUSES ANALYSIS

Intergranular brittle fracture may occur on the carburized parts if the prior austenite grain boundaries are embrittled. In general, such an embrittlement is associated with a carbide net or impurity element segregation, especially phosphorous, on the prior austenite grain boundaries, or with hydrogen absorption from the carburizing atmosphere. Another microstructural feature to consider when dealing with brittle fracture of carburized parts is the possible formation of surface intergranular oxidation if oxygen is present in the treatment atmosphere. From the observations and examinations in section above, no carbide network was identified within the carburized layer for various regions. It is highlighted that the chemical analysis of the splined-shaft material revealed a low phosphorous content (in agreement with the specification) and phosphorus segregation on the intergranular fracture surface was not probed by EDX. In order to determine if impurity segregation phosphorus associated with the grain boundary fracture noted on the carbrized layer, an Auger analysis should be performed [18]. In present case, the intergranular facets associated with "ductile tear" are presented only within about 20 μm depth from the surface, which corresponds to the internal oxidation depth in a case layer. Hence, the major role of phosphorus in the embrittlement process can be excluded. The intergranular embrittlement fracture should be more closely related to the presence of internal oxidation defect in the case layer and the structure anomaly can be regarded as a kind of weakened zone at the surface of carburized steel. Phosphorus segregation in the embrittlement process did not act a major role.

During carburizing of components, the oxygen diffuses into the steel and combines with certain alloying elements. In particular, chromium, silicon and manganese are readily oxidized. The internal oxidation propagated preferentially along the prior-austenitic grain boundaries, presenting intergranular precipitation of oxides in the case layer. Oxidation products may embrittle the initial austenite grain boundaries specially. The study's results also indicated that the formation of grain boundary "cavities" associated with the intergranular oxidation. Therefore, it can be expected that the crack would easily initiate and propagate in the structure of grain boundary "cavities." Finally, the intense intergranular oxide precipitates promoted the microstructural embrittlement of the case layer, which was associated with the presence of oxidation precracks to lead to the brittle fracture during the service. The fractographic results confirmed that cracking followed initially the intergranular oxidation path until a depth of approximately 20 μm.

In service, the splined-shaft bears torsion load. In general, the torsion shear stress increases from the center of the shaft to the surface along the radial direction. The outmost surface of the splined-shaft bears greater shear stress. Literature indicates that cracks usually form 45° under torsional nature of loading imposed on a component [19], while, the failed splined-shaft was not in this instance. The tooth end of splined-shaft was fully bound up by the sleeve and the shaft end was fixed tightly in the internal hole of the driving gear. From the design construction of the splined-shaft, the axial free length is relatively short (merely 6.0 mm at the fillet, see in Figures 17.18 and 17.22), equivalent to a pure notch in construction.

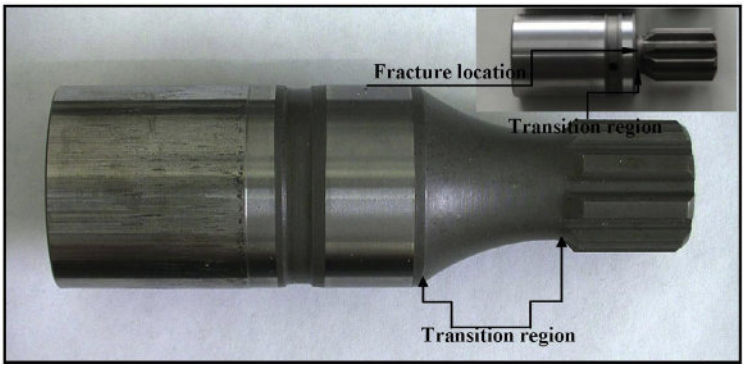

FIGURE 17.22

Improved splined-shaft with long transition between the tooth and the shaft.

Additionally, due to the presence of circular intergranular micro-cracks on the outer surface of the splined-shaft, the crack would propagate along the radial direction rather than propagating along the direction of 45° to the axial. At last the transverse fracture formed.

It should be pointed out that the presence of intergranular internal oxidation in the case layer is not enough to cause the splined-shaft to rupture prematurely. However, in combination with greater stress concentration at the fracture location resulting from over-short axial free length between the tooth portion and the cylinder portion, the probability of such an event is considerably increased. Similar failure did not occur on a new type of splined-shaft which had a suitable transition between the tooth and the cylinder (Figure 17.22), despite the occurrence of internal oxidation in the case layer.

4.4 CONCLUSION

The material of failed splined-shaft, the surface hardness, and the case depth corresponded to specifications. Internal oxidation phenomenon occurred on the carburized splined-shaft to lead to the formation of intergranular oxides of Cr, Mn, Si enveloping a "soft" zone of nonmartensitic structure alongside the grain boundaries of the carburized layer. The formation of grain boundary "cavities" associated with the intergranular oxidation. Grain boundary "cavities" promoted crack initiation and propagation. The fracture mechanism of the splined-shaft was ductile intergranular cracking. The premature failure of the splined-shaft was promoted by intergranular internal oxidation. Presence of intergranular internal oxidation in the case layer was not enough to cause the shaft to rupture prematurely. However, in combination with greater stress concentration at the fracture location resulting from over-short axial free length between the tooth portion and the cylinder portion, the probability of such an event was considerably increased.

5 RECOMMENDATIONS

1. Generally, internal oxidation is to be expected during carburizing because the carburizing media usually contains oxygen compounds (CO_2, CO, H_2O, and so forth) and the commercial case-hardening steels usually contain alloy elements with a higher affinity for oxygen than iron (Si, Cr, Mn, and so forth). But there are some possibilities of reducing the depth of oxides for a given steel by applying a high carbon-potential (a low CO_2 content). For avoiding internal oxidation, carburizing media without the presence of oxygen compounds has to be used; for example, carburizing with methane.
2. The configuration and degree on internal oxidation would be influenced by the type and the amount of its alloying elements. Exchange the material of splined-shaft and select the steels containing alloy elements (e.g., Mo, Ni) unsusceptible for internal oxidation.
3. Substitute the improved splined-shaft with long axial free length between the tooth portion and the cylinder portion for old type of splined-shaft to decrease the degree of stress concentration.

REFERENCES

[1] Brooks CR, Choudlhury A. Failure analysis of engineering materials. New York: The McGraw-Hill Companies, Inc.; 2002.
[2] ASM. Fractography. 9th ed. ASM handbook, vol. 12. Materials Park, OH: ASM International; 1987.
[3] ASM. Failure analysis and prevention. 10th ed. ASM metals handbook, vol. 11. Materials Park, OH: ASM International; 2002.
[4] Clegg RE. Failure of planetary pinions in earth moving equipment—failure analysis approach. Eng Fail Anal 2000;7:35–41.
[5] Klinger C, Bettge D. Axel fracture of an ICE3 high speed train. Eng Fail Anal 2013;35:66–81.
[6] Milan MT, Spinelli D, Bose Filjo WW, Montezuma MFV, Tita V. Failure analysis of a SAE 4340 steel locking bolt. Eng Fail Anal 2004;11:915–24.
[7] Mazur Z, Carvajal-Martínez A, Muñoz-Quezada R, García-Illescas R. Failure analysis of a leak-off pipe from injection valves of an off-shore operating diesel engine. Eng Fail Anal 2007;14:196–208.
[8] Straffelini G, Versari L. Brittle intergranular fracture of a thread: the role of a carburizing treatment. Eng Fail Anal 2009;16:1448–53.
[9] Krauss G. Steel: heat treatment and processing principles. Materials Park, OH: ASM International; 2000.
[10] Chatterjee-Fischer R. Internal oxidation during carburizing and heat treatment. Metall Trans 1978;9A:1553–60.
[11] Varin JD. Fracture characteristics of steering gear sector shafts. Pract Fail Anal 2002;2:65–9.
[12] Tawancy HM. Degradation of mechanical strength of pyrolysis furnace tubes by high-temperature carburization in a petrochemical plant. Eng Fail Anal 2009;16:2171–8.

[13] Tawancy HM. Failure of a furnace outlet pipe in a benzene plant by internal oxidation due to improper welding practice. Eng Fail Anal 2009;16:2179–85.
[14] Colombo RL, Fusani F, Lamberto M. On the soft layer in carburized gears. J Heat Treat 1983;3,126–8.
[15] Verhoeven JD, Chen N, Bevolo AJ. A scanning auger microscopy characterization of the internal oxidation produced on carburizing. J Heat Treat 1992;9(2):73–80.
[16] Koslovskii IS, Kalinin AT, Novokava AY, Lebedova EA, Feofanova AI. Internal oxidation during case-hardening of steels in endothermic atmospheres. Met Sci Heat Treat 1967;9(3 and 4):157–61.
[17] Asi O, Cetin Can A, Pineault J, Belassel M. The relationship between case depth and bending fatigue strength of gas carburized ASE 8620steel. Surf Coat Technol 2007;201:5979–87.
[18] George K. The microstructure and fracture of a carburized steel. Metall Trans 1978;9:1527–35.
[19] Jha AK, Sreekumar K, Mittal MC. Metallurgical studies on a failed EN19 steel shear pin. Eng Fail Anal 2008;15:922–30.

CHAPTER

18 Failure mechanisms and modes analysis of vehicle exhaust components and systems

Zhigang Wei*, Thomas Goehring*, Melany Mioduszewski*, Limin Luo*, Adam Kotrba*, Marek Rybarz†, Kay Ellinghaus‡, Markus Pieszkalla‡

*Tenneco Inc., Grass Lake, Jackson, Michigan, USA**

Tenneco Automotive Polska sp. z o.o. Rybnik, Poland†

Tenneco GmbH, Edenkoben, Germany‡

CHAPTER OUTLINE

Handbook of Materials Failure Analysis With Case Studies from the Aerospace and Automotive Industries.
http://dx.doi.org/10.1016/B978-0-12-800950-5.00018-1

1 INTRODUCTION

Exhaust components and systems can be found in a wide variety of vehicles, construction and agricultural equipment, ships, aircrafts, stationary machinery, and other applications. Figure 18.1 schematically shows an exhaust system in a passenger car. The basic functions of vehicle exhaust systems are to clean and transmit exhaust gas out of the vehicle to the atmosphere, reduce noise, make the drivers and passengers comfortable, and manage heat. Vehicle exhaust systems consist of many components, physically joined and functionally integrated. Typical gasoline exhaust components may include, but not limited to, manifolds, downpipes, flanges, catalytic converters, resonators, hangers, exhaust pipes, mufflers, and tailpipes. Diesel components may include diesel oxidation catalyst (DOC), diesel particulate filter (DPF), selective catalyst reduction (SCR), and many fluid delivery, injection, and decomposition components. Their wide range of types, sizes, operational conditions such as temperature, load and environment, design details result in a wide spectrum of possible failures, which are often difficult to examine and

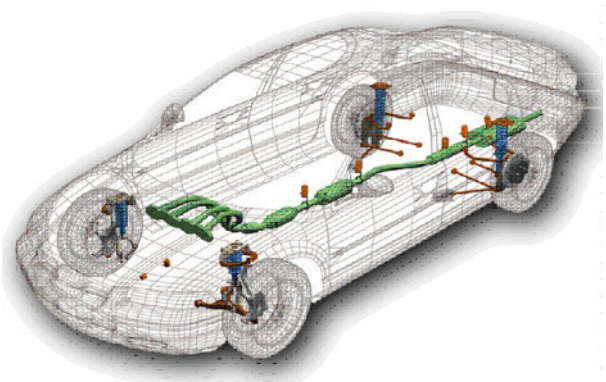

FIGURE 18.1

Schematic of an exhaust system in a passage car.

assess. The durability and reliability performance of vehicle exhausts as well as other vehicle components and systems is one of the most important concerns to product design and validation engineers [1–3]. Failure mode and effect analysis is often the first step of a durability and reliability assessment process. It involves reviewing parts and identifying failure mechanisms and modes, as well as their causes and effects. Failure probability can only be estimated and controlled by first understanding the failure mechanisms and failure modes. More important, an exhaust system is a chain of components, which must work together faultlessly. Like other systems in series [4], usually, an exhaust system is more unreliable as a whole than its weakest component. Faults in each of the exhaust components have potential negative effects on the performance and safety of exhaust systems as well as the vehicles.

Failure can be defined in several ways. Two typical definitions of failure that are often used include failure of functions and failure of materials and structures. The former one is related to the loss of functions such as power and control, while the latter one is linked to the loss of capability in load bearing and structural integrity, which is the focus of this chapter. Failure mechanisms and failure modes are often used interchangeably [5]. However, here in this chapter, the two definitions are treated separately to distinguish between the underlying driving forces of failure and the appearance of failure. In other words, failure mechanism is defined here as the mechanical, chemical, physical, or other processes that result in failure while failure mode is defined as the pattern, location, or other visible characteristics of the failure. In testing, several failure modes can be activated or suppressed, depending on the specific geometry and loading condition. For example, failure modes can be surface fatigue crack or subsurface fatigue crack [6–8], Mode-I (opening mode) fatigue crack or Mode-II (shearing mode) fatigue crack [9]. However, the sole failure mechanism for these failure modes is fatigue. Similarly, a single failure mode can be caused by a single failure mechanism, such as fatigue, or a combination of multiple failure mechanisms, such as fatigue, creep, oxidation, and corrosion [10,11].

Failure mechanisms and modes of exhaust components and systems greatly depend on materials, loading condition, and operating environment. Years of experience has shown that the prevailing failure modes in exhaust systems are cracks at welds between pipes and muffler/resonator/converter (360° welds), cracks at hanger-to-pipe welds (line welds) and broken hanger rods, and the dominant failure mechanism is fatigue [12,13]. Different failure mechanisms, such as corrosion, creep, oxidation, erosion, wear or their combinations are responsible for most other failures. Fatigue is essentially a cycle-dependent failure mechanism under vibration environment caused by engine vibration, road condition, thermal cycling, etc. Corrosion, creep, and oxidation are basically time-dependent failure phenomena [14]. Creep and oxidation of metals are usually issues for components such as vehicle manifolds operated at high temperature [14]. Corrosion in vehicle exhaust systems is usually caused by salt, condensate, urea, and other corrosive agents.

Decades of development in exhaust components and systems has made exhaust product design very sophisticated and mature. However, failure does occur, either unwanted or wanted. Unwanted failure is caused by many factors [15] such as limited knowledge and uncertainties about the failure nature of complex components and systems; new requirements in weight reduction, performance improvement and cost reduction push the application to new territories; new functions added with new unexplored engineering challenges; human errors in design, assembly, operation, and maintenance. It should be emphasized here that as soon as design and applications change, formerly successful solutions no longer satisfy the new requirements, and new failures appear. For example, with the advanced integrated mechanical and electrical systems, modern exhaust systems are becoming multi-functional, intelligent mechatronics systems. With the new systems, new failure mechanisms and modes occur, and the failure causes might no longer be limited to component hardware, but can also be extended to software, control, or communication systems. All of these provide new challenges as well as new opportunities to product design and validation engineers. In addition to the unwanted failure, in product design stage, attempts are often made to deliberately cause failures, in searching for possible failure mechanisms and modes, and to gain insight into the potential failure mechanisms and failure modes [5,15].

In this chapter, an overview of the trend of exhaust system development and products are reviewed in Section 18.1 followed by a discussion of the new challenges on materials failure mechanisms/modes in Section 18.2. The most common failure mechanisms, such as fatigue and corrosion, as observed in exhaust products are discussed in Section 18.3. In Section 18.4, a probabilistic failure data analysis method is presented to help identify the failure mechanisms followed by a discussion of a method for materials screening and ranking for cyclic oxidation, thermal cycling, and corrosion resistances in Section 18.5. Two case studies, applying the methods outlined in this chapter, are demonstrated in Section 18.6 followed by a final summary in Section 18.7. Based on the fact that there is very little information published-to-date specifically addressing failure mechanisms and modes of vehicle exhaust components and systems, this chapter offers a comprehensive and practical guide on the state-of-the-art methodologies for failure cause determination, effective remedies and prevention strategies for engineers, as well as managers, in their product design and validation.

2 TREND OVERVIEW OF EXHAUST DEVELOPMENT AND MATERIALS REQUIREMENTS

Increasingly stringent emission regulations drive demand for increased energy efficiency, reduced weight, and advanced aftertreatment strategies, which requires exhaust materials to meet the increasing demands in durability and reliability performance [16]. In this section, the historical development of exhaust systems,

especially the most recent trend in research and development (R&D), is provided. The development of advanced aftertreatment technologies and the associated materials aspects, in particular, material failure mechanisms, modes, and failure prevention are emphasized.

Exhaust systems have been applied to many engine configurations throughout the last century, and over the last 40 years catalytic converters have been integrated to reduce pollution [17]. But as of this most recent decade, enhanced catalysts and particulate filter systems are applied, driving the tailpipe emissions down to extremely low levels, referred to in the light-duty markets as super-ultra-low emissions vehicles. Regulations are spreading across many industrialized regions of the world and are driving lower levels to ensure appropriate public health, including those within highly commercial and populated areas. Pollution of concern is categorized as particulate matter (PM), carbon monoxide (CO), hydrocarbons (HC), and nitrogen oxides (NOx), but now with greenhouse gas emissions concerns, carbon dioxide (CO_2), methane (CH_4), ammonia (NH_3), and nitrous oxide (N_2O) also must be controlled. Furthermore, attention has been broadened beyond passenger cars and light trucks, and well into commercial vehicles, including trucks and off-road equipment in agriculture and construction, locomotive, and marine. As undesirable health and environment effects from pollution become well understood, further regulations and resulting changes to exhaust systems are expected.

As exhaust systems have recently evolved, applied materials and their failure modes have also changed. Some of these trends are described, including operational conditions, as well as material effects and failures. Most exhaust systems in regions with tightening regulations are expected to last the full useful life of the vehicle, exceeding 120,000 miles for light duty and 435,000 miles for heavy duty (US requirements). Most of the applied steel is now stainless, ensuring longevity against structural and environmental inputs, including temperature, vibrations, and corrosion. Tightening emissions regulations often drive catalysts closer to the engine to minimize the time it takes to light-off, achieving the temperature necessary to support the adequate conversions, but increasing applied thermal and vibration loads. With recent interests in climate control, fuel consumption is important as it contributes to global warming via CO_2 emissions, and light-weighting initiatives are critical. Many vehicle exhaust subsystems target weight reduction, pushing the boundaries on materials and their thicknesses, and increasing material failure mode risks, although low-stress areas are targeted. Materials technologies continue to advance to offset such risks, as with tailored blanks which combine sheets of varying thicknesses prior to stamping, applying thinner materials in areas with less thinning within the manufacturing process.

Diesel powertrains have experienced the greatest evolution over the last dozen years, integrating technologies to reduce harmful soot and NOx emissions [18]. Air quality has been affected in many industrialized regions as diesels increase in number, including on and off-road commercial vehicles such as long-haul trucks and construction equipment. DPFs are integrated within the exhaust and significantly

reduce PM by forcing the exhaust flow through porous walls to physically remove it, eliminating the infamous black plumes of soot coming from these engines, even under high-load conditions. DPFs are often ceramic, coming in various materials tuned for their applications needs, including cordierite, silicon carbide, and aluminum titanate. Metallic options with various designs for filtration efficiency are also available. Soot accumulates on the filter and requires a periodic cleaning, which is often catalytically supported, and exhaust temperatures are increased through fuel supplied through the engine (post-injection) or with secondary fuel injectors integrated within the exhaust [19]. Such events, referred to as active or passive regeneration, leverages the catalytic behavior of a DOC to oxidize the introduced fuel (active) or oxidize the NO to produce NO_2 (passive, reduces soot loads more slowly at lower temperatures than needed for active). Thermal stresses certainly occur, but systems must be designed to control their significance across the applied materials to avoid failures which could lead to leak paths, reducing the filtration effectiveness. As regeneration of the soot occurs, particularly active, exothermic response results in elevated outlet temperatures that must be managed, affecting peak downstream temperatures which in many cases require tailpipe coolers to avoid environmental exposure risks. As packaging, costs, and mass are tightened, DPFs merge with NOx reduction catalysts, further reducing NOx emissions as well as PM, but increasing their complexities and material risks that come with urea-selective catalytic reduction (SCR) systems.

NOx emissions are of concern since they are precursors to ambient ozone levels, and in extreme conditions result in smog and acid rain. The lean-burn nature of diesel applications (less fuel needed per given volume of air) drives its fuel efficiency benefit, but excess air results in NOx emissions since there is insufficient fuel to balance with the oxygen. Urea SCR systems target NOx emissions through the use of a reductant, urea, injected with controlled rates into the exhaust. With the exhaust heat, urea decomposes into ammonia, which selectively reacts with NOx to yield nitrogen (N_2) and water (H_2O). Ammonia is highly corrosive, and material grades have had to be adjusted to support such an internally corrosive environment. The urea injection is often supplemented with a mixer to promote droplet breakup and ammonia uniformity across the catalyst inlet. Urea dosing also must assure the avoidance of wall-wetting across all operating conditions, which could lead to pooling and the formation of problematic deposits, furthering the corrosion risks on material failures. Furthermore, sensors for diagnostics and controls must now be incorporated to accommodate the balance of injected urea with the anticipated NOx reduction, verifying adequate conversion, and avoidance of undesired byproducts, such as ammonia and nitrous oxide. Such systems have been overwhelmingly applied globally across markets and are being enhanced with new catalyst materials and reductant generation methodologies to enable further NOx reduction value, improving cold starts and low-load conditions such as city driving that may not produce sufficient exhaust heat for desired conversion.

Exhaust systems will continue to evolve as global warming concerns increase and CO_2 regulations tighten, driving needs for improved operational efficiencies both

from the engine as well as vehicle. Engine technologies continue to demonstrate efficiency improvements, influencing exhaust requirements, as with the direct injection of gasoline, promoting efficiencies but requiring exhaust particulate filters to offset the generated PM. Exhaust valves are integrated to balance acoustic requirements, improving attenuation as less cylinders are applied on demand. Further efficiencies are of interest, including the recovery of the exhaust heat, converting it into useful energy, either in the form of heat, electricity, or mechanical work. Heat exchangers are already applied, particularly in hybrid vehicle applications, transferring exhaust heat to the powertrain and drivetrain during cold starts to more quickly achieve operational efficiencies as well as cabin heating. Thermoelectric generators apply unique materials such as skutterudite to produce electrical power as thermal gradients occur across them, providing opportunities to unload alternators to save fuel. A Rankine cycle system offers the most effective conversion of heat, but comes with complexity and integration requirements, including the integration of an evaporator in the exhaust, integrated with a selected working fluid and expander to drive the mechanical shaft output torque, which can feed directly into the drivetrain or drive a generator. Over time, these systems and their materials and resulting failure modes will evolve via optimization as they spread across applications, markets, and regions.

In summary, exhaust systems undergo some of the harshest operating conditions in the vehicle, including excessive temperatures, vibrations, and environmental exposure, and as technologies are demonstrated and applied, their material selection and failure mode considerations are extremely important and must be part of the innovation and development process.

3 TYPICAL FAILURE MECHANISMS AND MODES IN VEHICLE EXHAUST SYSTEMS

Vehicle exhaust systems are complex constructions with different sections experiencing different operating conditions and eventually requiring different demands on durability and reliability performance [20]. Based on operating temperature, a vehicle exhaust system can be roughly divided into two parts: hot end or front part and cold end or rear part [21,22]. The hot end includes manifolds, front pipe or downpipe, and catalytic converter. The cold end includes the resonator, center pipe, muffler, and tail pipe. The threshold temperature is roughly about 400 to 500 °C. An intermediate part, (e.g., center muffler, connecting pipes, etc.) is sometimes added as the third part [21]. The heat source of the exhaust systems mainly comes from the engine. Other sources include the active thermal regeneration system for particulate matter reduction and elimination [16]. The peak temperature generated by spark plugs is usually greater than 6000 °C; the peak temperature in an internal combustion engine chamber is also high (e.g., about 2000 °C) [15]. Even though such high temperatures do not entirely transfer to the engine materials due to advanced thermal management technologies, thermal-fatigue and other high-temperature-related mechanisms are the dominant failure mechanisms for engine parts, such as

cylinder head, crankcase, piston, etc. [15]. The high-temperature exhaust gas generated in engines emits into exhaust manifolds and down through the exhaust system components to the tailpipe with continuously decreasing temperature level, and finally gets released to the atmosphere.

The hot end of exhaust systems, in particular, manifolds which are usually the hottest part with peak temperature of 1000 °C or higher [10] (Santacreu et al., 2013), are not only subjected to high temperature and temperature changes but also simultaneously subjected to external load either by the applied stress due to engine and road vibration loading or constraint, which also generates stress in the components. Thermal cycles such as engine start-up and shut-down cycles lead to nonuniform thermal expansion and contraction of exhaust components and systems, and eventually result in low-cycle thermal-fatigue failure. Under these complex thermal-mechanical loading and environmental conditions, oxidation, fatigue, creep or their combinations can be the major cause of the material failure. At the cold end of exhaust system, the temperature is lower and oxide formation is usually not a significant issue. Instead, pitting corrosion, crevice corrosion, and corrosion caused perforation are the primary corrosion mechanisms and modes. Mufflers are subject to severe corrosion both externally and internally, and the lifetime of a muffler is usually shorter than that of other parts of exhaust systems. The most critical zones in mufflers are the confined areas between shells and baffles, where the evacuation of acid solution is not facilitated, and crevice corrosion can develop and even lead to the perforation of mufflers. The primary corrosion agents of the internal corrosion is gas condensate while chloride-containing de-icing salts on the roads in cold counties are the main causes for corrosion on exterior surfaces. In fact, compared to the inner wet corrosion, the external corrosive loads through rainwater, road dust, slush and de-icing salts are almost negligible [23]. Corrosion caused perforation in mufflers not only leads to noise problems and back pressure change but also to exhaust gas leaks that can cause concerns as this may allow gas to enter the vehicle.

Failure assessment of failed components and systems can be conducted with the following steps to reveal the failure modes and the root causes of failures.

Step 1: Visual assessment: The first step in any failure analysis is visual inspection of damage to view the damaged exhaust, if possible on-site, which provide information regarding the manner in which the exhaust was operated, and the type of loads subjected.

Step 2: Laboratory tests: Metallographic, chemical analysis, strength, ultrasonic, scanning electron microscope (SEM), stereomicroscope, microhardness are often used to find the failure details and the failure mechanisms. Specimens usually need to be sectioned, mounted, polished, and etched before metallographic examination. Fatigue fracture surface would allow pinpointing of the fracture origin. However, very often, rubbing of the fracture surface and corrosion damage (after the fracture) obscure the fracture surface to such an extent that fracture morphology and the initiation site cannot be conclusively determined.

Step 3: Analysis: Based on the failure observations, simple mathematical calculation may be needed to estimate the operating conditions such as stress, strain, temperature, and to find the possible solutions to mitigate and to prevent failure. For example, some physical patterns can be used as temperature indicators (e.g., partially spheriodized silicon needles indicating temperature well under a certain degree). Computational tools such as computational fluid dynamics (CFD) and finite element analysis (FEA) and other virtual simulation tools can simulate the real failure events and to help find the failure causes and design flaws.

In the following sections, some of the most common failure mechanisms and modes as observed in vehicle exhaust components and systems are described.

3.1 MECHANICAL FATIGUE

The motion and vibration, compounded by elevated temperatures, make fatigue a major concern in the design and validation of the exhaust system. Elevated temperatures reduce the fatigue strength of the material. Systems are designed to prevent localized areas of high stress, particularly in areas where stress risers from manufacturing are present. These stress risers include bends in pipes where material thinning occurs during the forming process. Bends include the bending of the pipe to fit around other vehicle components such as axles, spare tires, and gas tanks. Bends may also be a radius that results from sizing the pipe or flaring a pipe for connecting one component to another. The most common stress risers occur at welds. Fatigue can also occur as the result of differences in thermal expansion and contraction during heating and cooling of the system. The differences may be due to variation of thermal expansion between two materials or the same material with different masses, larger masses heating and cooling at a slower rate than adjacent smaller mass. Fatigue cracks are generally in a straight line or following the contours of a stress riser and are trans-granular. There may be cracks parallel to the failure as a result of shifting stress concentration if there is not an apparent stress riser.

Welds are used to join pipes to other pipes or components such as catalytic converters, resonators, and mufflers. The weld is both a geometric and metallurgical stress riser. The heat affected zone in the parent material around the weld is an area of large grains which has lower fatigue life. The most common failures occur by initiating at a weld toe and propagating through the parent material in the heat affected zone of the weld or at the weld root and propagating through the weld and/or the parent material. Both the weld toe and root create a geometric notch that is a stress riser for fatigue initiation. The difference in microstructure between the weld, the parent material, and the heat affected zone in the parent material is a metallurgical stress riser. Examples of these failures can be seen in Figure 18.2a and b.

Fatigue is evidenced by striations on the fracture surface as seen in Figure 18.3a and b. Striations are not always visible under lower magnification. Larger striations

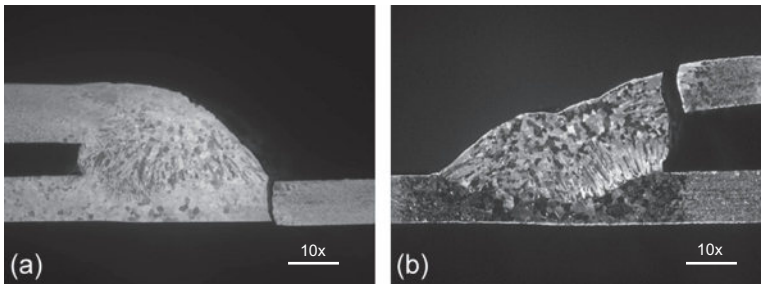

FIGURE 18.2

Fatigue failure at (a) weld toe and (b) weld root.

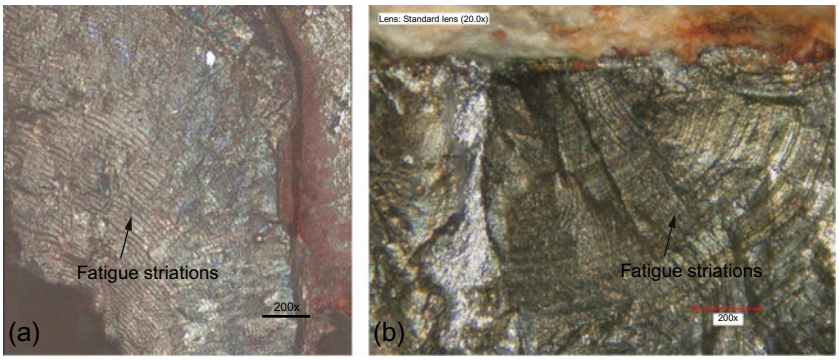

FIGURE 18.3

Fatigue striations on fracture surfaces.

usually indicate a high-load/low-cycle condition. Smaller striations indicate a low-load/high-cycle condition. Usually, the wider spacing of the fatigue striations and the presence of secondary cracking are evidence of the more rapid propagation of the fracture at that location. The striation pattern can also indicate the location of the crack initiation.

3.2 THERMAL FATIGUE

Thermal fatigue occurs at elevated temperatures and usually in combination with mechanical fatigue. Thermal fatigue consists of oxidation penetrating the material and forcing open a crack. Continued heating will propagate the crack through a cycle of oxidation opening the crack. These are typically trans-granular with multiple branch cracks filled with oxidation. Examples of thermal-fatigue cracks are shown in Figure 18.4a and b.

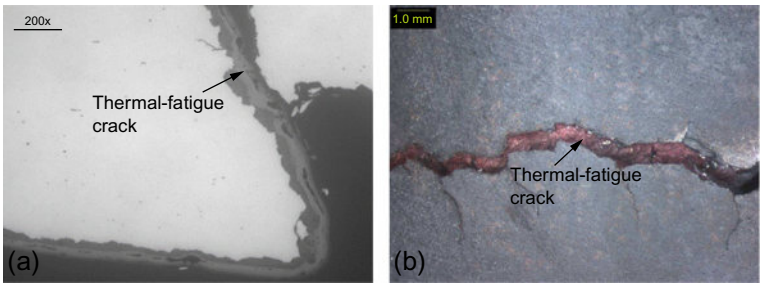

FIGURE 18.4

Thermal-fatigue cracks.

3.3 CORROSION

Corrosion is a complex time-dependent electrochemical process, in which an anodic reaction between metal and metal ions results in electrolytic removal of metal. There are many types of corrosion occurring in the exhaust systems: general corrosion, pitting corrosion, crevice corrosion, inter-granular corrosion, and oxidation, etc. [24,25]. In addition to corrosion, failure mechanisms of materials under combined mechanical loading, either applied stress or residual stresses, and corrosive environment, such as stress corrosion cracking (SCC) and corrosion-fatigue (CF), are also major engineering concerns in vehicle exhaust systems. Fluid flow introduced by modern injector systems cause erosion-corrosion damage. Corrosion failures may be perforation of components that allow exhaust leaks in internal components that result in noise issues due to a change in the muffler acoustics. Perforation can be a small area where pitting corrosion penetrates the material thickness. Complete failures can be overall corrosion that may not extend through the entire thickness but reduces the thickness sufficiently that allows premature fatigue or even a tensile failure.

Corrosion is highly dependent on the environment to which the exhaust is exposed. This includes the internal environment which can be affected by the fuel source, the fuel mixture (rich or lean), and the temperatures of the exhaust stream. Material selection is the most important aspect for preventing or at least minimizing corrosion. Ferritic or 400 series stainless steels are the most common materials used in exhaust system due to the chromium content. The chromium content affects the oxidation resistance and the type of ferritic stainless steel is usually based on the maximum service temperature. Aluminized ferritic stainless steels (hot dip coating of aluminum on the mill supplied material) have shown to greatly improve corrosion resistance. Aluminum is a sacrificial coating in a galvanic condition so that even if the steel is scratched from road damage or during forming operations and welding, the aluminum will corrode preferentially to the stainless steel.

If localized corrosion attack initiates on an open surface, it is called pitting corrosion; if corrosion occurs at an occluded site, it is called crevice corrosion [26]. This localized corrosion can lead to accelerated failure of structural components by

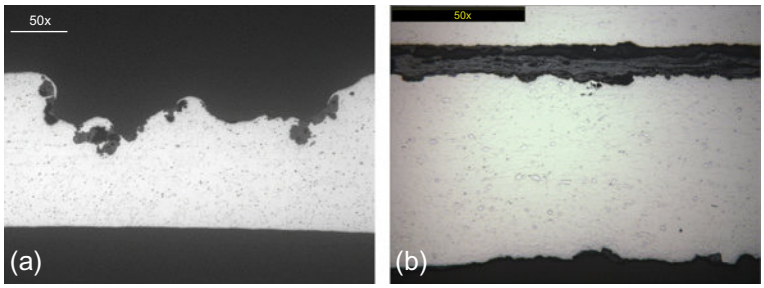

FIGURE 18.5

(a) Pitting corrosion on ferritic stainless steel and (b) crevice corrosion between two layers.

perforating and by acting as an initiation site for cracking [26]. Unlike general metal loss, which is defined as relatively uniform thinning over a significant area, localized metal loss such as pitting and crevice corrosion can vary significantly within a given area. Pitting corrosion is the most common and usually occurs at a surface imperfection as small as inclusions in the raw steel corrosion. Once corrosion initiates at a location, it can serve as a catalyst for more rapid corrosion resulting in a pit. Early in a corrosion environment, it is not unusual to see multiple spots of corrosion with adjacent areas having no corrosion attack. With continued exposure, the corrosion will eventually spread over an entire part. Crevice corrosion occurs when two materials are placed together and moisture wicks between the layers. This condition results in accelerated corrosion due to the trapped moisture and any corrosive materials in the moisture. Examples of pitting corrosion and crevice corrosion are shown in Figure 18.5.

While austenitic or 300 series stainless steels have superior corrosion resistance to the ferritics due to the addition of nickel in the alloys, the cost is usually higher and the risk of stress corrosion cracking is present. Stress corrosion cracking (SCC) occurs in materials that are susceptible (like austenitic stainless steel), under stress, and exposed to halogens including chlorides found in road salt or ocean air. The stress may only be residual stress from forming the material as well as static and dynamic stresses on the exhaust system on the vehicle. SCC cracks usually start very small and may open up as the stress on the material increases. The cracks are usually trans-granular and often have multiple branch cracks. Ferritic stainless steel is not susceptible to SCC. Figure 18.6 shows the stress corrosion cracking patterns in austenitic stainless steels.

Another corrosion mechanism is inter-granular corrosion due to sensitization of the grain boundaries. Sensitization occurs when the available chromium content at the grain boundaries is depleted and corrosion resistance is reduced. This occurs when the material is exposed to temperatures between 400 and 800 °C. At these temperatures, carbon and/or nitrogen migrates to the grain boundaries and forms chromium carbides and/or nitrides, depleting the chromium. If exposed to a corrosive environment, corrosion will rapidly propagate through the grain boundaries until the grains fall out or a continuous path through the material thickness results in

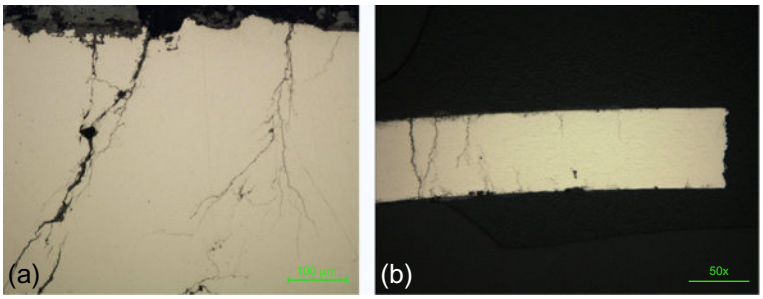

FIGURE 18.6

Stress corrosion cracking (SCC) in austenitic stainless steels.

failure. Ferritic stainless steels used in exhaust systems are stabilized with titanium and/or niobium (also known as columbium) in combination with low carbon content. Titanium and niobium have a greater affinity for carbon than chromium so that titanium and/or niobium carbides and/or nitrides are formed preferential to chromium carbides/and or nitrides. This allows the chromium to be available to provide corrosion resistance. Austenitic stainless steels are also susceptible to sensitization. Improper gas shielding during welding may allow nitrogen from the air to be absorbed in the weld. The excess nitrogen can exceed the needed ratio of carbon/nitrogen to titanium/niobium resulting in sensitization. Figure 18.7 shows the inter-granular corrosion due to sensitization of a ferritic stainless steel weld.

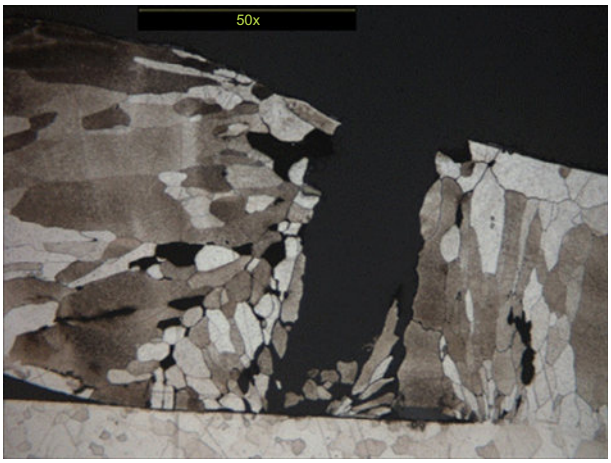

FIGURE 18.7

Inter-granular corrosion due to sensitization of a ferritic stainless steel weld.

3.4 TENSILE

A tensile failure may also be called a ductile failure. This simply occurs when the stress on a component exceeds the strength of the material. In exhaust applications, the main consideration is the temperature to which the system is exposed. Selection of an appropriate material and thickness of the structures alleviates any concern for tensile failures. In some cases, if a crack (e.g., fatigue crack) has propagated to a degree such that the remaining load-carrying cross-section is no longer able to carry the load, it breaks suddenly through the tensile failure mechanism, as so-called overload failure. Figure 18.8 shows an example of failure (necking and cracking) under tensile loading.

3.5 IMPACT

Impact failures occur when a sudden high load is applied to the component and the material fails. The failure would have an appearance of a brittle failure. Ferritic stainless steels are subject to a glass transition temperature, whereby at low temperatures, the ductility of the material is reduced. Impact is usually not a factor considered in exhaust design and validation processes.

3.6 OXIDATION

As previously stated in the section on corrosion, the chromium content affects the oxidation resistance of the stainless steel. Ferritic stainless steels tend to have better oxidation resistance than austenitic stainless steels. Failures due to oxidation are unusual and are likely the result of an unusual thermal event where temperatures exceed normal operating conditions. Shorter exposure to extreme high temperatures

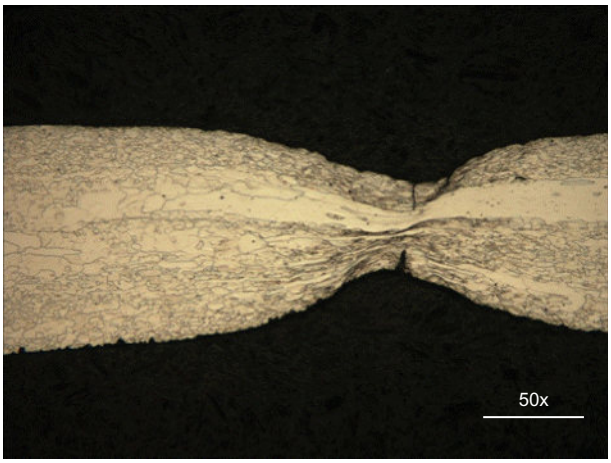

FIGURE 18.8

Tensile/ductile failure.

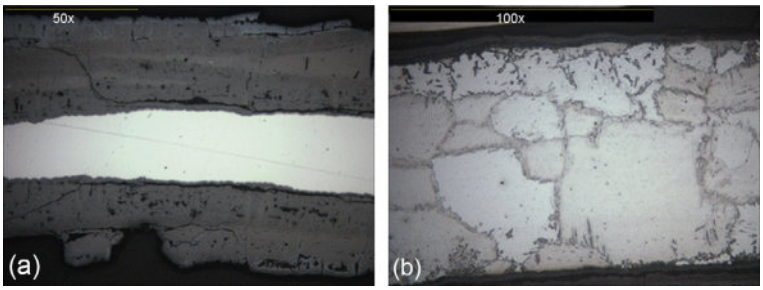

FIGURE 18.9

(a) Heavy oxidation from high temperatures and (b) grain growth and grain boundary liquation.

will also result in exaggerated grain growth and may result in a condition known as grain boundary liquation. Figure 18.9a and b shows the severe oxidation and grain boundary liquation, respectively.

3.7 UREA CORROSION

The use of urea as a redundant for SCR systems has introduced another corrosion concern. Ammonia is formed in the process and at high temperatures can result in intergranular corrosion termed as "dusting." This condition has been found in the lower alloy content ferritic stainless steels and austenitic stainless steels and is more severe at elevated temperatures. Higher chromium content ferritics stabilized with niobium has been found to be the optimum material for urea applications. Figure 18.10 shows the corrosion pattern caused by urea dusting in a 409 stainless steel.

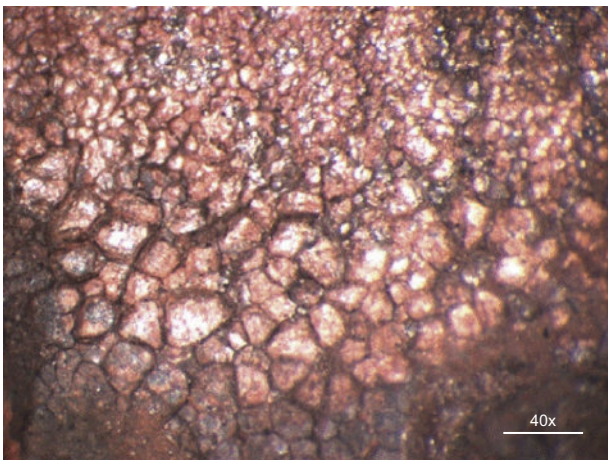

FIGURE 18.10

Urea dusting of 409 stainless steel.

3.8 EROSION-CORROSION

In SCR, urea solution is injected into exhaust systems by means of a spraying nozzle. As a result, in addition to conventional corrosion, some urea droplets can impact the shell of the exhaust systems with weakened resistance due to high-temperature influence. Solid particles in exhaust gas stream can severely cause erosion damage in exposed steel and lead to the reduction of wall thickness of exhaust systems. A simulated urea spraying process is shown in Figure 18.11a and a tested exhaust inner surface with erosion-corrosion characteristics is shown in Figure 18.11b. Erosion-corrosion process normally occurs under turbulent flow conditions, and the most severe erosion-corrosion occurs in the sudden geometrical changing area of a system, where the flow introduced pressure is usually high.

Another example is provided in Figure 18.12. A very early design model of a thermal regeneration system was subjected to approximately 3000 cycles of thermal-fatigue testing. Each cycle consisted of heating to around 1150 °C and cooling to about 150 °C with each cycle lasting about 15 min. The test results in oxidation thinning of the wall combined with pressure on the inside pushing out the thin wall that is further weakened under the elevated temperatures (Figure 18.12). Air flow makes the wall deform significantly as well as leads to erosion-oxidation, which is a common damage mechanism in combined high temperature and gas or fluid flow applications [27]. Creep may also play a role in the high-temperature deformation of the thin wall.

4 FAILURE MODELING AND DATA ANALYSIS

The phenomenal or qualitative analysis of failure mechanisms and modes discussed in Section 18.3 is the first step in understanding the possible failures of products in service. However, to more fully understand the physical failure process, the causes or driving forces behind the phenomena, a more quantitative analysis is needed. In other words, simple and predictive models are needed for product design, analysis, and validation. Mathematical and statistical tools are necessary for building up the rational framework, in which the material properties, such as composition, physical and mechanical properties are properly incorporated into the predictive models. With these aims, the modeling of failure in terms of both crack growth and total life approaches are presented in Section 18.4.1 to better understand the underlying driving forces of the observed failure phenomena. Subsequently, statistical and probabilistic test data analyses are introduced in Section 18.4.2 to help further reveal the failure mechanisms. The materials performance characterization, ranking and selection, which are critical to product design and validation, especially at early development stage, are discussed in Section 18.5.

4.1 FATIGUE FAILURE MODELING

Fatigue evaluation of engineering components and systems has become an integral part of design processes in many industries [1]. There are generally two types of methodologies for fatigue analysis: (1) safe-life approach based on total life using

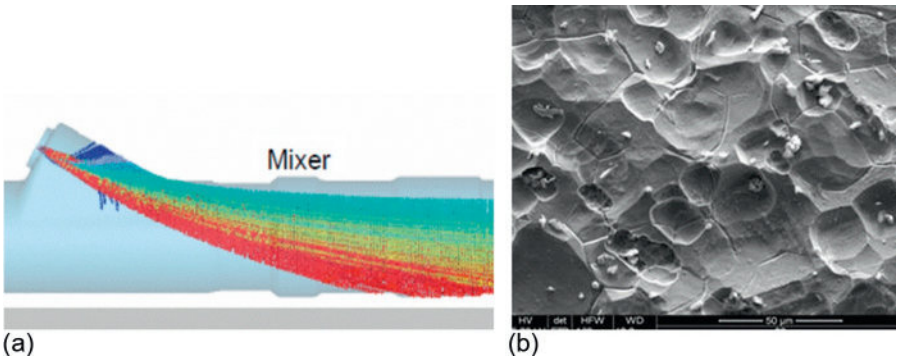

FIGURE 18.11

(a) Spraying simulation and (b) damage erosion-corrosion inner surface of an exhaust system.

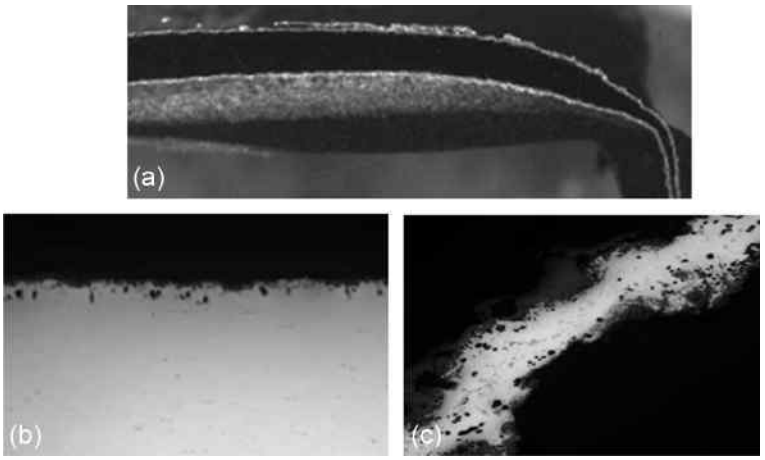

FIGURE 18.12

High-temperature oxidation-erosion, (a) wall-thinning, (b) modest eroded surface, and (c) severely eroded surface.

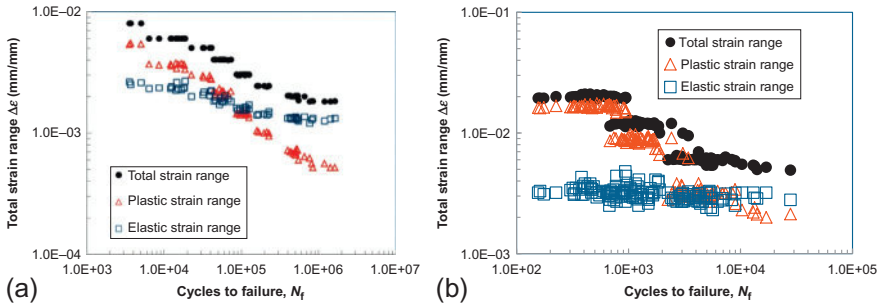

FIGURE 18.13

The raw data of elastic strain range, plastic strain range, total strain range as functions of cycles to failure for test data of (a) ASTM A969 and (b) 9Cr-1Mo steel [44].

fatigue stress-life $S-N$ or strain-life $\varepsilon-N$ data [28] and (2) damage tolerance approach based on crack growth using fracture mechanics theories [29]. At design stage, the safe-life approach is often used, while at the maintenance stage the damage tolerance approach is usually applied. The use of these methods is also industry dependent. For example, the total life approach is more commonly used in automotive industry, whereas the damage tolerance or crack growth approach is often used in nuclear power industry and aerospace industry, where the maintenance of aging equipment and fleets is a critical issue [30].

4.1.1 Crack Growth Approach

Fatigue damage is caused by fatigue crack initiation and crack growth. Under combined corrosion and fatigue or tensile loading, the failure modes are often localized, usually, in terms of crack growth. Therefore, crack growth modeling is a method used in engineering applications, and it is a proper way to understand the fatigue, corrosion-fatigue, stress corrosion cracking, and other environment assistant failures. It is noted that the elastic fracture mechanics is often used, but it is usually limited to relative large cracks. Additionally, the boundary between crack initiation and crack growth is usually not very clear.

For pure fatigue damage in metallic materials, the crack growth can be expressed by the following Paris law-type differential equation [31]:

$$\begin{aligned} \frac{\mathrm{d}a}{\mathrm{d}N} &= C_f(\Delta K)^m \\ \Delta K &= Y_f \Delta\sigma\sqrt{\pi a} \end{aligned} \tag{18.1}$$

where a, N, ΔK, and $\Delta\sigma$ are crack length, cycle, stress intensity factor range, and stress range, respectively. The stress range $\Delta\sigma = \sigma_{\max} - \sigma_{\min}$ is simply the difference between maximum and minimum stresses. C_f, Y_f, and m are material- or geometry-related constants. It should be noted that Equation (1) or its equivalents can be applied to different loading conditions: tension, compression, shear, bending, torsion, uniaxial, and multiaxial [9].

However, the one-parameter driving force (stress range or stress intensity factor range) fatigue models, such as Equation (1), fail to describe the observed effects of maximum stress intensity factor in fatigue crack growth, which are important for some nonwelded steels, aluminum alloys, brittle materials such as ceramics, and many other materials. It is generally believed that, under uniaxial fatigue loading, both maximum intensity factor and stress intensity factor ranges are the driving forces for fatigue crack growth [32]. Experimental results of fatigue crack growth have shown that the fatigue crack growth rate can be written as $\mathrm{d}a/\mathrm{d}N = D(K^*)^{\lambda}$ [33], where the damage parameter K^* is defined as $K^* = K_{\max}^{(1-\gamma)}\Delta K^{\gamma}$ and γ is a material constant. A similar two-parameter model $\mathrm{d}a/\mathrm{d}N = D(K_{\max})^p(\Delta K)^q$ is also widely used [32,34]. It should be noted that these two equations are equivalent with $\gamma = p+q$ and $\gamma = q/(p+q)$. Generally, for ductile metals the fatigue crack growth is found to be controlled by ΔK and the contribution from $K_{\max}$ term can be neglected, i.e., $p \ll q$. By contrast, for brittle materials such as ceramics, fatigue crack growth

rate is principally a function of K_{max} because the crack-advance mechanism is identical to that under static loading, thus $p \gg q$; for semi-ductile materials, both ΔK and K_{max} play comparable roles, $p \approx q$. Physically, K_{max} control the breaking of bonds that build up the required internal stresses and the dislocation substructure which governs crack nucleation and growth, while ΔK control the extent of plastic zone [32].

Similarly, the quantity $(1-\gamma)$ can be used as a measure of material's sensitivity to mean stress in fatigue life analysis [35,36]. The lower the value of γ the higher the sensitivity of a material to mean stress, e.g., a metal with $\gamma = 1$ is insensitive to mean stress, and one with $\gamma = 0$ is independent of stress range. With two-parameter driving force models, the crack growth rate and the final fatigue life can be determined by the competition between the stress range and mean stress. For example, for ductile materials, the fatigue life is dominated by stress range while the fatigue life is controlled by the mean stress for brittle materials. For semi-ductile materials, contributions from both stress range and mean stress are comparable. These conclusions are consistent with the fatigue crack growth observations.

The crack growth under tensile loading in corrosive environment is very complex. However, for engineering applications, the formulae for stress corrosion cracking can be expressed as [37]

$$\begin{aligned} \frac{da}{dt} &= C_c (K_{max})^n \\ K_{max} &= Y_c \sigma_{max} \sqrt{\pi a} \end{aligned} \tag{18.2}$$

where t, k_{max}, and σ_{max} are time, maximum stress intensity factor, and maximum stress, respectively. C_c, Y_c, and n are material- or geometry-related constants. Equation (2) is very similar to the creep-fatigue crack growth model developed for a creep-brittle material [38,39].

For environment-enhanced crack growth under stress corrosion cracking and corrosion-fatigue, a simple superposition theory [40,41] has been suggested and widely used. The theory states that, to a first order approximation, the total crack growth rate is simply the algebraic sum of the rates of growth of the cycle- and time-dependent components, mathematically, $da/dN = (da/dN)_{cycle} + (da/da)_{time}$. The mechanical component represents the rate of fatigue crack growth in the absence of the influences of an external environment and is determined experimentally by testing in an inert environment or in vacuum. The environmental component is to be determined from experimental crack growth data under sustained loading in the appropriate environment. The advantage of the linear superposition theory is the ability to predict the rates of fatigue crack growth in an aggressive environment directly from pure fatigue data and SCC test data and it would drastically reduce the amount of testing required. Then, the combined corrosion-fatigue crack growth can be expressed as:

$$\frac{da}{dN} = C_f (\Delta K)^m + C_c (K_{max})^n \Delta t \tag{18.3}$$

where Δt is hold (dwell) time. Oxidation effect [24] can also be modeled with Equation (3) [42].

However, interaction effect seems to be everywhere [38] and Equation (3) does not account this effect. Physically, when corrosion and fatigue occur simultaneously, the chemical attack can greatly accelerate fatigue crack growth. Frequently, fatigue or tensile stress corrupt the protective films that would normally slow the corrosive attack, allowing continued and accelerated attack. "Interaction" is the phenomenon of two or more things to produce a result greater or less than the sum of their individual effects. The superposition theory has been extended to a generalized nonlinear superposition theory [43], in which, a nonlinear interaction term is added to reflect the interaction effect.

$$da/dN = (da/dN)_{\text{cycle}} + (da/dN)_{\text{time}} + (da/dN)_{\text{Interaction}} \tag{18.4}$$

The first two items can be directly obtained from pure fatigue data and pure time-dependent crack growth test data. A definition of the interaction effect is defined as

$$\lambda = \frac{V_T - (V_1 + V_2)}{V_1^{\alpha} V_2^{1-\alpha}} \tag{18.5a}$$

or

$$V_T = V_1 + V_2 + \lambda V_1^{\alpha} V_2^{1-\alpha} \tag{18.5b}$$

In Equation (5a) and (5b), da/dN or da/dt is replaced with V for clarity purpose. λ is termed as the interaction factor measuring the severity of interaction effect. $\lambda = 0$, $\lambda > 0$, and $\lambda < 0$ represent no interaction, positive interaction, and negative interaction, respectively. $\alpha(0 < \alpha < 1)$ reflects the relative contribution from the two growth rate mechanisms to the interaction effect. The subscripts 1, 2, and T represent the component-1, component-2, and the total or combined one. The multiplication of terms with V_1 and V_2 is assumed to be the underlying mechanisms of interaction. The interaction factor λ can be directly calculated from Equation (5a), provided that test data V_1, V_2 and V_T are known [43].

4.1.2 Total Life Approach

For high-cycle fatigue, the most widely used power-law relationship between cycle and stress range is known as Wöhler curve [31]. The power-law relationship between cycle and plastic strain range (or strain amplitude) is known as the Manson-Coffin equation [31], which plays a prominent role in low-cycle fatigue. Wöhler and Manson-Coffin equations are accurate enough, respectively, at high-cycle and low-cycle regimes. However, in the middle of the two extremes, neither of these relationships is accurate, and it is more appropriate to use total strain range (or strain amplitude) to characterize fatigue. Clearly, the combination of the Wöhler curve for high-cycle fatigue and the Manson-Coffin equation for low-cycle fatigue is a natural step for fatigue modeling over the whole cycle range, and the solution is the double-term power-law approach, Equation (6a) and (6b), in which total strain range is decomposed into elastic part and plastic part [31]:

$$\Delta\varepsilon = \Delta\varepsilon_e + \Delta\varepsilon_p = (\sigma_e/E)N_f^{b_e} + (S_p)N_f^{b_p} \tag{18.6a}$$

or

$$\varepsilon_a = \Delta\varepsilon/2 = \varepsilon_{ae} + \varepsilon_{ap} = \sigma_f'(2N_f)^b/E + \varepsilon_f'(2N_f)^c \tag{18.6b}$$

Where ε_a is the strain amplitude, which is half of the total strain range $\Delta\varepsilon$; $2N_f$ is the number of reversal, and each cycle consists of two reversals. The terms σ'_f/E and ε'_f are strain intercepts at $2N_f = 1.0$, and b and c are slopes of the elastic and plastic lines, respectively, in log-log plot. In strain-life tests, a stress-strain hysteresis loop recorded near half of the fatigue life is usually employed to determine stable values of stress range $\Delta\sigma$, strain range $\Delta\varepsilon$, and plastic strain range $\Delta\varepsilon_p$. Both of these equations are commonly used in engineering applications [31]. In principle, there is no difference between Equation (6a) and (6b) and the usage is totally upon to engineers' preference and background.

It is also found [31] that all materials studied follow $\Delta\varepsilon = (3.5S_u/E)N_f^{-0.12} + (D)^{0.6}N_f^{-0.60}$. S_u, E, and $D = \ln[100/(100 - \%\text{RA})]$ are ultimate tensile strength, elastic modulus, and ductility, respectively. RA is the reduction of area in a tensile test. The elastic and the plastic lines have slopes of -0.12 and -0.6, respectively, for all 29 materials, which cover a wide range of strength and ductility, hence, the description "universal slopes." The universal model was further improved based on more added test data: $\Delta\varepsilon = 1.17(S_u/E)^{0.832}\ N_f^{-0.09} + 0.0266(D)^{0.155}(S_u/E)^{-0.53}N_f^{-0.56}$, which is obtained from the strain-life of 50 materials. Figure 18.13a and b shows the fatigue data collected with the method for two materials [44].

4.2 STATISTICAL AND PROBABILISTIC DATA ANALYSIS

The durability and reliability performance analysis is essentially based on test data and the accurate interpretation of the data. However, the inherent scatters in test data cannot be substantially reduced even under controlled testing conditions. The uncertainty of the cycles to failure for components, such as vehicle exhausts, comes from many sources, such as material uncertainty, loading uncertainty, and the uncertainty of the initial damage distribution. Therefore, a certain amount of repeats of tests are often required to capture the uncertainty, scatter characteristics, and failure probability of the test data. Probabilistic data analysis is not only vital to successful durability/reliability engineering designs but also critical to reveal failure mechanisms [7]. Oftentimes, with proper data transformation and linearization, test data can be curve/surface fitted using a probabilistic distribution function to gain physical understanding and quantitative descriptions. The basic characteristics of life data and the associated probabilistic distribution include mean, scatter, homoscedasticity and heteroscedasticity, skewness (symmetry), kurtosis, and entropy (uncertainty), etc. [45]. In many cases, especially for single failure modes, the continuous probability density functions (PDFs) and cumulative distribution functions (CDFs) of lognormal or Weibull distribution functions can be effectively used for characterizing the

scattered fatigue test data [5]. For failure with two or more failure mechanisms and modes, the fatigue data can be described using bimodal or multiple-modal distributions [7]. The preference of one PDF over another has to be determined by test data correlation. The goodness-of-fit with different distributions can be evaluated and compared using many methods such as Kolmogorov-Smirnov (KS) and Anderson-Darling (AD) methods [45]. AD statistic measures how well the data follow a particular distribution, especially in the tails of the distribution: the better the distribution fits the data, the smaller this statistic will be. The lognormal and Weibull PDFs are two of the most commonly used PDFs for fatigue reliability analysis. The three-parameter lognormal PDF is shown as follows:

$$f(x)=\frac{1}{\sigma(x-\delta)\sqrt{2\pi}}\exp\left[-\frac{1}{2}\left(\frac{\log(x-\delta)-\mu}{\sigma}\right)^2\right];\ \sigma>0,-\infty<x<\infty,x>\delta \tag{18.7}$$

where μ is the mean, σ is the standard deviation, and δ is threshold or shift parameter. When $\delta=0$, Equation (7) is the two-parameter lognormal PDF. If $\log(x)$ is further replaced with x, then we have a normal distribution: $f(x)=\frac{1}{\sigma\sqrt{2\pi}}\exp\left[-\frac{1}{2}\left(\frac{x-\mu}{\sigma}\right)^2\right]$.

The three-parameter Weibull PDF is as follows:

$$f(x)=\frac{\beta}{\eta}\left(\frac{x-\gamma}{\eta}\right)^{\beta-1}\exp\left[-\left(\frac{x-\gamma}{\eta}\right)^{\beta}\right];\ x\geq 0,\eta>0,\beta>0,x>\gamma \tag{18.8}$$

where η, β, and γ are scale, shape, and location or shift or threshold parameters, respectively. When $\gamma=0$, the three-parameter Weibull functions are the two-parameter Weibull distributions. The threshold parameters δ and γ give the lower bounds of the PDFs, explicitly indicating the existence of a physical threshold value. As the name implies, the threshold parameters locate the PDF along the abscissa (cycles to failure for the durability data). Changing the values of δ and γ has the effect of "sliding" the PDF to the right because values of δ and γ must be positive. The Weibull distribution function has several different physical implications depending on the value of β: early mortality rate ($\beta<1$), constant mortality rate ($\beta=1$), and decreasing mortality rate ($\beta>1$). Furthermore, the Weibull distribution can be reduced to exponential distribution function when $\beta=1$ and to the Raleigh distribution function when $\beta=2$. For $\beta=3.2$ or around, the Weibull distribution is very similar to the normal distribution.

The parameters of a distribution function can be estimated using several methods, among which the least square method (LS) and the maximum likelihood method (ML) are the two most commonly used [45]. The basic idea of the least square method is to find the parameters, e.g., θ_j for the expected best fit curve by minimizing the sum of the squares of residuals $R^2(\theta_j)=\sum\left[y_i-f(x_i,\theta_j)\right]^2$: $\partial(R^2)/\partial\theta_i=0$. By contrast, the maximum likelihood method finds the parameters that maximize the likelihood function $L=\prod_{j=1}^{N}f(\theta_j)$, e.g., by setting the partial derivative of the likelihood function to zero: $\partial\mathrm{Log}(L)/\partial\theta_j=0$.

Example: Probabilistic Distribution of Thermal-Fatigue Test Data

The V-shape specimen testing method [10,46] (Santacreu et al., 2013) has been developed to simulate manifolds fixed to the engines. The specimen is fixed on both sides creating an initially stress-free condition and then cyclically heated using resistance heating with the maximum temperature zone located at the center of the specimen [47] (Figure 18.14a). The specimens are defined as "failed" when the specimen separated into two pieces after a certain cycle N_f. Figure 18.14b shows the tested specimens, in which total separation occurred. Similar to other life test data, V-shape specimen test data always contain inherent scatters. Therefore, probabilistic approaches have to be used to interpret the test data in order to implement the observations into new product designs and to find the failure mechanisms. Two sets of thermal-fatigue test data, stainless steel (SS) 409 (ferritic) with 25 data points and SS309 (austenitic) with 23 data points from V-shape testing are used for probabilistic analysis. Two-parameter Weibull distribution function is used first to analyze the data and the results are shown in Figure 18.14c. From the data plots shown in Figure 18.14c, it can be clearly seen that the datasets do not fall on straight lines in the probability plot. Therefore, a more sophisticated function which can capture the major control parameters is needed to give a better data correlation. Further examination reveals that the major feature of these curves is the concave downward

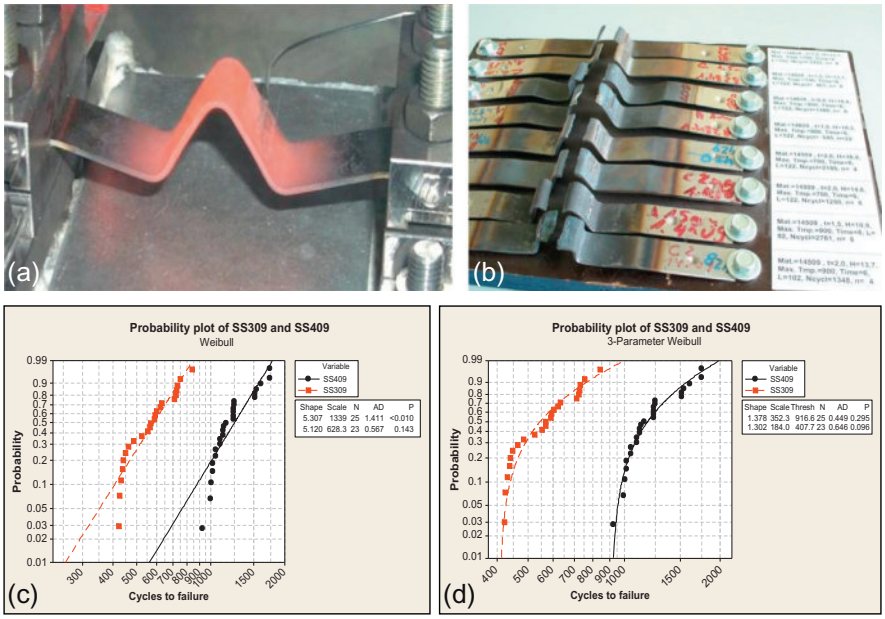

FIGURE 18.14

V-shape specimen for thermal-fatigue resistance testing, (a) V-shape test configuration and heating, (b) tested specimens, (c) probability plots of two-parameter Weibull CDFs for the test data, and (d) probability plots of three-parameter Weibull CDFs for the test data.

trend, theoretically, subtraction of a positive threshold γ in a three-parameter CDF function can improve the data fit. Eventually, three-parameter Weibull distribution function is used for data analysis, and the results are shown in Figure 18.14d. From the data plots shown in Figure 18.14d, it can be clearly seen that the data correlation is much better.

The values of fit parameters using the two distributions for the two materials are listed in Table 18.1. Clearly, the overall fits from the three-parameter Weibull distribution are much better than that of the two-parameter CDFs in terms of AD statistic, especially for SS409. The values of the threshold parameters obtained are $\gamma = 916.4$ and $\gamma = 407.7$, respectively, for SS409 and SS309 with the three-parameter Weibull CDF. The existence of a positive threshold parameter γ indicates the existence of a physical threshold value below which no failure occurs. These parameters γ provide an estimate of the earliest time-to-failure of the units under test, and they must be less than or equal to the first time-to-failure, i.e., the minimum extreme value.

How to quantitatively measure the uncertainty of tested failure data, in terms of probabilistic distribution is important in probabilistic analysis. Intuitively, the uncertainty parameter in a distribution function should be governed by the spread of the distribution. Parameters with such capabilities include the standard deviation in the normal distribution and the shape parameter in the Weibull distribution. However, these parameters belong to their respective specific distributions and cannot be used interchangeably. Also, the physical meanings and the mathematical expressions of these parameters are often different. For example, the standard deviation in a normal distribution represents the absolute range of the spread, whereas the shape parameter in a Weibull distribution represents the relative shape or profile of the distribution. Therefore, a unified parameter that gives a consistent uncertainty measurement regardless of specific distribution functions is needed. In fact, an uncertainty measure is already available in statistics field: Shannon entropy [48]. The mathematical formulae of Shannon entropy for all commonly used probabilistic distribution functions

Table 18.1 Values of Fit Parameters of Two- and Three-Parameter CDFs for SS409 and SS309 V-Shape Test

		Materials	
CDFs	**Parameters**	**SS409**	**SS309**
Two-parameter Weibull	Shape (β)	5.307	5.120
	Scale (η)	1339.0	628.3
	AD statistic	1.411	0.567
Three-parameter Weibull	Shape (β)	1.378	1.302
	Scale (η)	352.3	184.0
	Threshold (γ)	916.6	407.7
	AD statistic	0.449	0.646

can be found in related handbooks. However, the direct application of the Shannon entropy to fatigue failure analysis is very difficult because of its irrelevance in failure process interpretation. Inspired by the developments in complexity and uncertainty measurements in computational complexity, classical statistical physics and information theory, an uncertainty measure, which shows many advantages over the Shannon entropy, has been proposed [49]

$$U(X) = -4\int_{-\infty}^{\infty} R(x)\log R(x)\mathrm{d}x \tag{18.9}$$

where $R(x) = 1 - F(x)$ is reliability function. The uncertainty value for the uniform distribution is $b - a$; where a and b are lower and upper limits of a uniform distribution. Clearly, the value of uncertainty of the uniform distribution is proportional to the length of the interval, i.e., the bigger the range, the higher the uncertainty, which is intuitively correct. For the special case with $b = 1$ and $a = 0$, we have $U = 1$. Clearly, factor 4 in Equation (9) is a normalizing factor. Based on the values of the parameters listed in Table 18.1, the calculated uncertainty values for SS409 and SS309 are 233.6 and 130.5, respectively. The values calculated from the unified uncertainty parameter U can give the uncertainty estimate in an absolute and equivalent way, which cannot be reflected from the shape parameter of the Weibull distributions.

Overall, statistical [50] and probabilistic data analysis provides a valuable insight into the failure mechanisms as well as an invaluable tool for product design.

5 MATERIALS PERFORMANCE RANKING AND SELECTION

Generally speaking, the process of materials characterization, screening, ranking, and final selection is a lengthy and expensive process. Simple ranking formulae are provided in this section for two important failure mechanisms: (1) cyclic oxidation/thermal fatigue and (2) corrosion. In these formulae, the fundamental information about chemical composition, physical properties, mechanical properties are correlated to the performance of the materials. These simple formulae can help design engineers to quickly screen, rank, and select materials for exhaust system development even without conducting physical tests. The formulae can also help material engineers to develop new high-performance materials.

5.1 MATERIAL RANKING IN CYCLIC OXIDATION AND V-SPECIMEN THERMAL-CYCLING RESISTANCE

5.1.1 *Cycling Oxidation Tests*

Spalling of the surface oxide layer caused by cyclic oxidation is one of the major failure mechanisms at the vehicle hot end. It is also called dry corrosion [22]. In general, oxide layers can protect metals from further oxidation unless it is mechanically removed or cracked due to internal or external stress. However, most oxides have

different coefficients of thermal expansion from that of the base metals, and eventually thermal stresses can be generated in oxide layers when the temperature changes. Therefore, oxides that form at high temperatures may lose adherence to the base metals, especially when cyclically heated and cooled, and become nonprotective. Ceramics and oxides usually have lower values of thermal expansion than base metals. Oxidation and spalling not only result in metal loss of the exhaust system and negative impact on system integrity but also the generated flakes can cause blockage in the catalyst. Simulated test has been conducted at temperature up to 1000 °C [22], and the thermal cycle consists of about 20 min high-temperature hold time, about 5 min cooling time, and similar heating time. The samples were characterized by weight variation and the results for a temperature level were obtained. Overall, the ranking in oxidation resistance (from strongest to the weakest) is K41X (AISI 441), 18-9ED (AISI 304), and R20-12 (AISI 308 Si) [22]. It was found that the ferritic steels show better oxidation resistance than austenitic steels. The driving force for the spallation is believed to be the residual stress or thermal stress in the oxide even though there is no external load applied to the specimens [22].

5.1.2 V-Shape Specimen Thermal-Cycling Tests

V-shape testing as described in Section 18.4 can relatively quickly provide a rough indication about the materials' thermal-cycling resistance even without going into detailed and very sophisticated stress-strain analysis. Therefore, V-shape specimen testing is particularly useful in early design process for A-to-B comparison purposes, in which material screening, ranking, and selection are critical issues [10,47 (Santacreu et al., 2013). The V-shape specimen test results under thermal-cycling loading for several materials have been reported and the ranking in thermal-cycling resistance has been conducted based on the test data [47].

5.1.3 A Ranking Formula for Cyclic Oxidation and V-Shape Specimen Thermal Cycling

Both the cyclic oxidation and the V-shape specimen thermal-cycling tests are subject to two common conditions: (1) high-temperature environment and load (internal stress for cyclic oxidation and both internal and external stress for V-shape testing) even though the resistance assessment criteria are different for them, and (2) mass loss for the former and cycles to failure for the latter. Therefore, both could be treated in a unified way in materials ranking. Many physical properties, especially thermophysical properties, such as thermal expansion coefficient and thermal conductivity can significantly affect the thermal energy, thermal stress build-ups, and eventually change the mass loss or thermal-cycling life. Thermal conductivity is a parameter to measure the capability to disperse generated heat and the introduction of the thermal conductivity k reflects the transient nature of the cyclic oxidation and the thermal-cycling testing. Generally, the higher the value of the thermal conductivity, the faster the heat spreads and eventually the less the thermal stress. Thermal expansion coefficient reflects the capability of stress buildup for a given boundary condition. Generally, the higher the value of thermal expansion coefficient, the higher the thermal

stress. The thermal conductivity of ferritic steels is higher than that of austenitic steels: 25 versus 15 W/K m. The coefficient of thermal expansion of ferritic steels is significantly lower than austenitic steels: $(11-12)\times10^{-6}/°C$ for ferritic as compared to $(18-20)\times10^{-6}/°C$ for austenitic steels [10] (Santacreu et al., 2013). The specific heat (which characterizes the amount of heat required to change a substance's temperature by a given amount) and density are also important thermophysical properties, however, the differences in density and specific heat between ferritic and austenitic steels are not as significant as the differences in thermal conductivity and thermal expansion.

To reflect the above observations, a parameter $\lambda = k\sigma_f/E\alpha$, which was initially used for thermal shock resistance assessment [51], has been adopted for cyclic oxidation and thermal-cycling resistance ranking [47]. The introduction of σ_f reflects the materials' intrinsic capability to resist the exterior applied forces. The thermomechanical properties and the ranking of five stainless steels, which are commonly used in vehicle exhaust systems, are listed in Table 18.2 [47]. The predicted ranking based on λ and the ranking for both cyclic oxidation and V-shape testing are also provided for comparison. Clearly, the parameter λ provides a consistent correlation with all of these test data. It should be noted that all of the data used are based on room temperature.

5.2 MATERIAL RANKING IN CORROSION RESISTANCE

5.2.1 Pitting or Crevice Depth

The changes in specimen weight versus time are often used to calculate corrosion rates for general corrosion. However, measuring weight loss is unsuitable for localized corrosion effects such as pitting, crevice, and inter-granular attack since total weight loss can be minimal while local damage can be severe [21,23]. Therefore, the average depth of the pits does not illustrate the real dimension of the corrosion in some cases. Actually, maximum pit depth or crevice depth are more proper measurements of corrosion resistance [25]. A "dip & dry" apparatus has been developed to simulate corrosion on mufflers made of stainless steels, by cyclic dipping in an artificial condensate, drying and oxidizing specimens in an oven [22]. In these conditions and in order to simulate the most critical areas of the muffler, an artificial crevice was fixed on the lower part of the specimen. After test, the artificial crevice was removed and the maximum corrosion depth in the confined area was measured. Figure 18.15 shows results obtained for several stainless steels used for exhaust applications. It is found that the corrosive resistance ability can be ranked (from the worst to the best) as 409, 430, 441, 434, 434Ti, 304.

5.2.2 Pitting Corrosion Potential

In addition to the measurement of pit depth, there are several simpler ways to measure the pitting corrosion resistance such as potential, critical pitting temperature. Corrosion experts generally consider that materials exhibiting higher values of breakdown potential E are more resistant to pitting corrosion. Critical pitting

Table 18.2 Thermal-Mechanical Properties of Stainless Steels and Ranking of the Five Stainless Steels

Steel Names	Tensile Strength, σ_f MPa	Thermal Expansion Coefficient, $\alpha 10^{-6}/K$	Thermal Conductivity, k(W/m K)	$\lambda = k\sigma_f/E\alpha \times 10^{-3}$ W/m	λ Ranking	Oxidation Cycling Test Ranking	V-Shape Tests Ranking
441/439 (1.4509)	489	11.0	25.0	5.052	1	1	1
409 (1.4512)	378	11.0	25.7	4.052	2	–	2
309 (1.4828)	675	16.5	15.0	2.950	3	2	3
321 (1.4541)	620	18.5	16.1	2.698	4	–	4
304 (1.4301)	505	16.5	15.0	2.464	5	3	–

temperature (CPT) can be used, similar to pitting potential, as a means for ranking susceptibility to pitting corrosion; the higher the CPT, the more resistant the alloy is to pitting [26]. If crevice corrosion is the primary concern, creviced samples can be used to determine a critical crevice temperature (CCT), which is usually lower than the corresponding CPT [26]. The localized corrosion resistance of seven stainless steels was determined using the accelerated testing procedures with electrochemical critical pitting potential, and the results and ranking are provided in Figure 18.16. The ranking in pitting corrosion potential is: 1.4301 (304) > 1.4513(434Ti) > 1.4526(436) > 1.4113 (434) > 1.4509(441) > 1.4510(439) >1.4512(409) [27].

5.2.3 Pitting Corrosion Resistance Ranking with PREN

Since corrosion is dictated by material composition and associated physical and mechanical properties, which are usually already available in many handbooks as the fundamental database. Therefore, a formula based on the available data and information without conducting time-consuming and expensive tests is strongly desired. The method can then be used as a quick reference for engineering applications. Pitting resistance equivalent number (PREN) is such a method and it is widely used as a means of comparing the relative corrosion resistance of different steels. PREN is a theoretical way of comparing the pitting corrosion resistance of stainless steels, based only on their chemical compositions. The early use of the PREN can at least be traced back to the 1960s [52], since then, a number of empirical formulae for the PREN have been developed and the testing procedure has been specified in the ASTM G48 standard [53]. In general, the higher PREN-value is, the better the corrosion resistance.

The general linear expression of PREN can be expressed in the following form [52]:

$$\mathrm{PREN} = \%\mathrm{Cr} + m\%\mathrm{Mo} + n\%\mathrm{N} \tag{18.10}$$

where m and n are the factors for molybdenum and nitrogen. For steels, the two most commonly used formulae are PREN_{16}, in which the values of m and n are $m = 3.3$ and $n = 16$, and PREN_{30} in which the values of m and n are $m = 3.3$ and $n = 30$. In these formulae, nitrogen is 16 or 30 times more effective and molybdenum is 3.3 times more effective than chromium for chloride pitting resistance. Nitrogen is the element attributed the strongest beneficial on localized corrosion in the PREN formula. However, the value for N usually does not have a dramatic effect on ranking because the actual nitrogen levels are quite modest in most stainless steels.

It is a natural step to extend the linear model to a nonlinear form with interaction effect, Equation (11) [27].

$$\mathrm{PREN} = \%\mathrm{Cr} + m\%\,\mathrm{Mo} + n\%\mathrm{N} + l\%\,\mathrm{Mo}\%\mathrm{N} + + i(\%\mathrm{Mo})^2 + j(\%\mathrm{N})^{2+} + \cdots \tag{18.11}$$

A specific form of Equation (11) is given in Equation (12) [54] to model the observed interaction effect between Mo and N and the nonlinear effect of N.

$$\mathrm{PREN} = \%\mathrm{Cr} + 3.3\%\,\mathrm{Mo} + 51\%\mathrm{N} + 6(\%\mathrm{MoN}) - 1.6(\%\mathrm{N})^2 + \cdots \tag{18.12}$$

It should be noted that the standard PREN calculation used for stainless steels cannot be used for nickel alloys. For nickel-based corrosion-resistant alloys, e.g., Inconel 625, PRENs are calculated from Equation (13). For such alloys, molybdenum, chromium, tungsten, and niobium are the most influential alloying elements

$$\mathrm{PREN} = \%\mathrm{Cr} + 1.5(\%\,\mathrm{Mo} + \%\mathrm{W} + \%\mathrm{Nb}) \tag{18.13}$$

Additionally, there are correlations between PREN and other parameters. For example, $E = 2.94\exp(0.14\mathrm{PREN}_{16})$ has been established between potential and PREN [55].

The chemical composition of seven exhaust used steels, the values of PREN, and the predicted PREN ranking are listed in Table 18.3. The crevice depth test ranking as shown in Figure 18.15 and the pitting corrosion potential ranking as shown in Figure 18.16 are also provided for comparison purpose. Clearly, the rankings of the predicted and the tests match very well. However, PREN has some limitations [27].

6 CASE STUDIES

Practical experience shows that, similar to engine failure [15], a high percentage of failure in exhaust components and systems can be controlled and avoided. Technical shortcomings in design, defects caused in fabrication, incorrect assembly, unsuitable materials, operating errors, and insufficient maintenance are often the causes of failure. Design flaws include inadequate dimensioning, unsuitable shape, fits, tolerances, materials, heat treatment, manufacturing process, etc. Avoiding abrupt changes of sectional areas and high stress around stress risers such as fillets, welds, notches can improve durability performance. Materials performance, ranking, and the material selection should be considered in product design. Materials defects include contamination, bobbles, lamination in rolling, structural defects, and heat treatment defects. Welds quality is always a significant concern in design. Lack of fusion, burn-through, porosity, undercut, carbide precipitation at the grain boundaries, excessive grain growth are common issues. Manufacturing defects include: nonadherence to dimensions, tolerance, fits and clearances, and lack of alignment. Surface finish is also important factor. Tool marks, scratches, grooves, and indentations introduce local stress leading to fatigue crack initiation and propagation. Increase knowledge, awareness, and training of operating personnel should be enforced to reduce the operating and errors. Two case studies provided below show how to implement the knowledge gained into product design and validation.

6.1 CASE 1: MUFFLER BRACKET FATIGUE FAILURE

Left-hand (LH) and right-hand (RH) muffler assemblies bolted to each other by a bracket welded to the outlet head bead, were experiencing failures of the brackets while on the vehicle. A right-hand muffler assembly, which shows the placement of the bracket on the muffler head bead, is shown in Figure 18.17a. Analysis of

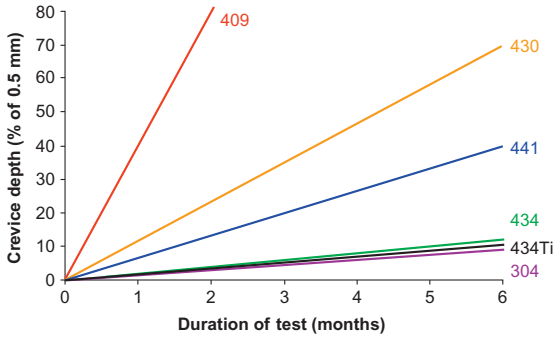

FIGURE 18.15

Crevice pitting resistance test ranking [22].

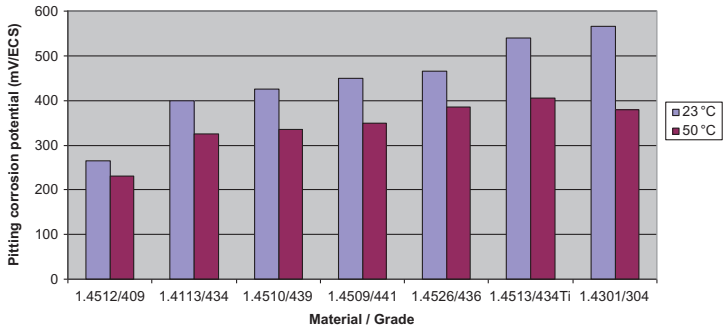

FIGURE 18.16

Pitting corrosion potential in NaCl solution, 0.02 M; pH 6.6.

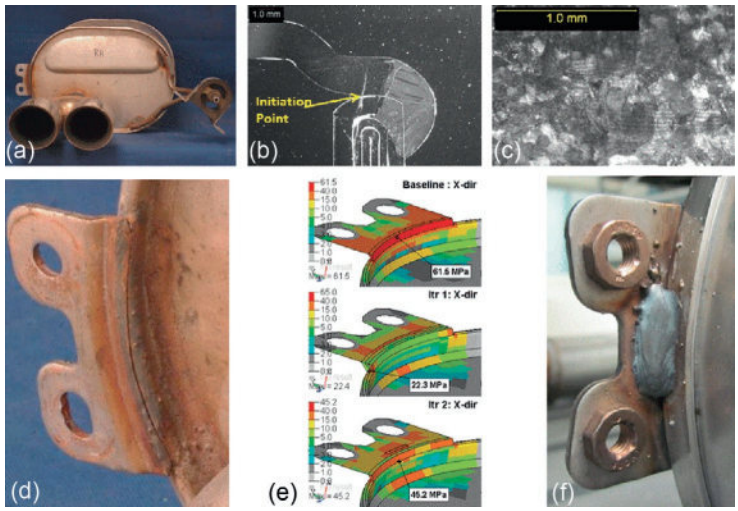

FIGURE 18.17

(a) Right-hand (RH) muffler assembly, rear view, (b) bracket weld cross-section, (c) fatigue striations, (d) baseline weld, (e) stress contour plot, x-direction, and (f) iteration2: bracket with 15 mm weld.

Table 18.3 Typical Chemical Composition (wt%) of Exhaust Stainless Steels and Corrosion Resistance Ranking [27]

Steel Names	Cr	Mo	N	Ni	$PREN_{16}$	$PREN_{16}$ Ranking	Crevice Depth Test Ranking	Pitting Corrosion Potential Ranking
444 (K44X)	19.0	1.9	0.015		25.5	1	–	–
309 (1.4828)	19.3		0.03	11.40	19.8	2	–	–
321 (1.4541)	18.0		0.1	9-12	19.6	3	–	–
304 (1.4301)	18.2		0.055	8.1	19.1	4	1	1
441 (1.4509)	17.8	0.1	0.015		18.4	5	2	2
430 (1.4016)	16.5		0.015		16.7	6	3	–
409 (1.4512)	11.5		0.01		11.7	7	4	3

the parts showed that the failures were the result of fatigue and the cracks initiated at the root of the weld, Figure 18.17b, and propagated through the bracket to head bead weld. The weld cross-section, with the initiation point noted on the image, is also shown in Figure 18.17b. Fatigue striations were visible on the fracture surfaces and are shown in Figure 18.17c. The originally designed weld setup consists of a weld extending the full length of the bracket on the rear face (when in vehicle position) after failure is shown in Figure 18.17d.

To remedy the failures, additional welds were considered to lower the stress on the bracket weld. FEA analysis was performed on the original weld design (Baseline), Figure 18.17d the original weld with the addition of a full-length weld on the front bracket face (Iteration 1), and the original weld with the addition of a 15 mm weld centered on the front bracket face (Iteration 2). The FEA analysis showed a stress reduction in Iteration 1 and Iteration 2 when both axial force and torque were applied to the bracket. Figure 18.17e shows a stress contour plot of x-direction axial force between the three weld scenarios with the area of highest stress noted. After consideration for the manufacturing and assembly process, the 15 mm weld was selected for additional testing as it showed a reduction in stress and had a reduced chance of interfering with the function of the bracket.

Bench testing of brackets with the original weld and Iteration 2 samples was performed to compare the fatigue durability of the two weld designs. The Iteration 2 test parts exceeded the cycles of the baseline parts in both vertical and longitudinal testing and the new weld design was implemented to resolve the bracket failures. Figure 18.17f shows the forward edge of the bracket from a left-hand (LH) muffler after the application of the 15 mm weld.

6.2 CASE 2: PROBABILISTIC THERMAL-FATIGUE LIFE ASSESSMENT

In high-temperature applications such as manifolds, thermal-fatigue resistance is the driving forces for material selection and product designs. However, thermal-fatigue testing of real exhaust components and systems are usually time-consuming and expensive. Eventually, verified, reliable and accurate virtual life-assessment tools are critically demanded. It is essential that analytical and numerical simulation techniques are employed at the earliest possible design stage, so that design errors can be identified and materials can be selected as early as possible. The virtual tools demonstrated here are based on computer-aided engineering (CAE), which include (a) CAD (computer-aided design) model, which is generated to represent the geometry of the designed components or systems, (b) finite element analysis (FEA), and (c) computational fluid dynamics (CFD). The procedure is first mesh the CAD model for FEA and CFD analyses. Subsequently, the CFD-generated temperature profile is mapped onto the meshed FEA model to generate nodal temperature profile, which will be used as the peak temperature in subsequent thermal-cycling analysis. Then, FEA is conducted to calculate the stress or strain. The definition of cumulative plastic strain amplitude $PEEQ\_A = \left(\varepsilon_{\mathrm{p}}^{n} - \varepsilon_{\mathrm{p}}^{n-1}\right)/4$

has been established as a proper damage parameter to assess the durability/reliability risk based on the established damage criteria. Where ε_p is cumulative plastic strain at cycle n, which is fixed in simulation for consistency purpose. The combined isotropic and kinematic hardening model, which is used for describing the behavior of materials under cyclic loading, is used to calculate ε_p. The plastic hardening parameters have been calibrated from cyclic test data for dozens of metallic materials for certain given temperature ranges, and these databases of the fitting parameters are readily available to engineers. With the obtained *PEEQ_A* and the temperature information, the thermal-fatigue life at a certain reliability level for all the elements can be calculated. Finally, the locations with the shortest life can be identified, and recommendations for product design can be made. More technical details can be found [56,57], in which a data-based probabilistic thermal-fatigue life-assessment procedure has been developed.

The thermal-fatigue test data obtained using V-shape specimen testing method for two stainless steels (i.e., a ferritic and an austenitic) were analyzed, and the fit parameters of probabilistic distribution functions for the data were estimated. The thermal-fatigue data, in terms of *PEEQ _A* -N or E (ordinate)-N(abscissa), of the two stainless steels are, respectively, plotted in Figure 18.18a and b, for three different respective peak temperatures. Different *PEEQ _A* levels at a temperature were achieved by changing the specimen thickness, fixture distance, etc. To protect the confidential information, all of the detailed values and units of the data shown in Figure 18.18 are concealed.

It is found from Figure 18.18a and b that as temperature increases, all of the two sets of data shift to left side indicating reduced cycles to failure at higher temperatures. Overall, the ferritic data, in terms of mean, show larger cycles to failure than those of the austenitic steel. Clearly, the two datasets in Figure 18.18 show some degrees of scatter at all temperature levels, and any attempts to make a deterministic life prediction are deemed to fail, and probabilistic description is needed. Additionally, all of the data show good linear patterns, therefore, linear curve-fitting methods can be used to extract the values of the fitting parameters.

A manifold design is shown in Figure 18.19a. The peak temperature distribution, which is obtained from the CFD simulation results, is shown in Figure 18.19b. The locations with two highest temperatures are also highlighted in Figure 18.19b. In FEA simulation, both the engine side (left side) and the down pipe side (right side) were fixed. The probabilistic life distributions of the manifold made of the austenitic steel for the calculated temperature distribution and *PEEQ _A* are plotted in Figure 18.20a–c, respectively, for reliability of 90%, 50%, and 10%. The shortest lives at one of the highlighted locations are, respectively, 38, 76, and 118 cycles, for reliability of 90%, 50%, and 10%, and the corresponding locations of the elements are also indicated in these figures. Similarly, the probabilistic life distribution of the manifold made of the ferritic steel are plotted in Figure 18.21a–c, respectively, for reliability of 90%, 50%, and 10%. The shortest lives at the same highlighted location are, respectively, 408, 491, and 553 cycles, for reliability of 90%, 50%, and 10%.

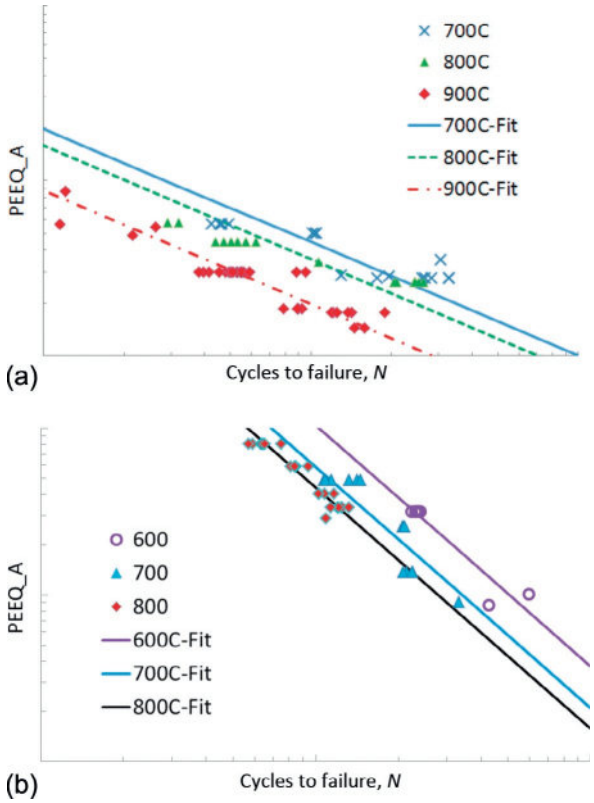

FIGURE 18.18

The data and fitted mean curves of (a) an austenitic stainless steel and (b) a ferritic stainless steel at three different peak temperatures.

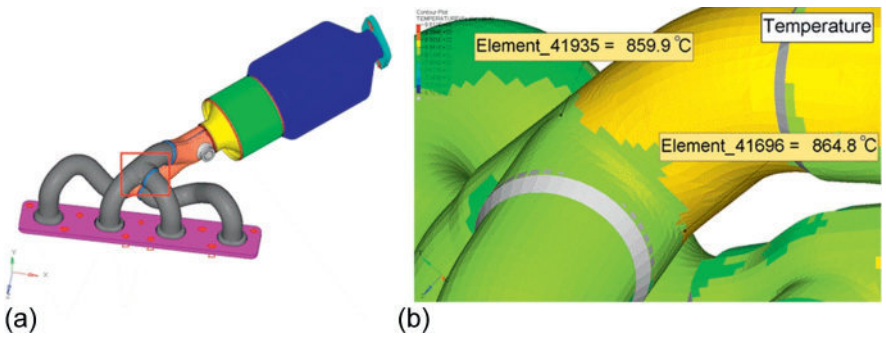

FIGURE 18.19

(a) The configuration of the manifold and (b) peak temperature distribution.

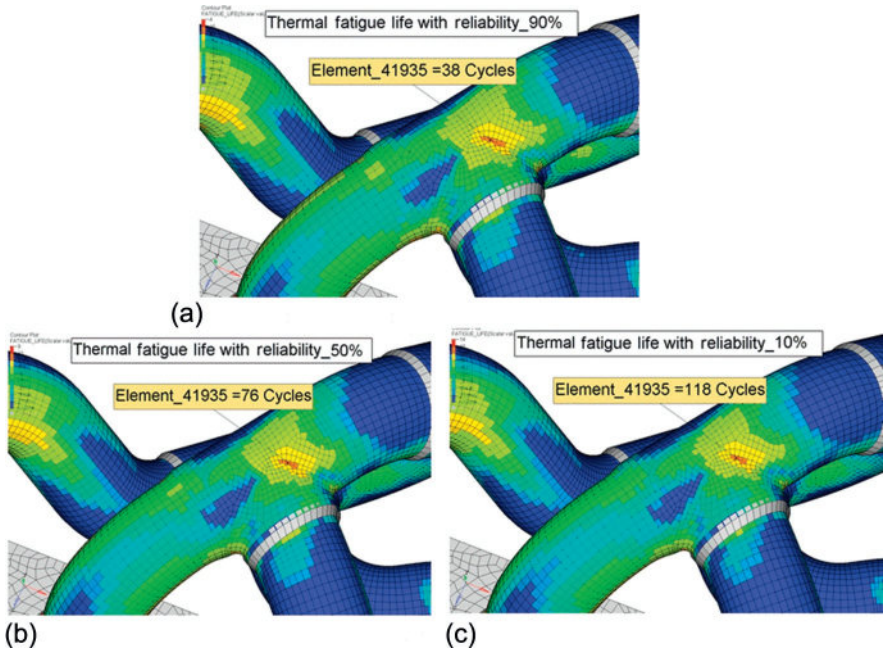

FIGURE 18.20

(a) Life distribution at reliability of 90%, (b) life distribution at reliability of 50%, and (c) life distribution at reliability of 10% for the austenitic steel.

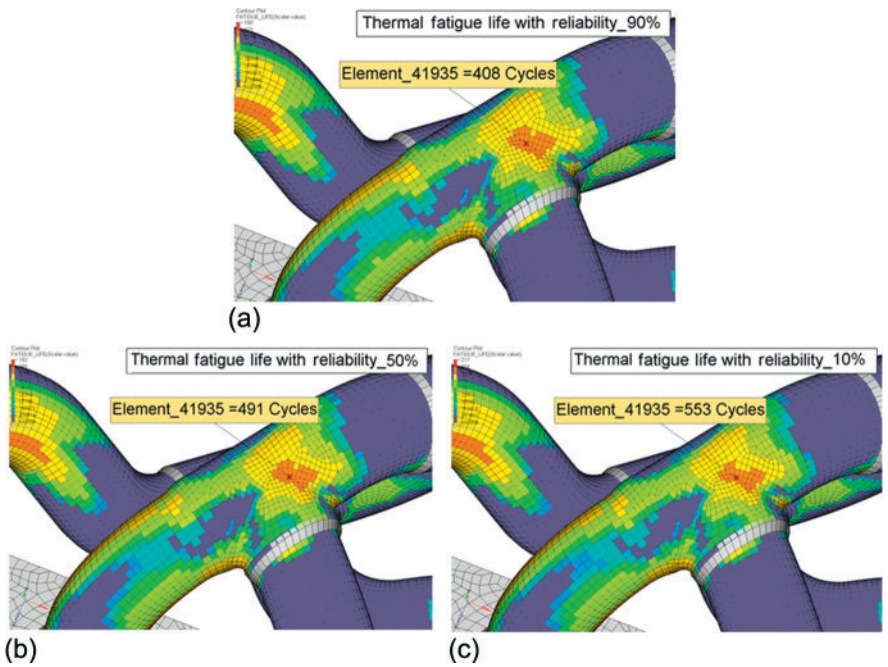

FIGURE 18.21

(a) Life distribution at reliability of 90%, (b) life distribution at reliability of 50%, and (c) life distribution at reliability of 10% for the ferritic steel.

It is noted that the lives of the ferritic manifold are much longer than those of the austenitic one at their respective reliability levels, in other words, more durable. The enhanced thermal-fatigue resistance of the ferritic steel over the austenitic steel is dictated by the *PEEQ_A–N* data as shown in Figure 18.18. Clearly, the probabilistic thermal-fatigue simulation results are consistent with the V-shape thermal-fatigue testing results and the ranking listed in Table 18.2.

7 CONCLUSION

Modern vehicle exhaust components and systems are exposed to increasingly complex operating conditions with high temperatures, severe loadings, and corrosive environments. Stringent government regulations on emissions and fuel economy further push the materials to their limits. Therefore, understanding the failure mechanisms and failure modes of the materials under adverse working conditions is essential to improving the durability and reliability performance of vehicle exhaust products to meet customer requirements.

In this chapter, an overview trend of the vehicle exhaust system development and products were reviewed followed by a discussion of the new challenges of materials failure mechanisms/modes. Some of the most common failure mechanisms, such as fatigue, creep, oxidation, and corrosion, as observed in exhaust products were thoroughly and systematically reviewed. A probabilistic failure data analysis method was described to help identify and to quantify the cause of failure mechanisms, as well as, to prevent failure occurrences. A method for screening and ranking materials based on cyclic oxidation, thermal cycling, and corrosion resistances was discussed. Simple ranking formulae were introduced, correlating fundamental information about chemical composition, physical properties, and mechanical properties to the performance of the materials. These simple formulae can help design engineers to quickly screen, rank, and select materials for vehicle exhaust system development even without conducting physical tests. Finally, two case studies were provided to illustrate the knowledge-based failure prevention, product design and validation procedure. In summary, this chapter offers a comprehensive and practical guide on the state-of-the-art methodologies for failure cause determination, effective remedies, and prevention strategies for engineers, as well as managers, in their product design and validation.

ACKNOWLEDGMENTS

The authors would like to thank Mr. Keith Prodin, Mr. Kevin Smith, Dr. Fulun Yang, Mr. Robert Rebandt, Mr. Henry Sullivan, Mr. Erwin Peters, Mr. Timothy Gardner, Mr.Yunfei Qu, Mr. Youngjae Kang, Mr. Devdutt Shende, Prof. Kamran Nikbin, Prof. D. Gary Harlow, Dr. Pierre Olivier Santacreu, for their helpful comments and contributions to works summarized in this chapter.

REFERENCES

[1] Lee YL, Pan J, Hathaway R, Barkey M. Fatigue testing and analysis: theory and practice. Boston, USA: Elsevier Butterworth-Heinemann; 2005.

[2] O'Connor P, Kleyner A. Practical reliability engineering. 5th ed. New York: Willy; 2012.

[3] Yang G. Life cycle reliability engineering. Hoboken, New Jersey: John Wiley & Sons, Inc.; 2007.

[4] Billinton R, Allan RN. Reliability evaluation of engineering systems: concepts and techniques. 2nd ed. New York and London: Plenum Press; 1992.

[5] Nelson WB. Accelerated testing: statistical models, test plans, and data analysis. Hoboken, New Jersey: John Wiley & Sons, Inc; 2004.

[6] Cashman G. A statistical methodology for the preparation of a competing modes fatigue design curve. J Eng Mater Technol 2007;129:159–68.

[7] Harlow DG. Statistical characterization of bi-modal behavior. Acta Mater 2011;59:5048–53.

[8] Jha SK, Larsen JM, Rosenberger AH. Towards a physics-based description of fatigue variability behavior in probabilistic life-prediction. Eng Fract Mech 2009;76:681–94.

[9] Socie DF, Marquis GB. Multiaxial fatigue. Warrendale, PA: Society of Automotive Engineers, Inc.; 2000.

[10] Santacreu PO, Faivre L, Acher A. Life prediction approach for stainless steel exhaust manifold. SAE Int J Passeng Cars-MechSyst 2012;5(2). http://dx.doi.org/10.4271/2012-01-0732.

[11] Santacreu PO, Simon C, Coleman A. Thermomechanical fatigue behavior of stainless steel grades for automotive exhaust manifold applications. In: McGaw MA, Kalluri S, Bressers J, Peteves SD, editors. Thermomechanical fatigue behavior of materials: 4th volume. West Conshohocken, PA: ASTM STP 1428, ASTM International; 2003, pp:227–239.

[12] Lin S. Exhaust system reliability evaluation. Int J Reliab Qual Saf Eng 2011;18:327–40.

[13] Rice RC, editor. SAE fatigue design handbook. 3rd ed. Warrendale, PA: Society of Automotive Engineers, Inc.; 1997, AE-22.

[14] Manson SS, Halford GR. Fatigue and durability of metals at high temperatures. Materials Park, Ohio: ASM International; 2009.

[15] Greuter E, Zima S. Engine failure analysis: internal combustion engine failures and their causes. Warrendale, PA, USA: SAE International, 400 Commonwealth Drive; 2012.

[16] Kotrba A, Yetkin A, Gough B, Gundogan A, Mastbergen D, Paterson C. Performance characterization of a thermal regeneration unit for exhaust emissions controls systems. SAE Technical Paper, 2011-01-2208, 2011.

[17] Heck RM, Farrauto RJ. Automobile exhaust catalysts. Appl Catal A Gen 2001;221: 443–57.

[18] Zheng G, Kotrba A, Golin M, Gardner T, Wang A. Overview of large diesel engine after treatment system development. SAE Technical Paper, 2012-01-1960, 2012.

[19] Kotrba A, Brockman A, Martin S, Mikovits A, Butzke GL, Richey Z, et al. Secondary fuel injection layout influences on DOC-DPF active regeneration performance. SAE Int J Commer Veh 2013;6(2):539–44. http://dx.doi.org/10.4271/2013-01-2465.

[20] Yasir M, Mori G, Wieser H, Schattenkirchner M, Hogl M. A new testing method for lifetime prediction of automotive exhaust silencers. Int J Corrosion 2011. http://dx.doi.org/10.1155/2011/689292, Article ID 689292.

[21] Hoffmann C, Gümpel P. Pitting corrosion in the wet section of the automotive exhaust systems. J Achiev Mater Manuf Eng 2009;34:115–21.

[22] Michel B, Saedlou S, Herbelin JM, Santacreu PO. Corrosion simulation tests on stainless for automotive applications. In: Karjalainen P, Hertzmann S, editors. Proceedings of 6th European stainless steel conference, Finland, June 12-13; 2008.
[23] Gümpel P, Schiller D, Arlt N, Bouchholz D. Simulation of corrosion behaviour of stainless steels in passenger car exhaust systems. ATZ Worldwide 2004;106:18–20.
[24] Birks N, Meier GH, Pettit FS. Introduction to the high temperature oxidation of metals. Cambridge, UK: Cambridge Press; 2006.
[25] Sabata A, Brossia CS, Behling M, Localized corrosion resistance of automotive exhaust alloys, Corrosion 98, March 22–27, 1998, San Diego, CA, NACE International.
[26] Frankel GS. Pitting corrosion. ASM handbook, volume 13A, corrosion: fundamentals, testing, and application. Materials Park, Ohio: ASM International; 2003, pp:236–241.
[27] Wei Z. Characterization of materials for exhaust systems under combined mechanical and corrosive environment. SAE Technical Paper, 2013-01-2420, 2013, http://dx.doi.org/10.4271/2013-01-2420.
[28] ASTM E739-10, Standard practice for statistical analysis of linear or linearized stress-life ($S-N$) and strain-life ($\varepsilon-N$) fatigue data. West Conshohocken, PA: ASTM International; 2010.
[29] API 579-1/ASME FFS-1 2007 Fitness-For-Service, The American Society of Mechanical Engineers and API; June 5, 2007.
[30] Sadananda K, Sarkar S, Kujawski D, Vasudevan AK. A two-parameter analysis of S-N fatigue life using both $\Delta\sigma$ and σ_{max}. Int J Fatigue 2009;31:1648–59.
[31] Manson SS, Halfold GR. Fatigue and durability of structural materials. Materials Park, Ohio: ASM International; 2006.
[32] Ritchie RO. Mechanisms of fatigue-crack propagation in ductile and brittle solids. Int J Fract 1999;100:55–83.
[33] Walker A. The effect of stress ratio during crack propagation and fatigue for 2024-T3 and 7075-T6 aluminum. In: Effects of environment and complex loading history on fatigue life. Philadelphia, PA: American Society for Testing and Materials; 1970. p. 1–14, ASTM STP 462.
[34] Noroozi AH, Glinka G, Lambert S. A two parameter driving force for fatigue crack growth analysis. Int J Fatigue 2005;27:1277–96.
[35] Dowling NE, Calhoun CA, Arcari A. Mean stress effects in stress-life fatigue and the Walker equation. Fatigue Fract Eng Mater Struct 2009;32:163–79.
[36] Dowling NE. Mean stress effects in strain-life fatigue. Fatigue Fract Eng Mater Struct 2009;32:1004–19.
[37] Congleton J, Charles EA, Sui G. Review on effect of cyclic loading on environmental assisted cracking of alloy 600 in typical nuclear coolant waters. Corros Sci 2001;43:2265–79.
[38] Saxena A, Dogan B, editors. J ASTM Int Select Technic Papers, ASTM STP 1539, Creep-fatigue interactions: test methods and models, West Conshohocken, PA; 2011.
[39] Wei Z, Yang F, Cheng H, Nikbin K. Probabilistic prediction of crack growth based on creep/fatigue damage accumulation mechanism. J ASTM Int 2011;8(5). http://dx.doi.org/10.1520/JAI103690.
[40] Wei RP. Some aspects of environment-enhanced fatigue crack growth. Eng Fract Mech 1970;4:633–51.
[41] Wei RP, Landes JD. Correlation between sustained-load and fatigue crack growth in high-strength steels. Mater Res Stand 1970;9:25–46.

[42] Wei Z, Yang F, Lin B, Luo L, Nikbin K. Deterministic and probabilistic creep-fatigue-oxidation crack growth modeling. Prob Eng Mech 2013;33:126–34.
[43] Wei Z, Luo L, Rybarz M, Clark D, Nikbin K. A new generalized nonlinear superposition theory and its applications in modeling corrosion-fatigue. In: Proceedings of the ASME 2013 pressure vessels & piping division conference, PVP2013-97633, Paris, France, July 14–18, 2013; 2013.
[44] Harlow DG. Low cycle fatigue: probability and statistical modeling of fatigue life, PVP2014-28114. In: Proceedings of the ASME 2014 pressure vessels & piping conference, Anaheim, California, USA, July 20–24; 2014.
[45] Neter J, Wasserman W, Kutner M. Applied linear statistical models. Homewood, IL: Richards D. Irwin, Inc.; 1990.
[46] Chinouilh G, Santacreu PO, Herbelin JM. Thermal fatigue design of stainless steel exhaust manifolds, SAE Technical Paper 2007-01-0564; 2007.
[47] Wei Z, Konson D, Yang F, Luo L, Ellinghaus K, Pieszkalla M. Thermal fatigue resistance characterization and ranking of materials using the V-shape specimen testing method. Fatigue Fract Eng Mater Struct 2014. http://dx.doi.org/10.1111/ffe.12154.
[48] Shannon CE. A mathematical theory of communication. Bell Syst Tech J 1948;27:379–423, 623-656.
[49] Wei Z, Lin S, Luo L, Gao L. Components durability, reliability and uncertainty assessments based on fatigue failure data. SAE Int J Mater Manf 2015;8(1):80–90. http://dx.doi.org/10.4271/2014-01-2308.
[50] Natrella M. Experimental statistics, handbook 91. Washington DC: National Bureau of Standards; 1966.
[51] Lu TJ, Fleck NA. The thermal shock resistance of solids. Acta Mater 1998;13:4755–68.
[52] Lo KH, Shek CH, Lai JKL. Recent developments in stainless steels. Mater Sci Eng R 2009;65:39–104.
[53] ASTM G48-11: Standard test methods for pitting and crevice corrosion resistance of stainless steels and related alloys by use pf ferric chloride solution. West Conshohocken, PA: ASTM International; 2011.
[54] Jargelius-Pettersson RFA. Application of the pitting resistance equivalent concept to some highly alloyed austenitic stainless steels. Corrosion 1998;54:162–8.
[55] Merrello R, Botana FJ, Botella J, Matres MV, Marcos M. Influence of chemical composition on the pitting corrosion resistance of non-standard low-Ni high-Mn-N duplex stainless steels. Corros Sci 2003;45:909–21.
[56] Wei, Z., Qu, Y., Yang, Y., Yang, F., Yule, M., Ellinghaus, K., Pieszkalla, M., Figen, L., Probabilistic thermal-fatigue life assessment for vehicle exhaust components and systems, 2014-01-2305, Rosemont, Illinois, USA; October 7–9, 2014.
[57] Wei Z, Luo L, Lin B, Yang F, Konson D, Ellinghaus K, Pieszkalla M, Avery K, Pan J, Engler-Pinto C. Hold-time effect on thermal-mechanical fatigue life and its implications in durability analysis of components and systems. Mater Performance Characterization, 2014;37(8):897–908. http://dx.doi.org/10.1520/MPC20140032, .

CHAPTER

Failure of structural parts for large road vehicles

19

Víctor H. Jacobo, Edgar I. Ramírez, Rafael Schouwenaars, Armando Ortiz
Department of Materials Science and Manufacturing, DIMEI Universidad Nacional Autónoma de México Avenida Universidad, Coyoacán, México D.F. Mexico

CHAPTER OUTLINE

1 INTRODUCTION

The production of large road vehicles, such as trucks and buses, represents an important economic activity in many emerging economies, where the combination of sufficiently skilled yet relatively cheap labor allows for efficient manufacturing. At the same time, economic growth produces increased needs for the transportation of goods and persons, providing extensive markets for the sale of these products.

Production of trucks and buses differs in many aspects from the production of automobiles and vans. The latter are almost exclusively designed, manufactured, and marketed by large multinational corporations. This results in very high numbers of the same model being built and therefore justifies large research and development divisions. Also, the socio-economic impact of road accidents has led to the development of ever more stringent safety regulations and mandatory crash testing for passenger vehicles. Even so, occasional failure still happens even in this kind of systems [1].

For large road vehicles, production series are typically much smaller and products are customized to the specific needs of the client. In this sense, city buses and coaches show little similarity between them and there are many different types of

Handbook of Materials Failure Analysis With Case Studies from the Aerospace and Automotive Industries.
http://dx.doi.org/10.1016/B978-0-12-800950-5.00019-3

medium-sized trucks which can be found in everyday traffic. Road conditions in emerging economies may be very different from what is considered standard in Europe and North America; use in pronouncedly mountainous terrain may modify the operation conditions as compared to original design specifications. Low-floor buses such as the ones found in many North-American and European cities would be impossible to operate on the outskirts of most Mexican cities.

Often, the chassis and suspension of the vehicles are designed and produced separately, while the body (for buses) or the cargo space (for trucks) may be designed and built by subcontractors or clients. With the exception of the largest multinational producers, design optimization is often performed by fairly classic engineering tools instead of the latest finite-element and vehicle dynamics software [2,3].

Because of the former, when failure occurs in critical components of such vehicles, all possible causes must be considered. In the present work, all studies were performed for local manufacturers and had the main purpose of incorporating process modifications or design changes, with the goal of product improvement and failure prevention. A first case study relates to the structural parts of the body of transit buses which showed extensive fracture propagating trough the structural and exterior parts of the body. A second case refers to the Z-bar of a passenger bus, which forms part of the air suspension system. The third study analyzes the sudden fracture of the transmission axle of a dump truck and the fourth one investigates the fatigue failure of the torsion bar of a long-haul passenger bus. Failure of the welded hollow structural sections threatens the integrity of the vehicle during usage, while the other three cases may severely affect the driveability of the vehicle, so all four cases present critical safety issues.

2 EXPERIMENTAL PROCEDURES

Because the analyses were performed on request of the various production plants involved, failed parts were retrieved by company personnel without any knowledge of failure analysis. This means that some of the evidence required for a full analysis may have been lost. Also, significant reluctance was met to disclose all the essential details which may facilitate the analysis, although generally this situation improved during the investigation, as plant engineers were presented with the available evidence and it was made clear that the failure analysis was used as a tool for quality improvement and not part of a judicial process.

All parts were observed visually and photographs at low magnifications were produced by digital camera and stereo microscopy. Fracture surfaces and metallographic sections were studied in a Philips XL20 SEM equipped with an EDAX energy dispersive X-ray spectrometer. Sections were prepared by standard metallographic practice and observed without etching to detect inclusions and after 5 s of etching in Nital (3% nitric acid in ethanol) to reveal microstructure. Surface hardness and hardness profiles (Rockwell C) were determined according to ASTM E 18-98 [4]. Chemical composition was determined by spark emission spectroscopy using a Spectrolab M8 equipment according to ASTM-E415 [5]. All failed parts involved in the study were subject to an analysis with penetrating liquids to detect the presence

of additional crack initiation sites, but none were found. In the transmission shaft, which had already been cut into pieces before the failure analysis, an additional flaw was discovered during SEM-observation.

It shall be noted that in all studies, the number of images, micrographs, chemical analyses, and mechanical properties collected was significantly larger than what can be presented here. Only the most relevant evidence is provided in this chapter, to give a general overview of the problems encountered.

3 CASE STUDIES

3.1 WELDED HOLLOW STRUCTURAL SECTIONS

The first set of failure cases refers to the structural parts of the body of high-floor transit buses with front engine. The frame of the body consists of hollow structural sections. This frame is critical in providing bending and torsional stiffness. The latter aspect is one of the main problems to be considered in the design of the frame and is made complicated by the necessary presence of doors, where diagonal stiffeners cannot be used [3]. Figure 19.1 shows a transverse stiffener used in the front of the bus, the shape is determined by the front-engine design of the vehicle. This beam transfers a significant part of the frame and passenger weight to the front suspension. Figure 19.2 shows

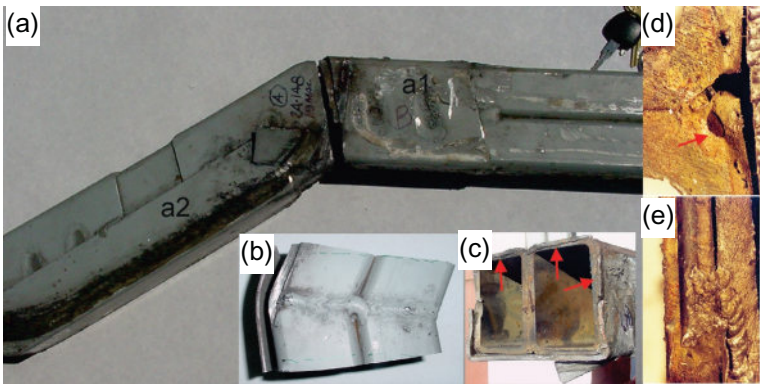

FIGURE 19.1

Failure of the transversal stiffener in a front-engine transit bus. (a) Shows the failed part, which was reinforced by plates which were welded onto the original design (a1 and a2). (b) Shows a reference part without failure. (c) Presents the cross-section of the failed part. The arrows indicate the weld material, which covers the structural section only superficially. (d) Indicates a low-quality joint, with inclusions and discontinuities between the weld and base metal and incomplete penetration of the weld material into the union between the two hollow sections. (e) Likewise indicates an incomplete weld which fails to fully join both sides of the structural section.

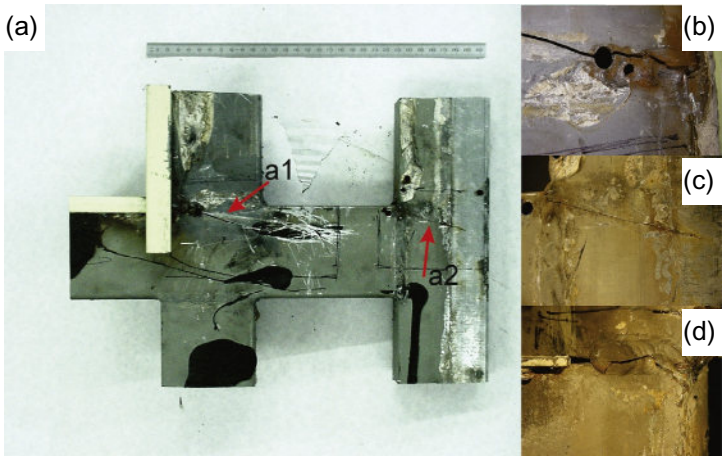

FIGURE 19.2

Cross and T-junction of the portal of the descent door of a transit bus. (a) Presents the assembly with cracks marked by arrows a1 and a2. (b) Gives a close-up of crack a1, which runs through a hole drilled in the profile. The origin of the crack is found in the weld joint seen in the left-hand side of (b); the holes, which were drilled to affix accessories in the bus interior after production did not seem to affect the propagation of the fatigue cracks in any significant manner. (c) Presents a close-up of crack a2, while (d) shows the origin of the crack in the weld material of the T-joint.

failed T and cross unions of welded sections retrieved from the frame around the descent (rear) door (notice the cross union consists in fact of two separate T-joints).

In the case of the transverse stiffener, square butt joints were produced from the same material as used in the original product; one set of samples was manufactured using the E6013 electrodes used by the subcontractor and one set using E7018 electrodes as deemed more appropriate by the present authors. Five tensile samples were produced from each set, with the welding seam at the center. For the E6013 electrode, an ultimate tensile strength of 380 MPa was obtained with an elongation at failure of 4.6%, for the E7018 electrode, the values were 470 MPa and 7.2%, respectively. In the first case, fracture occurred in the weld, in the second case, it was the base material that failed in a ductile manner.

In both cases presented above, the failure mode was fatigue (Figures 19.3 and 19.4). In the first one, fatigue propagation was strictly limited to the weld material for the simple reason that the metallurgical union between weld and base material was almost nonexistent, as seen in Figures 19.1c and 19.5a. Only a thin overlay connects the two halves of the structural section. In the same way, the reinforcement plates applied to the original design are so poorly welded that their effect is negligible. The reason for the failure is the selection of the welding electrodes, which provide insufficient strength and poor penetration of the base material by the welding seem, but allow relatively fast production rates. The problems are exacerbated by the extremely poor execution of the welds, as evidenced by their macroscopic appearance and the presence of oxide inclusions and shrink porosity.

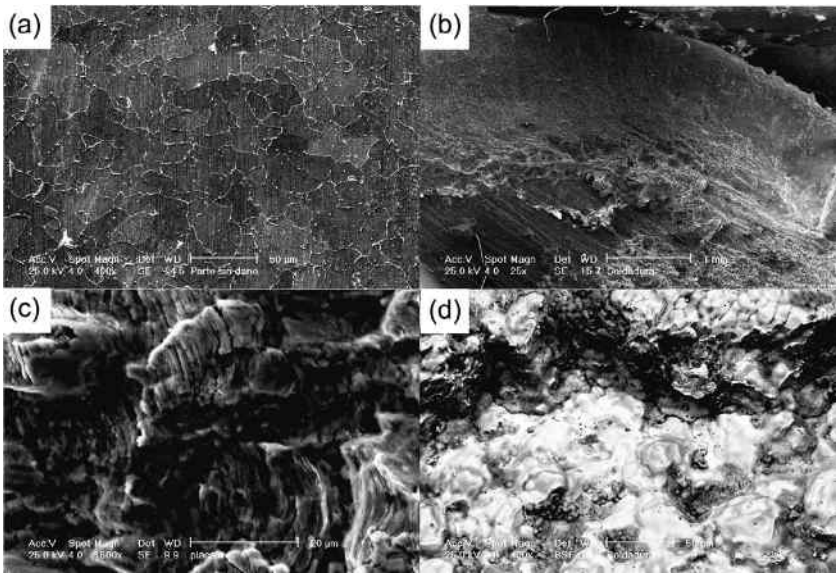

FIGURE 19.3

SEM-images corresponding to the failure shown in Figure 19.1. (a) Shows the typical microstructure of a low-carbon steel. (b) Presents a fatigue failure of the weld, as evidenced by the detail in (c) The lower part of (b) presents the surface of the structural profile which still shows the cutting marks produced when the section was cut to size during manufacturing and was not affected by the welding. (d) Shows a part of the fracture surface within the weld material where oxide inclusions and shrinking porosity are found.

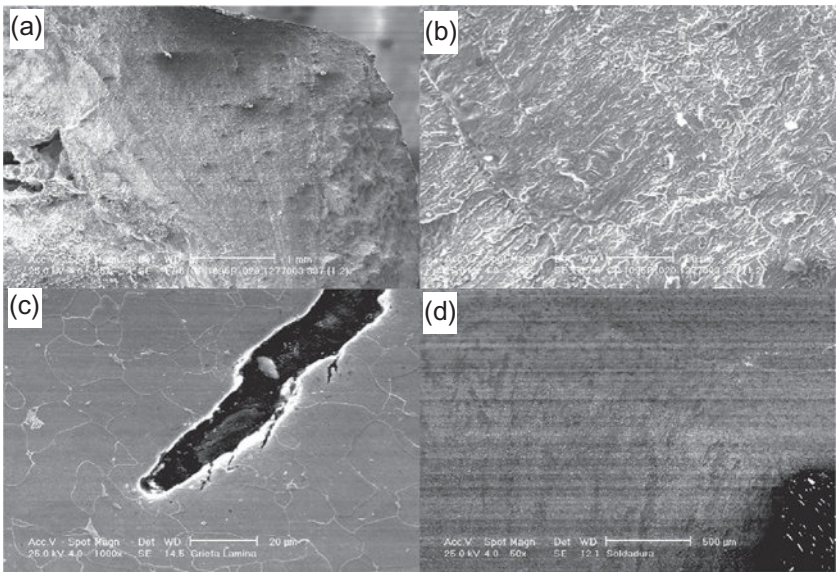

FIGURE 19.4

SEM-observations of the hollow structural sections of Figure 19.2. (a) Shows fatigue crack propagation through the profile wall, the complex propagation pattern as observed in (b) indicates a strong shear component in the loading cycle. (c) Shows a blunted crack tip in a typical low-carbon steel microstructure. (d) Shows the weld, the HAZ and base material in a continuous transition which indicates the formation of a sound metallurgical joint.

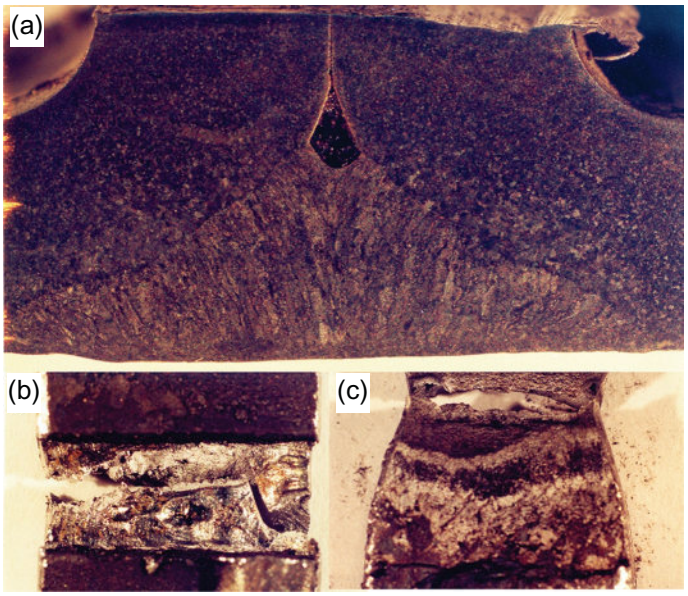

FIGURE 19.5

(a) Presents a cross-section of the welds used in the transversal stiffener. No weld penetration is observed, the heat-affected zone is small and recognized by some limited grain growth. (b, c) Represent butt joints after tensile testing. In (b), the E6013 electrodes used in production were employed; the sample fails through the weld material. In (c), an E7018 electrode was used, which causes tensile failure to occur in the base metal while the weld material is intact.

In the second case, the welds are of a good metallurgical quality. On the sides of the junctions, where the welds are flat, execution is satisfactory. In the corners, where accessibility is limited, the welds are discontinuous and badly executed. Torsional loading is the main design concern of the structural frame, and that this will lead to local shear loading on the junctions, causing elevated stresses exactly at these corners.

It is concluded that in the first case, extreme cost-cutting through materials selection and the use of unqualified labor is entirely responsible for the failure. In the second case, process control is also insufficient and the use of underqualified labor may be a factor. However, considering the specific initiation sites for fatigue, design changes may be required to provide additional stiffness to the frame around the doors of the bus, with the goal of reducing the stress concentrations in the corners of the unions between the hollow sections.

3.2 Z-BAR OF AIR SUSPENSION

The Z-bar is part of the rear suspension of a transit bus. This element consists of a stiff spring whose section is designed to assure constant bending stresses along the part's length (Figure 19.6a). The left side acts directly on the chassis, with the central

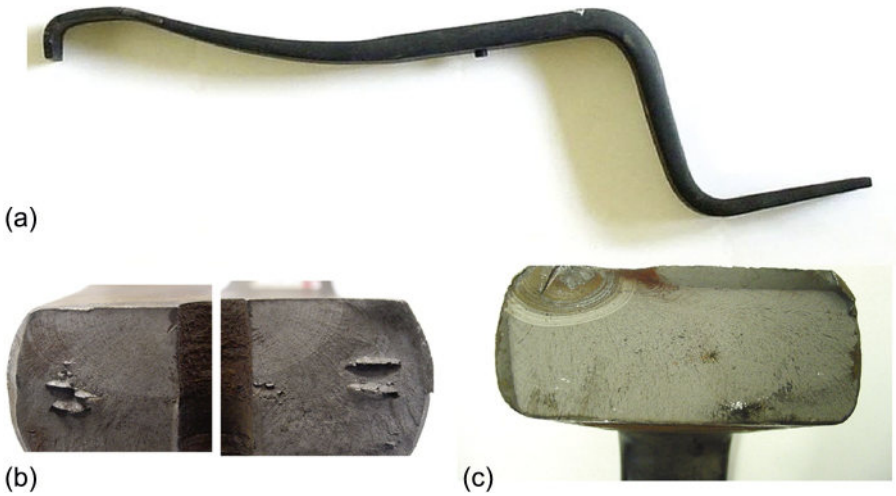

FIGURE 19.6

(a) Represents the original design of the Z-bar. The horizontal dimensions of the part, as pictured, are 1.2 m. The pin at the center locks into the top of the rear axis assembly. (b) Presents the failure due to the addition of a bolt to the right of the pin, the bolt was used to add a reinforcing plate to the original design. Notice the delamination failure in parts of the section outside the concentric fatigue marks. (c) Corresponds to fatigue failure initiated by fretting between the reinforcement plate and the original part.

pin locking into the rear axis assembly, which is allowed to pivot when the bar is bent. Two clamps (not shown) assure rigid contact between the rear axis assembly and the Z-bar. The horizontal extension at the right supports an air suspension unit. Figure 19.6a presents the original design of the part. Fracture occurred systematically in the sharp bend to the right of the central pin. As an improvised remedy, this section was "reinforced" by drilling two holes through the section and retrofitting a steel plate with bolts. After this "correction," failure became even more frequent. The reasons can be seen in Figure 19.6b, c. In Figure 19.6b, the corners of the drilled hole serve as the stress concentrators for fatigue. In Figure 19.6c, fretting wear between the bolted plate and the original Z-bar served as the fatigue initiator.

Chemical analysis indicated that the material corresponds to the required AISI5160 specification. However, a hardness of 39 HRC was measured, as compared to the design specification of 44.5-48.5 HRC. This corresponds roughly to a yield strength of 1.2 GPa as compared to the 1.4 GPa specified in the design. Additionally, the material showed a strongly banded microstructure with large longitudinal inclusions. The latter are the cause of the delamination features observed in the brittle fracture zone of Figure 19.6b.

Figure 19.7 represents the finite-element analysis of the original design as well as the effect of the additional hole. It is seen that in the curved sections of the bar, the stress reaches 500 MPa. Given the strength of the material as derived from hardness

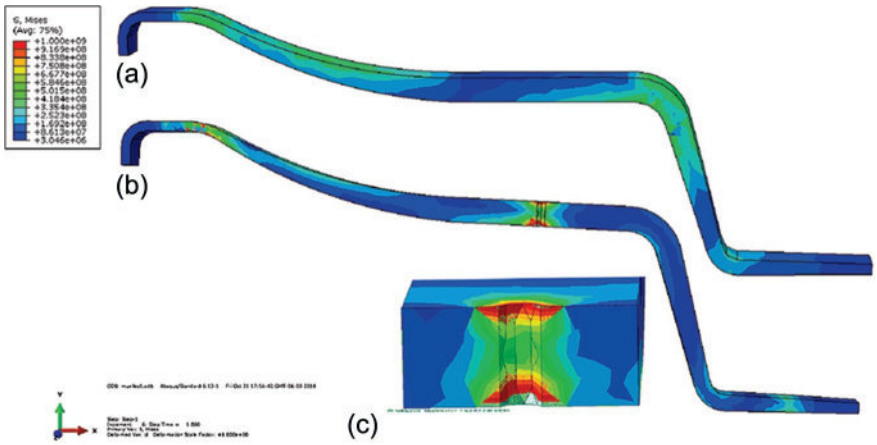

FIGURE 19.7

Finite element analysis of the Z-bar. (a) Represents the original design. The simulation was made for loads of 75 kN, which is twice the static design load. Stresses of 500 MPa are reached in the bent parts of the bar. (b) Presents the same simulation with a single bolt hole. Its presence alters the distribution of the stresses and provides stress concentrations (c) at the point where fatigue initiation was observed (Figure 19.6b).

measurements, this stress level could be below the fatigue limit of the material. However, dynamic effects were taken into account by multiplying the static service load by a factor of 2. This factor may be too low to simulate operation conditions, especially if road conditions are bad. A full analysis of the vehicle dynamics would be required to answer these questions into detail. Also, overloading of the bus cannot be excluded. The large inclusions, the banded microstructure, and the insufficient hardness of the material may also be contributing factors in the failure. A simulation with the bolt hole present shows the significant stress concentration at the position of fatigue initiation seen in Figure 19.6b. The absolute values of the stresses in this case are not representative, as the precise data on the reinforcing plate were unknown to the authors. However, comparison of Figure 19.6 to Figure 19.7 is sufficient to explain why the "correction" of the design exacerbated the failure problem, as a new stress raiser was introduced at a critical position of the component.

3.3 TRANSMISSION AXLE

This analysis corresponds to a transmission axle for a dump truck for use at construction and excavation sites. Failure occurred during dynamometer testing at the assembly plant and was detected by excessive vibration. The shaft was cut into four quarters at the plant, almost obliterating the crack initiation site (Figure 19.8). Surface markings indicating plastic deformation were generated after initial failure as the part is restricted by a heavy metal sleeve which permitted torque to be transmitted

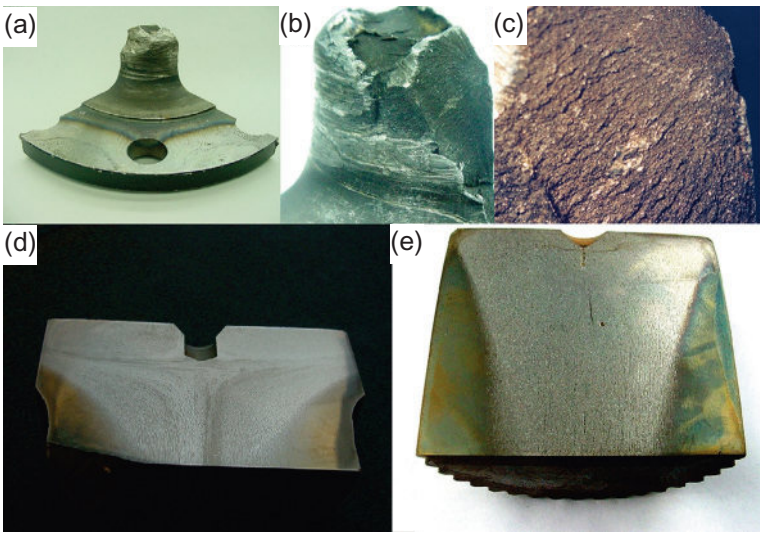

FIGURE 19.8

Fractured truck axle. The fracture originated from a flaw which was almost cut away by improper handling of the part before starting a professional failure analysis (a, b). The fracture surface has a complex morphology and emanates from a single point near the surface, as shown in (c). Macro-etched sections of a reference part (d) and of the opposite end of the axle (e) provide an impression of some of the metallurgical aspects of the case. The quenching depth can easily be determined; (d) shows clear evidence of the complex flow pattern induced by the forging process, while (e) indicates a strongly banded microstructure with centerline porosity and inclusions.

along the interlocked halves of the broken shaft. The geometry of the fracture is significantly more complex than what is expected in fragile failure under torsion (Figure 19.8b). The Chevron-marks in Figure 19.8c point toward the initial flaw.

Metallographic analysis of the shaft indicated poor metallurgical quality of the steel. In Figure 19.8d and e., macroetching revealed a banded microstructure with centreline porosity. Both effects indicate inadequate cooling conditions after ingot casting and, while the former defect can be eliminated by prolonged homogenization, porosity, and the accompanying oxide film remain present even after forging. Porosity and large inclusions were also present in a reference piece which was chosen at random from available stock. Additional evidence of poor steel quality was found in the form of a 10-mm long internal crack intersecting the fracture surface (which means the crack was originally longer that what could be measured) (Figure 19.9a). Abundant oxides were present in the crack zone (Figure 19.9b), while oxide-free parts showed the presence of two parallel microcracks, bridged occasionally by transverse cracks (Figure 19.9c). Martensite colonies were not intersected by the defects, but delimited by them, indicating the flaw was present before quenching.

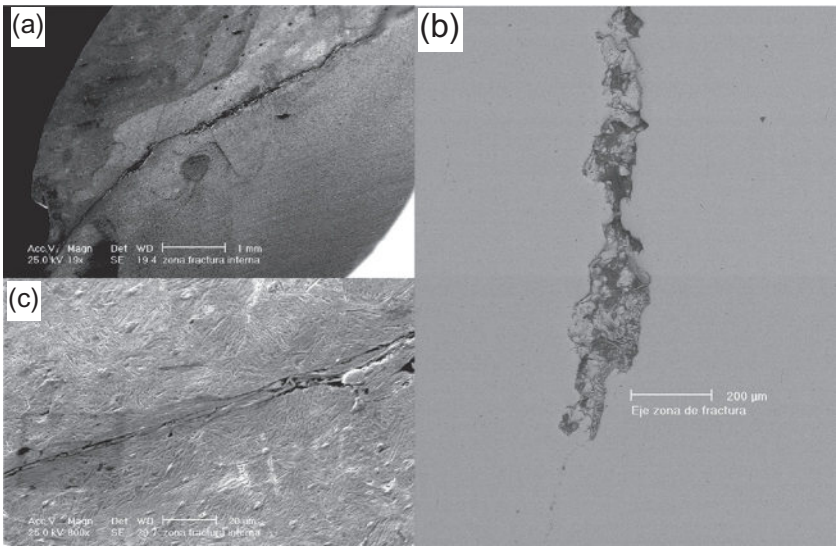

FIGURE 19.9

SEM-observation of truck axle. (a) Shows a large flaw intersecting the fracture surface which is at the left. (b) Shows significant oxide inclusions, (c) shows the thin cracks connecting different zones of oxide inclusions along the defect.

The composition corresponds to AISI1048 carbon steel with enhanced manganese content as specified by the client. Hardness was found to be low in the center of the shaft (10.5 HRC), At 11 mm from the surface 31HRC was found, 10 points below minimum specifications and at the surface, HRC63 was measured, slightly above the specified range of 54-60 HRC. The very low value in the center is probably caused by the slowly cooled, coarse microstructure but is not likely to have a large effect on the failure case at hand.

Finite element analysis (Figure 19.10) shows that the crack initiation site is outside the zone of maximum stresses. The exact nature of the initial flaw cannot be reconstructed, because it became part of the fracture surface and was partially obliterated by undue handling of the failed part. However, the presence of a second flaw, at least 10 mm in extent in the same zone, explains the reasons for failure. The base material used in the forging is ingot cast; continuously cast material is always to be preferred due to its better homogeneity and smaller grain size. Large inclusions also point to a poor metallurgical quality of the base material. According to the flow patterns, very large strains are found in the fracture zones (Figure 19.8d). Large shear strains are responsible for the propagation of shear cracks which initiate at the oxide inclusions and connect stringers of the same. Although some uncertainty exists with respect to the critical stress intensity of circumferential flaws under torsion conditions, similar defects (but of lesser size) were found to be responsible for the fatigue failure of the axle of a high-speed train carriage [6].

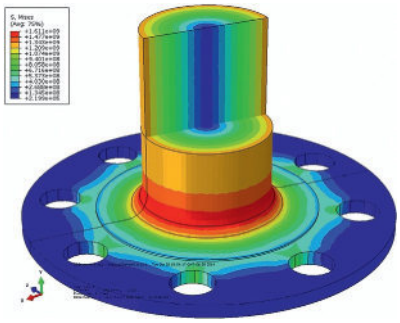

FIGURE 19.10

Finite element analysis of the failed axle. Maximum stresses are found at the fillet between the axle and the flange. The fracture initiated outside the zone of maximum stress, indicating that the presence of the pre-existing flaws was responsible for the failure, not sudden overload which would have caused fracture initiation at the fillet.

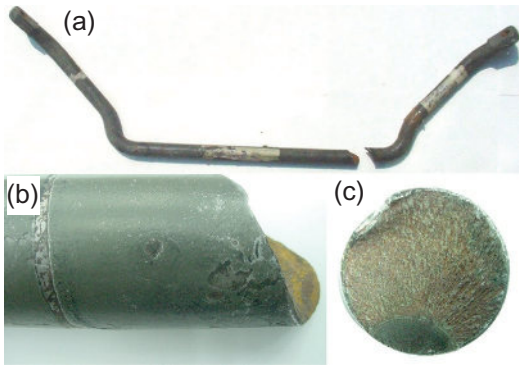

FIGURE 19.11

(a) Represents the entire torsion bar. The horizontal dimensions of the part, as pictured, are 2.4 m. The bar is attached by pins to the wheel assembly on both ends and supported to the chassis by clamps which are separated from the bar by rubber sleeves. (b) Shows the position of the clamps. Point-like contact damage and fretting damage are observed at the surface in the fracture zone. (c) Shows the concentric fatigue pattern and the chevron marks from the ensuing brittle failure.

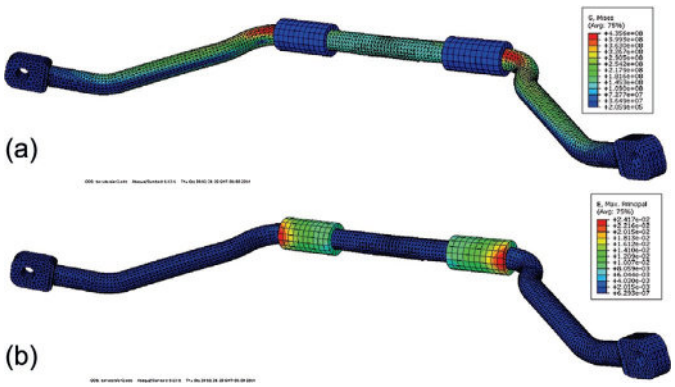

FIGURE 19.12

Finite element models of the torsion bar. (a) Represents the Von Mises equivalent stresses which are maximum at the points of maximum curvature of the part. (b) Represents the strain in the sleeves, which can take fairly high levels.

3.4 TORSION BAR

The last case corresponds to the torsion bar of the suspension of a long-haul coach. This component is used to transfer load from the wheels at the inside of turns toward the outside, by applying spring action on the chassis which is induced by the rolling movement caused by centrifugal inertia. By exerting an upward force on the chassis at the inside of the turn, roll is reduced, while at the same time a downward force is exercised on the wheels at the outside of the turn and increases grip. Failure of this part results in a sudden change in the force equilibrium of the vehicle suspension, inducing strong dynamic effects accompanied by a loss of grip with the road surface. Significant driver skill is required to prevent severe accidents in such event.

Failure occurred in three different coaches in short succession. The coaches had between 333,000 and 375,000 km of service. The torsion bars show a typical pattern of a semi-elliptical fatigue crack emanating from a point at the surface followed by brittle fracture under torsion (Figure 19.11). Brittle fracture occurs at relatively small extents of fatigue crack propagation. In two out of three cases studied, the initiation point had the characteristic features of an indentation and together with other types of surface damage it was concluded that metal-metal contact occurred in this zone, which corresponds to the area where the bar is clamped to the chassis. In the third case, fatigue was initiated outside the clamping zone, at a point where the curvature of the bar was strongest. The material of the bar corresponds to AISI 5155 steel with increased Cr-content and shows a homogenous bainitic microstructure, with very limited banding and without large inclusions. A uniform hardness of 44HRC was measured, indicating a high-quality material subject to excellent thermal treatment.

Finite element simulations of the torsion bars are presented in Figure 19.12. Figure 19.12a shows the stress analysis under operating conditions of a torsion bar, taking into account the presence of rubber sleeves at the point where the bar supports the chassis. The maximum stress occurs at the point of maximum curvature, which corresponds to the failure of one of three cases studied. Figure 19.12b shows the corresponding strains. If the rubber sleeves are substituted by two rigid supporting points, maximum stresses occur at these contact points while the stress in the curvature of the bar is unchanged.

Material quality or manufacturing defects could be excluded as failure causes. The fact that one of the bars failed at the point of maximum curvature indicates that insufficient attention was paid to the effect of curvature as a stress raiser. The other two cases are somewhat more complex, because, while there is clear evidence of localized contact provoking surface damage to the torsion bars, such contact is supposedly prevented by the presence of a rubber sleeve. The surface damage could be unequivocally identified with the fatigue crack initiation.

An explanation can be found by the fact that coaches operating on long-distance services from central Mexico (2200 m above sea level) to the coast manage a continuous sequence of sharp curves in temperatures which are generally above 30 °C and, during certain seasons, above 40 °C. The accumulated heat caused by cyclic

compression of the rubber, combined with the impossibility to transfer this heat to the environment, leads to thermal degradation of the sleeve [7–10], to the point where it no longer fulfills its intended function.

3.5 DISCUSSION

Within the field of terrestrial transportation, relatively few failure cases related to welding and forging have been published in open literature over the last two decades (with the exception of spot welds, which present a field to broad to discuss here). One of the reasons is that the production of passenger cars is highly standardized and supported by multinational research and development departments where sufficient expertise is present to remember the lessons from past failures. Confidentiality doubtlessly is another reason why so few cases are reported. A limited review with statistical relevance was given by Heyes in 1998 [1].

Classical arc welding is not used in conventional production of automobiles. It is important in the custom production of specialized road vehicles, either for cargo or for passenger transport. Significant attention has been given to the fatigue failure of such welds in civil construction [11,12]. The lack of attention to the topic in vehicle construction is illustrated by the two cases presented here, as failure was a clear consequence of insufficient care for the process on behalf of subcontractors. Improper electrode selection, with the goal of increasing productivity, results in rapid fatigue failure of the welded structures. Even with reasonable materials selection, lack of attention to the weld quality in cross and T junctions leads to fatigue starting from the angles of the junctions, where stresses are highest. Rapid fatigue propagation has been reported due to the improper application of weld material for the repair of other automotive components as well [13,14]. Part of the reason for the many defects observed is the perception that shielded arc welding is a simple process that can be performed by low-skilled personnel, which is definitely not true for parts which are subject to dynamic loading.

With respect to forged parts, crankshafts seem to be the most critical component according to literature reports [14–19]. In all cases but one, reports relate to heavy engines for trucks and generators, which are produced in significantly smaller series than standard combustion engines for passenger cars. The same observation holds for the few available reports on the failure of axles [6,13,20,21]. In this chapter, improper repairs (or reinforcements) were present in two cases out of five; in one case the repair showed no effect at all, in the other one the consequences were deleterious. It can be concluded that knowledge about structural mechanics and materials failure is often insufficient at the operational level to take decisions with respect to the reparation or redesign of structural components which are subject to dynamic loads.

An additional factor is the lack of detailed data on vehicle dynamics and precise operation conditions. This is reflected in the finite-element analysis of the individual parts, where uncertainties on the precise loading conditions may yield results which

are either above or below the safety limit of a component, depending on the hypotheses made. Methods are available to resolve this uncertainty by iterative refinement of vehicle dynamics and analysis of the entire structure, but these are expensive in terms of human resources [2,3]. In the present work, the finite-element models serve to illustrate the essential features of each failure case, without providing fully quantitative proof of the hypotheses; classical fracture analysis provides the additional evidence required to reach conclusions.

4 CONCLUSION

For the hollow structural sections studied in this overview, material selection and poor manufacturing were the main causes for failure, with design coming in as a secondary factor. The need for high-quality welds in structural parts subject to dynamic loading and fatigue was not recognized at the production level. In one case reviewed here, the failure of a forged axle was directly due to the quality of the material employed, while the design of the forging process and the heat treatment may have had a secondary influence. Surprisingly, similar failure causes were reported for the axle of advanced carriages for a high-speed railway which are subject to more stringent quality control procedures. In a second case, the quality of the material was a secondary factor, with the design of the part being primary. Specifically, the failure to take into account curvature as a stress raiser under bending-torsion conditions led to the underestimation of the dimensions of the Z-bar studied. Also in the case of the torsion bars, which showed excellent material quality and manufacturing, the effect of curvature was underestimated. The presence of unforeseen operation conditions exacerbated the problem, resulting in the thermal degradation of elastomer parts which were assumed to prevent the type of damage initiation which was observed.

ACKNOWLEDGMENTS

We acknowledge technical assistance by E. Ramos, I. Cueva, J. Romero, and G. Álvarez as well as financial support by DGAPA grants IN117412 and PE102612.

REFERENCES

[1] Heyes AM. Automotive component failures. Eng Fail Anal 1998;4:129–41.
[2] Reyes Ruiz CA, Ramírez Díaz EI, Ruiz Cervantes O, Schouwenaars R, Ortiz A. Modelling of the suspension of a passenger bus by finite element software. In: EngOpt 2012—3rd international conference on engineering optimization, Rio de Janeiro, Brazil, 01–05 July; 2012.
[3] Ruíz O, Ramírez EI, Jacobo VH, Schouwenaars R, Ortiz A. Efficient optimisation of the structure of a passenger bus by iterative finite element models with increasing degrees of

complexity. In: EngOpt 2012—3rd international conference on engineering optimization, Rio de Janeiro, Brazil, 01–05 July; 2012.
[4] ASTM E 18–98. Standard test methods for rockwell hardness and rockwell superficial hardness of metallic materials. West Conshohocken, PA: American Society for testing Materials; 2000.
[5] ASTM-E415. Standard test method for optical emission vacuum spectrometric analysis of carbon and low-alloy steel. West Conshohocken, PA: American Society for Testing Materials; 2000.
[6] Klinger C, Bettge D. Axle fracture of an ICE3 high speed train. Eng Fail Anal 2013;35:66–81.
[7] Molinari A, Germain I. Self heating and thermal failure of polymers sustaining a compressive cyclic loading. Int J Solids Struct 1996;33:3439–62.
[8] Ovalle Rodas C, Zaïri F, Naït-Abdelaziz M. A finite strain thermo-viscoelastic constitutive model to describe the self-heating in elastomeric materials during low-cycle fatigue. J Mech Phys Solids 2014;64:489–93.
[9] Han C, Zhang J, Liang Z. Thermal failure of rubber bushing of a Positive Displacement Motor: study based on thermo-mechanical coupling. Appl Therm Eng 2014;67:489–93.
[10] Zhang J, Liang Z, Han C. Failure analysis and finite element simulation of key components of PDM. Eng Fail Anal 2014;45:15–25.
[11] Cho HN, Lim JK, Choi HH. Reliability-based fatigue failure analysis for causes assessment of a collapsed steel truss bridge. Eng Fail Anal 2001;8:311–24.
[12] Mashiri FR, Zhao XL, Grundy P. Fatigue tests and design of welded T connections in thin cold-formed square hollow sections under in-plane bending. J Struct Eng 2002;128:1413–22.
[13] Asi O. Fatigue failure of a rear axle shaft of an automobile. Eng Fail Anal 2006;13:1293–302.
[14] Fonte M, Li Bin, Reis L, Freitas M. Analysis of a diesel generator crankshaft failure. Eng Fail Anal 2009;16:2333–41.
[15] Ktari A, Haddar N, Ayedi HF. Fatigue fracture expertise of train engine crankshafts. Eng Fail Anal 2011;18:1085–93.
[16] Jiménez Espadafor F, Becerra Villanueva J, Torres García M. Analysis of a diesel generator crankshaft failure. Eng Fail Anal 2009;16:2333–41.
[17] Pandey RK. Failure of diesel-engine crankshafts. Eng Fail Anal 2003;10:165–75.
[18] Asi O. Failure analysis of a crankshaft made from ductile cast iron. Eng Fail Anal 2006;13:1260–7.
[19] Yu Z, Xu X. Failure analysis of a diesel engine crankshaft. Eng Fail Anal 2005;12:487–95.
[20] Hirakawa K, Toyama K, Kubota M. The analysis and prevention of failure in railway axles. Int J Fatigue 1998;20:135–44.
[21] Alihosseini H, Dehghani K. Modeling and failure analysis of a broken railway axle: effects of surface defects and inclusions. J Fail Anal Prev 2010;10:233–9.

CHAPTER

Failure of steel couplings used in railway transport

20

Teresa L.M. Morgado

Engineering Departmental Unit of Tomar Polytechnic Institute, Escola Superior de Tecnologia de Abrantes do Instituto Politécnico de Tomar, Abrantes, Portugal

ICEMS-IST-UL—Institute of Materials and Surfaces Science and Engineering, Lisbon University, Lisboa, Portugal

CHAPTER OUTLINE

1 INTRODUCTION

Railway structures and components, like rails, gearboxes, couplings, wagons, etc., are subject to fatigue problems that can lead to complete failure. With the exception of the rails in which a major mechanism of damage is the freight forwarding and fatigue of bearing, as documented in Ref. [1], to remaining structural components, the main aspect to be taken into account in the design is definitely structural fatigue.

Handbook of Materials Failure Analysis With Case Studies from the Aerospace and Automotive Industries.
http://dx.doi.org/10.1016/B978-0-12-800950-5.00020-X

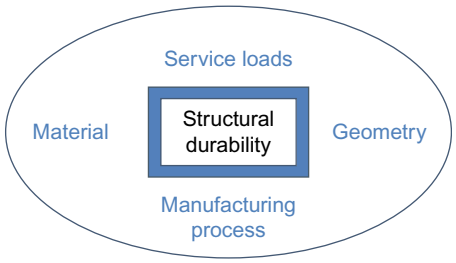

FIGURE 20.1

Structural durability parameters.

As is shown in Figure 20.1, the parameters that influence the structural durability of mechanical components are service loads, material properties, geometry, and the manufacturing process. The interaction of these four parameters must be taken into account at the design stage, in order to define the component lifetime.

Structural fatigue, often originates in cracking in critical areas [2–4], is caused by the dynamic loads that are exerted by various effects with varying importance depending on machines element or structural component type.

In fatigue design of railway components it is necessary to take into account the following requirements: weight loads and transported loads, transmissions loads and torque, centrifugal and inertial forces, irregularities of the rails, aerodynamic and environmental effects. All these scenarios contain vibrational phenomena that are time dependent. Therefore, to ensure safety for life without failure problems, the structural components must be designed to fatigue. In other words, the structural durability of the components must be taken into account [5].

In contrast to the case of the static design based on the yield strength or ultimate tensile strength of the material, that is the allowable or permissible stresses, the design of fatigue is based on the SN curves for a range of constant load or fatigue life curves for loads of varying amplitude [6] or on strain-based approach [7].

In the study of the loads influence on fatigue life (number of fatigue cycles), it is observed that in the case of variable amplitude loading, the fatigue life depends on the cumulative frequency distribution (spectrum shape), and may be several orders higher than that seen in constant amplitude loading [5,8]. As load-time histories depend on the particular application (offshore, aeronautics, railways, automotive, bridges, etc.) and function of the components. In the past 80 years, different application related to the standard spectra were developed [9] and are still under development.

The importance of the "load spectrum" by Ernest Gaβner was recognized in 1938, with procedures formulated for simulating the variable amplitude loading for aeronautical structures. In the 1960s, with the emergence of servo hydraulic testing machines, the historical program "eight-block-program test" could be replaced by more realistic load versus time process, using the cumulative frequency distribution known as the Gaussian function.

In mechanical systems, the load applied or processed material defects are stochastic variables. In recent years, an effort was made to employ the probability theories in the mechanical component's design. Currently, building codes such as Eurocode 3 [10] already consider probabilistic databases.

This chapter presents the study case results obtained in a failure analysis carried out on a cast steel railway component in an electric trains used for coal transportation.

2 PROBLEM DEFINITION

A significant number of failures have occurred in mechanical components (couplings) of the coal freight trains (Figure 20.2) which led to disruption of service and economic losses. The couplings were obtained by sand casting process, with ASTM A148 90-60 specifications [11], and the owner being a multinational thermoelectric company, Tejo Energia S.A Company.

The cracks exhibit the classical mechanisms of fatigue cracks under dynamic loads. Cracks, detected during the maintenance work, propagated from the transition radius between the "head" and the "body" of the railway coupling (Figure 20.3), which is a zone of stress concentration.

The first failure study in a coupling railway (diesel locomotive) has been conducted by the author [11], where strain gauge data was analyzed from which data fatigue cycles were derived.

A second failure study was made when the line became electrified and will be presented and discussed in this chapter. The coal, that will be transformed in electric power, is loaded in an electric freight train which consists of 22 wagons and 2 locomotives, corresponding to a total of 2154 tons. These trains make two travels of about 334 km each, 300 days a year. These travels includes one way in the South

FIGURE 20.2

Out of service cast steel railway couplings.

FIGURE 20.3

Crack localization.

to North direction, fully loaded, and then returns empty in the North to South direction. To study service solicitations, the loading data were obtained while the train was in service, during two routine journeys: with loaded train from Sines Harbour to Ermidas village (47 km) and with empty train, from Ermidas to Sines Harbour. These journeys were chosen because the track profile is the most accidental one; in other words, present the highest altitude differences of the travel.

3 MATERIAL AND GEOMETRY OF THE RAILWAY COUPLING

For performing the required function, the railway coupling component has to show certain strength, depending on the material, manufacturing, and geometry. In Figure 20.4, the interior complex geometry of the coupling "head" can be observed.

The casting process offer unique cost advantages over other manufacturing methods for many components, especially those having complex three-dimensional geometry such as the railway coupling. Nevertheless, several classes of defects can develop in the casting process. While some defects can affect only the exterior appearance, others can have major adverse effects on the structural integrity of the manufactured parts, including fatigue problems.

The problem of the fatigue strength estimation of materials/components containing natural defects, inclusions, or inhomogeneities is of great importance from both a scientifically or industrial point of view. Undoubtedly, an important factor affecting failure of components and structures is the presence of flaws due to processing, manufacturing, or mechanical damage occurring during service. The presence of flaws in the materials leads to failures even if low stresses are applied. It is therefore of primary importance to consider such defective features such as input parameters in fatigue limit assessment. The fatigue limit of cast materials is mainly controlled by the presence of casting defects like micro shrinkages or dross defects [12–14].

FIGURE 20.4

Complex geometry of the coupling "head."

But there are few models that can predict the effect of nonmetallic inclusions on fatigue strength. This may be because adequate and reliable quantitative data on nonmetallic inclusions are hard to obtain. Murakami and coworkers [14] have investigated the effects of defects, inclusions, and inhomogeneities on fatigue strength of high-strength steels and expressed the fatigue limit as a function of Vickers hardness and the square root of the projection area of an inclusion or small defect (Equation 20.1).

$$\sigma_{w(1)} = \frac{C(\mathrm{Hv}+120)}{(\sqrt{\mathrm{area}})^{1/6}}\left[\frac{1-R}{2}\right]^{\alpha} \tag{20.1}$$

where Hv is Vickers hardness in kgf/mm^2, $\sqrt{\mathrm{area}}$ come in μmm, constant C is equal to 1.43 for superficial inclusion and defects and $C = 1.41$ for inclusion and defects inside of the component, α variable is given by Equation (20.2).

$$\alpha = 0.026 + \mathrm{Hv} \times 10^{-4} \tag{20.2}$$

That model does not specify the effect of the number of cycles to failure. Bathias and Paris [15] considered a new empirical formula (20.3) that included the number of cycles to failure.

$$\sigma_{w(2)} = \frac{\beta(\mathrm{Hv}+120)}{(\sqrt{\mathrm{area}})^{1/6}}\left[\frac{1-R}{2}\right]^{\alpha} \tag{20.3}$$

where R is stress ratio ($R = \sigma_{\min}/\sigma_{\max}$), the variable β is given by Equation (20.4) in case of inclusions and defects inside the component and by Equation (20.5) in case of inclusions and defects at the surface of the component.

$$\beta = 3.09 - 0.12 \ln N_f \tag{20.4}$$

$$\beta = 2.79 - 0.108 \ln N_f \tag{20.5}$$

Morgado and Brito [16] had discussed the casting defects influence on the railway component fatigue limit by the application of Murakami-Endo´s model and the Bathias and Paris model. In the comparative study of the nonmetallic inclusions, porosities, and shrinkage cavities in the inside and at the surface of the component, when comparing fatigue strength, the model of Bathias and Modified Paris presented a percentage of error in relation to the maximum experimental fatigue strength, (for errors values until 10%) which was lower than the presented ones for the model of Murakami. Therefore, more research is needed in this field.

3.1 MATERIAL CHARACTERIZATION

There are some basic categories of casting defects standardized by "International Committee of Foundry Technical Associations," as cited by Kalpakjian [17]. Among them "cavities" consists of rounded or rough internal or exposed cavities, including blowholes, pinholes, pipes, shrinkage areas, and porosity. Because of their thermal expansion characteristics, metals shrink during solidification, and cooling to ambient temperature. Shrinkage cause dimensional changes and sometimes cracking and cavities; therefore, it is an important parameter to consider when determining the resistance and toughness of the casting mechanical components. Porosity may be caused by shrinkage and/or off gassing during solidification. It causes adverse effects on the mechanical properties of the castings and may affect the fatigue resistance of the component.

The railway coupling's chemical composition showed that the cast material is that of a low-alloy manganese steel with 0.31% carbon, 1.7% manganese, 0.37% silicon, and small percentages of additional elements.

Cast steels containing those percentages of manganese and silicon present good mechanical properties that can improved by heat treatment. The sulfur and phosphorus contents are below the minimum imposed by ASTM requirements for this class of steel casting. Furthermore, manganese tends to inhibit the effect of sulfur promoting intergranular weakness.

Tensile test on the mechanical properties of the railway coupling that was obtained for the study presented the following mean values [11]: 0.2% yield stress, $S_y = 463.95$ MPa; ultimate tensile stress, $S_{ut} = 659.58$ MPa; rupture strain, $\varepsilon = 28.5\%$; reduction of area, $q = 47.9\%$; Young modulus, $E = 207$ GPa; ratio Poisson, $v = 0.3$.

From results of chemical analysis and mechanical tests, as it has been said before, the steel in study was included in class 90-60 of ASTM A-148 Standard—Steel casting for structural applications.

3.2 METALLOGRAPHIC ANALYSIS

Several samples, obtained from the critical zone of the piece (Figure 20.3), were prepared for microstructural analysis. Samples preparation followed normal metallographic procedures. After polishing the surfaces, previous microscopic observations were made without etching to visualize porosities and other casting defects.

Micrographs were obtained from an OLYMPUS DP10 digital camera attached to a Metallurgical Microscope OPTISHOT of Nikon Corporation and the software used was OLYMPUS C-Y95.

Relevant features exhibited were the great density of spherical micro-porosities distributed in a band adjacent to the periphery of the samples. The porosity observed was spherical with smooth walls; which could be due to dissolved gases expelled from the solution during cooling. Pipes and rounded or rough cavities, which had larger dimensions than the porosities, were also detected, very often in the core of the sample. Both types of irregularities were compared with those specified by Standard Reference Photographs for Casting Solidity—AAR-M; 211-92. Results were inconclusive for the purpose since this standard did not make any reference to the resistance required of the component for each function.

For microstructure identification, posterior etching was made by 25 s Nital or Vilela reagent. Light microscopy analysis demonstrated that the microstructure present was predominantly low-carbon tempered martensite. Due to high temper temperature (close 700 °C), a great amount of fine carbide dispersion was found, mainly on the prior austenite grain boundaries. Other features exhibited by the microstructure were some proeutectoid ferrite, within the interior or outlining the previous austenite grain. Also, impurity segregations, which are oxides from the casting process, were observed in some regions of the samples.

3.3 QUANTITATIVE ANALYSIS OF CASTING DEFECTS

Quantitative analysis of the casting defects was performed by a specific computer program Matrox Inspector® of Matrox Electronic Systems, Ltd. suited for microstructural defect inspection. Due to its localization in a band close to the outer surface of the piece, porosities were quantified while comparing the total photomicrographs area. Furthermore, pipes and shrinkage cavities were compared with the total sample area because of their small number and bigger dimensions.

The counting method used was based on the minimum area of the defects and in their types forming by this way classes/categories. Frequency bar graphs presented in Figures 20.5 and 20.6, detail the types of nonmetallic inclusions, porosities, and shrinkage cavities as well as types of tempered martensite, fine carbide, and acicular ferrite, respectively. Minimum areas in [mm^2], considered were the following:

- Porosities, shrinkage cavities, and nonmetallic inclusions: [8.16×10^{-3}], [8.82×10^{-3}], [4.41×10^{-3}], [2.20×10^{-3}], [4.41×10^{-4}], [8.82×10^{-6}], [4.41×10^{-6}], [2.20×10^{-6}];
- Tempered martensite, fine carbide, and acicular ferrite: [3.53×10^{-5}], [1.77×10^{-5}], [8.83×10^{-6}], [3.53×10^{-3}], [5.50×10^{-7}], [2.75×10^{-7}], [2.20×10^{-7}], [1.37×10^{-7}], [2.75×10^{-8}].

Of the analyses that were carried through descriptive statistics, it was verified that of the defects observed of nonmetallic inclusions, porosities, and shrinkage cavities types, 64.4% were inside of the component and 78.75% were at the surface and belonged to

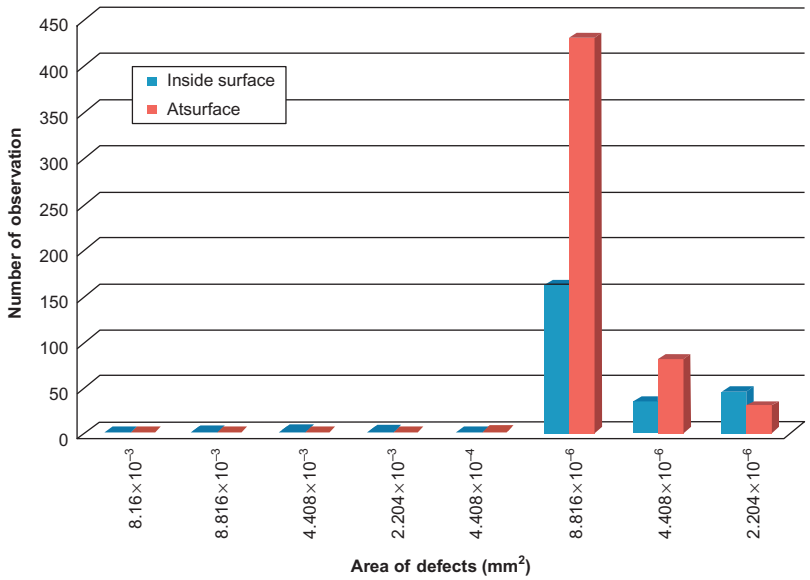

FIGURE 20.5

Total of nonmetallic inclusions, porosities, and shrinkage cavities defects observed.

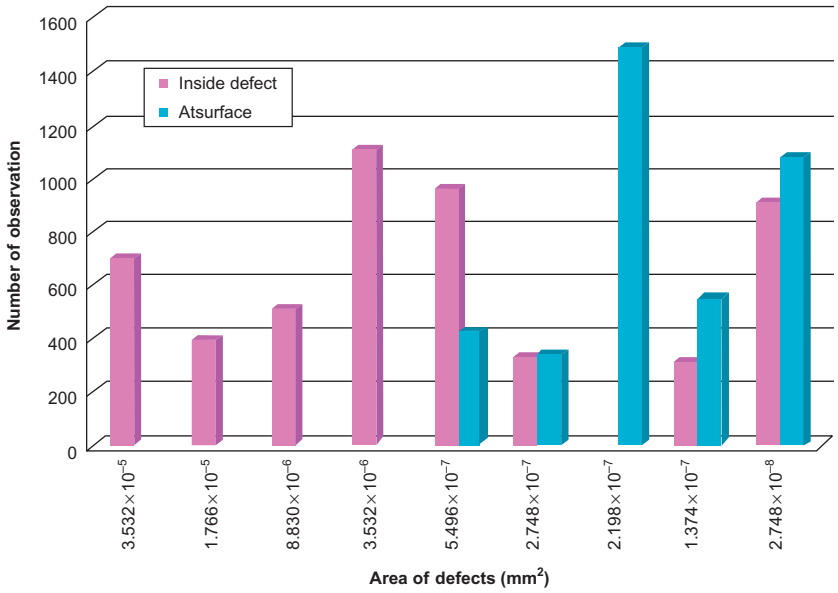

FIGURE 20.6

Total of tempered martensite, fine carbide, and acicular ferrite details observed.

the [8.816×10^{-6}] mm^2 categories; observed details of type tempered martensite, fine carbide and acicular ferrite were verified that the [2.20×10^{-7}] mm^2 and [3.53×10^{-6}] mm^2 categories corresponded, respectively, to 38.21% of defects present at the surface of the component and 21.08% were inside of the component.

4 FATIGUE TESTS: GENERATE LIFE FATIGUE CURVE

Initiation fatigue crack tests are based on the following procedure in which a sample or component is subjected to a cyclic loading up to failure. A large part of the cycles in these trials was used for crack initiation. Despite the fact that fatigue tests conducted on small specimens did not establish precisely the fatigue life of the component, these tests provided data on the intrinsic behavior on the initiation crack of the metal or alloy. As a result, this data can be used to develop criteria to prevent fatigue life situations, involving damaged coupling replacements.

Twelve machined specimens with cylindrical geometry were tested according to the standard ASTM E8 [18], in the Mechanical Testing Laboratory of the Mechanical Engineering Department of Lisbon University. The specimens were tested in tensile with constant amplitude alternating cycles. The stress ratio value was $R = 0.05$. The frequency of the cycles used in the tests was 8-10 Hz. The test ended when more than 6,000,000 cycles were obtained [11].

Microscopy observations of longitudinal sectional view of specimens tested to the fatigue were made. The results of specimens 7 and 9 can be observed in Figure 20.7. The conclusions of the microscopy observation was that there is a direct relationship between fatigue resistance, size distribution, and porosity, expressed by a marked decrease in the fatigue life of samples containing larger pores and distribution of nonmetallic inclusions.

Casting defects measured in the specimens are acceptable in accordance with the present criteria railway sector. To guarantee the highest fatigue strength values, the

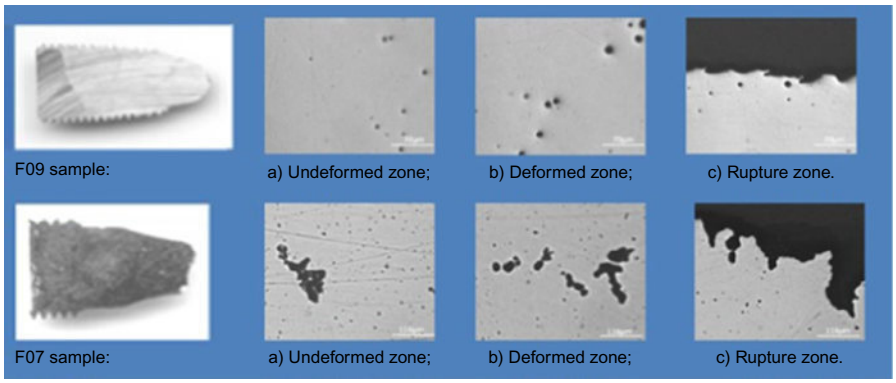

FIGURE 20.7

Microscopy observations of longitudinal sectional view of F07 and F09 fatigue specimens.

component must present a raised level of health in order to avoid the significant increase of the dimension of defects that occurs when the component is requested to the fatigue criteria.

Data that present a scatter pattern within the results requires a proper statistical treatment as proposed in ASTM E739-91 [19].

The slope of the fatigue life curve was obtained for the number of cycles $N = 1 \times 10^4$ and $N = 1 \times 10^7$. On the log-log scale, the part of an S-N curve is given by the relation (20.6).

$$Y = a + bX \tag{20.6}$$

Where $Y = \log N$, $X = \log S$, $a = \log C$ and $b = -m$, N is the number of elapsed cycles, S is the applied nominal stress, and both a and b are constants of the S-N curve.

Parameters a and b must be estimated from the data points (S_i, N_i), $i = 1, 2, \ldots, n$. Using the method of least squares, a and b are estimated by $\hat{a}$ and $\hat{b}$. The "best-fit" line or least-squares line is given by Equation (20.7).

$$\hat{Y} = \hat{a} + \hat{b}X \tag{20.7}$$

Where, $\hat{Y}$ is the estimate of Y, the mean of Y at given X. Thus, N is the estimate of the median of $N|S$.

Log-normal life distribution can be used to determine any probability of failure, P_f. The probability of survival is defined as follow (Equation 20.8).

$$P_s = 1 - P_f \tag{20.8}$$

S-N curves are obtained from the results of fatigue tests with normalized specimens from a real component. Therefore, it is necessary to consider reduction factors, identified by Marin [20], which quantified the effects of surface condition, size, loading, temperature, and miscellaneous items. The Marin Equation (20.9) is written as:

$$S_e = K_a K_b K_c K_d K_e S'_e \tag{20.9}$$

where K_a is the surface condition modification factor, K_b is the size modification factor, K_c is the load modification factor, K_d is the temperature modification factor, K_e is the miscellaneous effects modification factor, and S'_e is the experimental endurance limit.

Life fatigue curves considering the finishing adjustments of laminated ($K_a = 0.80$) and hot-rolled specimens ($K_a = 0.53$) [6,21] are given for a reliability of 50%, 90%, 95%, 99% in a Log-Normal distribution, according to expressions (20.10)–(20.13), respectively.

$$NS^{10.147} = 6.95 \times 10^{29} \tag{20.10}$$

$$NS^{8.8335} = 8.81 \times 10^{25} \tag{20.11}$$

$$NS^{8.4654} = 7.14 \times 10^{24} \tag{20.12}$$

$$NS^{7.7693} = 6.15 \times 10^{22} \tag{20.13}$$

5 SERVICE ACQUISITION AND DATA TREATMENT

Strain gauge-based techniques were used to measure strain and subsequent stresses in the rail components. As been said before, in this study case, service tests have been carried out on the representative journeys of the coal transportation train. Continuous acquisition of measurements of the strain gauges rosettes were carried out over 48 km, on the coupling between the locomotive and the first wagon (Figure 20.8), where higher loads were expected.

The procedure followed in this study case determined the strain state at one point or multiple points of the component from a set of conditions that included its shape or geometry, its connection to the external environment and the type of requirements to which these components have to comply with. Stress state information combined with mechanical properties of the material was used to predict the damage of the mechanical component analyzed. The stress ranges were compared with the material yield stress to predict or explain the occurrence of ruptures caused by fatigue. Two approaches will be presented in this chapter, one using the Palmgren-Miner Rule modified by Haibach and the other using Palmgren-Miner Rule and Goodman relation.

5.1 STRAIN GAUGE ACQUISITION

To determine the component strains and respective principal stresses while in service, 10 electric strain gauges of the type 45° rosette have been bonded. These type of rosettes have three strain gauges that make 45° between them; one longitudinal/axial direction, other oblique, and the other transversal to the axial direction. Figures 20.9 and 20.10 illustrate, by scheme and by photography of the respective strain gauges bonding on the real component, the positions of rosettes (R1, R2, R3, R4, R5, R6, R7, R8, R9, and R10) and their respective directions. Rosettes 1 and 6 were bonded at the crack zone showed in Figure 20.3 and labeled with a red circle in Figure 20.9.

In the acquisition process, it was necessary to use only 30 channels on the dynamic strain gauge bridge (National Instruments' SCXI-1001 chassis with 4

FIGURE 20.8

Coupling instrumented.

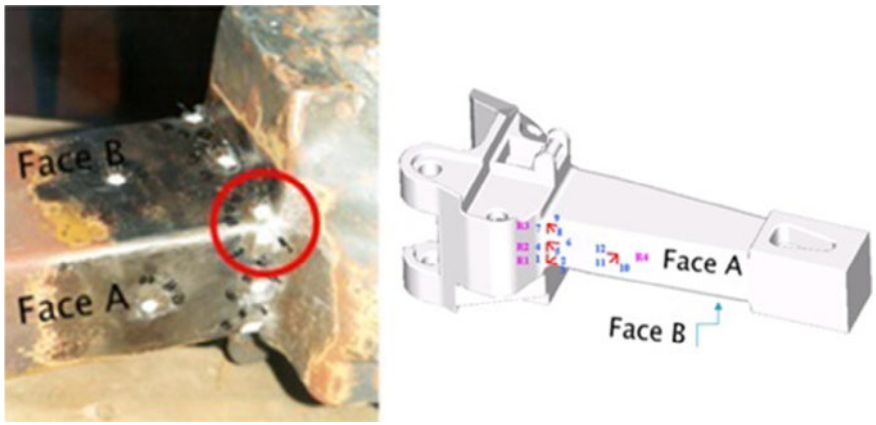

FIGURE 20.9

Position of R1, R2, R3, and R4 rosettes.

SCXI-1520 modules of 8 channels each belonging to the Mechanical Testing Laboratory of Mechanical Engineering Department—University of Lisbon), in quarter bridge configuration. The acquisition frequency was set at 30 Hz. The data was collected with a portable PC and a LabView 7.0 processing system was used for treatment and analysis of the signals [22].

From the data obtained, it was verified that the highest values of strains occurred on longitudinal direction, with strain gauge 3 of rosette 1 (Figure 20.11) and strain gauge 18 of rosette 6 (Figure 20.12; see also Figures 20.9 and 20.10). So the most "critical" rosettes were rosette 1 and 6, with strain spectra shown in Figures 20.11 and 20.12, respectively. Strain spectrum of strain gauge 18 presented the highest values, 1500 μstrain, as can be observed in Figure 20.12.

5.2 UNIAXIAL BEHAVIOR

The uniaxial or biaxial nature of the stress states is appraised by the value of the angle, θ_1, between the largest strain value and principal direction 1. This angle, represented in Figure 20.13, was calculated using Equation (20.14).

$$\tan 2\theta = \frac{2\varepsilon_b - \varepsilon_a - \varepsilon_c}{\varepsilon_a - \varepsilon_c} \tag{20.14}$$

Where $\varepsilon_a, \varepsilon_b$ and ε_c represents the three strains gauges values obtained in each rosette; and these values must respect the following: $\varepsilon_a > \varepsilon_b > \varepsilon_c$ and $\varepsilon_b > (\varepsilon_a + \varepsilon_c)/2$.

The principal and equivalent stresses have been calculated using the expressions (20.15) and (20.16).

$$\sigma_{1,2} = \frac{E}{2}\left(\frac{(\varepsilon_a + \varepsilon_c)}{1+v} \pm \frac{\sqrt{2}}{1+v}\sqrt{(\varepsilon_a - \varepsilon_b)^2 + (\varepsilon_b - \varepsilon_c)^2}\right) \tag{20.15}$$

$$\sigma_{eq} = \frac{1}{\sqrt{2}}\sqrt{(\sigma_1 - \sigma_2)^2 + \sigma_2^2 + (-\sigma_1)^2} \tag{20.16}$$

FIGURE 20.10

Position of R5, R6, R7, R8, R9, and R10 rosettes.

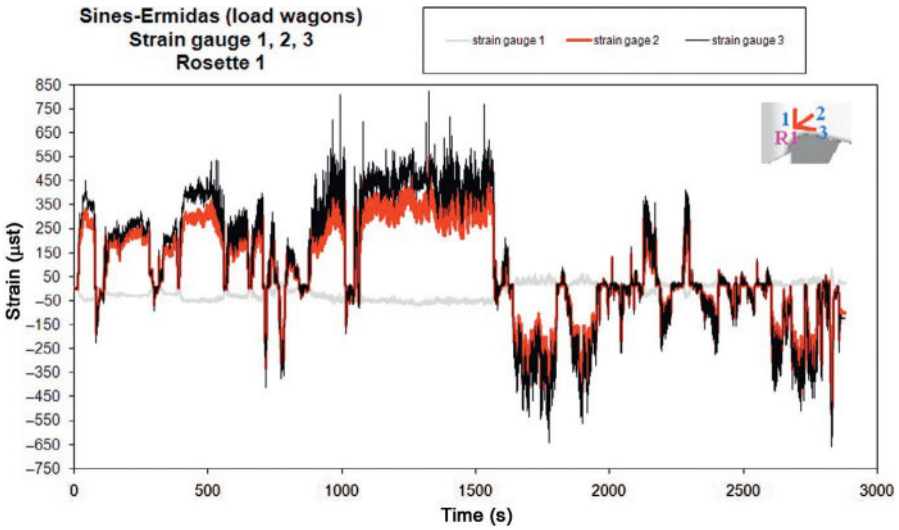

FIGURE 20.11

Strain spectra of strain gauges 1, 2, 3 of rosette 1.

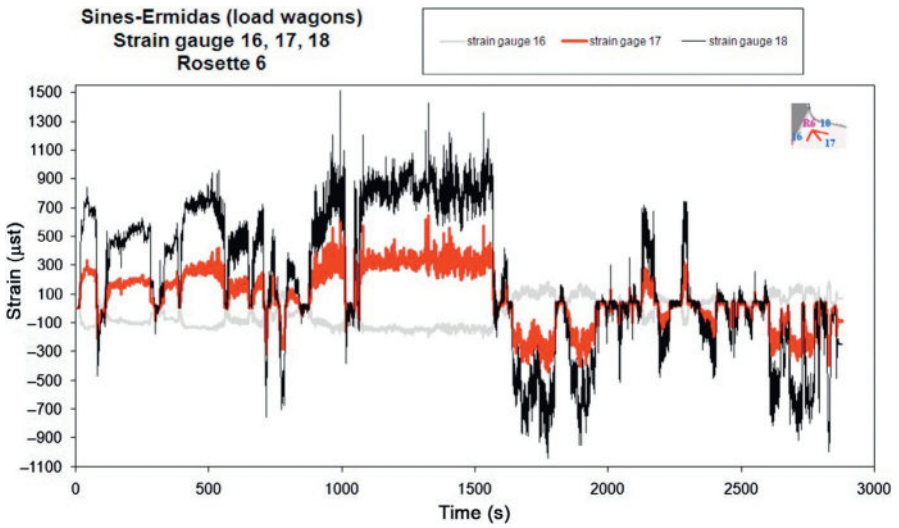

FIGURE 20.12

Strain spectra of strain gauges 16, 17, 18 of rosette 6.

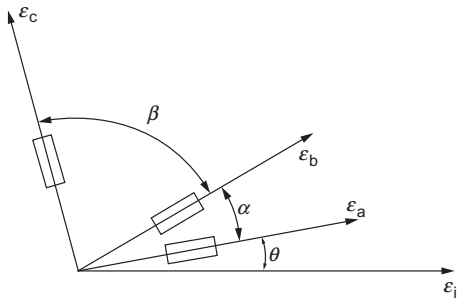

FIGURE 20.13

Schematic representation of strain gauges on a rosette [23].

where σ_1 and σ_2 are the longitudinal and transversal stresses to the movement/travel direction, respectively, and σ_{eq} represents the equivalent stress on the plane.

Diagrams of the longitudinal angle versus principal stresses, σ_1, below 50 MPa and above 50 MPa of rosette 6 (as been denominated before, the most "critical" one) can be observed in Figures 20.14 and 20.15, respectively. Results of Figure 20.14 show that the angle values are high in the beginning of the journey, when the stresses are very low, therefore these results are not representative of the service solicitations and must not be taken into consideration. In Figure 20.15, where stresses are higher than 50 MPa, the angle is lower than 6°; so it can be said that the component is subjected mainly to tensile loads.

5.3 SERVICE STRESS ANALYSIS

Once the stress spectrum is obtained, it is necessary to characterize the stress cycles and its counting. The most usual methods are Range-Pair Method, Leving-Crossing Method, and Rainflow Counting [24]. In this study case, the Rainflow method [25] was selected using the equivalent stresses.

One routine was developed for the purpose of counting fatigue cycles where stress data were organized in 2 MPa amplitude classes (Sturges rule) considering only the stresses above 50 MPa. The results were plotted in terms of stress levels as a function of the accumulated number of cycles. Figure 20.16 reflects the maximum equivalent stresses of rosettes 1, 6, and 7 (see Figures 20.9 and 20.10). From the Figure 20.16 analysis, it can be concluded that the maximum service stresses using the equivalent stress criterion remain below the yield stress of the material. The number of accumulated cycles varied between 3570 (rosette 1) and 7997 (rosette 6), while the peak stresses varied between 126 MPa (rosette 7) and 308 MPa (rosette 6). Of these conclusions, it can be considered that rosette 7 gave the "nominal" data, that is, the reference data because it is far away from the stress concentration zone (see Figure 20.3).

The stress ratio ($R = \sigma_{min}/\sigma_{max}$) is an important fatigue parameter in the stochastic loads case, and in some life prediction approaches is taken into account. For this

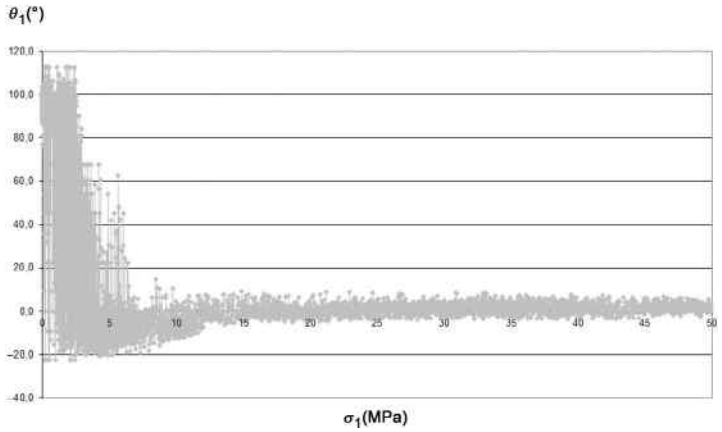

FIGURE 20.14

Rosette 6 diagram of the longitudinal angle versus principal stress σ1 lower than 50 MPa.

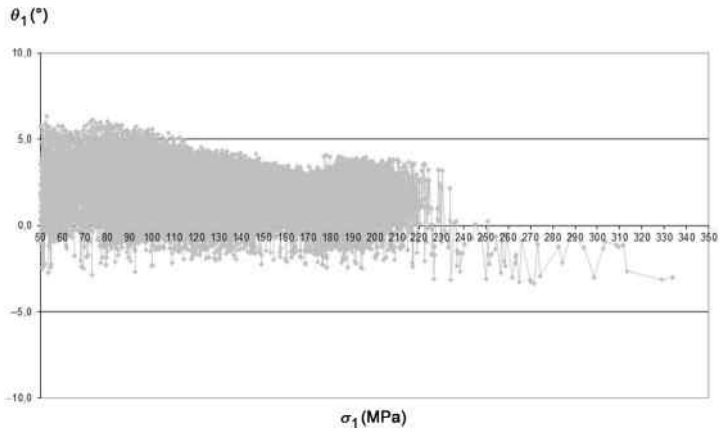

FIGURE 20.15

Rosette 6 diagram of the longitudinal angle versus principal stress σ1 higher than 50 MPa.

railway component, a service stress ratio study was made. Figure **20.17** presents the stress ratio versus number of accumulated cycles of fatigue diagramed for rosette 6. It can be observed that for the values in [0.97; 0.98] and [0.98; 0.99], the stress ratio classes corresponded respectively to 632 and 802 fatigue cycles while the [0.99; 1] class presented 1749 accumulated fatigue cycles, for a total of 7997 accumulated cycles.

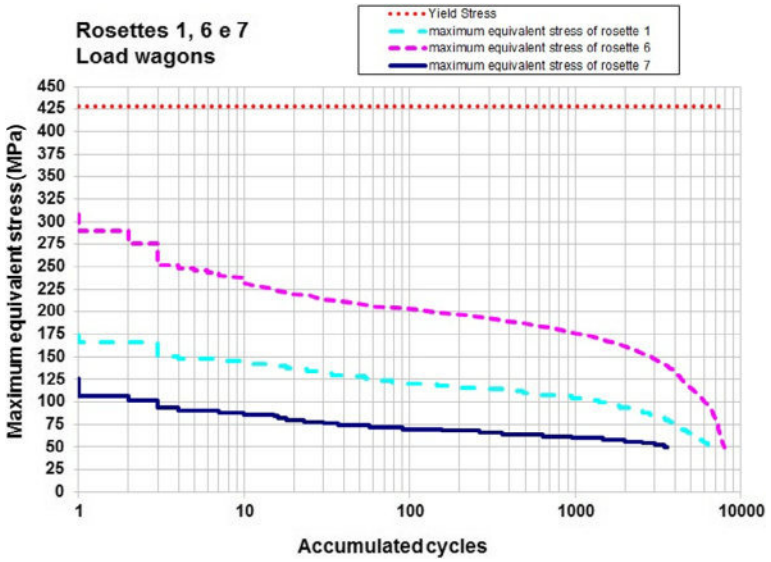

FIGURE 20.16

Maximum equivalent stresses of rosette 1, 6, and 7 versus accumulated cycles.

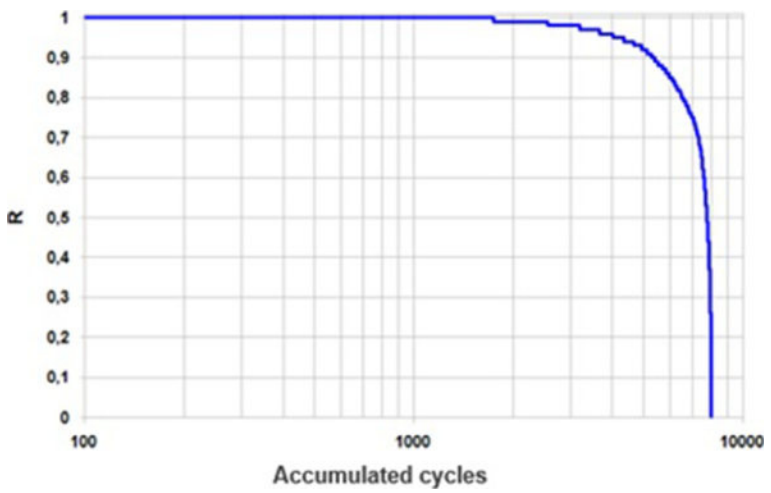

FIGURE 20.17

Diagram of the stress ratio versus accumulated cycles for rosette 6 [22].

6 LIFE PREDICTION APPROACHES

There are a variety of life prediction approaches based on ε-N or S-N curves. With S-N curve different criteria can be used, like Goodman, Soderberg, ASME, etc., [21] with Palmgren-Miner Rule [26], or Palmgren-Miner Rule modified by Haibach [9,27] to predict the damage and the life of a component.

Morgado conducted a failure analysis in gearboxes housing of railway vehicles [28], where loading data was also obtained while in service, using strain gauge, in two routine journeys: Lisbon-Oporto intercity train, with maximum speed of 160 km/h, and Entroncamento-Guarda freight train, with a maximum speed of 120 km/h, with Goodman diagrams employed.

Study of the elastic and plastic deformations, promoted by the stress concentration in the railway coupling, using the Local Approach with Morrow equation and Muralidharan and Manson equation were also presented and discussed by Morgado [7].

As it has been said before, in this study case two approaches based on S-N curves are presented, compared and discussed with important conclusions made.

6.1 LIFE PREDICTION USING PALMGREN-MINER RULE MODIFIED BY HAIBACH

The fatigue Damage (represented by variable D) was calculated considering Palmgren-Miner rule modified by Haibach [9], where the damage content of a spectrum with size L_s, is determined by the expression (20.17) and with that value, D_{spec}, the real damage sum, was calculated from the experimental results, using the expression (20.18) and S-N curves of different reliabilities using Equations (20.10)–(20.13).

$$D_{spec} = \sum_{i=1}^{n} \frac{n_i}{N_i} \tag{20.17}$$

$$D_{real} = \frac{D_{spec}}{L_s} \bar{N}_{exp} \tag{20.18}$$

where n_i is the number of cycles for each range stress class on histogram, N_i is the number of cycles for each range stress class histogram in curves S-N, L_s is the spectrum size, and $\bar{N}_{exp}$ is the size of standardized variable in Gaussian distribution.

Therefore in this method, the cumulative frequency distribution of stress range must be determined for each rosette. Several cumulative frequency distributions of equivalent stress ranges (spectrum) are presented in Figure 20.18.

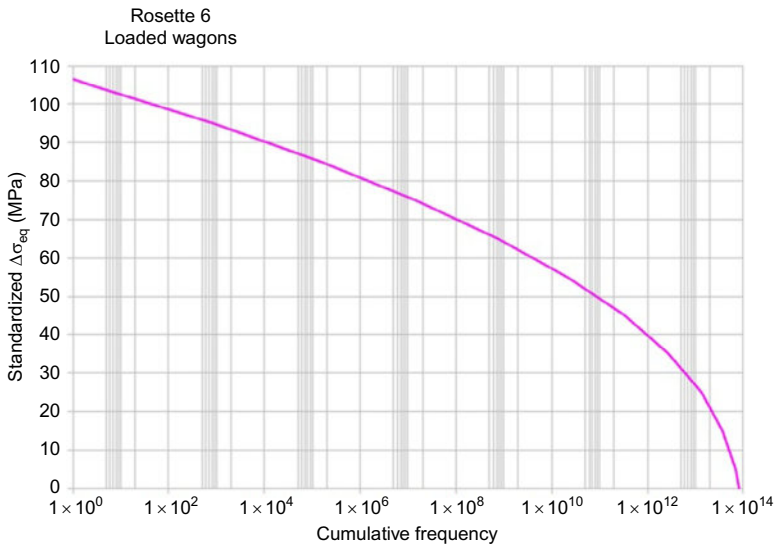

FIGURE 20.18

Cumulative frequency distribution of equivalent stress of rosette 6.

Life prediction, in years, considering the most critical rosettes 1 and 6, for the reliabilities of 50%, 90%, and 95% (Equations 20.10–20.12) are presented in Figure 20.19. It can be observed that for 95% of the reliability, rosette 6 has a life prediction of 7 years, while the life prediction for reliability of 90% is that of 13 years. The author has determined that by the life predictions for all the other rosettes with the respective cumulative frequency distribution of equivalent stress ranges, it can be concluded that for reliabilities upper than 95% the life prediction is higher than 26 years [6].

6.2 LIFE PREDICTION USING PALMGREN-MINER RULE AND GOODMAN EQUATION

Figure 20.20 represents the damage calculation routine used by the author to determine fatigue damage. In this method, the damage was calculated considering the linear model of accumulation of damage using Miner's rule [26]. The damage results were obtained for the maximum equivalent stresses using the S-N curves for 50%, 90%, 95%, and 99% reliability levels. And once the mean stress is not constant, the damage calculation was carried out one cycle at a time using the Goodman equation. As showed in Figure 20.20, the Goodman equation considers the stress ratio, R, cycle by cycle.

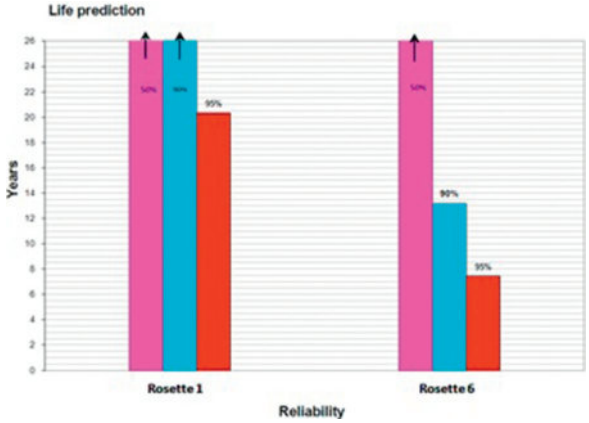

FIGURE 20.19

Life prediction for railway casting steel couplings.

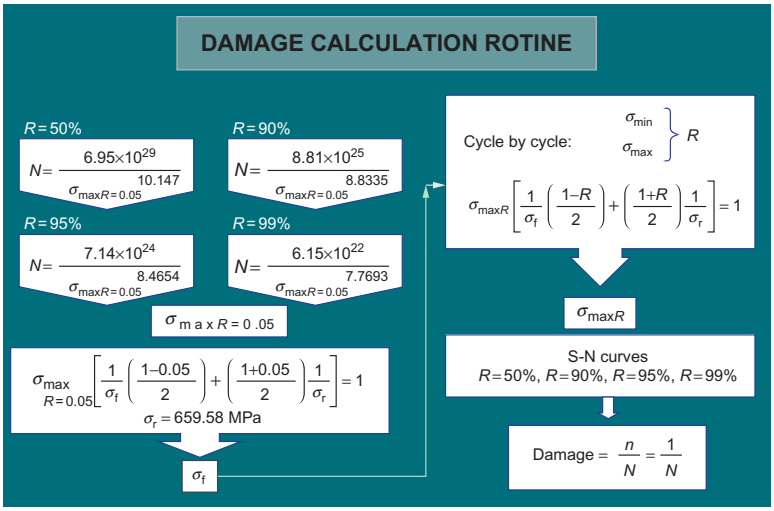

FIGURE 20.20

Damage calculation methodology using Palmgren-Miner rule and Goodman equation.

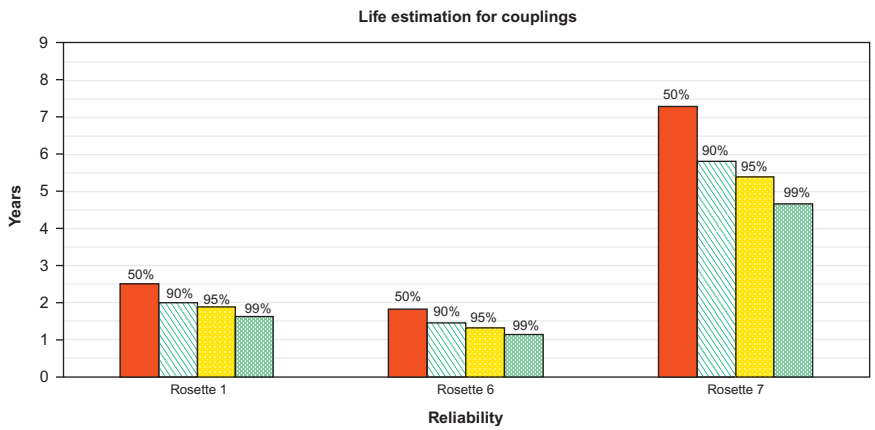

FIGURE 20.21

Life prediction for railway casting steel couplings using Goodman equation.

Life prediction using the data acquisition of rosettes 1, 6, and 7 is shown in Figure 20.21 where can be observed that for all rosettes and all reliabilities the life prediction is low; lower than 2 years for rosette 6 and lower than 7.5 years for rosette 7 (the "nominal" one).

7 RESULTS AND DISCUSSION

A detailed analysis of the morphology and casting defects distribution on the tested specimen revealed areas with high porosities, densities, and the presence of some inhomogeneity. The presence of porosities and shrinkage cavities of varying diameter, were at the periphery of the piece and in greater concentration along the line of agreement with the head of the railway coupling where the crack appeared (Figure 20.3). Nevertheless, was verified by author that, the porosities density measured in the samples is acceptable in accordance with the current railway industry criteria. But the component was requested to fatigue, so the complex geometry railway component should have had a higher level of homogeneity, in the other words, less manufacturing defects/intrinsic defects, like porosities and shrinkages cavities, to ensure greater resistance to fatigue and greater service safety to avoid the increase of that defects.

Service life assessments can and must be performed by measuring service strain and deriving stress spectra, because the designer needs to reliably assess/and have knowledge of the stochastic service loads.

From the maintenance service records, is known that cracks do not appear on rosette 7 zone, so the Goodman equation on this case does not apply as it is too conservative. Nevertheless is known that cracks appeared on rosettes 1 and 6 zones, so the life prediction using Goodman equation for all the reliabilities presented in Figure 20.21, was confirmed by the maintenance service record. Therefore, by Figure 20.19, it can be said that, for this study case, life prediction using Palmgren-Miner Rule modified by Haibach is too optimist and cannot be used.

8 CONCLUSION

The present work shows the importance of the service loads, material properties, geometry, and the manufacturing process interaction on the structural durability of mechanical components. This interaction must be taken into account at the design stage. This study also shows that there is not a successful life estimation model and the research needs to be done to improve in this scientific area, this issue in particular, needs the collaboration of industries like the railway, aeronautics, automobile industries as well as manufacturers of mechanical components.

REFERENCES

[1] Baskett D. Gauge corner cracking: an affliction for rails and headache of railways. J EIS 2002, January.

[2] Branco CM, Fernandes AA, Castro PMST. Fatigue in welding structures. 2nd ed. Fundação Calouste Gulbenkian; 1999, ISBN: 972-31-0139-4 [in Portuguese].

[3] Radaj D, Sonsino CM, Frickle W. Fatigue assessment of welded joints by local approaches. 2nd ed. Cambridge, England: Woodhead Publishing Limited; 2006 ISBN: 13: 978-1-84569-188-2.

[4] SAE. Fatigue design handbook. Society of Automotive Engineers; 2001.

[5] Berger C, Eulitz K-G, Heuler P, et al. Betriebsfestigkeit in Germany—an overview. Int J Fatigue 2002;24:603–25.

[6] Morgado TLM. Structural integrity of a railway component [Ph. D thesis]. Portugal: Lisbon University; 2009 [in Portuguese].

[7] Morgado TLM, Branco CM. Life estimation study of a steel railway component. In: Fifth international conference on engineering failure analysis 2012, 1–4 July. The Hague, The Netherlands: Elsevier; 2012.

[8] Sonsino CM. Fatigue design and testing of components. In: 6th fracture conference—O´ Porto, Portugal, abstract book, SPM; 1998. p. 3–46.

[9] Heuler P, Klaütschke H. Generation and use of standardized load spectra and load–time histories. Int J Fatigue 2005;27(8):974–90.

[10] prEN 1993-1-9: 2004 (E). Eurocode 3: design of steel structures—part 1–1: general rules.

[11] Infante V, Branco CM, Brito AS, Morgado TLM. Failure analysis of cast steel railway couplings used for coal transportation. Eng Fail Anal 2003;10:475–89.

[12] Murakami Y, Endo M. Effects of defects, inclusions and inhomogeneities on fatigue strength. Int J Fatigue 1994;16(3):163–82.

[13] Beretta S, Blarasin A, Endo M, Giunti T, Murakami Y. Defect tolerance design for automotive components. Int J Fatigue 1997;19(4):319–33.

[14] Murakami Y. Metal fatigue: effect of small defects and nonmetallic inclusions. Elsevier; 2002, ISBN: 0-08-044064-9.

[15] Bathias C, Paris PC. Gigacycle fatigue in mechanical practice. Marcel Dekker; 2005, ISBN: 0-8247-2313-9.

[16] Morgado TLM, Brito AS. Study of casting defects and fatigue limit models of a railway component. In: Thirteenth international ASTM/ESIS symposium on fatigue and fracture mechanics (39th national symposium on fatigue and fracture mechanics), November 13–15; 2013.

[17] Kalpakjian S. Manufacturing engineering and technology. 2nd ed. New York: Addison Wisley Longman Publishing Company; 2000, ISBN: 0201508060/ISBN-13: 9780201508062.

[18] ASTM E8M-04. Standard test methods for tension testing of metallic materials [Metric]. Developed by Subcommittee: E28.04, Book of Standards Volume: 03.01, West Conshohocken, USA.

[19] ASTM E739-91. Standard practice for statistical analysis of linear or linearized stress-life (S-N) and strain-life (E-N) fatigue data. Developed by Subcommittee E08.04, Book of Standards Volume: 03.01, West Conshohocken, USA; 2004.

[20] Marin J. Mechanical behavior of engineering materials. Englewood Cliffs, NJ: Prentice-Hall; 1962, p. 224.

[21] Shigley JE, Mischke CR. Mechanical engineering design. 8th ed. McGraw-Hill; 2006, ISBN: 0−390−76487−6.
[22] Morgado TLM, Branco CM, Infante V. Reliability fatigue analysis of steel couplings used in railway transport of coal. In: Second international conference on material and component performance under variable amplitude loading, proceedings, vol. II. p. 715–22, ISBN: 978-3-00-027049-9.
[23] Branco CM. Mechanics of materials. 4th ed. Lisbon: Fundação Calouste Gulbenkian; 2006, ISBN: 972-31-1147-0 [in Portuguese].
[24] Stephens RI, Fatemi A, Stephens RR, Fuchs HO. Metal fatigue in engineering. 2nd ed. John Wiley & Johns, Inc.; 2001, ISBN: 0-471-51059-9.
[25] ASTM Standard E1049 1985. Standard practices for cycle counting in fatigue analysis. West Conshohocken, PA: ASTM International; 2011. http://dx.doi.org/10.1520/E1049-85R11E01.
[26] Miner DE. Cumulative damage in fatigue. Trans ASME 1945;67(A):159–64.
[27] Sonsino CM. Principles of variable amplitude fatigue design and testing: fatigue testing and analysis under variable amplitude loading conditions. In: McKeigham PC, Ranganathan N, editors. ASTM STP, vol. 1439. West Conshohocken, PA: ASTM International; 2005. p. 3–23.
[28] Morgado TLM, Branco CM, Infante V. A failure study of housing of the gearboxes of series 2600 locomotives of the Portuguese Railway Company. Eng Fail Anal 2008;15:154–64.

CHAPTER

Failure analysis and prevention in powertrain systems

21

Mohammad Azadi

Fatigue and Wear in Materials (FWM) Workgroup, Irankhodro Powertrain Company (IPCO), Tehran, Iran

CHAPTER OUTLINE

1 INTRODUCTION

Most engineering components are working under fatigue-loading conditions. Generally, there are various types of cyclic loadings based on different criteria. These categories of fatigue-loading conditions can be found in Figure 21.1.

One typing set can be isothermal fatigue (IF) and unisothermal fatigue (UIF) loadings. At IF loadings, the temperature is constant during cycles. However, there is a thermal transient behavior under UIF loadings, such as a thermomechanical fatigue (TMF) condition. For TMF loadings, there are two types of conditions, including in-phase (IP) and out-of-phase (OP) states [1]. Under OP conditions, the compressive stress occurs at maximum temperatures and the tensile stress occurs

Handbook of Materials Failure Analysis With Case Studies from the Aerospace and Automotive Industries.
http://dx.doi.org/10.1016/B978-0-12-800950-5.00021-1

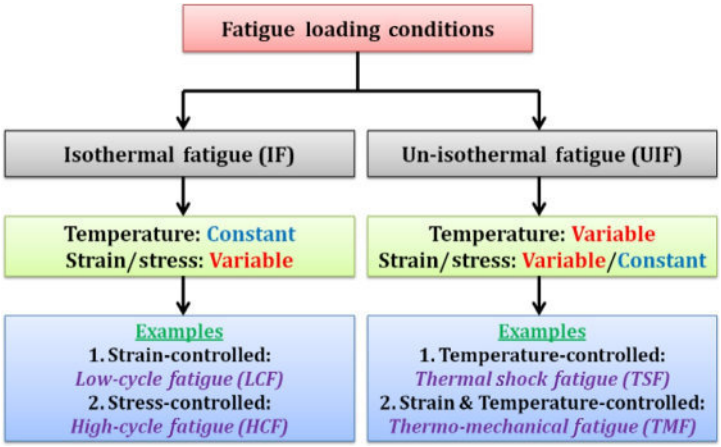

FIGURE 21.1

Different categories of fatigue-loading conditions.

at minimum temperatures. This condition is vice versa under IP loadings. Another typing set is according to the cycle number, including high-cycle fatigue (HCF) and low-cycle fatigue (LCF) regimes. As known, the strain controls the fatigue lifetime under LCF loadings. However, the stress controls the fatigue lifetime under HCF loadings. Based on this statement, strain-controlled and stress-controlled fatigue tests would be performed for LCF and HCF regimes, respectively. It should be noted that the transition cycle is usually 10^3-10^4 million cycles between HCF and LCF regimes. In some cases, a combination of these different fatigue loadings would be imposed to engineering components. For an instance, in engine cylinder heads, TMF-superimposed HCF behaviors should be considered (as shown in Figure 21.2). Based on start-stop cycles in engines, cylinder heads are imposed to LCF loadings. Besides, when the engine is working, the temperature on the cylinder head surface has its maximum value according to the combustion process. However, when the engine is off, the temperature decreases to the environment temperature. This loading type has OP-TMF conditions. In addition, during the combustion process, the combustion pressure on the cylinder head is changing during cycles at maximum temperatures. This phenomenon imposes HCF loadings to the cylinder head. In this case, since the temperature variation in solids would be damped in less than 0.1 mm of the wall thickness, the thermal transition can be neglected for the HCF regime. Therefore, TMF-superimposed HCF behaviors should be investigated in the design of cylinder heads.

Generally, in powertrain systems, engine components have been imposed to cyclic loadings. Therefore, the utilized material in such components should have enough strength under such HCF, LCF, and TMF conditions or a combination of these loadings. This chapter has presented failures in engine components under

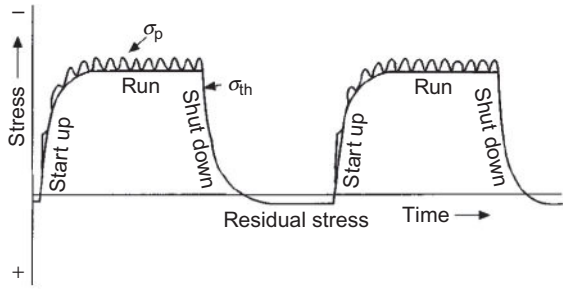

FIGURE 21.2

Different types of fatigue loadings in engine cylinder heads [11].

fatigue-loading types. Therefore, two case studies on cracked cylinder heads and damaged valves in internal combustion engines have been analyzed in this chapter. After the failure analysis of damaged components, some improvement methods were proposed to prevent such failures.

In the first case, a failure analysis on a failed intake valve in a gasoline engine was presented. During an endurance test, an intake valve was broken and caused some other damages on the piston and the cylinder. Material examinations (by a light microscopy and a scanning electron microscopy) were conducted on the fracture surface of the intake valve shaft. Obtained results demonstrated that no pores or defects could be observed, the microstructure and the hardness of the material were conformed to the specification (the standard map, extracted by the manufacture). However, a mechanical factor caused the damage, which consisted of a fully reversed bending load due to the misalignment of the valve shaft. The misalignment was caused by the thermal deformation in the valve shaft. The engine was working under a hot condition. In addition, it was a reversed condition (with zero mean stress) due to the rotation of the valve shaft during engine working. In addition, the fracture surface demonstrated beach marks due to cyclic loadings. In this case study, it was found that cracks initiated from the outer surface of the valve shaft and propagated through the inside zone of the fracture surface.

In the second case, a failure analysis was conducted on a gasoline engine cylinder head, made of aluminum alloy, which has been used in passenger cars. During an endurance test, a crack initiated from the interior wall of a hole in the center region of the cylinder head and then, propagated through the wall thickness of the cylinder head. Metallurgical examinations were conducted in the cracked zone. Obtained results showed that there were many casting pores due to poor quality of casting in the failed cylinder head, which has certainly played a crucial role in initiating the crack. The finite element analysis of the cylinder head was also performed to identify stress components. Modeling of a bolt for the hole showed that plastic stresses occurred. Moreover, lower strength of the material due to high assembly stress caused the failure in the cylinder head.

2 FAILURE ANALYSIS OF A BROKEN INTAKE VALVE [2]

2.1 FAILURE HISTORY

Valves are important components in internal combustion engines, which are responsible for the air entrance and the smoke exit from the combustion chamber [3]. Their operation has a direct effect on performance parameters (i.e., power, torque, fuel consumption, etc.) and engine emissions.

Applied stresses on valves during their service lifetimes are generated by valve train dynamics and the combustion pressure [3]. During the combustion process, the temperature of the intake valve reached to nearly 550 °C. This temperature for the exhaust valve is between 700 and 900 °C and is dependent on the engine [3,4]. In addition, due to this nature of work, valves are subjected to severe cyclic loading stresses, which are applied by the camshaft. Therefore, the material should have proper fatigue strength.

Fatigue failures can occur in three cases. One can be at the head area of valves, which leads to radial cracks due to stresses generated by temperature gradient. This is a thermal fatigue failure. The second can be near to seat face, which leads to transversal cracks due to mechanical bending stresses. The third can be in the groove area, which leads to transversal cracks due to the stress concentration [3]. Other failures in engine valves can occur due to oxidation or corrosion phenomena.

In the case of the failure analysis and the fatigue analysis of valve systems, several studies have been reported. Voorwald et al. [3] presented the fatigue strength of X45CrSi93 stainless steel, which is used in internal combustion engine valves. Their results illustrated significant increase of the axial fatigue strength in the martensitic X45CrSi93 steel after nitriding, compared to results of chrome-plating specimens. Ipohorski et al. [5] conducted a failure analysis of a steam valve stem. They demonstrated that the failure was attributed to the low toughness of the material and a nitrided layer on roots of the threaded zone.

A failure analysis of the exhaust valve stem in a gas engine was performed by Kwon and Han [6]. They showed that the failure was a result of the overheating. The significant hardness loss, the extensive surface oxidation, and fretting/galling on the valve stem were indicative of the overheating. Yu and Xu [7] performed a failure analysis and metallurgical investigations of diesel engine exhaust valves. Their fractographic studies indicated that the fatigue was the dominant mechanism of the failure in the exhaust valve.

This part presents a case study for a failure analysis of a broken intake valve. This fracture took place in a gasoline engine (designed for passenger cars) during an endurance test (entitled 500 h general cycles). During this durability test, the engine torque reduced sharply and therefore, the test was stopped after 161 h. After more investigations, it was observed that one of intake valves in the cylinder number 1 was broken. This event also caused other damages on the piston and the cylinder head. These failures in the intake valve are shown in Figures 21.3 and 21.4.

This damage in the valve was repeated three times in the same engine. The first time occurred after 242 h of such a durability test. This failure took place in the

FIGURE 21.3

The broken intake valve in a gasoline engine during an endurance test [2].

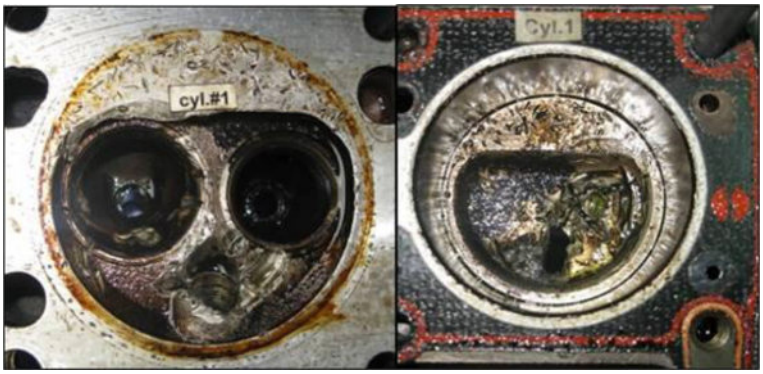

FIGURE 21.4

Damages on piston and cylinder head faces according to failures [2].

intake valve of the cylinder number 1 at the same condition. It means that the failure location in the intake valve was the same in two cases. The second time occurred after 60 h of another test (entitled 165 h over-speed cycles). In this case, the exhaust valve (in the cylinder number 1) was broken. According to this failure history, the damage mode was chosen for accurate investigations due to its repeatability.

For the failure analysis of the intake valve, two types of root causes were considered which include mechanical and material phenomena. Mechanical problems include:

- The nonconformance of the geometric dimension and the tolerance of the intake valve in comparison to the specification (the standard map)
- A problem in the oil lubrication of the valve system
- Increase in the clearance of the valve shaft and the valve guide

- The misalignment of the valve seat with the valve guide
- The nonplanar of the valve guide on the combustion chamber (of the cylinder head)

Other mechanical problems are due to piston crashing, valve opening according to uncorrect timing, etc. Material problems include:

- The nonconformance of the chemical composition with the specification (the standard map)
- Defects in the microstructure of the intake valve
- Low hardness of the intake valve and the valve guide
- The existence of inclusions in the intake valve

To investigate these factors, specimens were taken from the failed intake valve and prepared by standard methods for metallurgical examinations (including the microstructure investigation and the fractography). The chemical composition of the intake valve was determined by a spectroscopy chemical analysis.

The valve shaft was cut near the fracture surface to measure the hardness. A Rockwell C test with 150 Kg force was performed for 15 s and it was repeated four times according to ASTM-E18-08 standard [8].

According to the specification (the standard map), the material of the intake valve shaft is made of 1.4718 steel (X45CrSi9-3) which includes chrome and silicon elements [9]. It should be mentioned that the heat treatment process of the valve system has two types. One process is annealing at 780-820 °C and the other consists of solution at 1000-1050 °C, quenching in hot oil and tempering at 780 °C in the water or the air [9]. The first one is for the intake valve shaft according to the specification (the standard map of the component). It should be mentioned that the exhaust valve shaft has both heat treatment processes.

To investigate the fractography, pictures of the material microstructure were taken by a light microscope after grinding, polishing, and etching the specimen surface [10]. The microstructure of specimens and fractured surfaces were studied by a scanning electron microscopy (SEM). In addition, accurate measurements on the valve system of this engine were conducted by a coordinate measuring machine (CMM).

2.2 RESULTS AND DISCUSSIONS

2.2.1 *Mechanical Investigations*

Dimensions of several parts in the valve system were measured by the CMM. First, accurate measurements were conducted for the diameter of the valve shaft (the external diameter) and the valve guide (the internal diameter) and also its clearance. These results are shown in Table 21.1.

The clearance can be calculated as a difference of the internal diameter of the valve guide and the external diameter of the valve shaft. It should be mentioned that these dimensions could not be measured for the failed intake valve (in the cylinder number 1) due to its damages. Table 21.1 demonstrates that the clearance increases by performing the endurance test. In addition, as another result, the clearance after

Table 21.1 Diameters of the Valve Shaft and the Internal Diameter of the Valve Guide

Intake Valve Number		1	2	3	4
External diameter (mm)	Before test	7.911	7.911	7.909	7.906
	After test	7.903	7.900	7.896	7.897
Internal diameter (mm)	Before test	7.929	7.928	7.933	7.935
	After test	Damaged	7.947	8.012	7.944
Clearance (mm)	Before test	0.018	0.017	0.024	0.029
	After test	Damaged	0.047	0.116	0.047

Table 21.2 Values of Parameters in the Valve System Which Are Measured After the Test

Intake Valve Number	1	2	3	4
Deviation from cylindricity of valve guide (mm)	Damaged	0.038	0.078	0.009
Misalignment of valve seat and guide (mm)	Damaged	0.036	0.006	0.072
Deviation from cylindricity of valve shaft (mm)	Damaged	0.005	0.004	0.012
Misalignment of valve seat and shaft (mm)	Damaged	0.295	0.096	0.065

the test in the cylinder number 3 was more than other cylinders. The reason can be described by occurring higher temperatures in this cylinder. It means that the maximum temperature of the cylinder head occurred in the cylinder number 3 in this gasoline engine, which was measured during a temperature survey test [4].

Results of measuring the deviation value from the valve guide cylindricity and the misalignment value of the valve seat and guide (nonconcentricity) are shown in Table 21.2. It should be mentioned that these measurements data are conducted after the test (there is no available data before the test) and could not be performed for the cylinder number 1 due to its damages. In addition, accurate measurement results of the valve shaft parameters are also shown in Table 21.2. These parameters include the deviation value from the cylindricity of the valve shaft and the misalignment value of the valve seat and shaft (nonconcentricity).

As demonstrated in Table 21.2, the maximum value for the deviation from the cylindricity of the valve guide was measured in the cylinder number 3. In addition, the nonconcentricity value of the cylinder number 4 is more than other cylinders. The maximum value of the deviation from the cylindricity of the valve shaft was measured for the cylinder number 4. However, the misalignment value of the valve seat and shaft for the cylinder number 1 is more than other cylinders. These misalignments can be produced by thermal deformations. Moreover, thermal deformation can be produced when the engine is working in an ultra-hot condition according to various reasons.

As mentioned, one important factor in these thermal deformations is the heat transfer in the engine. The temperature difference between inlet and outlet of coolant temperatures can describe thermal conditions of the engine. This value is shown in Figure 21.5 for two different engine speeds (3000 and 5000 rpm at full-loaded conditions) during two endurance tests on the same engine (without any failures during 500 h of testing), comparing to this engine, where the intake valve was broken at 161 h. These results demonstrated that the temperature difference between inlet and outlet of coolant temperatures for this engine (with the failed intake valve) was higher than the other one, which had no failures. This value was about 8 °C for the failed engine in comparison to 6 °C (as an average value) in the engine without failures.

It means that the heat transfer system of the failed engine was not working in a proper situation comparably to the other engine. This phenomenon can be due to various reasons such as pump defects. In other words, the engine has worked in a hot condition and, one reason for breaking of the intake valve can be this hot condition of the engine.

Higher temperature leads to excessive thermal expansions in the valve shaft. Then, the valve can be exposed to the misalignment and therefore can be exposed to an external bending force. As the valve rotates; while the engine is working, this force becomes a reversed cyclic loading in the valve shaft. Finally, the valve can be locked in its guide due to an unallowable deformation. This locking of the valve system causes the valve to remain opened and then causes crashing of the piston and thus, leads to damages in both the piston and the cylinder head (as shown in Figure 21.2).

2.2.2 Material Investigations

In the first step, the fracture surface of the broken intake valve was investigated as shown in Figures 21.6 and 21.7. In these figures, beach marks can be observed due to cyclic loadings and the fatigue fracture. As it is known, the valve rotates when the engine works and a reversed bending load is applied to the valve shaft. The fracture surface on the valve shaft shows macroscopic lines, which illustrate the cracks growth path. On the other side of the valve shaft, the fracture surface was damaged due to the impact after the failure in the engine.

A visual inspection of beach marks on the valve shaft surface shows two crack initiation zones (as illustrated in Figure 21.5, in two left and right sides). These regions are demonstrated with arrows (entitled “Crack 1” and “Crack 2”) in Figure 21.5. As shown in Figure 21.5, cracks initiate at the outer surface of the valve shaft. This phenomenon occurs mostly in HCF regime. Then, this pattern shows a fully reversed bending as the loading type in the valve system [12]. In other words, the mean stress is zero and the stress ratio is minus one ($R = -1$). This bending force is applied due to the misalignment, reported in Table 21.2. As mentioned before, this misalignment can be produced by thermal deformations due to hot working of the engine.

SEM images of the fracture surface are shown in Figure 21.8. A defect near the outer surface of the valve shaft (shown in the right side of Figure 21.8 which is that

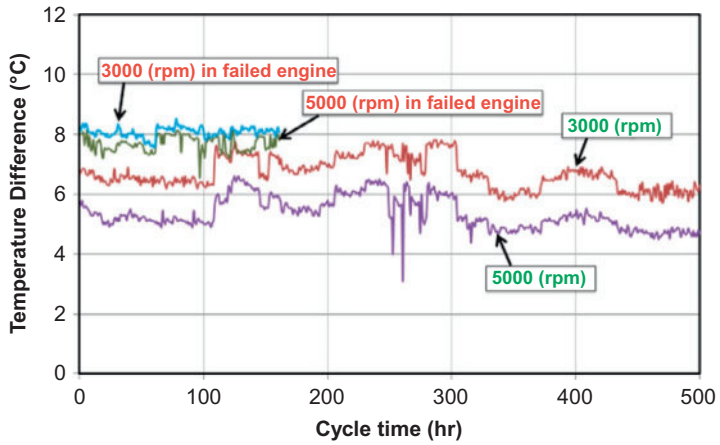

FIGURE 21.5

Temperature differences between inlet and outlet of coolant temperatures [2].

FIGURE 21.6

The fracture surface of the broken intake valve with beach marks [2].

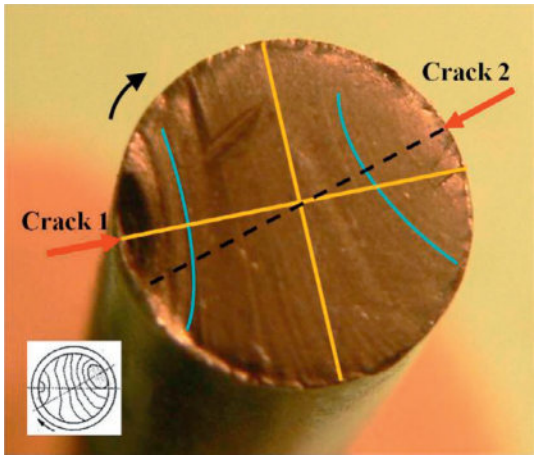

FIGURE 21.7

Beach marks and crack initiation zones on the valve shaft surface [2].

region entitled "Crack 1" in Figure 21.7) existed which could cause a crack initiation. This zone is a three-dimensional dislocation which has become active during the fatigue failure. In addition, the oxide and carbide particles can be probably observed (shown by arrows in Figure 21.8) near the crack initiation zone.

The element composition of the failed valve shaft is shown in Table 21.3. The result demonstrated that there is a conformation for the chemical composition of the valve shaft to the specification (the standard map of the component) and the material standard [9].

The average hardness of the material was determined to be 33 HRC, which is in the range of mentioned values in the specification (the standard map of the component). In this standard map, the value is mentioned as 24.8-34.5 HRC. Thus, there is no conformation for the hardness of the material in the valve shaft.

In Figure 21.9, it can be seen that the microstructure of the valve shaft material consisted of a tempered martensite [3,12]. This microstructure confirms the heat treatment process, which is also revealed by the hardness. As mentioned before, the material of the intake valve shaft is made of 1.4718 steel (X45CrSi9-3) which includes chrome and silicon elements [9].

The microstructure of the material has a conformation with the specification (the standard map) of the valve system. As it can be seen in Figure 21.7, there exist no unusual pores or defects due to the casting process or the heat treatment process in the material of the valve shaft.

These material investigations illustrate that the damage was not due to material defects and the failure caused by a mechanical factor. In the previous part, it was shown that the heat transfer system of the engine was not working in a proper condition and therefore, a misalignment occurred in the valve shaft. Then, this phenomenon led to an external bending force. According to the valve rotation, a reversed bending load caused fatigue damages. Finally, an unallowable thermal deformation in the valve shaft caused locking of the valve system and led to failures in both the piston and the cylinder head.

Table 21.3 The Chemical Composition of the Failed Intake Valve Shaft

Elements	Failed Component	Material Standard [9]
C	0.45	0.40-0.50
Si	3.24	2.70-3.30
Mn	0.40	0.80
Cr	9.15	8.00-10.00
Ni	0.17	0.60
P	0.02	0.04
S	0.01	0.03
Fe	Rem.	Rem.

2.3 REMARKABLE NOTES

In the presented part, various tests and inspections (include material investigations and accurate measurements) were conducted to study reasons of the broken intake valve in a gasoline engine. Results demonstrate that:

- The microstructure and the hardness of the material had conformations to the specification (the standard map) of the valve system. No unusual pores or defects can be observed in the material of the valve shaft according to the casting process and the heat treatment process.
- Cracks initiated from the outer surface of the valve shaft and propagated through inside of the fracture surface. On the fatigue fracture surface, beach marks can be observed due to a reversed bending load. The reversed condition is due to the rotation of the valve during engine working. The bending force is also due to the misalignment of the valve shaft, which was caused by a thermal deformation during testing.

3 FAILURE ANALYSIS OF A CRACKED CYLINDER HEAD [13,14]

3.1 FAILURE HISTORY

Cylinder heads are exposed to thermomechanical cyclic loadings from the combustion chamber (thermal stresses) and bolts (mechanical stresses). Therefore, the important parameter in the design of cylinder heads is known as the TMF strength. Since the correct performance of the cylinder head influences parameters of engines such as the power, the torque, the fuel consumption, and environmental pollutions, the design of this component according to fatigue lifetimes has a high importance. Some actions, such as the material selection, the heat treatment process, and manufacturing methods have more effect on the service lifetime of cylinder heads.

During an endurance test (500 h off-road cycles), a cylinder head, casted from the $AlSi_8Cu_3$ aluminum alloy, failed. According to this failure, a crack initiated inside a hole in the center (between cylinder numbers 2 and 3). That hole was used for a support during the casting process. After 434 h of engine working, the test was stopped, since the coolant fluid entered the combustion chamber. This event was repeated in another endurance test (400 h thermal change cycles) after 125 h of engine working. Due to this repeated failure, the failure mode was chosen for an investigation. Two root causes are considered, which include mechanical and material phenomena. Mechanical factors include following parameters:

- The nonconformance of the geometric dimension and the tolerance of the cylinder head (such as the thickness around the hole) and the bolt according to drawing
- A problem in fastening of the bolt
- The existence of the excessive distortion in the cylinder head

- Excessive stresses due to fastening of the bolt and the subsequent influence on the fatigue
- Defects in cooling and lubricating systems of the engine

The material factors include following parameters:

- The nonconformance of the chemical composition with the specification
- Defects in the microstructure near the cracked zone
- The existence of inclusions in the cylinder head
- Low strength and low hardness

Because of these events, metallurgical investigations, the fractography observation, the finite element analysis, and some other measurements on the failed cylinder head were conducted.

3.2 RESULTS AND DISCUSSIONS

3.2.1 Observation Results

The cracked zone is shown in Figure 21.10. Checking cooling and lubricating systems of the engine showed no issue. The differences between coolant inlet and outlet temperatures were constant during the endurance test, and there was no leakage. Twenty hours before stopping the engine, the ECU sensed a knock and both the engine torque and engine power decreased because of retarding of the ignition time. After checking the engine performance condition by the defect analyzer device, it was found that there were no knocks. This was due to the crack initiation and decreasing of the cylinder head stiffness. It should be mentioned that until 300 h of the endurance test, the fuel type was gasoline and was then changed to the compressed natural gas type. As a result, the mean power of the engine increased from 100 to 110 kW, which could be a cause of higher thermal stresses.

3.2.2 Measurements

The bolt type that was tightened in the hole was DIN-906, which had a conical shape. In Figure 21.11, its dimensions are shown. Results of measuring the bolt diameter and the bolt length as well as the thickness of the cylinder head (area 1 and area 2 in Figure 21.12) showed a good conformance to drawings. There was no plastic deformation noted during the visual inspection of bolt threads. However, within the hole, the threads were deformed. It should be mentioned that the material of the bolt is steel alloy in comparison to the hole made of the aluminum alloy. The bolt pitch according to a straight line was 1.5 mm; however, for the hole thread, pitches were 1.50, 1.49, 1.52, 1.49, 1.46, and 1.51 mm, which indicated the plastic deformation.

As it is well known, the deformation of a cylinder head has two modes including bending and torsion. The tightening torque of cylinder head bolts was 20 Nm, continued with twisting of 120°. The removal torque of cylinder head bolts and the surface flatness of the cylinder head could have approximately showed the overall deformation. The cylinder head flatness was measured as 56 μm, which was below

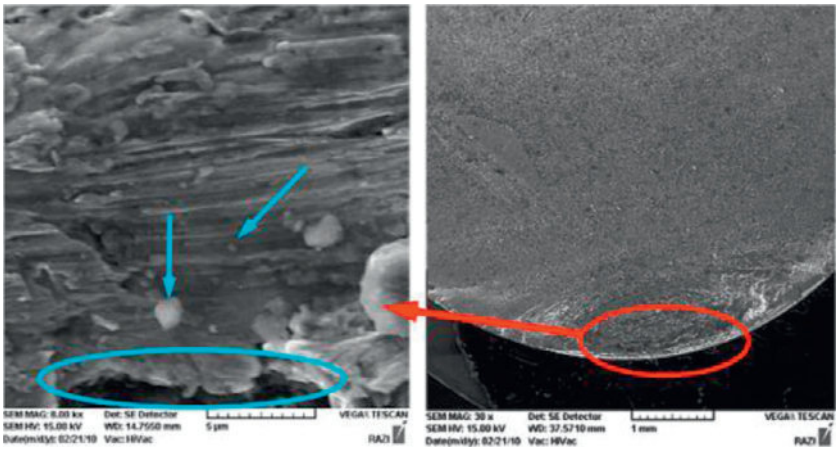

FIGURE 21.8

SEM images of the fracture surface with different magnifications [2].

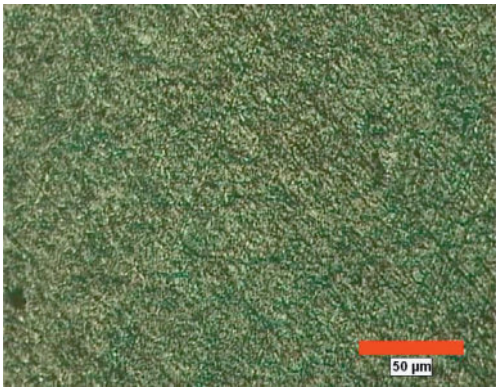

FIGURE 21.9

The microstructure of the valve shaft made of 1.4718 steel (X45CrSi9-3) [2].

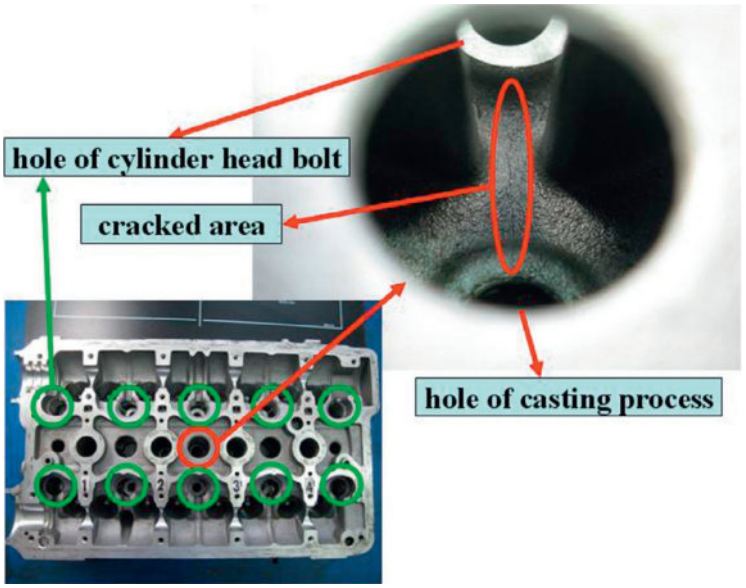

FIGURE 21.10

The cracked zone on the cylinder head [13,14].

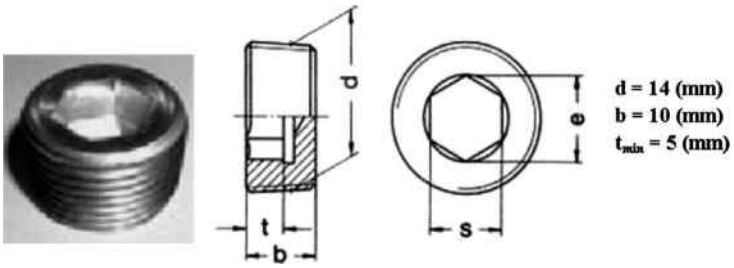

FIGURE 21.11

Dimensions of the bolt according to DIN906 standard [13,14].

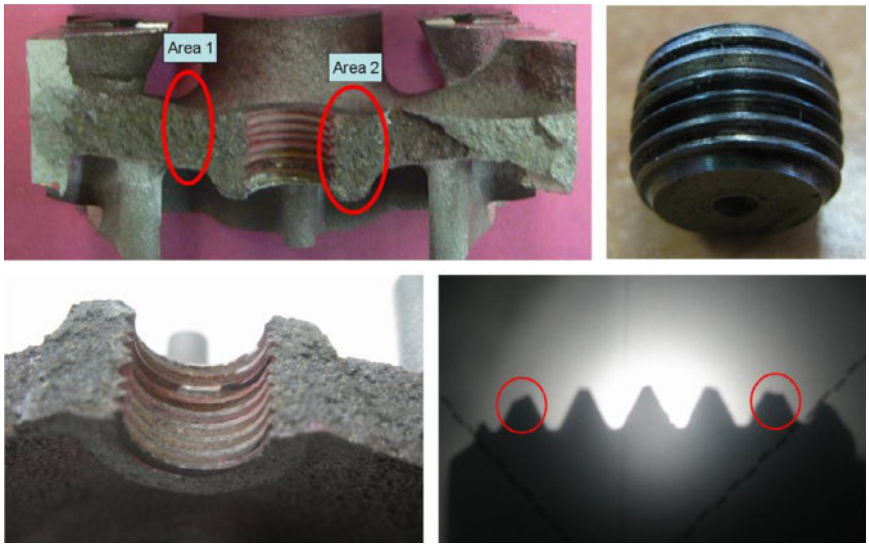

FIGURE 21.12

The shape of the bolt and the hole [13,14].

the specification (100 μm as the maximum value). The reported flatness was the difference between deepest valleys and highest peaks of the surface roughness. Bolt lengths during the test were measured by the ultrasonic device. Stress relaxations were calculated and are shown in Table 21.4. Results showed that after the running-in test, the bolt lengths increased and then decreased due to the stress relaxation. The changes in lengths were symmetric.

3.2.3 Material Investigations

The cracked zone was fully opened to investigate the fracture surface. Figure 21.13 shows crack origins and the direction of the propagation. The visual inspection revealed pores around the hole because of poor quality of the casting process, which

Table 21.4 Stress Relaxations in Cylinder Head Bolts During the Endurance Test

	Bolt Length (mm)				Stress Relaxation (MPa)	
No.	Initial	Before Running-In	After Running-In	After Test	Before and After Running-In	Before and After Test
1	138.98	141.19	140.86	140.85	−479.142	−14.554
2	138.87	140.72	140.40	140.39	−466.174	−14.601
4	138.97	141.20	140.84	140.78	−522.663	−87.333
5	137.90	140.35	140.04	140.01	−452.797	−43.916
6	139.22	141.40	141.01	141.00	−565.417	−14.538
7	138.42	141.00	140.55	140.52	−654.255	−43.757

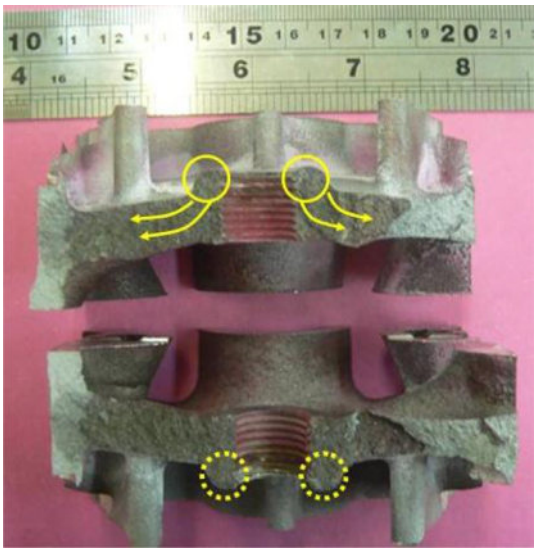

FIGURE 21.13

The surfaces after opening cracked zone [13,14].

needs an optimization in melting, degassing, casting, and molding methods. The existence of these pores could produce a stress concentration for crack initiations and growths.

The chemical composition of the failed cylinder head material was determined by the spectrographic chemical analysis method. The results are shown in Table 21.5. The cylinder head alloy conformed to the standard (of the $AlSi_8Cu_3$ aluminum alloy), except for higher silicon content [15,16]. This element not only increases the strength and the hardness but also decreases the elongation to fractures.

Table 21.5 The Chemical Composition of the Cracked Cylinder Head (%)

Cylinder Head	Si	Fe	Cu	Mn	Mg	Zn	Ni	Ti	Al
Cracked case	9.7	0.37	2.40	0.40	0.42	0.57	0.01	0.11	Base
EN-46200 [15]	8.5-9.5	0.3-0.7	2.3-2.6	0.35-0.50	0.25-0.50	0.5-0.7	0.30 max	0.08-0.012	Base

Brinell hardness tests [16,17] with 250 kg force and a steel indentor with 5-mm diameter were performed with 15-s intervals on the specimen surface. It should be mentioned that the average hardness of the material was determined to be 121 HB 5/250, which is higher than the lower limit of the specification (90 HB) due to the higher amount of silicon.

To investigate the microstructure and the heat treatment of the cylinder head material, a part of the cylinder head near the cracked zone was separated (as shown in Figure 21.14). Fractographical pictures [18,19] were taken after grinding, polishing, and etching the specimen surface in Keller's reagent for 10 s. In Figure 21.15, it is seen that the microstructure of the cylinder head material consisted of a solid solution of aluminum-silicon (the rich phase was made of aluminum) and a uniform distribution of a eutectic silicon phase and intermetallic phases. In general, the microstructure conforms to the standard [20,21], but pores, which are near the surface, could be a place of the stress concentration and could be a site of crack initiations during cyclic thermomechanical loadings.

According to the standard [20], the allowable limit for the porosity is 5% in a reference surface (which is 3 mm by 4 mm). In addition, 500 μm is the limit between micro- and macro-porosities. A macro pore is a pore, which could be seen visually without any microscope. The porosity was measured as 3% for the surface in Figure 21.14, which is below the standard limit [20]; however, the diameter of pores

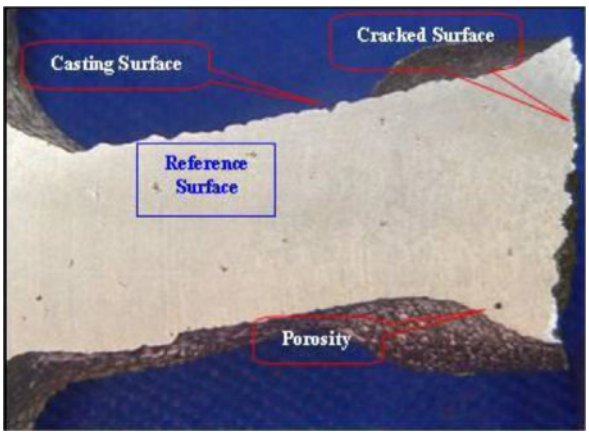

FIGURE 21.14

The zone below cracked surface [13,14].

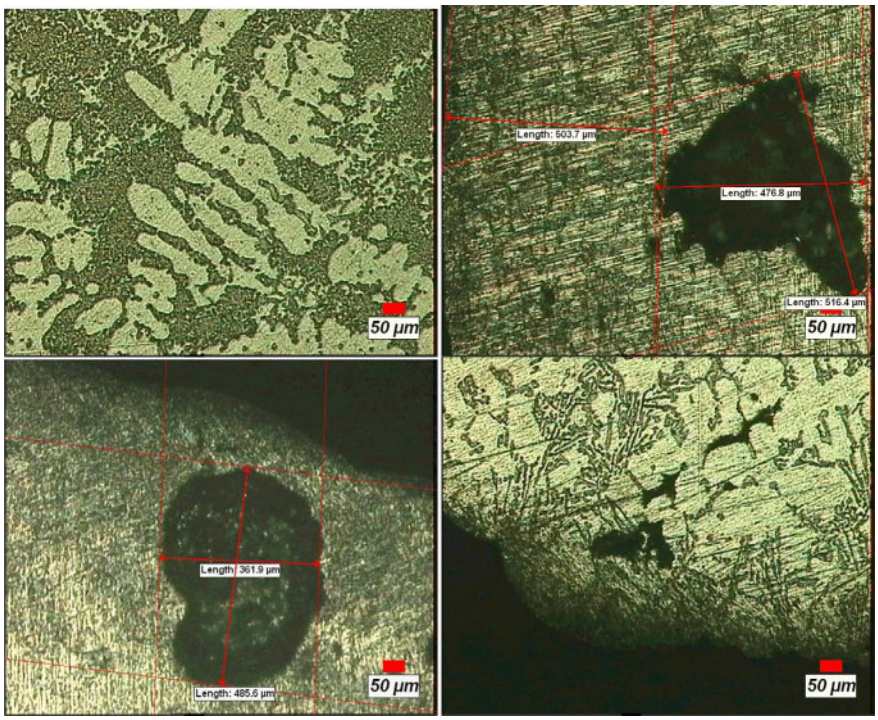

FIGURE 21.15

Microstructures of cracked zones [13,14].

was more than 500 µm. As seen in the figure, the porosity distribution was high near the surface, and this could cause lower fatigue lifetime.

To investigate the cracked surface more accurately, a SEM investigation was conducted, and results are shown in Figure 21.16 with different magnifications. According to Figure 21.16, casting defects and pores were observed near threads. It should be mentioned that the diameter of pores was about 450 µm.

3.2.4 Mechanical Investigations

The finite element analysis of the cylinder head with and without modeling of the bolt for the hole was performed at rated power conditions of the engine, including the combustion pressure, the temperature distribution, and assembly loadings. The analysis included following steps:

- The thermal analysis for finding the temperature distribution
- The structural analysis with assembly loads (bolt forces, press-fits, conical bolt forces, and shrink-fits), the thermal load, the thermal load, and the gas pressure in cylinder number 2, the thermal load and the gas pressure in cylinder number 1

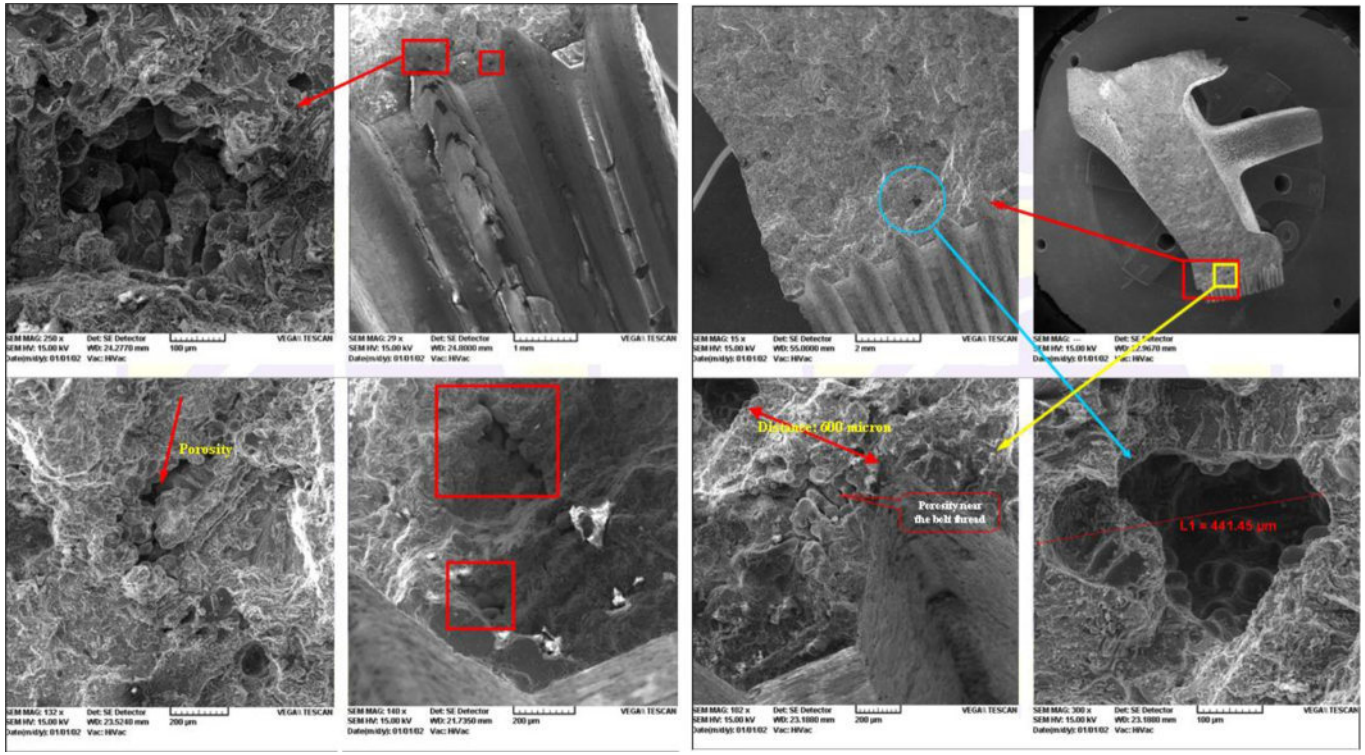

FIGURE 21.16

Results of SEM investigations near the cracked surface [13,14].

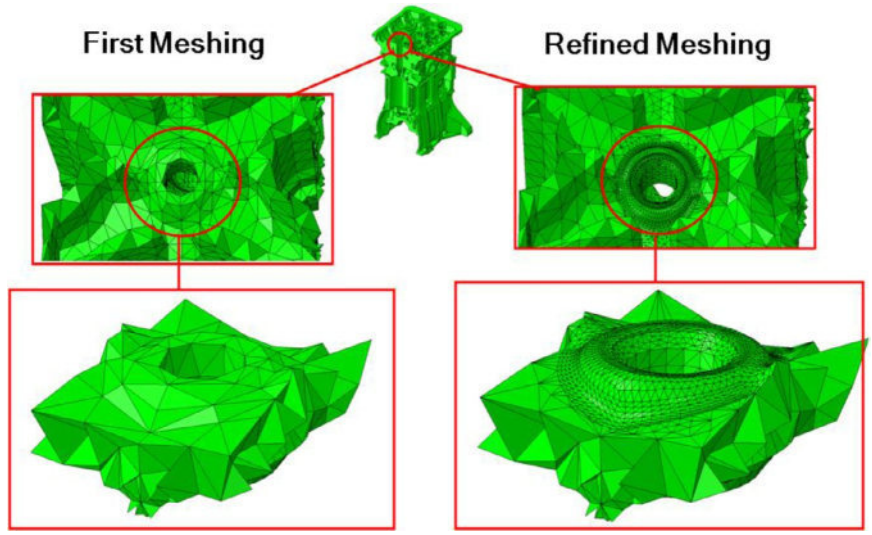

FIGURE 21.17

The finite element model with and without refined meshing [13,14].

To model the cylinder head and the engine block, nonlinear gasket elements and sliding contact definitions were used (Figure 21.17). The full model size was reduced to 1/2 that of the model, and linear material models [13,14] utilized to simplify the calculation procedure. To model the bolt force, an external displacement of 0.235 mm on the 1/3 top of the bolt length was applied to the hole, as shown in Figure 21.18. The resulting Von-misses stress around the hole is shown in Figure 21.18, which includes plastic deformations. The stress component in the *x*-direction (the crack growth direction) and the maximum principal stress are shown in Figure 21.19. As seen in the figure, by considering the bolt model, both stresses (x-component and maximum principal ones) increased.

3.3 REMARKABLE NOTES

Different tests were conducted to investigate root causes of the cracked cylinder head. Obtained results showed as follows:

- Cracks initiated from the interior wall of the hole on the cylinder head and propagated through the thickness.
- The chemical composition of the failed cylinder head basically corresponded to the specified range except for higher silicon content.
- Higher silicon content causes higher hardness, higher strength, and lower elongation of the material.
- Casting pores were seen on the fracture surface, where their volume fraction was in the range of the standard [20]; however, diameters were more than the allowable amount, to some extent. In addition, deformations on threads were also observed.

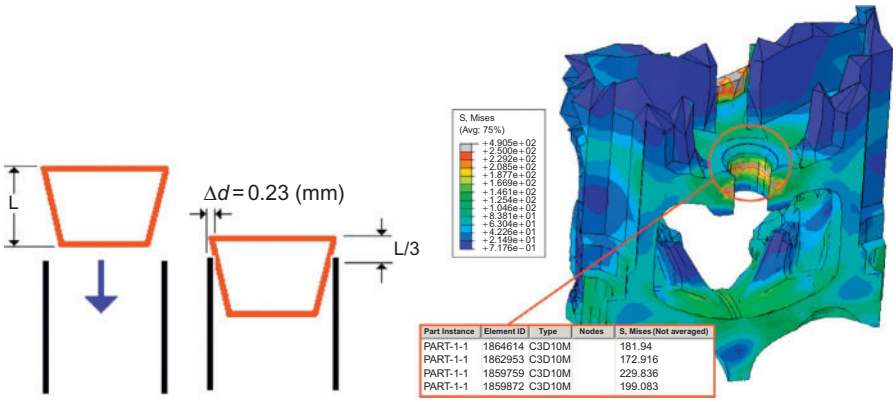

FIGURE 21.18

Dimensions of the bolt and the hole and Von-misses stresses around the hole [13,14].

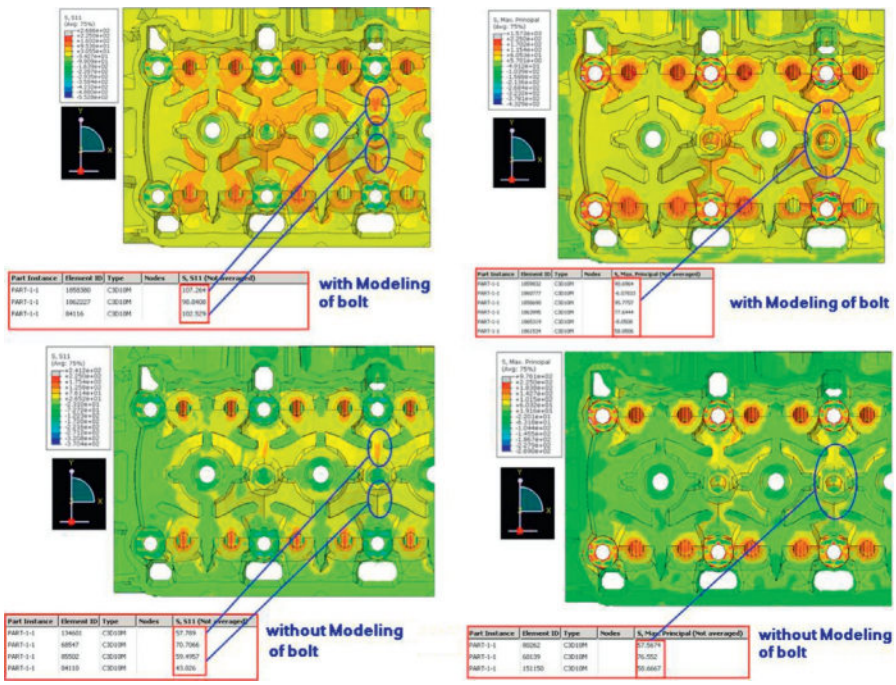

FIGURE 21.19

Stress distributions including stress component in *x*-direction and maximum principal stress around the hole [13,14].

However, these defects could not lead to a premature fracture of the cylinder head; the main reason for cracking was the high stress and the plastic strain due to the bolt assembly in the hole, which could be a cause of crack initiations. Subsequently, pores near the surface of threads as well as cyclic thermomechanical loadings on the cylinder head could be a cause of the crack growth. To prevent this failure mode in the cylinder head, the hole could be eliminated, the type of the bolt could be changed, or the fastening torque could be adjusted.

REFERENCES

[1] Azadi M. A thermo-mechanical fatigue life prediction model for aluminum alloy (A356.0) with thermal barrier coating [Ph.D. thesis]. Tehran, Iran: Sharif University of Technology; 2013.

[2] Azadi M, Roozban M, Mafi A. Failure analysis of an intake valve in a gasoline engine. J Engine Res 2012;26:3–9.

[3] Voorwald HJC, Coisse RC, Cioffi MOH. Fatigue strength of X45CrSi93 stainless steel applied as internal combustion engine valves. Procedia Eng 2011;10:1256–61.

[4] Azadi M. General temperature survey of cylinder block and head, Test Report, No. 410018R001, Irankhodro Powertrain Company (IPCO), Tehran, Iran; 2010.

[5] Ipohorski M, Luppo MI, Castillo-Guerra R, Ovejero-Garcia J. Failure analysis of a steam valve stem. Mater Characterization 2003;50:23–30.

[6] Kwon OG, Han MS. Failure analysis of the exhaust valve stem from a Waukesha P9390 GSI gas engine. Eng Fail Anal 2004;11:439–47.

[7] Yu ZW, Xu XL. Failure analysis and metallurgical investigation of diesel engine exhaust valves. Eng Fail Anal 2006;13:673–82.

[8] Standard test methods for Rockwell hardness of metallic materials, Standard No. ASTM-E18–08; 2008.

[9] ASM. Properties and selection: irons, steels, and high-performance alloys. ASM metals handbook, vol. 1; 1990.

[10] ASM. Metallography and microstructures. ASM metals handbook, vol. 9; 1990.

[11] Azadi M, Winter G, Farrahi GH, Eichlseder W. Design of cylinder head and block in internal combustion engines based on fatigue strength of materials. In: 8th Conference on Internal Combustion Engines and Oil, Iran; 2014. p. 37.

[12] Sachs NW. Practical plant failure analysis, a guide to understanding machinery deterioration and improving equipment reliability. New York: Taylor and Francis Group; 2007.

[13] Azadi M, Mafi A, Roozban M, Moghaddam F. Failure analysis of a crack gasoline engine cylinder head. J Fail Anal Prev 2012;12(3):286–94.

[14] Azadi M, Mafi A, Abbadzadeh Y, Moghaddam F. Investigation of damage causes in a cracked cylinder head and finite element simulation. In: Proceeding of 7th International Conference on Internal Combustion Engines, Iran; 2011. p. 57.

[15] Aluminum and aluminum alloys—castings—chemical composition and mechanical properties, Standard No. DIN-EN-1706; 1998.

[16] $AlSi_9Cu_3$ aluminum alloy permanent mold casting alloy material specification, Standard No. IK-150–11–1–0014; 2007.

[17] Test method for Brinell hardness test of metallic materials, Standard No. ASTM E10–06; 2006.
[18] ASM. Properties and selection: nonferrous alloys and special-purpose materials. ASM metals handbook, vol. 2; 1990.
[19] ASM. Failure analysis and prevention. ASM metals handbook, vol. 11; 1990.
[20] Porosity classification and requirements for casting parts, Standard No. IK-150–11–1–0010; 2006.
[21] Volume defects of castings made from non-ferrous metal, Standard No. IK-150–11–1–0011; 2006.

Index

Note: Page numbers followed by *f* indicate figures and *t* indicate tables.

C

D

E

F

G

H

I

K

L

M

N

O

P

R

S

T

U

V

W

X

Z